DEVELOPMENT OF EROSION - CORROSION WEAR RESISTANT COATINGS ON SUPERALLOYS

A THESIS

Submitted in partial fulfilment of the requirements for the award of the degree of

DOCTOR OF PHILOSOPHY

in

METALLURGICAL AND MATERIALS ENGINEERING

By

SURYANARAYAN BHOLANATH MISHRA

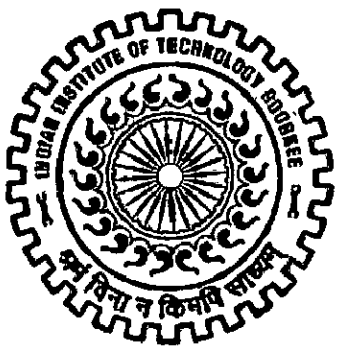

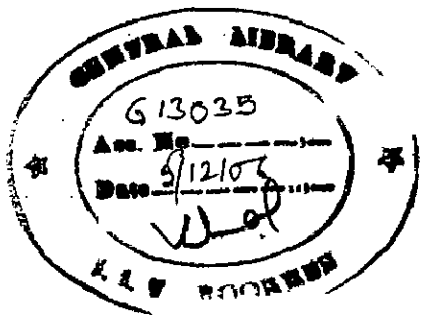

DEPARTMENT OF METALLURGICAL AND MATERIALS ENGINEERING
INDIAN INSTITUTE OF TECHNOLOGY ROORKEE
ROORKEE-247 667 (INDIA)

MARCH, 2006

6th Annual Convocation- 2006
Degree conferred on 11.11.2006

Supdt. (PGS&R)

INDIAN INSTITUTE OF TECHNOLOGY ROORKEE
ROORKEE

CANDIDATE'S DECLARATION

I hereby certify that the work which is being presented in the thesis, entitled **"DEVELOPMENT OF EROSION-CORROSION WEAR RESISTANT COATINGS ON SUPERALLOYS"** in partial fulfilment of the requirements for the award of the Degree of Doctor of Philosophy and submitted in the Department of Metallurgical and Materials Engineering of the Institute is an authentic record of my own work carried out during a period from July, 2002 to March, 2006 under the supervision of **Dr. Satya Prakash** and **Dr. Kamlesh Chandra**.

The matter presented in this thesis has not been submitted by me for the award of any other degree of this or any other University/Institute.

(SURYANARAYAN BHOLANATH MISHRA)

This is to certify that the above statement made by the candidate is correct to the best of our knowledge.

(Dr. KAMLESH CHANDRA)
Assistant Professor

(Dr. SATYA PRAKASH)
Professor

Department of Metallurgical and Materials Engineering
Indian Institute of Technology Roorkee
Roorkee – 247 667, India

Date: 16.03.2006

The Ph.D. Viva-Voice examination of **Suryanarayan Bholanath Mishra**, Research Scholar, has been held on 9 Sept 2006.

Signature of Supervisor(s)

Signature of External Examiner

ABSTRACT

Degradation of materials due to erosion either at room temperature or at elevated temperature is encountered in a large variety of engineering industries. Solid particle erosion is the loss of material that results from repeated impact of small solid particles. In industrial applications, solid particles are produced during the combustion of heavy oils, synthetic fuels, and pulverized coal, and causes erosion of materials. Boilers and other power plant equipments suffer severe erosion and erosion-corrosion problems resulting in substantial losses. Fly ash content of the Indian coal is very high and causes severe erosion and erosion-corrosion of the materials in the power plants, resulting in increased forced shut down and repair. This is one of the major reasons for shortage of power, which further increases the cost of power for industries, thus affecting the overall growth of the country. These facts emphasize the need to develop more erosion and erosion-corrosion resistant coatings to protect the materials (metals and alloys) used in energy generation systems.

Currently superalloys are being used to increase the service life of the boilers, especially in the superheater zones of the boilers and new generation ultra and supercritical boilers. Although the superalloys have adequate mechanical strength at elevated temperatures, they often lack resistance to erosion-corrosion environments. Protective coatings are primarily used to restrict the surface damage of the components in practice. Suitable coating techniques also allow for regeneration of parts that have been rendered unusable by erosion.

Among the various techniques used for deposition of coatings, plasma spraying is a most flexible and versatile thermal spray process with respect to the sprayed materials. Plasma spraying has been a successful and reliable cost-effective solution for many industrial problems. It allows the spraying of a wide range of high performance materials from superalloys and refractory intermetallic compounds to ceramics with continuously increasing commercial applications. It does not cause deterioration of the substrate alloys, and relatively thick coatings can be formed with high deposition rates.

Coatings of a wide variety of materials are often applied to improve resistance to erosion and corrosion. However, the mechanisms of coating damage depend on the coating material and its thickness, the properties of the interface, the substrate

material and the test conditions. Ni- based coatings are used in applications where wear resistance combined with high temperature corrosion resistance is required. Thus from application point of view, the Ni-based powders are selected as coating materials in the present investigation.

It has been reported in the literature that the diffusion may take place between the substrate and the spray material during the plasma spraying. Further it has been opined by some researchers that the diffusion of elements can have a major influence on coating performance. Taking into consideration the above facts for the effect of substrate on the plasma sprayed coatings, five different superalloys which are used for high temperature application have been selected for spraying three coatings. The analysis could further be beneficial to understand the effect of the substrate superalloys, if any, on the performance of the different coatings.

The plasma spray coatings were deposited at Anod Plasma Limited, Kanpur (India) on five superalloy substrates. These superalloys were procured from Mishra Dhatu Nigham Ltd., Hyderabad (India). Three types of coatings were formulated Ni-22Cr-10Al-1Y (NiCrAlY), Ni-20Cr and Ni_3Al. The NiCrAlY has also been used as a bond coat to provide rough surface for mechanical bonding before applying the final coating in all cases. The coatings were characterised by optical microscopy, microhardness testing, X-ray Diffractometry (XRD), scanning electron microscopy (SEM) and electron probe micro analyser (EPMA).

All the coatings were successfully obtained on the given Ni-, Fe- and Co- based superalloys. The plasma sprayed coatings were found to have some porosity. The microhardness of the coatings was found varying with the distance from the coating-substrate interface. Maximum value of microhardness was shown by Ni-20Cr coating and a minimum by Ni_3Al coating. NiCrAlY and Ni-20Cr coatings had shown lamellar structure with distinctive boundary along the cross-section, whereas Ni_3Al coating showed relatively massive structure. XRD analysis of the as-sprayed coatings indicated the formation of solid solutions, whereas EDAX analysis confirmed the presence of basic elements of the coating powders. The marginal diffusion of various elements from the substrate into the plasma sprayed coatings has been indicated by EPMA. The diffusion between the bond coat and top coat was relatively high. Quantitatively aluminium was found to be the most vulnerable element to the diffusion phenomenon.

Erosion tests were carried out using an 'Air Jet Erosion Test Rig' at Defence Metallurgical Research Laboratory, Hyderabad, India. Erosion studies were conducted on uncoated as well as plasma spray coated superalloy specimens at room temperature. The experiments were carried out at an impact velocity of 40 ms^{-1} and impingement angles of 30° and 90°. Silica sand particles of average size 180 μm (range of 150-220 μm) were used as erodent. The dry sliding wear behaviour of all the superalloys and coatings on one of these superalloy substrates namely Superfer 800H have been determined using pin-on-disc machine against a counterface of En-32 steel hardened to HRC 62 to 65, at room temperature.

Erosion-corrosion study of the plasma coatings and superalloys are also carried out in the coal-fired boiler of a thermal power plant. The samples were hanged in the low temperature primary super heater zone with the help of stainless steel wire and a rigid support of stainless steel rod through the soot blower dummy points at 36.7 m height from the base of the boiler. The average temperature observed was about 540°C with full load of 210 MW. The samples were exposed to this environment for 10 cycles each of 100 hours duration and followed by 1 hour cooling at ambient conditions (total 1000 hours exposure).

All the samples subjected to erosion and wear in the laboratory test rigs were analysed using Scanning Electron Microscope with EDAX attachment. Also Optical Profilometer was used to assess the surface roughness of eroded samples. Whereas the samples from actual boiler environment were subjected to measurement of scale thickness, X- Ray Diffractometry, Scanning Electron Microscopy with EDAX attachment (SEM/EDAX) and Electron Probe Micro Analyser (EPMA).

In room temperature erosion studies, on superalloys at 30° impact angle, no significant difference in the erosion rate was found, whereas at 90° impact angle, the Ni-based superalloys have shown relatively better erosion resistance as compared to Fe- and Co- based superalloys.

The sequence of superalloys based on the erosion resistance at 90° impact angle is:

Superni 718 > Superni 75 > Superni 600 > Superco 605 > Superfer 800H

Comparing the erosion resistance of NiCrAlY, Ni-20Cr and Ni_3Al coatings in the room temperature erosion condition at 30° impact angle, sequences observed for the different coated superalloys are as follows:

Ni_3Al > NiCrAlY > Ni-20Cr	for	Superni 75, Superfer 800H and Superni 718
NiCrAlY > Ni_3Al > Ni-20Cr	for	Superni 600 and Superco 605

Comparing the erosion resistance of NiCrAlY, Ni-20Cr and Ni_3Al coatings in the room temperature erosion condition at 90° impact angle, sequences observed for the different coated superalloys are as follows:

Ni_3Al > Ni-20Cr > NiCrAlY	for	Superni 75 and Superni 718
Ni_3Al > NiCrAlY > Ni-20Cr	for	Superni 600 , Superfer 800H and Superco 605

The sequence for the overall protective behaviour of coatings in room temperature erosion condition can be arranged as:

Ni_3Al > NiCrAlY > Ni-20Cr

Ni_3Al coating has shown better erosion resistance at 90° impact angle amongst the coated superalloys which may be attributed to its higher ductility. The volumetric erosion loss of the Ni_3Al coated superalloys is significantly lower than that for the NiCrAlY and Ni-20Cr coated superalloys under the room temperature erosion conditions.

The relatively lower erosion rates for all the uncoated superalloys as compared to their coated counterparts at both the impact angles were shown by steady state erosion rate graph. The higher volumetric erosion rate of the plasma sprayed coatings in general might be attributed partly to the presence of some porosity in the coatings. In case of the coated specimens, relatively higher erosion rates were observed in some early cycles of the study, followed by steady state conditions. The early higher weight loss might be attributed to the porosity and the surface roughness of the coatings. Further, the coatings showed good adherence to their respective substrates during the exposure.

Under the sliding wear study, Superni 600 superalloy has given highest specific wear rate, followed by Superni 75 amongst the uncoated superalloys. Whereas Superfer 800H has shown the lowest value of specific wear rate followed by Superco 605 superalloy. The Ni-20Cr coating is having the highest hardness amongst the coatings,

which might be one of the cause for its better wear resistance. Whereas the inferior wear resistance of Ni_3Al coating may be due to its lower hardness.

Superni 600 superalloy has shown the highest average coefficient of friction amongst the worn superalloys, whereas that of Superco 605 superalloy was found to be least. Further the difference in coefficient of friction for Superni 75 and Superfer 800H superalloy is marginal. Amongst the plasma sprayed coatings the highest coefficient of friction is revealed for Ni-20Cr coating whereas least average coefficient of friction was given by NiCrAlY coating.

All the superalloys exposed in the low temperature primary superheater zone of boiler at 540°C have shown weight loss thereby suggesting the contribution of erosion. The deposits on the surfaces of the exposed superalloys consisted of oxides of silicon and aluminium (fly ash constituents) along with some other oxides. From this it can be inferred that the superalloys have also been oxidised to some extent accompanied with erosion by fly ash impact. The embedment of ash particles in the top layers of exposed superalloys have been also confirmed by the EPMA analysis. The superalloys depending on their on their weight loss can be arranged as

Superni 600 > Superfer 800H > Superni 75 > Superni 718.

Comparing the erosion-corrosion loss of NiCrAlY and Ni-20Cr coated superalloys in boiler environment, it can be inferred that the difference in thickness loss with respect to substrate is negligible. In case of Ni_3Al coated superalloy the thickness loss is perceptible and is follows:

Superfer 800H > Superni 600 > Superni 718 > Superni 75

Further all the coated superalloys are partially oxidised upto the coating substrate interface. The substrate superalloys remain unaffected by the environment attack. Amongst the three coatings, Ni-20Cr coated superalloys have provided maximum resistance against the fly ash impact at 540°C. The slightly higher thickness loss has been shown by NiCrAlY coated superalloys. The Ni_3Al coated superalloys have shown similar thickness removal as obtained for uncoated superalloys. Although the thickness removal is low for the coated superalloys, the thickness of partially oxidised layer is significant. The EDAX and EPMA analysis have indicated the partial oxidation of the coated superalloys upto the coating thickness. From the EDAX and EPMA analyses of the coated samples, it is clear that the Ni exists at the centre of splats and remains unoxidised. Oxygen penetrates along the interconnected splat boundaries of the plasma sprayed coatings and pores, and oxidises mainly Al and Y present at the periphery of

splats alongwith the Cr. These oxides might be responsible for blocking/slowing down the transport of oxygen along the splat boundaries and pores. Thus in the boiler environment coating layers get partially oxidised, and acts as a perfect barrier against erosion-corrosion of superalloys. Further the partially oxidised coatings remain intact even after 1000 hours cyclic exposure, thus it can be presumed that it will enhance the life of boiler tube in the evaluated environment.

Fly ash deposited together with scale formed by slower oxidation rate at 540°C in the boiler environment might be promoting denser and more impact resistant top layers, resulting in lower metal loss.

The superalloys with the coatings may be used in the boiler environment as they will provide the requisite protection against erosion-corrosion. The coatings have not been very effective in improving the wear resistance under sliding condition. The erosion behaviour at room temperature of these alloys and coatings indicate that the coatings are having relatively higher erosion rates. But these coatings are adherent and will definitely be useful in protecting the substrate alloy against erosion and will act as a sacrificial material.

ACKNOWLEDGEMENTS

I have great privilege and pride to express my sincere thanks and immense gratitude to **Dr. Satya Prakash**, Professor, Department of Metallurgical and Materials Engineering (MMED), Indian Institute of Technology, Roorkee for his valuable and intellectual guidance throughout the tenure of this work. He has been a motivating and driving force where targets appeared to be arduous during the course of work. His timely help, constructive criticism, positive attitude and painstaking efforts, have made it possible to complete this thesis in the present form. I am highly grateful to **Dr. Kamlesh Chandra**, for his continuous encouragement and support as a co-supervisor.

I am highly indebted to Dr. V. K. Tiwari, Ex-Head, Dr. P. S. Mishra, Head, MMED for their co-operation in extending the necessary facilities and supports during the concluding phase of this work. I wish to record my deep sense of gratitude to Head, Institute Instrumentation Centre (IIC), Indian Institute of Technology Roorkee for extending necessary facilities during the course of experimental and analysis work.

I am highly thankful to Dr. B. Venkataraman, Group Head, Surface Engineering, Defence Metallurgical Research Laboratory (DMRL), Hyderabad, for his support and interaction in extending the erosion test facility. I am grateful to Dr. Ajay Gupta, Director IUC DAE, Indore, Dr. M. Chakraborty, Professor, Metallurgical and Materials Engineering Department, IIT, Kharagpur, Shri B. P. Shrama, Head, Material Science Division (MMD), BARC, Mumbai and Dr. G. B. Kale, Scientist Officer, Material Science Division (MMD), BARC, Mumbai, for extending their facilities to perform the analysis work. Special thanks are due to Mr. R. K. Tandon, Managing Director, Anod Plasma Spray Ltd., Kanpur for kindly providing plasma spray facility.

I owe my sincere thanks to Dr. D. M Phase and Mr. Vinay Ahire of IUC DAE, Indore and Mr. Dr. Rabindranath Maiti of CRF IIT Khargpur for performing SEM/EDAX analysis. Thanks are due to Dr. P. Sengupta of BARC, Mumbai for conducting EPMA analysis. I am highly grateful to Anod Plasma Spray Limited, Kanpur, India for providing the facility of the plasma spray coating. The support of Mr. J. K. N. Murthy, Scientist, Mr. Nageswar Rao, DMRL, Hyderabad for conducting erosion experiments

during this work is also gratefully acknowledged. I wish to thank the Mishra Dhatu Nigam Limited, Hyderabad, India for supplying the superalloys.

I would like to record my sense of gratitude for the library staff of IIT Roorkee, IIT Mumbai, IIT Kharagpur, IIT Madras, DMRL, Hyderabad and BARC Mumbai for their kind co-operation to carry out the literature survey. Thanks are also due to Mr. Sunil Sharma, Librarian of MMED for providing all the necessary help.

I wish to record my deep sense of gratitude to Sr. Exe. Er. Davinder Singh, Asstt. Exe. Er. J. S. Bhatia, Asstt. Exe. Er. Kulwant Saini, Shri K. C. Sharma, Shri V. S. Kushwaha and other staff of maintenance department, S. G. G. S. Super Thermal Power Plant, Ropar, Punjab, India for their kind support and help to carry out the experimentation work in the industrial environment.

I am highly obliged and wish to owe my sincere thanks to the technical and administrative staff, especially to Mr. R. K. Sharma, Mr. Rajinder S. Sharma, Mr. S. K. Seth, Mr. Vidya Prakash, Mr. Shamsher Singh, Mr. T. K. Sharma, Mr. S. M. Giri, Mr.. Shakti Gupta, Mr. Dhan Prakash, Mr. M. Pandey, Mr. B. D. Sharma, Mr. H. K. Ahuja, Mr. V. P. Verma, Mr. Naresh Sharma, Mr. Ashish of the MMED and Mr. Jasbir Singh, Mr. Jagpaal Singh and other staff of MIED, who helped me in all possible ways during the experimental work.

I would like to express my sincere thanks to Mr. Shiv Kumar, Mrs. Rekha Sharma, and Dr. T. K. Ghosh of IIC, IIT, Roorkee for carrying out XRD, SEM and EPMA work respectively. Thanks are also acknowledged to Mr. Puran Sharma for preparing high quality micrographs. Sincere thanks are acknowledged to Mr. Narendra Kumar for typesetting of thesis manuscript.

I wish to thank my friends and colleagues for their moral support and camaraderie help to keep things in perspective. Thanks are due to Dr. Gitanjali, Dr. Buta Singh Sidhu, Dr. Harpreet Singh, Mr. T. S. Sidhu, Mr. Anupam Singhal, Mr. M. R. Ramesh, Mr. Sanjay Panwar, Mr. N. Arivazhagan, Mr. M. K. Kushwaha, Mr. Lenin, Mr. Sandeep Bansal, Mr. S. Kulkarni and Mr. Ravinder Kumar. Special thanks to Mr. Girish Desale, Mr. Manish Rana, Mr. Amod Kulkarni, Mr. Amrish K. Panwar and Mr Pawan Kumar Sapra for their everlasting support.

I would like to express my reverence and great admiration for my parents, who have always been the guiding and encouraging force for me. I would like to humbly dedicate my thesis to my parents. A sense of forgiveness is recorded for my brother and for their moral support during the course of this work.

A sense of apology is due to my loving sons Aayush and Ankush, who probably missed many precious moments of fatherly love and care. My wife Sandhya deserves special thanks and grand appreciation for her persistent moral support and capability to rejuvenate me during the leaning phases of the work. I am falling short of words to express gratitude to her for the determination shown to bear extra household responsibilities during the tenure of this work.

Above all, I am highly indebted to almighty God who blessed me with spiritual support and fortitude at each and every stage of this work.

(SURYANARAYAN B. MISHRA)

PREFACE

The entire work carried out for this investigation has been presented into nine chapters.

Chapter-1 contains the introductory remarks about erosion and erosion-corrosion and sliding wear phenomenon and their impact on the various engineering equipments and components. The ways to counteract this problem are also briefly presented.

Chapter-2 begins with a critical review of the existing literature pertaining to the erosion studies conducted by various researchers relevant to the current work. The studies related to erosion-corrosion behaviour of plasma spray coatings have also been reviewed. It is followed by a comprehensive review of the sliding wear behavior of the superalloys and protective coatings. The various preventive measures have been summarised and the plasma spray process is discussed in detail. The problem has been formulated after critical analysis of the available literature towards the end of this chapter.

Chapter-3 presents the experimental techniques and procedures employed for applying the coatings and their characterization, the erosion wear and erosion-corrosion studies and analysis of their products. The details of the various equipments and instruments used for the present investigation are given.

Chapter-4 includes the findings and discussions of the investigation regarding the characterisation of as-sprayed coatings.

Chapter-5 contains the results of the erosion studies performed on uncoated and coated superalloys in an air jet erosion test rig. It also includes the critical discussion of results in view of the existing literature to suggest the plausible erosion mechanisms.

Chapter-6 contains the results and discussion pertaining to the sliding wear characteristics of the plasma sprayed coatings on Superfer 800H substrate and all the five superalloys.

Chapter-7 includes the findings regarding the behaviour of coated and uncoated superalloys for the erosion-corrosion in the coal-fired boilers of Thermal Power Plant, along with discussion of results.

In chapter-8 the important results of the present study have been discussed. It includes comprehensive discussions on the results obtained in laboratory and industrial environment with respect to the available literature. Further the comparative resistances of different coatings in similar environments have also been reported.

Chapter-9 presents the major conclusions of the study on the characterisations of plasma sprayed NiCrAlY, Ni-20Cr and Ni_3Al coatings, erosion and sliding wear behaviour for the uncoated and coated superalloys in the laboratory and the erosion-corrosion behaviour of the superalloys and coatings exposed to the boiler of coal fired thermal power plant.

CONTENTS

Page No.

Candidate's Declaration i

Abstract ii

Acknowledgements viii

Preface xi

List of Figures xiii

List of Tables xxxv

Research Papers Presented/Published xxxvi

Abbreviations xxxviii

CHAPTER 1 INTRODUCTION 1

CHAPTER 2 LITERATURE REVIEW 6

2.1 EROSION WEAR 6

2.1.1 Mechanisms of Erosion 9

2.1.1.1 Erosion Mechanisms of Ductile Materials 9

2.1.1.2 Erosion Mechanisms of Brittle Materials 15

2.1.1.3 Erosion Mechanisms of Coatings 16

2.1.1.4 Erosion Mechanisms at High Temperature 20

2.1.2 Factors Affecting Erosion 24

2.1.3 Types of Erosion Test Rig 26

2.1.4 Erosion Rate 26

2.2 EROSION IN ENERGY GENERATION AND COAL GASIFICATION SYSTEMS 27

2.3 BEHAVIOUR OF VARIOUS METALS AND ALLOYS IN VARIOUS EROSIVE CONDITIONS 29

2.3.1 Erosion of Superalloys 30

2.3.2 Energy Generation Systems 33

2.4 ADHESIVE OR SLIDING WEAR 37

2.5 MEANS OF COMBATING EROSION AND EROSION-CORROSION WEAR 42

2.5.1 Modification of Impingement Conditions 42

2.5.2 Materials Selection 42

2.5.3 Use of Protective Coatings 43

2.5.3.1 Processes Used For Applying Coatings 45

2.6 THERMAL SPRAYING 46

2.7 PLASMA SPRAYING 47

2.7.1 Plasma Spraying-The Process 48

2.7.1.1 Plasma Jets 48

2.7.1.2 Coating Formulation 49

2.7.1.3 Adhesion of the Plasma Sprayed Coatings 50

2.7.1.4 Plasma Spray Process Variables 54

2.7.2 Process Variants of Plasma Spraying 55

2.7.2.1 Atmospheric Plasma Spraying (APS) 55

2.7.2.2 Vacuum (VPS) or Low Pressure Plasma Spraying (LPPS) 55

2.7.2.3 Shrouded Plasma Spraying (SPS) 57

2.7.2.4 Controlled Atmosphere Plasma Spraying (CAPS) 57

2.8 ROLE OF COATINGS IN VARIOUS EROSIVE CONDITIONS 57

2.8.1 MCrAlY Coatings 61

2.8.2 Nickel-Chromium coatings 62

2.8.3 Nickel Aluminide Coatings 64

2.9 FORMULATION OF PROBLEM 65
2.9.1 Scope 65
2.9.2 Aim 67

CHAPTER 3 EXPERIMENTAL TECHNIQUES AND PROCEDURES 70

3.1 SELECTION OF SUBSTRATE MATERIALS 70

3.2 DEVELOPMENT OF COATINGS 70
3.2.1 Preparation of Substrate Materials 70
3.2.2 Alloy Powders for Coatings 70
3.2.3 Formulation of Coatings 72

3.3 CHARACTERISATION OF COATINGS 73
3.3.1 Measurement of Coating Thickness 73
3.3.2 Measurement of density and bond strength of the Coatings 73
3.3.3 Measurement of Porosity and oxides contents 73
3.3.4 Metallographic Studies 74
3.3.5 Measurement of Microhardness 74
3.3.6 X-Ray Diffraction (XRD) Analysis 74
3.3.7 Scanning Electron Microscopy (SEM) and Energy Dispersive X-Ray (EDAX) Analysis 75
3.3.8 Electron Probe Micro Analyser (EPMA) 75

3.4 ROOM TEMPERATURE EROSION TESTS 76
3.4.1 Experimental Setup 76
3.4.2 Erosion Studies in an Air Jet Erosion Test Rig 76
3.4.3 Analysis of eroded surfaces 77
3.4.3.1 Visual Observation 77
3.4.3.2 Erosion rate from weight loss data (g/g) 77

3.4.3.3 Erosion Rate in Terms of Volume Loss (cm^3/g) 80
3.4.3.4 *SEM/EDAX Analysis* 80
3.4.3.4.1 Surface Morphology 80
3.4.3.4.2 Cross-Sectional Morphology 80
3.4.3.5 Surface Roughness of the Eroded Zone 80

3.5 SLIDING WEAR STUDIES USING PIN-ON-DISC WEAR TEST RIG 80
3.5.1 Experimental Setup 80
3.5.2 Sliding Wear Studies 81
3.5.3 Analysis of Sliding Wear Study 83
3.5.3.1 Friction and Wear Rate 83
3.5.3.2 Examination of Worn Surfaces and Wear Debris 83

3.6 EROSION-CORROSION STUDIES IN ACTUAL INDUSTRIAL ENVIRONMENT 84
3.7 ANALYSIS OF EROSION-CORROSION PRODUCTS IN BOILER ENVIRONMENT 86
3.7.1 Visual Observation 86
3.7.2 Thermogravimetric Studies 86
3.7.3 Measurement of Scale Thickness 86
3.7.4 X-Ray Diffraction (XRD) Analysis 86
3.7.5 SEM/EDAX Analysis 87
3.7.5.1 Surface Morphology 87
3.7.5.2 Cross-Sectional Morphology 87
3.7.6 Electron Probe Micro Analyser (EPMA) 87

CHAPTER 4 CHARACTERISATION OF SUPERALLOYS AND PLASMA SPRAYED COATINGS 88

4.1 MICROSTRUCTURES OF THE SUBSTRATE SUPERALLOYS 88

4.2 PLASMA SPRAYED COATINGS 88

4.2.1 Coating Powders 88

4.2.2 Visual Examination of the Coatings 89

4.2.3 Measurements of Coating Thicknesses 89

4.2.4 Porosity and Oxide Contents, Density and Bond Strength of Coatings 96

4.2.5 Evaluation of Microhardness 96

4.2.6 Metallographic Studies for the Coatings 97

4.2.6.1 Surface Structure 97

4.2.6.1.1 NiCrAlY Coating 97

4.2.6.1.2 Ni-20Cr Coating 97

4.2.6.1.3 Ni_3Al Coating 97

4.2.6.2 Cross-Sectional Structures 97

4.2.7 XRD Analysis 106

4.2.8 SEM / EDAX Analysis 106

4.2.9 EPMA Analysis 106

4.3 DISCUSSION 122

CHAPTER 5 EROSION STUDIES IN AN AIR JET EROSION TEST RIG 125

5.1 RESULTS 125

5.1.1 Uncoated Superalloys 125

5.1.1.1 Visual Examination 125

5.1.1.2 Erosion Rate 125

5.1.1.3 SEM/EDAX Analysis 126

5.1.1.3.1 Surface Morphology 126
5.1.1.3.2 Cross-sectional Analysis 135
5.1.1.4 Surface Roughness 135
5.1.2 NiCrAlY Coating 135
5.1.2.1 Visual Examination 135
5.1.2.2 Erosion Rate 135
5.1.2.3 SEM/EDAX Analysis 136
5.1.2.3.1 Surface Morphology 136
5.1.2.3.2 Cross-sectional Analysis 148
5.1.2.4 Surface Roughness 148
5.1.3 Ni-20Cr Coating 148
5.1.3.1 Visual Examination 148
5.1.3.2 Erosion Rate 148
5.1.3.3 SEM/EDAX Analysis 149
5.1.3.3 .1 Surface Morphology 149
5.1.3.3 .2 Cross-sectional Analysis 161
5.1.3.4 Surface Roughness 161
5.1.4 Ni_3Al Coating 161
5.1.4.1 Visual Examination 161
5.1.4.2 Erosion Rate 161
5.1.4.3 · SEM/EDAX Analysis 162
5.1.4.3.1 Surface Morphology 162
5.1.4.3.2 Cross-sectional Analysis 174
5.1.4.4 Surface Roughness 174
5.2 SUMMARY OF RESULTS 174
5.3 DISCUSSION 178
5.3.1 Uncoated Superalloys 179
5.3.2 NiCrAlY Coating 185
5.3.3 Ni-20Cr Coating 188
5.3.4 Ni_3Al Coating 189

5.4 EFFECT OF HARDNESS AND POROSITY ON THE EROSION BEHAVIOUR OF THE COATINGS 190

CHAPTER 6 SLIDING WEAR STUDIES USING PIN-ON-DISC WEAR TEST RIG 195

6.1 RESULTS 195

6.1.1 Frictional Behaviour 195

6.1.2 Wear 196

6.1.3 SEM Analysis 196

6.1.3.1 Morphology of worn samples 196

6.1.3.2 SEM of wear debris 202

6.1.4 XRD Analysis 202

6.2 SUMMARY OF RESULTS 202

6.3 DISCUSSION 203

CHAPTER 7 EROSION-CORROSION STUDIES IN INDUSTRIAL ENVIRONMENT 211

7.1 RESULTS 211

7.1.1 Uncoated Superalloys 211

7.1.1.1 Visual Examination 211

7.1.1.2 Thermogravimetric Data and Thickness Monitoring 211

7.1.1.3 X-ray Diffraction Analysis 212

7.1.1.4 SEM/EDAX Analysis 212

7.1.1.4.1 Surface Morphology 212

7.1.1.4.2 Cross-Sectional Analysis 220

7.1.1.5 EPMA Analysis 220

7.1.2 **Ni-Cr-Al-Y Coating** 220

7.1.2.1 Visual Examination 220

7.1.2.2 Thermogravimetric Data and Thickness Monitoring 220

7.1.2.3 X-ray Diffraction Analysis 221

7.1.2.4 SEM/EDAX Analysis 221

7.1.2.4.1 Surface Morphology 221

7.1.2.4.2 Cross-Sectional Analysis 221

7.1.2.5 EPMA Analysis 236

7.1.3 **Ni-20Cr Coating** 236

7.1.3.1 Visual Examination 236

7.1.3.2 Thermogravimetric Data and Thickness Monitoring 236

7.1.3.3 X-ray Diffraction Analysis 237

7.1.3.4 SEM/EDAX Analysis 237

7.1.3.4.1 Surface Morphology 237

7.1.3.4.2 Cross-Sectional Analysis 237

7.1.3.5 EPMA Análisis 250

7.1.4 **Ni_3Al Coating** 250

7.1.4.1 Visual Examination 250

7.1.4.2 Thermogravimetric Data and Thickness Monitoring 250

7.1.4.3 X-ray Diffraction Analysis 251

7.1.4.4 SEM/EDAX Analysis 251

7.1.4.4.1 Surface Morphology 251

7.1.4.4.2 Cross-Sectional Analysis 251

7.1.4.5 EPMA Analysis 264

7.2 **SUMMARY OF RESULTS** 264

7.3 DISCUSSION 267
7.3.1 Uncoated Superalloys 267
7.3.2 Ni-Cr-Al-Y coating 272
7.3.3 Ni-20Cr Coating 273
7.3.4 Ni_3Al Coating 276

CHAPTER 8 COMPARATIVE DISCUSSION 280
8.1 Room Temperature Erosion Studies 280
8.2 Sliding Wear Sudies 281
8.3 Erosion-Corrosion in Low Temperature Primary Superheater of coal-fired Boiler at 540°C for 1000 hours 285

CHAPTER 9 CONCLUSIONS 289

SUGGESTIONS FOR FUTURE WORK 293

APPENDIX 294
Table A-1 294
Table A-2 303
Table A-3 307

REFERENCES 315

LIST OF FIGURES

Figure No.	Particulars	Page No.
Fig. 2.1	A schematic view of solid particle erosion of material (Buckley, 1981).	8
Fig. 2.2	Schematic views of the sections through impact sites formed by hard particles on a ductile metal. The impact direction is from left to right. (a) Ploughing mechanism by spherical shape solid particle; (b) Cutting mechanism by an angular particle, rotating backwards during impact (Winter and Hutchings, 1974).	11
Fig. 2.3	Schematic view of (a) type I cutting by an angular particle, rotating forwards during impact: (b) type II cutting by an angular particle, rotating backwards during impact (Hutchings, 1979).	11
Fig. 2.4	Schematic diagram illustrating the types of cracking events that occur during loading by single particles (Zambelli and Levy, 1981).	18
Fig. 2.5	Simplified schematic drawing of crack formation from a single particle impact (Wensink and Elwenspoek, 2002).	18
Fig. 2.6	Schematic diagram showing the types of degradation that can occur under conditions of combined oxidation-erosion (Barkalow and Pettit, 1979).	21
Fig. 2.7	Classification of erosion-corrosion (Kang et al, 1987).	21
Fig. 2.8	Classifications of erosion-corrosion (Rishel et al, 1990).	22
Fig. 2.9	Summary of erosion regimes observed at high temperatures (Stephenson, 1989 and Stephenson and Nicholls, 1993).	25

Fig. 2.10	Weight loss against temperature for IN 800 H and IN 800 H preoxidized in H_2-10% H_2O after exposure for 24 and 72 h in the UMIST erosion-corrosion apparatus (Stack et al, 1992).	38
Fig. 2.11	Model illustrating the oxide formation during oxidation and erosion–corrosion at 550 °C (Norling and Olefjord, 2003).	38
Fig. 2.12	Schematic microstructure of thermal spray coating consisting of splats, unmelted particles, pores and cracks (Kucuk et al, 2001).	51
Fig. 2.13	The plasma spraying process (Batchelor et al, 2003)	52
Fig. 2.14	Temperature distribution and geometry of plasma jet (Knotek, 2001).	53
Fig. 2.15	The structure of plasma sprayed film (Batchelor et al, 2003)	53
Fig. 2.16	Plasma spray process variables (Bhusari, 2001).	56
Fig. 3.1	A schematic view of an air jet erosion test rig.	78
Fig. 3.2	Scanning electron micrograph of the silica sand particles.	79
Fig. 3.3	A photograph of the Pin-on-disc wear test rig and its controller.	82
Fig. 4.1	Optical micrographs of the substrate superalloys (a) Superni 75 (b) Superni 600 (c) Superfer 800H (d) Superco 605 (e) Superni 718	90
Fig. 4.2	Scanning electron micrographs showing morphology of powders used for plasma coatings (a) Ni-22Cr-10Al-1Y powder (b) Ni-20Cr powder (c) Ni_3Al powder	91
Fig. 4.3	X-ray diffraction patterns of the coating powders (a) Ni-22Cr-10Al-1Y powder (b) Ni-20Cr powder (c) Ni_3Al powder.	92
Fig. 4.4	Surface macrographs of as-sprayed plasma coated specimens (a) NiCrAlY coating (b) Ni-20Cr coating (c) Ni_3Al coating.	93

Fig. 4.5	BSEI scanning electron micrograph showing cross-sectional morphology of NiCrAlY plasma sprayed coatings on superalloy substrates (a) NiCrAlY coating on Superfer 800H (b) NiCrAlY coating on Superco 605.	94
Fig. 4.6	BSEI scanning electron micrographs showing cross-sectional morphology of plasma sprayed Ni-20Cr coatings with bond coat of NiCrAlY coating on superalloy substrates (a) Ni-20Cr coating on Superfer 800H (b) Ni-20Cr coating on Superco 605.	94
Fig. 4.7	BSEI scanning electron micrographs showing cross-sectional morphology of plasma sprayed Ni_3Al coatings with bond coat of NiCrAlY coating on superalloy substrates (a) Ni_3Al coating on Superfer 800H (b) Ni_3Al coating on Superco 605.	95
Fig. 4.8	Microhardness profiles of plasma sprayed NiCrAlY coating for different substrate superalloys along the cross-section.	98
Fig. 4.9	Microhardness profiles of plasma sprayed Ni-20Cr coating with NiCrAlY bond coat for different substrate superalloys along the cross-section.	98
Fig. 4.10	Microhardness profiles of plasma sprayed Ni_3Al coating with bond coat of NiCrAlY for different substrate superalloys along the cross-section.	99
Fig. 4.11	Optical micrographs showing surface morphology of plasma sprayed NiCrAlY coating on substrate superalloys (a) Superni 75 (b) Superni 600 (c) Superfer 800H (d) Superco 605 (e) Superni 718.	100

Fig. 4.12	Optical micrographs showing surface morphology of plasma sprayed Ni-20Cr coating on substrate superalloys (a) Superni 75 (b) Superni 600 (c) Superfer 800H (d) Superco 605 (e) Superni 718	101
Fig. 4.13	Optical micrographs showing surface morphology of plasma sprayed Ni_3Al coating on substrate superalloys (a) Superni 75 (b) Superni 600 (c) Superfer 800H (d) Superco 605 (e) Superni 718	102
Fig. 4.14	Optical micrographs along the cross-section of plasma sprayed NiCrAlY coating on different substrate superalloys. (a) Superni 75 (b) Superni 600 (c) Superfer 800H (d) Superco 605 (e) Superni 718	103
Fig. 4.15	Optical micrographs along the cross-section of plasma sprayed Ni-20Cr coating with bond coat of NiCrAlY on different substrate superalloys. (a) Superni 75 (b) Superni 600 (c) Superfer 800H (d) Superco 605 (e) Superni 718	104
Fig. 4.16	Optical micrographs along the cross-section of plasma sprayed Ni_3Al coating with bond coat of NiCrAlY coat on different substrate superalloys. (a) Superni 75 (b) Superni 600 (c) Superfer 800H (d) Superco 605 (e) Superni 718	105
Fig. 4.17	X-ray diffraction patterns for the plasma sprayed NiCrAlY coating on different superalloy substrates.	108
Fig. 4.18	X-ray diffraction patterns for the plasma sprayed Ni-20Cr coating on different superalloy substrates.	109
Fig. 4.19	X-ray diffraction patterns for the plasma sprayed Ni_3Al coating with bond coat of NiCrAlY on different superalloy substrates.	110
Fig. 4.20	SEM/EDAX analysis of the plasma sprayed coatings on Superni 75 superalloy substrate showing elemental composition (Wt.%) at selected points (a) NiCrAlY coating (b) Ni-20Cr coating (c) Ni_3Al coating	111

Fig. 4.21	BSEI and elemental X-ray mappings of the cross-section of plasma sprayed NiCrAlY coating on Superni 75 superalloy.	112
Fig. 4.22	BSEI and elemental X-ray mappings of the cross-section of plasma sprayed NiCrAlY coating on Superni 600 superalloy.	113
Fig. 4.23	BSEI and elemental X-ray mappings of the cross-section of plasma sprayed NiCrAlY coating on Superfer 800H superalloy.	114
Fig. 4.24	BSEI and elemental X-ray mappings of the cross-section of plasma sprayed NiCrAlY coating on Superco 605 superalloy.	115
Fig. 4.25	BSEI and elemental X-ray mapping of the cross-section of plasma sprayed Ni-20Cr coating with bond coat of NiCrAlY on Superni 600 superalloy.	116
Fig. 4.26	BSEI and elemental X-ray mappings of the cross-section of plasma sprayed Ni-20Cr coating with bond coat of NiCrAlY on Superco 605 superalloy..	117
Fig. 4.27	BSEI and elemental X-ray mappings of the cross-section of plasma sprayed Ni-20Cr coating with bond coat of NiCrAlY on Superni 718 superalloy.	118
Fig. 4.28	BSEI and elemental X-ray mappings of the cross-section of plasma sprayed Ni_3Al coating with bond coat of NiCrAlY on Superni 600 superalloy.	119
Fig. 4.29	BSEI and elemental X-ray mappings of the cross-section of plasma sprayed Ni_3Al coating with bond coat of NiCrAlY on Superco 605 superalloy.	120
Fig. 4.30	BSEI and elemental X-ray mappings of the cross-section of plasma sprayed Ni_3Al coating with bond coat of NiCrAlY on Superni 718 superalloy.	121
Fig. 5.1	Macrographs of uncoated superalloys eroded at a velocity of 40 ms^{-1} and impact angles of 30° and 90°. (a) and (a1) Superni 75; (b) and (b1) Superni 600; (c) and (c1) Superfer 800H; (d) and (d1) Superco 605 (e) and (e1) Superni 718.	127

Fig. 5.2	Erosion rate (g/g) against cumulative mass of erodent for uncoated superalloys at a velocity of 40 ms^{-1} and 30° impact angle.	128
Fig. 5.3	Erosion rate (g/g) against cumulative mass of erodent for uncoated superalloys at a velocity of 40 ms^{-1} and 90° impact angle.	128
Fig. 5.4	A histogram illustrating the steady-state erosion rate of superalloys subjected to erosion at a velocity of 40 ms^{-1} and impact angle of 30° and 90° using silica sand of average size 180 μm as erodent.	129
Fig. 5.5	Scanning electron micrographs of eroded superalloys subjected to erosion at a velocity of 40 ms^{-1} and impact angle of 30° and 90°. (a) and (a1) Superni 75; (b) and (b1) Superni 600; (c) and (c1) Superfer 800H.	130
Fig. 5.6	Scanning electron micrographs of eroded superalloys subjected to erosion at a velocity of 40 ms^{-1} at impact angle of 30° and 90°. (a) and (b) Superco 605 at impact angle of 30°; (a1) Superco 605 at impact angle of 90°; (c) and (c1) Superni 718 at impact angle of 30° and 90° respectively.	131
Fig. 5.7	Scanning electron micrographs with compositions of the eroded superalloys. (a) Superni 75 at 30° impact angle (e) Superfer 800H at 90° impact angle. (b), (c), (d), (f), (g) and (h) respectively are the compositions at positions 1, 2, 3, 4, 5 and 6 of the surface micrographs (a) and (e).	132
Fig. 5.8	Scanning electron micrographs with compositions of the eroded Superco 605 superalloy. (a) 30° impact angle and (e) 90° impact angle. (b), (c), (d), (f), (g) and (h) respectively are the compositions at positions 1, 2, 3, 4, 5 and 6 of the surface micrographs (a) and (e).	133

Fig. 5.9	Scanning electron micrographs with compositions of the eroded Superni 718 superalloy. (a) 30° impact angle and (e) 90° impact angle. (b), (c), (d), (f), (g) and (h) respectively are the compositions at positions 1, 2, 3, 4, 5 and 6 of the surface micrographs (a) and (e).	134
Fig. 5.10	Scanning electron micrographs across the cross-section at different positions from the eroded area of Superni 600 superalloy eroded at 90° impact angle.	137
Fig. 5.11	3D optical profile of the eroded superalloys. (a) and (b) Superni 75, (c) and (d) Superni 600, (e) and (f) Superfer 800H, respectively at 30° and 90° impact angle. Dimension of scanned area is 591 μm × 449 μm.	138
Fig. 5.12	3D optical profile of the eroded superalloy (a) and (b) Superco 605, (c) and (d) Superni 718, respectively at 30° and 90° impact angle. Dimension of scanned area is 591 μm × 449 μm.	139
Fig. 5.13	Macrographs of plasma sprayed NiCrAlY coating on superalloys substrates eroded at a velocity of 40 ms^{-1} and impact angle of 30° and 90°. (a) and (a1) Superni 75; (b) and (b1) Superni 600; (c) and (c1) Superfer 800H; (d) and (d1) Superco 605; (e) and (e1) Superni 718.	140
Fig. 5.14	Erosion rate (g/g) against cumulative mass of erodent for uncoated and plasma sprayed NiCrAlY coated superalloys at a velocity of 40 ms^{-1} and 30° impact angle.	141
Fig. 5.15	Erosion rate (g/g) against cumulative mass of erodent for uncoated and plasma sprayed NiCrAlY coated superalloys at a velocity of 40 ms^{-1} and 90° impact angle.	142
Fig. 5.16	A histogram illustrating the steady-state erosion rate of plasma sprayed NiCrAlY coating on different superalloy substrates subjected to erosion at a velocity of 40 ms^{-1} and impact angle of 30° and 90° using silica sand particle of average size 180 μm as erodent.	143

Fig. 5.17	Scanning electron micrographs of eroded plasma sprayed NiCrAlY coating on different superalloys substrates subjected to erosion at a velocity of 40 ms^{-1} and impact angle of 30° and 90°. (a) and (a1) Superni 75; (b) and (b1) Superni 600; (c) and (c1) Superfer 800H.	144
Fig. 5.18	Scanning electron micrographs of eroded plasma sprayed NiCrAlY coating on different superalloys substrates subjected to erosion at a velocity of 40 ms^{-1} and impact angle of 30° and 90°. (a) and (a1) Superco 605; (b) and (b1) Superni 718.	145
Fig. 5.19	Scanning electron micrographs with compositions of the eroded NiCrAlY coating superalloy substrates at 30° impact angle. (a) Superfer 800H and (e) Superco 605. (b), (c), (d), (f), (g) and (h) respectively are the compositions at positions 1, 2, 3, 4, 5 and 6 of the surface micrographs (a) and (e).	146
Fig. 5.20	Scanning electron micrographs with compositions of the eroded NiCrAlY coating on Superni 718 superalloy at 90° impact angle. (a) surface micrograph; (b), (c) and (d) are the compositions at positions 1, 2 and 3 respectively of the surface micrograph (a).	147
Fig. 5.21	Scanning electron micrographs across the cross-section at different positions from the eroded region showing damage in NiCrAlY coating on Superni 600 superalloy eroded at 30° and 90° impact angle. (a), (b) and (c) at 30° impact angle (a1) and (b1) at 90° impact angle.	150
Fig. 5.22	3D optical profile of the eroded NiCrAlY coated superalloys (a) & (b) Superni 75; (c) & (d) Superni 600; (e) & (f) Superfer 800H; respectively at 30° and 90° impact angle. Dimension of scanned area is 591 μm × 449 μm.	151

Fig. 5.23	3D optical profile of the eroded NiCrAlY coated superalloys (a) & (b) Superco 605; (c) & (d) Superni 718 respectively at 30° and 90° impact angle. Dimension of scanned area is 591 μm × 449 μm.	152
Fig. 5.24	Macrographs of plasma sprayed Ni-20Cr coated superalloys eroded at a velocity of 40 ms^{-1} and impact angles of 30° and 90° respectively. (a) and (a1) Superni 75, (b) and (b1) Superni 600, (c) and (c1) Superfer 800H, (d) and (d1) Superco 605, (e) and (e1) Superni 718.	153
Fig. 5.25	Erosion rate (g/g) against cumulative mass of erodent for uncoated and plasma sprayed Ni-20Cr coated superalloys at a velocity of 40 ms^{-1} and 30° impact angle.	154
Fig. 5.26	Erosion rate (g/g) against cumulative mass of erodent for uncoated and plasma sprayed Ni-20Cr coated superalloys at a velocity of 40 ms^{-1} and 90° impact angle.	155
Fig. 5.27	A histogram illustrating the steady-state erosion rate of plasma sprayed Ni-20Cr coating on different superalloys substrates subjected to erosion at a velocity of 40 ms^{-1} and impact angle of 30° and 90° using silica sand of particle average size 180 μm as erodent.	156
Fig. 5.28	Scanning electron micrographs of plasma spray Ni-20Cr coated superalloys subjected to erosion at a velocity of 40 ms^{-1} at impact angle of 30°. (a) and (a1) Superni 75 (b) and (b1) Superni 600. (c) and (c1) Superfer 800H.	157
Fig. 5.29	Scanning electron micrographs of plasma sprayed Ni-20Cr coating on different superalloys substrates subjected to erosion at a velocity of 40 ms^{-1} at impact angle of 30° and 90°. (a) and (a1) Superco 605; (b) and (b1) Superni 718.	158

Fig. 5.30	Scanning electron micrographs with compositions of the Ni-20Cr coating on superalloy substrates eroded at 90° impact angle. (a) Superfer 800H and (e) Superco 605. (b), (c), (d), (f), (g) and (h) respectively are the compositions at positions 1, 2, 3, 4, 5 and 6 of the surface micrographs (a) and (e).	159
Fig. 5.31	Scanning electron micrographs with compositions of the eroded Ni-20Cr coating on Superni 718 superalloy substrate. (a) 30° impact angle and (d) 90° impact angle. (b), (c), (e) (f) and (g) respectively are the compositions at positions 1, 2, 3, 4 and 5 of the surface micrographs (a) and (d).	160
Fig. 5.32	Scanning electron micrographs across the cross-section at different positions from the eroded area of Ni-20Cr coating on Superni 600 superalloy eroded at 30° and 90° impact angle. (a), (b) and (c) at 30° impact angle; (a1) and (b1) at 90° impact angle.	163
Fig. 5.33	3D optical profile of the eroded Ni-20Cr coated superalloys (a) & (b) Superni 75, (c) & (d) Superni 600, (e) & (f) Superfer 800H, respectively at 30° and 90° impact angle. Dimension of scanned area is 591 μm × 449 μm.	164
Fig. 5.34	3D optical profile of the eroded Ni-20Cr coated superalloys (a) & (b) Superco 605, (c) & (d) Superni 718, respectively at 30° and 90° impact angle. Dimension of scanned area is 591 μm × 449 μm.	165
Fig. 5.35	Macrographs of plasma sprayed Ni_3Al coated superalloys eroded at a velocity of 40 ms^{-1} and impact angle of 30°. (a) and (a1) Superni 75; (b) and (b1) Superni 600; (c) and (c1) Superfer 800H; (d) and (d1) Superco 605; (e) and (e1) Superni 718.	166

Fig. 5.36	Erosion rate (g/g) against cumulative mass of erodent for uncoated and plasma sprayed Ni_3Al coated superalloys at a velocity of 40 ms^{-1} and 30° impact angle.	167
Fig. 5.37	Erosion rate (g/g) against cumulative mass of erodent for uncoated and plasma sprayed Ni_3Al coated superalloys eroded at a velocity of 40 ms^{-1} and 90° impact angle.	168
Fig. 5.38	A histogram illustrating the steady-state erosion rate of plasma sprayed Ni_3Al coating on different superalloys substrates subjected to erosion at a velocity of 40 ms^{-1} and impact angle of 30° and 90° using silica sand particles of average size 180 μm as erodent.	169
Fig. 5.39	Scanning electron micrographs of plasma spray Ni_3Al coated superalloys subjected to erosion at a velocity of 40 ms^{-1} at impact angle of 30° and 90°. (a) and (a1) Superni 75; (b) and (b1) Superni 600; (c) Superni 600 of 30° impact angle at higher magnification.	170
Fig. 5.40	Scanning electron micrographs of plasma spray Ni_3Al coated superalloys subjected to erosion at a velocity of 40 ms^{-1} at impact angle of 30° and 90°. (a) and (a1) Superfer 800H; (b) and (b1) Superco 605; (c) and (c1) Superni 718.	171
Fig. 5.41	Scanning electron micrographs with compositions of the Ni_3Al coating on Superco 605 superalloy substrate eroded at 90° impact angle. (a) Superco 605. (b), (c) and (d) respectively are the compositions at positions 1, 2 and 3 of the surface micrographs (a).	172
Fig. 5.42	Scanning electron micrographs with compositions of the eroded Ni_3Al coating on Superni 718 superalloy substrate. (a) 30° impact angle and (e) 90° impact angle. (b), (c), (d), (f), (g) and (h) respectively are the compositions at positions 1, 2, 3, 4, 5 and 6 of the surface micrographs (a) and (e).	173

Fig. 5.43	Scanning electron micrographs across the cross-section at different positions from the eroded region of Ni_3Al coating on Superni 600 superalloy eroded at 30° and 90° impact angle. (a) 30° impact angle (b) 90° impact angle.	180
Fig. 5.44	3D optical profile of the eroded Ni_3Al coated superalloys (a) & (b) Superni 75; (c) & (d) Superni 600; (e) & (f) Superfer 800H; respectively at 30° and 90° impact angles. Dimension of scanned area is 591 μm × 449 μm.	181
Fig. 5.45	3D optical profile of the eroded Ni_3Al coated superalloys (a) & (b) Superco 605, (c) & (d) Superni 718, respectively at 30° and 90° impact angle. Dimension of scanned area is 591 μm × 449 μm.	182
Fig. 5.46	A schematic diagram showing the erosion scar produced, in general, on all the materials tested at 90° and 30° impact angle.	183
Fig. 5.47	A schematic diagram showing probable erosion mechanism of superalloys when impacted by silica sand particles at a velocity of 40 ms^{-1} and impact angle of 30°	186
Fig. 5.48	A schematic diagram showing probable erosion mechanism of superalloys when impacted by silica sand particles at a velocity of 40 ms^{-1} and impact angle of 90°	187
Fig. 5.49	A schematic diagram showing probable erosion mechanism of plasma spray coated superalloy when impacted by silica sand particles at a velocity of 40 ms^{-1} and impact angle of 30°	192
Fig. 5.50	A schematic diagram showing probable erosion mechanism of plasma spray coated superalloys when impacted by silica sand particles at a velocity of 40 ms^{-1} and impact angle of 90°	193

Fig. 5.51	Variation of steady state erosion rate (volumetric loss, cm^3/g) against increasing microhardness for all the plasma sprayed coatings eroded at a Velocity 40 ms^{-1} and impact angle of 30° using silica sand particles of average size180 μm as erodent.	194
Fig. 5.52	Variation of steady state erosion rate (volumetric loss, cm^3/g) against increasing microhardness for all the plasma sprayed coatings eroded at a Velocity 40 ms^{-1} and impact angle of 90° using silica sand particles of average size180 μm as erodent.	194
Fig. 6.1	Coefficient of friction versus sliding time curves of superalloys at a normal load of 9.8 N and sliding velocity of 1 ms^{-1}.	197
Fig. 6.2	Coefficient of friction for plasma sprayed coatings on Superfer 800H superalloy substrate versus sliding time curves at a normal load of 9.8 N and sliding velocity of 1 ms^{-1}.	197
Fig. 6.3	Variation of cumulative wear volume of superalloys with sliding distance at a normal load of 9.8 N and sliding velocity of 1 ms^{-1}.	198
Fig. 6.4	Variation of cumulative wear volume of plasma sprayed coatings on Superfer 800H superalloy substrate with sliding distance at a normal load of 9.8 N and sliding velocity of 1 ms^{-1}.	198
Fig. 6.5	Variation of specific wear rate of superalloys with sliding distance at a normal load of 9.8 N and sliding velocity of 1 ms^{-1}.	199
Fig. 6.6	Variation of specific wear rate of plasma sprayed coatings on Superfer 800H superalloy substrate with sliding distance at a normal load of 9.8 N and sliding velocity of 1 ms^{-1}.	199

Fig. 6.7	Scanning electron micrographs of worn surfaces of superalloys subjected to sliding distance of 3000 m at an average sliding speed of 1 ms^{-1} on a pin-on-disc wear test rig. (a) Superni 75 (b) Superni 600 (c) Superfer 800H (d) Superco 605 (e) Superni 718.	200
Fig. 6.8	Scanning electron micrographs of worn surfaces of plasma sprayed coatings on Superfer 800H superalloy substrate subjected to sliding distance of 1200 m at an average sliding speed of 1 ms^{-1} on a pin-on-disc wear test rig. (a) NiCrAlY coating (b) Ni-20Cr coating (c) Ni_3Al coating.	201
Fig. 6.9	Scanning electron micrographs of wear debris of superalloys subjected to sliding distance of 3000 m at an average sliding speed of 1 ms^{-1} on a pin-on-disc wear test rig. (a) Superni 75 (b) Superni 600 (c) Superfer 800H (d) Superco 605 (e) Superni 718.	204
Fig. 6.10	Scanning electron micrographs showing wear debris of plasma sprayed coatings on Superfer 800H superalloy substrate subjected to sliding distance of 1200 m at an average sliding speed of 1 ms^{-1} on a pin-on-disc wear test rig. (a) NiCrAlY coating (b) Ni-20Cr coating (c) Ni_3Al coating.	205
Fig. 6.11	X-ray diffraction profile of wear debris of Superni 75 superalloy substrate subjected to sliding wear studies at a normal load of 9.8 N and sliding velocity of 1 ms^{-1}.	206
Fig. 6.12	X-ray diffraction profile of wear debris of Superni 600 superalloy substrate subjected to sliding wear studies at a normal load of 9.8 N and sliding velocity of 1 ms^{-1}.	206

Fig. 6.13	X-ray diffraction profile of wear debris of Superfer 800H superalloy substrate subjected to sliding wear studies at a normal load of 9.8 N and sliding velocity of 1 ms^{-1}	207
Fig. 6.14	X-ray diffraction profile of wear debris of Superco 605 superalloy substrate subjected to sliding wear studies at a normal load of 9.8 N and sliding velocity of 1 ms^{-1}	207
Fig. 6.15	X-ray diffraction profile of wear debris of Superni 718 superalloy substrate subjected to sliding wear studies at a normal load of 9.8 N and sliding velocity of 1 ms^{-1}	208
Fig. 6.16	X-ray diffraction profile of wear debris of plasma sprayed NiCrAl Y coating on Superfer 800H superalloy substrate subjected to sliding wear studies at a normal load of 9.8 N and sliding velocity of 1 ms^{-1}	208
Fig. 6.17	X-ray diffraction profile of wear debris of plasma sprayed Ni_3Al coating on Superfer 800H superalloy substrate subjected to sliding wear studies at a normal load of 9.8 N and sliding velocity of 1 ms^{-1}	209
Fig. 7.1	Macrographs of uncoated superalloys subjected to coal-fired boiler at 540°C for 1000 hours. (a) Superni 75 (b) Superni 600 (c) Superfer 800H (d) Superni 718.	213
Fig. 7.2	Weight change against time in hours plot for uncoated superalloys exposed to the coal fired boiler for 1000 hours at 540°C.	214
Fig. 7.3	Bar chart indicating the total thickness loss in mm by the uncoated superalloys after 1000 hours exposure to the coal fired boiler at 540°C.	214
Fig. 7.4	SEM back scattered electron image along the cross-section for the uncoated superalloys exposed to the coal-fired boiler at 540°C for 1000 hours. (a) Superni 75 (b) Superni 600 (c) Superfer 800H (d) Superni 718	215

Fig. 7.5	X-ray diffraction profiles for superalloys exposed to Low Temperature Primary Super Heater of the coal fired boiler for 1000 hours at 540°C. (a) Superni 75 (b) Superni 600.	216
Fig. 7.6	X-ray diffraction profiles for superalloys exposed to Low Temperature Primary Super Heater of the coal fired boiler for 1000 hours at 540°C. (a) Superfer 800H (b) Superni 718.	217
Fig. 7.7	SEM micrographs showing the surface morphology and EDAX analysis of superalloys exposed to coal-fired boiler for 1000 hours at 540°C. (a) Superni 75 (b) Superni 600.	218
Fig. 7.8	SEM micrographs showing the surface morphology and EDAX analysis of superalloys exposed to coal-fired boiler for 1000 hours at 540°C. (a) Superfer 800H (b) Superni 718.	219
Fig. 7.9	Oxide scale morphology and elemental composition variation across the cross-section of Superni 600 superalloy exposed to boiler of thermal power plant for 100 hours at 540°C.	222
Fig. 7.10	Oxide scale morphology and elemental composition variation across the cross-section of superalloys exposed to boiler of thermal power plant for 1000 hours at 540°C. (a)Superfer 800H (b) Superni 718.	223
Fig. 7.11	BSEI and X-ray elemental mapping of the cross-section of Superni 75 superalloy exposed to the boiler of the thermal power plant at 540°C for 1000 hours.	224
Fig. 7.12	BSEI and elemental X-ray mapping of the cross-section of Superni 600 superalloy substrate exposed to boiler of thermal power plant for 1000 hours at 540°C.	225
Fig. 7.13	BSEI and elemental X-ray mapping of the cross-section of Superfer 800H superalloy substrate exposed to boiler of thermal power plant for 1000 hours at 540°C.	226

Fig. 7.14	BSEI and elemental X-ray mapping of the cross-section of Superni 718 superalloy substrate exposed to boiler of thermal power plant for 1000 hours at 540°C.	227
Fig. 7.15	Macrographs of plasma sprayed NiCrAlY coating on superalloys subjected to boiler at 540°C for 1000 hours. (a) Superni 75 (b) Superni 600 (c) Superfer 800H (d) Superni 718.	228
Fig. 7.16	Weight change versus time in hours plot for uncoated and NiCrAlY coated superalloys exposed to the coal fired boiler for 1000 hours at 540°C.	229
Fig. 7.17	Bar chart indicating the total thickness loss in mm for NiCrAlY coating on different superalloy substrates after 1000 hours exposure to the coal fired boiler at 540°C.	229
Fig. 7.18	SEM back scattered electron image along the cross-section for the NiCrAlY coated superalloys exposed to the coal-fired boiler at 540°C for 1000 hours. (a) Superni 75 (b) Superni 600 (c) Superfer 800H (d) Superni 718	230
Fig. 7.19	X-ray diffraction profiles for Plasma Spray NiCrAlY coating on Superni 75, Superni 600, Superfer 800H and Superni 718 superalloy substrates exposed to Low Temperature Primary Super Heater of the coal fired boiler for 1000 hours at 540°C.	231
Fig. 7.20	SEM micrographs showing the surface morphology and EDAX analysis for NiCrAlY coating on superalloys exposed to coal fired boiler for 1000 hours at 540°C (a) Superni 75 (b) Superni 600.	232
Fig. 7.21	SEM micrographs showing the surface morphology and EDAX analysis for NiCrAlY coating on superalloys exposed to coal fired boiler for 1000 hours at 540°C. (a) Superfer 800H (b) Superni 718.	233
Fig. 7.22	Oxide scale morphology and elemental composition variation across the cross-section of NiCrAlY coated Superni 600 superalloy exposed to boiler of thermal power plant for 1000 hours at 540°C.	234

Fig. 7.23	Oxide scale morphology and elemental composition variation across the cross-section of NiCrAlY coating on superalloys exposed to boiler of thermal power plant for 1000 hours at 540°C (a)Superfer 800H (b) Superni 718.	235
Fig. 7.24	BSEI and elemental X-ray mapping of the cross-section of NiCrAlY coating on Superni 75 superalloy substrate exposed to boiler of thermal power plant for 1000 hours at 540°C.	238
Fig. 7.25	BSEI and elemental X-ray mapping of the cross-section of NiCrAlY coating on Superni 600 superalloy substrate exposed to boiler of thermal power plant for 1000 hours at 540°C.	239
Fig. 7.26	BSEI and elemental X-ray mapping of the cross-section of NiCrAlY coating on Superfer 800H superalloy substrate exposed to boiler of thermal power plant for 1000 hours at 540°C.	240
Fig. 7.27	BSEI and elemental X-ray mapping of the cross-section of NiCrAlY coating on Superni 718 superalloy exposed to boiler of thermal power plant for 1000 hours at 540°C.	241
Fig. 7.28	Macrographs of plasma sprayed Ni-20Cr coating with bond coat of NiCrAlY coating on superalloys subjected to coal-fired boiler at 540°C for 1000 hours (a) Superni 75 (b) Superni 600 (c) Superfer 800H (d) Superni 718.	242
Fig. 7.29	Weight change versus time in hours plot for uncoated and Ni-20Cr coated superalloys with bond coat of NiCrAlY coating exposed to coal fired boiler for 1000 hours at 540°C.	243
Fig. 7.30	Bar chart indicating the total thickness loss in mm for Ni-20Cr coating on different superalloy substrates after 1000 hours exposure to the coal fired boiler at 540°C.	243

Fig. 7.31	SEM back scattered electron image along the cross-section for the Ni-20Cr coating on different substrate superalloys exposed to the coal-fired boiler at 540°C for 1000 hours. (a) Superni 75 (b) Superni 600 (c) Superfer 800H (d) Superni 718.	244
Fig. 7.32	X-ray diffraction profiles for Plasma Sprayed Ni-20Cr coating with bond coat of NiCrAlY coating on Superni 75, Superni 600, Superfer 800H and Superni 718 superalloys substrates exposed to Low Temperature Primary Super Heater of the coal fired boiler for 1000 hours at 540°C.	245
Fig. 7.33	SEM micrographs showing the surface morphology and EDAX analysis for Ni-20Cr coating with bond coat of NiCrAlY coating on superalloys exposed to coal fired boiler for 1000 hours at 540°C. (a) Superni 75 (b) Superni 600.	246
Fig. 7.34	SEM micrographs showing the surface morphology and EDAX analysis for Ni-20Cr coating with bond coat of NiCrAlY coating on superalloys exposed to coal fired boiler for 1000 hours at 540°C. (a) Superfer 800H (b) Superni 718.	247
Fig. 7.35	Oxide scale morphology and elemental composition variation across the cross-section of Ni-20Cr coating with bond coat of NiCrAlY on Superni 600 superalloy exposed to boiler of thermal power plant for 1000 hours at 540°C.	248
Fig. 7.36	Oxide scale morphology and elemental composition variation across the cross-section of Ni-20Cr coating with bond coat of NiCrAlY on superalloys exposed to boiler of thermal power plant for 1000 hours at 540°C (a) Superfer 800H (b) Superni 718.	249

Fig. 7.37	BSEI and elemental X-ray mapping of the cross-section of Ni-20Cr coating on Superni 75 superalloy with bond coat of NiCrAlY exposed to boiler of thermal power plant for 1000 hours at 540°C.	252
Fig. 7.38	BSEI and elemental X-ray mapping of the cross-section of Ni-20Cr coating on Superni 600 superalloy with bond coat of NiCrAlY exposed to boiler of thermal power plant for 1000 hours at 540°C.	253
Fig. 7.39	BSEI and elemental X-ray mapping of the cross-section of Ni-20Cr coating with bond coat of NiCrAlY on Superfer 800H superalloy substrate exposed to boiler of thermal power plant for 1000 hours at 540°C.	254
Fig. 7.40	BSEI and elemental X-ray mapping of the cross-section of Ni-20Cr coating on Superni 718 superalloy with bond coat of NiCrAlY exposed to boiler of coal fired thermal power plant for 1000 hours at 540°C.	255
Fig. 7.41	Macrographs of plasma sprayed Ni_3Al coating with bond coat of NiCrAlY coating on superalloys subjected to coal-fired boiler at 540°C for 1000 hours (a) Superni 75 (b) Superni 600 (c) Superfer 800H (d) Superni 718.	256
Fig. 7.42	Weight change versus time in hours plot for uncoated and Ni_3Al coated superalloys with bond coat of NiCrAlY coating exposed to coal fired boiler for 1000 hours at 540°C.	257
Fig. 7.43	Bar chart indicating the total thickness loss in mm for Ni_3Al coating on different superalloy substrates after 1000 hours exposure to the coal fired boiler at 540°C.	257
Fig. 7.44	SEM back scattered electron image along the cross-section for the Ni_3Al coating on different substrate superalloys exposed to the coal-fired boiler at 540°C for 1000 hours. (a) Superni 75 (b) Superni 600 (c) Superfer 800H (d) Superni 718	258

Fig. 7.45	X-ray diffraction profiles for Plasma Sprayed Ni_3Al coating with bond coat of NiCrAlY coating on Superni 75, Superni 600, Superfer 800H and Superni 718 superalloys substrates exposed to Low Temperature Primary Super Heater of the coal fired boiler for 1000 hours at 540°C.	259
Fig. 7.46	SEM micrographs showing the surface morphology and EDAX analysis for Ni_3Al coating with bond coat of NiCrAlY coating on superalloys exposed to coal fired boiler for 1000 hours at 540°C (a) Superni 75 and (b) Superni 600.	260
Fig. 7.47	SEM micrographs showing the surface morphology and EDAX analysis for Ni_3Al coating with bond coat of NiCrAlY coating on superalloys exposed to coal fired boiler for 1000 hours at 540°C (a) Superfer 800H and (b) Superni 718.	261
Fig. 7.48	Oxide scale morphology and elemental composition variation across the cross-section of Ni_3Al coating with bond coat of NiCrAlY on Superni 600 superalloy exposed to boiler of thermal power plant for 1000 hours at 540°C.	262
Fig. 7.49	Oxide scale morphology and elemental composition variation across the cross-section of Ni_3Al coating with bond coat of NiCrAlY on superalloys exposed to boiler of thermal power plant for 1000 hours at 540°C (a) Superfer 800H (b) Superni 718.	263
Fig. 7.50	BSEI and elemental X-ray mapping of the cross-section of Ni_3Al coating on Superni 75 superalloy with bond coat of NiCrAlY exposed to boiler of thermal power plant for 1000 hours at 540°C.	268
Fig. 7.51	BSEI and elemental X-ray mapping of the cross-section of Ni_3Al coating on Superni 600 superalloy with bond coat of NiCrAlY exposed to boiler of thermal power plant for 1000 hours at 540°C.	269

Fig. 7.52	BSEI and elemental X-ray mapping of the cross-section of Ni_3Al coating on Superfer 800H superalloy with bond coat of NiCrAlY exposed to boiler of thermal power plant for 1000 hours at 540°C.	270
Fig. 7.53	BSEI and elemental X-ray mapping of the cross-section of Ni_3Al coating on Superni 718 superalloy with bond coat of NiCrAlY exposed to boiler of thermal power plant for 1000 hours at 540°C.	271
Fig. 7.54	Schematic diagram showing probable erosion-corrosion mechanism for the uncoated Superni 600 superalloy exposed to boiler environment at 540°C for 1000 hours.	274
Fig. 7.55	Schematic diagram showing probable erosion-corrosion mode for the NiCrAlY coated Superni 600 superalloy exposed to boiler environment at 540°C for 1000 hours.	275
Fig. 7.56	Schematic diagram showing probable erosion-corrosion mode for the Ni-20Cr coated Superni 718 superalloy exposed to boiler environment at 540°C for 1000 hours.	278
Fig. 7.57	Schematic diagram showing probable erosion-corrosion mode for the Ni_3Al coated Superfer 800H superalloy exposed to boiler environment at 540°C for 1000 hours.	279
Fig. 8.1	Bar chart indicating volumetric erosion rate in cm^3/g for the coated and uncoated superalloys subjected to erosion at a velocity of 40 ms^{-1} and impact angle of 30° using silica sand of average particle size 180 μm as erodent.	282
Fig. 8.2	Bar chart indicating volumetric erosion rate in cm^3/g for the coated and uncoated superalloys subjected to erosion at a velocity of 40 ms^{-1} and impact angle of 90° using silica sand of average particle size 180 μm as erodent.	282
Fig. 8.3	Schematic diagram of plasma sprayed coatings on different superalloy substrates indicating minor diffusion of elements from substrate into the coatings. (a) Superni 75 (b) Superni 600 (c) Superfer 800H (d) Superco 605 (e) Superni 718	283
Fig. 8.4	A histogram illustrating the specific wear rate of different superalloys and plasma sprayed coatings on Superfer 800H superalloy substrate.	284

Fig. 8.5 A histogram illustrating the average coefficient of friction for different superalloys and plasma sprayed coatings on Superfer 800H superalloy substrate. 284

Fig. 8.6 Bar chart indicating total extent of thickness loss in mm of uncoated and NiCrAlY, Ni-20Cr and Ni_3Al coated superalloys when exposed to the Low Temperature Primary Superheater of coal fired boiler at 540°C for 1000 hours. 287

LIST OF TABLES

Table No.	Particulars	Page No.
Table 3.1	Nominal composition and industrial applications of the superalloys	71
Table 3.2	Parameters of the argon shrouded plasma spray process	72
Table 3.3	Erosion conditions	77
Table 3.4	Chemical composition (wt %) of the En-32 steel disc	81
Table 3.5	Coal analysis data	85
Table 3.6	Chemical analysis of ash and flue gases inside the boiler	85
Table 4.1	Composition, particle size and designation of the coating powders	89
Table 4.2	Average density, coating thickness range, porosity content range and oxides content ranges of the plasma sprayed coatings	96
Table 5.1	Summary of the results for coated and uncoated superalloys eroded at a velocity of 40 ms^{-1} at impingement angle of 30^{o} using silica sand (150-250 μm size, Knoop Hardness of 880) as erodent	175
Table 6.1	Summary of the results for coated and uncoated superalloys subjected to pin-on-disc wear test rig at a normal load of 9.8 N and a constant sliding velocity of 1 ms^{-1}	202
Table 7.1	Summary of the results for coated and uncoated superalloy after 1000 hours of exposure to the low temperature primary superheater of the coal fired boiler at around $540^{0}C$	264
Table A.1	Mechanisms of erosion of various metals, alloys and coatings as reported by various researchers	294
Table A.2	Factors affecting erosion	303
Table A.3	Summary of sliding wear studies of superalloys and coatings relevant to the present study.	307

RESEARCH PAPERS PRESENTED/PUBLISHED

1. S.B. Mishra, S. Prakash and K. Chandra, (2006), "Studies on Erosion Behaviour of Plasma Sprayed Coatings on a Ni-Based Superalloy," Wear, Vol. 260, Issue 4-5, pp. 422-432.
2. S.B. Mishra, K. Chandra, S. Prakash and B. Venkataraman, (2005), "Characterisation and Erosion Behaviour of a Plasma Sprayed Ni_3Al Coating on a Fe-Based Superalloy," Materials Letters, Vol. 59, Issue 28, pp.3694-3698.
3. S.B. Mishra, K. Chandra, S. Prakash and B. Venkataraman, (2006) "Erosion Performance of Coatings Produced by Shrouded Plasma Spray Process on a Co-Base Superalloy," Surface and Coatings Technology, accepted for publication, in press.
4. S.B. Mishra, K. Chandra and S. Prakash, (2006) "Characterisation and Erosion Behaviour of Plasma Sprayed NiCrAlY and Ni-20Cr Coatings on a Fe-based Superalloy," Journal of Tribology (ASME Journal), accepted for publication.
5. S.B. Mishra, S. Prakash and K. Chandra, "Erosion of Some Superalloys and Role of Plasma Spray Coatings –A Review," Presented and published in the proceedings of the Indo Japan Conference on Damage Tolerant Design and Materials, held at Mechanical Engineering Department, Indian Institute of Technology Madras, Chennai, December 16-18, 2004, pp.220-225.
6. S.B. Mishra, S. Prakash and K. Chandra, "Characterisation of Plasma Sprayed NiCrAlY, Ni-20Cr And Ni_3Al Coatings on a Ni-Based Superalloy Inconel 718," Presented and published in the proceedings of the 'International Symposium of Research Students on Material Science and Engineering', held at Metallurgical and Materials Engineering Department, Indian Institute of Technology Madras, Chennai, December 20-22, 2004, pp.1-8.
7. S.B. Mishra, S. Prakash and K. Chandra, (2005), "Characterisation and Erosion of Plasma Sprayed Coating on a Ni-Based Superalloy," Published in the Proc. of the "Conference on Materials Degradation: Innovation, Inspection, Control and Rehabilitation", held at METSOC, Calgary, Alberta, Canada on August 21-24, pp. 403-414.

8. S.B. Mishra, K. Chandra and S. Prakash, (2005), "Solid Particle Erosion Behaviour of Plasma Sprayed Coatings on a Fe-Based Superalloy," Published in the Proc. of the "World Tribology Congress III", held at Washington Hilton, Washington D.C., USA, on September 12-16, paper no. WTC2005-63877.
9. S.B. Mishra, K. Chandra and S. Prakash, "Characterisation and Erosion Behaviour of NiCrAlY Coating Produced by Plasma Spray Method on Two Different Ni-based Superalloys," Accepted for oral presentation in The International Conference on Metallurgical Coatings and Thin Films-ICMCTF 2006, to be held at San Diego, California, USA from May 1-5, 2006. Paper will be published in the journal **Surface & Coatings Technology**.
10. S.B. Mishra, K. Chandra and S. Prakash, "Erosion-corrosion performance of NiCrAlY coating produced by shrouded plasma spray process in a coal-fired thermal power plant," Accepted for presentation in the Second International Conference on Engineering Failure Analysis to be held at Toronto, Canada from Sept. 13-15, 2006. Paper will be published in the journal of **Engineering Failure Analysis**.
11. S.B. Mishra, K. Chandra and S. Prakash, "An Overview on Erosion Behaviour of Plasma Sprayed Coatings," Accepted for oral presentation in the COM 2006 - 45th International Conference of Metallurgists organized by METSOC - the Metallurgical Society of CIM to be held at Montreal, Quebec, Canada from October 1-4, 2006.

ABBREVIATIONS

APS	Air Plasma Spray
Bal	Balance
BSEI	Back Scattered Electron Image
RBSD	Robinson Back Scattered Detector
EDAX	Energy Dispersive X-ray Analysis
EPMA	Electron Probe Micro Analyser
hr	Hour
HVOF	High Velocity Oxy-Fuel
LPPS	Low Pressure Plasma Spray
min	Minute
Ni-20Cr	Ni-20 Wt% Cr
NiCrAlY	Ni-22Cr-10Al-1Y
SEM	Scanning Electron Microscopy
VPS	Vacuum Plasma Spray
Wt%	Weight Percentage
% age	Percentage
Wt. Gain	Weight Gain
XRD	X-ray Diffraction
TBC	Thermal Barrier Coating

Chapter 1

INTRODUCTION

Through the years the erosive wear which occurs when solid particles entrained in a fluid stream strike a surface has been a serious and continuing problem in many industrial operations (**Finnie, 1995**). Erosion is the progressive loss of original material from a solid surface due to mechanical interaction between that surface and a fluid, a multi-component fluid, or impinging liquid or solid particles (**ASTM standard G76-95**). Erosion occurs when solid particles entrained in a fluid stream (gaseous or liquid) strike a surface. In many industries, such as marine, offshore, process, aeronautical and mining, there is a regular requirement for components such as valves, pumps, pipework, extrusion dyes, powder mixers, turbine and helicopter blades to perform in aggressive environments which are erosive. Sand particles suspended in the water or entrained into airflow can impact on the internal or external surfaces of these components resulting in expensive erosion damage (**Wood, 1999**). In industrial applications, such as coal-fired boilers, fluidized beds, and gas turbines, solid particles are produced during the combustion of heavy oils, synthetic fuels, and pulverized coal and causes erosion of materials (**Zhang et al, 2000**).

Control valves are extensively used in the petrochemical and process industries for the regulation of fluid flow. Some of these operating conditions are extremely aggressive being not only corrosive but also erosive due to the entrainment of sand into the production flow. A survey by BP found that out of a sample of 258 choke valves that had failed over a 2-year period, 35% could be attributed to erosion. The costs incurred in the replacement of these damaged valves are estimated to be in the region of £300,000 per valve; this figure does not include unscheduled shutdowns or lost production. In addition to these considerable difficulties are often experienced in the replacement operations. These could be reduced either by design considerations or by coating the internal components with ultra-hard wear–resistant facings (**Wood and Wheeler, 1998**).

Gas and steam turbines operate in environments where the ingestion of solid particles is inevitable. In commercial and military aircraft and naval installations, some of the mechanisms that cause solid particle ingestion are vortices generated during landing and take-off, and storms, volcanic ash and thrust reverser efflux at low speed

which blows sand, ice and dust into engines. In steam turbines, the solid particles are principally boiler scale, mainly iron oxide that break off and become entrained in the steam. Filters and separators can remove a large percentage of the solid particles, but significant amounts of small particles still pass through and enter the engines. Due to their high inertia solid particles deviate from the flow streamlines, impact the blade surfaces and causes severe erosion damage. This damage is manifested by pitting and cutting of the blade's leading and trailing edges and results in an increase in the blade surface roughness. The overall effects of the above phenomena are to increase the pressure loss and change the blade geometry. Continued operation under particulate flow conditions adversely affects the performance of the engines, as well as their lives, and can be detrimental to their reliability (**Tabakoff, 1995**).

Particle erosion has become an increasingly important material property, particularly in the field of alternative energy technology (**Soderberg et al, 1981**). One of the most serious problems associated with fluidized bed combustors (FBC) technology is the material loss of the combustor wall and the in-bed tubes. The term 'wastage' is commonly used for this phenomenon, which is generally accepted to be a result of erosion or abrasive wear that may be accelerated by oxidation or high-temperature corrosion (**Stringer et al, 1989**). According to **Lindsley et al (1995)** for fluidized bed combustors installations, lost revenue during downtime is approximately $50000 per day for an average size unit and annual maintenance costs approaching a million dollars per year. **Stein et al (1999)** have reported that for the electric power industry solid particle erosion cost an estimated US$150 million a year in lost efficiency, forced outages, and repair costs. Erosion damage to steam turbine components is also a costly problem estimated to cost the utility industry about $150 million per year (**Walsh and Tabakoff, 1990**).

According to **Krishnamoorthy et al (1993)** a performance review of thermal power stations in India indicates that erosion problems contribute significantly towards partial unavailability of power in India. Boilers and other steam power plant equipments suffer severe erosion and corrosion problems resulting in substantial losses (**Prakash et al, 2001**). The data covering one-year duration for the boiler tube failure in the coal fired power plant in northwestern region of India indicates that out of the 89 number of failures, 62 failures were attributed to the erosion-corrosion by fly ash. Moreover fly ash content of the Indian coal is very high and causes severe erosion-corrosion of the materials in the power plants.

According to **Hidalgo et al (2001A and 2001B)** erosive, high temperature wear of heat exchanger tubes and other structural materials in coal-fired boilers are recognized as being the main cause of downtime at power-generating plants. As suggested by them these could account for 50-75% of their total arrest time. They reported that further maintenance costs for replacing broken tubes in the same installation are also very high, and can be estimated at up to 54% of the total production cost. Therefore, they suggested that the development of wear and high temperature oxidation protection system in industrial boilers is very important from both engineering and economic perspective.

The combined erosion-corrosion of materials at elevated temperature is a degradation mechanism that occurs in coal burning energy generation equipment that contain small, moving solid particles in reactive gases, such as fluidized bed combustors and coal gasifiers. It is important to have an understanding of how the rates and mechanisms of material loss in these devices are affected by the differences in compositions of the material and the variations in exposure conditions **(Levy et al, 1989)**. If the mechanism of degradation operating in a particular practical system can be identified, this can help in finding remedial measures. Hence in view of the quantum of the loss due to erosion-corrosion wear it becomes imperative for an engineer to develop better defence against such degradation by exploring newer erosion-corrosion wear resistant materials for the industrial applications.

When a metal is subjected to erosion and oxidation simultaneously at high temperature, the metal surface takes on certain features that reflect the nature of the attack and the conditions under which it occurs **(Peterson et al, 1995)**. According to them, there are two distinct primary regions of erosion-corrosion interaction. In the first, the erosion removes the surface of the growing oxide scale without affecting the metal-scale interface or the metal below. In this regime, the eroded oxide surface shows evidence of cutting, removal and displacement that reflect various degrees of plastic displacement or removal of the oxide. The scale surface remains flat and does not develop any other topographical features. In the second primary regime of interaction, in which the erosion component is substantially more vigorous, the distinct scale no longer forms and the erosive particles impact the metal substrate, causing substantial plastic deformation of the metal. In this case, the metal surface shows features similar to those

found on the thick oxide surface. At longer exposure times, surface features develop that are on a much larger scale. These features include hills and valleys and ripple formations.

Several studies concerning the interaction between erosion and a surface oxide film have been reported in the literature. Mechanisms of material removal have been proposed which include oxide fracture and chipping, oxide spallation at the metal-oxide interface and plastic deformation of metal substrate resulting in both oxide and metal loss. The choice of material depends on the mechanical strengths that the material can provide at the operating temperature. Material chemistry which provides mechanical strength may not be able to provide sufficient erosion-corrosion resistance **(Singh, 2003)**.

A superalloy is an alloy developed for elevated-temperature service, usually based on group VIIIA elements, where relatively severe mechanical stressing is encountered, and where high surface stability is frequently required **(Li et al, 2003)**. Iron-, nickel- and cobalt- base superalloys are the commercial alloys commonly used for the high temperature applications e.g. manufacture of components used in aggressive environments of gas turbines, steam boilers etc. The superior mechanical performance and good corrosion resistance of the superalloys, especially the nickel-base superalloys at high temperature make them favourites as base materials for power generation systems, industrial gas turbines and other energy conversion systems. However, the presence of fly ash, combustion gases constitutes an extreme environment, and erosion, erosion-corrosion and hot corrosion is inevitable when alloys are used at high temperatures for long periods of time **(Goebel et al, 1973, Tabakoff, 1995, 1999A and Kamaraj, 2003)**. To improve the oxidation and corrosion resistance of superalloys and to increase the service life of superalloy components at high temperatures, two approaches have been employed, adding fair amounts of Al, Cr, and Ti, and small amounts of Y, Zr and Hf to the alloy, which help to improve oxidation and corrosion resistance. Another method is coating the alloy with a protective layer using various surface treatment techniques **(Wang et al, 1989)**. Wear and corrosion resistance of components can be greatly increased by protective coatings and this is a growing industry of considerable economic importance **(Hocking, 1993)**.

Coatings provide a way of extending the limits of use of materials at the upper end of their performance capabilities, by allowing the mechanical properties of the substrate materials to be maintained while protecting them against wear or corrosion **(Sidky and Hocking, 1999)**. Coating technology is one of the more rapidly growing

technologies in the field of materials. A combination of the development of materials specifically designed for erosion-corrosion resistance and the appropriate technique for the application of these materials, as a coating would be the optimum solution. Suitable coating techniques also allow for regeneration of parts that have been rendered unusable by erosion. Coatings are primarily used to restrict surface damage of components in practice **(Stringer, 1998)**. It has been reported that the thermal spray is a technique that produces a wide range of coatings for diverse applications. Thermal-sprayed coatings are economical, can be produced by relatively simple techniques and offer excellent corrosion and wear protection. Moreover, other favorable properties can be produced at the coating or component surface. As a result, these coatings have found use in various industrial applications **(Tabakoff, 1999B and Wielage et al, 1998)**.

Among the thermal-spray techniques, plasma spraying is the most flexible and versatile process with respect to the sprayed materials. Almost any material can be used for plasma spraying on almost any type of substrate. The high temperatures of plasma-spray processes permit the deposition of coatings for applications in areas of corrosion and wear protection as well as special applications for thermal, electrical and biomedical purposes **(Knotek, 2001 and Pfender, 1988)**. The development of anti-wear protection elements for boilers using thermal spraying requires careful evaluation of their service performance **(Hocking et al, 1989)**. This evaluation would help to establish the influence of the coating technique on their erosion behaviour **(Hidalgo et al, 2000)**. It is important to understand the nature of all types of environmental degradation of metals and alloys as vividly as possible so that preventive measures against metal loss and failures can be economically devised to ensure safety and reliability in the use of metallic components **(Chatterjee et al, 2001).**

The present study has been performed to evaluate the behaviour of the plasma sprayed coatings on superalloys in room temperature erosion test rig, pin-on-disc sliding wear test rig and erosion-corrosion performance in actual industrial environment. Behaviour of these coatings under different degrading environments once evaluated will be helpful in choosing the suitable coating for the given environment.

Chapter 2

LITERATURE REVIEW

This chapter contains a critical review of the existing literature on erosion and erosion-corrosion behaviour of metals, alloys and protective coatings; including a comprehensive review of the sliding wear behaviour of some metals, alloys and protective coatings are also included in this chapter. This is followed by the detailed description of Plasma spray coating process. The problem has been formulated after critical analysis of the literature towards the end of this chapter.

2.1 EROSION WEAR

The loss of material caused by the impingement of tiny, solid particles, which have a high velocity and impact on the material surface at defined angles, is called erosive wear **(Guo et al, 1995)**. According to ASTM standard **G76-95 (2000)**, erosion is the progressive loss of original material from a solid surface due to mechanical interaction between that surface and a fluid, a multi-component fluid, or impinging liquid or solid particles. Erosion is a serious problem in many engineering systems, including steam and jet turbines, pipelines and valves used in slurry transportation of matter, and fluidized bed combustion system **(Kosel, 1992)**. A schematic view of erosion wear is shown in Fig. 2.1.

According to **Kosel (1992), solid particle erosion** refers to a series of particles striking and rebounding from the sliding of abrasive particles across a surface under the action of an externally applied force. He further reported that solid particle erosion is expected whenever hard particles are entrained in a gas or liquid medium impinging on a solid at any significant velocity (greater than 1m/s). In both the cases, particles are accelerated or decelerated, and their directions of motion can be changed by the fluid, this is more significant in liquid media, and slurry erosion is treated as different though related subject. In some of the cases solid particle erosion is a useful phenomenon, as in sandblasting and high speed abrasive water-jet cutting, but is a serious problem in many engineering systems, including steam and jet turbines, pipelines and valves carrying particulate matter, and fluidized bed combustion (FBC).

Liquid impingement erosion has been defined as progressive loss of original material from a solid surface due to continued exposures to impacts by liquid drops or jets. Liquid impingement erosion connotes repeated impacts or collisions between the surface being eroded and small discrete liquid bodies. It is quite difficult to propel liquid droplets to high velocities without breaking them up, and liquid impingement erosion has become a practical problem primarily where a target body moves at high speeds and collides with liquid drops that are moving much more slowly. Almost all the work done in this subject has been in connection with just two major problems: "moisture erosion" of low-pressure steam turbine blades operating with wet steam, and "rain erosion" of aircraft or missile surfaces and helicopter rotors. Whenever vapor or gas flows carrying liquid droplets impinge upon solid surfaces- as in nuclear power plant pipes and heat exchangers, erosion can occur **(Heymann, 1992)**.

In **Slurry erosion,** slurry can be described as a mixture of solid particles in a liquid of such a consistency that it can be readily pumped. The term slurry erosion is strictly defined as that type of wear, or loss of mass that is experienced by a material exposed to a high velocity stream of slurry. Slurry erosion is caused by the interaction of a liquid suspension of solid particles and a target which experiences loss of material by the repeated impact of suspension particles **(Clark, 1992)**.

Cavitation Erosion is the mechanical degradation caused by cavitation in liquids. The mechanical loading of a solid surface i.e. due to a cavitating liquid is caused by asymmetrical collapse of cavities either at or near the surface. These asymmetrical collapses result in liquid microjets that are directed towards the solid surface. The mechanical loads are much localized, and because of the concerted collapse of the cavity cluster can be extremely severe resulting in the deformation of surface. The repeated loading eventually leads to removal of material from the surface **(Hansson and Hansson, 1992)**.

One of the most serious problems associated with fluidized bed combustors (FBC) technology is the material loss of the combustor wall and the in-bed tubes. The term 'wastage' is commonly used for this phenomenon, which is generally accepted to be a result of erosion or abrasive wear that may be accelerated by oxidation or high-temperature corrosion **(Stringer et al, 1989)**. Unacceptable levels of surface degradation of metal containment walls and heat exchanger tubing by a combined erosion-corrosion (E-C) mechanism have been experienced in some boilers, particularly

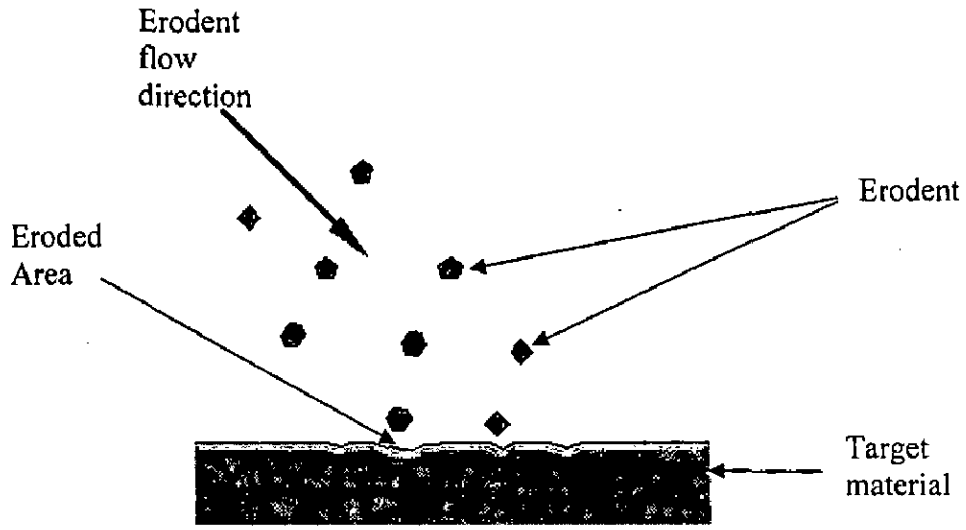

Fig. 2.1 A schematic view of solid particle erosion of material (Buckley, 1981).

fluidized bed combustors by **Levy (1993).** According to **Kosel (1992), erosion-corrosion** refers to the simultaneous, synergistic interaction between the solid particle erosion and corrosion. Erosion-corrosion is of considerable technical importance in several types of applications, including coal gasification or liquidification, steam turbines, jet turbines, and in the in-bed evaporator tubes, waterwalls, and convection pass surfaces of FBC systems. Material losses due to combined effect of erosion and corrosion is a problem in many industrial applications such as hydraulic turbines, slurry pumps, valves, pipelines conveying solid particles **(Das et al, 2005).**

2.1.1 Mechanisms of Erosion

In erosion, the detailed process that cause material removal is still poorly understood **(Gee et al, 2003). Finnie's (1960)** analysis of the cutting action of a single particle launched against a ductile target was the first model of solid particle erosion capable of predicting material removal rate. Several researchers have reported the material removal mechanisms of erosion for different alloys and these are as follows.

2.1.1.1 Erosion Mechanisms of Ductile Materials

Finnie's analysis *(1958) of the cutting action of a single particle launched against a ductile target was the first model of solid particle erosion capable of predicting material removal rate.* **In his scheme, the particles were assumed to be non-deforming and impacting a target, which was assumed to reach a constant flow pressure (i.e. the target is assumed perfectly plastic) immediately upon impact. By assuming that no rotation of the particles occurs during the impact process, he could solve for the trajectory of the particle in closed form as it cuts the surface, and thus predict material removal rates. This theory formed the foundation for later rigid-plastic models, which removed the restriction of particle rotation during impact. Finnie (1960)** developed an analytical model to predict erosion rates that were based on the assumption that the mechanism of erosion was that of **micromachining.** According to him the impacting particle penetrates the target by a small amount, translates along the surface removing material ahead of it in a machining mode and finally leaves the surface. A refined model has been developed for this mechanism by **Finnie and McFadden (1978)** utilizing the equation of motion of the particle tip to define an amount of target material that would be removed.

Bitter (1963 A, B) and Neilson and Gilchrist (1968) have further modified this *micromachining* mechanism and model, primarily to account for erosion at large impingement angle. They have all tended to use the equation of motion of the particle translating along the surface of the specimen as a starting point for developing an analytical model. **Bitter (1963 A ,B)** has reported the two types of erosion wear, one caused by repeated deformation during collisions, eventually resulting in breaking loose pieces of the material, and other caused by the cutting action of the free-moving particles.

Some researchers [**(Sheldon and Kanhere (1972), Hutchings and Winter (1974), Winter and Hutchings (1974, 1975), and Christman and Shewmon (1979)**] have used the large single particle, millimetre in diameter, and impacted them individually at the target surface to study the mechanism of erosion from a physical standpoint. **Winter and Hutchings (1974)** have identified the two different regimes of deformation, referred to as ploughing and cutting (Fig. 2.2). According to them ploughing tends to occur at large negative rake angles; i.e. when the angle between the surface and the leading edge of the particle is small. If other impact conditions are kept constant, material is removed by ploughing when a critical impact velocity is exceeded. They further added that ploughing deformation is, however, discouraged if the particle executes a rolling type rotation during its time of contact with the surface rather than sliding along it. Whereas at more positive rake angle cutting deformation occurs; however, in every case studied rolling caused the cutting edge of the particle to penetrate deeply into the metal surface rather than perform the scooping action required for material removal.

Hutchings (1979) further modified the above regimes using the impact of single particle on to metals at 30° impact angle and subdivided the cutting type into two basic types of impact damages, as illustrated in Fig. 2.3. According to him rounded particles deform the surface by ploughing, displacing material to the side and in front of the particle. Further impacts on neighbouring areas lead to the detachment of heavily-strained material from the rim of the crater or from the terminal lip. He further reported that this type of deformation embraces both the ploughing and wedges-forming modes of abrasion shown in Fig. 2.3 (a) and Fig. 2.3 (b). The deformation caused by an angular particle depends on the orientation of the particles as it strikes the surface, and on whether the particle rolls forwards or backwards during contact. He proposed that in the

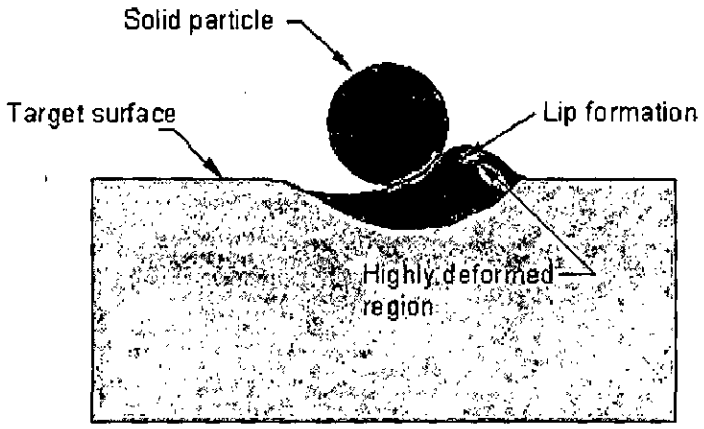

(a) Ploughing mechanism

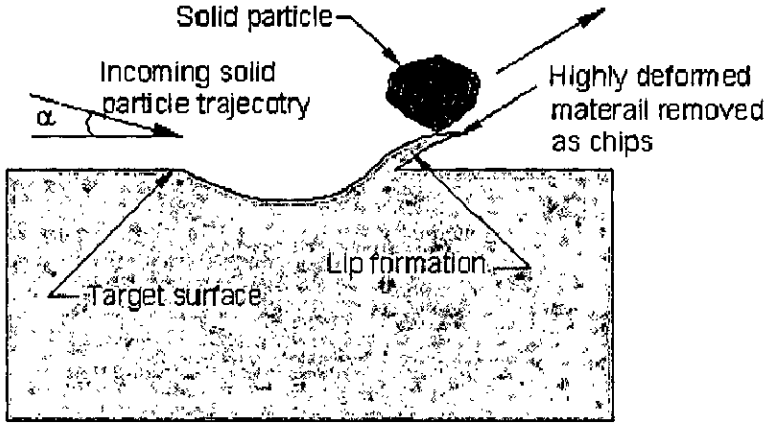

(b) Cutting mechanism

Fig. 2.2 Schematic views of the sections through impact sites formed by hard particles on a ductile metal. The impact direction is from left to right. (a) Ploughing mechanism by spherical shape solid particle; (b) Cutting mechanism by an angular particle, rotating backwards during impact **(Winter and Hutchings, 1974)**.

(a) Type I cutting

(b) Type II cutting

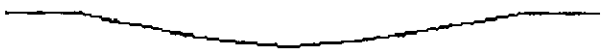

Fig. 2.3 Schematic view of (a) type I cutting by an angular particle, rotating forwards during impact: (b) type II cutting by an angular particle, rotating backwards during impact **(Hutchings, 1979)**.

mode which has been termed type I cutting (Fig. 2.3 (a)), the particle rolls forward, indenting the surface and raising material into a prominent lip, which is vulnerable to removal by subsequent nearby impacts. He further suggested that if the particle rolls backward (Fig. 2.3 b), a true machining action can occur, in which the sharp corner of the abrasive grain cuts a chip from the surface. The type II cutting occurs over only in a narrow range of particles geometries and impact orientations as suggested by him.

Further he added that a clear distinction can be drawn between these three types of deformation (Fig. 2.2 and Fig. 2.3) when single particle strikes a plane surface, classification is not yet so simple when randomly oriented particles of irregular shape impinge on a previously eroded and thereby roughened surface. Nevertheless, features similar to those caused by single particle impacts can be distinguished on surfaces eroded by the impact of many particles. According to him erosive wear is associated with the detachment by plastic rupture of metal displaced from the impact sites into raised crater rims and lips. Although each impact displaces material from the indentation formed, it will often not become detached as wear debris until it has experienced several cycles of plastic deformation and becomes severely work-hardened.

Bellman and Levy (1981) have investigated the erosion mechanism in ductile metals. According to them, an eroded surface is one that had many numbers of particles impacted on it and a steady state surface has been eroded to the condition where erosion rate has reached a constant value. They reported that when an impacting particle causes a local depression of surface it creates an **impact crater**. The entrance side of the impact crater is the side at which the tip of the particle first penetrated the target surface. The exit side is that side from which the damaging particle tip left the surface. According to them impact craters are always much smaller than the particles that cause them, implying that only a portion of a particle enters and exits an impact crater. The balance of the particle provides mass for the total kinetic energy of the particle, its driving force. They reported that the impact craters on a fresh surface are of three types: **indentation craters; smear craters; ploughing craters**. Indentation craters exhibit some evidence that the initial surface has been depressed into their walls and the craters have some plastically deformed material raised above the initial plane of the surface (called as hump) on the exit side. Smear craters occur when a flat portion of a particle damages the surface over a large area but only to a shallow depth. Usually a ridge of sheared material is pushed to the exit side. The ridge may be strongly or weakly attached to the

surrounding metal. Ploughing craters occur when a projecting corner or a sharp point on a particle forces its way deeply into the surface and then translates along the surface for a distance. This causes projecting lips to be uplifted along either side of the crater formed. The traverse of the particle also forms a hump on the exit side. They further opined that on a steady state surface, smear and indentation craters predominate. The smear craters are larger than those formed during the initial stages of erosion and do not form ridges. Thin platelets of severely deformed metal that extend outward above the adjacent erosion surface occur along the exit and sides of the smear crater. Because they lack any bonding to adjacent surfaces, these platelets are only slightly anchored to a portion of the smear crater and are very vulnerable to being knocked off. Indentation craters on a steady state surface do not form a hump and tend to be somewhat less deep than those on a non-steady state surface. The edges of the indentation crater have platelet protrusions similar to those on a smear crater.

They further reported that the extrusion is the initiation of mechanism of platelet erosion. They described that the loss of metal from an eroding surface appears to occur by a combined extrusion forging mechanism. Evidence indicates that the platelets are initially extruded from shallow craters made by the particle impact. Once formed, they are forged into a distressed condition, in which they are vulnerable to being knocked off the surface in one or several pieces. The lip of the platelets extruded out of the crater by the first impact is identical with one shown by **Gulden et al (1982)**. Similar extruded lips are also reported by **Winter and Hutchings (1975)**. **Soderberg et al (1981)** have tested about 50 metals and alloys and further have classified them with respect to erosion mechanism. Their result indicates that almost all the metals and alloys lose material by formation of lip or platelet and their subsequent fracture.

A theoretical model which predicts the extent of lip formation as well as the weight loss using the single impact experiments is presented by **Sundararajan (1983)**. The model postulates that the lip formation is the result of localization of deformation in the near-surface regions of the target and that the lip is removed either by inertial-stress-induced tensile fracture or by separation across adiabatic shear bands formed at the base of the lip. He used the single impact data's for copper, brass, thoria dispersed (TD) Nickel and nickel targets. **Sundararajan and Shewmon (1983)** had proposed the new theoretical model for the erosion of metals by particles at normal incidence which employs a criterion of critical plastic strain to determine when the material will be

removed. This critical plastic strain is defined as the strain at which the deformation in the target localizes and hence results in the lip formation. They have concluded that under typical erosion conditions the "localization" model is more appropriate than the "fatigue" models. **Brach (1988)** has developed an analytical model for the energy loss suffered by an arbitrarily shaped, rigid particle impacting the surface of a massive target material at any impact angle. By further assuming that the erosion rate should be proportional to the energy loss suffered by the particle during impact, he had demonstrated that the erosion response will be ductile (i.e. a maximum in the erosion rate at intermediate impact angles) or brittle (a maximum in the erosion rate at normal impact angles), depending on the relative magnitudes of the energy absorbed due to tangential (i.e. frictional) and normal inelasticity effects.

Hutchings and Levy (1989) had discussed the mechanisms of erosion in ductile metals subjected to the impact of solid particles and also presented the experimental observations. They reported the possible effects associated with the local temperature rise caused by particle impact. They found that heat conduction play an important role in reducing the maximum temperature rise in all practical cases of erosion and had reported the negligible cumulative effect on the temperature rise of successive impacts. They described the observed erosion mechanism in terms of three distinct phases, which occurred sequentially at any one location. According to them in the steady state condition all the three phases occur simultaneously at different locations over the surface. In the initial phase an impacting particle forms a crater and material is extruded or displaced from the crater to form a raised lip or mound. In the second phase the displaced metal is deformed by subsequent impacts; this may lead to lateral displacement of the material and can be accompanied by some ductile fracture in heavily strained regions. Finally after a relatively few impacts, the displaced material becomes so severely strained that it is detached from the surface by ductile fracture. They reported this mechanism of erosion as the "platelet" mechanism defined by **Levy et al (1984)** and differs from the micromachining model proposed by **Finnie (1960)** in that it is postulated that in most cases the impact of several particles is necessary in order to remove a fragment of metal from the surface (**Hutchings and Levy, 1989**). Further they opined that the "platelet" mechanism was observed over all impact angles up to 90°. At shallow angles of 20° or less, all three phases of the mechanism can occur in a single continuous action during the impact of a single particle resulting in removal of material in a process

indistinguishable from micromachining. With subsequent increments of impacting particles, the mass loss rate increased until it reached steady state condition where each increment of particles caused the same metal-loss rate to occur. Steady-state conditions occurred after a relatively short exposure period as discussed by **Levy (1982).**

Later **Sundararajan (1991)** developed a model valid for all impact angles as an extension of the earlier model **(Sundararajan, 1983)** proposed specifically for normal impact erosion. This model **(Sundararajan, 1991)** is based on the assumption that the localization of plastic flow underneath the impacting particle is responsible for lip formation and hence erosion. He reported that it is capable of rationalizing the important experimental observations related to erosion, namely the effects of material properties, impact velocity and angle and particle shape.

2.1.1.2 Erosion Mechanisms of Brittle Materials

Solid particle erosion damage of brittle materials has been investigated by **Sheldon and Finnie (1966)** who studied the erosive regime, usually referred to as hertzian fracture, where the contact between the particle and the body is exclusively elastic. In their analysis they considered dynamic forces between the surface and the particle and this resulted in a prediction of the volume removed for a material with specific properties. They also concluded that the fracture at the surface is a function of the volume of material constrained in the primary erosion zone in relation to the surface and volume flows.

Zambelli and Levy (1981) investigated the erosion behaviour of brittle oxide scales on ductile alloy substrates. They interpreted the erosion damage of the NiO scales using simplified postulates based on fracture propagation concepts. They reported the removal of NiO duplex scale in a two-step mechanism. Plastic flow indentation and lateral crack growth in the columnar outer layer is the first step in the erosion mechanism. In the second step, pits are produced from hertzian cone fractures formed in the inner layer. The oxide is removed by the chipping away of the cracked scale of the outer and inner layers, which enlarges the pits. At greater velocities, particles sizes and impingement angles the erosion of the thinner oxide scales to the bare nickel occurred in times of the order of seconds. It was suggested that the strengths of the bonds between the two scale layers and between the scale and the metal substrate were directly related to the erosion behaviour.

They further added that NiO scale thicker than 50 μm introduced some protection during the initial period of erosion of the outer scale. They concluded that the microstructure, mechanical properties and bonding state of the oxide layers are important parameters in the erosion behaviour of oxide scales. A schematic representation showing a proposed sequence of crack initiation events as the result of single-particle impacts as illustrated by them is shown in Fig. 2.4. They assumed that at impact loading subsurface lateral cracks formed beneath the plastically deformed indentation pit which propagate almost parallel to the surface in the columnar outer layer. They reported that lateral crack propagation can also be induced at the interface between the scale layers resulting in a loss of scale by exfoliation of the outer layer. Further they opined the formation of ring cracks at the interface between the two layers. They concluded that as a result of many particle impacts downward propagation of these ring cracks proceeds along trajectories so as to form a hertzian-type truncated cone (frustum cone) fracture.

Wensink and Elwenspoek (2002) reported that the brittle erosion deals with material removal due to crack formation as illustrated in Fig. 2.5. When a brittle material is impacted by a hard sharp particle, the contact area is plastically deformed due to the high compressive and shear stresses and a radial crack is formed. After the impact, the plastic deformation leads to large tensile stresses that result in lateral cracks causing the material removal.

2.1.1.3 Erosion Mechanisms of Coatings

The erosion behaviors of several types of coatings have been evaluated in the laboratory by **Levy (1988)**. He reported that in general, metals, alloys and coatings on metallic substrate erode by one of the two basic mechanisms, i.e. either by plastic deformation to failure of material or cracking and chipping of a brittle material. Further coatings that have some degree of ductility erode by a plastic deformation mechanism, whereas brittle coatings erode by cracking and chipping mechanism. The erosion mechanisms by which ductile and brittle coatings are removed are basically different. He opined that ductile materials including materials with relatively little measurable ductility (1% - 2% elongation) fail as a result of impacting particles causing localized plastic flow that exceeds the critical strain to failure in local areas. Structural alloys, MCrAlY coatings and other primarily metallic coatings will erode by this mechanism. When erodent particles in a gas or liquid carrier fluid strike the surface of a ductile

material they initially extrude thin microplatelets of the base materials from craters, which are formed at the sites of the impacts. The platelets are then further flattened, i.e. pancake forged, by subsequent particles striking the initially deformed material. After a small number of particles have impacted the same localized area, whose size is from a few micrometers to as many as 100 μm in major diameter, part or even all of the initially extruded platelets will have been strained to their critical strain and fracture of portions of the platelets will occur.

Further he reported that the coatings that form a layer of oxidized scale in service erode-corrode by the erosion of the scale and its replacement by oxidation of the base metal via cation diffusion. He concluded that the erosion rates of thermally sprayed coatings vary directly with their grain size and level of porosity. The presence of cracks in diffusion-type coatings results in higher erosion rates. Whereas plasma-sprayed ceramic coatings for use as thermal barriers are somewhat porous and brittle materials, that are eroded by cracking and chipping mechanism. Moreover when the grain size of the coating is very small and there is a minimum of pores, the material loss rate is very low. Thus the greater the porosity of the coating, the easier it is for the erodent particles to knock off pieces of exposed ceramic pore walls, and the greater is the removal rate. He also proposed that the compositions and hardness of the coatings do not correlate with the loss rates, but their morphologies do.

The erosion characteristics of PVD titanium nitride coated high speed steel using alumina particles as erodent have been studied by **Hedenqvist and Olsson (1990).** They classified the damage resulting from single particle impacts into three types:

1) indentation-like impact craters
2) impact craters causing detachment of coating fragments
3) impact craters with lip formation.

They further reported that of these, damage of type 1 is a predominant whereas damage of type 2 and 3 cause actual coating removal. The dominance of damage of type 1 is mostly due to geometrical reasons: the 90° angle of incidence favours this type of damage over the other two. According to them damage of type 1 is favoured by low substrate hardness and high coating thickness. Whereas damage of type 2 and 3 are favoured by low coating thickness, while the influence of substrate hardness seems to be

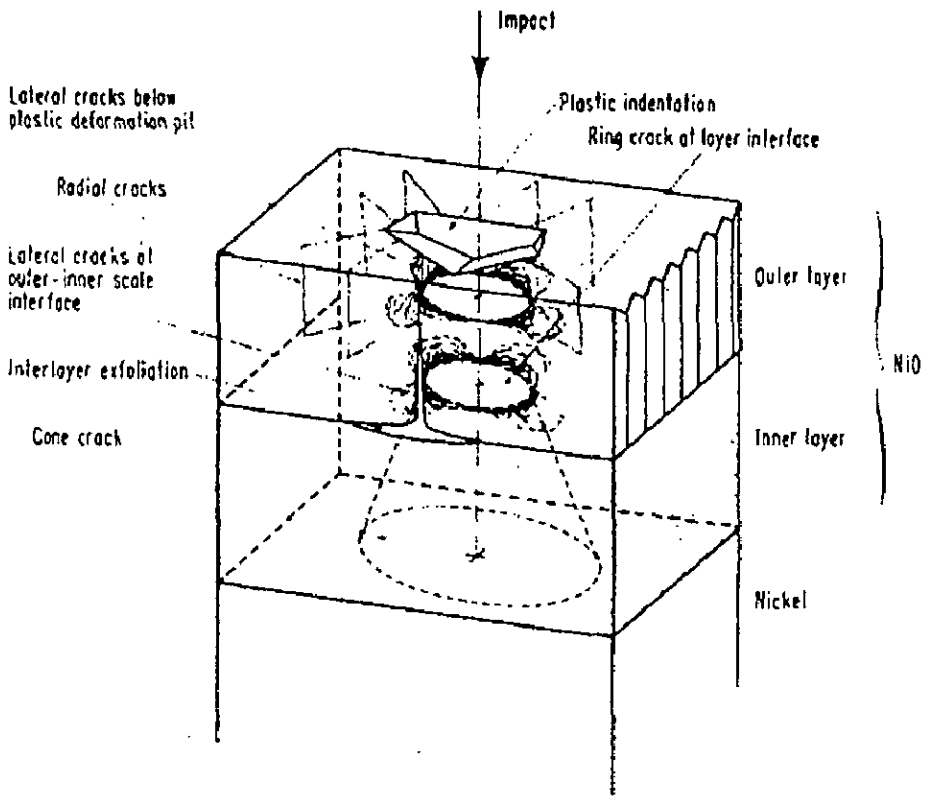

Fig. 2.4 Schematic diagram illustrating the types of cracking events that occur during loading by single particles **(Zambelli and Levy, 1981)**.

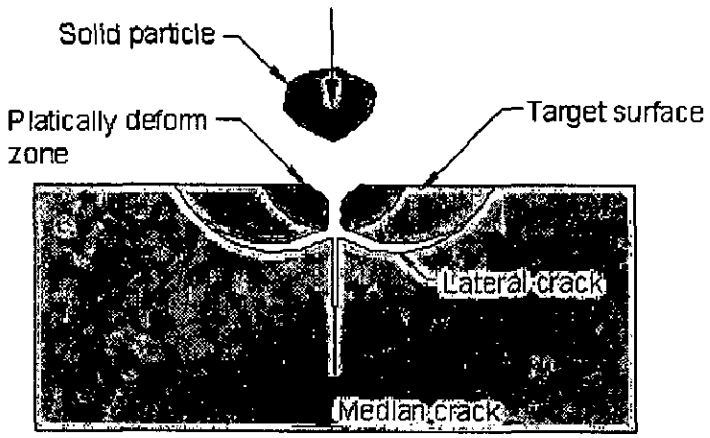

Fig. 2.5 Simplified schematic drawing of crack formation from a single particle impact **(Wensink and Elwenspoek, 2002)**.

more complex: the relative occurrence of both types of damages increase with increasing substrate hardness for the thinnest coating, but no clear relationship can be discerned for the other coating thicknesses. It is concluded that on increasing the particle dose, adjacent crack systems in the coating interact and TiN fragments gets detached. They proposed that numbers of particle impacts are needed to produce this effect and referred this coating removal mechanisms as erosive fatigue wear.

Further, reported the significant contribution of cutting erosion to the erosion wear. Also lip formations of coating/substrate composite material originating from type 3 damage are removed by subsequent particle impacts. They proposed that at a certain critical particle dose TiN fragments, 10-50μm in diameter, detached by interfacial spalling. The spalling takes place at the Ti/TiN interface, i.e. not along the high speed steel/ Ti interface. Once initiated the spalling mechanism proceed primarily by the detachment of coating fragments from the rim of the initial spalling. Finally they concluded that interacting spalling rapidly causes complete coating failure over a large area by this spalling wear mechanism.

Wood et al (1997) studied the erosion resistance of a WC-Co-Cr (detonation gun) thermally sprayed coating under slurry erosion conditions at jet velocities of 16.4 and 26.0 m/s and concluded the two erosion mechanisms:

1) Microcutting and microploughing of the relatively soft binder materials result in the harder particles being exposed. These are then gouged out by the impact of eroding particles and cause further cutting on removal. They concluded that this appeared to be a less significant mechanism, although important at lower kinetic energies and lower impact angles.
2) The particle impact results in the coating experiencing a fluctuating stress which allows the propagation of subsurface cracks by a fatigue mechanism. Cracks initiated at defects in the coating and when these cracks interlink, large areas of coating were removed in sizes 10-400 μm in diameter. According to them the splat geometry was found to determine the crack growth path with existing coating defects such as cracks perpendicular to the substrate interface cause significant material removal. Further they concluded that this mechanism was found to be dominant at higher angles of incidence and for higher kinetic energies.

2.1.1.4 *Erosion Mechanisms at High Temperature*

Several studies concerning the interaction between erosion and a surface oxide film have been conducted **[Barkalow and Pettit (1979), Kang et al (1985), Stephenson et al (1985, 1986), Stephenson and Nicholls (1990), Wright et al (1991) and Stack et al (1991)]**. Mechanisms of material removal have been proposed which include oxide fracture and chipping, oxide spallation at the metal-oxide interface and plastic deformation of metal substrate resulting in both oxide and metal loss.

Such interactions have been summarised by **Barkalow and Pettit (1979)** using schematic diagrams typical of Fig. 2.6 which shows that for low energy particles, scale fracture does not occur and therefore metal recession rates will be determined by the oxidation process only. As the impact energy is increased and damage to the oxide scale occurs, an interaction between erosion and oxidation will result in accelerated metal loss. At still higher impact energies, deformation of the substrate produces metallic erosion. It is suggested that for materials to operate successfully at high temperatures a key requirement is the formation and maintenance of a protective oxide scale. The particle impingement conditions for which oxide failure occurs must therefore be quantified if material behaviour is to be predicted.

Kang et al (1987) had suggested that the exact behaviour and the resulting morphology of the metal surface depend on the severity of erosion and the oxidation rate (Fig. 2. 7). Pure erosion of the oxide dominates at high temperatures where the oxidation rate is high, while pure erosion of metal occurs at low temperature. In the erosion-enhanced oxidation regime a steady-state oxide thickness develops, with the rate of oxide formation equal to the rate of scale removal by erosion. When the erosion rate is high as compared with the scaling rate, the oxidation-affected erosion regime is entered and under these conditions a continuous oxide scale is unable to form and the metal surface comprises a composite layer of oxide, embedded erodent fragments and extruded metal. **Rishel et al (1990)** modified the above model by subdividing the 'erosion-enhanced oxidation regime' into three categories: Type I, Type II and Type III, as illustrated in Fig. 2.8. The intermediate category, Type I, is the regime in which the thickness loss due to erosion is balanced by the thickness gain due to oxidation. This sub-division was carried out on the basis of microscopy of the eroded surfaces in the various corrosion environments.

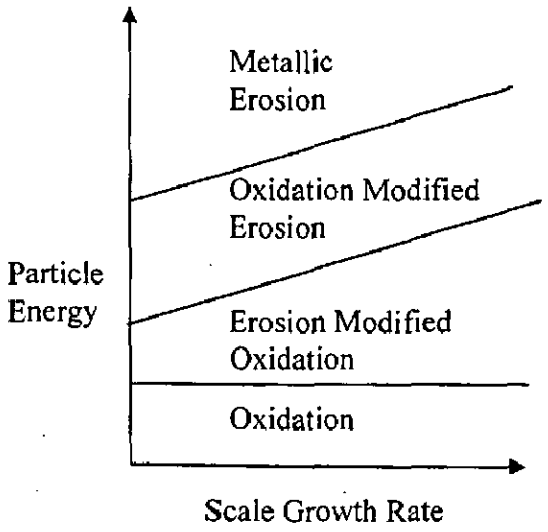

Fig. 2.6 Schematic diagram showing the types of degradation that can occur under conditions of combined oxidation-erosion (**Barkalow and Pettit, 1979**).

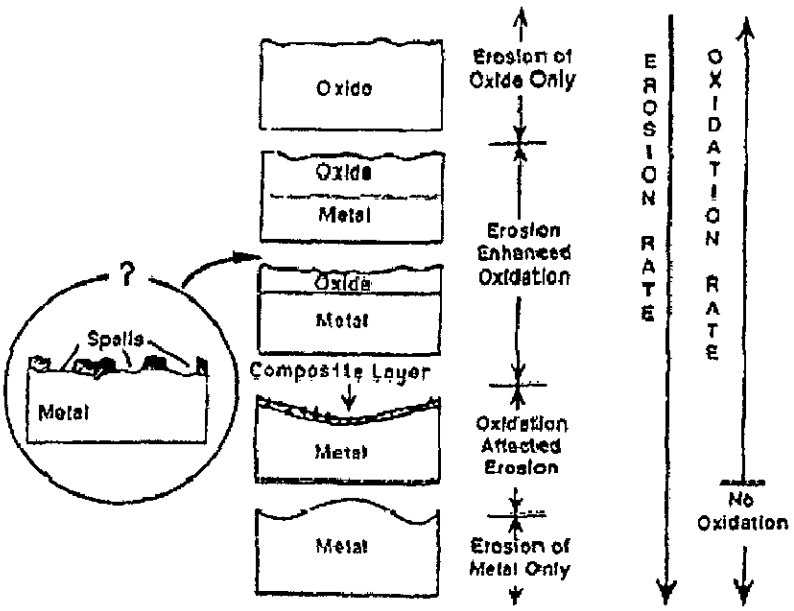

Fig. 2.7 Classification of erosion-corrosion (**Kang et al, 1987**).

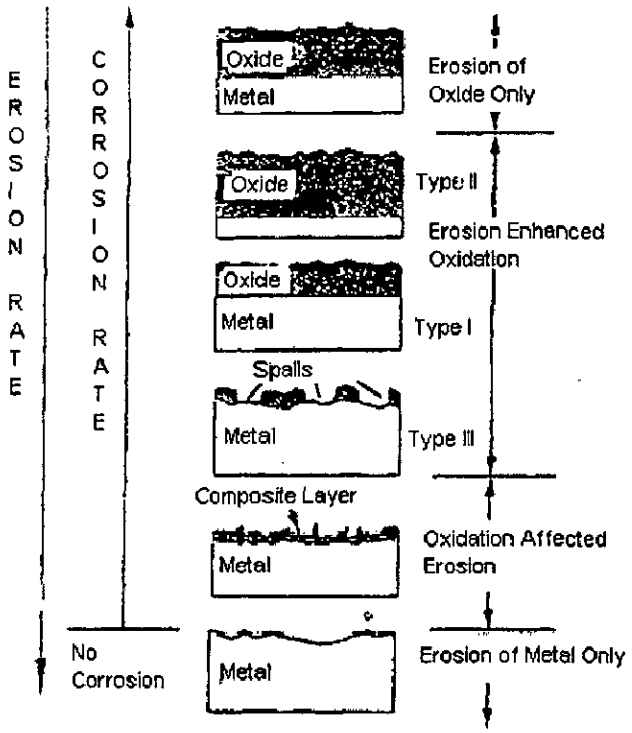

Fig. 2.8 Classifications of erosion-corrosion (**Rishel et al, 1990**).

Hancock and Nicholls (1988) assumed in the first instance that oxide scales respond in a brittle manner and therefore their fracture behaviour must be quantified whereas erosion of the metallic substrate is controlled by localised plastic deformation and therefore high temperature strength must be considered. They proposed that the fracture stress of oxides can be determined using acoustic emission or resonant frequency techniques and have demonstrated the importance of both temperature and scale thickness. They estimated the localised deformation behaviour of the metallic substrate from hot hardness testing. They concluded that structural, high temperature alloys such as the nickel base superalloys maintain their strength up to temperatures of 700°C however, at higher temperatures result in a sharp reduction in strength **(Stephenson and Nicholls, 1990).**

Stephenson (1989) and Stephenson and Nicholls (1993) have proposed four regimes of erosion (Fig. 2.9). According to them when the impact conditions are such that no damage results, Fig. 2.9 (a), metal loss will be predicted from the standard oxidation kinetics. Further if the erosion damage is highly localised at the surface such that only loss of oxide occurs, for example by localised fracture and chipping, Fig. 2.9 (b), but the scale remains protective, then metal loss can be expected to increase due to enhanced oxidation. In this oxide dominated regime the boundary conditions for the on-set of damage require that the fracture stress of the oxide is exceeded and that the oxide behaves as though it were of infinite thickness. They estimated this latter requirement from the modelling work of **Halling and Arnell (1984)** and depends on the ratio of the particle-target contact radius "*a*" and oxide thickness "*x.*" The analysis showed that the substrate has no influence on the scale surface properties when $x/a > 0.23$.

Further they proposed that the oxide modified regime (Fig. 2.9 c) occurs when the fracture strength of the oxide is exceeded and x/a is below 0.23, i.e. for relatively thin oxide scales. They reported that damage morphologies vary from through thickness scale fracture to oxide spallation, although damage to the substrate is not observed. They suggested that in this regime metal loss rates are likely to be high since the surface oxide is non-protective and linear kinetics prevails.

According to them as the relative thickness of oxide is reduced, the maximum normal force at the oxide-metal interface will increase and if the particle velocity is sufficiently high, plastic deformation of the substrate will occur. It is proposed that in this substrate dominated regime (Fig. 2.9 d) material removal is primarily from the substrate with a contribution from the surface oxide. Metal loss rate is determined by the

erosion resistance of the metal substrate and oxidation makes only a minor contribution to the degradation process. They suggested that an interesting condition can exist where the oxide film does not fracture and its effect is to reduce the force applied to the substrate. Thus, when this applies the erosion rate will be reduced. They concluded that from knowledge of the particle, oxide and substrate properties and the impact dynamics, the boundary conditions between each regime can be quantified by considering the contact conditions at the oxide surface and how these change with oxide thickness. They also reported that the conditions for scale fracture can be determined by calculating the maximum radial tensile stress at the oxide scale surface for a given impact event and comparing this with the fracture stress values. They estimated the contact radius assuming Hertzian behaviour with the 'effective' elastic properties of the surface which are determined using the **Halling and Arnell (1984)** analysis, which could be used to evaluate both the oxide dominated and oxide modified regimes. There are two important factors which differentiate the high temperature erosion of metals from their low temperature behaviour **(Stephenson and Nicholls, 1995)**:

(i) the surface properties of the metal may change significantly with time due to the growth of a surface oxide. The rate of growth of the oxide is a function of the temperature.

(ii) the mechanical properties of oxide and metal may change with temperature and time.

Several other researchers have reported mechanisms of erosion for various metals, alloys and coatings under different test conditions and are been summarised in **Appendix A.1.**

2.1.2 Factors Affecting Erosion

It is well understood that the erosion rates are affected by various factors **[Kosel (1992), Levy (1995), Sundararajan (1984) and Tilly (1973)]**. Some of these important factors are impact velocity, impact angle, particle concentration, particle shape, particle size, particle density, particle friability, temperature, particle hardness, material hardness, toughness, microstructure, chemical composition etc. The various factors affecting erosion are summarised in Appendix A.2.

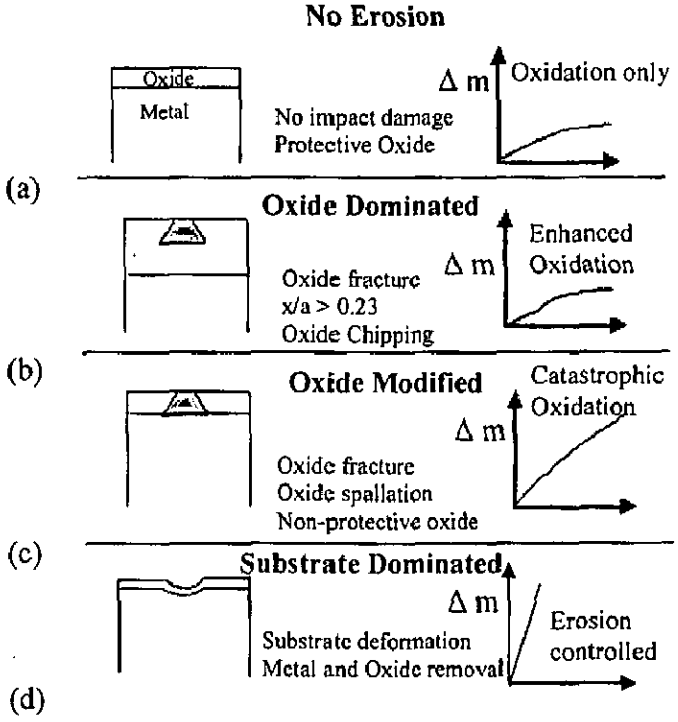

Fig. 2.9 Summary of erosion regimes observed at high temperatures (**Stephenson ,1989 and Stephenson and Nicholls, 1993**).

2.1.3 Types of Erosion Test Rig

There are number of designs of erosion rig in use around the world (**Wood and Wheeler, 1998**). These rigs fall into four main types (**Soderberg et al, 1981**):

1. The sand or gas-blast rig
2. Reciprocating liquid slurry loop
3. Centrifugal accelerator
4. Whirling arm rig

In the gas-blast rig, particles are introduced into a fast-moving gas-stream and accelerated down an acceleration tube before impact with the test piece. While in slurry type, gas-stream is replaced by water-stream. In these test rigs the motion of gas and water stream are linear. Whereas the centrifugal accelerator and whirling arm rig involve circular motion. In the centrifugal accelerator the test samples are held stationary at the rim of the rotor and the sand particles are fed into the center being accelerated radially onto the target surface. Here test duration is often long. In whirling arm rig, the samples are mounted onto the end of arms, which are attached to a rotor. This is rotated at high speed and erodent is fed onto the target surface.

2.1.4 Erosion Rate

As per ASTM standard erosion value is the volume loss of specimen material divided by the total mass of abrasive particles that impacted the specimen (mm^3g^{-1}) (**ASTM Standard G75-96**). Normalized Erosion Rate is calculated by dividing the erosion value of the specimen by erosion value of reference material (**Hansen, 1979**). According to **Tabakoff and Shanov (1995)** the erosion rate is defined as the ratio between the change in the sample mass and the mass of the impacting particles. **Hansen (1979)** compared the erosion rates of alloys, ceramics, and cermets. He proposed that the order of material rankings would change with any change of variables such as velocity, particle type or size, and angle of impingement. He performed the erosion tests using 27 μm Al_2O_3 particles at normal incidence and 170m/s at 20°C and 700°C in nitrogen. Hansen also conducted the tests with a gas-jet erosion apparatus in which particles are fed from a hopper into a nozzle, where they mix with and are accelerated by a flowing gas stream (ASTM G76). He normalized the erosion rates by defining the relative erosion factor (REF) as specimen volume loss divided by that of a standard material,

stellite 6B. He concluded that REFs of most of the metals were similar at 20°C and 700°C, typically within about 20%.

2.2 EROSION IN ENERGY GENERATION AND COAL GASIFICATION SYSTEMS

Many power plant engineers, as well as researchers of industrial wear problems are of the opinion that ash impacting erosion wear is the principal cause of boiler tube failure in economiser, primary superheater and reheater groups of boiler tubes (**Suckling and Allen, 1995**).

According to them wear of boiler tubes in pulverized fuel power stations by erosion is a serious problem that often leads to unscheduled and costly outages. They reported that the combustion products of pulverised coal for the purposes of generating heat in a thermal power station are: coarse ash, fly ash, as well as the accompanying flue gases. The coarse ash, or boiler bottom ash consists of 10-20% of the total ash load and comprises of particles ranging in size between 0.075 μm to as large as 500 μm. The fly consists of 80-90% of the total ash load, and has a particle size range from 2 μm to 500 μm. As suggested by them the term "boiler bottom ash" is the coarse ash that drops out of the bottom of the boiler under the influence of gravity after combustion, whilst the fly ash entrained in the gas is ducted out. Further the nature of the fly ash is such that at high temperature it will form deposits on the boiler tubes in its path. However, when passing through the latter stages of the boiler where the temperatures are substantially lower, the fly ash displays rebound as opposed to captive behaviour. They proposed that this causes localised erosive wear that can lead to unscheduled and costly boiler tube failures.

Simms et al (1995) reported that the development of coal-fired combined cycle power generation systems is receiving considerable worldwide interest. These systems, utilising both steam and gas turbines, have many advantages over conventional coal-fired power generation systems, which include increased efficiency of the electricity production and lower environmental emissions (specifically CO_2, SO_x and NO_x). According to them the influence of materials on the development of these systems can be considerable as it is necessary that components have adequate lifetimes in their operational environments. They further added that successful development and commercialisation of these new systems require that all the component parts are

manufactured from appropriate materials and that these materials give predictable in-service performance.

In coal-fired power stations, about 20% of the ash produced in the boilers is deposited on the boiler walls and superheater tubes **(Mbabazi et al, 2004)**. This deposited ash is subsequently discharged as slag and clinker during the soot blowing process. Whereas the rest of the ash is entrained in the stream of flue gas leaving the boiler. They reported that the ash-laden flue gas passes through the narrow passages between the corrugated steel plates that constitute the air heater elements. Then the ash particles collide with the surfaces of the steel air heater elements and material is eroded from the surfaces. Further in advanced stages of erosion, the plates become perforated. The air heater elements fail once they cannot maintain their structural integrity. According to them such erosion, together with the processes of blocking, fouling and corrosion, shortens the service life of the air heater elements. Once this happens, the power station unit has to be shut down in order to replace the damaged air heater elements. The resulting penalty is not only the cost of replacing the elements but also the cost of stoppage of power production. They proposed that it is desirable to predict the rate of erosion of the air heater elements in order to plan systematically for the maintenance or replacement of the air heater elements to avoid forced outages.

They further opined that in large coal-fired power stations, pulverised coal is burnt in the burners of the boilers. To improve upon the overall thermal efficiency of the boiler plant, heat exchangers are used to extract residual heat energy from the flue gas before it is released to the atmosphere and to transfer it to the combustion air supplied to the boiler burners. According to them part of the air supplied, the 'primary air', is fed to the coal mills and is used to dry the pulverised coal and to transport the coal to the burners in the furnace. Whereas the greater part of the air supplied, the 'secondary air', is used in burning the coal. Further the heat exchangers used for preheating the combustion air are of the rotary regenerative type, commonly referred to as "air heaters". While these air heaters are prone to erosion, corrosion, blocking and fouling, particularly if the coal is of relatively poor quality, as is often the case in large South African power stations (ash content typically above 25%).

Krishnamoorthy et al (1993) reported that the coal used in Indian power stations has large amounts of ash (about 50%) which contains abrasive mineral species such as hard quartz (up to 15%) which increase the erosion propensity of coal. They also reported that a performance review of thermal power stations indicated that erosion

problems contribute significantly towards partial unavailability of power in India. They added that in coal-fired boilers, the pulverized fuel (PF) is transported to the boiler using a network of PF pipes. Components such as PF bends and elbows, multiple-port outlets, the orifice and the burner assembly are prone to high erosion wear, especially in certain locations oriented favourably for impacting wear particles.

Heat exchanger tubes immersed within a bubbling fluidized bed combustor (BFBC) often experience unacceptably high levels of thinning on their outer diameter and this loss in wall thickness is typically concentrated on the lower half of tubes and is frequently termed metal wastage **(Stringer and Wright, 1987 and MacAdam and Stringer, 1995)**. They reported that this is consistent with aggregate impacts or any process associated with an upward particle flow. According to them, the wastage is primarily due to mechanical wear by bed particles in contact with the tubes, though an oxidation or corrosion component cannot be ruled out. They proposed that there are several macroscopic bed conditions that lead to particles with sufficient energy to cause wear. They opined that some of these are related to characteristics of the bed design or individual component failures, and others are related to intrinsic or unintentionally induced long-range flow patterns within the bed. Further they suggested that there is a general consensus however, that some of the worst wear is associated with energetic events intrinsic to bubbling bed combustors and that these events are associated in some way with bubbles themselves. They further reported that bubbles rising through tube banks are known to throw highly energetic dense aggregates of defluidized particles against tube bottoms. Also, voids, which can form beneath tubes as the entire bed undulates, will collapse against the underside of tubes with a similar effect. They concluded that the bottom of a tube is intermittently hammered by particle aggregates that strike and slide across the surface before dropping away.

2.3 BEHAVIOR OF VARIOUS METALS AND ALLOYS IN VARIOUS EROSIVE CONDITIONS

The solid particle erosion behavior of various metals and alloys at elevated temperatures varies depending on whether the tests are conducted below or above about 0.35 Tm, where Tm is the melting point of the eroding material **(Singh & Sundararajan, 1990)**. It was reported that at test temperatures below about 0.35 Tm or at higher temperatures with an inert atmosphere, the erosion behavior of ductile materials

appears to be deformation controlled as at room temperature. Further they suggested that at higher temperature due allowance should be made for the alteration of mechanical behavior of the eroding material as caused by recovery and recrystallization. They added that much of erosion data in these regimes indicates very clearly that the velocity and impact angle dependence of the erosion rate at elevated temperatures is similar to that obtained at room temperature. Also **Singh and Sundararajan (1990)** have demonstrated that the mechanism of erosion under such conditions is identical to that obtained at room temperature. They reported that beyond a test temperature of about 0.35 Tm the oxidation of the eroding material becomes important and thus the nature of the interaction between erosion and oxidation becomes relevant and should be necessarily incorporated in the erosion model.

2.3.1 Erosion of Superalloys

The erosion behaviour of superalloys had been reported by number of researchers using their own laboratory test rig. The effect of impact angle, velocity, temperature and many other parameters were found to be affecting the erosion rate of superalloys. The mechanism of erosion of superalloys at room temperature and elevated temperature is ductile in nature as reported by numbers of researchers.

Wright et al (1986) reported that in the case of the nickel-, iron- and cobalt-based alloys a comparison of the erosion behaviour at elevated temperatures in an inert atmosphere (no oxidation) and in an oxidizing atmosphere (E-O regime) indicates that the erosion rate is always higher in the E-O regime and also that the difference between the erosion rates (E and E-O conditions) increases with increasing hardness of the eroding material.

Restall & Stephenson (1987) reported the erosion and corrosion behavior of aluminized Mar M002 and IN738. They found that under the erosion/ corrosion conditions encountered for example in a marine gas turbine, the use of surface coatings will lead to considerable improvements in component lifetime and their behaviour is dependent on the impurity level, particle loading and temperatures of the hot gas stream. Damage morphologies on components reflect the changes which occur in the surface oxide film and the coating properties. According to them the particular importance are of the oxide plasticity and the ductile to brittle transition temperature range of the coating. They concluded that the greatest benefits from the use of surface coatings under erosion

conditions are realized at high temperatures (> 850°C for aluminide type coatings) and in corrosive environments.

The erosion behaviour of a number of alloys normally used for their abrasive wear resistance or their high strength at elevated temperatures was investigated by **Ninham (1988)**. He tested the alloys in two conditions; the annealed condition and the strengthened condition, by either mechanical or heat treatment as appropriate for the alloy. He proposed that the aging or work-hardening treatments carried out on the high temperature alloys had essentially no effect on erosion rates. Further the abrasion-resistant alloys generally eroded at higher rates than the high temperature alloys. According to him the carbides were deleterious to erosion resistance. He suggested the general mechanism seen to be one of gouging (type I cutting, as defined by Hutchings (1979)) in which material is raised above the mean surface, followed by deformation during subsequent impacts and ultimately removal of the deformed volume. Further there will be considerable variation in the number of impacts required to remove any given volume of material, according to the orientation and shape of the particle and its contact point relative to the displaced material. He proposed that final removal may involve cutting, strain, to failure or some combination of these two processes. He concluded that the erosion response of high strength materials, particularly when eroded by quartz, is only weakly dependent upon impact angle. Most of these materials give rise to rather flat erosion vs. angle plot, with a peak at roughly at 60° impact. He has indicated from the experimental evidence and theoretical considerations that very high temperature excursions of very small duration occur on eroding surfaces; temperature rise is greater for high strength alloys than for low strength alloys. Further the high temperature of a deforming volume, in combination with extremely high strain rates, lead to viscous flow and is also only weakly sensitive to the alloy's physical properties (composition). It was proposed by them that high strain rate, short contact time, and essentially adiabatic nature of erodent particle are responsible for the near-constant erosion rates of the high temperature alloys. He suggested that the impacts must be either entirely elastic or plasticity limited to the erodent, since impulsive pressures are generated during impacts which may be considerably greater than the yield pressure of either erodent or target.

Chinnadurai and Bahadur (1995) investigated the erosion mechanisms and effect of temperature (240°C to 800°C) on two heat resistant superalloys, Haynes-188 and Waspaloy at the impingement velocity of 50m/s. They have shown flake formation and ploughing as two types of erosion mechanisms. According to them flake formation

occurs when the surface undergoes plastic deformation because of the repeated impacts of erodent particles. These impacts produce a fine layered structure. The extremities of these layers are severely work hardened and so develop radial cracks. Successive particle impacts break these outer layers thereby causing the erosive loss of material. Flakes are formed during impacts predominantly at high impingement angles and low operating temperatures. They reported that in a ploughing process, erodent particles penetrate the surface and travel a short distance thereby tearing the substrate and removing the material. Ploughing occurs predominantly at high operating temperatures. It was concluded that the surface eroded in the 24-200°C temperature range exhibited predominantly the flaky appearance while those eroded in the 500 to 800°C range had more of the ploughing effect.

Tabakoff (1995) studied the high temperature erosion resistance of nickel-based MAR-M246 and cobalt- based X-40 superalloys in an erosion wind tunnel (high temperature), which simulates the operating conditions of steam and gas turbines. He concluded that these superalloys showed maximum erosion rates at 45° impingement angle. Further both alloys showed good erosion resistance for turbomachinery uses exposed to high temperatures and velocities. **Tabakoff (1999A and 1999B)** also investigated the erosion behaviour of INCO 718, Waspaloy, INCO 738 and MAR-246. The effects of the impact angle, particle velocity and temperature on the erosion rate of these superalloys have been experimentally investigated by him and it was established that these superalloys exhibit ductile erosion pattern and the erosion rate was found to be strongly dependent on the particle velocity. He concluded that the alloy INCO 718 wears less at elevated temperatures, while the Waspaloy deterioration is enhanced by raising the temperature. **Shanov et al (1997)** investigated the erosion behavior of a nickel-based superalloy Waspaloy. They reported that Waspaloy behaved as a ductile material because the maximum erosion was between 30° and 45° impact angle. They also found that the sample temperature has a significant effect on the material erosion rate. They further inferred that the erosion resistance of the Waspaloy decreases at elevated temperatures and was proportional to the particle impact velocity to the power n. They had also shown that the size and shape of erodent affects the erosion of materials. The investigators also studied the effect of mass of erodent particles on the erosion rate of TiC coating on Waspaloy.

Erosion rates of NiO scale having two different thicknesses (100μm and 20μm) were determined as a function of impact velocity, impact angle and erodent size and compared with that of substrates obtained by machining the oxide scale **(Roy et al, 1998)**.

They reported that under the condition when deformed zone is confined within oxide scale the erosion rate of the oxide scale is higher than the erosion rate of the substrate by four times during normal impact and by two times during oblique impact. According to them transition from metal erosion to oxide erosion occurs slowly through a regime where erosion takes place from a deformed layer containing the oxide scale and the substrate metal. Further this transition takes place as the ratio of the oxide thickness to the depth of deformation increases from 0.5 to 3.0.

The erosion-corrosion degradation behaviour of cobalt-based alloy along with nickel-based tungsten carbide and a tungsten carbide copper-based solid cermet have been investigated by **Reyes and Neville (2003)**. It is proposed that under severe impingement conditions the cobalt based alloy shows superior erosion-corrosion resistance to the two metal-matrix composites.

2.3.2 Energy Generation Systems

Tiainen et al (1987) have exposed a variety of materials in a 14 MWth AFBC (Atmospheric Fluidized Bed Combustors) in Finland for 1500 hours. The surface temperature of the tube was between 400 and 450°C. They studied one set in the splash zone of the bed and the other was higher up, in the free board. They concluded that all the samples in the splash zone suffered weight loss; plasma sprayed alumina (0.3 mm thick) and zirconia (0.4 mm thick) coatings were quite severely damaged, being totally worn away from the bottom of the tube. The weight loss of plasma-sprayed FeCrAlY alloy (0.25 mm thick) was ≈ 7 mg/cm^2 after 1500 hour exposure. For comparison, Incoloy 800H and 310 stainless steel showed higher weight losses, with slightly lower losses being measured for 347 stainless steel, while the weight loss for 253 MA, an austenitic stainless steel, was about half that of the FeCrAlY coating. Whereas they reported that the samples in the freeboard showed weight gain resulting from oxidation. They observed some spalling of the plasma-sprayed zirconia coating, caused by oxidation at the metal-coating interface.

Levy et al (1989) exposed a number of in-bed tube sections of different steel alloys in the Point Tupper atmospheric fluidized combustor (AFBC) by the Canada Center for Mineral and Energy Technology (CANMET) at temperatures from 450 to 850°C for time periods from 1000 to 10000 hours. The authors reported the upper surfaces of in-bed tubes in FBCs have a segmented scale morphology and resulting in

lower metal wastage rates than the bottom surfaces which lose material by a faster, scale-spalling mechanism.

The combined erosion-corrosion behaviour of a group of chromium containing steels used in chemical process and energy production equipment was investigated by **Levy and Man (1989)**. The tests were carried out in an elevated temperature nozzle-type erosion tester at 850°C and particle velocities of 35 and 70 ms^{-1}. The Al_2O_3 erodent particles of round-shaped (100-150 μm) were impacted at a particle flux of 2.5g/min. They concluded that erosion of oxide scale formed on the surface was the dominant surface degradation mechanism on all of the steel at all tests conditions.

Stack et al (1991, 1992) exposed the pre-oxidized alloys in the simulated fluidized bed environment. Specimens of Incoloy 800H and FeCrAlY alloys were preoxidized to produce chromia and alumina-rich surface scales respectively. The treatment was carried out in air, oxygen or H_2/H_2O and specimens were subsequently exposed at 500°C in the fluidized bed apparatus for up to 168 h. The specimen velocity was 1.9 ms^{-1} and the bed material consisted of rounded silica particles with diameter of ≈ 200 μm. They found that the scales formed in air and oxygen were up to 6 μm thick and were rich in iron oxides (for the Incoloy 800H substrate). The 1-2 μm thick scales which formed in H_2-10%H_2O were the most resistant to particle impacts, probably due to greater adherence and lower stresses. They reported that the lower wastage of the preoxidized FeCrAl alloy compared with the preoxidized Incoloy 800 H does not necessarily indicate that alumina scales are more resistant to erosion-corrosion than chromia scales; and this result was probably due to a lower wastage rate for the FeCrAl alloy substrate than the Incoloy 800 H substrate, associated with their initial (or transient) oxidation rates.

Stack et al (1992) also exposed the samples of ground Incoloy 800 H and preoxidized alloy over a range of temperatures (Fig. 2.10) in the fluidized bed test rig. They reported that after 24 hour the wastage of the preoxidized alloy typically fell with increasing temperature, while the ground alloy exhibited the characteristic maximum in material loss at intermediate temperatures. They found that the mass loss from the preoxidized steel after 72 h was similar to that of the unprotected alloy exposed for 24 h, although the loss was slightly less at lower temperatures. It is likely therefore that most of the preformed scale had been removed after 72 h. According to them, at lower temperatures, erosion thinned the preformed scale which, once removed, caused the

material to behave as the ground alloy. Whereas at high temperatures, the preoxidized scale was capable of absorbing more stress by plastic deformation and showed some ability to self-heal by oxidation. The authors suggested that the scale may deform initially, developing a 'glaze'-like surface (particularly at higher temperature), followed by initiation of cracks on, or beneath the surface of the oxide. According to them the scale failure might have resulted from the linking of cracks within the oxide, followed by local spallation. They proposed preoxidation to be beneficial only where the erosion is corrosion-dominated (i.e. at higher temperatures and lower velocities). Further for metal temperatures < 500 °C, where the alloy shows higher rates of loss, preoxidation is likely to provide only short-term protection. While preoxidation may be useful at metal temperatures close to those where a protective oxide will grow, at lower temperatures such a layer may be of limited use.

Wang (1996) evaluated the erosion-corrosion resistances of HVOF Cr_3C_2-NiCr coating and several other thermal sprayed coatings in an elevated temperature blast erosion nozzle tester using varieties of bed ash and fly ash as erodent. He reported that the ashes retrieved from biomass-fired CFBCs demonstrated high erosivity due to high concentrations of SiO_2 and the presence of chemically active compounds in the ash. The author also observed that in elevated temperature erosion tests (300°C and 450°C) involving fly ashes with high concentrations of chemically active compounds bearing Cl, K, Na, S, and P, the major mechanism of material wastage was erosion-stimulated corrosion and corrosion-accelerated erosion.

Hidalgo et al (2001A) reported that erosive, high temperature wear of heat exchanger tubes and other structural materials in coal-fired boilers are recognized as being the main cause of downtime at power-generating plants, which could account for 50-75% of their total arrest time. According to them maintenance costs for replacing broken tubes in the same installations are also very high, and can be estimated at up to 54% of the total production costs. Further high temperature oxidation and erosion by the impact of fly ashes and unburned carbon particles are the main problems these applications. Therefore he suggested that the development of wear and high temperature oxidation protection systems in industrial boilers is a very important topic from both engineering and an economic perspective. They further reported that the free oxygen content in power plant boiler atmospheres is sufficient to account for a combined erosion-corrosion process, consisting of an oxidizing gas at elevated temperature carrying erosive fly-ashes which impact against metallic surfaces. Moreover these

erodent particles can deposit or embed themselves on the test surface in quite significant quantities, and chemical reactions of erodent particles and oxide scales can develop on the eroding surface, so that the erosion rate is also dependent on the oxidation kinetics and erodent particle reactivity.

Norling and Olefjord (2003) have investigated the erosion-corrosion behaviour of four steels (Fe2.25Cr1Mo, Fe9Cr1Mo, AISI 304, 353 MA) and one Ni-base superalloy (Inconel 625). The alloys were exposed in a test rig at 550°C in air for one day, one week and three weeks at the particle velocity of 1.2 ms^{-1}. The exposure temperature of 550°C was chosen because it is a target temperature for eroded parts in new and future combustion plants, e.g. superheater tubes positioned within the loop seal of a circulating fluidized bed combustor as reported by **Nafari and Nylund (2002)**. They reported the measured wastage of the alloys was in the range of 58-270 μm/1000 h and the oxide formed during erosion was up to 30 times thicker than the oxide formed during pure oxidation. They proposed that enhanced oxidation during erosion was caused by inward transport of molecular oxygen through cracks and other defects created by particle bombardment. **Norling and Olefjord (2003)** have also proposed a model for oxide formation and cracking of the oxide for the higher alloyed Fe- and Ni-based alloys exposed to the above conditions (Fig. 2.11). They concluded that the strong oxide forming elements (Cr and Mn) were enriched in the thin oxide formed on the surface of the non-eroded areas. Whereas they concluded that the thick crack oxide products were present on the eroded area of the Fe-based alloys. It was found that steady state is reached within 1 day (except for the Fe2.25Cr1Mo alloy). Further chromium and manganese were not enriched in the oxide and corresponds to the composition of the alloy. They reported the same behaviour for initial oxidation of these types of alloys at this temperature. They concluded that the composition of the oxide formed during short exposure reflects the alloy composition reported by **Olefjord (1975)**. They further reported that during erosion–corrosion, fragments of alumina particles are embedded into the surface oxide. It was found that the alumina particles are partly coated with erosion products from the rig. This fact made the quantitative analysis of the oxide formed on the Inconel 625 relatively complex.

Hou et al (2004) reported that above 500°C, wastage is higher and is clearly controlled by oxidation, where an oxide layer would grow to a limiting thickness, spall under impact, and then reform. At intermediate temperatures, 400-500°C, wastage is

very sensitive to the level of fine sub-micron dust within the bed and to the bed composition. Rapid decrease in wastage occurs when the condition allowed the development of a protective deposit layer that consisted of sub-micron deformable bed particles on the specimen surface. These particles deposited on bulk bed particles to form an encasing layer. This material then transfers to the specimen surface during particle impact. If the deposit layer can build up in thickness faster than the erosion processes, it will protect the underlying metal from wastage. The condition at which this layer forms depends on the amount of fine dust particles retained in the bed, which is closely related to the composition of the bed, the specimen and bed temperatures and the oxidation rate of the specimen.

2.4 ADHESIVE OR SLIDING WEAR

According to **Bhunshan (2002), adhesive or sliding wear** occurs when two nominally flat bodies are in sliding contact whether lubricated or not. Adhesion (or bonding) occurs at the asperity contacts at the interface and these contacts are sheared by sliding, which may result in detachment of a fragment from one surface and attachment to the other surface. As the sliding continues, the transferred fragments may come off the surface on which they are transferred back to the original surface, or else form loose wear particles. Some are fractured by a fatigue process during repeated loading and unloading action resulting in formation of loose particles. He reported that **abrasive wear** occurs when asperities of a rough, hard surface or hard particles slide on a softer surface and damage the interface by plastic deformation or fracture. There are two general situations for abrasive wear. In the first case, the hard surface is the harder of two rubbing surfaces (two-body abrasion), for example, in mechanical operations, such as grinding, cutting and machining; and in the second case, the hard surface is a third body, generally a small particle of abrasive, caught between the two other surfaces and sufficiently harder that it is able to abrade either one or both of the mating surfaces (three-body abrasion), for example, in free-abrasive lapping and polishing. In many cases, the wear mechanism at the start is adhesive, which generates wear particles that get trapped at the interface, resulting in a three-body abrasive wear.

Dry sliding wear of various metals, alloys and coatings have long been the object of research. Intensive investigations have been conducted by various investigators to

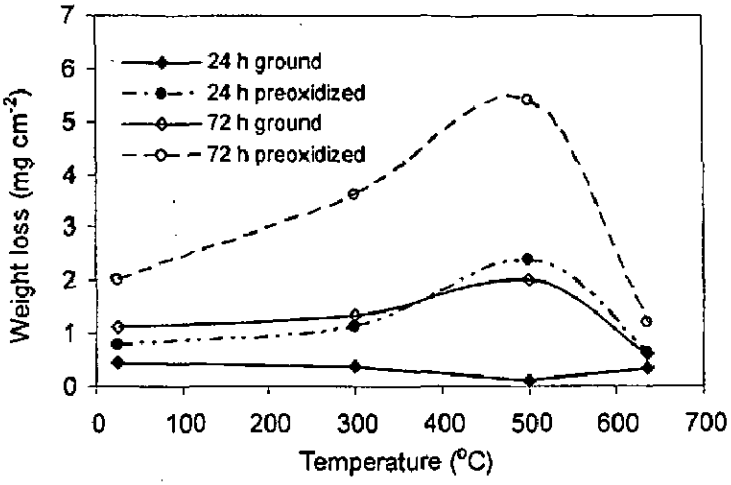

Fig. 2.10 Weight loss against temperature for IN 800 H and IN 800 H preoxidized in H_2-10% H_2O after exposure for 24 and 72 h in the UMIST erosion-corrosion apparatus (**Stack et al, 1992**)

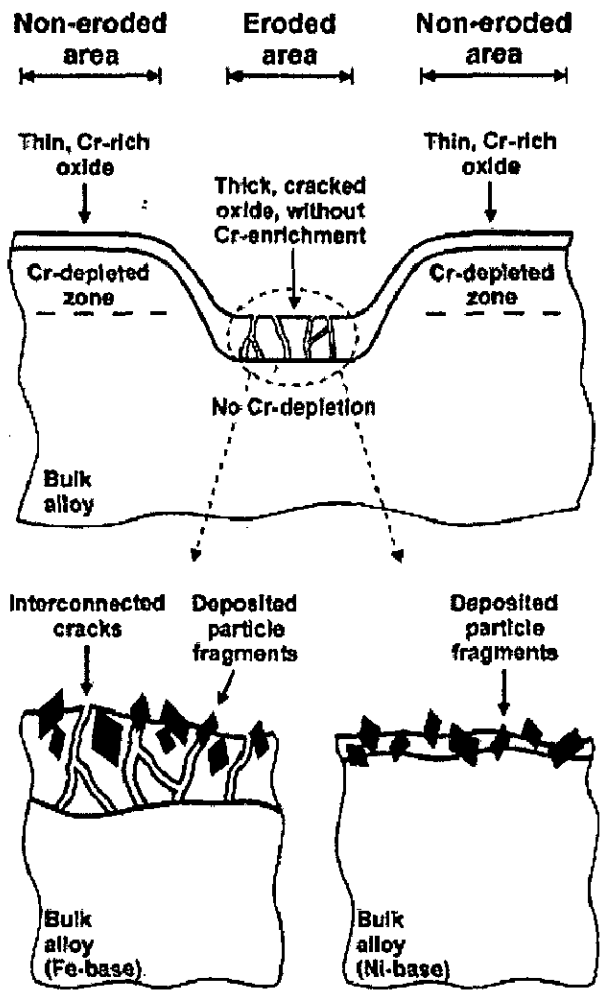

Fig. 2.11 Model illustrating the oxide formation during oxidation and erosion–corrosion at 550 °C (**Norling and Olefjord, 2003**).

explore different aspects of dry sliding wear behaviour of metals, alloys and coatings under different conditions. Research has mainly been centered on investigating the effects of sliding conditions like load, sliding velocity, initial surface roughness, microstructure, mechanical properties, environment, etc., and at the same time to detect the mechanisms of wear operating under these conditions. Some sliding wear studies which may be relevant to the present work has also been summarised in Appendix A-3.

An excellent review on the role of oxidation in the wear of alloys has been reported by **Stott (1998)**. He reviewed some of the models developed to account for the generation of oxide during sliding and the effects of such oxides on the rates of wear. He emphasized on high-speed unidirectional sliding, where frictional heat can lead to surface temperatures that are sufficiently high to result in relatively thick oxides on the contacting surfaces. It is suggested that wear is caused by spallation of oxide from the contacting asperities; this occurs when the oxide attains a critical thickness, leading to mild-oxidational wear. At very high speeds, surface temperatures may be high enough for the oxide to melt, leading to severe-oxidational wear. He suggested that during low-speed, reciprocating sliding, under conditions where debris can be retained between the contacting surfaces, such debris can be compacted into the surfaces, giving effective wear protection. A model to account for the observed wear rates has shown that increased temperatures facilitate the generation of oxide debris and assist in compaction of the debris to develop the wear-protective layers. He concluded that oxidation can have a beneficial effect in reducing wear during sliding of metals and alloys, particularly by preventing metal–metal contact. The heat required for oxidation can be induced by friction or can be applied externally.

The structure and mechanism of formation of the 'glaze' oxide layers produced on nickel-based alloys during wear at high temperatures has been explained by **Stott and Jordon (2001)**. They reported that transitions to low wear rates often occur during sliding between contacting metal surfaces, due to the establishment of high-resistance load-bearing layers. According to them such layers are developed from compaction of wear debris particles, with adhesion between the particles being an important factor in determining whether the layers are maintained, leading to wear protection, or break down, leading to abrasive wear. They are formed more easily and retained more effectively at higher temperatures, due to increased sintering and adhesion between the debris particles and to enhanced oxidation of these particles. They concluded that complex relationships occur between the effects of increased load in producing larger

debris particles, in decreasing the critical particle size for establishing the layers and in decreasing the separation between the sliding surfaces, and the effects of hardness of the substrates on the sizes and amounts of wear particles and on the topographies of the scars. They reported that the relationships are complicated further by oxidation and sintering of debris particles, leading to development of oxide or oxide-containing 'glaze' surfaces, and subsequent breakdown of the layers during sliding.

Panagopoulos et al (2003) have investigated the sliding wear behaviour of nickel superalloy CMSX-186 against stainless steel spheres in a pin-on-disk apparatus. The weight loss of CMSX-186 during their experimental procedure was found to increase with increasing applied load for a constant value of sliding speed. They inferred that the main wear mechanism of Ni superalloy CMSX-186 might be attributed to the ductile and brittle friction mechanism. They concluded that the collected debris consisted of the fundamental faces of Ni and $Ni(Al,Ti)_3$ of CMSX-186 in addition to elements such as Fe and C, which probably sprang from the counter material.

The sliding wear of Nimonic 80A against counterforce alloy, Stellite, 6 at 20°C using a speed of 0.314 m/s under a load of 7 N have been investigated by **Du et al (2003).** They indicated the formation of a wear resistant nano-structured glazed layer. According to them the improved wear resistance of such a layer has been attributed to the absence of Hall-Petch softening and the lack of significant degree of work hardening and enhanced fracture toughness of the surface.

Li et al (1998) have studied the different degradation mechanisms that may occur on MCrAlY coatings (CoNiCrAlY) which were thermal sprayed under various atmospheres (air, argon, vacuum) on a nickel-based superalloy (Hastelloy X). They evaluated the friction behaviour of these coatings sliding against a low-pressure plasma sprayed NiCoCrAlYTa coating under fretting conditions. Depending on the coating microstructure, two kinds of damage were reported: particle detachment and microstructural transformation (tribologically transformed structure). They also studied the adhesion and oxidation wear. They reported that after 100 cycles, tribologically transformed structures were observed on the wear tracks of the three CoNiCrAlY coatings. This brittle structure led to debris formation. They concluded that this was the main wear mechanism occurring in longer tests conducted with the ASPS CoNiCrAlY, which has a homogeneous structure. It was proposed that oxides and porosity present in APS and HVOF CoNiCrAlY induced detachment of entire splats and more severe wear. In all cases adhesive transfer from the counterbody was observed and debris was oxidized.

Edrisy et al (2001) investigated the sliding wear behavior of low carbon steel coatings deposited on 319 Al alloy substrates using a plasma transfer wire arc (PTWA) thermal spraying process. They concluded that wear mechanisms of the coating were associated with surface oxidation, splat tip fracture and surface hardening during wear. According to them splat delamination or removal of individual steel splats as a result of crack growth along the FeO veins within the coating was seldom. They classified the wear rates and mechanisms as:

1. Oxidation (formation of Fe_2O_3) as the main wear mechanism at low load and velocity.
2. At low velocity and high load the high wear rate was associated with severe deformation of the steel splat tips and eventually splat fracture and fragmentation. In addition, tribological layers consisted of a mixture of Fe_2O_3, FeO, and Fe_3O_4 formed on the contact surfaces.
3. At high load and velocity the wear rates decreases. Evidence was found for two different mechanisms that could account for the relatively low wear rates. The first mechanism was the formation of a thick protective mixed oxide layer on the wear track. The second mechanism was a pronounced hardening of the iron coating.
4. The wear rates were the lowest at high velocity and low load conditions, where there was no evidence for the splat tip fracture mechanism and the surfaces were covered with oxide rich tribolayers.

Lin et al (1973) concluded that mechanisms for the room-temperature wear of the Nimonic 75, 263, Nimonic 108 and Incoloy 901 alloys are associated with their strength properties. According to them, the initial wear rate of these alloys depends largely on their initial strengths, while the subsequent wear and friction behaviour can be correlated to work hardening of the contact areas. They explained that for instance, N108 has an initially relatively high strength and the contact areas subsequently work harden quite rapidly. Consequently, the initial, rapid wear rate, which is lower than those of the weaker alloys, N75 and C263 soon drops to a relatively low value. However the load-bearing areas of Incoloy 901 apparently work harden at a much lower rate and consequently the initial, rapid wear rate persists for a much longer period. There was no evidence that oxide films formed on the load-bearing areas ever become thick enough or thermally softened enough to have much effect on the friction and wear behaviour of these alloys.

Allen and Ball (1996) reviewed the performance of engineering materials under wear situations in South African industries. According to them wear of materials can be regarded as two stage process. The accumulation of strain precedes microfracturing events. An ability to absorb strain by transformation or work-hardening without the initiation of fracture, together with an ability to resist the propagation of the eventual fracture process, will provide good wear resistance. They concluded that hard, brittle particles or coatings that are mechanically incompatible and incoherent with the matrix material initiate and propagate wear processes. They further suggested that the synergistic corrosion and oxidation can accelerate wear in aggressive environments.

2.5 MEANS OF COMBATING EROSION AND EROSION-CORROSION WEAR

2.5.1 Modification of Impingement Conditions:

If possible, the geometry and/or fluid dynamics should be modified to reduce the amount of liquid impacting the exposed surfaces, to reduce the impact velocity of the droplets (or change the impact angle to reduce the normal component of impact velocity), to reduce the droplet size, or to reduce time of operation under the most severe conditions. Other measures include design, air injection, and control of the operating temperature and pressure.

2.5.2 Materials Selection

Materials selection for erosion resistance should be based on the ability of alloys to absorb the impact energy by a nondestructive strain mechanism, such as twinning, stacking fault formation, or a stress-induced martensitic type phase transformation. Generally, materials selected for a particular duty will last an adequate length of time, provided the designer has taken a proper account of all the factors affecting life. The lifetime is determined by some degradation process, which may be mechanical-fatigue, in the case of materials serving a low-temperature function where the stress varies, or creep, for a material subjected to high stress at elevated temperatures—or one of the processes listed later. In some cases, the separation of these processes is not so clear—thus, pits on a turbine blade will act as stress raisers, and accelerate fatigue failure. Loss of section as a result of general corrosion or erosion will result in an increase in the stress experienced by a component and result in accelerated creep failure. Loss of load-bearing

section, for example by internal penetration of corrosion or by near-surface depletion of strengthening alloy elements, will have the same effect. The surface degradation processes may also adversely affect the performance of components—an example is the solid particle erosion (SPE) of steam turbine blades by spalled oxide particles entrained in the steam, in which the most important economic effect is the degradation of the performance of the turbine, rather than any macroscopic failure of components **(Stringer, 1998)**.

2.5.3 Use of Protective Coatings

Coating technology is one of the more rapidly growing technologies in the field of materials. A combination of the development of materials specifically designed for erosion resistance and the appropriate technique for the application of these materials, as a coating would be the optimum solution. Suitable coating techniques also allow for regeneration of parts that have been rendered unusable by erosion. Coatings are primarily used to restrict surface damage of components in practice, where other requirements prevent the substitution of an inherently resistant material **(Stringer, 1998)**.

Increasingly greater demand imposed on materials makes it more difficult or, at the current stage of development, even impossible to combine the different properties required in one single material. Therefore, a composite system of a base material providing the necessary mechanical strength with a protective surface layer different in structure and/or chemical composition and supplied by a surface treatment can be an optimum choice in combining material properties. Although protective surface treatments are widely used at low temperature, the use of these at elevated temperature is more recent. Current high temperature applications are limited largely to the aerospace industry. An enormous challenge exists now to develop and apply these techniques to other high temperature applications **(Stroosnijder et al, 1994 and Li et al, 2003)**.

The coating can be defined as a layer of material, formed naturally or synthetically or deposited artificially on the surface of an object made of another material, with the aim of obtaining required technical or decorative properties **(Burakowski and Wierzchon, 1999)**. There are three main kinds or compositions of barriers: Inert or essentially inert, inhibitive and sacrificial. Various combinations of these types are found in coating systems designed to use some or all of the several protective advantages provided. It must be remembered that there is no such thing as a

"perfect" coating in a practical sense so none of these types or any combination can be expected to give perfect protections **(Hamner, 1977)**.

Generally speaking, coatings can be regarded as materials with greater resistance to the significant surface degradation process. In the case of corrosion, the coating itself has a greater resistance to the corrosive environment. In the case of erosion or wear, the coating is resistant to this aspect. However, the coating has a number of other important requirements **(Stringer, 1998)**. In brief, these are:

(1) The coating must have good adherence to the substrate, throughout the range of conditions that the component is exposed in service. Most obviously, it must tolerate without spalling from the surface the temperature variations that the component experiences in service; and the strains and strain variations that the component will normally impose on the coating. This latter is because the coating is normally thin in comparison to the substrate, and thus will be forced to match the substrate *strains*.

(2) A coating must not only be resistant to the condition for which it has been chosen, but any other condition to be experienced by the component. For example, in the case of a high-temperature coating, susceptibility to water damage of any kind when the system is down and the surface is cool is very undesirable.

(3) The conditions required for the coating process must be consistent with the system to be coated: a process requiring a high vacuum is not appropriate for coating a boiler water wall in place.

(4) The coating process must not damage the substrate. In general, this means that any process which involves heating the substrate to high temperatures needs to be assessed carefully.

(5) A very similar issue is that during the coating process or use, interdiffusion of any species between the coating and the substrate must also be assessed carefully.

(6) The coating must not induce failure in the substrate. This means that the system should not allow a crack formed in the coating to propagate into the substrate, for example.

(7) Interface properties are very sensitive to the presence of minor impurities, since chemisorptions (for example) can result in the formation of a complete monolayer of an element at an interface even if volumetrically the concentration is very low. These impurities may come from the substrate itself, the coating process, or the environment.

The development of modern coal fired power generation systems with higher thermal efficiency requires the use of construction materials of higher strength and with improved resistance to the aggressive service atmospheres. These requirements can be fulfilled by protective coatings (**Nickel et al, 2002**). **Wang and Luer (1994)** have reported the recent use of coatings to protect the heat exchanger tubes of fluidized bed combustor from erosion-corrosion problems. **Hidalgo et al (1997 and 2000)** have further discussed the use of plasma sprayed thin anti wear and anti oxidation coatings to take care of the high temperature erosion and corrosion problems in energy generation systems.

2.5.3.1 Processes Used for Applying Coatings

A wide range of processes are used to deposit metal, ceramic, and organic coatings or combinations of these materials (composite coatings). Each of these processes has their own distinct processing parameters (e.g., temperature, pressure, and time), advantages and limitations. A comprehensive list of the various coatings materials or coatings methods as reported by **Davis (2001)** is as follows:

(i) Organic coatings and linings
(ii) Ceramic coatings
(iii) Hot dip metallic coatings
(iv) Electroplating (metal or composite coatings)
(v) Electroless plating (metal or composite coatings)
(vi) Weld overlays (metal or ceramic coatings)
(vii) Thermal spraying (metal, plastic, ceramic, or composite coatings)
(viii) Cladding (thick metal coatings)
(ix) Chemical vapor deposition (metals, graphite, diamond, diamondlike carbon, and ceramics)
(x) Physical vapor deposition (metals, ceramics, or solid lubricants)
(xi) Thermoreactive deposition/diffusion process (carbides, nitrides, or carbonitrides).

From a production point of view, three methods are in current use, these being thermal spraying (TS), chemical vapour deposition (CVD) from a pack and physical vapour deposition (PVD) (**Strafford et al, 1984**), of these, thermal sprayed coatings are economical, can be produced by means of relatively simple techniques and offer

excellent corrosion and wear protection. Moreover, other favourable properties can be produced at the coating or component surface. As a result, these coatings have found use in various industrial applications **(Wielage et al, 1998)**.

2.6 THERMAL SPRAYING

Thermal spraying is a generic term for a group of processes that apply a consumable in the form of a spray of finely divided molten or semimolten droplets to produce a coating **(Davis, 2001)**. Thermal spraying has emerged as an important tool of increasingly sophisticated surface engineering technology. The different functions of the coating, such as wear and corrosion resistance, thermal or electrical insulation can be achieved using different coating techniques and coating materials **(Yamada et al, 2002)**.

Thermal spraying has grown into a well accepted technology for the production of overlay protective coatings and is used extensively in industry servicing a range of components. Metallic and ceramic coatings allow engineering components to operate under extreme conditions of wear, corrosion and high-temperature exposure. More than 35 years ago, plasma spraying was established as a commercial process, but only last two decade some serious attempts have been reported to establish a solid scientific base for this technology **(Pfender, 1988; Sampath et al, 2003)**.

Thermal spray coatings consist of microstructural units called splats, which form from the splashing of particles with high temperature and velocity on the substrate (Fig. 2.12). A schematic microstructure of thermal spray coating consisting of splats, unmelted particles, pores and cracks **(Kucuk et al, 2001)** has been shown in Fig 2.12. Thermal spraying is the application of a material (the consumable) to a substrate by melting the material into droplets and impinging the softened or molten droplets on a substrate to form a continuous coating. Most thermal spray processes require abrasive blasting or a bond coat to optimise the coating adhesion **(Budinski, 1998)**. One of the advantages of thermal spraying is the fact that the molten or partly molten coating material droplets are deposited on to a substrate material without melting and only slight heating of the substrate occurs. Therefore, usually no influence on heat treatments, chemical compositions, etc., is observed due to the moderate heat input by thermal spray coating processes and substrate temperatures seldom exceed 150 ^{0}C **(Knotek, 2001)**.

Thermal spray coatings are especially interesting for their cost/performance ratio. Unique alloys and microstructures can be obtained with thermal spraying which are not possible with a wrought material. This includes continuously graded composites and corrosion resistant amorphous phases. Thermal spray coatings additionally offer the possibility of on-site application and repair of components, given a sufficient accessibility for the sprayer and his equipment. However, thermal spraying in the workshop is preferred, whenever possible, to achieve optimum results **(Heath et al, 1997)**.

The industrial applications of thermally sprayed coatings largely depend on the bond quality between the coating and substrate. Therefore, a thorough substrate surface preparation is necessary. Contaminants such as rust, scale grease, moisture, etc. must be removed from the surface. After cleaning usually a roughening of the substrate surface follows to ensure coating adhesion. Common methods for surface roughening, which are often combined **(Knotek, 2001)**, are:

- Dry abrasive grit blasting.
- Machining or macro roughening.
- Applying a bond coat.

The thermal spray coating process should start as soon as possible after the surface preparation is completed, since the prepared surface is very active and oxidation, recontamination, etc., should be avoided **(Knotek, 2001)**.

2.7 PLASMA SPRAYING

Plasma spraying is the most flexible/versatile thermal spray process with respect to the sprayed materials and offers a reliable cost-effective solution for many industrial problems. The high temperatures of plasma spray processes permit the deposition of coatings for applications in areas of liquid and high temperature corrosion and wear protection and also special applications for thermal, electrical and biomedical purposes **(Knotek, 2001)**. It allows the spraying of a wide range of materials from superalloys and refractory intermetallic compounds to ceramics. This technology encompasses also the manufacture of net shapes which can be used directly as engineered materials **(Vardelle et al, 1996)**. Plasma spraying is part of thermal spraying, a group of processes in which finely divided metallic and non-metallic materials are deposited in a molten or semi-molten state on a prepared substrate **(Fauchais, 2001)**.

In the fifties, the plasma torches were developed to test materials at high enthalpies for simulated re-entry vehicles. Then in late fifties and early sixties, the first

serious attempts were reported using plasma torches for spraying of primarily refractory materials. Almost any material can be used for plasma spraying on almost any type of substrate. This flexibility is probably one of the major reasons for the rapid expansion of this technology **(Pfender, 1988).** The high temperatures enable the use of coating materials with very high melting points such as ceramics, cermets and refractory alloys **(Fauchais et al, 1991).**

Plasma techniques are capable of producing thick coatings films more than 100 μm at high production rates with no degradation of the mechanical properties of the alloy substrate **(Yoshiba, 1993).** But problems that may be encountered are porosity and poor adhesion, especially in case of adhesion of ceramics to metals. Further, adhesion can be improved by the use of bond coat interlayer and /or powder of small particle size.

Plasma sprayed coatings are used today as thermal barriers and abrasion, erosion or corrosion resistant coatings in a wide variety of applications. The aviation industry is a large consumer of thermal barrier coatings, but also of abrasion and erosion resistant coatings. Thermal or plasma sprayed coatings are often used to restore dimensions of worn or damaged components as well **(Westergard et al, 1998).** A new application of plasma spraying is in producing hydroxyapatite coatings onto the stems of orthopaedic endoprostheses **(Batchelor et al, 2003).**

2.7.1 Plasma Spraying-The Process

2.7.1.1 Plasma Jets

A plasma torch or gun consists of a water cooled copper anode and a thoriated (2 wt%) tungsten cathode as shown in Fig. 2.13. Argon gas flows around the cathode and through the anode. The shape of the anode is made as a constricting nozzle. A gas, usually argon or nitrogen or a mixture of these with hydrogen or helium flows around the cathode and exits through the anode nozzle. The typical value of the flow rate of the gas as reported by **Sidky and Hocking (1999)** is 3.5 L min^{-1}. Further material used for the anode is usually high purity oxygen free copper **(Fauchais, 2004).**

A dc arc is maintained between the electrodes and plasma of ions and atoms emerges at a temperature of 6,000-12,000^{0}C at a distance of 1 cm form the nozzle, decreasing rapidly to 3000^{0}C at a distance of 10 cm from the nozzle. The gas plasma generated by the arc consists of free electrons, ionised atoms and some neutral atoms and undissociated diatomic molecules if nitrogen or hydrogen is used as reported by **Tucker (1994).** The point of entry of the powder into the plasma jet is usually in the diverging portion of the nozzle or sometimes the powder is fed externally. In some applications RF

(Radio frequency) discharges are used as heat sources instead of dc arc. Compared to dc arc troches the main difference is in the torch internal diameter, resulting in flow velocities below 100 ms^{-1} and the axial injection of particles **(Fauchais, 2004)**.

Plasma gas velocities with most conventional torches are subsonic, but supersonic velocities can be generated by using converging-diverging nozzles with critical exit angles. The most important parameters relative to the powder particles at impact on the surface are their temperature, velocity and extent of reaction with the gaseous environment **(Tucker, 1994)**. Near the nozzle, the gas velocity is 200-600 ms^{-1} but the particle velocity is only 20 ms^{-1}. However the particle acceleration (due to gas frictional forces) is 100 000 g so that 18 μm particles reach a maximum velocity of 275 ms^{-1} at a distance of 6 cm from the nozzle **(Sidky and Hocking, 1999)**.

The very high temperature generated in plasma spray process melts even the most refractory particles. But at the same time low melting point materials such as plastics can also be sprayed. The temperature of the core of the plasma may exceed 30,000^{0}C **(Tucker, 1994)**. A schematic of a typical distribution of temperature in the plasma has been shown in Fig. 2.14 **(Knotek, 2001)**. Further, Plasma spraying operates at high energy levels; the power consumption of a typical coating unit is approximately 50 kW with an electric current of several hundred amperes flowing in the plasma arc **(Batchelor et al, 2003)**.

The plasma jet is typically 5 cm in length and distance form the substrate is of the order of 15 cm. Oxidation is minimal because of low dwell time and use of a reducing gas. The temperature of the substrate rarely exceeds of 320^{0}C and is often below 150^{0}C.. Plasma spraying process is a process which causes no distortion of the substrate **(Sidky and Hocking, 1999)**.

2.7.1.2 Coating Formulation

For strong dense plasma sprayed coatings, most of the particles must be molten before impingement and must have sufficient velocity to splat into the irregularities of the previous splats. Many coatings contain readily oxidised elements (e.g. aluminium, molybdenum and titanium) for which plasma spraying at low pressure (20 mbar) or in argon is advantageous. Underwater plasma spraying offers much scope for deposition of wear and corrosion resistant coatings on submerged substrates such as offshore structures **(Sidky and Hocking, 1999)**.

The high impingement speeds of the molten particles during spraying are intended to ensure that the molten droplets disintegrate on contact instead of remaining as discrete

droplets, this process is known as splat formation. The structure of the plasma sprayed coatings can be envisaged as a series of interlocking splats **(Batchelor et al, 2003)**. The splats have columnar or equi-axed structures with grain sizes between 50 and 200 nm. However this fine structure is altered by grain size effect, large volume fraction of internal interfaces, voids, pores and so on **(Fauchais, 2004)**. Further a rapid quenching of the sprayed particles takes place due to the radial spreading and increase in surface area of rather small mass of the spray particles. The necessary time for solidification is between about 10^{-8} and 10^{-6} seconds **(Knotek, 2001)**. The solidification is generally achieved before the next particle impacts at the same location **(Fauchais, 2004)**.

The distance between the plasma spraying gun and the substrate can be allowed to vary up to 10mm without significant effect on the coating quality. The coating deposition rates in plasma spraying are typically range from 1 to 10 kilograms of coating per hour. Plasma spraying offers a faster coating rate than most of the other coating techniques **(Batchelor et al, 2003)**.

The extent of reaction of the powder with its gaseous environment during transit depends both on the composition of the plasma gas and the amount of intermixing of the plasma gas with the ambient gas between the nozzle and the substrate. It is generally assumed that argon and helium are inert and no degradation of the powder occurs in the torch when they are used as only plasma gases **(Tucker, 1994)**. The plasma spray is often done in closed chamber filled with inert gas, to prevent the escape of any polluting or toxic debris from the process and to suppress the oxidation of the metal powder during the plasma spraying. Oxide contamination can greatly weaken the sprayed coating as oxides act as brittle inclusions within the microstructure of the coatings. The splat structure of a plasma sprayed coating and the destructive role of oxide inclusions are illustrated in Fig. 2.15 **(Batchelor et al, 2003)**. Further the use of inert gas atmospheres, argon shroud or low pressure chamber are reported to decrease the porosity of the coatings. In addition, the plasma jet becomes longer and therefore the nozzle-workpiece distance is increased substantially, which increases the dwell time in the plasma resulting in more uniform particle heating **(Nicoll, 1984)**.

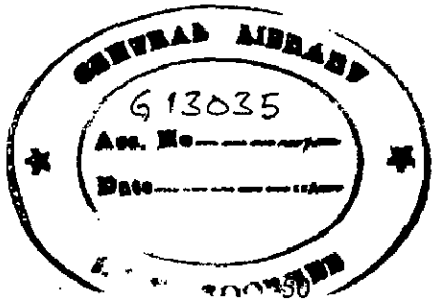

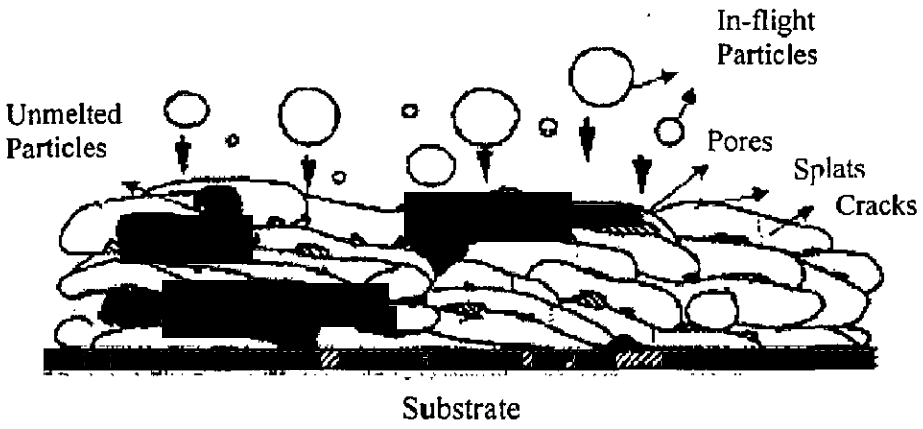

Fig. 2. 12 Schematic microstructure of thermal spray coating consisting of splats, unmelted particles, pores and cracks (Kucuk et al, 2001).

PLASMA SPRAYING APPARATUS

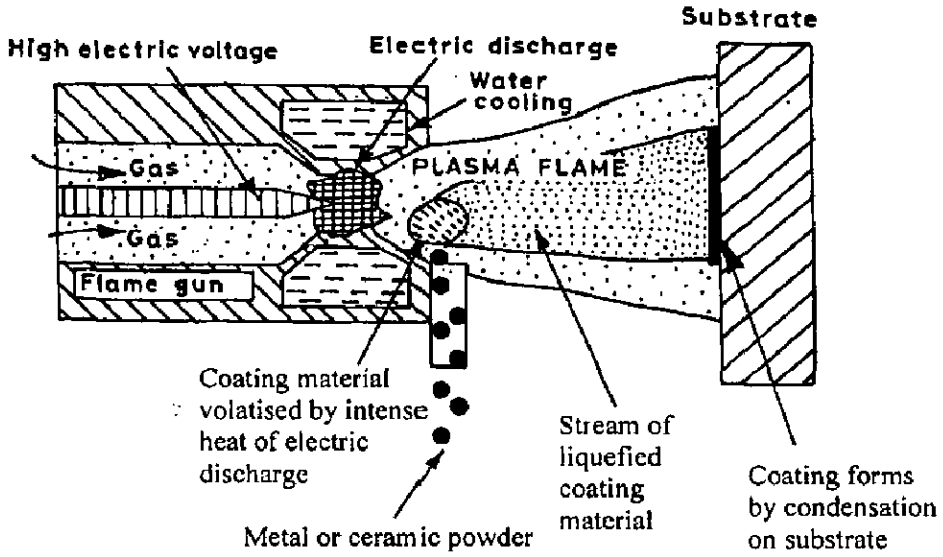

MECHANISM OF COATING DEPOSITION

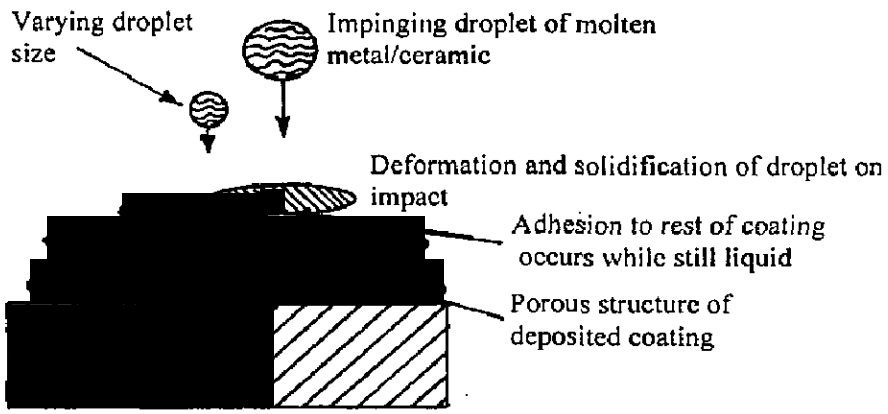

Fig. 2.13 The plasma spraying process (Batchelor et al, 2003)

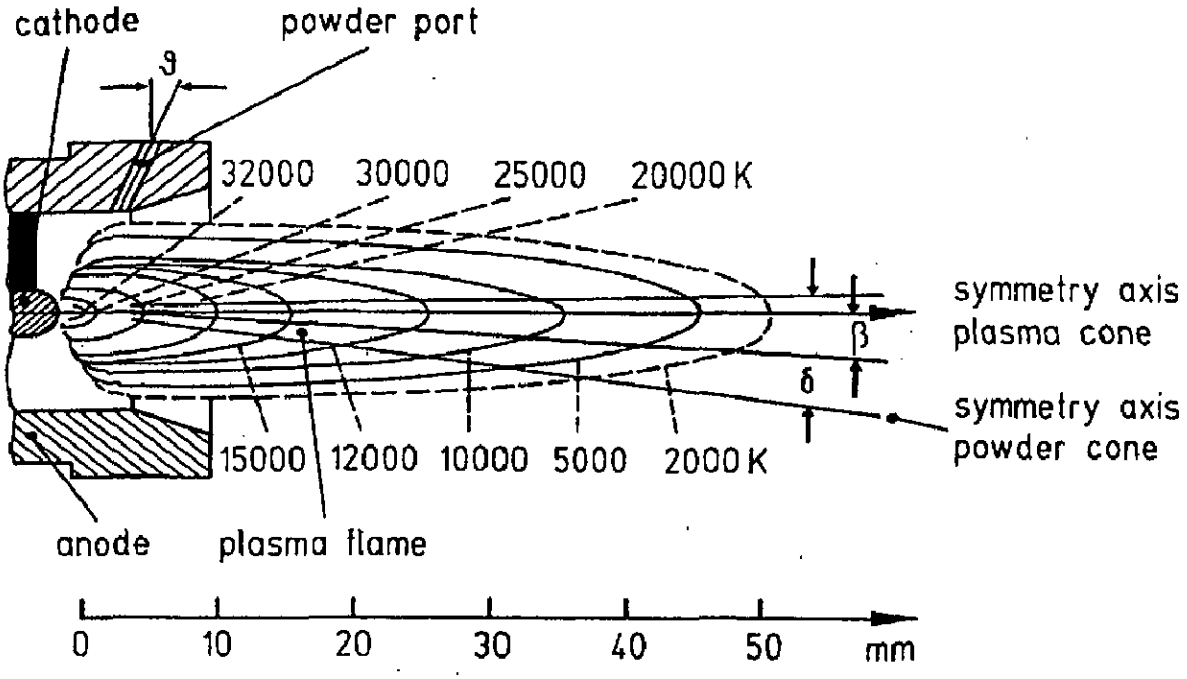

Fig. 2.14 Temperature distribution and geometry of plasma jet (Knotek, 2001).

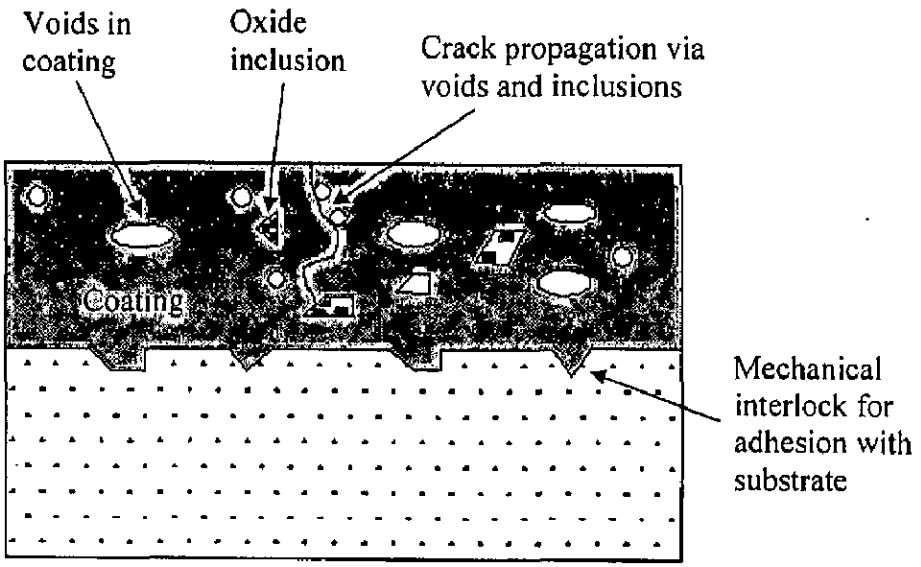

Fig. 2.15 The structure of plasma sprayed film (Batchelor et al, 2003).

2.7.1.3 *Adhesion of the Plasma Sprayed Coatings*

The strength of adhesion or bonding between the coating and substrate is critical to the performance of the coating. Usually the surface to be plasma sprayed is roughened by mechanical means such as abrasive blasting, grit blasting or rough turning, which also activate and clean the surfaces prior to coating. With plasma spraying the bonding is suggested to be obtained from the mechanical interlock and solid state adhesion between the atoms in the coatings and substrate. Mechanical interlocking is physical keying between an often deliberately roughened substrate and a coating that is in very close contact with the substrate. Adhesion mechanisms between the coating and interface are illustrated in Fig.2.15 (**Batchelor et al, 2003**). The quenching stresses within the spray particles increase the interlocking effects (**Knotek, 2001**).

Solid state adhesion involves either electron transfer between the outermost atoms of the coating and the substrate or the formation of a much thicker layer of a compound material. It is modelled that the molten droplets dissolve or sweep away any oxide and contaminants that cover a metal surface. The cleaned metal substrate then reacts with the molten droplets before they solidify (**Batchelor et al, 2003**).

Coating properties are also governed by the splat layering which further depends on the particle parameters at impact, the shape and topology of already deposited layers, the ability of the flattening particle to accommodate their pores, asperities etc, and finally, of their temperature at the moment of impact. Also the substrate and coating temperature influence the coating properties. These temperatures control the inter-lamellar contacts, the residual stress distribution within the coating and the pass temperature. For instance, if the pass temperature is high, the sticking of the small particles resulting from the re-condensation of vaporised sprayed material will occur and create defects between passes (**Fauchais, 2004**).

2.7.1.4 *Plasma Spray Process Variables*

Bhusari (2001) has summarised the plasma spray process variables as shown in Fig. 2.16. According to him, the thermal sprayer responsible for the application of the plasma sprayed coatings need not be a trained scientist, however should be at least aware of the issues detailed in the Fig. 2.16.

2.7.2 Process Variants of Plasma Spraying

The plasma spray process can take place in different atmospheres at different pressure levels and the various process variants as discussed by **Knotek (2001)** are:

Atmospheric Plasma Spraying (APS)

Vacuum (VPS) or Low Pressure Plasma Spraying (LPPS)

Shrouded Plasma Spraying (SPS)

Controlled Atmosphere Plasma Spraying (CAPS)

2.7.2.1 Atmospheric Plasma Spraying (APS)

Atmospheric plasma spraying (APS) is the most economical process variant which is carried out in air. The powder particles can interact with the air atmosphere, which may limit the choice of the spray material, since the originating oxides are built into the coating. The major fields for APS-applications are coatings for wear and corrosion (liquid and gaseous) protection, often based on oxide ceramic materials. Other typical coating materials are metals and some alloys especially insensitive to oxidation. The porosity of APS-coatings is generally between 1 and 5%.

2.7.2.2 Vacuum (VPS) or Low Pressure Plasma Spraying (LPPS)

The coating process of VPS takes place in a closed chamber with reduced pressure. The coating process, started after the chamber is evacuated to pressures $< 10^{-1}$ mbar and refilled with an inert gas atmosphere, takes place at about 50 to 400 mbar. To be able to constantly follow the working chamber pressure, efficient pump systems have to be employed in order to remove the steadily injected plasma gases. These methods are used for the metals that are too reactive to be sprayed in air. The increase in particle velocity results in high quality pure coatings. The jet velocity is Mach 3, giving low porosity and strong adhesion (**Sidky and Hocking, 1999**).Another advantage of VPS technology is the option to clean the substrate surface especially from oxide layers and preheat the substrate, both giving better adhesion. The main drawback of the system is high technical effort/expense for achieving the vacuum conditions. For some application using low melting point material as substrates, there is insufficient convective heat transfer within the chamber.

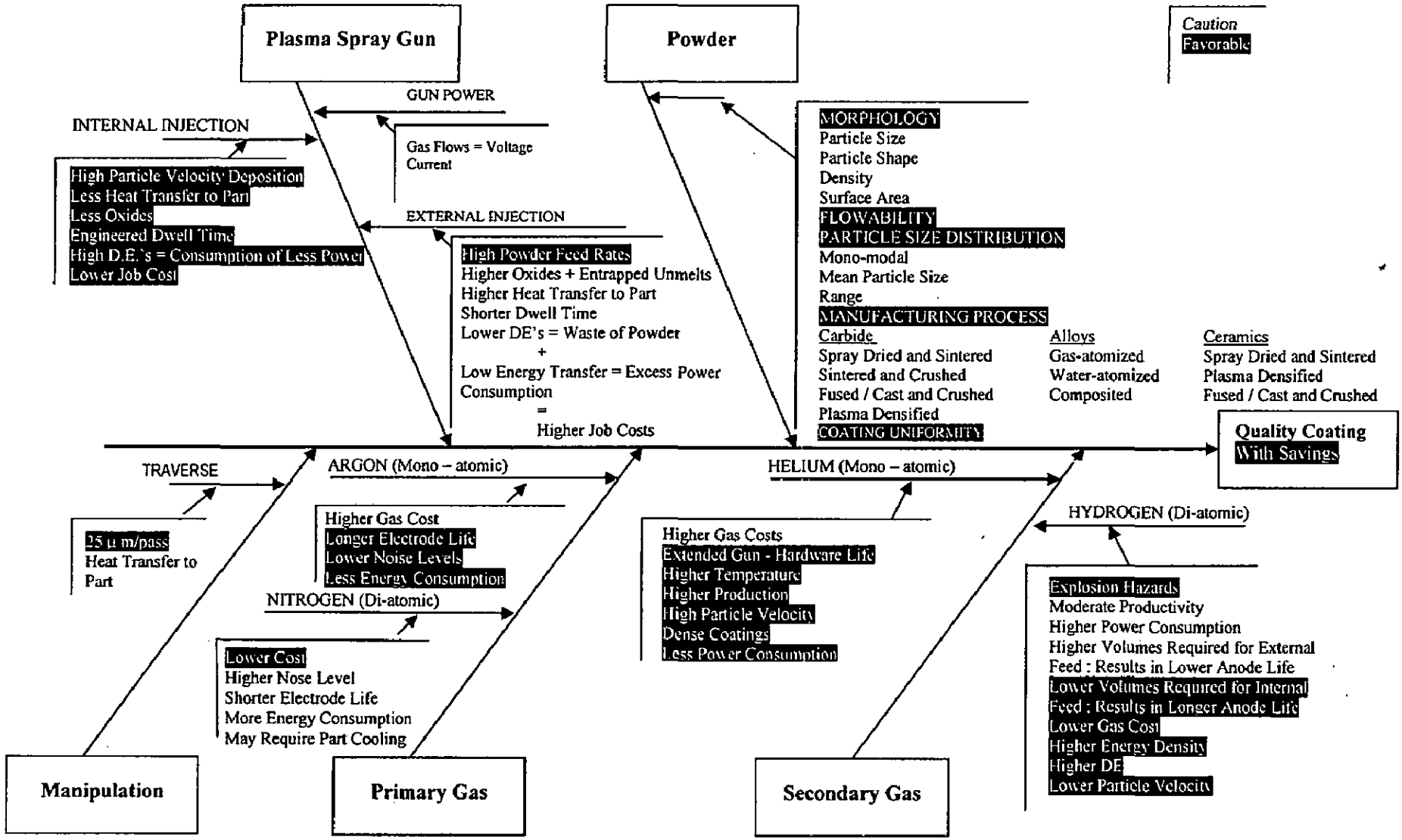

Fig. 2.16 Plasma spray process variables (Bhusari, 2001).

2.7.2.3 *Shrouded Plasma Spraying (SPS)*

Shrouded plasma spraying has been developed to reduce the effort for chamber and pumping system for less expensive applications. Similar to shrouded welding processes, envelope of an inert gas, which is not ionized, protects the plasma jet from the surrounding oxygen containing atmosphere and also improves substrate cooling. Both argon-shrouded and low pressure, inert-gas-chamber spray coating methods are used in the commercial production of the very reactive MCrAlY coatings on gas turbine components (**Tucker, 1994**).

2.7.2.4 *Controlled Atmosphere Plasma Spraying (CAPS)*

Combining vacuum plasma spraying and inert-gas plasma spraying in one system leads to controlled atmosphere plasma spraying (CAPS). For a pressure range from 50 to 400 mbar VPS-coatings are deposited, whereas at pressures around 1 bar inert gas plasma spray coatings are produced. Further with pressures up to 4 bar high pressure plasma spay coatings are deposited.

2.8 ROLE OF COATINGS IN VARIOUS EROSIVE CONDITIONS

Many researchers have investigated different types of coatings for preventing the degradation of the metals and alloys under different conditions. Research and development work on arc-sprayed coatings stemmed from the needs to develop coatings that (**Dallaire, 2000**):

- resist the impact of large mineral particles or oxide scales,
- posses good erosion-oxidation characteristics up to high temperatures,
-resist the impact of high velocity particles impacting with low and high angles,
-can be easily and safely arc sprayed with air on site and in shops.

Davis et al (1986) reported that the processing controls designed to improve thermal fatigue resistance such as an increase in the porosity, the use of mixed phases and partially stabilized phases and the introduction of segmentation with micro-cracking may have detrimental effects on a coating's erosion resistance. A study was made to relate the erosion behavior of several experimental zirconia- base ceramic thermal barrier coatings to their processing parameters and microstructure. It was reported that the initial erosion rates of partially stabilized, plasma-sprayed, zirconia-base ceramic thermal

barrier coatings were directly related to their initial surface roughness. They reported that the apparent porosity of coating was found to be influencing erosion directly whereas hardness and microcracking were not observed to be dominating factors. Also adherence at the bond-coat ceramic coat interface was not related to erosion behavior in the plasma sprayed coating systems.

Takeda et al (1993) investigated the application of low-pressure plasma spraying technique to the formation of some coatings of cermet and metallic alloy materials (Cobalt base, stellite-6, etc.) with high resistance against the cavitation and rain erosion damage. By using plasma spraying, some coatings were prepared and tested for cavitation erosion behavior. Cobalt base alloy coating showed much more excellent resistance to the erosion than that of Stellite-6. According to them the superiority of the Co base alloy coatings in the erosion resistance has been attributed to the unique microstructure caused by the rapid solidification during the deposition. Further the rapid solidification of the Co base alloy coating results in the extended solid solubility of the alloying elements, which restricts the precipitation of chromium carbide. In case of stellite sheet, SEM micrograph and EPMA images show that the carbon and chromium enrich at the same positions, where cobalt rarely exists. They reported that in the Stellite-6, chromium carbide forms as a second phase. They also found that the ZrB_2-CoCrAlY cermet coating forms a very hard surface but the erosion resistant property is insufficient for practical usage. They further reported that the erosion resistance of the Co base alloy coating decreases with the increase of the chromium carbide.

Different superalloys and coatings were tested in an erosion wind tunnel (high temperature), which simulates steam and gas turbines (**Tabakoff, 1995**). The erosion behavior of MAR-M246 and cobalt based X-40 superalloys and LC-1H (chromium carbide-nichrome), LC-1B 9 (nichrome), RT22 (platinum aluminide), and RT22B (rhodium platinum aluminide) coatings were studied. He reported that diffusion techniques are frequently used for aluminiding of Ni and Co superalloys. He concluded that the coatings RT22 (platinum aluminide) and RT22B (rhodium platinum aluminide) exhibit maximum erosion rates at 30° impingement angles for a temperature at 815°C and particle velocity of $366ms^{-1}$. He also suggested that these coatings are excellent for turbomachinery use and are ten times better in erosion resistance compared with the superalloys MAR and X-40.

Tabakoff and Shanov (1995) investigated the erosion behaviour ceramic (titanium carbide) coating deposited by the chemical vapour deposition (CVD) process

on nickel and cobalt based superalloys. The tests specimens were exposed to particle laden flow at velocities of 305 and 366 m s^{-1} and temperatures of 550°C and 815°C. From the graph of erosion rate against impingement angle they have shown that initially for the TiC coating erosion rate increases with the impingement angle up to 45°, after which it does not change significantly. They also compared this with previous result of **Tabakoff (1995)** for RT22 coating applied on the same substrate (M246) and concluded the lower erosion rate of titanium carbide coating. They also concluded that the same ceramic coating did not indicate any improvement of erosion behaviour compared to RT44 coating for protection of X40 superalloy. They proposed that a CVD titanium carbide coating on M246 superalloy substrate provides a very good erosion resistance when subjected to impact by fly ash and chromite particles.

Shanov and Tabakoff (1996) investigated the erosion resistance of titanium carbide (TiC) coating by CVD technique on Ni- base alloy INCO 718 and on AISI 410 substrates. This study demonstrated that the CVD titanium carbide coating provides excellent erosion protection for INCO 718 and stainless steel 410 when subjected to impact by chromite particles at elevated temperatures.

A series of coatings with different average splat size, sprayed from pure alumina powders of different particle size using an axial-injection plasma-spray torch under optimized conditions to obtain the best microstructures was investigated by **Hawthorne et al (1997).** They observed that increasing the splat size by using larger precursor powder particles gave coatings with improved microstructure integrity and hardness. They revealed that the erosion resistance of the alumina coatings depends upon their microstructure integrity.

Hidalgo et al (1997) investigated the erosion wear of nickel-based, iron-based and chromium-nickel plasma sprayed coatings on a carbon steel AISI 1025 and an AISI 304 austenitic stainless steel. The erosion tests were performed at 600 and 800°C for 9h under impact angles of 30 and 90°. Good average adherence values in the range of 40-50 MPa between coatings and substrates had been obtained. The high temperature erosion wear values of the three different plasma-sprayed coatings measured in a combustion unit operating under the same conditions as encounterd in an industrial boiler were very close, and similar to the behaviour of the stainless steel substrate.

Westergard et al (1998) evaluated erosion and abrasion characteristics of a series of plasma sprayed alumina coatings. They indicated that hydrogen concentration,

nozzle size and precursor powder type and size influence the erosion and abrasion characteristics of the coatings.

Eaton and Zajchowski (1999) investigated the erosion behavior of plasma sprayed yttria stabilized zirconia (YSZ) coatings of different powder size sprayed by Plasmadyne SG-100, Metco 3MB, Metco 7MB, Plasma Technic F-4 and Plasma Technic F-1-45 mini-gun systems. Their study showed that different plasma spray systems can produce different porosity levels in similar YSZ powders. They inferred that the fine particle size distributions of powders results in lower erosion rates in comparison to coarser distributions. Porosity level was shown to be moderately correlated to measured erosion rates.

Tabakoff (1999A) studied the erosion behaviour of plasma sprayed chromium carbide plus FeCrAlY coating on AISI 410 steel at 550°C temperature and 228m/s velocity. He investigated the variation of coating erosion rate with temperature at constant impact angle and velocity. He reported the coating as most readily erosive and maximum erosion was at 90° impact angle. He also evaluated the erosion behaviour of chromium carbide(LC-1B) and carbide nichrome (LC-1H) detonation gun coatings, plasma sprayed chromium coating, platinum aluminized (RT22), rhodium platinum aluminized (RT22B) and chromium (SDG-2207) super D-gun coating, including TiC, TiN, Al_2O_3 CVD and PVD coatings. He concluded that of the coatings for steam turbine, SDG-2207 and LC-1H exhibited the lowest erosion rates at low angles. Further he reported that the platinum aluminide coatings at 815°C and 366 ms^{-1} indicated the enhanced erosion resistance. It was also concluded that amongst the CVD coatings, TiC coatings offered the best erosion resistance. He also proposed that the TiN PVD coating exposed to high temperature and larger 300μm particles did not perform well after 30 and 40° particle impacts. In an another investigation of the similar coating, **Tabakoff (1999B)** proposed that the TiC coating offers the best erosion resistance, followed by the TiN coating. Further he reported no evidence of coating deformation, cracking or spallation. He concluded that the durability test of PVD coating confirmed that TiN coating can be successfully applied to compressor blades to extend compressor life.

Effect of laser melting on the erosion behaviour of plasma sprayed copper-ceramic coatings was evaluated by **Dallaire et al (1999).** They reported the poor erosion resistance of as sprayed plasma coatings. They concluded that the improvement in erosion resistance of laser-melted coatings was attributed to the formation of large clusters of boride particles upon laser melting plasma sprayed copper-boride coatings.

They reported the rounded boride islands were large enough to deflect the incoming eroding particles and the plastic copper phase dissipates the energy of particles with a high impingement angle.

Westergard et al (2000) in other study of plasma sprayed ceramic coatings made from alumina, chromia and alumina-titania powders, reported that among the alumina coatings, those deposited from sapphire powders gave the best results in the wear tests. An addition of titania to alumina had a favorable effect in most tests. They reported that in abrasion, one chromia coating displayed a wear resistance comparable to the dense sintered alumina reference. Whereas they inferred that the erosion rates were several times higher for all sprayed coatings compared to the reference alumina.

Branco et al (2004) reported the room temperature erosion behaviour of zirconia and alumina-based ceramic coatings, with different levels of porosity and varying microstructure and mechanical properties. They opined that the erosion models based on hardness alone cannot account for experimental results, and suggested that there is a strong relationship between the erosion rate and the porosity.

Barber et al (2005) reported the results of study on sub-surface cracks in eroded thermally sprayed WC-Co-Cr material. They proposed that during erosion test cracks are initiated at voids close to the surface and voids acts as stress raiser thus providing initiation site for cracks. These cracks then grow until they link up with transverse cracks and material removal takes place.

Bose et al (2005) reported the dominant solid particle erosion mechanisms of boron carbide and diamond coatings produced by chemical vapour deposition (CVD) when subjected to high energy particle impacts. The erosion tests were performed on a gas blast erosion rig using spherical soda-lime glass beads, angular quartz silica sand and diamond grit, at impingement velocities between 130 and 270 m/s and an erodent particle flux of 0.5 $kgm^{-2}s^{-1}$.

2.8.1 MCrAlY Coatings

MCrAlY coatings (CoNiCrAlY) were thermal sprayed under various atmospheres (air, argon, vacuum) on a nickel-based superalloy (Hastelloy X). These coatings formed by thermal spray methods are commonly used to protect gas turbine components from high-temperature oxidation and corrosion. The friction behavior of these coatings sliding against low- pressure plasma sprayed NiCoCrAlYTa coating was

evaluated under fretting conditions. The study focused mainly on the different degradation mechanisms (**Li et al 1998**).

For counteracting high temperature oxidation and hot corrosion of materials such as blades, duct segments etc., MCrAlYs are amongst the most protective coating materials used. Due to the particulate nature of the exhaust, such components are also exposed to erosion. **Zhao et al (2004)** studied the wear and erosion behavior of HVOF sprayed NiCoCrAlY coating with and without Al_2O_3 strengthening. Under selected sliding test conditions both coatings systems presented almost the same wear rates. Examination of the eroded surface on the NiCoCrAlY coating revealed ductile erosion behavior whereas the eroded surface of the Al_2O_3 strengthened NiCoCrAlY coating revealed mixed brittle and ductile erosion mechanism. The Al_2O_3 strengthened coating showed a higher erosion rate.

Metallic bond coats (NiCrAlY) between the substrate metal and the ceramic coating did not differ substantially in composition, appearance or thickness among the plasma-sprayed systems. In general, plasma-sprayed coatings will be well bonded to properly prepared substrate.

2.8.2 Nickel-Chromium Coatings

Nickel-chromium alloys have already been used as coatings to deal with oxidation environments at high temperature. When nickel is alloyed with chromium, this element oxidizes to Cr_2O_3 at rates which could make it suitable for use up to about 1473 k, although in practice, its use is limited to temperatures below about 1073 K (**Goward, 1986**). Thermal sprayed 50/50 nickel-chromium alloy is usually recommended as an erosion-corrosion protection for boiler tubes in power generation applications (**Grainger and Blunt, 1998**).

The high temperature erosion behavior of commercial thermally sprayed metallic and cermet coatings (WC, Cr and Ni-based) on boiler tube materials by using silica sand as erodent was studied **Hoop and Allen (1999)**. It has been reported that the coatings which contain large quantities of defects, particularly porosity, do not provide good erosion resistance to materials. They suggested that to provide good erosion resistance, coatings must have fine homogenous structures.

(Hidalgo et al, 2001A) investigated the erosion wear of plasma sprayed and flame sprayed coatings of nickel-chromium with small additions of aluminium and

titanium (NiCrAlTi). The substrate materials were austentic stainless steels (AISI 304,310 and 316). The erosion tests were performed at 500 and 800°C for 24h under impact angles of 30 and 90°. They reported that the porosity and oxide content of plasma-sprayed coatings are much lower than the flame-sprayed coatings. They suggested that the higher microhardness determined for the as-sprayed modified Ni-Cr flame-sprayed coatings as compared with the plasma-sprayed ones can be explained due to its higher oxide volume content. On the other hand they obtained a significant increase in the coating hardness after exposing it for 24h at 800°C. They concluded that the erosion behaviour of nickel-chromium flame and plasma sprayed coatings at medium temperature (500°C) was characterized by low erosion rates and a ductile erosion mechanism. Whereas they reported the erosion mechanism at higher temperature (800°C) could be defined as corrosion wear. They proposed very useful erosion behaviour of plasma-sprayed coating in the latter case.

Also they **(Hidalgo et al, 2001B)** studied the high temperature erosion-wear of plasma sprayed NiCrBSiFe and 35%WC-65%NiCrBSiFe onto the fully annealed AISI 304 austentic stainless steel. They found that the adherence of NiCrBSiFe in the as-sprayed condition and after high-temperature treatments was very good. However it was noted that the 35%WC-NiCrBSiFe coating adherence showed an important decrease after 800°C heat treatment and after thermal fatigue conditions. They concluded that the high temperature erosion behaviour of plasma-sprayed NiCrBSiFe coatings had proven to be very promising when compared with stainless steels, other Ni-Cr alloys and Cr_3C_2 cermets. On the contrary the high temperature erosion behaviour of 35%WC-NiCrBSiFe coating was suggested to be very poor.

Link et al (1998) exposed pure nickel, Ni-20Cr and Ni-30Cr alloys to conditions of erosion and corrosion simultaneously at 700°C and 800°C. The exposures were made using normal impact of an air stream loaded with 20-μm alumina at the velocities of 75 and 125 m/s. They reported that under simple oxidation, the alloy specimens developed a thin protective layer of chromia. Further they added that under erosion-corrosion conditions, this protective scale was prevented from forming and the alloys were found to undergo aggressive attack at a rate that was the same as that experienced for pure nickel, the surface oxides were identified as Cr_2O_3 and NiO. They proposed that, under erosion-corrosion, the erosive stream prevents the formation of a continuous layer of chromia by removing the oxide faster than it can spread laterally. The specimen is said to be in a state of erosion-maintained transient oxidation. This mechanism implies that it

would be difficult for protective scales to form in the presence of erosion and the oxidation behavior of an alloy cannot be used as a guide to its resistance to erosion-corrosion. The investigators concluded that that nickel, Ni-20Cr and Ni-30Cr degrade at the same rate under identical conditions of erosion- oxidation.

Roy et al (1999) studied the influence of erosion-induced roughness on the oxidation kinetics of Ni and Ni-20Cr alloys. They eroded the Ni and Ni-20Cr alloy at two different impact velocities (35 and 65 m/s) and for two different impact angles (90° and 30°). They reported that the oxidation rate of Ni increased as the roughness of the surface prior to oxidation was increased by erosion. Whereas the oxidation rate of Ni-20Cr largely remain unaffected by an increase in roughness of the surface prior to oxidation obtained by erosion at increased impact angles.

2.8.3 Nickel Aluminide Coatings

Sundararajan and Roy (1997) had reported that the erosion rates of intermetallics were lower than that of the erosion rates of the base material (from comparison of the erosion rates of Ti_3Al based alloys with Ti). **Sahoo et al (1981)** investigated the erosion behaviour of Ni-base intermetallics (IC-50 and IC-218) at an impact velocity of 25 m/s using SiC as erodent at impingement angles of 90° and 30°. They found that the steady state erosion rate at 30° impingement angle is higher than that at 90° impingement angle. They have reported the comparable erosion rates and ductile erosion response were the characteristics of nickel aluminide based intermetallics.

The erosion behaviour of HVOF sprayed NiAl intermetallic compound (IMC) coatings over a range of angles and particle velocities in air at room temperature was investigated by **Hearley et al (1999).** They proposed that the maximum erosion was achieved at the highest velocity for all angles. Further they reported that maximum erosion was achieved at 90° for all velocities suggesting the coating behaved in a brittle manner. Whereas from morphological examination of the coatings it was suggested that coating removal takes place by a ductile mechanism. They concluded that the well established empirical guideline that erodent impact angle can be an indicator of erosion mechanism does not apply to HVOF NiAl IMC coatings eroded by angular silica particles of nominal size 125-150 μm. They also concluded that the HVOF NiAl IMC coatings showed lower erosion rates than both metallic and ceramic air plasma sprayed coatings.

Wang et al (2003) investigated the effect of CeO_2 and Cr additives, and found that the NiAl coating containing CeO_2 and Cr exhibits lower erosion rate. Also they confirmed that a material with higher hardness often exhibits a better resistance to erosion degradation, however the enhancement in erosion rate appeared not proportional to the change in hardness and Young's modulus. They concluded that this inconsistency may be caused by the different erosion mechanisms occurred during erosion of the intermetallic- based alloy coatings.

Zhang and Li (2000) studied the effects of oxygen-active elements, yttrium and cerium, on the resistance of an iron-aluminide coating to corrosive erosion in sand containing salty and acidic slurries, respectively. They concluded that the addition of yttrium and cerium significantly enhanced the dry sand erosion resistance of the aluminide coating.

2.9 FORMULATION OF PROBLEM

2.9.1 Scope

Erosion is a serious problem in power generation equipments, industrial gas turbines, steam turbines and coal- utilization turbines for ships and aircrafts and in other energy conversion and chemical process systems (**Westergard et al, 2000**). The examples of surface damage in the electricity generation components as suggested by **Stringer (1998)** are:

1. Exfoliation of oxide in steam-side of boilers, leading to erosion of down-stream valves and steam turbine components.
2. Wastage (erosion or abrasive wear, sometimes coupled with corrosion) of fireside components in fluidized bed combustors, both bubbling and circulating.
3. Fireside erosion in coal-fired boilers; fly ash erosion and soot-blower erosion.
4. Erosion of combustion turbine components in dusty environments; e.g. expander turbines in pressurized fluidized bed combustors (PFBC).
5. Erosion of combustion turbine first stage vanes and blades by carbon shed by improperly operating combustors, or by material collected by, and shed by, the compressor.

The simultaneous action of high-temperature oxidation and mechanical erosion on a metal surface constitutes a mechanism of metal wastage that is of considerable

importance in a number of processes where, for instance, the ability to handle hot, dusty gas streams is of vital importance for process economics **(Wright et al, 1995)**. The collision of solid particles with metal surfaces on which oxide scales are actively growing gives rise to complicated interactions that presents a severe challenge.

According to **Lin et al (1973)** the high cost of repairing or replacing gas-turbine engine components has increased interest in the wear and friction properties of alloys, such as nickel-base alloys, cobalt-base alloys, titanium alloys and chromium-rich steels, which are the materials most involved in such problems. They suggested that, as much of the damage to components in gas-turbine engines is likely to occur during the warming-up and cooling-down periods, when the temperatures are low, understanding of the nominally room-temperature tribological properties of such alloys is of paramount importance.

According to **Takeda et al (1993)** abrasion, erosion and corrosion resistance of components can be greatly increased by protective coatings and this is a growing industry of considerable economic importance. They opined that coal gasification electric power generation and waste incineration involves severe conditions and thick coatings have proved effective. Among the various coating methods thermal spraying fosters progress in both development of materials and modern coating technology because of advances in powder and wire productions. Thermally sprayed coatings are widely used in various applications (air crafts, textile, automobile, mining, etc.) to combat various surface degradation processes such as erosion, wear, corrosion etc **(Murthy et al, 2001)**. Although physical, chemical and mechanical properties of turbine alloys and coatings are documented satisfactorily, there is insufficient data about their rebound and erosion behavior **(Tabakoff, 1992)**.

As learnt form the literature that almost any material can be used for plasma spraying on almost any type of substrate, this flexibility is probably one of the major reasons for the rapid expansion of this technology. Major advantages of plasma spraying lie in reduced coating porosity and increased adhesion to the substrate, coupled with very limited heating of the substrate material. It is often possible to produce types of coatings by these methods, which are not obtainable in any other way. The plasma spray coatings are generally applied for protection against erosion, wear and corrosion, to prevent erosion or cavitations, and to provide electrical insulation or conductivity.

2.9.2 Aim

Currently superalloys are being used to increase the service life of the boilers, especially in the superheater zones of the boilers and new generation ultra and supercritical boilers. Although the superalloys have adequate mechanical strength at elevated temperatures, they often lack resistance to erosion-corrosion environments **(Singh, 2005)**. Ni based coatings are used in applications when wear resistance combined with oxidation or hot corrosion resistance is required **(Rosso et al, 1998)**. Nickel based alloys represent a significant part of overall thermal spray business. These materials are widely used as bond coats and top coats in number of applications requiring combination of properties, such as good wear resistance and corrosion resistance at the same time **(Hidalgo et al, 1997 and Ilavsky et al, 2000)**.

It has been reported in the literature that the diffusion may take place between the substrate and the spray material during the plasma spraying **(Berndt and McPherson, 1979, and Steffens and Mack, 1990)**. Further it is stated that diffusion of elements can have a major influence on coating performance **(Nicholls, 2000)**. Moreover the erosion resistance of coatings is strongly dependent on the coating process and on the substrate material **(Shanov and Tabakoff, 1996)**.

Taking into consideration the above facts for the effect of substrate on the plasma sprayed coatings, five different superalloys (namely Superni 75, Superni 600, Superni 718, Superfer 800H and Superco 605 supplied by Mishra Dhatu Nigam Limited, Hyderabad, India) have been selected for spraying three different coatings. The analysis could further be beneficial to understand the effect of the substrate superalloys, if any, on the performance of the different coatings. The present investigation is aimed to analyze the following performances of plasma sprayed Ni-22Cr-10Al-1Y, Ni-20Cr and Ni_3Al coatings on Ni-, Fe- and Co- based superalloys:

1. The erosion behaviours of the selected superalloys and coatings using room temperature erosion test rig.
2. The sliding wear behaviour of superalloys and these coatings on one of the substrates using Friction Wear Test Rig.
3. The erosion-corrosion performances of the coated and uncoated superalloys in actual industrial environment.

Severe failures of tubes due to erosion-corrosion in the Low Temperature Primary Super Heater has been encountered by maintenance department of the coal fired Thermal Power Plant, Ropar, Punjab, India. This zone has been selected to investigate the erosion-corrosion performance of the specimens for a total duration of 1000 hours.

Erosion resistance must generally be determined by laboratory techniques since the complexity of most eroding systems renders testing under service conditions difficult (**Soderberg et al, 1981**). It was planned to carry out the erosion tests at impact velocity of 40 ms^{-1} and two impingement angles of 30° and 90° at room temperature. These two impingement angles have been selected to distinguish the ductile or brittle behaviour of the materials (**Levy and Hickey, 1986**). The ash composition has been obtained for fly ash from the concerned thermal power plant where it contained around 55% silica, alumina (30%), etc (**Singh, 2003**). **Wells et al (2005)** and **Stringer (1995)** have also reported quartz as one of the main constituents in the ash. Keeping the composition of ash in mind, silica sand particles were found to be a good choice to simulate the condition in the actual boilers. Thus silica sand has been selected as erodent material. Further the fly ash has a particle size ranging from 5 μm to 500 μm (**Suckling and Allen, 1995**). **Wang (1995)** had also reported the mean particle size of approximately 158 μm with high concentration of Si in the fly ash which is retrieved from an operating biomass-fired boiler. The most appropriate average size of 180 μm has been used in the present study.

To evaluate the erosion behaviour of the selected coatings and superalloys in the industrial environment for predicting the actual service behavior it was planned to hang the samples for experimentation by making hole in them. From the literature review and the concerned plant, it is perceived that the erosion by impact of fly ash is severe in the temperature range between 400 and 550°C. Therefore, it was decided to expose the samples to fly ash impact for 10 cycles each of 100 hours duration in the Low Temperature Primary Super Heater zone of the boiler where temperature is around 540°C. For the specimens kept in boiler environment it was also planned to visually examine the samples after each cycle and record the changes in colour, luster, adherence-spalling tendency, and growth of cracks in the coatings/oxide scales formed.

Standard techniques such as Scanning Electron Microscope (SEM), X-ray Diffractometer (XRD), Energy Dispersive X-ray Analysis (EDAX) and Electron Micro Probe Analyser (EPMA) were chosen to characterise the as sprayed coating, erosion, wear and erosion-corrosion products, with an attempt to understand and propose mechanisms of

degradation, wherever possible. The kinetics data of high temperature erosion-corrosion and other data and analysis of the results would be useful to assess the effectiveness of the chosen coatings in providing resistance to erosion-corrosion wear for the superalloys and, to compare the performance of the different coatings under study. The analysis would further be beneficial to understand the effect of the substrate superalloys, if any, on the performance of the different coatings.

Chapter 3

EXPERIMENTAL TECHNIQUES AND PROCEDURES

This chapter presents the experimental techniques and procedures employed for applying the coatings and their characterisation, the erosion wear, sliding wear and erosion-corrosion studies and analysis of their final products. Specifications of the equipments and other instruments used for the present investigation are also incorporated.

3.1 SELECTION OF SUBSTRATE MATERIALS

Selection of the substrate material for the present study has been made after discussion with Mishra Dhatu Nigham Ltd, Hyderabad (India), who has developed the materials, which are basically Ni-, Fe- and Co- based superalloys having Midhani Grades Superni 75, Superni 600, Superni 718, Superfer 800 and Superco 605. The alloys were procured in rolled sheet form with each alloy sheet having different thickness within a range of 2-6 mm. Nominal composition and industrial applications of these alloys are given in Table 3.1.

3.2 DEVELOPMENT OF COATINGS

3.2.1 Preparation of Substrate Materials

Specimens with dimensions of approximately 30mm × 30mm × 5mm were cut from the alloy sheets for erosion studies in room temperature erosion test rig whereas specimens with dimensions of approximately 50mm × 20mm × 4mm were cut for erosion test in the boiler of Thermal Power Plant. Also some cylindrical pin shaped specimens of approximately 30mm length and 5mm diameter were prepared for sliding wear test on pin on disc wear test rig.

3.2.2 Alloy Powders for Coatings

Three types of coating powders namely Ni-22Cr-10Al-1Y (NI-343), Ni-20Cr (NI-105) and Ni_3Al (Ni and Al in the stoichiometric ratio of 3:1) were chosen for plasma

Table 3.1 Nominal composition and industrial applications of the superalloys.

Sr. No.	Alloy Midhani Grade *(Similar grade)*	Chemical Composition (wt. %)												Recommended Application (Manufacturer's Catalogue)	Density (g/cm^3)
		Fe	**Ni**	**Cr**	**Co**	**Cu**	**Al**	**Mo**	**Mn**	**Ti**	**Si**	**C**	**Others**		
1	Superni 75 *(Nimonic 75)*	3	Bal	19.5	-	-	-	-	-	0.3	-	0.1	-	Gas Turbine, boiler parts	8.41
2	Superni 600 *(Inconel 600)*	10 max	Bal	15.5	-	-	-	-	0.5	-	-	0.1	-	Furnace parts, heat treatment jigs	8.39
3	Superfer 800 *(Incoloy 800)*	Bal	32	21	-	-	0.3	-	1.5 max	0.3	1 max	0.1 max	-	Steam boilers, furnace equipment, heat exchangers and piping in chemical industry, reformer, baffle plates/tubes in fertilizer plants	7.95
4	Superco 605 *(KC 20WN L605)*	3	10	20	Bal	-	-	-	1.5	-	0.3	0.08	W-15	Gas Turbines, furnace equipment	8.19
5	Superni 718 *(Inconel 718)*	18.5	Bal	19	-	0.15	0.5	3.05	0.18	0.9	0.18	0.04	Cb + Ta -5.13	Jet engines, pump bodies and parts	9.10

spray deposition on the five types of superalloy substrates. In the last two cases of Ni-20Cr and Ni_3Al coatings, Ni-22Cr-10Al-1Y was also used as a bond coat, whereas entire coating of the Ni-22Cr-10Al-1Y powder was applied to constitute the first coating for the present study. The Ni_3Al coating powder was prepared in the laboratory whereas the first two coating powders were commercially available. Nickel powder with minimum assay 99.5% and size 200 mesh (Art. 4860) and aluminium fine powder with minimum assay 99.7% (Art. 880) supplied by Loba Chemical were mixed in stochiometric ratio 3:1 in the laboratory ball mill for 15 hrs to form a uniform mixture of Ni_3Al powder. Chemical composition and particle size of all the coating powders have been reported in Chapter 4 of the present study.

3.2.3 Formulation of Coatings

The specimens were polished with SiC papers down to 180 grit and subsequently grit blasted by alumina (Grit 60) before application of the coatings by shrouded plasma spray process. The coating work was carried out by a commercial firm namely Anod Plasma Ltd. Kanpur (India). The coatings were deposited on the substrates using 40 kW Miller Thermal (USA) plasma spray apparatus. Argon was used as powder carrying and shielding gas. All the process parameters were kept constant throughout the coating process while spraying distance was maintained in a narrow range of 90-110 mm. Ni-22Cr-10Al-1Y powder was deposited as a bond coat around 150 μm thick before applying the final coatings. The process parameters for the shrouded plasma spray process employed for applying the coatings are summarised in Table 3.2.

Table 3.2 Parameters of the argon shrouded plasma spray process

Arc current (A)	700
Arc voltage (V)	35
Powder flow rate (rev./min)	3.2
Spraying distance (mm)	90-110
Plasma arc gas (Argon) (psi)	59
Carrier gas (psi)	40
Spray gun nozzle diameter (mm)	6

3.3 CHARACTERISATION OF COATINGS

3.3.1 Measurement of Coating Thickness

Thickness of the coatings was continuously monitored during the process of plasma spraying with Minitest-2000 made in Germany. Efforts were made to obtain coatings of uniform thickness. In order to verify the thickness of coatings some of as sprayed specimens were cut along the cross-section and mounted as explained in the Section 3.3.3. Scanning Electron Microscope (LEO 435VP) with attached Robinson Back Scattered Detector (RBSD) was used to obtain the BSE images. The average thickness of the coating was then measured from these BSE images and the same has been reported in Chapter 4 of the present study.

3.3.2.1 Measurement of Density and Bond Strength of the Coatings

The densities of the coatings were measured using the following procedure. Firstly the superalloy substrate samples were polished and cleaned with acetone and dried. The weight with accuracy of 0.0001 gm and dimensions (using micrometer screw gauge with least count of 0.001 mm) of the samples were measured and numbers were marked on them, since each sample is having different weight and dimension. After depositing plasma coatings on these samples, again weight and dimensions were measured. The density was calculated by dividing the difference in mass by difference in volume of the sample before and after the coating. The density data obtained has been reported in chapter 4. The bond strength of the coatings was measured according to ASTM standard C633-01 at Defence Metallurgical Research Laboratories, Hyderabad, India. Also the bond strength of the coatings was measured at Anod Plasma Spray Limited, Kanpur using standard tensile test machine. The results obtained have been reported in chapter 4.

3.3.3 Measurement of Porosity and Oxides Contents

Porosity and oxides contents measurements for the plasma sprayed coatings have been made from the cross-sectional micrographs of the specimens. Porosity and oxides contents of the coated samples were measured on a Zeiss Axiovert 200 MAT Inverted optical microscope fitted with imaging software Zeiss AxioVision Release 4.1 (Germany). Ten values of porosity and oxides contents have been measured for each coated specimens and their averages are reported in Chapter 4.

3.3.4 Metallographic Studies

For metallographic studies across the cross-section, the plasma spray coated specimens were cut along their cross-section with diamond cutter (Buehler's Precision Diamond Saw, Model ISOMET 1000, USA make). Thereafter, the cut sections were hot mounted in Buehler's transoptic powder (20-3400-080) so as to show their cross-sectional details. This was followed by polishing of the mounted specimens by a belt sanding machine having emery belt (180 grit). The specimens were then polished manually down to 1000 grit using SiC emery papers. Final polishing was carried out using cloth polishing wheel machine with 1 μm lavigated alumina powder suspension. Specimens were then washed and dried before being examined under Zeiss Axiovert 200 MAT Inverted Optical Microscope interfaced with imaging software Zeiss AxioVision Release 4.1, Germany. The same microscope was used to obtain surface microstructures of the coatings. Cross-sectional as well as surface microstructures of the specimens used in the current study are presented in Chapter 4.

3.3.5 Measurement of Microhardness

Microhardness of the coatings was measured by Leitz's Hardness Tester Mini Load-2 (Made in Germany). 15-gram load was provided to the needle for penetration and a hardness value was based on the relation

$$Hv = 1854.4 \times \frac{P}{d^2}$$

(Where P is the load in gram, and d is the mean of the indentation diagonal length in mm).

Microhardness values were calculated by taking average of 10 measurements at each distance. These microhardness values are plotted as a function of distance from the coating/substrate interface in Chapter 4.

3.3.6 X-Ray Diffraction (XRD) Analysis

The plasma sprayed specimens were subjected to XRD analysis to identify various phases formed on their surfaces. Diffraction patterns were obtained by Bruker AXS D-8 Advance Diffractometer (Germany) with CuK_α radiation and nickel filter at 20 mA under a voltage of 35 kV. The specimens were scanned with a scanning speed of 1 Kcps in 2θ range of 10 to 110^0 and the intensities were recorded at a chart speed of 1 cm/min with

1^0/min as Goniometer speed. Assuming height of the most prominent peak as 100%, the relative intensities were calculated for all the peaks. The diffractometer being interfaced with Bruker DIFFRAC^{plus} X-Ray diffraction software which provides 'd' values directly on the diffraction pattern. These'd' values were then used for identification of various phases with the help of inorganic ASTM X-Ray diffraction data cards.

3.3.7 Scanning Electron Microscopy (SEM) and Energy Dispersive X-Ray (EDAX) Analysis

Surface morphology of the as-sprayed coatings was also studied with the help of Scanning Electron Microscope (LEO 435VP) with an aim to understand the structure of the coatings and identify oxide inclusions, unmelted particles, pores etc. Also surface SEM/EDAX analysis of some specimens was performed at Inter University Consortium (IUC) for Department of Atomic Energy (DAE) Facilities, Indore (India). The equipment consisted of a Scanning Electron Microscope of JEOL with EDAX attachment of Oxford model Flex Scan 520, England make. Although the compositions correspond to selected points on the as-sprayed surfaces, still the data could be useful to understand the formation of desired compositions in the coatings. SEM morphologies and the elemental analysis for the as sprayed coatings have been reported in Chapter 4 of this thesis.

3.3.8 Electron Probe Micro Analyser (EPMA)

For detailed cross-sectional analysis, the specimens were cut along the cross-section, mounted and polished in accordance with the procedure already discussed in section 3.3.4 and subjected to EPMA analysis. The EPMA analysis was performed on the mounted specimens after applying carbon coating on them. The EPMA analysis consisted of recording BSE Image and elemental X-ray mappings for representative area of each specimen. The selected area could have the three regions i.e. base specimen, coating and some epoxy region adjacent to the scale. X-ray mappings were obtained for all the elements of the substrate and the coatings and are reported in Chapter 4. EPMA analysis was done at Institute Instrumentation Centre (IIC), Indian Institute of Technology Roorkee, Roorkee (India) on JXA-8600M microprobe.

3.4 ROOM TEMPERATURE EROSION TESTS

3.4.1 Experimental Setup

Erosion testing was carried out using a room temperature solid particle erosion test rig (Fig. 3.1) at the Defence Metallurgical Research Laboratory, Hyderabad, India. The rig consisted of an air compressor, and particle feeder, an air particle mixing and accelerating chambers. Dry compressed air was mixed with the particles, which were fed at a constant rate from a conveyor belt type feeder in the mixing chamber and then accelerated by passing the mixture through a tungsten carbide converging nozzle of 4 mm diameter. These accelerated particles impacted the specimen, which could be held at various angles with respect to the impacting particles using an adjustable sample holder. The feed rate of the particles could be controlled by monitoring the distance between the particle feeding hopper and the belt drive carrying the particles to the mixing chamber. The impact velocities of the particles could be varied by varying the pressure of the compressed air. The velocity of the eroding particles was determined using a rotating double-disc method as described by **Ruff and Ives (1975)**.

3.4.2 Erosion Studies in an Air Jet Erosion Test Rig

The studies were performed for uncoated as well as coated specimens for the purpose of comparison as discussed in section 3.4.1. The erosion test conditions utilized in the present study are listed in Table 3.3. A standard test procedure was employed for each erosion test. The uncoated as well as the coated specimens were polished down to 1μm alumina wheel cloth polishing to obtain similar condition on all the samples before being subjected to erosion run. The samples were cleaned in acetone, dried, weighed to an accuracy of 1×10^{-5} g using an electronic balance, eroded in the test rig for 5 min and then weighed again to determine weight loss. The ratio of this weight loss to the weight of the eroding particles causing the loss (i.e., testing time x particle feed rate) was then computed as the dimensionless incremental erosion rate. This procedure was repeated until the erosion rate attained a constant steady-state value as per **ASTM standard G76-95 (2000)**. In the present study standard silica sand (ρ=2600 kg/m^3; Knoop hardness 880) was used as erodent (Fig. 3.2). Test has been repeated three times for all the materials and the average data for mass loss after each interval of time has been used for the analysis of erosion rate.

Table 3.3 Erosion conditions

Erodent material	Silica sand (Irregular shape)
Particle size (μm)	Average 180 (range 150–250)
Particle velocity (m/s)	40 ± 3
Air Pressure (kg/cm^2)	2.0
Erodent feed rate (g/min)	5 ± 0.4
Impact angle (^{0})	30, 90
Test temperature	Room Temperature
Nozzle diameter (mm)	4
Test time (min)	Cycles of 5 minutes
Sample size (mm × mm × mm)	30 × 30 × 5

3.4.3 Analysis of eroded surfaces

All the specimens subjected to erosion wear were analysed for the characterisation of erosion products. The analysis was performed for the surface and cross-section of the eroded specimens from room temperature studies. The specimens were analysed using surface SEM, EDAX and measurement of surface roughness using optical profilometer. Also some of these samples were subjected to cross-sectional SEM analysis.

3.4.3.1 Visual Observation

For the specimens eroded in laboratory test rig, visual examination was made after the completion of erosion cycles and the macrographs of the eroded specimens were taken.

3.4.3.2 Erosion rate from weight loss data (g/g)

The erosion rate data as obtained in section 3.4.2 was plotted with respect to cumulative mass of erodent and the plots have been given in chapter 5.

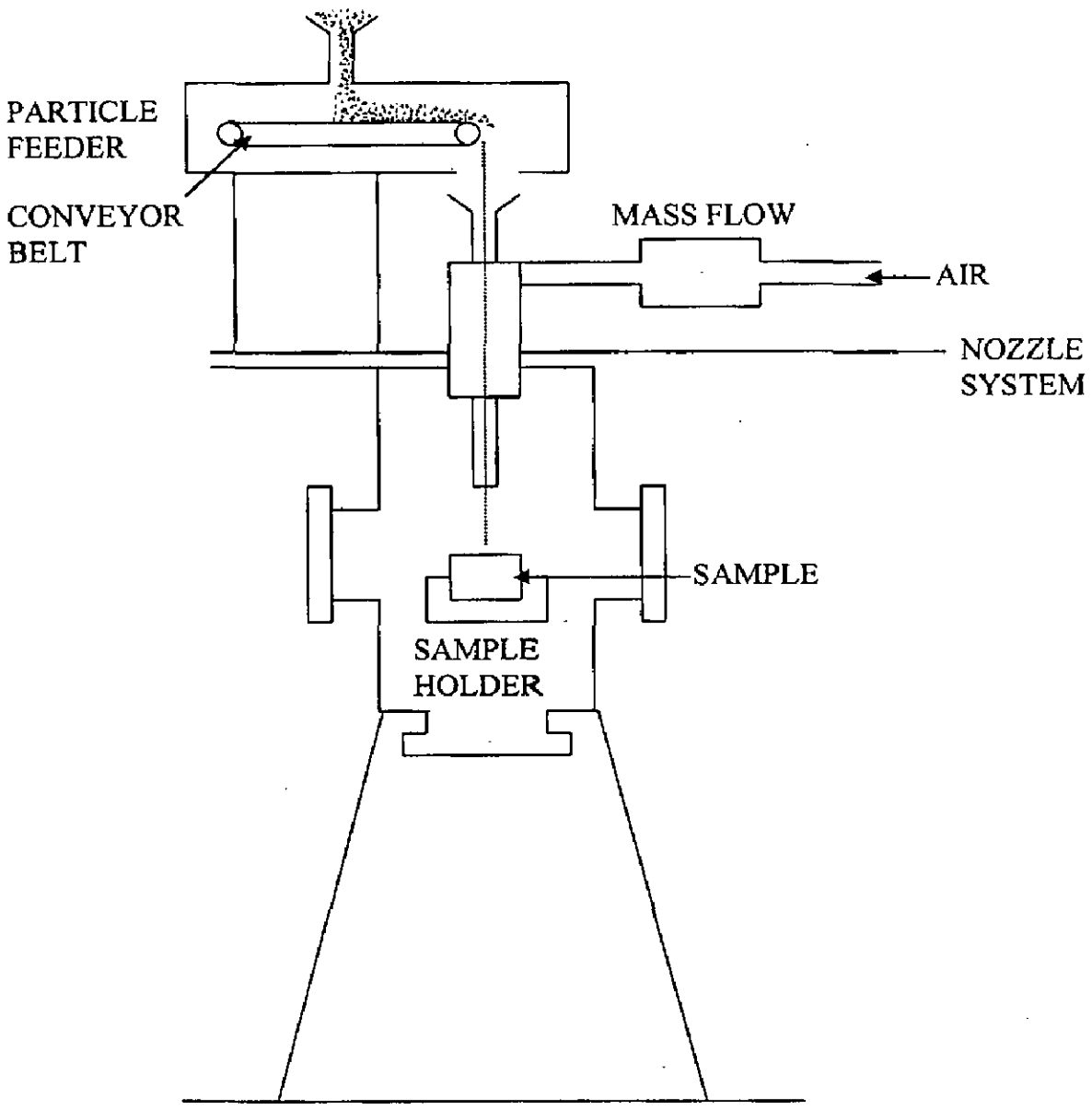

Fig. 3.1 A schematic view of an Air Jet Erosion Test Rig

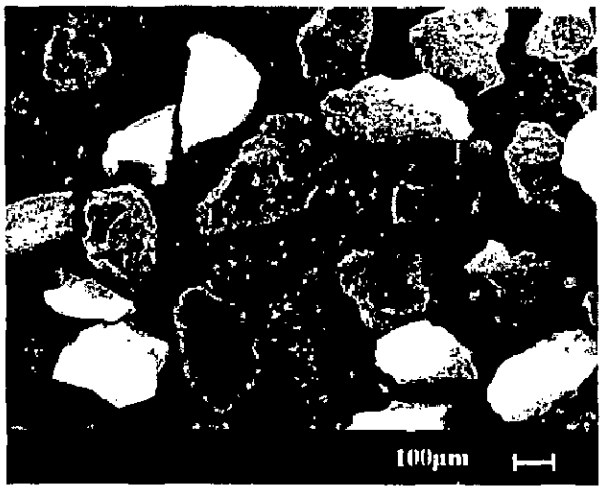

Fig. 3.2 Scanning electron micrograph of the silica sand particles.

3.4.3.3 Erosion Rate in Terms of Volume Loss (cm^3/g)

The constant value of the incremental erosion rate has been defined as the steady-state erosion rate. This constant value of incremental erosion rate was converted into volume wear rate by dividing it with the density of the target material to take into account the different densities of the coating material and the substrate. The histograms illustrating the steady state erosion rates in terms of volume loss (cm^3/g) have been plotted to compare erosion rates of different superalloys and coatings, and have been discussed in chapter 5.

3.4.3.4 SEM/EDAX Analysis

3.4.3.4.1 Surface Morphology

Surface SEM analyses of eroded samples were conducted using Scanning Electron Microscope (LEO 435VP) at IIC, IITR, Roorkee. Also SEM/EDAX analysis for some of the selected specimens was carried out at Inter University Consortium (IUC) for Department of Atomic Energy (DAE) Facilities, Indore (India).

3.4.3.4.2 Cross-Sectional Morphology

The eroded specimens after all surface analysis were cut across the cross-section from the eroded zone and polished as discussed in section 3.3.4. The cross-sectional SEM of some of the selected specimens was taken and is discussed in the chapter.

3.4.3.5 Surface Roughness of the Eroded Zone

The surafce roughness of all the eroded samples was measured from 5 different places from the eroded area using Veeco Optical Profilometer (USA make) and their average values have been reported in chapter 5. Also 3-Dimensional surface topography illustrating the surface roughness profiles of the eroded superalloys and coatings were taken.

3.5 SLIDING WEAR STUDIES USING PIN- ON -DISC WEAR TEST RIG

3.5.1 Experimental set up

Dry sliding wear tests for the superalloys and plasma sprayed coatings have been conducted using a sturdy pin-on-disc machine model TR-20E, supplied by M/S

DUCOM, Bangalore (INDIA). A complete photograph of the set up of the machine is shown in Fig. 3.3. The tests have been conducted in air having relative humidity in range from 40 to 75 pct. Wear tests have been conducted using pin samples that had flat surfaces in the contact region and the rounded corner. The pin is held stationary against the counterface of a 100 mm diameter rotating disc made of En-32 steel hardened to 62-65 HRC as provided in the pin-on disc machine. The composition of the material of the steel disc is given in Table 3.4. The En-32 steel is a plain carbon steel case hardened to attain a hardness of 62-65 HRC.

Table 3.4 Chemical composition (wt %) of the En-32 steel disc

C	Si	Mn	S	P
0.42 (max)	0.05-0.35	0.40-0.70	0.05 (max)	0.05 (max)

3.5.2 Sliding Wear Studies

The uncoated superalloys as well as one set of plasma spray coated specimens were prepared for sliding wear studies as discussed in section 3.2.1. The pins have been polished up to 4/0-grade emery paper and both the disc and the pin were cleaned by acetone and dried before carrying out the test. The pin is loaded against the disc through a dead weight loading system. The wear tests for superalloys and coatings have been conducted under the normal load of 9.8 N and at a fixed sliding velocity of 1 ms^{-1}. The track radii for the pin are kept at 43 mm. The rpm of the rotation of disc is adjusted so as to keep the linear sliding speed at a constant value of 1 ms^{-1}. A variation of ±5 rpm is observed in the rpm of the disc. The pilot experiments on as-coated superalloy pins were carried out by varying the coating time and the results were used to select the sliding distance for a particular load so that the wear is confined within the coating primarily throughout the test. The time interval of measuring the weight loss of the pin was so adjusted that at least five data points were obtained over the total sliding distance. Wear test on bare superalloys have been carried out for a total sliding distance of about 3000 m (10 cycles of 5 min. duration). Whereas for coated specimens, wear test has been carried out for a total sliding distance of 1200 m (10 cycles of 2 min. duration), so that only top coated surface is exposed for each sample. Tangential force is monitored continuously

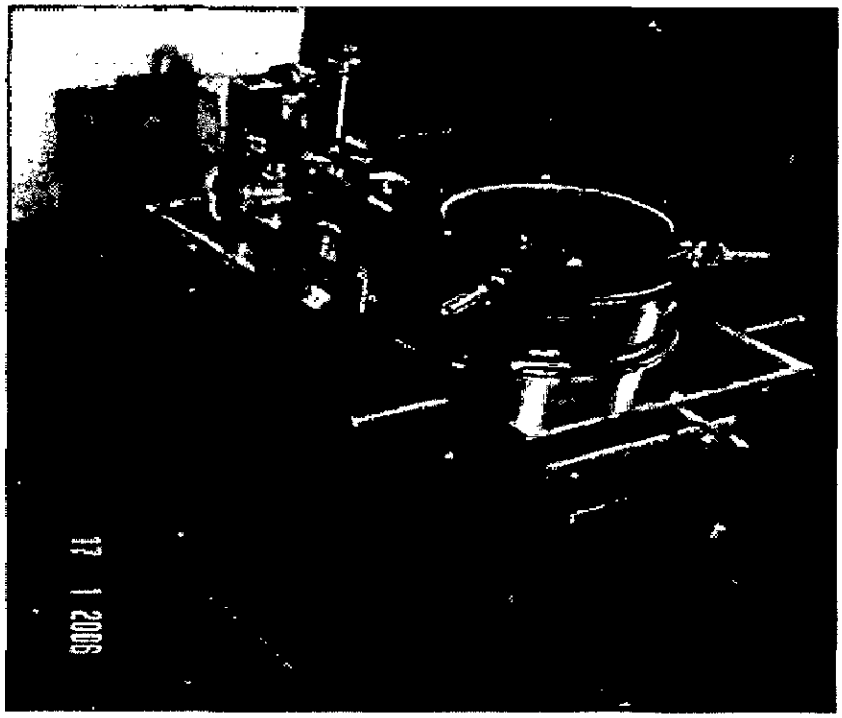

Pin-on-disc wear test rig

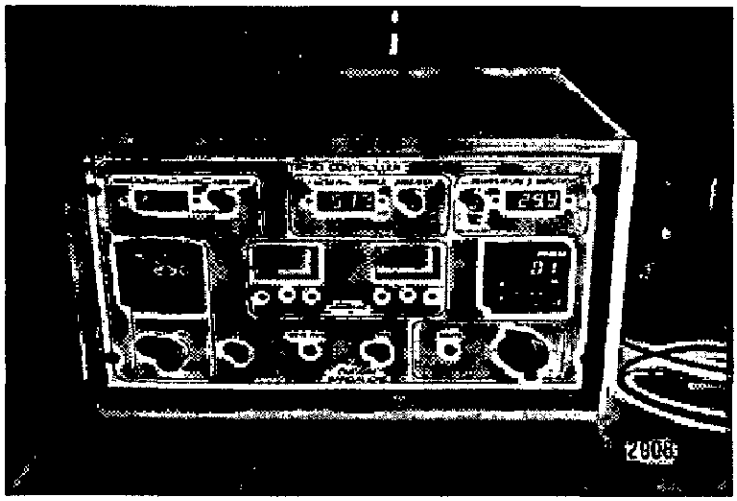

Controller of Pin-on-disc wear Tribotester

Fig. 3.3 A photograph of the Pin-on-disc wear test rig and its controller.

during the wear test. Weight losses of pins have been measured at different intervals of time to determine wear loss. The pin is removed from the holder after each run, cooled to room temperature, brushed lightly to remove loose wear debris, weighed and fixed again in exactly the same position in the holder so that the orientation of the sliding surface remains unchanged. The weight has been measured by a micro balance to an accuracy of 1×10^{-4} g. Each test at a given load and sliding velocity has been repeated three times and the average data for mass loss after each interval of time has been used for the analysis of wear rate. The coefficient of friction has been determined from the friction force and the normal loads; only precalibrated dead loads have been used.

3.5.3 Analysis for Sliding Wear Study

All the specimens subjected to sliding wear were analysed for the characterisation of wear surfaces and wear debris. The worn surfaces and wear debris of the specimens have been examined under scanning electron microscope.

3.5.3.1 Friction and Wear Rate

The coefficient of friction determined from the frictional force and the normal loads has been plotted against sliding time to give the friction behaviour of the superalloys and coatings. The weight loss data has been converted to volume loss data using the density of the superalloys and the coatings. The wear rate data were plotted with respect to sliding distance for superalloys and coatings, and the plots have been given in the subsequent chapter. The specific wear rates **(Ramesh et al, 1992)** of the superalloys and coatings were obtained by

$$W = \delta m / L\rho F \tag{1}$$

where W denotes specific wear rates in mm^3 /N-m,

δm the weight loss measured in mg,

L the sliding distance in m,

ρ the density of the worn material in mg/mm^3 and

F the applied load in N.

3.5.3.2 Examination of Worn Surfaces and Wear Debris

The worn surfaces of all the tested specimens were analysed using SEM facility at IIT Roorkee. The examination of the nature of wear debris provides basic information

regarding the degree of work hardening or the composition of the transferred layer. The debris material generated during wear experiments were carefully collected during dry sliding wear of all the specimens. These samples of wear debris are examined under scanning electron microscope and the salient features have been photographed.

For identification of different phases formed, X-ray diffraction analysis of wear debris collected for all the specimens was conducted on the diffractometer described in section 3.3.5. and the results of all the analysed samples have been presented in Chapter 6.

3.6 EROSION-CORROSION STUDIES IN ACTUAL INDUSTRIAL ENVIRONMENT

The samples were also subjected to actual industrial environment in the Low Temperature Primary Super Heater (LTSH) of Guru Gobind Singh Super Thermal Plant, Ropar, Punjab (India). This zone is selected, since severe failure due to erosion-corrosion has been reported by the concerned power plant. Two specimens of each coated and uncoated superalloys were prepared for this study as per procedure discussed in section 3.2.1, further 2 mm holes were drilled to hang these samples for experimentation. The uncoated as well as the coated specimens were polished down to 1μm alumina wheel cloth polishing to obtain similar condition on all the samples before being subjected to boiler environment. Also physical dimensions of the specimens were then measured carefully with digital Vernier Caliper to evaluate their surface areas. To evaluate the thickness loss of the samples during the exposure period, the average thickness (average of 20 measurements in each samples) is measured using micrometer screw gauge. The samples were hanged in the boiler with the help of stainless steel wire and a rigid support of stainless steel rod through the soot blower dummy points at 37.6 m height from the base of boiler. The temperature of the hanging zone was measured at regular intervals during the study and the temperature was about 540 ^{o}C with full load of 210 MW. The coal analysis data is reported in Table 3.5 whereas the chemical analysis of the flue gas and ash present inside the boiler is given in Table 3.6. The samples were exposed to combustion gases for 10 cycles each of 100 hours duration, followed by 1 hour cooling at ambient conditions. After the end of each cycle the samples were visually observed for any change on surface and weight of samples were measured subsequently. The total air flow is 725-790 T/hr. Analysis of flue gases showed presence of 14-16.5% CO_2 and 2.5-5% O_2 in it.

Table 3.5 Coal analysis data

Constituent	**Wt. % age**
Total moisture (inherent + surface)	10.43
Inherent moisture	7.55
Ash	34.74
Ash on fire basis (actual)	33.64
Volatile metal	21.59
GC_v (Gross calorific value) in Kcal/ kg	4187
GC_v on fire basis in Kcal/ kg	4055
Net GC_v in Kcal/ kg	3834
Unburnt carbon in fly ash	1.35
Unburnt carbon in bottom ash	5.75

Table 3.6 Chemical analysis of ash and flue gases inside the boiler

Ash		Flue Gases (Volumetric flow, 231 m^3/sec)	
Constituent	Wt. %age	Constituent	Value relative to flue gases
Silica	54.70	SO_x	236 mg/m^3
Fe_2O_3	5.18	NO_x	1004 $\mu g/m^3$
Al_2O_3-Fe_2O_3/Al_2O_3	29.56	CO_2	14-16.5%
Calcium oxide	1.48	O_2	2.5-5 %
Magnesium oxide	1.45		
SO_3	0.23		
Na_2O	0.34	40% excess air was supplied to the boiler for the combustion of coal.	
K_2O	1.35		
Ignition loss	4.31		

3.7 ANALYSIS OF EROSION-CORROSION PRODUCTS IN BOILER ENVIRONMENT

The surface and cross-section of the eroded-corroded specimens from boiler environment were analysed by XRD, SEM, EDAX, measurement of scale thickness and EPMA analysis.

3.7.1 Visual Observation

For the specimens kept in boiler environment, visual examination was made after each cycle and changes in colour, luster, adherence-spalling tendency, and growth of cracks in the coatings/oxide scales were recorded. After the completion of 10 cycles (each cycle of 100 hr and 1 hour cooling), the exposed specimens were finally carefully visually examined and their macrographs were taken.

3.7.2 Thermogravimetric Studies

The weight change values were calculated at the end of each cycle with the aim to approximate the kinetics of erosion-corrosion for the specimens kept in boiler environment. The weight change data were plotted with respect to number of cycles for each specimen and the plots have been given in the subsequent chapters.

3.7.3 Measurement of Scale Thickness

The eroded-corroded specimens after 1000 hours exposure in the boiler were cut across the cross-section and polished as discussed in section 3.3.4. In some cases, Scanning Electron Microscope (LEO 435VP) with attached Robinson Back Scattered Detector (RBSD) was used to obtain the BSE images at the areas where the scale thickness was observed to be the least. Average thickness of the scales was then measured from the respective BSE images and the data has been presented in Chapter 7.

3.7.4 X-Ray Diffraction (XRD) Analysis

For identification of different phases formed in the eroded-corroded specimen surfaces after 1000 hours exposure in the boiler, X-ray diffraction analysis of all those specimens was conducted on the diffractometer described in section 3.3.6 and results of all the analysed samples have been presented in Chapter 6.

3.7.5 SEM/EDAX Analysis

3.7.5.1 Surface Morphology

SEM/EDAX analysis of the eroded-corroded specimen surfaces after 1000 hours exposure in the boiler of thermal power plant, Ropar was conducted at CRF, Indian Institute of Technology, Kharagpur (India) using JEOL (JSM-5800) Scanning Electron Microscope fitted with EDAX attachment of Oxford (Model-6841) made in England. The equipment could directly indicate the elements or phases (oxides) present at a point alongwith their compositions (weight %) based on built-in EDAX software, which is a patented product of Oxford ISIS300. Although these compositions correspond to selected points on the surfaces, still the data could be useful to support the formation of various phases in the layers. The specimens were scanned under the microscope and the critical areas of interests were photographed with an aim to identify the micro cracks and morphology of the surface scale.

3.7.5.2 Cross-Sectional Morphology

SEM/EDAX analysis for some of the selected specimens was carried out along their cross-sections at Inter University Consortium (IUC) for Department of Atomic Energy (DAE) Facilities, Indore (India). The equipment consisted of a Scanning Electron Microscope of JEOL with EDAX attachment of Oxford model Flex Scan 520 England make. Cross-sectional BSE images were taken and some points of interest were identified on these images including scale/coating and substrate. EDAX analysis was then conducted to ascertain elemental composition (weight %) for these points. Although these compositions correspond to selected points along the cross-sections, still the data could be useful to approximate the distribution of various elements across the thickness of the scales. In some cases, the scale thickness was also measured from these BSE images.

3.7.6 Electron Probe Micro Analyser (EPMA)

All the exposed specimens were subjected to EPMA analysis. The details regarding the EPMA equipment and preparation of the specimens have already been mentioned in Section 3.3.8 of this chapter. Besides, some specimens were analysed at Material Science Division, Bhabha Atomic Research Centre, Trombay, Mumbai (India) using Cameca SX100, 3 Wavelength Dispersive Spectrometer, made in France.

During EPMA analysis, BSEI and elemental X-ray mappings were obtained for some critical area of interest on each specimen. The selected area could have three regions i.e. base specimen, coating and scale. X-ray mappings were obtained for all the elements present in the substrate, the coatings and the environment of study, but only those maps in which an element was identified in substantial concentrations have been reported in the respective Figures.

Chapter 4

CHARACTERISATION OF SUPERALLOYS AND PLASMA SPRAYED COATINGS

This chapter deals with critical examination of the substrate superalloys and the various coatings applied on them. The results of metallographic examination of substrate superalloys as well as the plasma spray coatings have been discussed. The physical properties like porosity, oxide content, microhardness and bond strength of as sprayed coatings have been reported and discussed with respect to the results reported in the literature. The results of XRD, SEM/EDAX and EPMA analysis of the coatings have been incorporated.

4.1 MICROSTRUCTURES OF SUBSTRATE SUPERALLOYS

Optical microstructures of the substrate superalloys are shown in Fig. 4.1, which are explained with reference to atlas of microstructures for industrial alloys (Metals Handbook, 1972 and ASM Handbook, 1995). The microstructures of Superni 75 and Superni 718, Fig. 4.1 (a) and (e) respectively can be characterised by a nickel-rich γ-solid solution matrix. In case of Superni 75, fine carbide particles are dispersed in the gamma matrix mainly along the grain boundaries. The microstructure of Superni 600 shows Ni-Cr-Fe solid solution containing fine as well as coarse carbides in the grains and along the grain boundaries, refer Fig. 4.1 (b). Twin boundaries are also visible in the structure of Superni 600. Whereas the microstructure of the Superfer 800H (Fig. 4.1 (c)) consists of a solid solution matrix in which some of the grains are delineated by particles of precipitated carbides at the grain boundaries and by twinning lines (Metals Handbook, 1972). The microstructure of Superco 605 superalloy (Fig. 4.1 (d)) shows carbide stringers with Co-rich phase. In γ matrix of the Superni 718, carbide segregation in the form of stringers is revealed.

4.2 PLASMA SPRAYED COATINGS

4.2.1 Coating Powders

The composition and designations of the various coating powders are given in Table 4.1. Three types of coating powders (Table 4.1) were deposited by argon shrouded

plasma spray process on five different superalloy substrates (Table 3.1). The scanning electron micrographs indicating morphology and X-ray diffraction profiles of the coating powders are shown in Fig. 4.2 and Fig. 4.3 respectively.

Table 4.1 Composition, particle size and designation of the coating powders

Coating powder	Composition (wt %)	Particle size	Designation
Ni-22Cr-10Al-1Y (Praxair NI-343), also sprayed as a bond coat for other two coatings	Cr (22), Al (10), Y (1), Ni (bal.)	-45 μm+10 μm	NiCrAlY
Ni-20Cr (Praxair NI-105)	Ni (80), Cr (20)	-45 μm+5 μm	Ni-20Cr
Nickel and Aluminium	Stochiometric ratio 3:1 (Ni:Al) Ni (min. assay 99.5%) and Al (min. assay 99.7%) mixed in laboratory ball mill for 8 hrs	Ni- about 74 μm Al- (40 ± 15 μm)	Ni_3Al

4.2.2 Visual Examination of The Coatings

Macrographs for the as coated samples are shown in Fig. 4.4. NiCrAlY and Ni-20Cr coatings have the smooth surfaces with dull green appearance, whereas Ni_3Al coating has shining grey colour with comparatively rough surfaces. These coatings are found to be free from surface cracks.

4.2.3 Measurements of Coating Thickness

SEM Back Scattered Electron Images (BSEI) were taken along cross-sections of the plasma sprayed coated specimens and are shown in Figs. 4.5 to 4.7. In case of Figs. 4.5 (a) and (b), only single layer of NiCrAlY coating is visible. While in each of the micrographs shown in Figs. 4.6 and 4.7, inner layer represents the bond coat of NiCrAlY coating whereas outer layer the particular type of coating. Thickness of the coatings has been measured from BSEI micrographs (Figs. 4.5 to 4.7) and has been reported in Table 4.2. In each case, thickness of the bond coat and the outer coat has been measured separately.

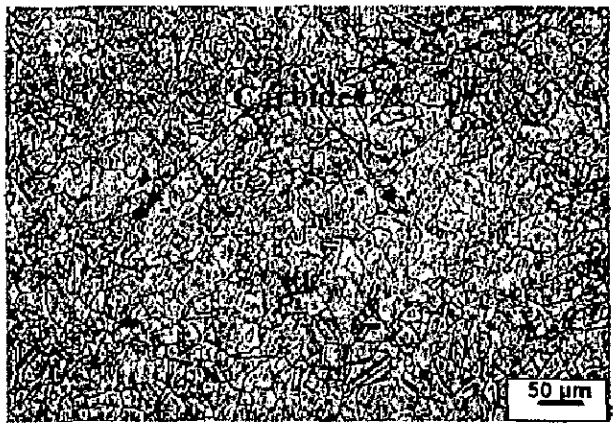

(a)

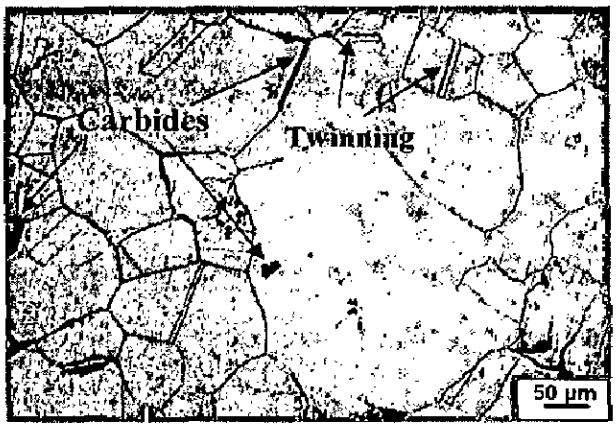

(b)

(c)

(d)

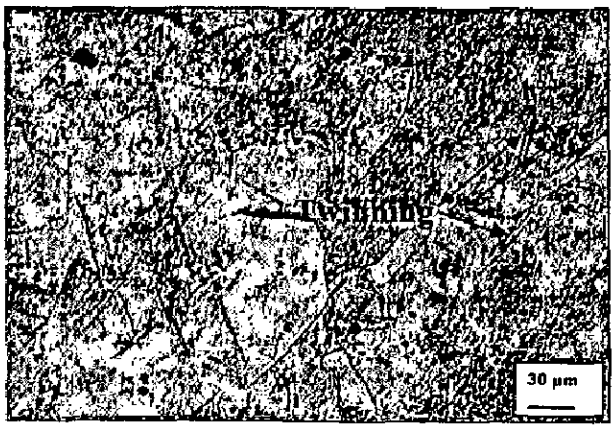

(e)

Fig. 4.1 Optical micrographs of the substrate superalloys

(a) Superni 75 (b) Superni 600 (c) Superfer 800H

(d) Superco 605 (e) Superni 718

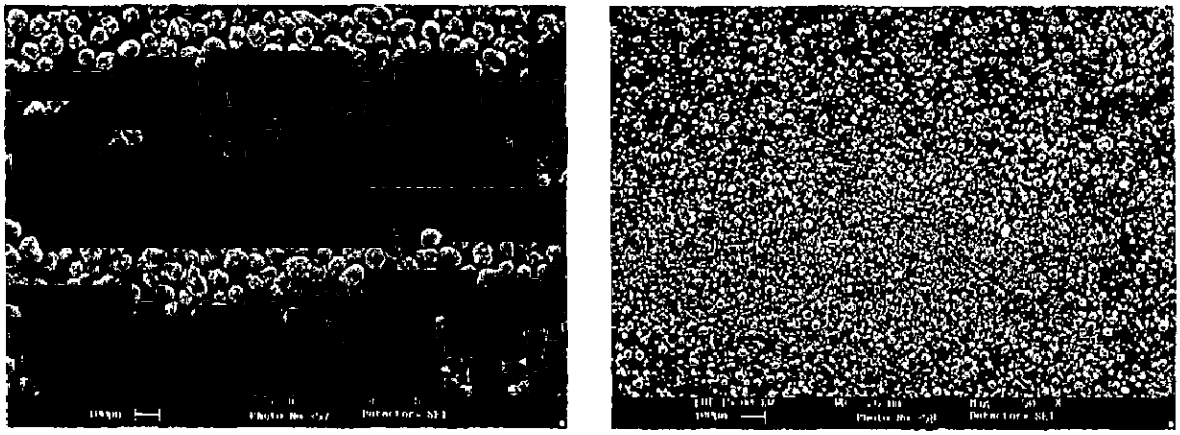

(a) (b)

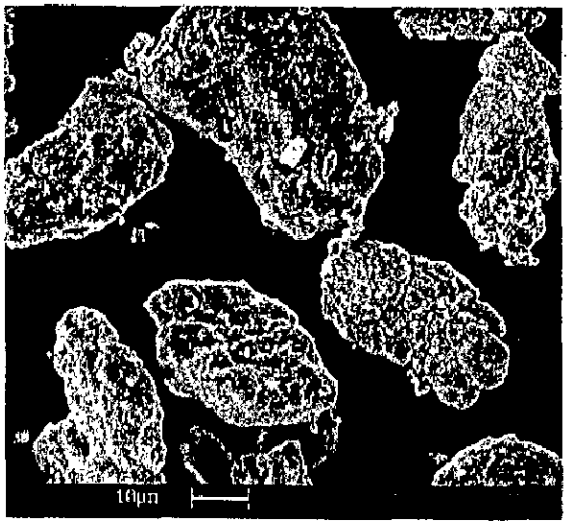

(c)

Fig. 4.2 Scanning electron micrographs showing morphology of powders used for plasma coatings

(a) Ni-22Cr-10Al-1Y powder (b) Ni-20Cr powder

(c) Ni_3Al powder

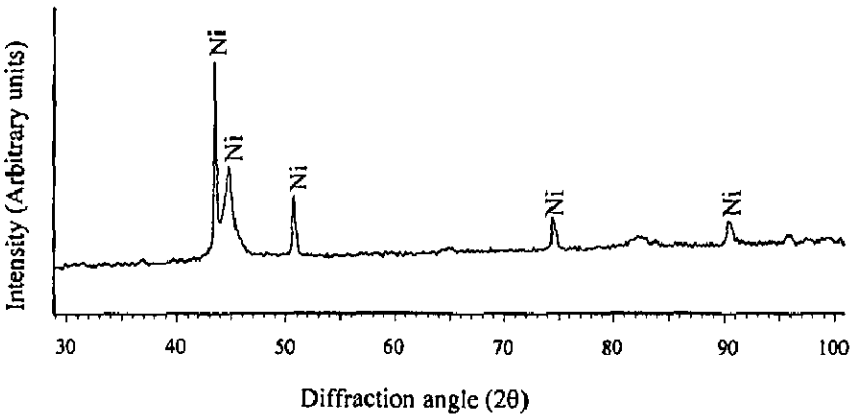

(a)

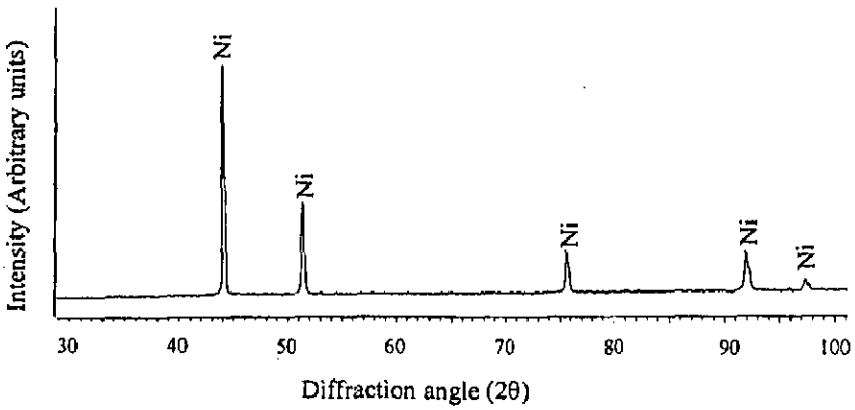

(b)

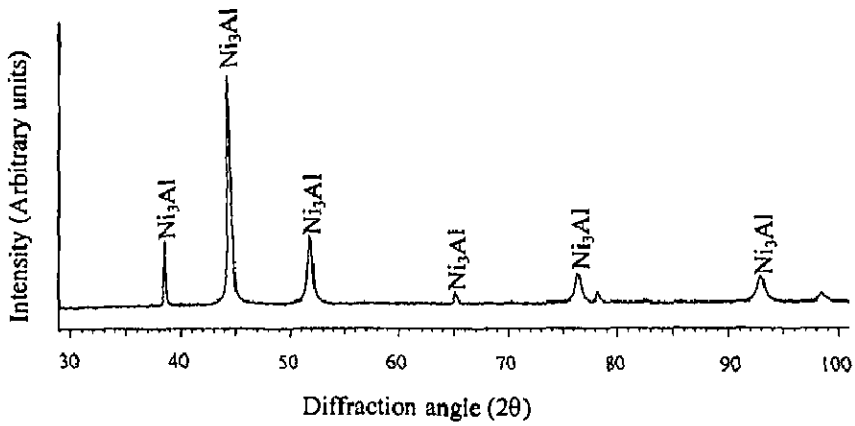

(c)

Fig. 4.3 X-ray diffraction patterns of the coating powders

(a) Ni-22Cr-10Al-1Y powder (b) Ni-20Cr powder

(c) Ni_3Al powder

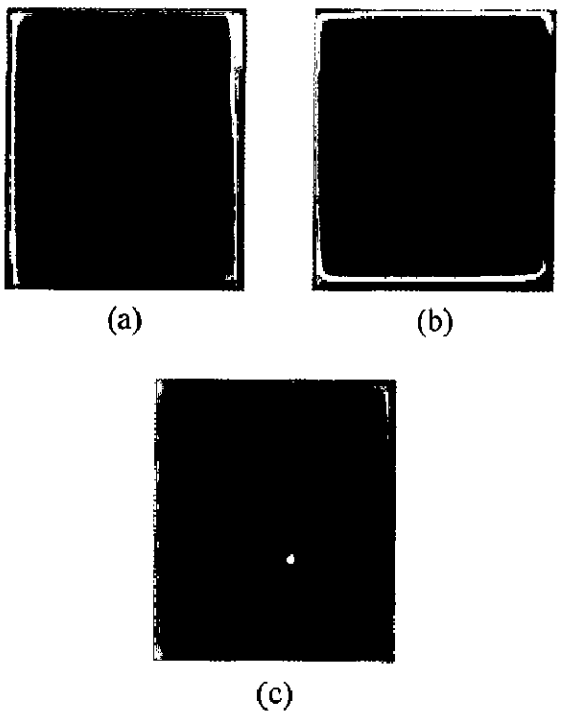

Fig. 4.4 Surface macrographs of as-sprayed plasma coated specimens
(a) NiCrAlY coating (b) Ni-20Cr coating
(c) Ni_3Al coating.

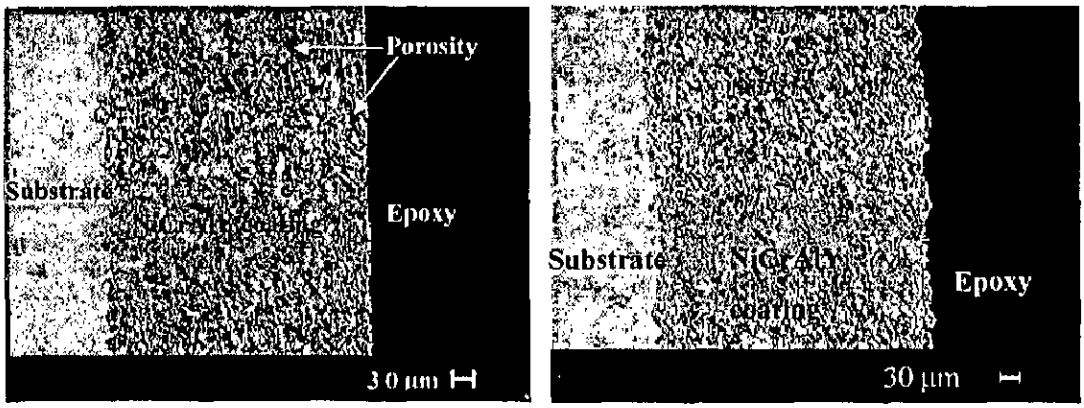

(a) (b)

Fig.4.5 BSEI scanning electron micrograph showing cross-sectional morphology of NiCrAlY plasma sprayed coatings on superalloy substrates
(a) NiCrAlY coating on Superfer 800H (b) NiCrAlY coating on Superco 605.

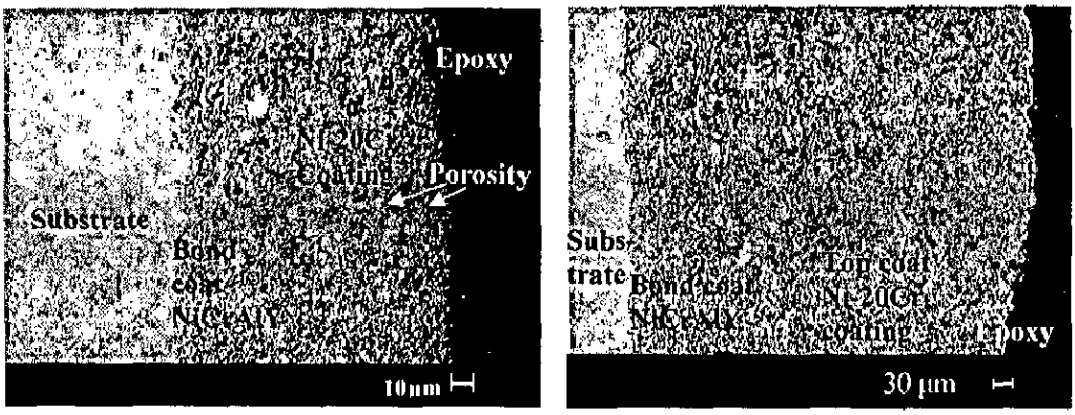

(a) (b)

Fig.4.6 BSEI scanning electron micrographs showing cross-sectional morphology of plasma sprayed Ni-20Cr coatings with bond coat of NiCrAlY coating on superalloy substrates
(a) Ni-20Cr coating on Superfer 800H (b) Ni-20Cr coating on Superco 605.

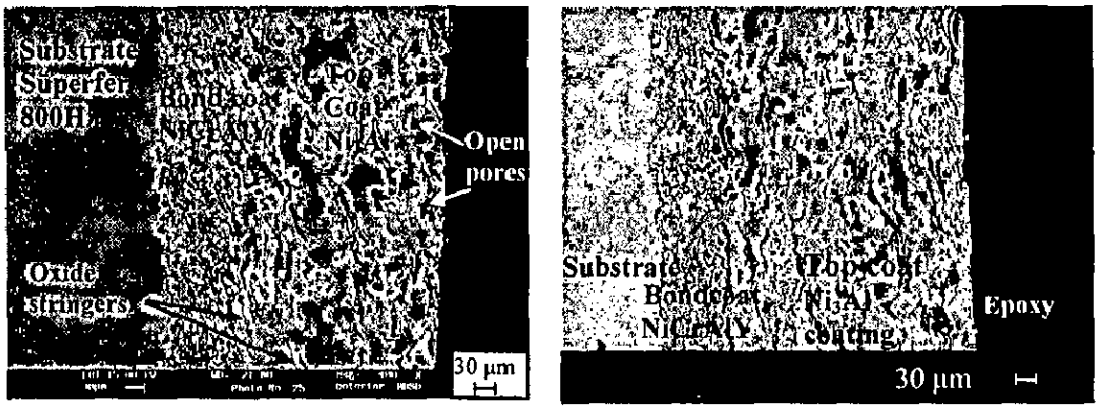

(a) (b)

Fig.4.7 BSEI scanning electron micrographs showing cross-sectional morphology of plasma sprayed Ni_3Al coatings with bond coat of NiCrAlY coating on superalloy substrates

(a) Ni_3Al coating on Superfer 800H (b) Ni_3Al coating on Superco 605.

4.2.4 Porosity, Oxide Contents, Density and Bond Strength of Coatings

Porosity of the coatings has a significant role to play on the erosion and corrosion resistance of plasma sprayed coatings. Dense coatings usually provide better erosion and corrosion resistance than the porous coatings. Porosity and oxides contents measurements were made for the plasma sprayed coatings, which are found to be in a range of 1.4-5.0% and 1-5% respectively (Table 4.2). The densities and bond strengths of the coatings have also been reported in the Table 4.2.

Table 4.2 Average density, coating thickness range, porosity content range and oxides content ranges of the plasma sprayed coatings

Coating	Average density (g/cm^3)	Bond Strength (MPa)	Coating thickness range (μm)			Porosity range (%age)	Oxides content range (%age)
			Bond coat (NiCrAlY)	Outer coat	Total		
NiCrAlY	6.8	40	398-440	--	398-440	2.0-4.5	1-4
Ni-20Cr	6.87	24	90-155	220-288	324-394	2.2-5.0	1-3
Ni_3Al	6.95	17.6	120-168	305-320	413-473	1.4-4.2	2-5

4.2.5 Evaluation of Microhardness

Microhardness of the coatings on different substrate superalloys has been measured along the cross-section. Profiles for microhardness versus distance from the coating-substrate interface are depicted in Fig. 4.8 to 4.10. The average microhardness values for Superni 75, Superni 600, Superfer 800H, Superco 605 and Superni 718 superalloys are observed to be 324, 260, 320, 512 and 478 Hv respectively. Microhardness of the NiCrAlY coating has been found to be in a range of 325 to 568 Hv. From the microhardness profiles it is obvious that the Ni-20Cr coating sprayed on Superfer 800H substrate has shown a maximum microhardness of the order of 658 Hv (Fig. 4.9), followed by NiCrAlY coatings (Fig. 4.8). Whereas the Ni_3Al coating has indicated the least microhardness with a maximum value of the order of 344 Hv (Fig. 4.10), which is just about 53% of that for the Ni-20Cr coating.

4.2.6 Metallographic Studies for the Coatings

4.2.6.1 Surface Structure

Optical micrographs showing the various plasma sprayed coatings (Fig. 4.11 to Fig. 4.13) reveal some voids and oxide inclusions in general with multiphase matrices. The existence of pores has also been indicated.

4.2.6.1.1 NiCrAlY Coating

Figure 4.11 shows optical micrographs for the plasma sprayed NiCrAlY coating on the different superalloys. The microstructures can be characterised by irregularly shaped grains with black phase distributed at intergranular sites.

4.2.6.1.2 Ni-20Cr Coating

Microstructures of the Ni-20Cr coated superalloys which is typical for a shrouded plasma spray process, consist mainly of melted splats providing matrix dispersed with dark coloured phase where unmelted oxide particles and voids are also seen. There is certain directionality indicated by the matrix phase. The melted splats can be recognized as white and nearly columnar grains in the micrographs. Fig. 4.12 depicts the microstructures of the Ni-20Cr coated superalloys which are typical for a shrouded plasma spray process.

4.2.6.1.3 Ni_3Al Coating

Optical micrographs of the Ni_3Al coatings on different superalloy substrates are shown in Fig. 4.13. It can be seen that the deposited coating is having massive structure indicating large size splats which form the matrix with voids and unmelted oxides. Some pores are also seen in the structures. Microstructures revealed are typical for a plasma spray process consisting of splats which are irregular shaped with distinct boundaries.

4.2.6.2 Cross-Sectional Structures

All the coatings were deposited on the stationary substrates by moving the plasma gun and the required thicknesses of the coatings have been obtained by varying number of passes. This might have led to the generation of lamellar structure of the coatings, as is obvious from the micrographs in Fig. 4.14 to Fig. 4.16. Oxide inclusions, in general can be seen in all the cases. The microstructures for the NiCrAlY coatings (Fig. 4.14) and Ni-20Cr coatings (Figs. 4.15) consist of fine grains which are elongated in longitudinal direction, whereas those for the Ni_3Al coatings (Figs. 4.16) are found to be massive.

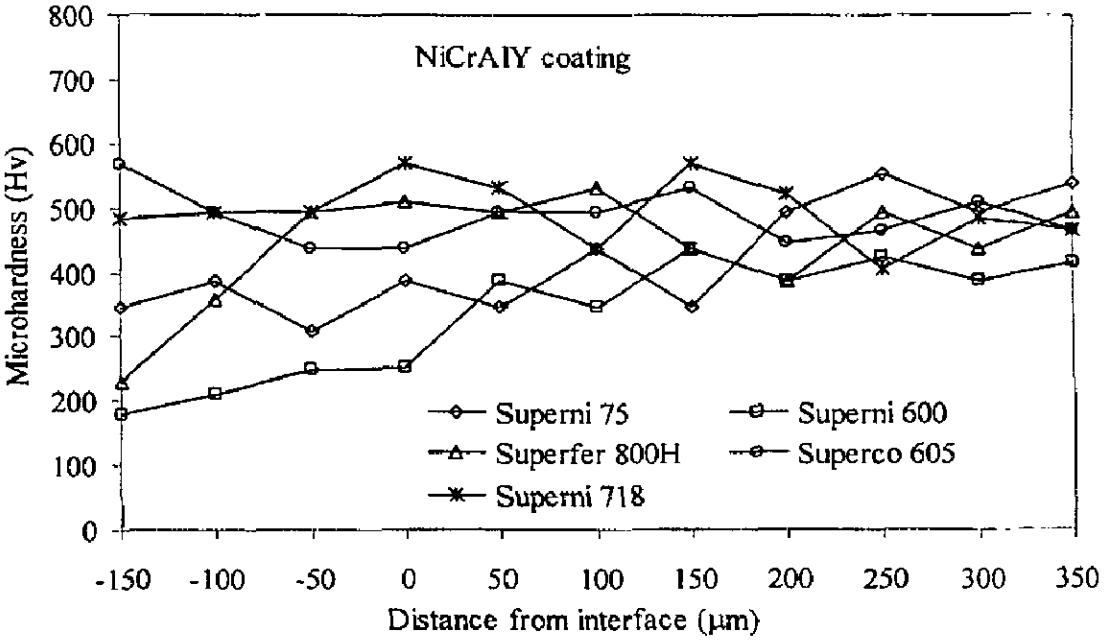

Fig. 4.8 Microhardness profiles of plasma sprayed NiCrAlY coating for different substrate superalloys along the cross-section.

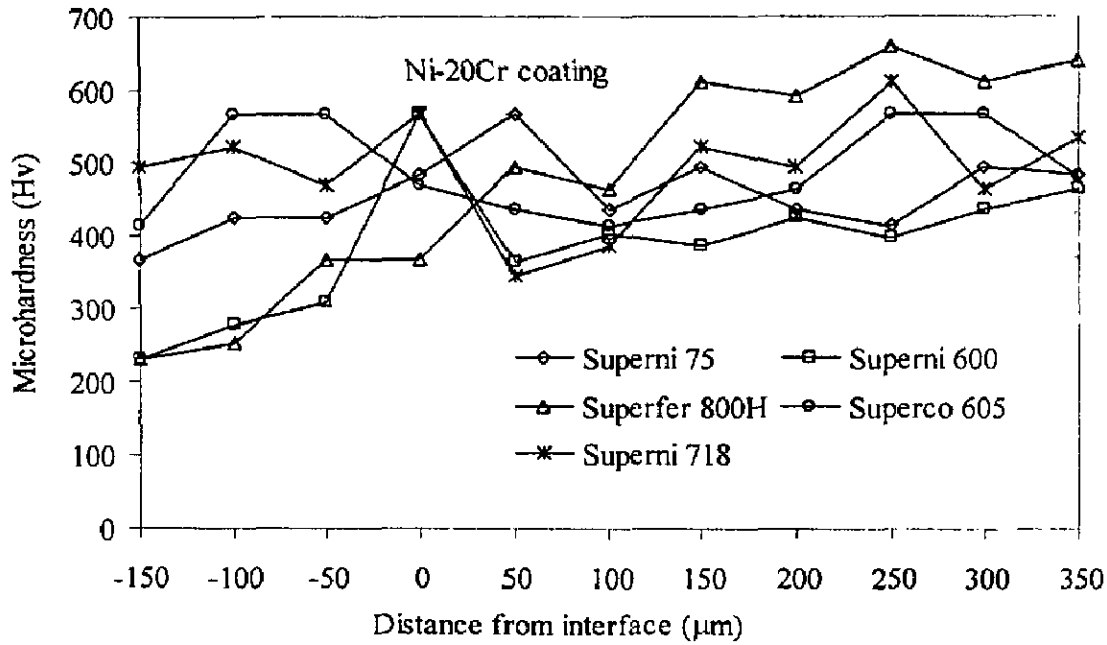

Fig. 4.9 Microhardness profiles of plasma sprayed Ni-20Cr coating with bond coat of NiCrAlY for different substrate superalloys along the cross-section.

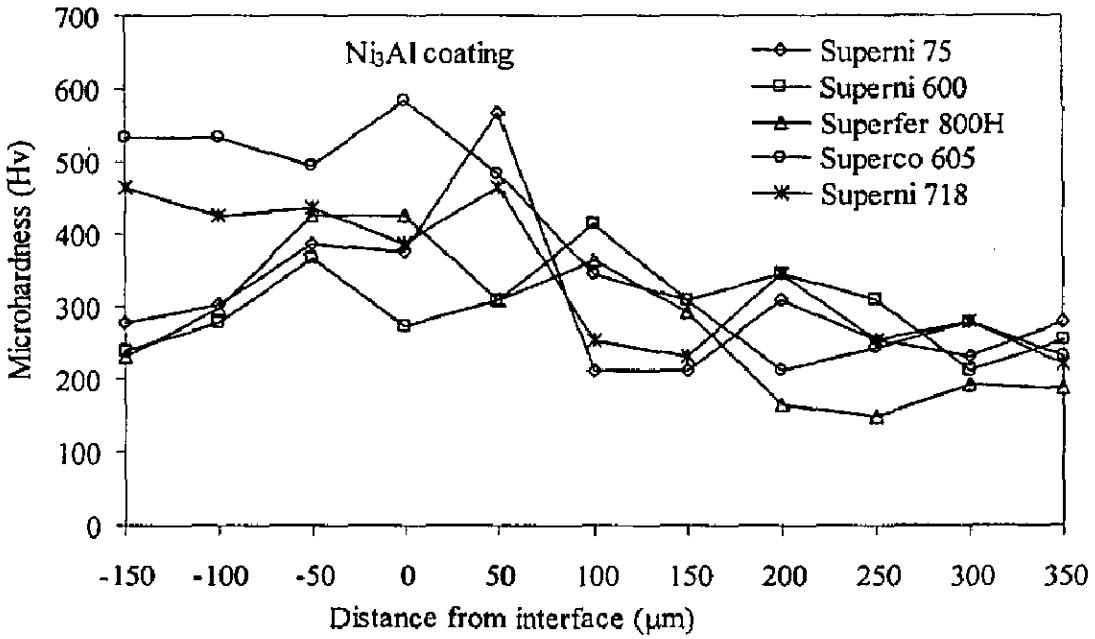

Fig. 4.10 Microhardness profiles of plasma sprayed Ni_3Al coating with bond coat of NiCrAlY for different substrate superalloys along the cross-section.

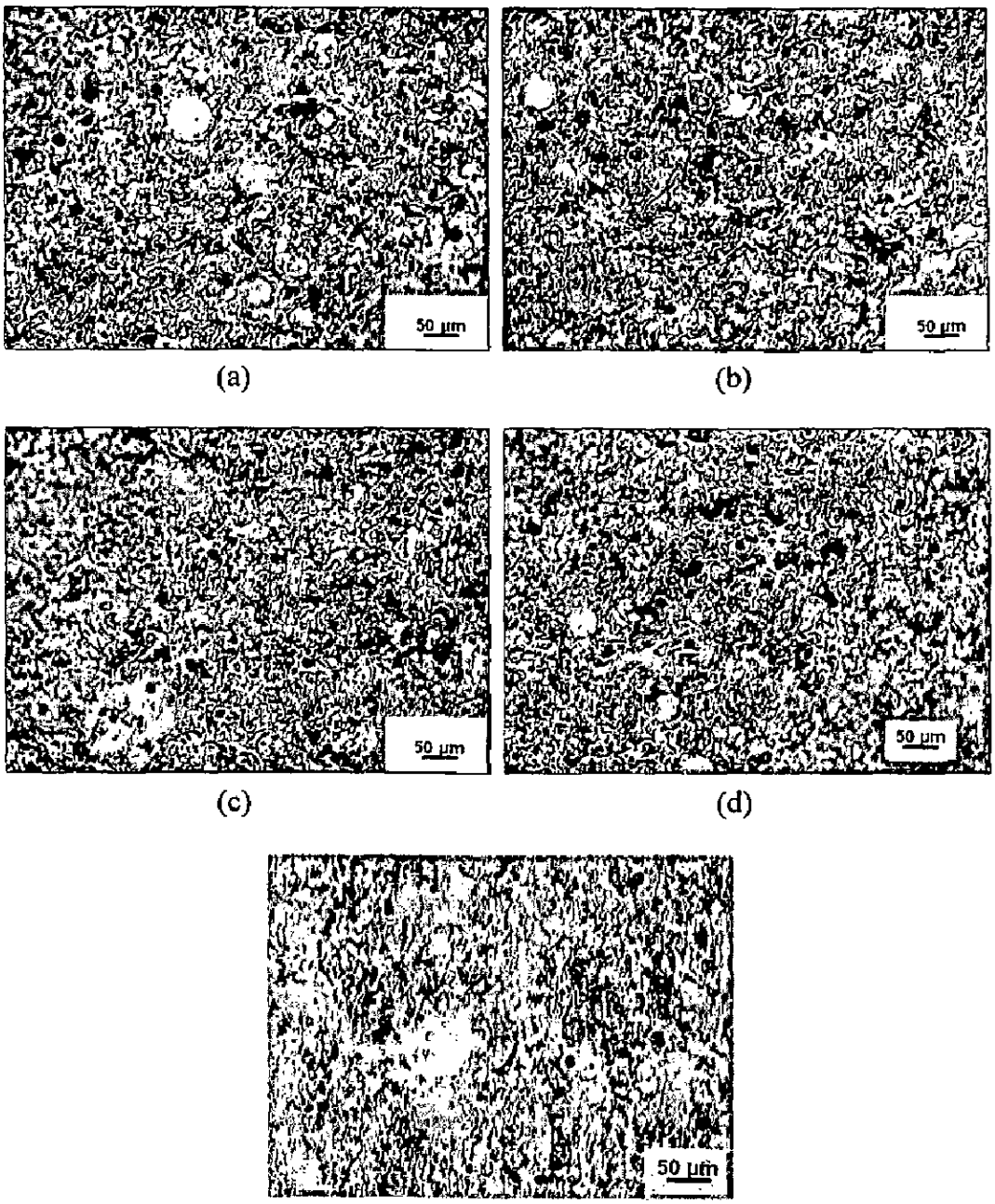

Fig. 4.11 Optical micrographs showing surface morphology of plasma sprayed NiCrAlY coating on substrate superalloys

(a) Superni 75 (b) Superni 600 (c) Superfer 800H

(d) Superni 605 (e) Superni 718

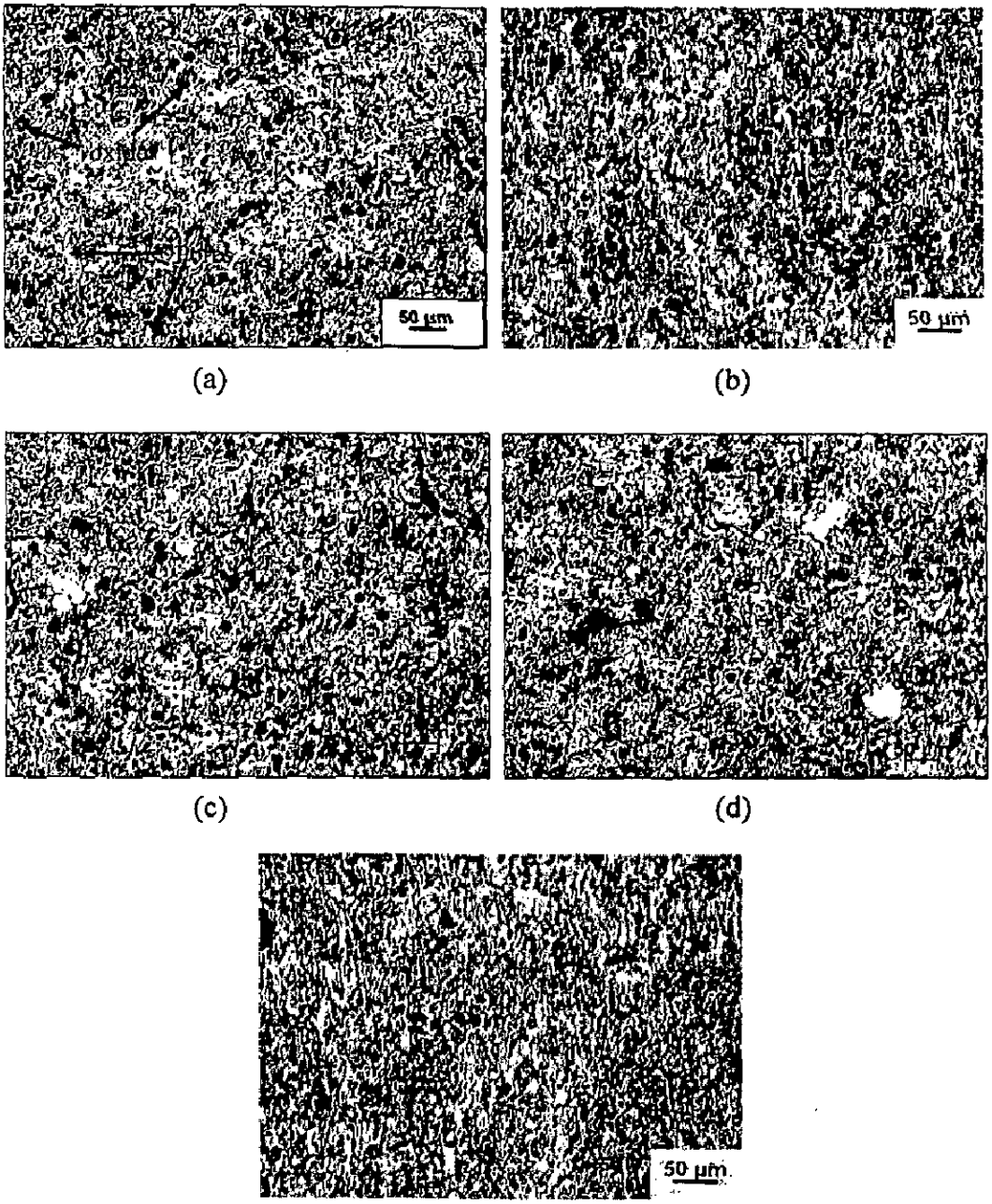

(a) (b)

(c) (d)

(e)

Fig. 4.12 Optical micrographs showing surface morphology of plasma sprayed Ni-20Cr coating on substrate superalloys

(a)Superni 75 (b) Superni 600 (c) Superfer 800H

(d) Superni 605 (e) Superni 718

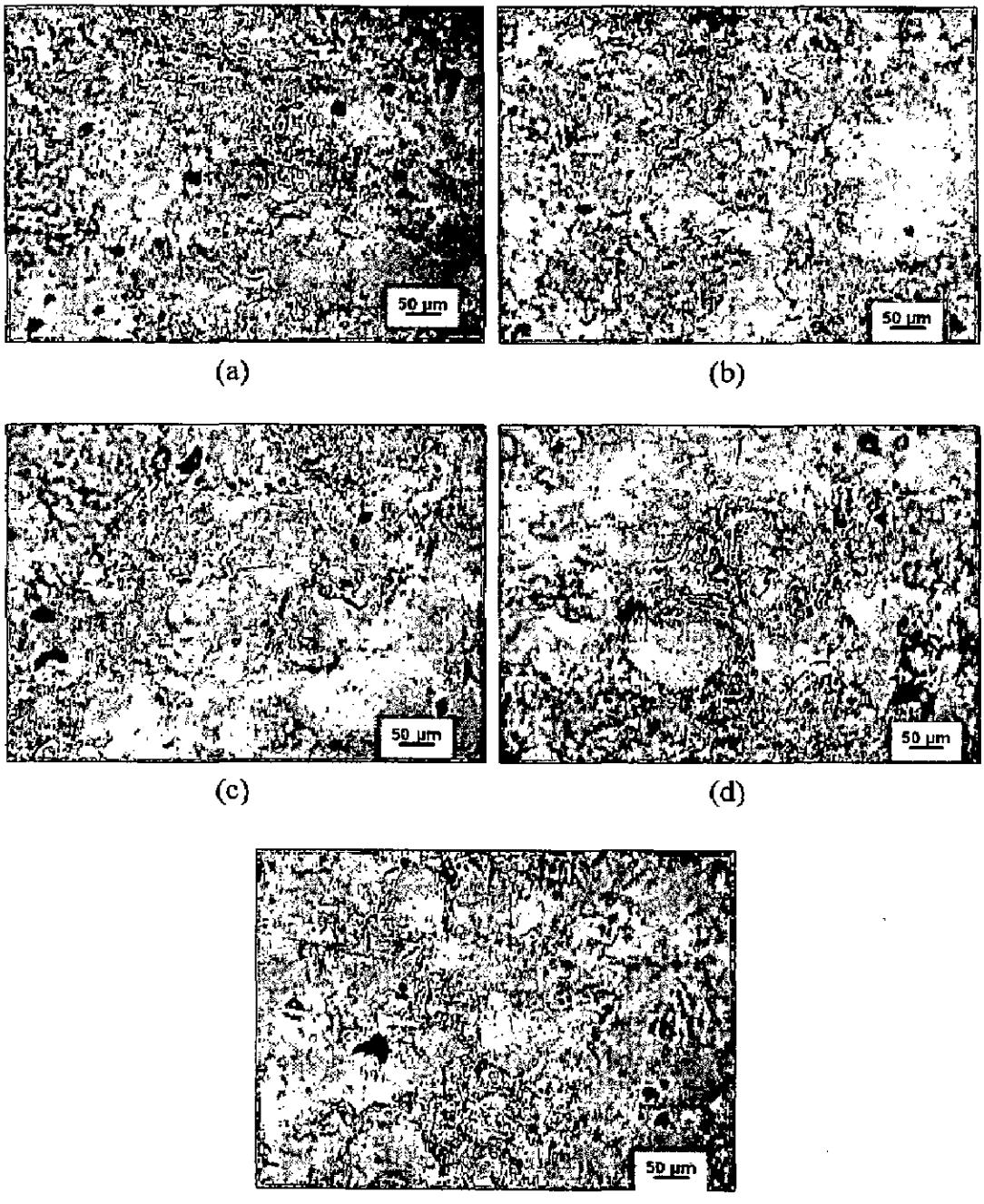

(a) (b)

(c) (d)

(e)

Fig. 4.13 Optical micrographs showing surface morphology of plasma sprayed Ni_3Al coating on substrate superalloys.

(a)Superni 75 (b) Superni 600 (c) Superfer 800H

(d) Superni 605 (e) Superni 718

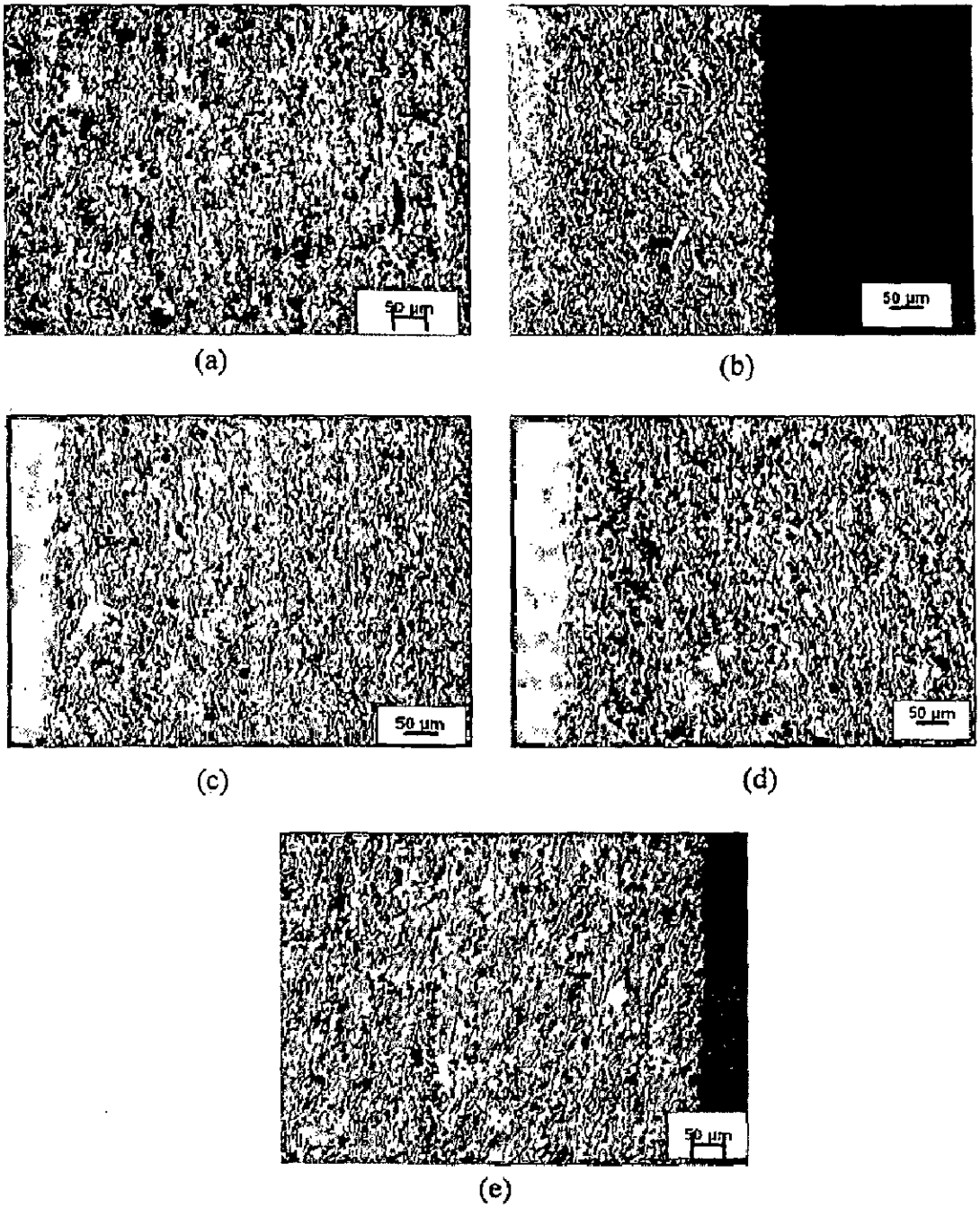

Fig. 4. 14 Optical micrographs along the cross-section of plasma sprayed NiCrAlY coating on different substrate superalloys.

(a) Superni 75 (b) Superni 600 (c) Superfer 800H

(d) Superco 605 (e) Superni 718

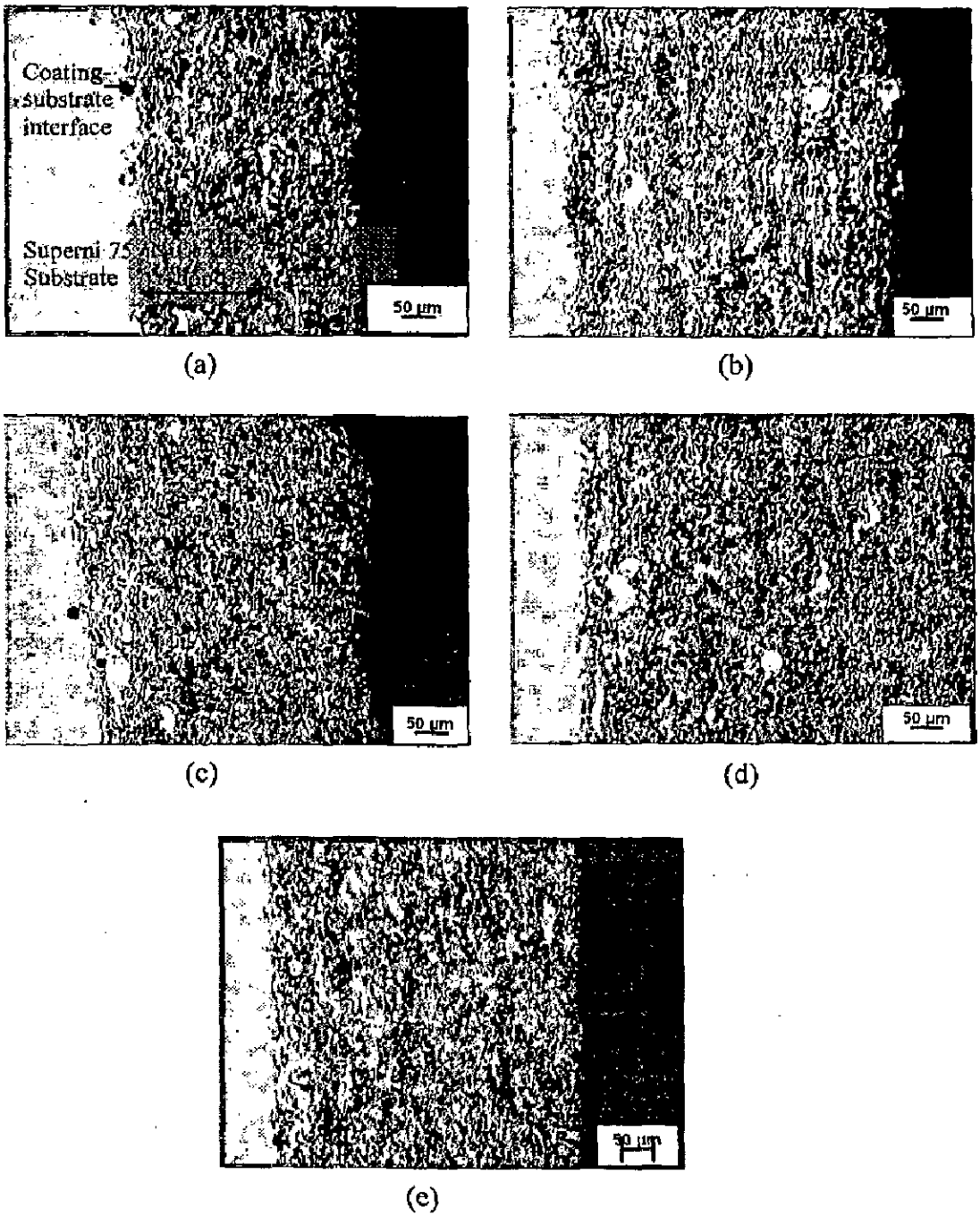

Fig. 4.15 Optical micrographs along the cross-section of plasma sprayed Ni-20Cr coating with bond coat of NiCrAlY on different substrate superalloys.
(a) Superni 75 (b) Superni 600 (c) Superfer 800H
(d) Superco 605 (e) Superni 718

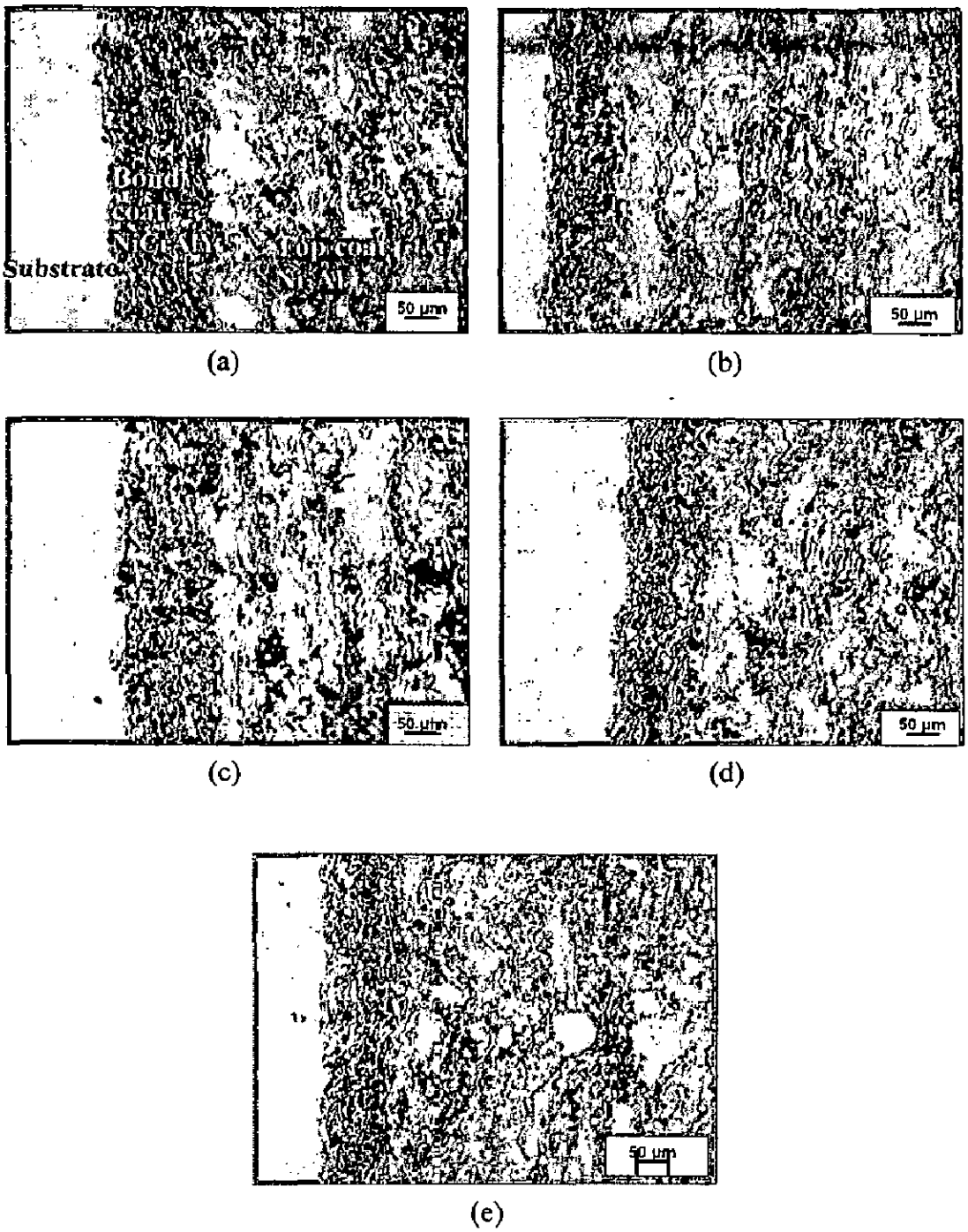

(a) (b)

(c) (d)

(e)

Fig. 4.16 Optical micrographs along the cross-section of plasma sprayed Ni_3Al coating with bond coat of NiCrAlY on different substrate superalloys.

(a) Superni 75 (b) Superni 600 (c) Superfer 800H

(d) Superco 605 (e) Superni 718

The splat size is larger in the case of Ni_3Al coatings as compared to that in the NiCrAlY and Ni-20Cr coatings. Layers of the bond coats and upper coats can easily be identified in the micrographs for the as sprayed Ni_3Al coatings, Fig. 4.16, alongwith the presence of some unmelted particles. The presence of few comparatively large blackish patches in the micrographs might be indicating voids in the coatings. Indications of globules near splat boundaries can be observed in most of the micrographs, which are most likely unmelted particles. These unmelted particle stick to surface due to high impact during plasma spray process and subsequently they cool and precipitate near splat boundaries as can be seen in the respective figures.

4.2.7 XRD Analysis

XRD patterns for the surfaces of the plasma sprayed NiCrAlY, Ni-20Cr and Ni_3Al coatings have been shown in the Fig.4.17 through Fig. 4.19 respectively on reduced scales. The NiCrAlY coated specimens have shown the presence of γ-Ni and γ'-Ni_3Al as main phases, Fig. 4.17. Whereas XRD patterns of the Ni-20Cr coatings have revealed γ-Ni as the main phase without formation of any intermetallic phase (Fig. 4.18). In case of Ni_3Al coatings, formation of the Ni_3Al as a main phase has been confirmed by XRD as can be seen in Fig.4.19.

4.2.8 SEM / EDAX Analysis

SEM micrographs, Fig. 4.20 indicate typical splat morphologies for the all the coatings in general with some indications of unmelted particles. EDAX analysis for NiCrAlY coating (Fig. 4.20 a) confirms the formation of required composition. Ni-20 Cr coating (Fig. 4.20 b) has shown two phases, the white one nearly corresponds to 18% Cr, thereby indicating probable formation of γ' phase, whereas the black phase has higher amount of Cr i.e. 29% which may be due to formation of γ phase as per Ni-Cr phase diagram. Fig. 4.20 (c) indicates the formation of Ni_3Al crystalline phase.

4.2.9 EPMA Analysis

Cross-sectional BSEI of the as-sprayed NiCrAlY coatings show distinct layers of the coatings and the substrates (Fig. 4.21 to Fig. 4.24). The elemental mappings for all the NiCrAlY coated superalloys show that the basic elements of the alloy powder viz. Ni, Cr, Al and Y are uniformly distributed within the coated region. Minor diffusion of titanium, iron, manganese, cobalt and tungsten has been indicated into the coating from the different superalloy substrates, depending upon the respective constituents of superalloys.

BSEIs for the Ni-20Cr coatings (Fig. 4.25 to Fig. 4.27) show two distinct zones in the coatings, where the top zone represents the Ni-20Cr top coat and the inner zone the bond coat. The top coat seems to be dense as compared to the bond coat. The elements of substrate, coating and bond coat are mainly confined to their original places except aluminum and to some extent titanium, tantalum, iron, cobalt and manganese. Some yttrium has also migrated to these places. Ti, Ta, Fe and Mn have also been noticed in very small but almost uniformly distributed concentration in the top coat as well as in the bond coat (Fig. 4.27). This indicates probable diffusion of these elements from the substrate superalloy.

X-ray mappings for the Ni_3Al coatings as depicted in Fig. 4.28 to Fig. 4.30 also indicate the minor diffusion of some elements from the substrate superalloys and bond coats to the top coats. Chromium is generally seen around the aluminium rich areas in the top coat region. Yttrium has also diffused to the top coat in small quantities and is present along the sides of aluminium rich areas. Iron, tantalum, titanium and manganese have also diffused from the substrate into the top coating in minor concentration and are distributed in an undefined pattern. The bond coat/substrate interface is distinct, and also clear demarcation can be seen between the bond coat and the top coat in all the Ni_3Al coated samples.

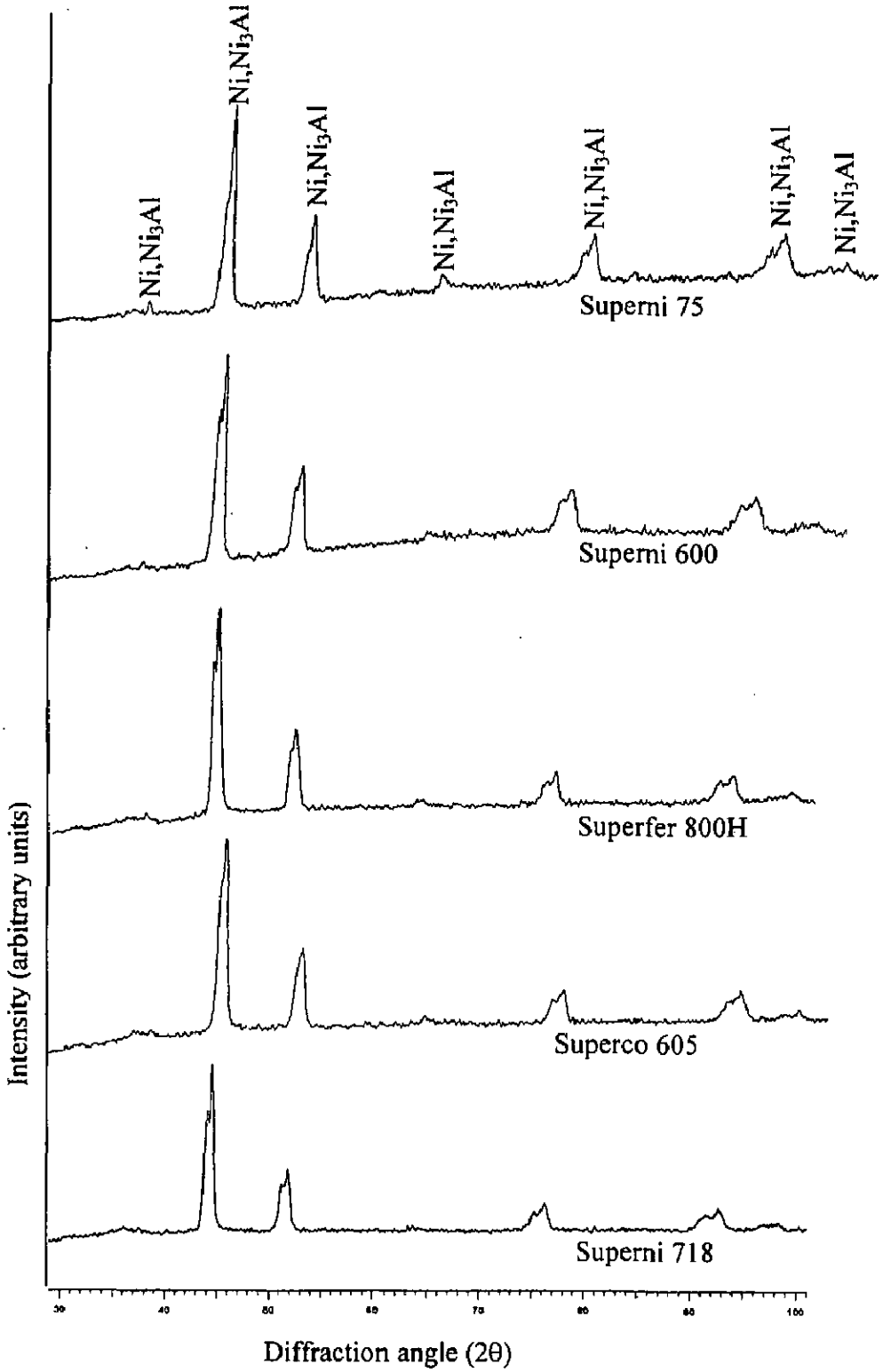

Fig. 4.17 X-ray diffraction patterns for the plasma sprayed NiCrAlY coating on different superalloy substrates.

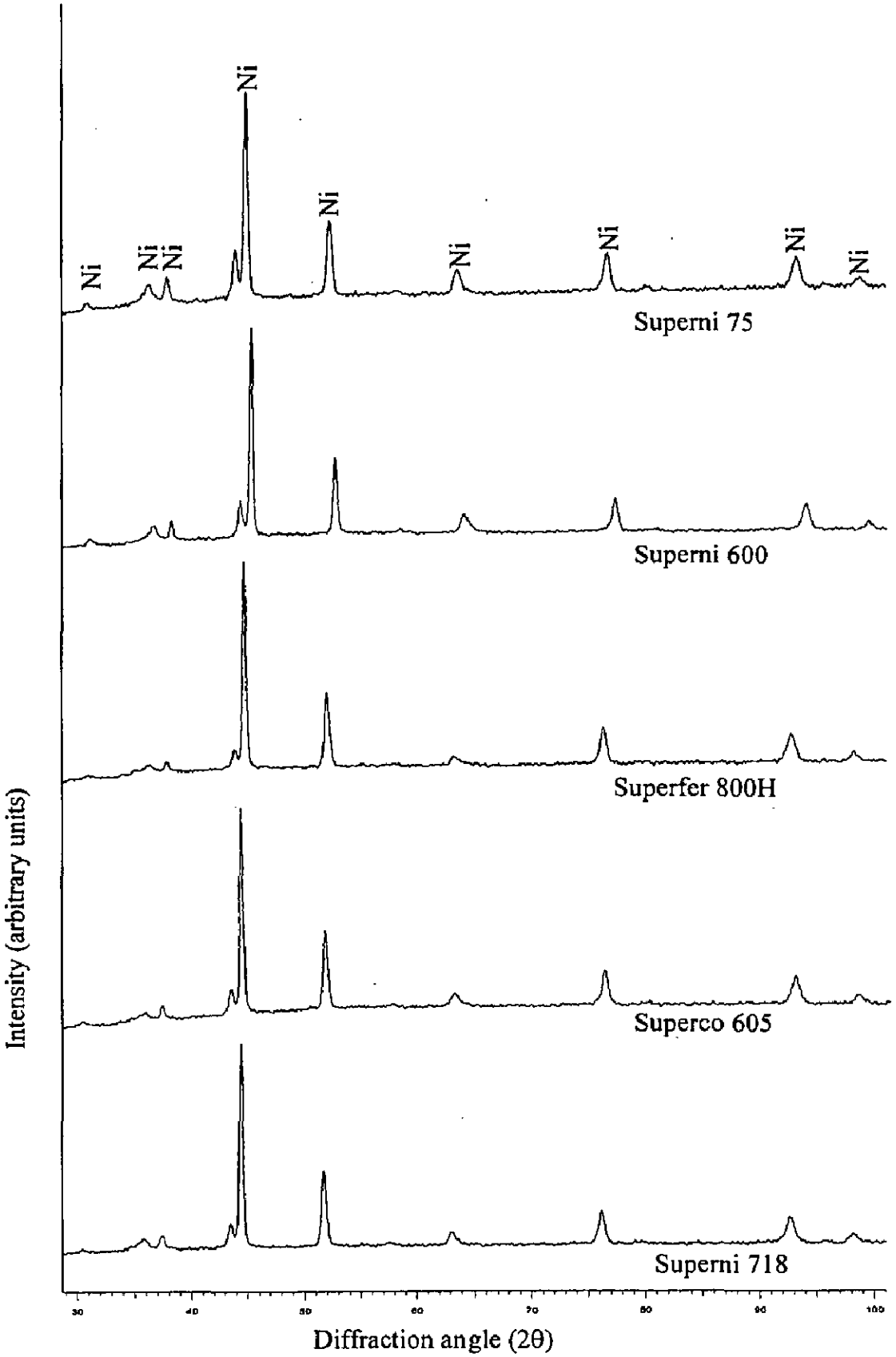

Fig. 4.18 X-ray diffraction patterns for the plasma sprayed Ni-20Cr coating with bond coat of NiCrAlY on different superalloy substrates.

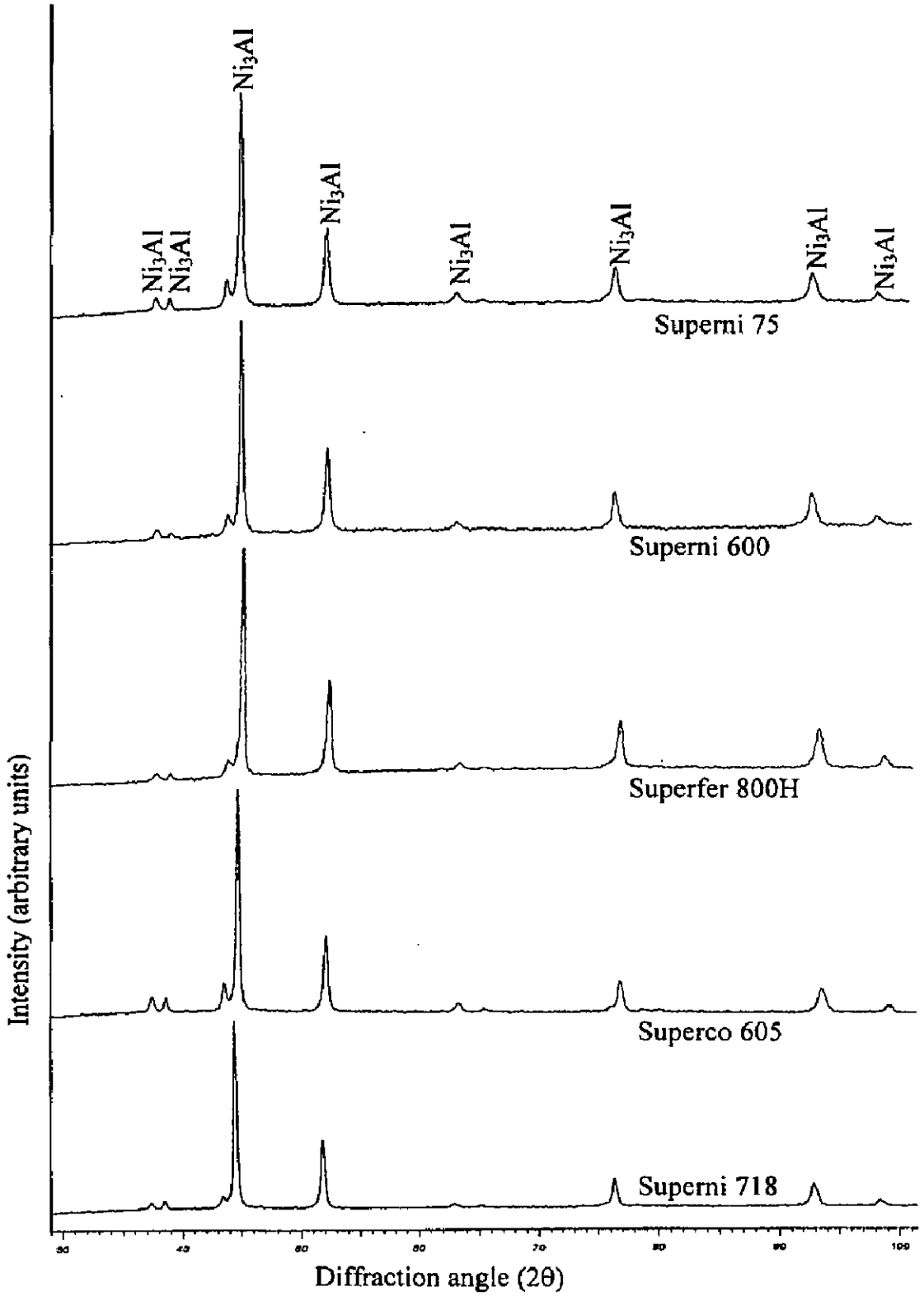

Fig. 4.19 X-ray diffraction patterns for the plasma sprayed Ni_3Al coating with bond coat of NiCrAlY on different superalloy substrates.

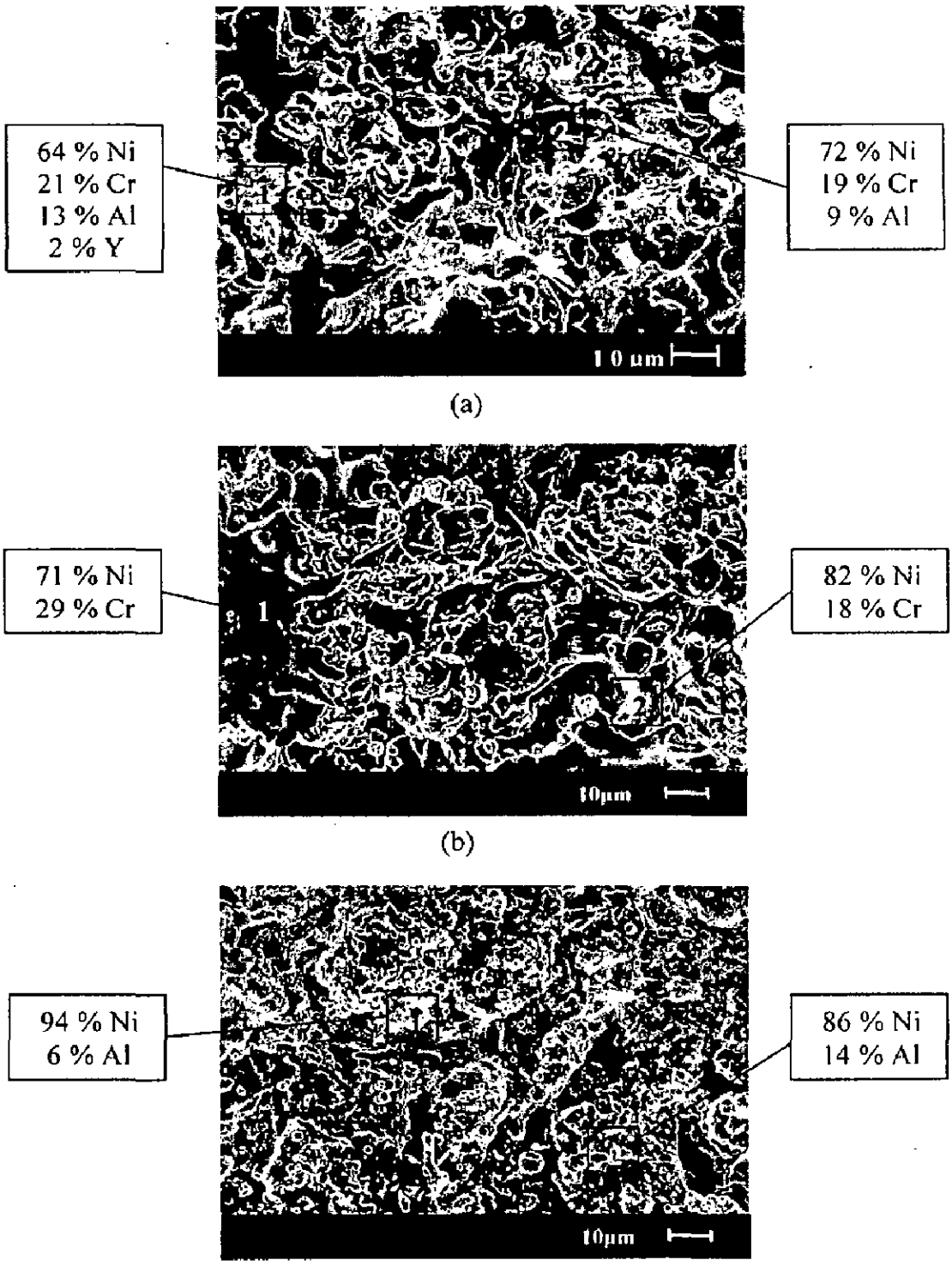

Fig. 4.20 SEM/EDAX analysis of the plasma sprayed coatings on Superni 75 superalloy substrate showing elemental composition (Wt.%) at selected points

(a) NiCrAlY coating (b) Ni-20Cr coating (c) Ni_3Al coating

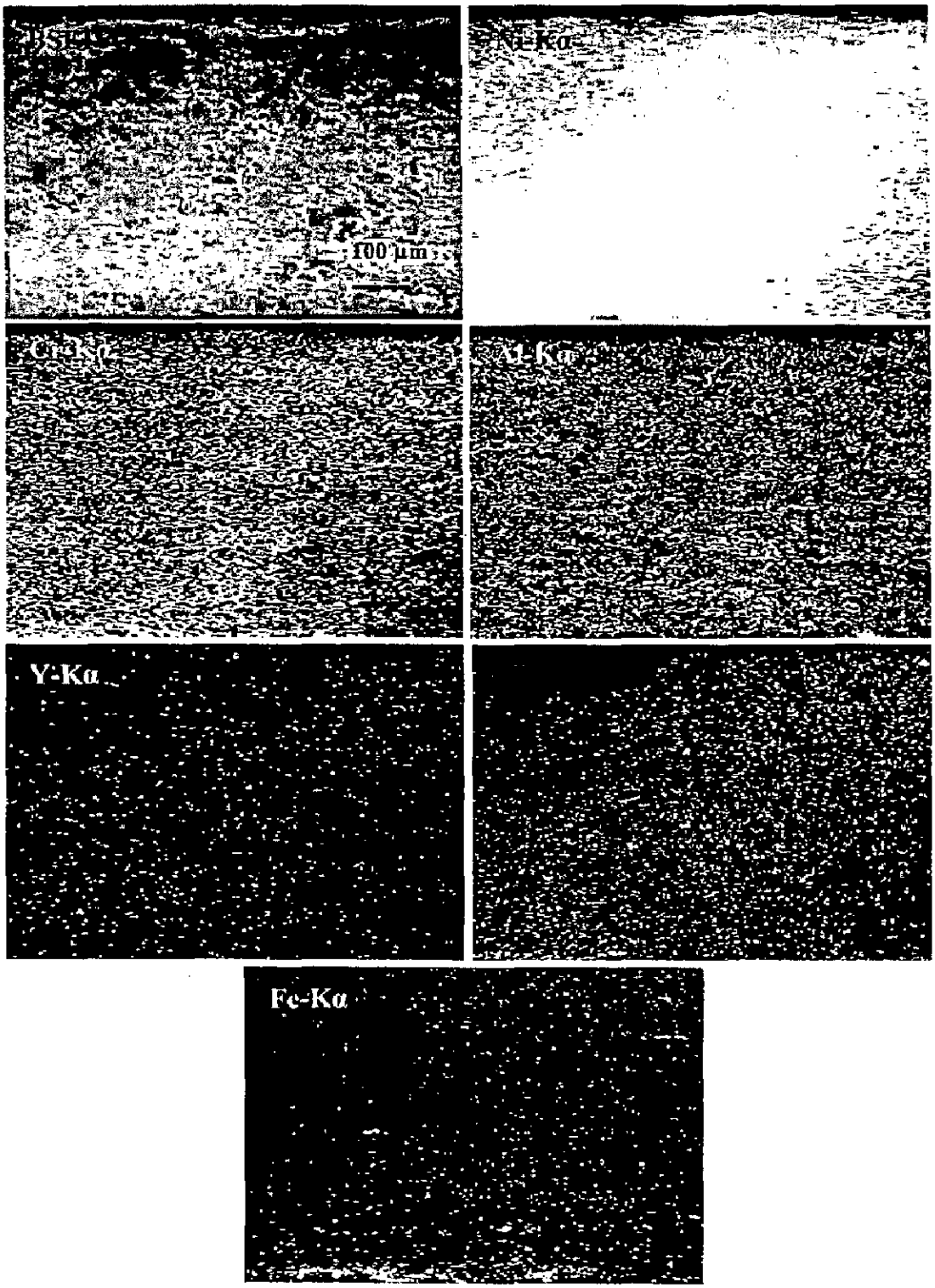

Fig. 4.21 BSEI and elemental X-ray mappings of the cross-section of plasma sprayed NiCrAlY coating on Superni 75 superalloy.

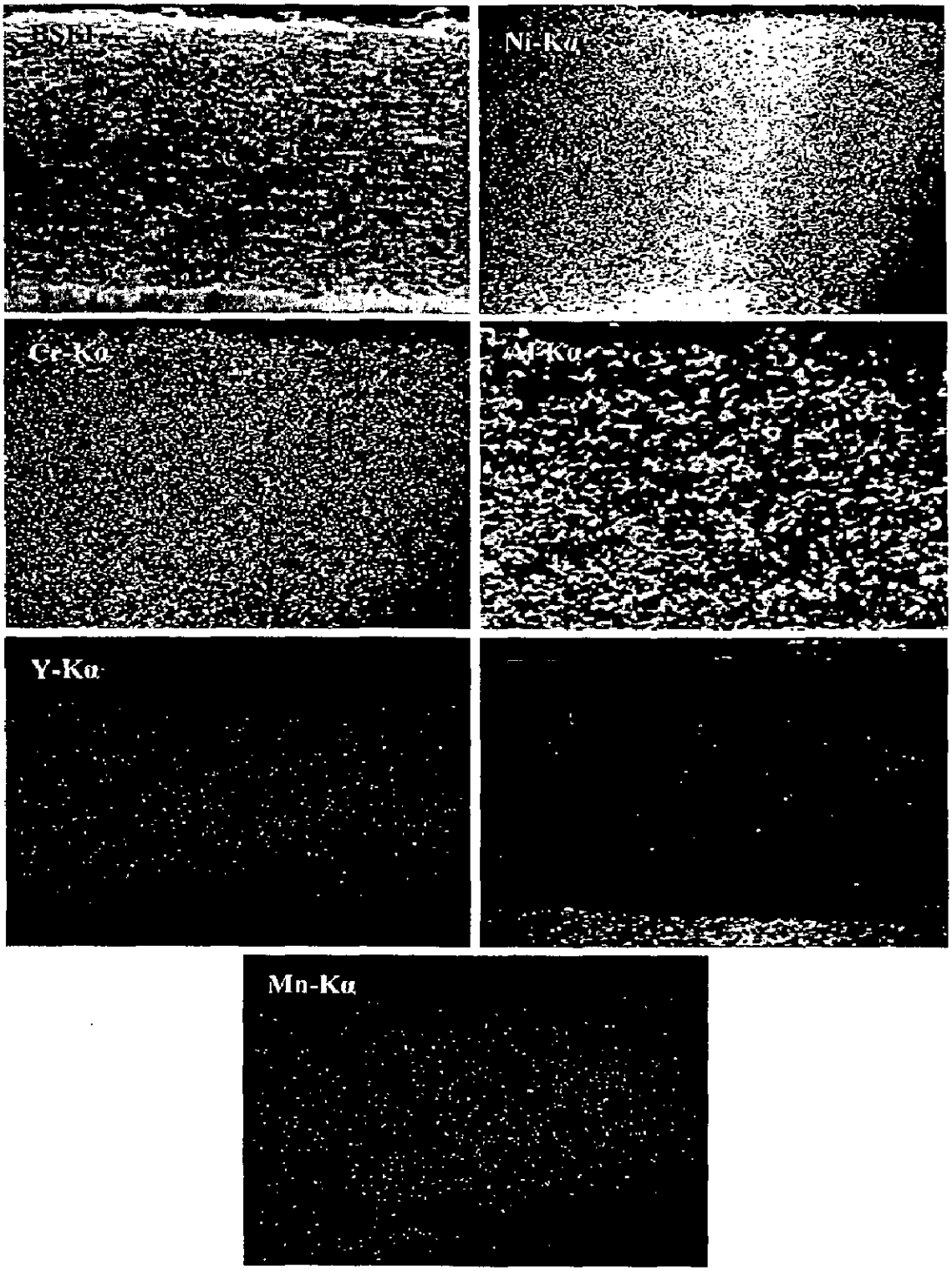

Fig. 4.22 BSEI and elemental X-ray mappings of the cross-section of plasma sprayed NiCrAlY coating on Superni 600 superalloy.

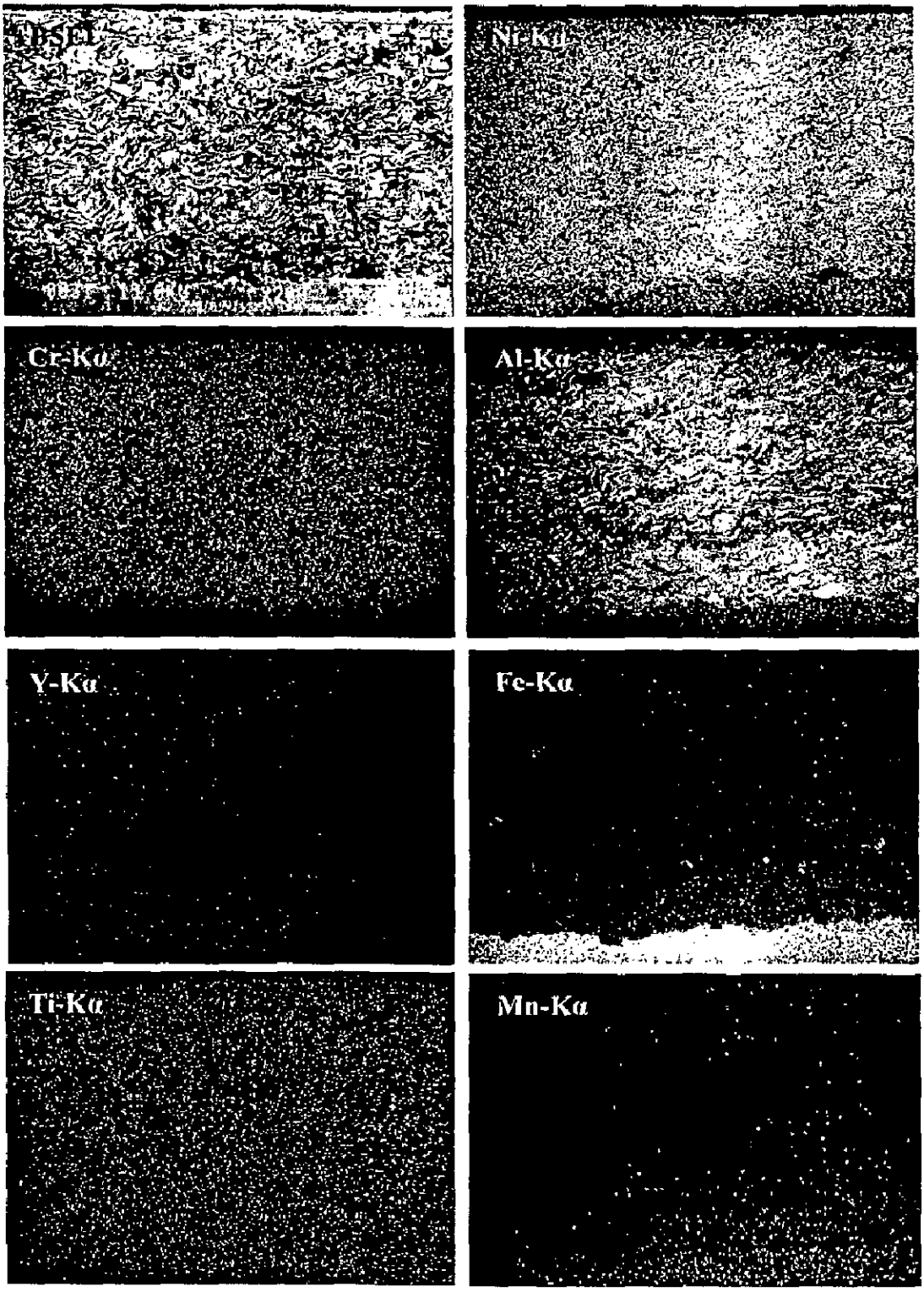

Fig. 4.23 BSEI and elemental X-ray mappings of the cross-section of plasma sprayed NiCrAlY coating on Superfer 800H superalloy.

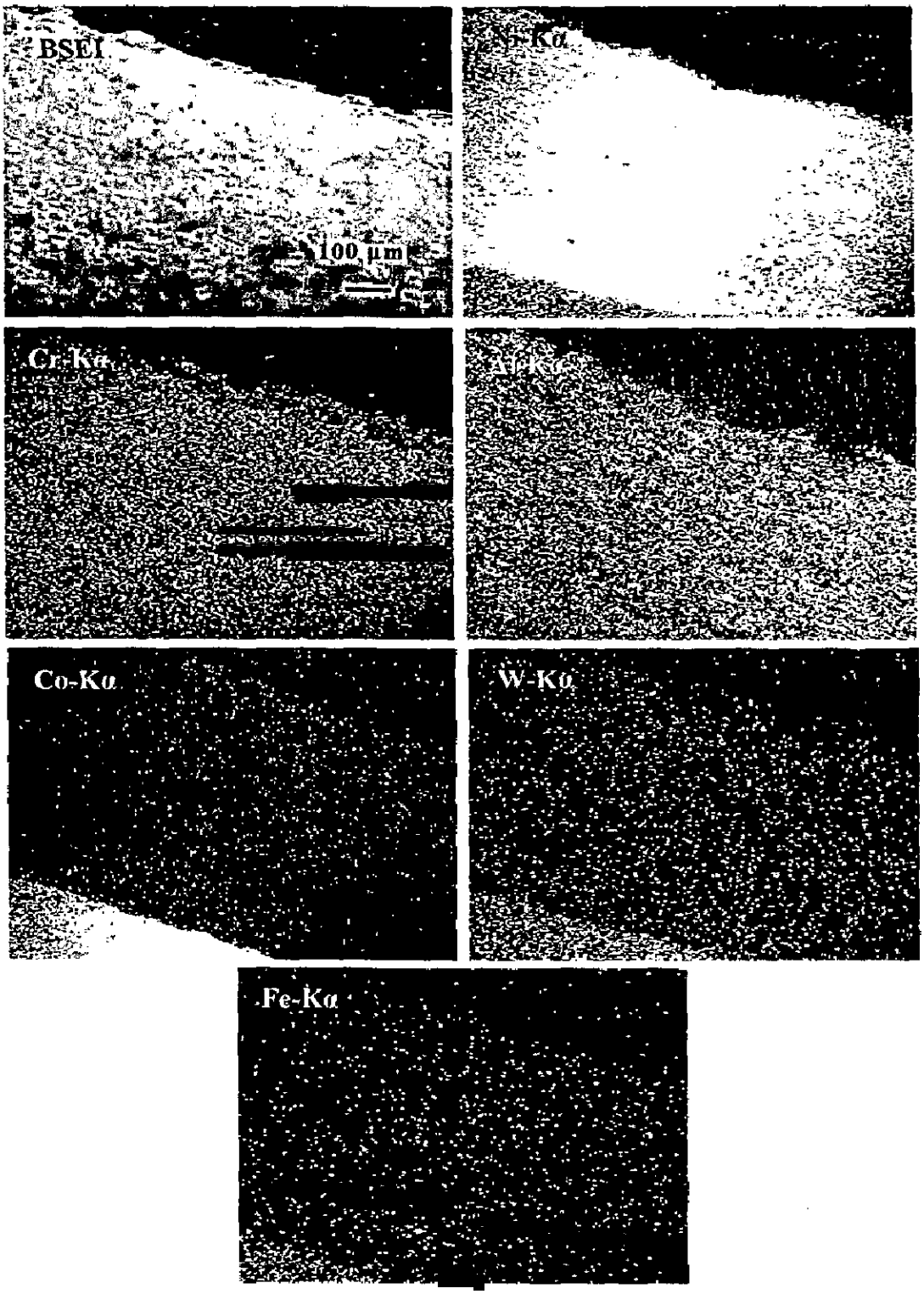

Fig. 4.24 BSEI and elemental X-ray mappings of the cross-section of plasma sprayed NiCrAlY coating on Superco 605 superalloy.

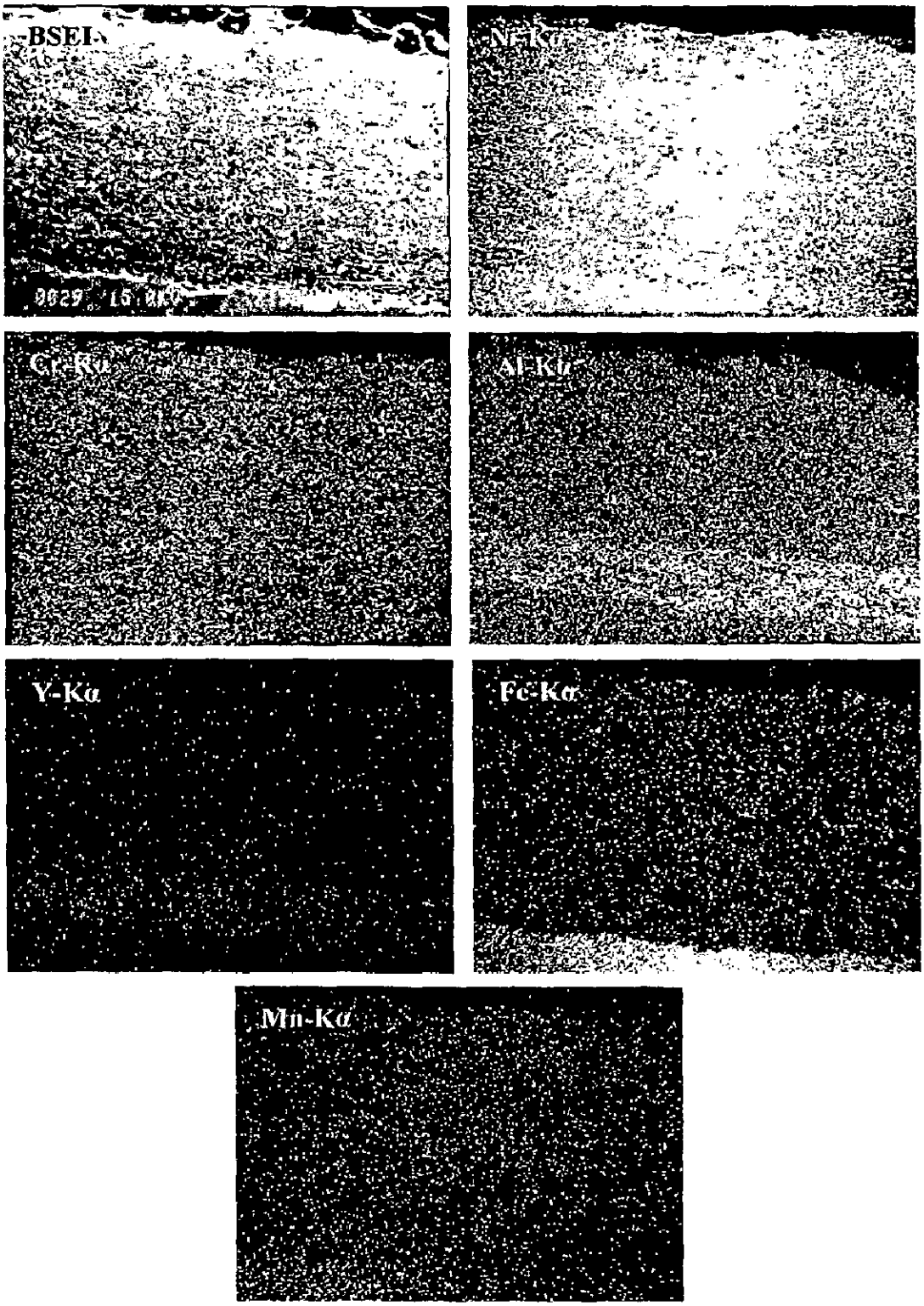

Fig. 4.25 BSEI and elemental X-ray mapping of the cross-section of plasma sprayed Ni-20Cr coating with bond coat of NiCrAlY on Superni 600 superalloy.

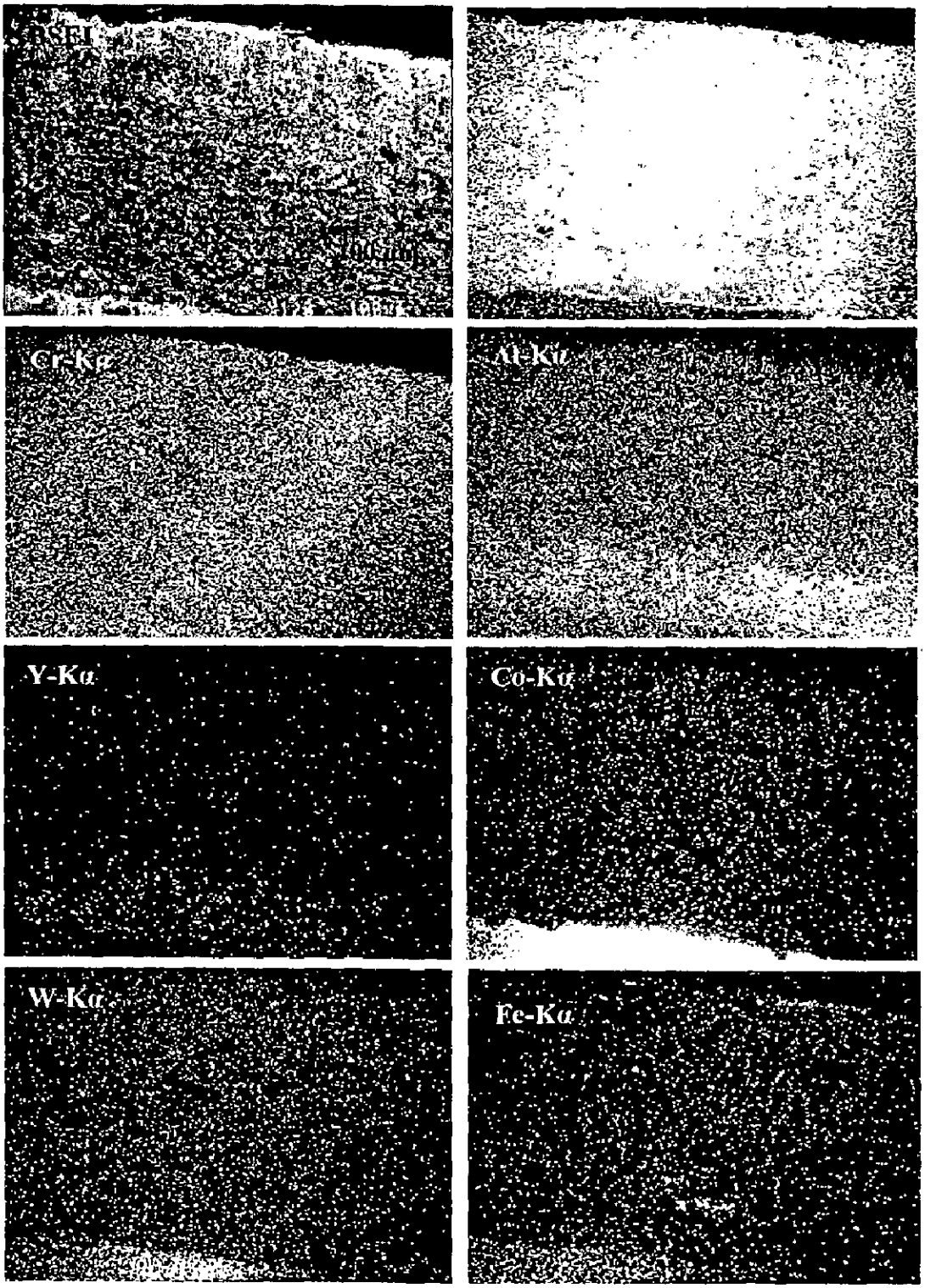

Fig. 4.26 BSEI and elemental X-ray mappings of the cross-section of plasma sprayed Ni-20Cr coating with bond coat of NiCrAlY on Superco 605 superalloy.

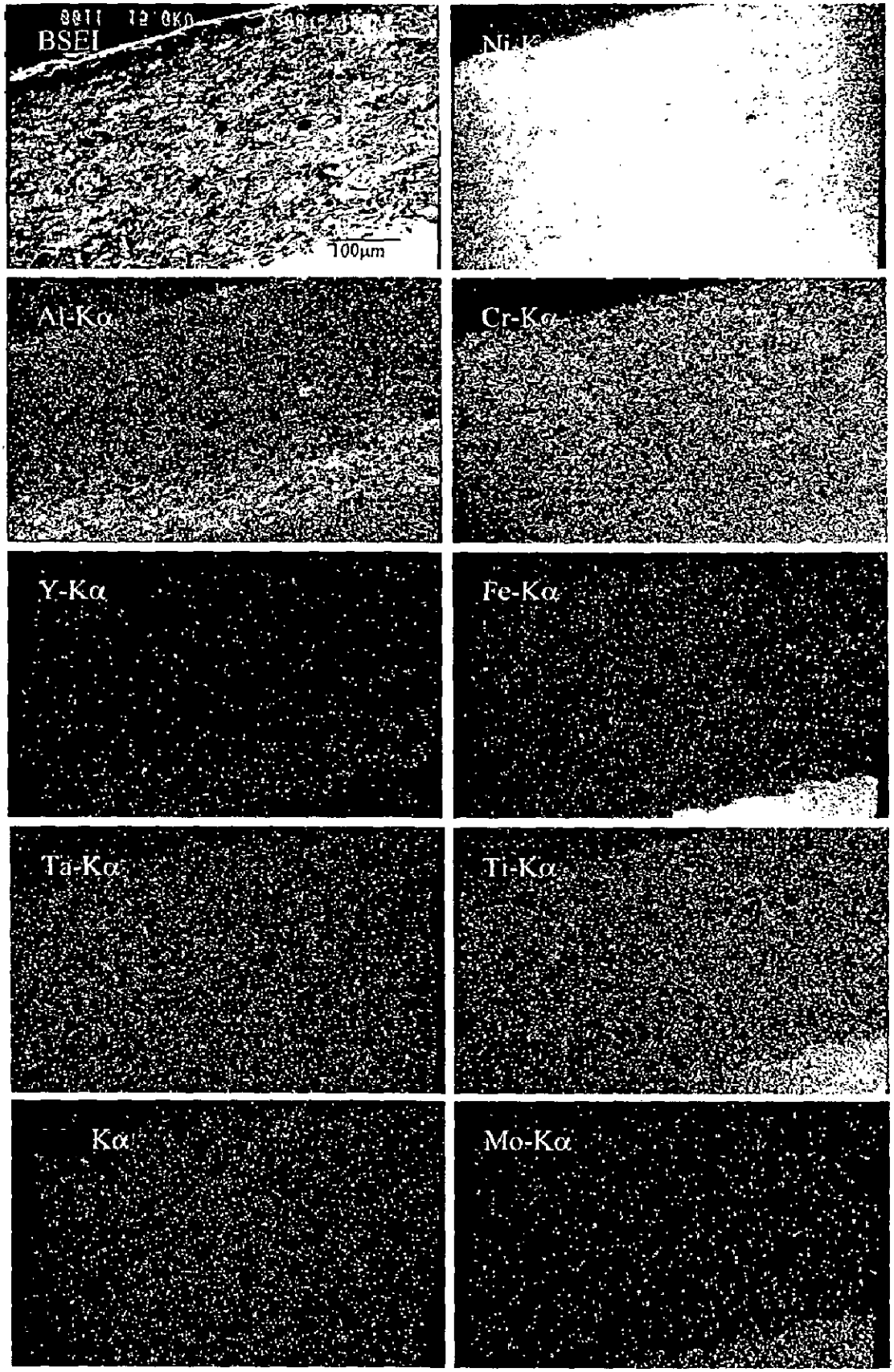

Fig.4.27 BSEI and elemental X-ray mappings of the cross-section of plasma sprayed Ni-20Cr coating with bond coat of NiCrAlY on Superni 718 superalloy.

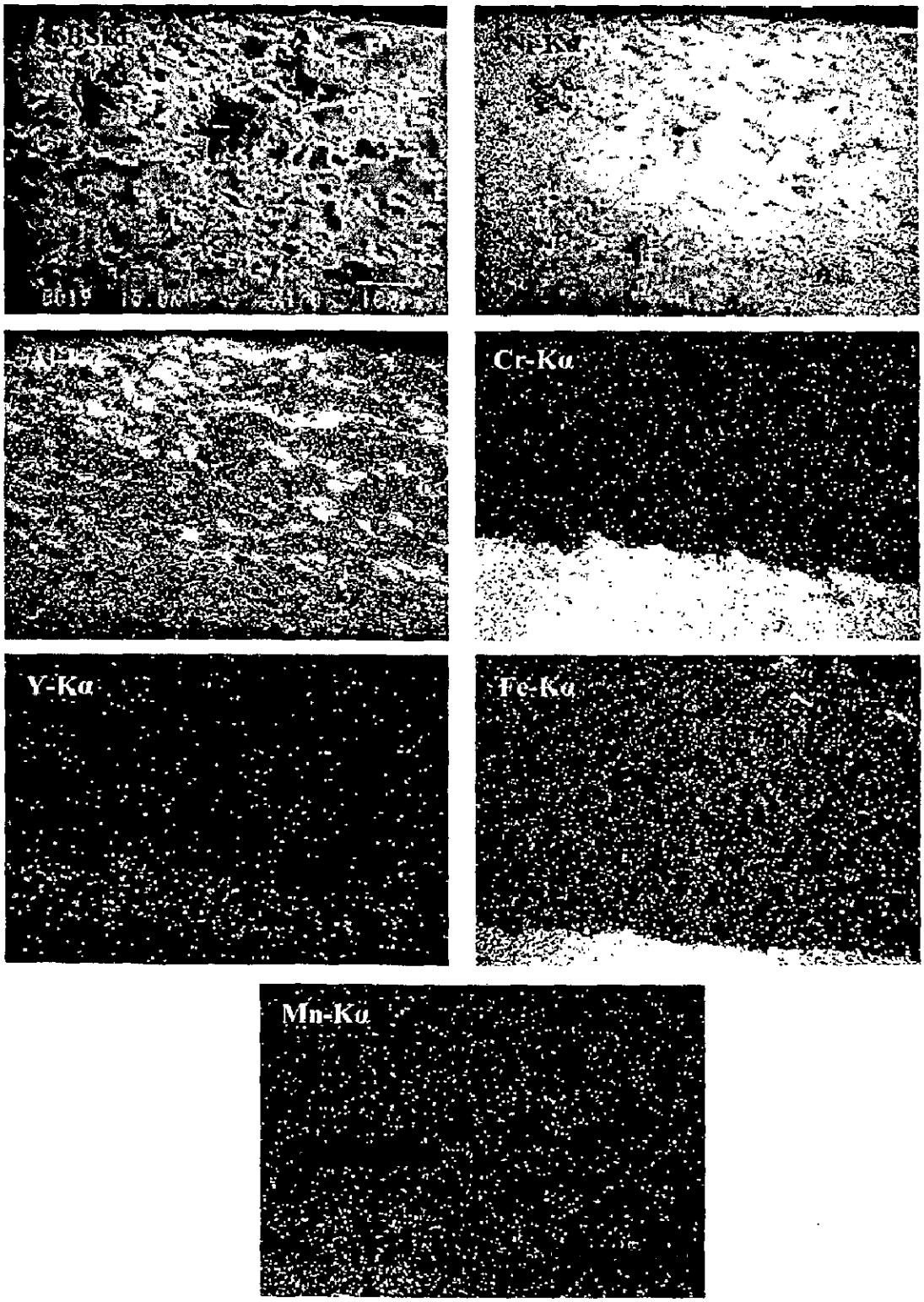

Fig. 4.28 BSEI and elemental X-ray mappings of the cross-section of plasma sprayed Ni_3Al coating with bond coat of NiCrAlY on Superni 600 superalloy.

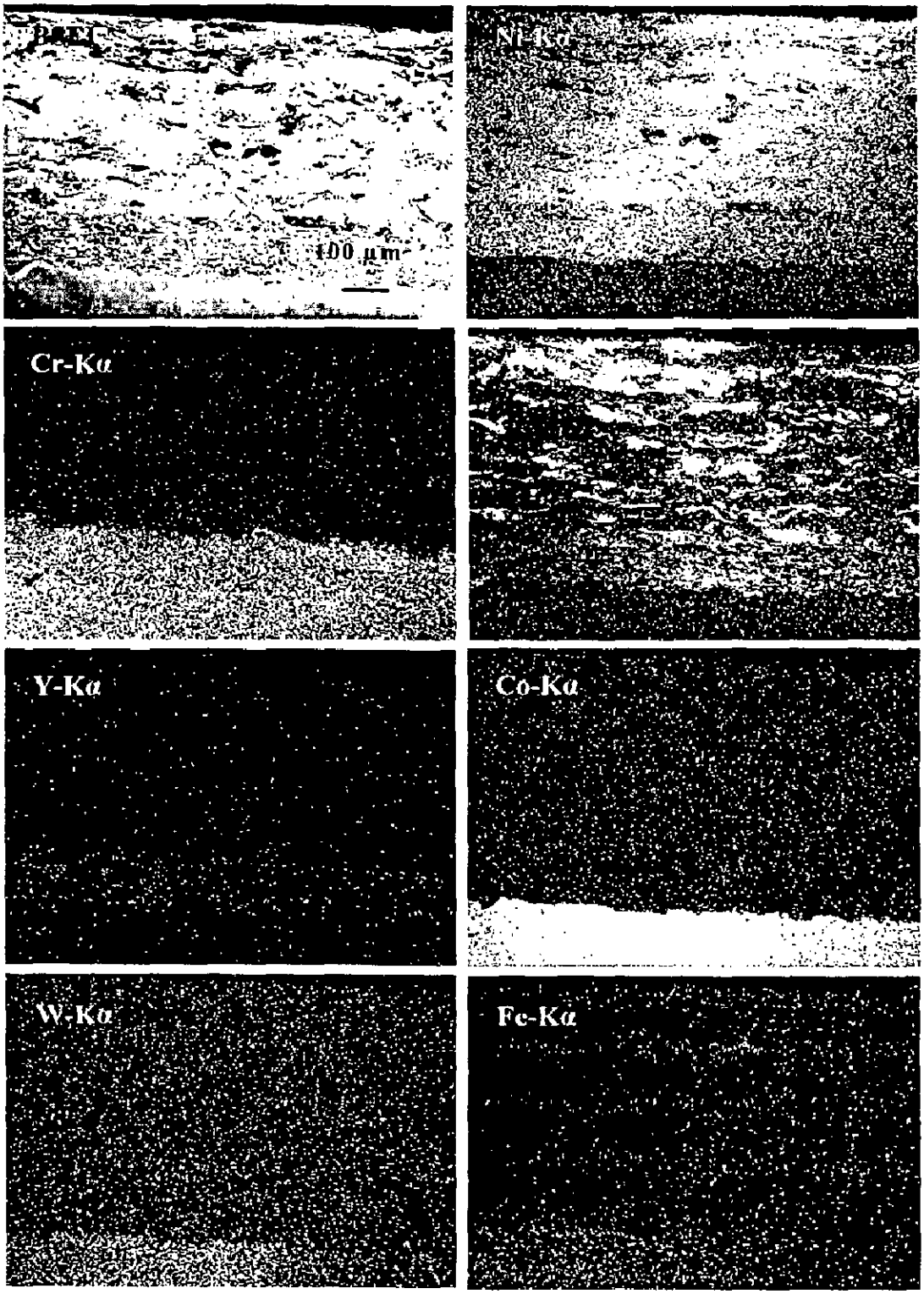

Fig. 4.29 BSEI and elemental X-ray mappings of the cross-section of plasma sprayed Ni_3Al coating with bond coat of NiCrAlY on Superco 605 superalloy.

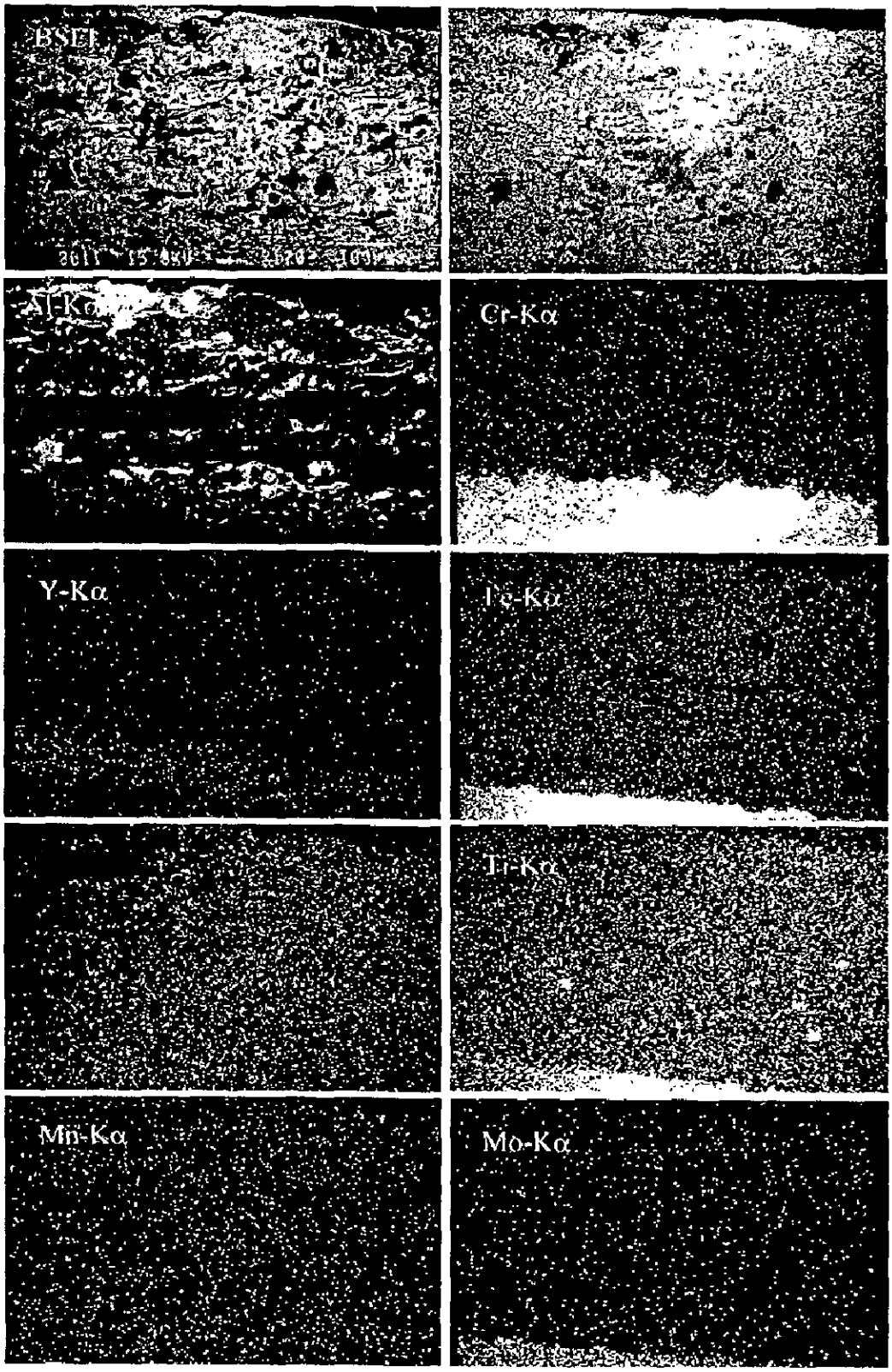

Fig. 4.30 BSEI and elemental X-ray mappings of the cross-section of plasma sprayed Ni_3Al coating with bond coat of NiCrAlY on Superni 718 superalloy.

4.3 DISCUSSION

Microstructural studies have revealed that the matrix for all the superalloys under study is a solid solution. The microstructures of these superalloys are compared with the standard microstructures from Metals Handbook (1972) and ASM Handbook (1995). The formation of carbides has been revealed invariably in all the cases, which could again be characterised with reference to the data available in the said handbooks. Basically strength of the Ni-base superalloys depends on the mechanism of solid solution hardening and precipitation hardening, singly and in combination. The main carbides which have the possibility of their formation by precipitation in the Ni- and Co- based superalloys under study are MC, M_7C_3 and $M_{23}C_6$, keeping in view the role of various alloying elements towards formation of particular carbide. Among them, $M_{23}C_6$ has the strongest possibility of formation in all the cases under study, as it is mainly promoted by Cr (ASM Handbook, 1995). Further, $M_{23}C_6$ carbide has tendency to precipitate at the grain boundaries. The possible carbides in case of Fe-based superalloy Superfer 800H are $M_{23}C_6$ and MC. Some large globules as could be seen in Fig. 4.1 (c) might be indicating the presence of MC (TiC) phase.

The plasma spray coatings were deposited at Anod Plasma Ltd. Kanpur (India) using a 40 kW Miller Thermal Plasma Spray apparatus. It was aimed to produce thicker coatings because thicker coatings are generally required for the components of energy generation systems. In the present study it was possible to obtain a thickness in the range of 350-550 μm for the NiCrAlY, Ni-20Cr and Ni_3Al coatings. Coating thickness of approximately 150 μm for the bond coat was selected as threshold limit. After spraying the coating thickness was measured along the cross-section for some randomly selected samples as has been reported in Table 4.2.

The porosity measurements for the plasma sprayed coatings are summarised in Table 4.2. The values of porosity (1.40-5.00 %) are in close agreement with the findings of Demirkiran et al (1999), Miguel et al (2003), Erickson et al (1998), and Singh et al (2003), and are reported by the author in his earlier publication (Mishra et al, 2005 and 2006). The coatings have shown oxide contents upto 5%. Although coatings have been sprayed under argon shrouding, some oxides are formed. The oxides may form due to the in-flight oxidation during spraying process and/or preexisting in the feed material (Bluni and Mardar, 1996). The latter reason for the oxides formation in the structure of coatings under

study looks to be more relevant as the chances of in-flight oxidation are fewer in case of the shrouded plasma spraying.

The bond strength of different coatings was measured using ASTM C-633 standard and the strength of Ni_3Al coating was found to be 17.6 MPa. Whereas Ni-22Cr-10Al-1Y and Ni-20Cr coatings showed bond strength greater than 20 MPa (failure takes place along the layer of glue used as adhesive). However, Anod Plasma Spray Limited, Kanpur, who developed this plasma spray coatings reported that the minimum values of the bond strengths of Ni-22Cr-10Al-1Y and Ni-20Cr coatings are 40 MPa and 24 MPa respectively as indicated in Table 4.2.

A slight increase in the values of microhardness values for the substrate superalloys has been observed near the interface between the bond coat and the substrate in all the cases. The hardening of the substrates as observed in the present study might have been occurred due to the

i) work hardening effect of sandblasting of the substrates prior to the coating and

ii) the high speed impact of the coating particles during plasma spray deposition.

The effect has also been reported by Singh (2003) and Hidalgo et al (2000). The observed non-uniformity in the hardness values along the thickness of the coatings may be due to the microstructural changes along the cross section of the coatings. Further the variation in the microhardness may also be attributed to minor diffusion of elements from the substrate to the coatings as seen from EPMA analysis. The observed microhardness values for the coatings have been compared with those reported by Miguel et al (2003), Mateos et al (2001), Hoop and Allen (1999), Chen et al (1993) and Sampath et al (2004), and are found to be in similar range.

Under the given spray condition, plasma sprayed coatings deposited on superalloys have a uniform microstructure. The NiCrAlY and Ni-20Cr coatings have shown fine size splats in their structures, Figs. 4.11 & 4.12 respectively. Comparatively larger sized splats are formed in the Ni_3Al coatings as indicated in Fig. 4.13. Most of the splats are well formed without any sign of disintegration. Micrographs similar to those of present study i.e. lamellar structures with voids and oxide inclusions have also been reported by Bluni and Mardar (1996), Erickson et al (1998), Westergard et al (1998), Ilavsky et al (2000), Margadant et al (2001), and Sidhu et al (2004 and 2005).

The distinctive boundaries in the microstructures across the cross-section of the coatings (Figs. 4. 14 to 4. 16) are due to different passes of the spray gun. Zhang et al (1997) suggested that the distinctive boundaries could be identified as a less dense structure between

the passes than within individual passes, owing to the flattened splats having got cooled and solidified before the next pass started.

From the XRD phases (Fig. 4. 17) of NiCrAlY coatings on different superalloy substrates, it can be inferred that the structure of the NiCrAlY coatings consist mainly of γ (nickel solid solution) and γ' (Ni_3Al) phases. The presence of γ-Ni and γ'-Ni_3Al as main phases in NiCrAlY coatings has also been reported by Wang et al (2003) for arc ion plated NiCrAlY coatings. The γ-Ni phase shown by XRD of as sprayed Ni-20Cr coating is the indication of the formation of nickel solid solution matrix in the coating. SEM/EDAX of the Ni-20Cr coating has revealed this matrix as white phase (point 2) as can be seen in Fig. 4.20 (b). Similar observation has been made by Sundararajan et al (2003A) for air plasma sprayed Ni-20Cr coating where they have indexed XRD pattern for the coating to mainly Ni solid solution γ (fcc) phase.

In case of Ni_3Al coating, the formation of Ni_3Al as the main phase has been confirmed by XRD. EDAX analysis of this coating has also shown the presence of Ni and Al. The similar XRD peaks have been reported by La et al (1999) and Liu and Gao (2001). Further the method of preparation of Ni_3Al powder for the present study had also been used by Sidhu & Prakash (2003) and La et al (1999).

The marginal diffusion of various elements from the substrate into the plasma sprayed coatings has been observed from the EPMA (Fig. 4.21 through 4.30). Relatively the diffusion between bond coat and top coat is observed to be higher as compared to that from the base alloys to the bond coat. Aluminium is found to be the most vulnerable element to the diffusion phenomenon. Cr, Ti, Ta, Fe, Co, W and Mn are some of the other elements which are prone to minor diffusion. Mazar et al (1986) have also reported limited interdiffusion in the Ni-Cr-Al-Y/Ni-based, Ni-Cr-Al-Y/Fe-based and Co-Cr-Al-Y/Fe-based systems during studies on the diffusion degradation of these systems. Further Nicholls (2000) has pointed out that the diffusion of elements between the substrate and coating can have a major influence on coating performance. He suggested that some interdiffusion is necessary to give good adhesion. Interdiffusion observed in the present study is very minor and might be helpful for providing better adhesion between the substrate, bond coat and the top coat.

Chapter 5

EROSION STUDIES IN AN AIR JET EROSION TEST RIG

Erosion behaviour of the superalloys as well as plasma sprayed coatings on the superalloy substrates, investigated in the present study has been described in this chapter. The erosion experiments were carried out using an air-jet erosion test rig at a velocity of 40ms^{-1} and impingement angles of 30° and 90°. The silica sand particles of average size 180 μm (between 150 and 220 μm) were used as erodent. The specimens were visually examined at the end of each cycle during the course of study.

The erosion rate data (g/g) have been plotted against cumulative mass of erodent for substrate superalloys and plasma spray coated superalloys. Steady state erosion rates in terms of volumetric loss (cm^3/g) for different uncoated and coated superalloys are compared. The eroded samples were analysed with SEM/EDAX and optical profilometer. The erosion rate data for each coated superalloy has been plotted alongwith uncoated superalloy in order to assess the coating performance. Efforts have been made to understand the mode of erosion.

5.1 RESULTS

5.1.1 Uncoated Superalloys

5.1.1.1 Visual Examination

Surface macrographs of the uncoated Superni 75, Superni 600, Superfer 800H, Superco 605 and Superni 718 superalloys eroded at 30° and 90° impact angles are shown in Fig. 5.1.

5.1.1.2 Erosion Rate

Fig. 5.2 shows the erosion rate of the uncoated Superni 75, Superni 600, Superfer 800H, Superco 605 and Superni 718 superalloys at an impact velocity of 40ms^{-1} and impingement angle of 30°. From the graph, it can be inferred that the erosion rate of Superco 605 is marginally higher than that for the other superalloys, whereas erosion rate of Superni 600 and 718 are lowest amongst the superalloys at 30° impact angle. Fig. 5.3 depicts the graph of erosion rate against cumulative mass of erodent for 90° impact

angle. From the plot it is apparent that the erosion rate of Superco 605 and Superfer 800H are marginally higher, while those of the Superni 75 and 718 are lower amongst the superalloys. Form Fig. 5.2 and 5.3, it can be revealed that up to the fifth cycle, variation in erosion rate is more and after sixth cycle becomes approximately constant at both the impact angles. A histogram illustrating the steady state erosion rate (volumetric loss) of the superalloys subjected to erosion is shown in Fig. 5.4. From the graph it can be seen that the steady state erosion rates of all the tested superalloys are not much different at 30° impact angle whereas the difference is appreciable at normal impact angle with maximum for Superfer 800H and minimum for Superni 718.

5.1.1.3 SEM/EDAX Analysis

5.1.1.3.1 Surface Morphology

The SEM observations (Figs. 5.5 to 5.9) are made on the eroded surface of all the superalloys at both the impact angles on reaching steady-state erosion condition. These micrographs reveal severe plastic deformation at the surfaces. No cracks are visible in these micrographs. Fig. 5.5 and Fig. 5.6 show the surface micrographs of all the three superalloys eroded at 30° and 90° impact angles. It is observed from the SEM (Fig. 5.5 and Fig. 5.6) of the eroded surfaces of superalloys at 30° impact angle that the material gets removed due to cutting and plastic deformation of the material in the flow direction of the impacting particles. The cutting scar (marked as CS) with lip (indicated as L) and crater (indicated as C) formed on the surfaces of the Superalloys eroded at 30° impact angle are clearly visible in these micrographs (Fig. 5.5). Wider craters and platelets formed on the surfaces of superalloys with plastic deformation when eroded at a 90° impact angle (Fig. 5.5 and Fig. 5.6).

SEMs of some of these eroded superalloys with compositions at selected points have been shown in Figs. 5.7 to 5.9. EDAX of Superni 75 superalloy eroded at 30° impact angle gave the weaker peaks of elements at eroded region from where it seems that material has been removed (marked as 1 in Fig. 5.7 a). Whereas EDAX analysis at different positions marked in the Figs. 5.7 to 5.9 have indicated the desired compositions of the superalloys. Further Fig. 5.8 (a) shows a smearing crater (SC) that resulted in the formation of a sharp ridge line on the right side by the solid particle impact. Also a series of slip bands (S) along one side is visible in the Fig. 5.8 (e). Broken pieces of sand particles embedded in the material are also revealed in some micrographs (Figs. 5.8a and 5.9b).

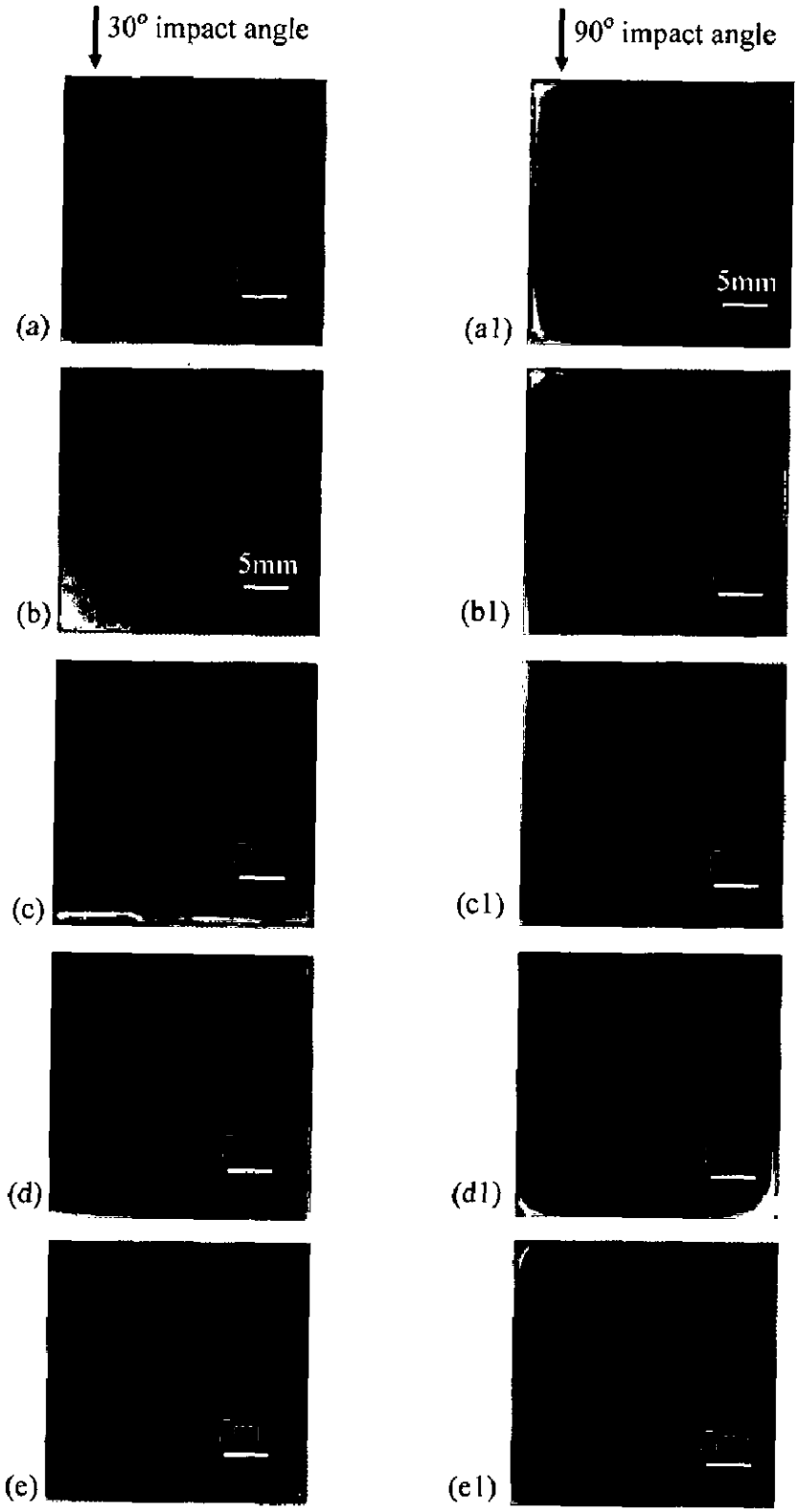

Fig. 5.1 Macrographs of uncoated superalloys eroded at a velocity of 40ms^{-1} and impact angles of 30° and 90°.

(a) and (a1) Superni 75; (b) and (b1) Superni 600; (c) and (c1) Superfer 800H; (d) and (d1) Superco 605; (e) and (e1) Superni 718.

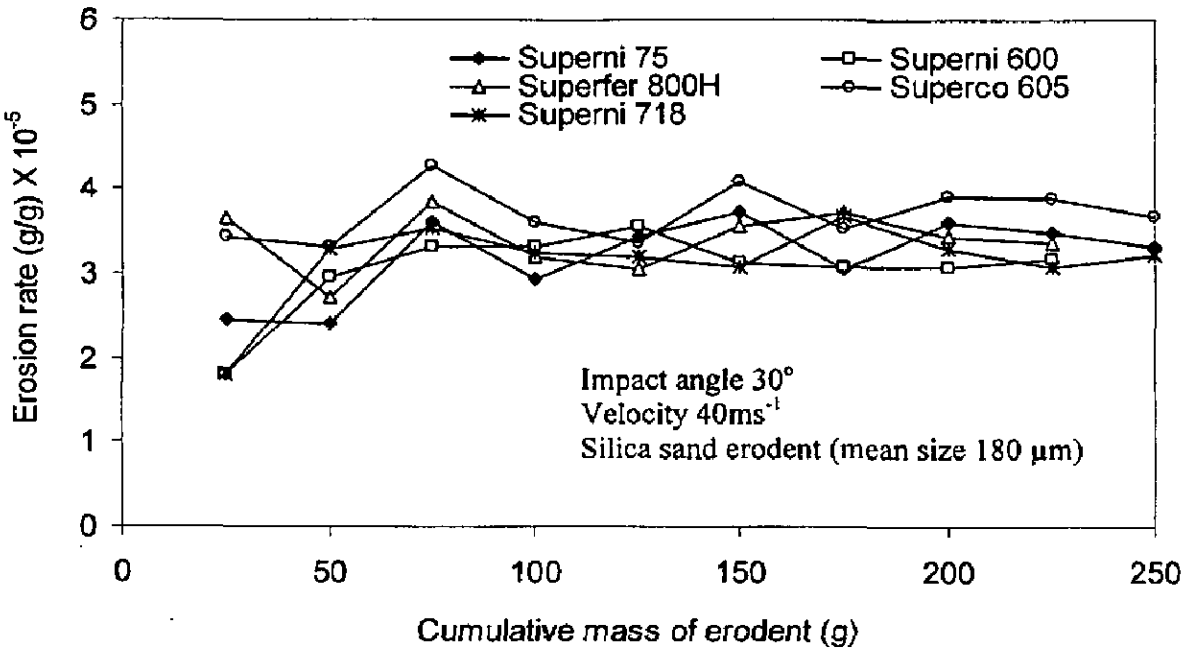

Fig. 5.2 Erosion rate (g/g) against cumulative mass of erodent for uncoated superalloys at a velocity of 40 ms^{-1} and 30° impact angle.

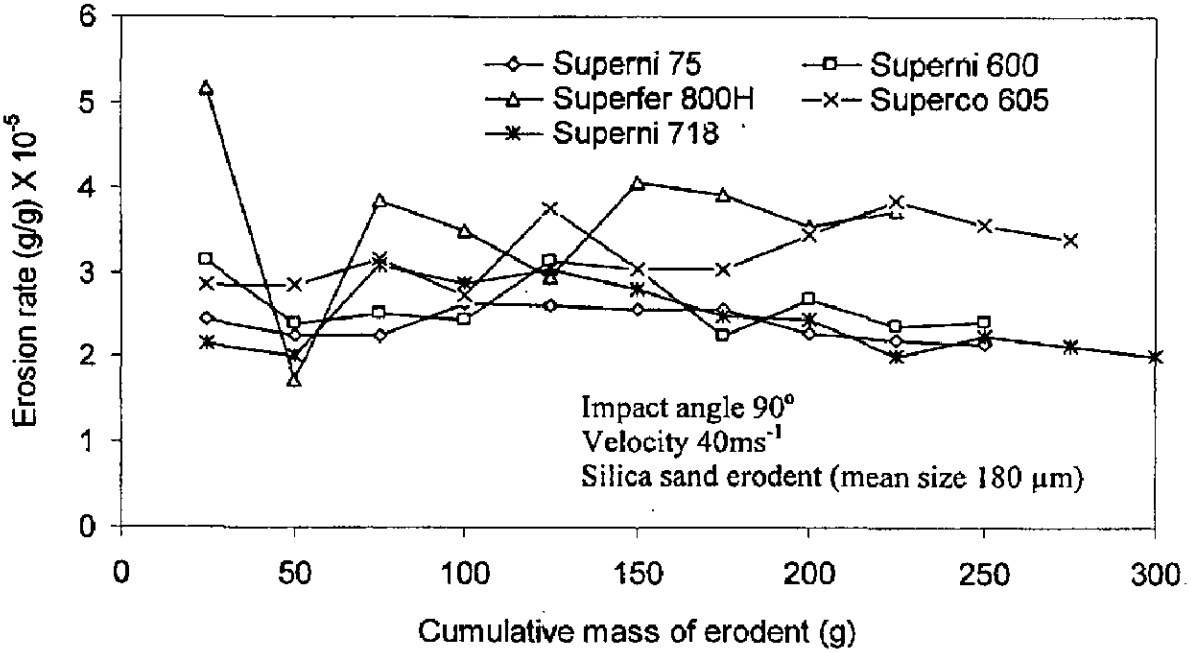

Fig. 5.3 Erosion rate (g/g) against cumulative mass of erodent for uncoated superalloys at a velocity of 40 ms^{-1} and 90° impact angle.

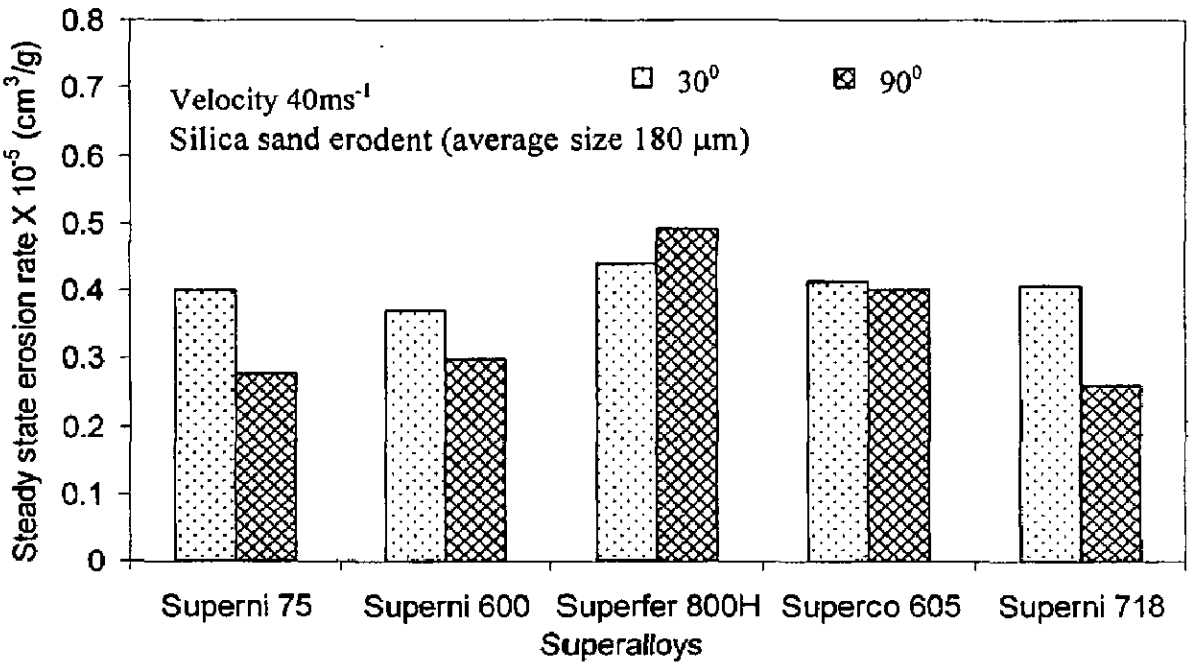

Fig. 5.4 A histogram illustrating the steady-state erosion rate of superalloys subjected to erosion at a velocity of 40 ms^{-1} and impact angle of 30° and 90° using silica sand of average size 180 μm as erodent.

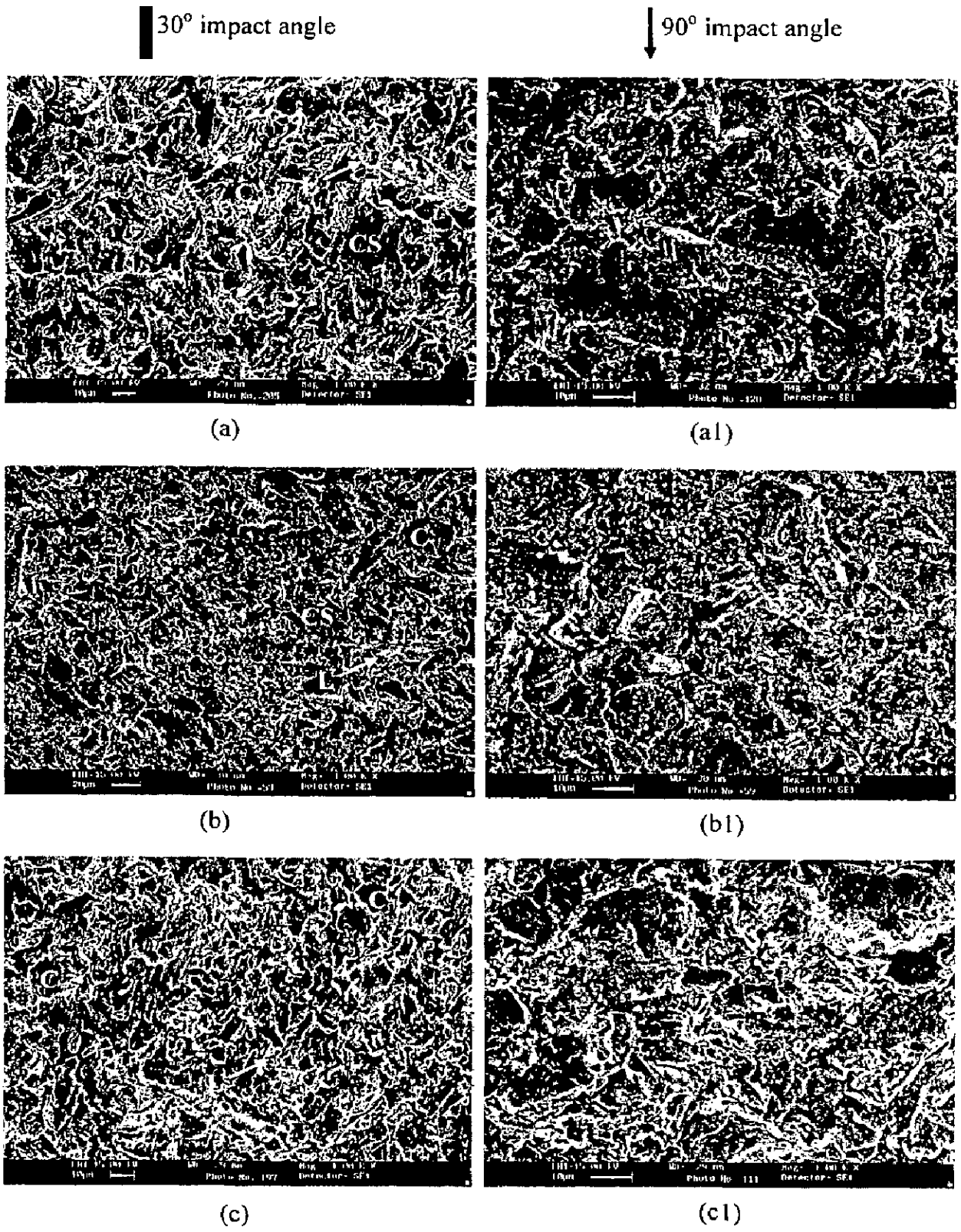

Fig.5.5 Scanning electron micrographs of eroded superalloys subjected to erosion at a velocity of 40 ms^{-1} and impact angle of 30° and 90°.

(a) and (a1) Superni 75; (b) and (b1) Superni 600;

(c) and (c1) Superfer 800H.

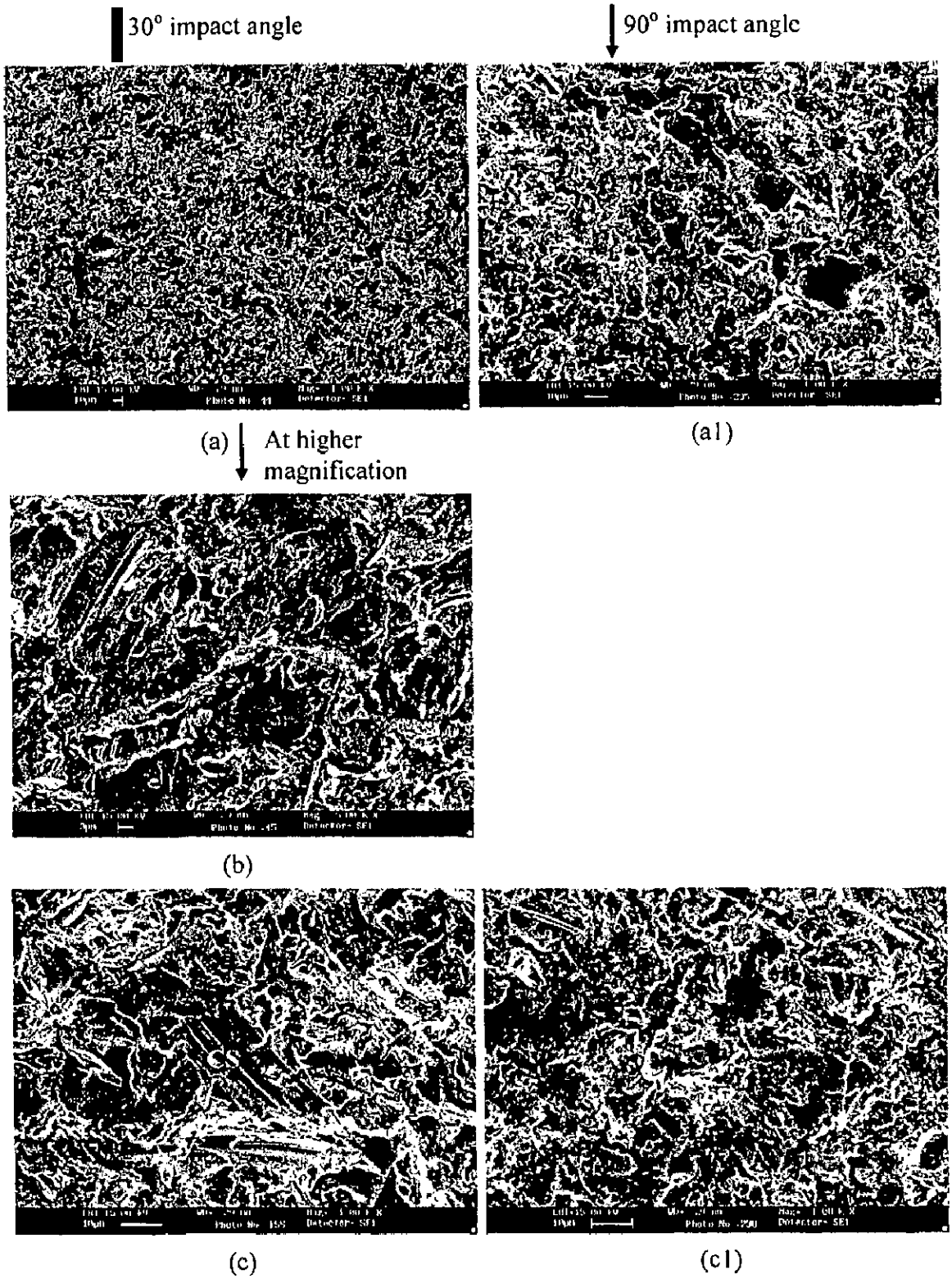

Fig. 5.6 Scanning electron micrographs of eroded superalloys subjected to erosion at a velocity of 40 ms^{-1} at impact angle of 30° and 90°.

(a) and (b) Superco 605 at impact angle of 30°;

(a1) Superco 605 at impact angle of 90°;

(c) and (c1) Superni 718 at impact angle of 30° and 90° respectively.

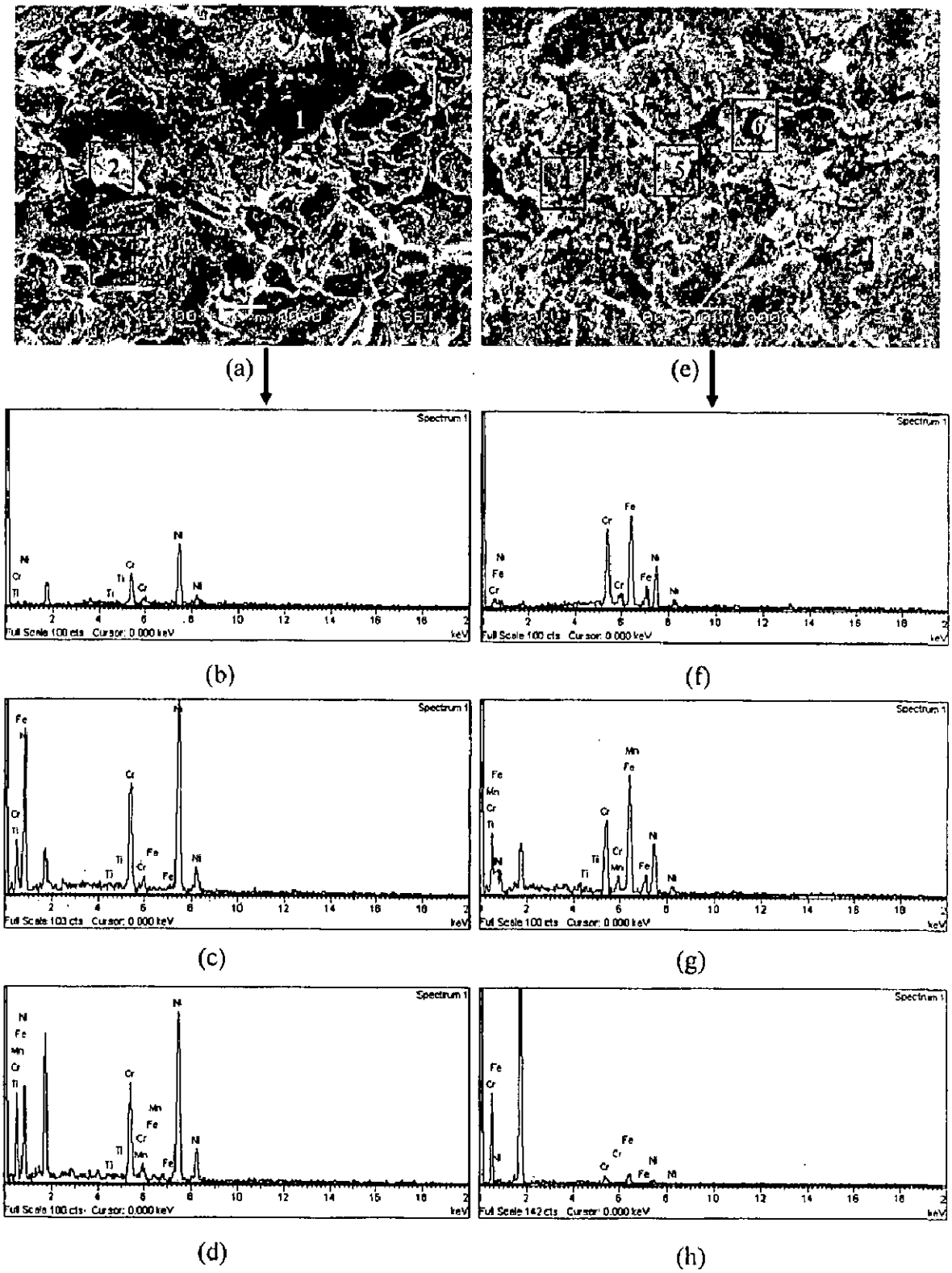

Fig. 5.7 Scanning electron micrographs with compositions of the eroded superalloys.

(a) Superni 75 at 30° impact angle (e) Superfer 800H at 90° impact angle.

(b), (c), (d), (f), (g) and (h) respectively are the compositions at positions 1, 2, 3, 4, 5 and 6 of the surface micrographs (a) and (e).

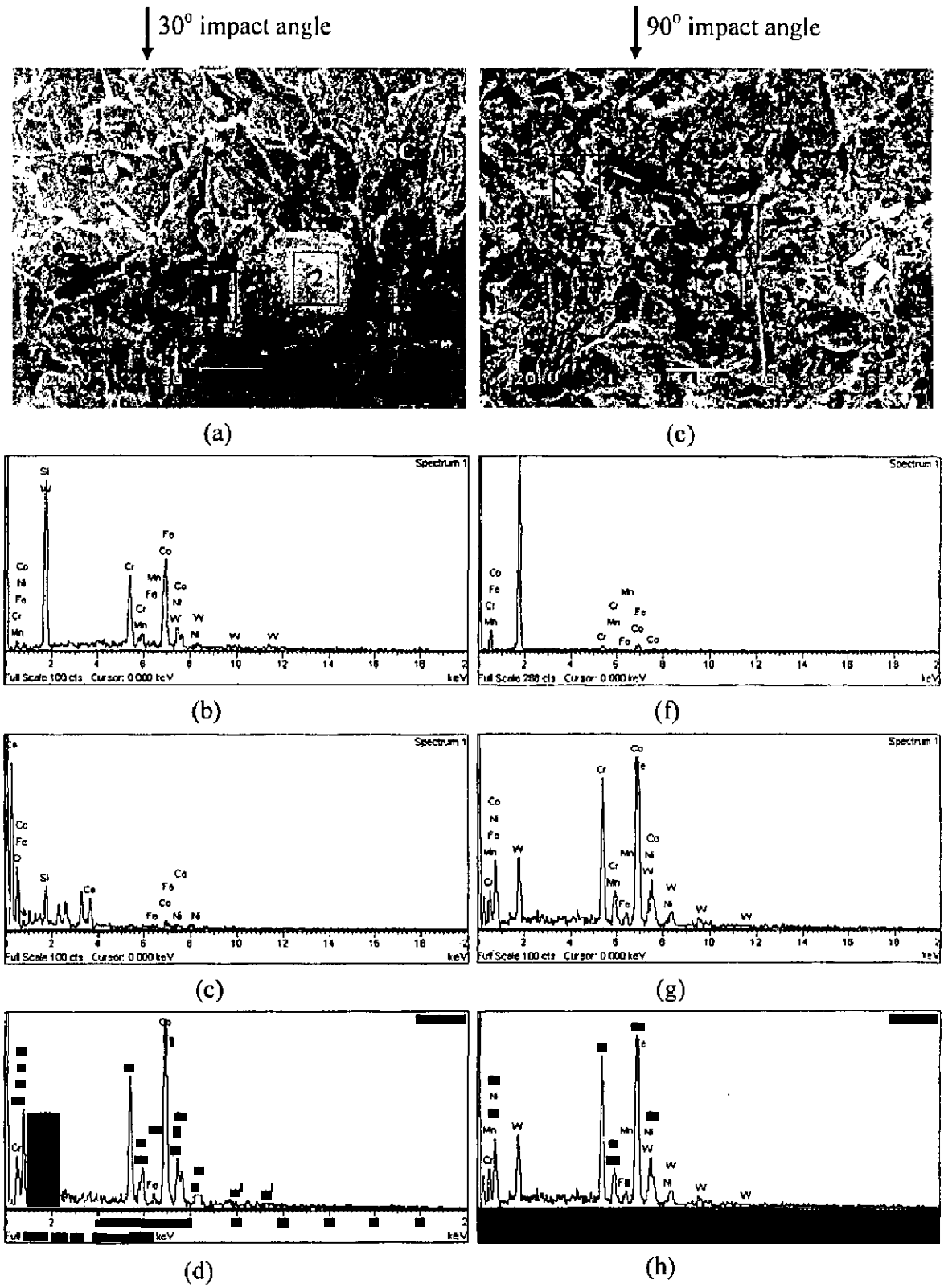

Fig. 5.8 Scanning electron micrographs with compositions of the eroded Superco 605 superalloy. (a) 30° impact angle and (e) 90° impact angle.

(b), (c), (d), (f), (g) and (h) respectively are the compositions at positions 1, 2, 3, 4, 5 and 6 of the surface micrographs (a) and (e).

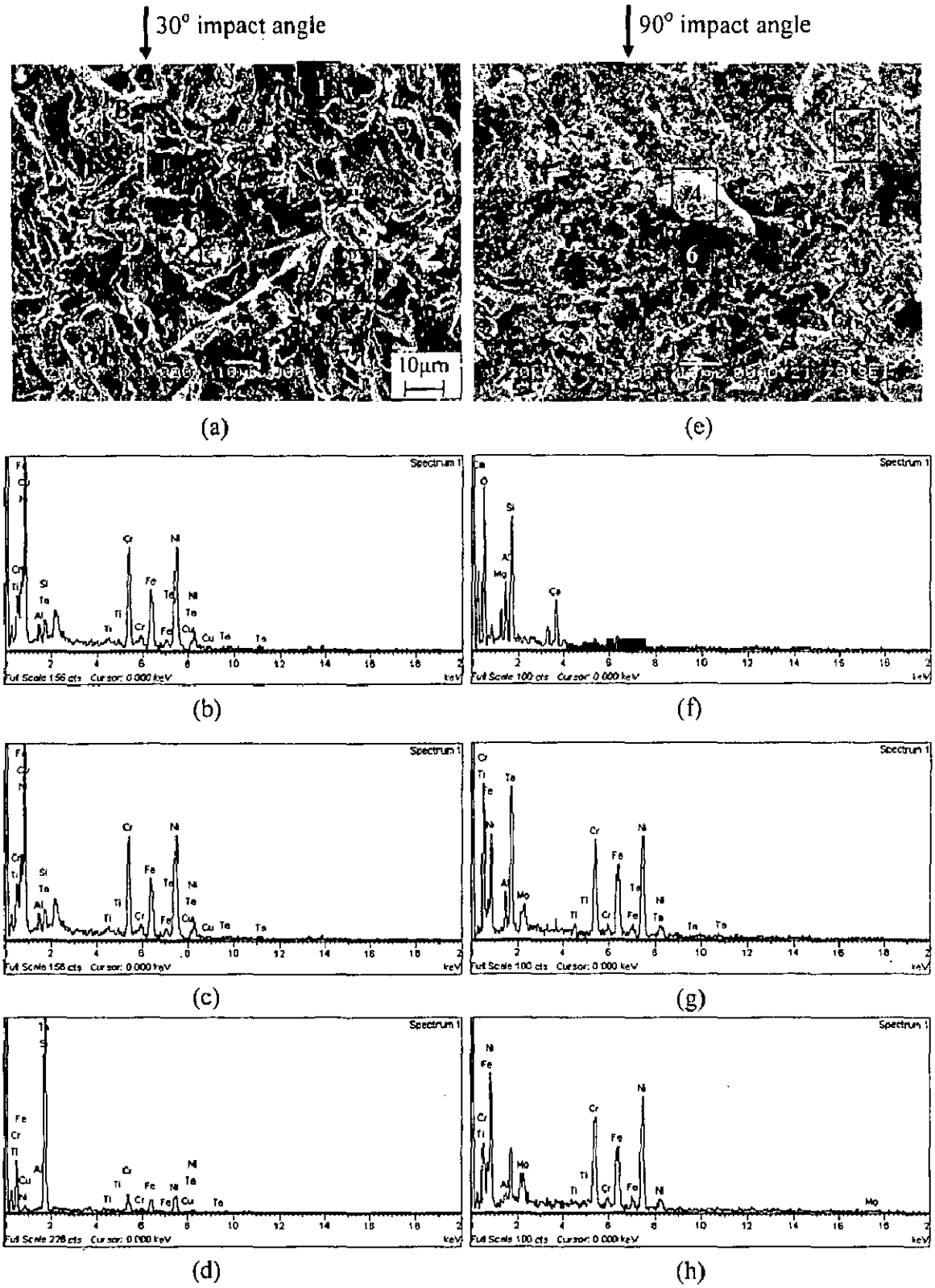

Fig. 5.9 Scanning electron micrographs with compositions of the eroded Superni 718 superalloy. (a) 30° impact angle and (e) 90° impact angle.

(b), (c), (d), (f), (g) and (h) respectively are the compositions at positions 1, 2, 3, 4, 5 and 6 of the surface micrographs (a) and (e).

5.1.1.3.2 Cross-sectional Analysis

In order to study the mechanisms of material removal, the eroded samples were cut along the cross-section through erosion zone by a diamond cutter and mounted using transoptic powder. The cross-sectional SEM of Superni 600 eroded at 90° impact angle has been depicted in Fig. 5.10. The micrographs indicate that the cavities are developed as a result of sand particles impact. Surface hillocks are also observed at various places which represent the portion of the alloy being partly removed from the surface of the specimens.

5.1.1.4 Surface Roughness

The surface roughnesses of all the eroded surfaces of the superalloys were measured and are reported in Table 5.1. The surface roughness is found to be in the range of 1.28-1.53 μm for 30° impact angle, and in the range of 1.28-1.62 μm or normal impact angle. The 3-Dimensional topography illustrating the surface roughness profiles of the eroded superalloys are shown in Figs. 5.11 and 5.12.

5.1.2 NiCrAlY Coating

5.1.2.1 Visual Examination

Surface macrographs of the plasma sprayed NiCrAlY coating on Superni 75, Superni 600, Superfer 800H, Superco 605 and Superni 718 superalloys eroded at 30° and 90° impact angles are shown in Fig. 5.13. From the Fig. 5.13, it can be inferred that for the coated Superni 600 and Superfer 800H eroded at 90° impact angle, the central eroded area is darker than that for the coated Superco 605 and Superni 718.

5.1.2.2 Erosion Rate

The erosion rate for the NiCrAlY coated superalloys eroded at an impact velocity of 40ms^{-1} and impingement angle of 30° has been compiled in Fig. 5.14. The graph (Fig. 5.14) reveals that the plasma sprayed NiCrAlY coating on Superco 605 superalloy eroded at 30° impact angle, gave the lowest erosion rate amongst these coated samples, while the coating is giving the highest erosion rate on Superni 718.

Fig. 5.15 shows the erosion rate graphs of the plasma spray NiCrAlY coating on Superni 75, Superni 600, Superfer 800H, Superco 605 and Superni 718 superalloys eroded at an impact velocity of 40ms^{-1} and impingement angle of 90°. From the graph, it can be observed that the erosion rate of NiCrAlY coating on Superni 75 is the highest, whereas that of the coating on Superfer 800H is the lowest amongst the coated superalloys at 90° impact angle. A histogram illustrating the steady state erosion rate in terms of volumetric loss for the plasma spray coated superalloys subjected to erosion under the given conditions is shown in Fig. 5.16.

5.1.2.3 SEM/EDAX Analysis

5.1.2.3.1 Surface Morphology

Scanning electron micrographs of plasma spray NiCrAlY coated superalloys subjected to erosion at a velocity of 40 ms^{-1} at impingement angles of 30° and 90° are shown in Figs. 5.17 and 5.18. The SEM studies provide useful information on the mechanism of erosion. Because of the different impingement angles of the sand particles, the eroded scars have different lengths and shapes. The morphologies of eroded surfaces at 30° impingement angle indicate that the failure is due to sand erosion where cutting and/or ploughing and lip fracture are dominant. The cutting scar and lips or ridges formed by the impacts of erodent particles at 30° impingement angle can be seen from the micrographs of the plasma sprayed NiCrAlY coating on all the superalloys. The platelets and craters formed by the plastic deformation of the NiCrAlY coating at normal impact angle on different superalloys can be seen from Figs. 5.17 and 5.18. The crater formed by the blunt erodent particle is visible in Fig. 5.18 (b1). The micrographs of the coatings eroded at normal impact angle indicate larger size craters whereas those at a 30° impact angle have deeper and stretched out.

EDAX analyses of some of these eroded surfaces are shown in Figs. 5.19 and 5.20. EDAX of point 1 and 3 marked in Fig. 5.19 (a) gives the composition of the coating whereas a large pit (marked as 2) shows only weak peaks of Ni and Cr. The broken piece of sand particle (Fig. 5.19 (e) and Fig. 5.20) embedded on the eroded surface of the NiCrAlY coating is confirmed by EDAX analysis. The EDAX analysis of eroded surface of the coating at 90° impact angle as depicted in Fig. 5.20 indicates the composition of NiCrAlY coating itself.

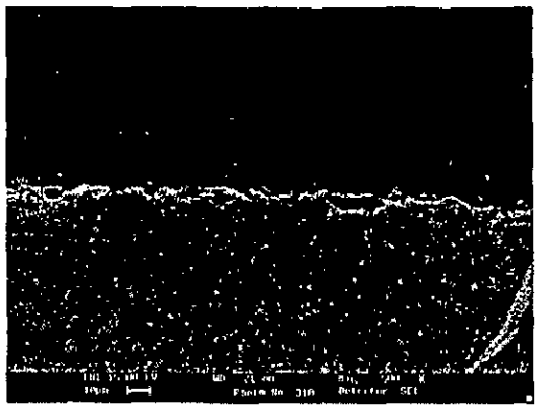

(a)

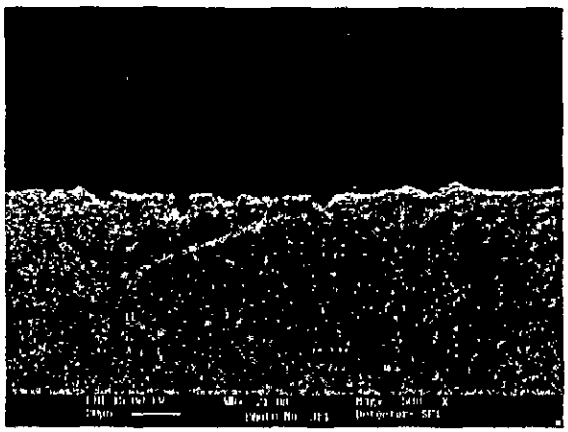

(b)

Fig. 5.10 Scanning electron micrographs across the cross-section at different positions from the eroded area of Superni 600 superalloy eroded at 90^0 impact angle.

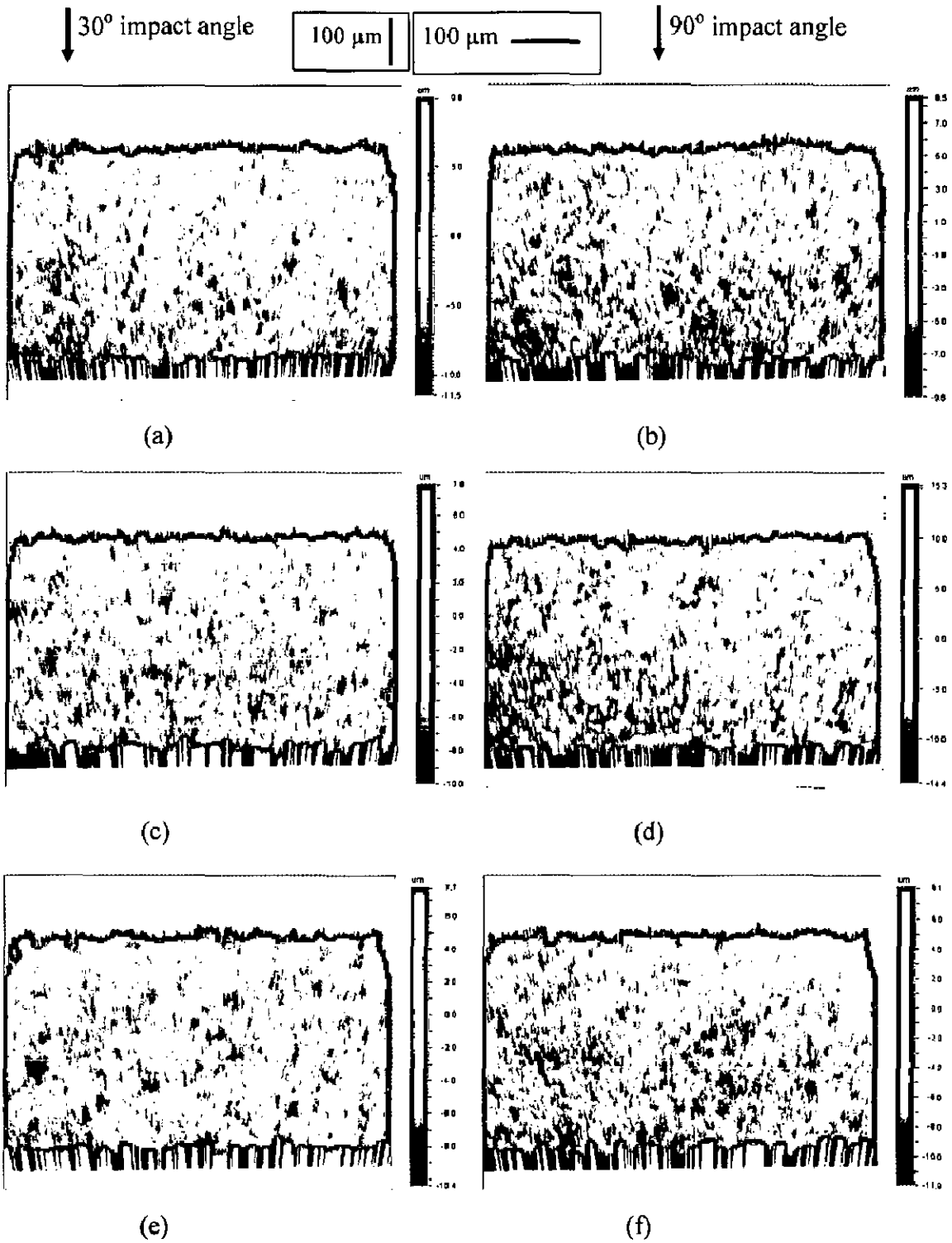

Fig. 5.11 3D optical profile of the eroded superalloys. (a) & (b) Superni 75, (c) & (d) Superni 600, (e) & (f) Superfer 800H, respectively at 30° & 90° impact angle. Dimension of scanned area is 591 μm × 449 μm.

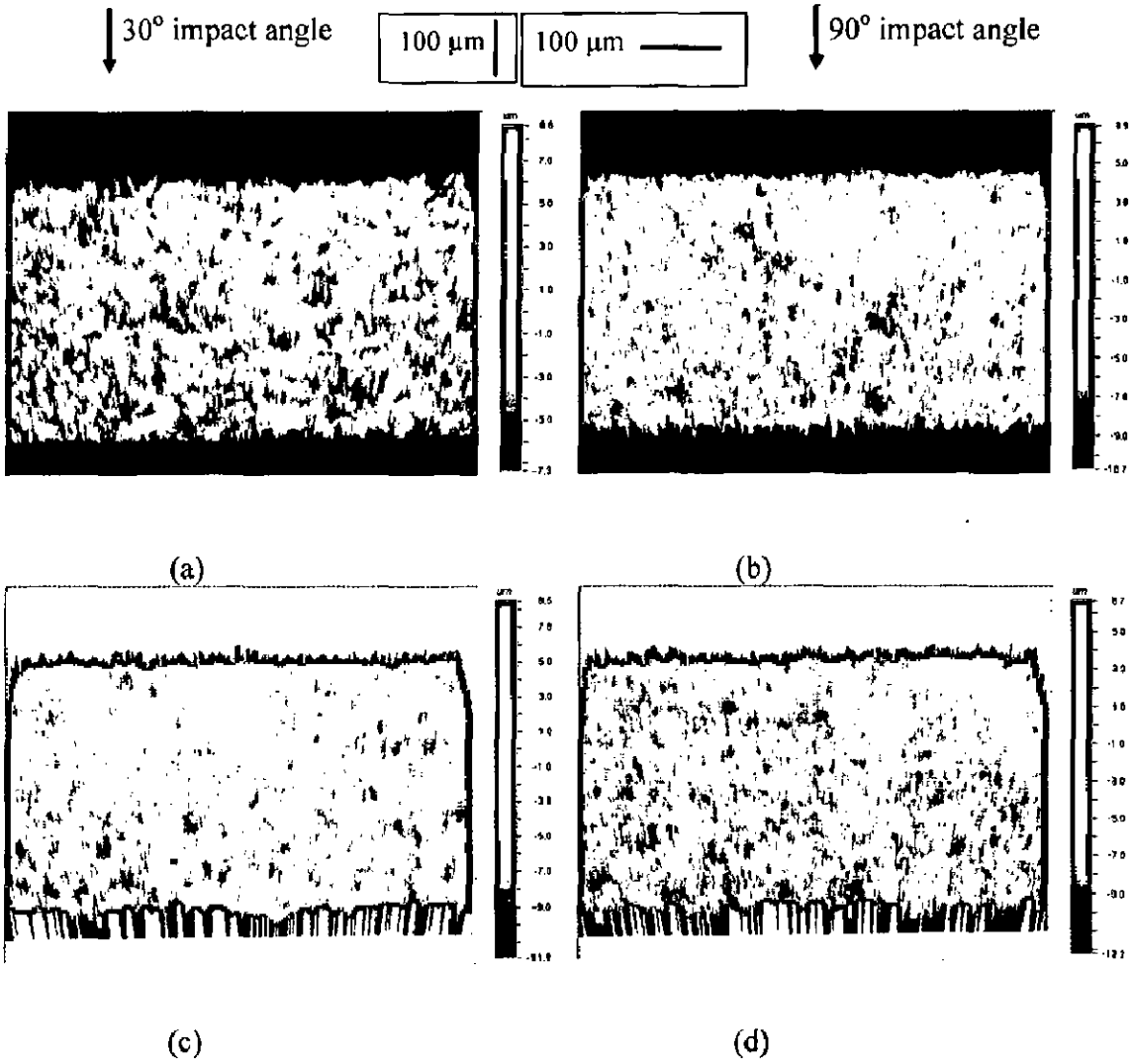

Fig. 5.12 3D optical profile of the eroded superalloy (a) & (b) Superco 605, (c) & (d) Superni 718, respectively at 30° and 90° impact angle. Dimension of scanned area is 591 µm × 449 µm.

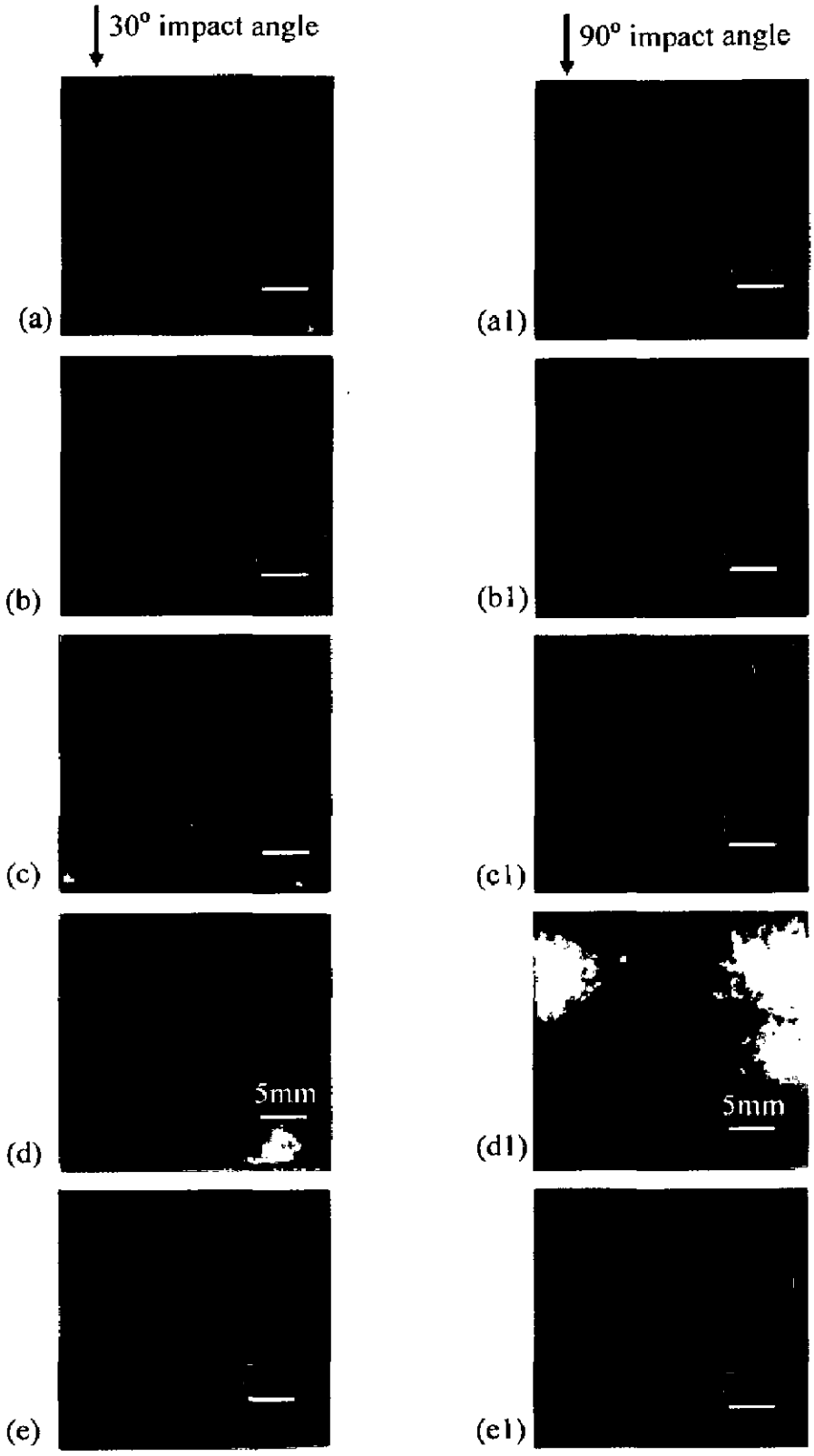

Fig. 5.13 Macrographs of plasma sprayed NiCrAlY coating on superalloys substrates eroded at a velocity of 40 ms^{-1} and impact angle of 30° and 90°. (a) and (a1) Superni 75; (b) and (b1) Superni 600; (c) and (c1) Superfer 800H;(d) and (d1) Superco 605; (e) and (e1) Superni 718.

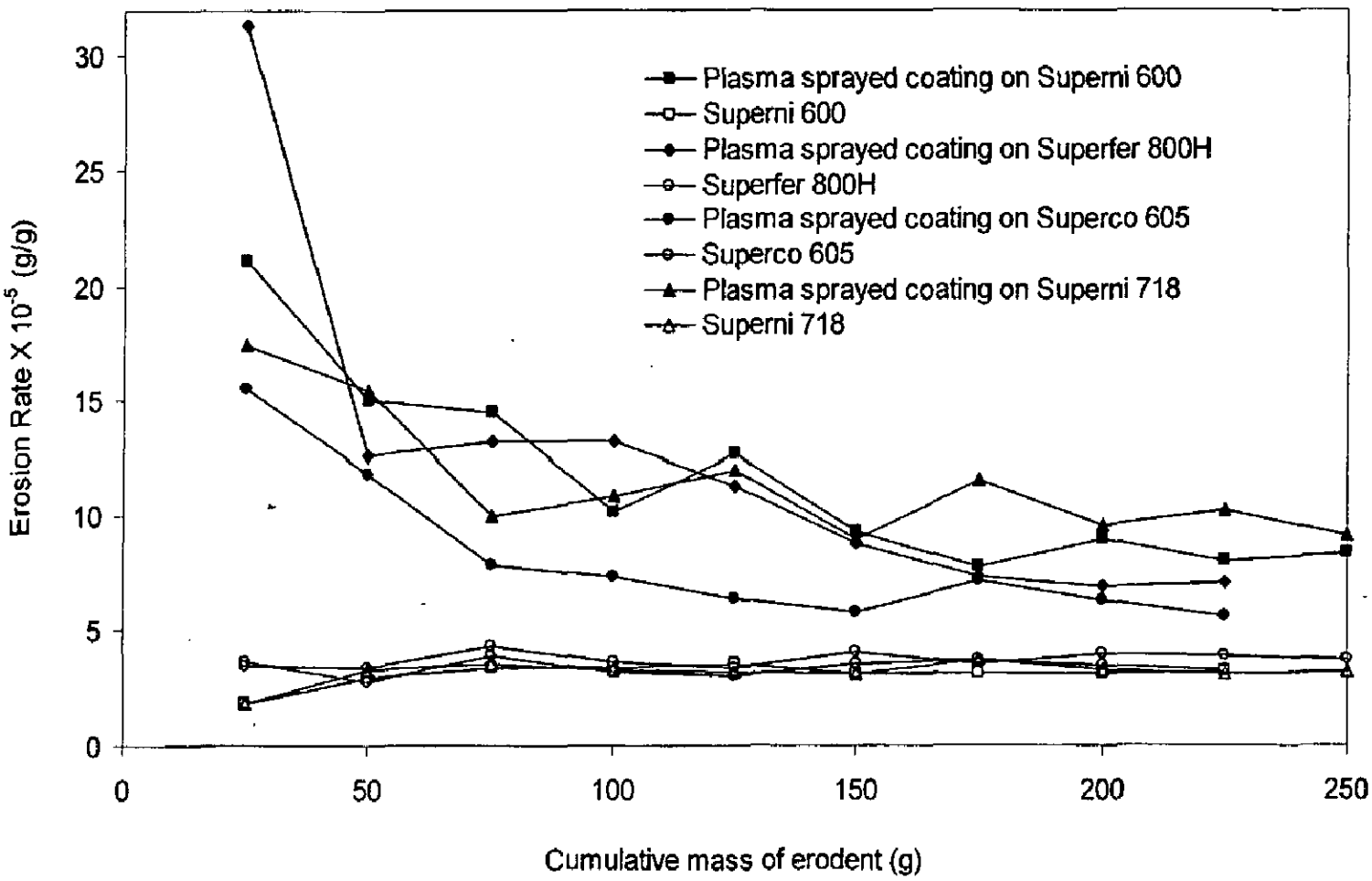

Fig. 5.14 Erosion rate (g/g) against cumulative mass of erodent for uncoated and plasma sprayed NiCrAlY coated superalloys at a velocity of 40 ms^{-1} and 30° impact angle.

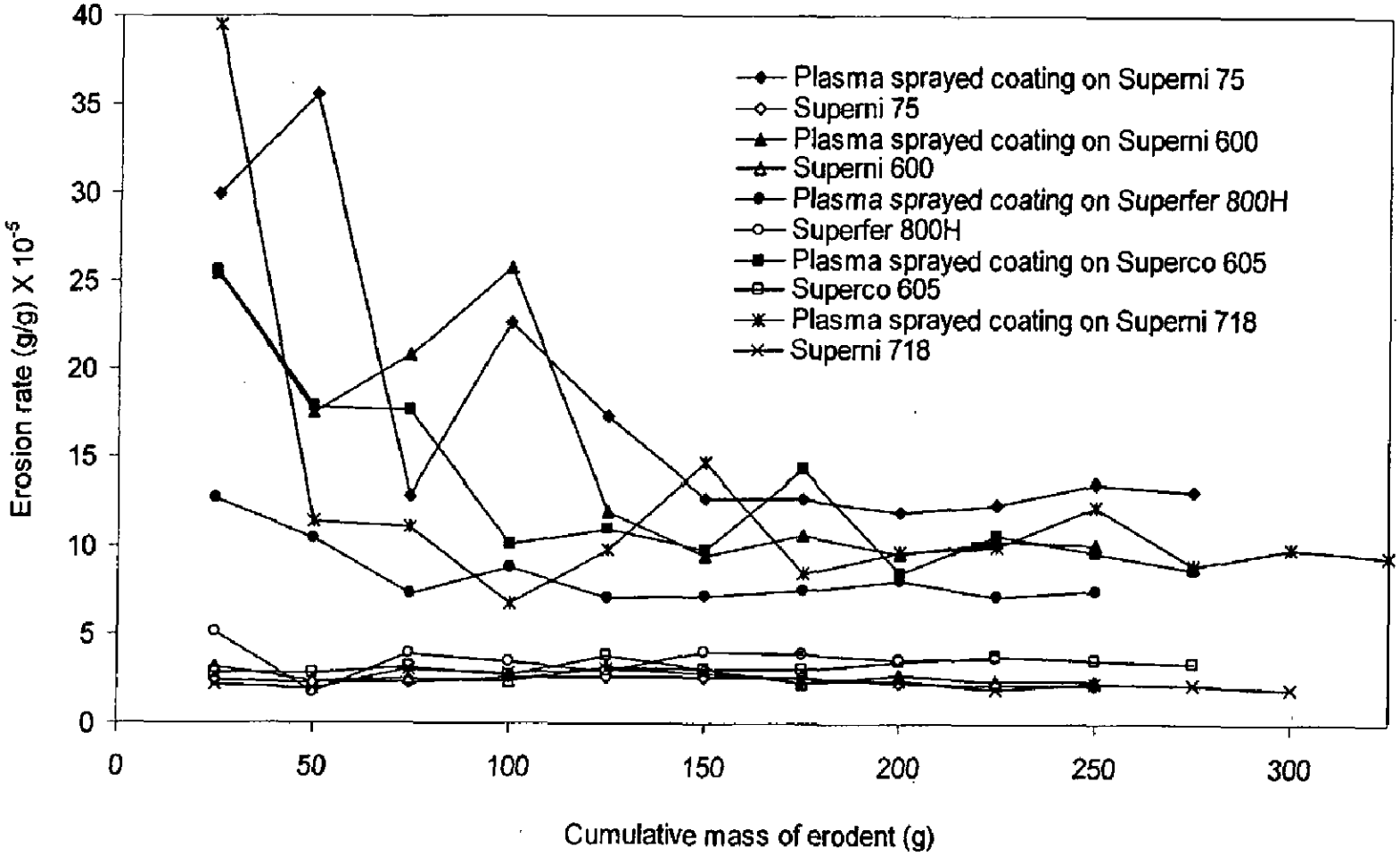

Fig. 5.15 Erosion rate (g/g) against cumulative mass of erodent for uncoated and plasma sprayed NiCrAlY coated superalloys at a velocity of 40 ms^{-1} and 90° impact angle.

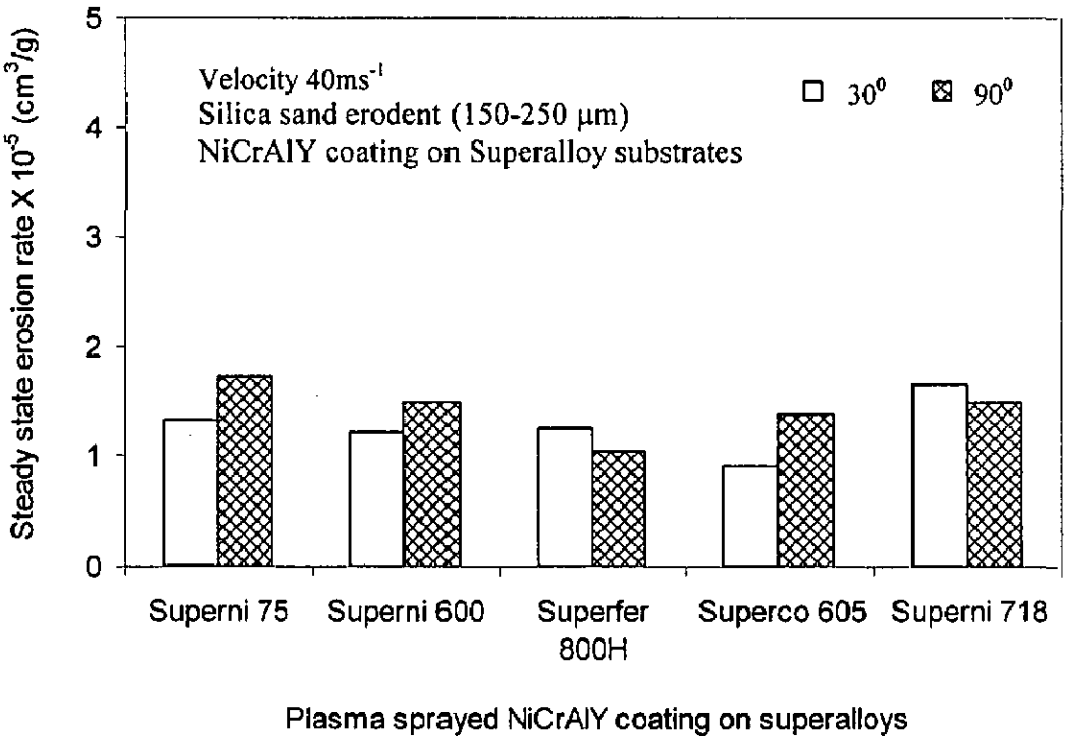

Fig. 5.16 A histogram illustrating the steady-state erosion rate of plasma sprayed NiCrAlY coating on different superalloy substrates subjected to erosion at a velocity of 40 ms^{-1} and impact angle of 30° and 90° using silica sand particle of average size 180 μm as erodent.

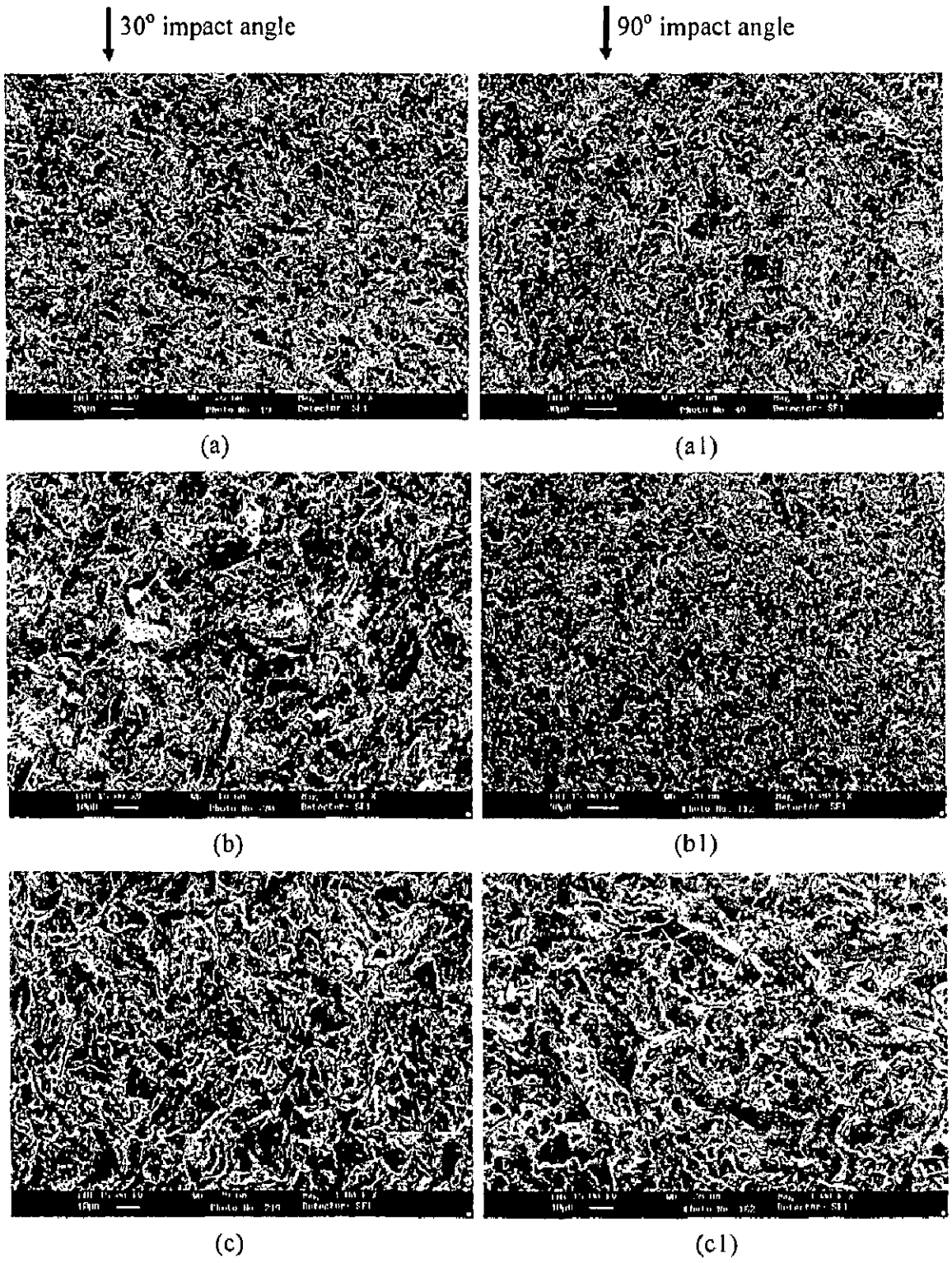

Fig.5.17 Scanning electron micrographs of eroded plasma sprayed NiCrAlY coating on different superalloys substrates subjected to erosion at a velocity of 40 ms^{-1} and impact angle of 30° and 90°.

(a) and (a1) Superni 75; (b) and (b1) Superni 600;

(c) and (c1) Superfer 800H.

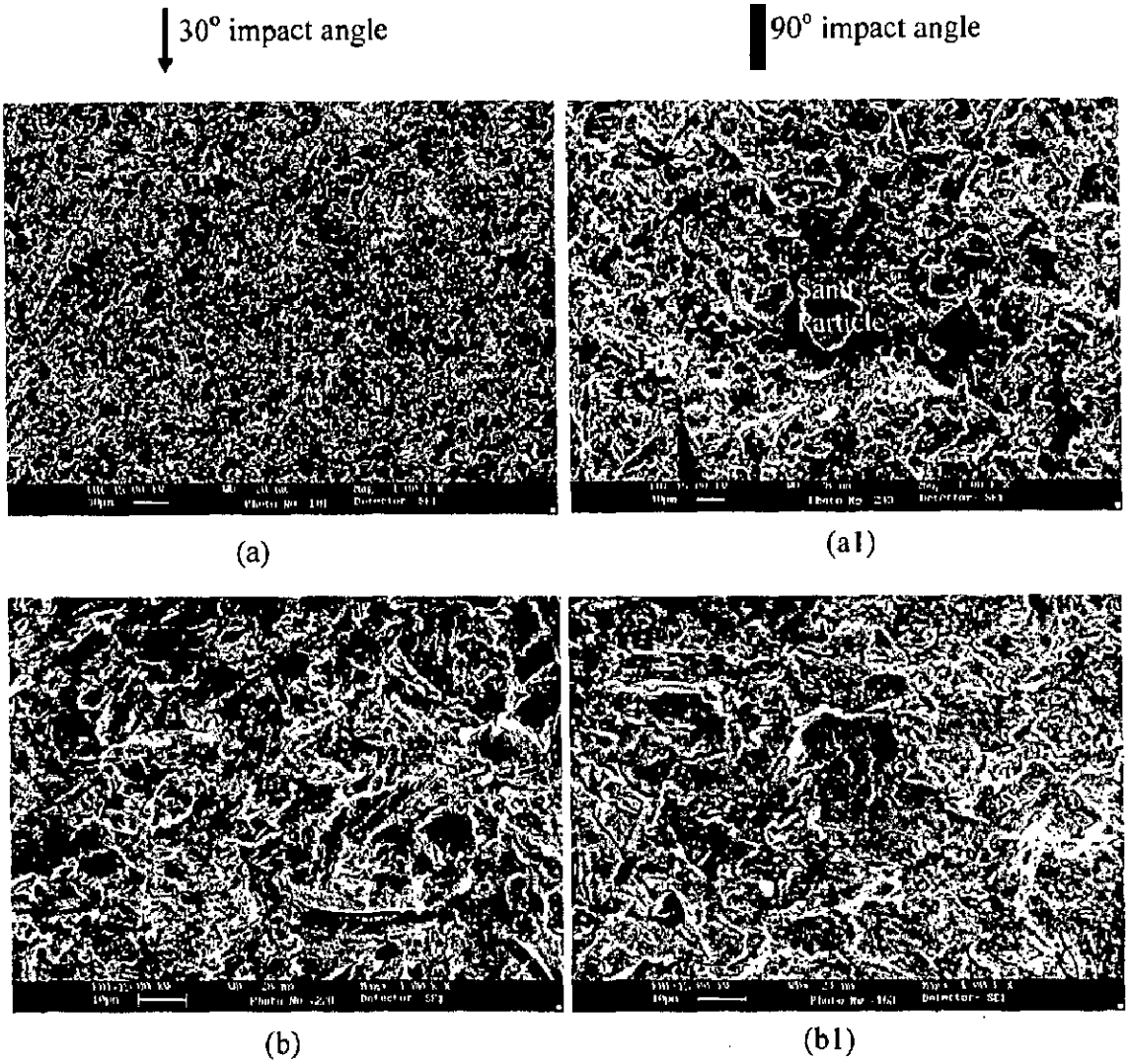

Fig.5.18 Scanning electron micrographs of eroded plasma sprayed NiCrAlY coating on different superalloys substrates subjected to erosion at a velocity of 40 ms^{-1} and impact angle of 30° and 90°.

(a) and (a1) Superco 605; (b) and (b1) Superni 718.

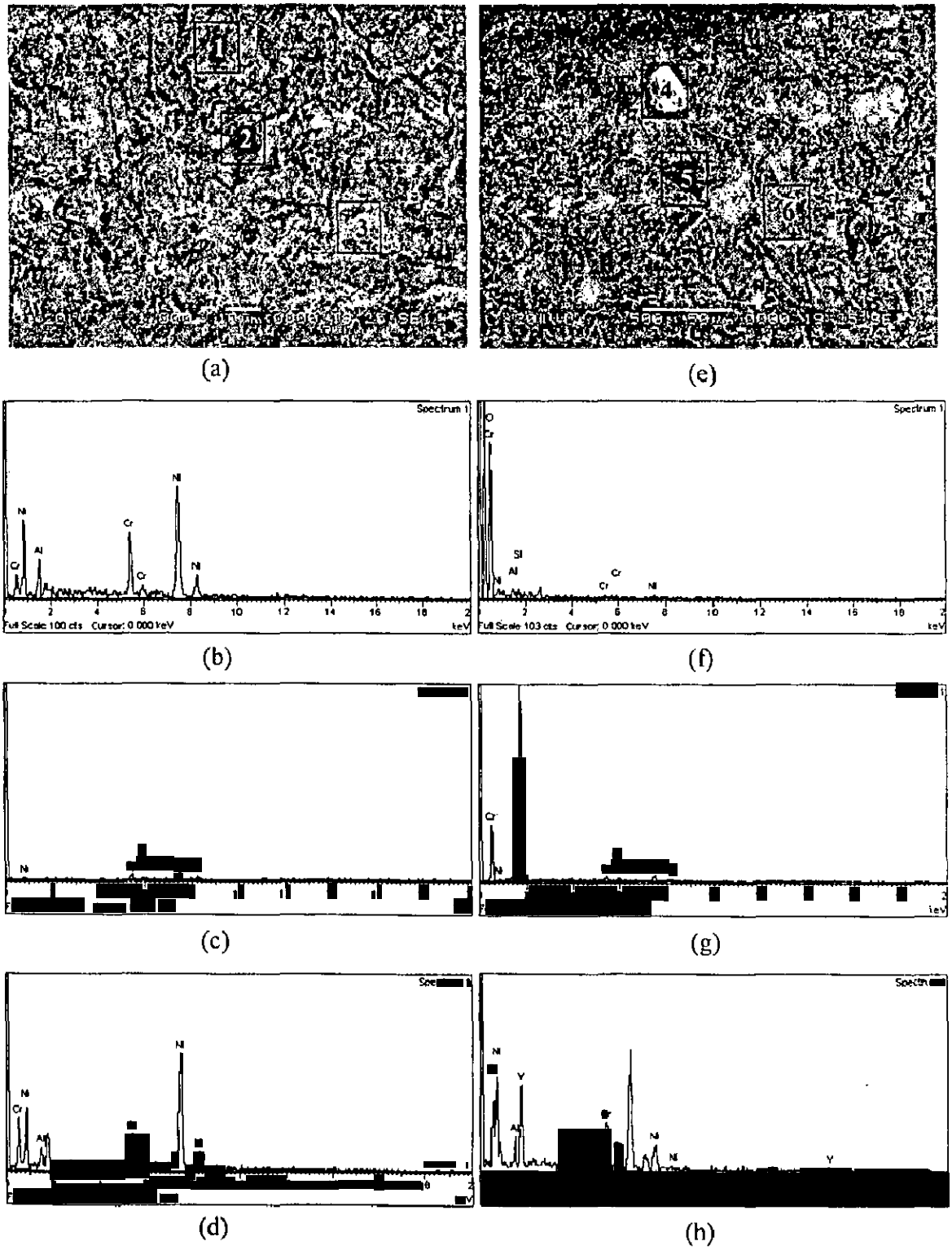

Fig. 5.19 Scanning electron micrographs with compositions of the eroded NiCrAlY coating superalloy substrates at 30° impact angle. (a) Superfer 800H and (e) Superco 605. (b), (c), (d), (f), (g) and (h) respectively are the compositions at positions 1, 2, 3, 4, 5 and 6 of the surface micrographs (a) and (e).

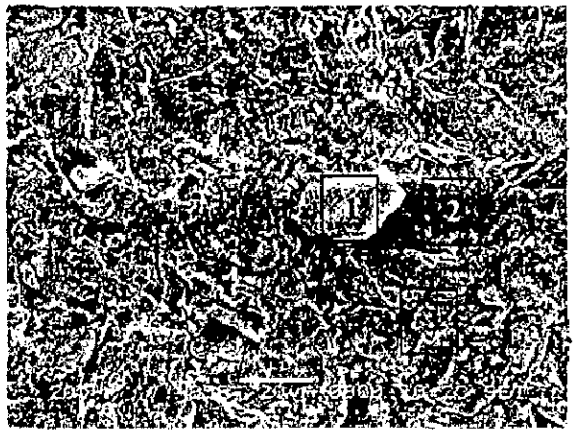

(a)

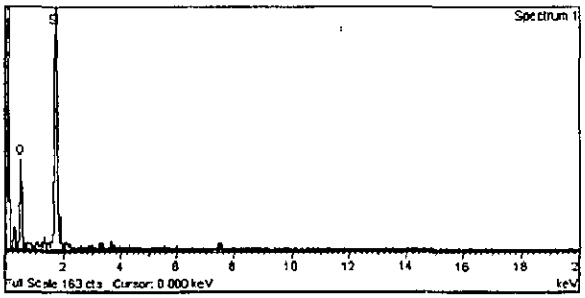

(b)

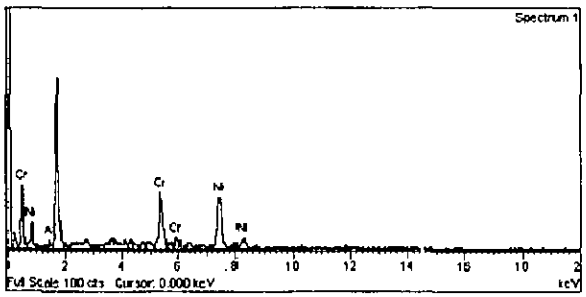

(c)

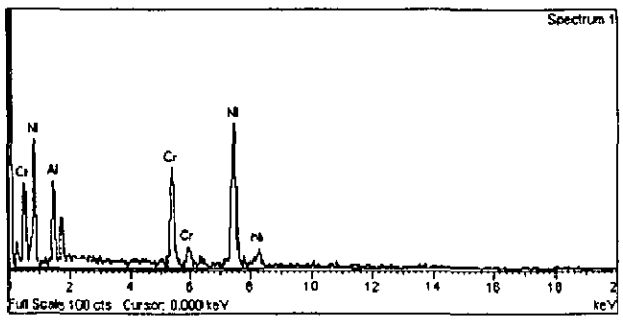

(d)

Fig. 5.20 Scanning electron micrographs with compositions of the eroded NiCrAlY coating on Superni 718 superalloy at 90° impact angle. (a) surface micrograph; (b), (c) and (d) are the compositions at positions 1, 2 and 3 respectively of the surface micrograph (a).

5.1.2.3.2 Cross-Sectional Analysis

The cross-sectional SEMs of NiCrAlY coating on Superni 600 superalloy substrate eroded at 30° and 90° impact angle have been depicted in Fig. 5.21.

5.1.2.4 Surface Roughness

The surface roughnesses of the eroded plasma spray NiCrAlY coated superalloys are reported in Table 5.1. The surface roughness of all the coated superalloys eroded at 30° impact angle were found to be in the range of 2.31-3.13 μm, whereas for normal impact angle the surface roughness lie in the range of 2.20-3.16 μm. The maximum value of average surface roughness was found to be 3.13 μm for coated Superfer 800H, whereas the minimum was 2.31 μm for Superco 605 at 30° impact angle. At 90° impact angle, the highest value of average surface roughness was obtained for coated Superco 605, whereas lowest for Superfer 800H. The 3-Dimensional surface roughness profiles of the eroded plasma sprayed NiCrAlY coating on different superalloys are shown in Figs. 5.22 and 5.23.

5.1.3 Ni-20Cr Coating

5.1.3.1 Visual Examination

Surface macrographs of the plasma sprayed Ni-20Cr coating on Superni 75, Superni 600, Superfer 800H, Superco 605 and Superni 718 superalloys eroded at 30° and 90° impact angles are shown in Fig. 5.24.

5.1.3.2 Erosion Rate

The erosion rate graph for the Ni-20Cr coated superalloys eroded at an impingement angle of 30° has been compiled in Fig. 5.25, which reveals that the plasma sprayed Ni-20Cr coating on Superni 718 substrate eroded at 30° impact angle, gave the highest erosion rate amongst the coatings, whereas the coating on Superni 75 and 600 gave the lower erosion rate. Further from the graph it can be also seen that the erosion rate of coating on Superfer 800H is also higher but lies slightly below than the coating on Superni 718.

Fig. 5.26 depicts the erosion rate graphs of the plasma sprayed Ni-20Cr coating on Superni 75, Superni 600, Superfer 800H, Superco 605 and Superni 718 superalloys eroded at an impingement angle of 90°. From the graph, it can be inferred that the erosion rate of Ni-20Cr coating on Superfer 800H was the highest amongst these coated superalloys, whereas that of the coating on Superni 718 gave the lowest amongst the superalloys at 90° impact angle. A histogram illustrating the steady state erosion rate of the plasma spray coated superalloys subjected to erosion is shown in Fig. 5.27. It can be clearly seen from the graph that the steady state erosion rate for Ni-20Cr coating on Superni 718 was highest at 30° impact angle. Whereas the graph (Fig. 5.27) reveals that steady state erosion rate is highest at 90° impact angle for Ni-20Cr coating on Superfer 800H substrate.

5.1.3.3 SEM/EDAX Analysis

5.1.3.3.1 Surface Morphology

SEM micrographs for the plasma spray Ni-20Cr coated superalloys after erosion at the impingement angles of 30° and 90° have been reported in Figs. 5.28 and 5.29. The cutting scar (CS), crater (C) and Lip (L) as seen are marked in the micrographs of superalloys eroded at impingement angle of 30°. The unmelted particles (marked as U) are visible in Figs. 5.28 (a), (b) and 5.29(a). The micrographs (Figs. 5.28 and 5.29) of the Ni-20Cr coated superalloys eroded at normal impact angle show that the highly plastic deformed surface with platelets and lips or ridges. Also unmelted particles are visible in Fig. 5.28 (c1).

EDAX analysis of the points 1, 2, 3 and 4 in the Fig. 5.30 (a) and (e) gives the composition of NiCr coating whereas it shows the higher chromium and some aluminium content at point 6 marked in the Fig. 5.30 (e). From the EDAX analysis of Fig. 5.31 (a) it can be seen that the pit region (marked as 1) is rich in chromium, while the white uneroded region (indicated as 2) has the composition of the Ni-20Cr coating. The distortion of the splat boundaries forming grooves in the coating can be seen in Fig. 5.31d (indicated as A) along with the plastic deformation of the coating. EDAX analysis of point 5 (Fig. 5.30 (e)) and point 4 of Fig. 5.31 (d) from the eroded surfaces of the Ni-20Cr coating confirms the embedment of the broken pieces of sand particle.

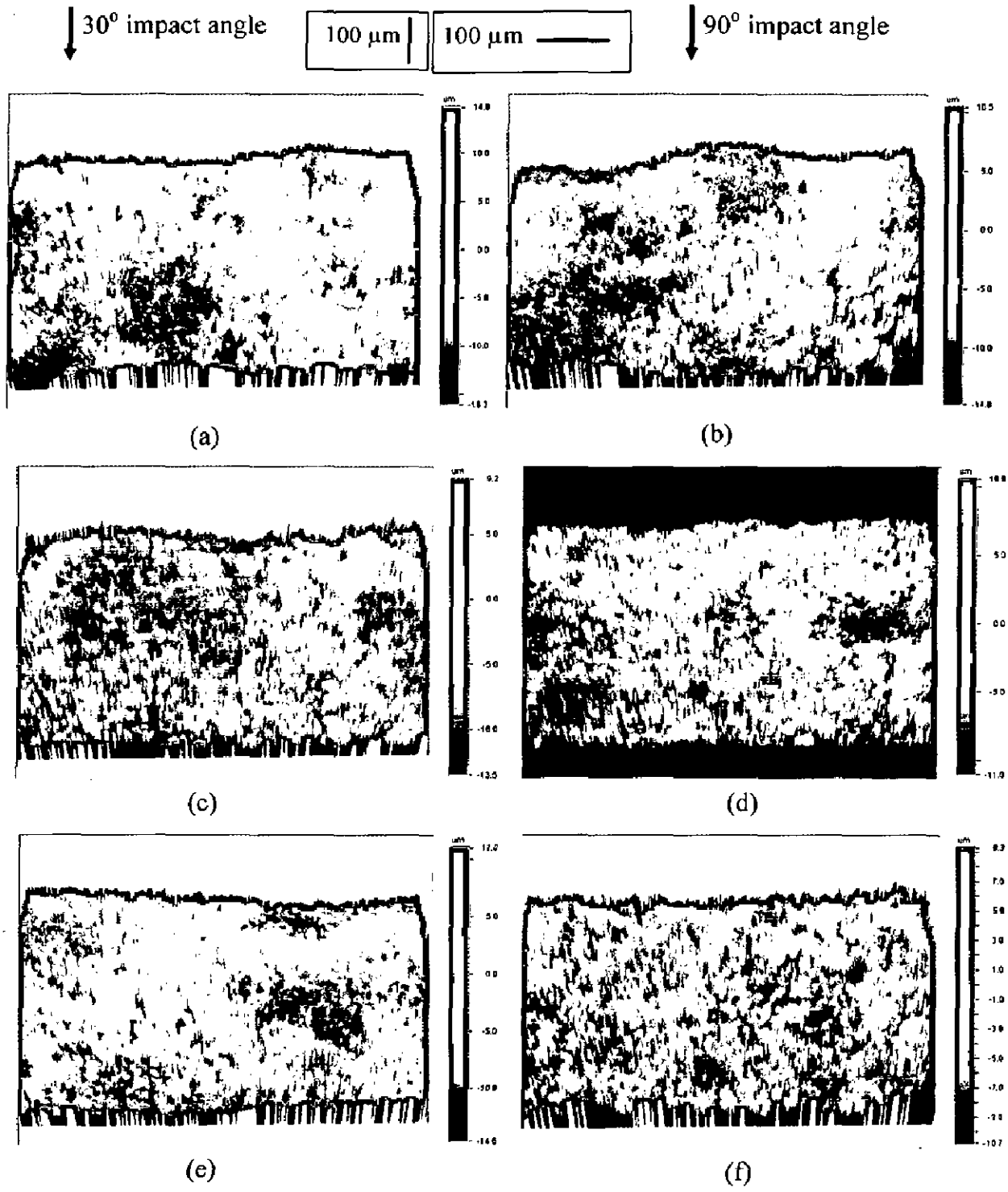

Fig. 5.22 3D optical profile of the eroded NiCrAlY coated superalloys (a) & (b) Superni 75; (c) & (d) Superni 600; (e) & (f) Superfer 800H; respectively at 30° and 90° impact angle. Dimension of scanned area is 591 μm × 449 μm.

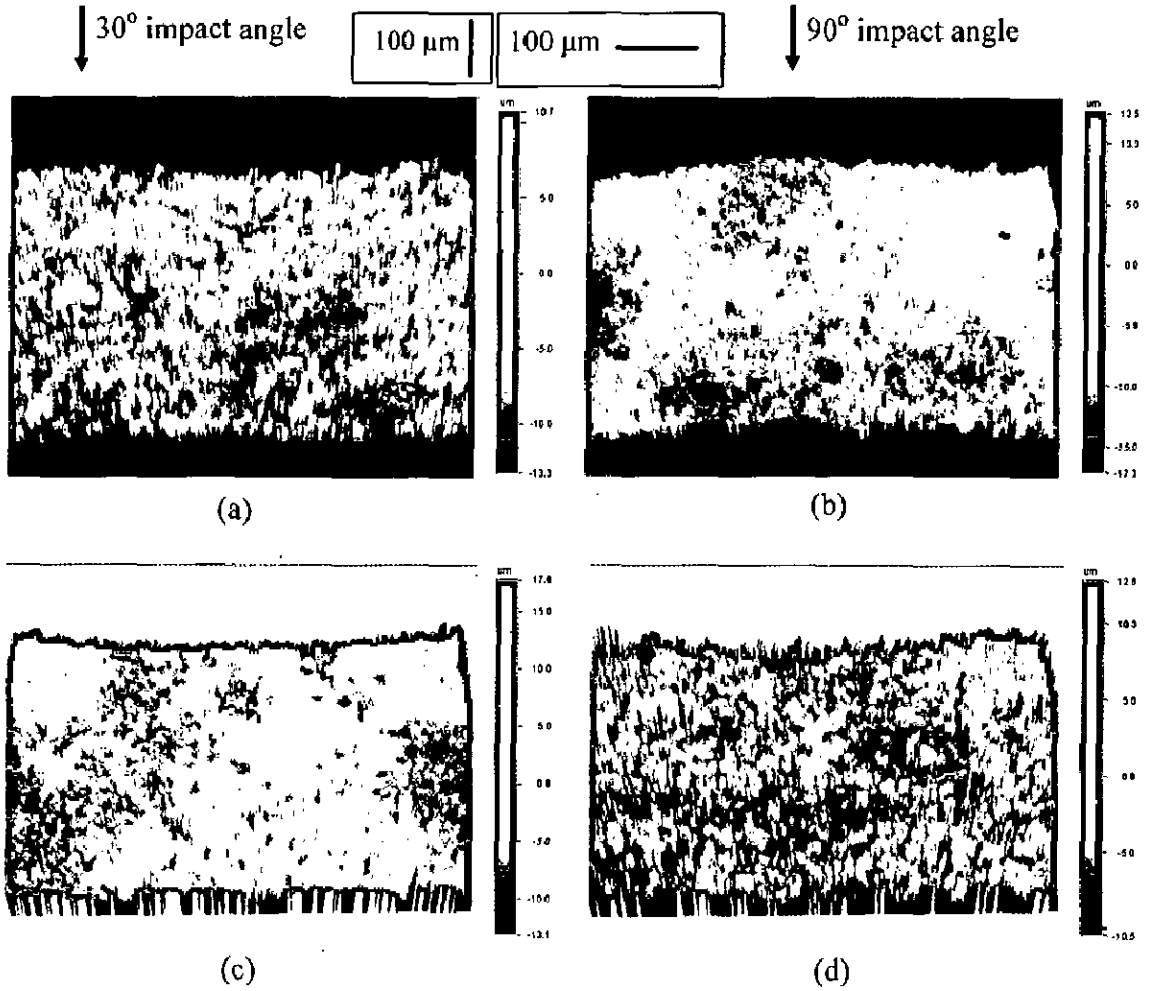

Fig. 5.23 3D optical profile of the eroded NiCrAlY coated superalloys (a) & (b) Superco 605; (c) & (d) Superni 718, respectively at 30° and 90° impact angle. Dimension of scanned area is 591 µm × 449 µm.

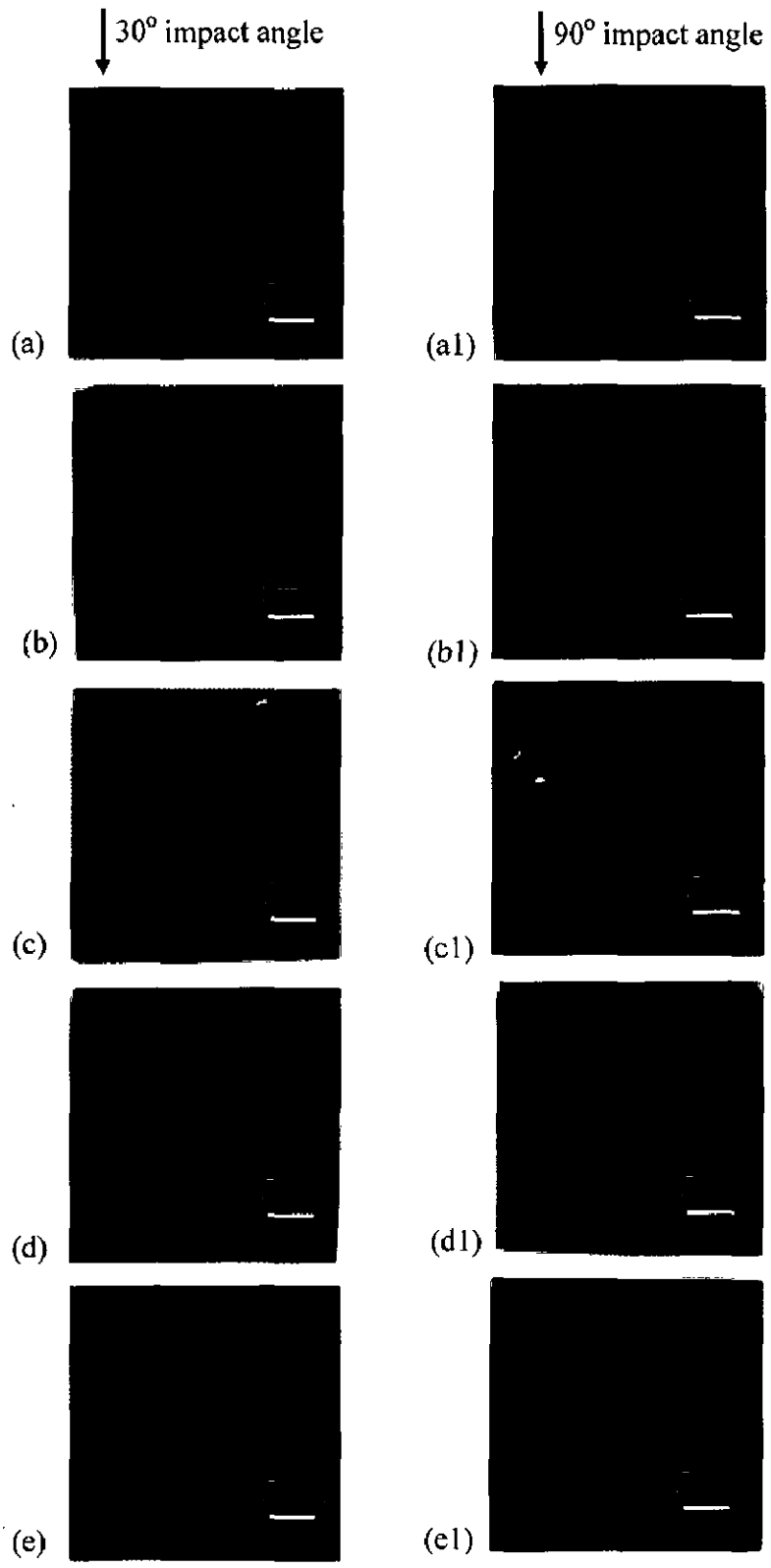

Fig. 5.24 Macrographs of plasma sprayed Ni-20Cr coated superalloys eroded at a velocity of 40 ms^{-1} and impact angles of 30° and 90° respectively.
(a) and (a1) Superni 75; (b) and (b1) Superni 600; (c) and (c1) Superfer 800H; (d) and (d1) Superco 605; (e) and (e1) Superni 718.

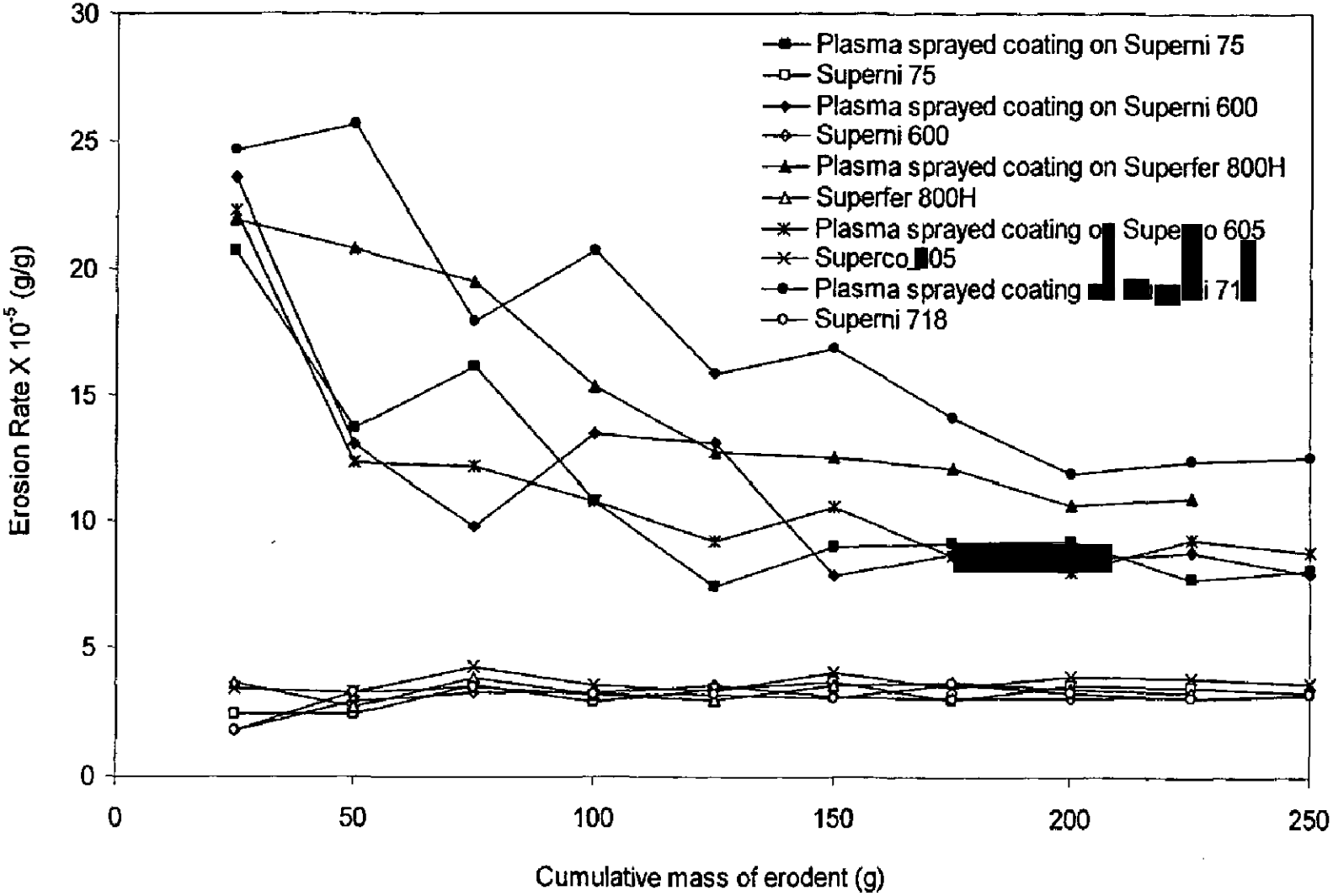

Fig. 5.25 Erosion rate (g/g) against cumulative mass of erodent for uncoated and plasma sprayed Ni-20Cr coated superalloys at a velocity of 40 ms^{-1} and 30° impact angle.

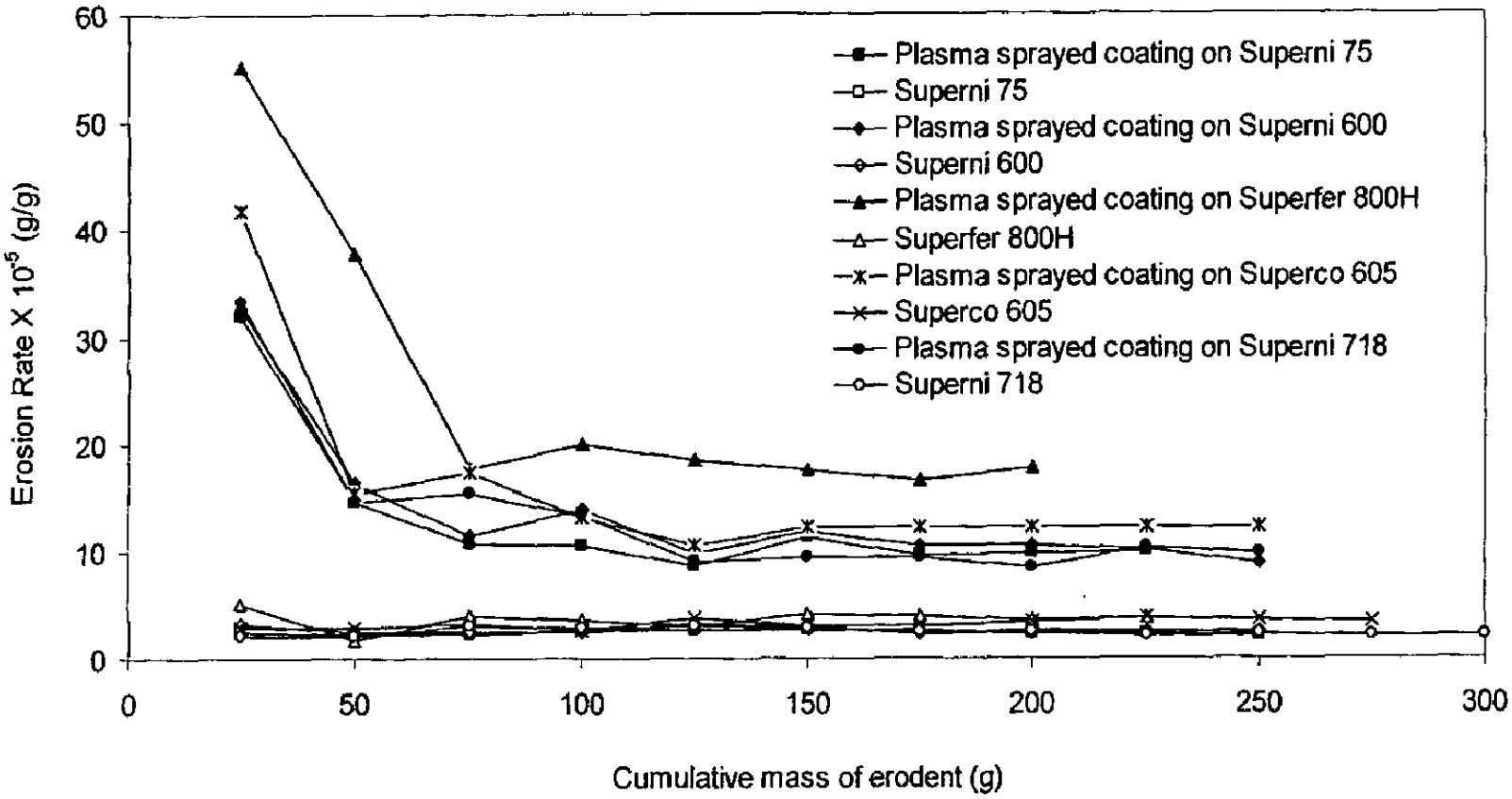

Fig. 5.26 Erosion rate (g/g) against cumulative mass of erodent for uncoated and plasma sprayed Ni-20Cr coated superalloys at a velocity of 40 ms^{-1} and 90° impact angle.

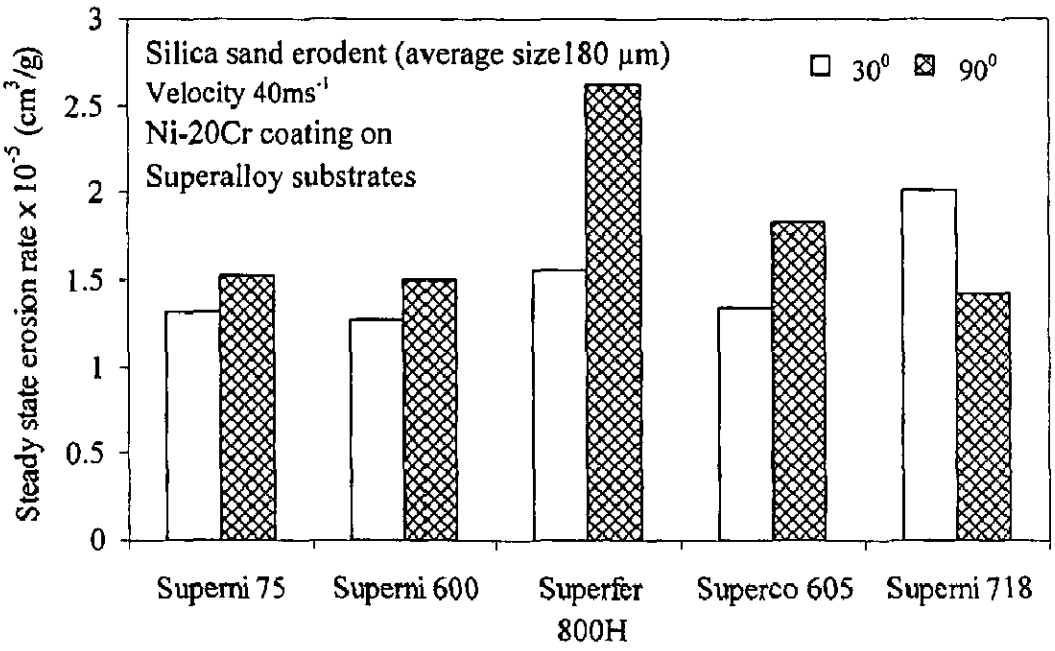

Fig. 5.27 A histogram illustrating the steady-state erosion rate of plasma sprayed Ni-20Cr coating on different superalloys substrates subjected to erosion at a velocity of 40 ms^{-1} and impact angle of 30° and 90° using silica sand of particle average size 180 μm as erodent.

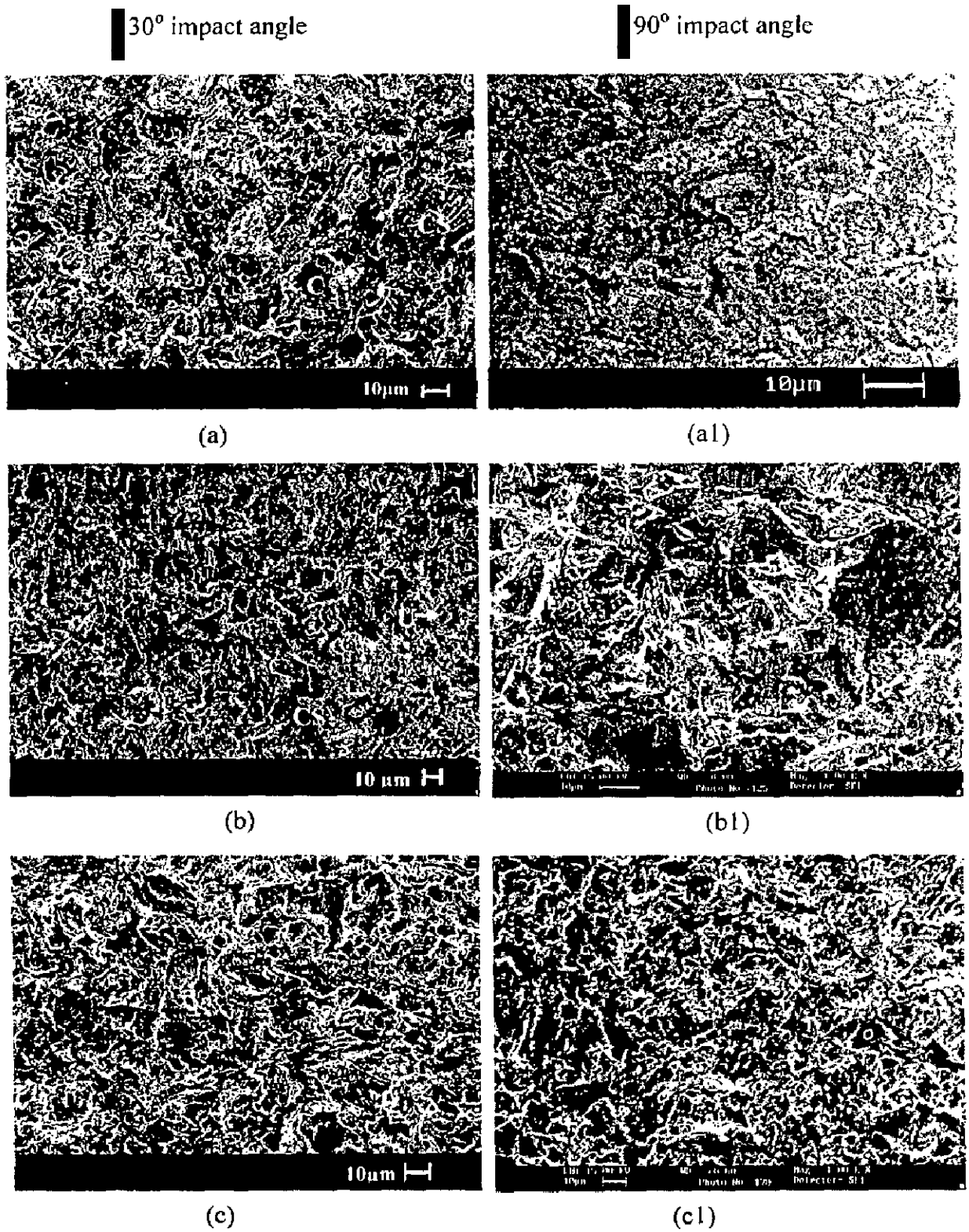

Fig. 5.28 Scanning electron micrographs of plasma spray Ni-20Cr coated superalloys subjected to erosion at a velocity of 40 ms^{-1} at impact angle of 30°.

(a) and (a1) Superni 75 (b) and (b1) Superni 600

(c) and (c1) Superfer 800H.

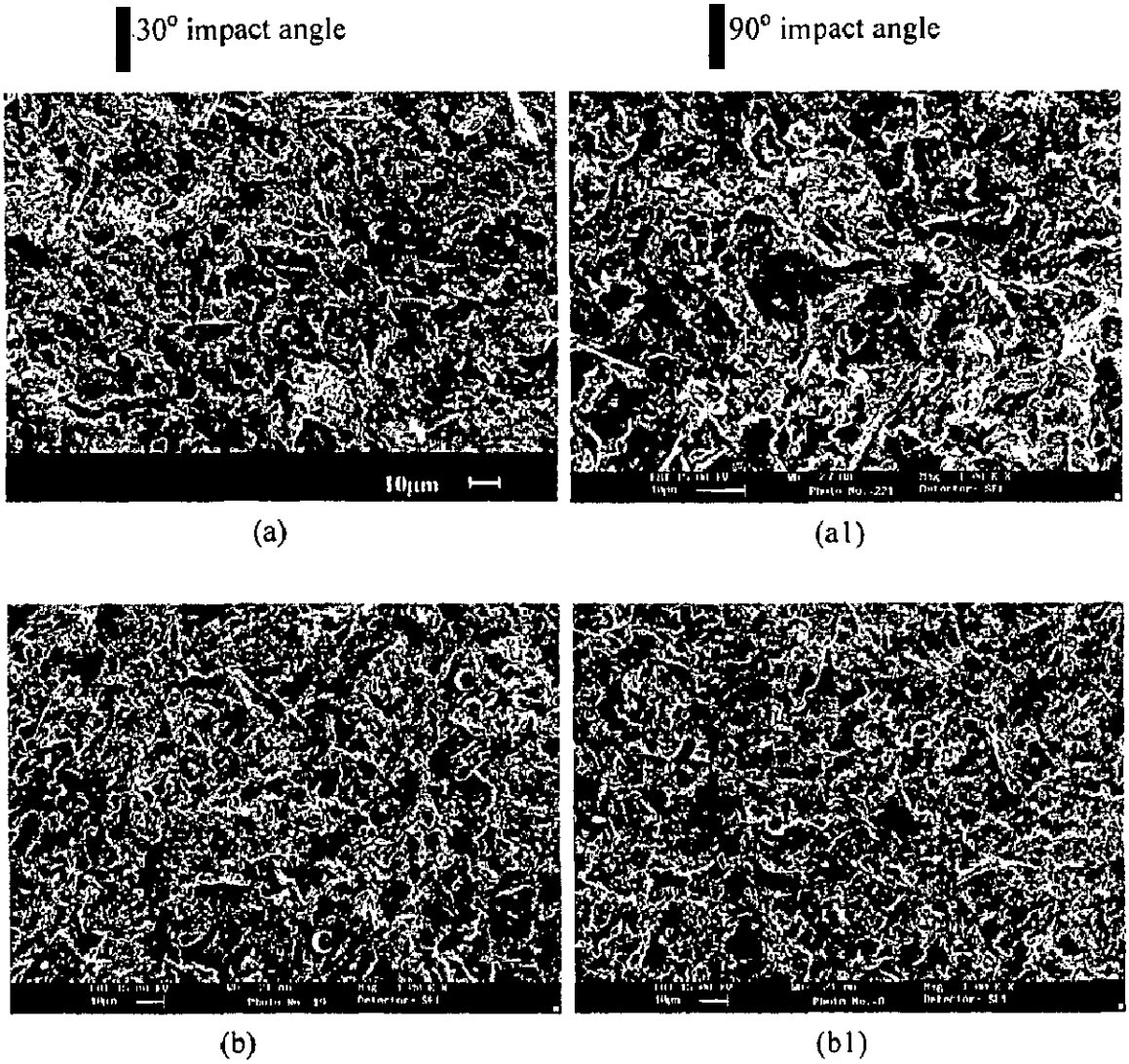

Fig. 5.29 Scanning electron micrographs of plasma sprayed Ni-20Cr coating on different superalloy substrates subjected to erosion at a velocity of 40 ms^{-1} at impact angle of 30° and 90°.

(a) and (a1) Superco 605; (b) and (b1) Superni 718.

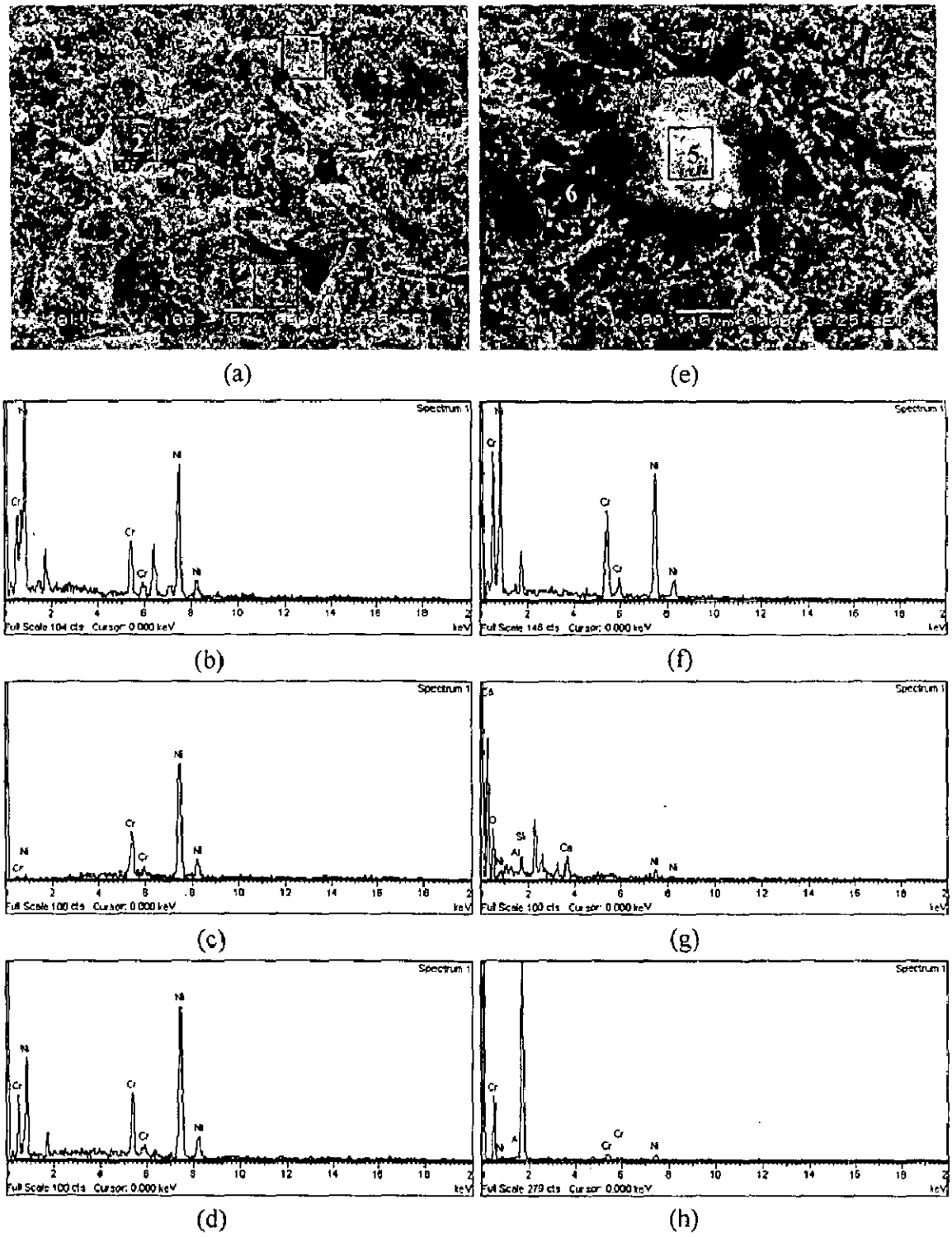

Fig. 5.30 Scanning electron micrographs with compositions of the Ni-20Cr coating on superalloy substrates eroded at 90° impact angle. (a) Superfer 800H and (e) Superco 605. (b), (c), (d), (f), (g) and (h) respectively are the compositions at positions 1, 2, 3, 4, 5 and 6 of the surface micrographs (a) and (e).

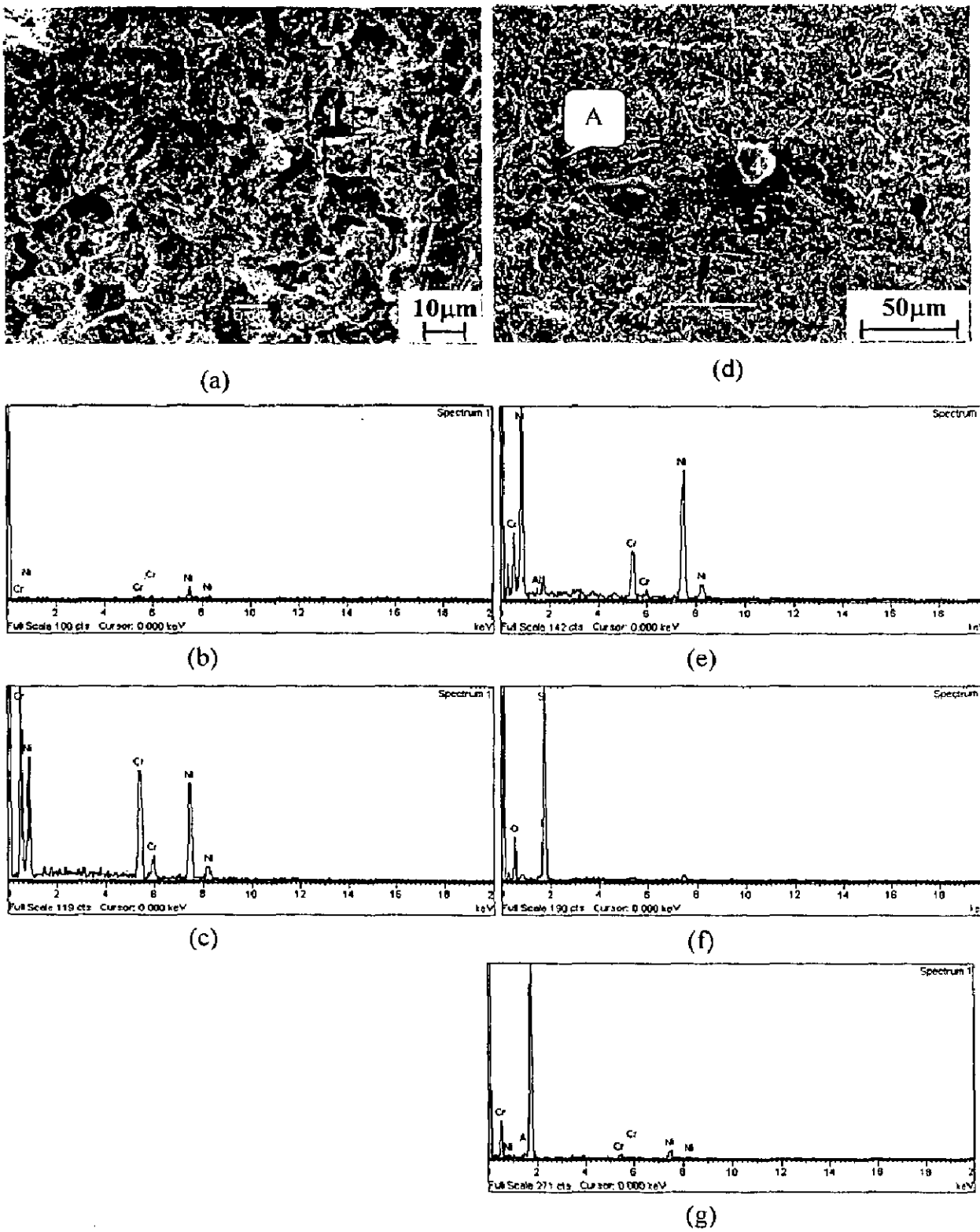

Fig. 5.31 Scanning electron micrographs with compositions of the eroded Ni-20Cr coating on Superni 718 superalloy substrate. (a) 30° impact angle and (d) 90° impact angle. (b), (c), (e) (f) and (g) respectively are the compositions at positions 1, 2, 3, 4 and 5 of the surface micrographs (a) and (d).

5.1.2.3.2 Cross-Sectional Analysis

The cross-sectional SEMs of the Ni-20Cr coating on Superni 600 superalloy substrate eroded at 30° and 90° impact angle have been depicted in Fig. 5.32. The micrographs of the coating eroded at 30° impact angle shown in Fig. 5.32 (a), (b) and (c) indicate some cavities and hillocks at several locations in the subsurface region as a result of sand particles impact. Surface hillock with cracks along its corners is clearly visible in Fig. 5.32 (b1) of the coating eroded at normal impact angle, which may get removed by subsequent impacts of the sand particles.

5.1.3.4 Surface Roughness

The surface roughnesses of the eroded plasma spray Ni-20Cr coated superalloys are reported in Table 5.1. The surface roughness of all the coated superalloys eroded at 30° impact angle was found to be in the range of 2.67-3.88 μm, whereas for normal impact angle the surface roughness lies in the range of 2.18-2.80 μm. The maximum value of average surface roughness was found to be 3.88 μm for coated Superni 600, whereas the minimum was 2.67 μm for coated Superni 75 at 30° impact angle. At 90° impact angle, the highest value of average surface roughness was 2.8 μm, obtained for coated Superni 718, whereas lowest was 2.18 μm for coated Superni 75. The 3D surface roughness optical profiles of the eroded plasma sprayed Ni-20Cr coating on different superalloys are shown in Figs. 5.33 and 5.34.

5.1.4 Ni_3Al Coating

5.1.4.1 Visual Examination

Surface macrographs of the plasma sprayed Ni_3Al coating on Superni 75, Superni 600, Superfer 800H, Superco 605 and Superni 718 superalloys eroded at 30° and 90° impact angle are shown in Fig. 5.35.

5.1.4.2 Erosion Rate

The erosion rate for the Ni_3Al coated superalloys eroded at an impact velocity of 40ms^{-1} and impingement angle of 30° has been compiled in Fig. 5.36. The plot (Fig. 5.36) reveals that the plasma sprayed Ni_3Al coating on Superni 75 superalloy eroded at 30° impact angle, has the lowest erosion rate amongst these samples, while the coating

gives the highest erosion rate on Superni 718 superalloy as substrate. Fig. 5.37 shows the erosion rate graphs of the plasma spray Ni_3Al coating on Superni 75, Superni 600, Superfer 800H, Superco 605 and Superni 718 superalloys eroded at an impingement angle of 90°. From the graph, it can be observed that the differences in erosion rate of Ni_3Al coated and uncoated superalloys are marginal.

A histogram illustrating the steady state erosion rate of the plasma spray coating on different substrate superalloys subjected to erosion is shown in Fig. 5.38. It can be clearly seen from the graph that the steady state erosion rate of coated Superni 600, Superco 605 and Superni 718 superalloys are marginally higher at 30° impact angle. Whereas the graph further reveals that steady state erosion rate for coated Superni 75 was greater at 90° impact angle and lower at 30° impact angle.

5.1.4.3 SEM/EDAX Analysis

5.1.4.3.1 Surface Morphology

Scanning electron micrographs for all the Ni_3Al coated superalloys eroded at 30° and 90° impact angle are shown in Fig. 5.39 and Fig. 5.40. Eroded surfaces from 30° impact angle indicate the microploughing and microcutting marks in general. The micrograph of the eroded surface of the plasma sprayed Ni_3Al coating on Superni 75 substrate at a 30° impact angle shows a triangular portion of a raised lip formed on the exit side of an impact crater can be seen from the lower left side of Fig. 5.39 (a). The craters and lips formed with plastic deformation can be seen from the SEM micrographs of the samples eroded at a 30° impact angle. Also cutting scar (CS) is visible in the micrograph (Fig. 5.39 c) of Ni_3Al coated Superni 75 at 30° impact angle.

Scanning electron micrographs (Figs. 5.39 and 5.40) for all the Ni_3Al coated superalloys eroded at 90° impact angle also show the lips (indicated as L) and craters (Indicated as C) formed by severe plastic deformation of the surfaces.

Figs. 5.41 and 5.42 reveal the broken pieces of sand particles embedded in the surfaces of the samples. EDAX analysis indicates the formation of Ni_3Al phase with the possibility of minor diffusion of chromium from the bond coat.

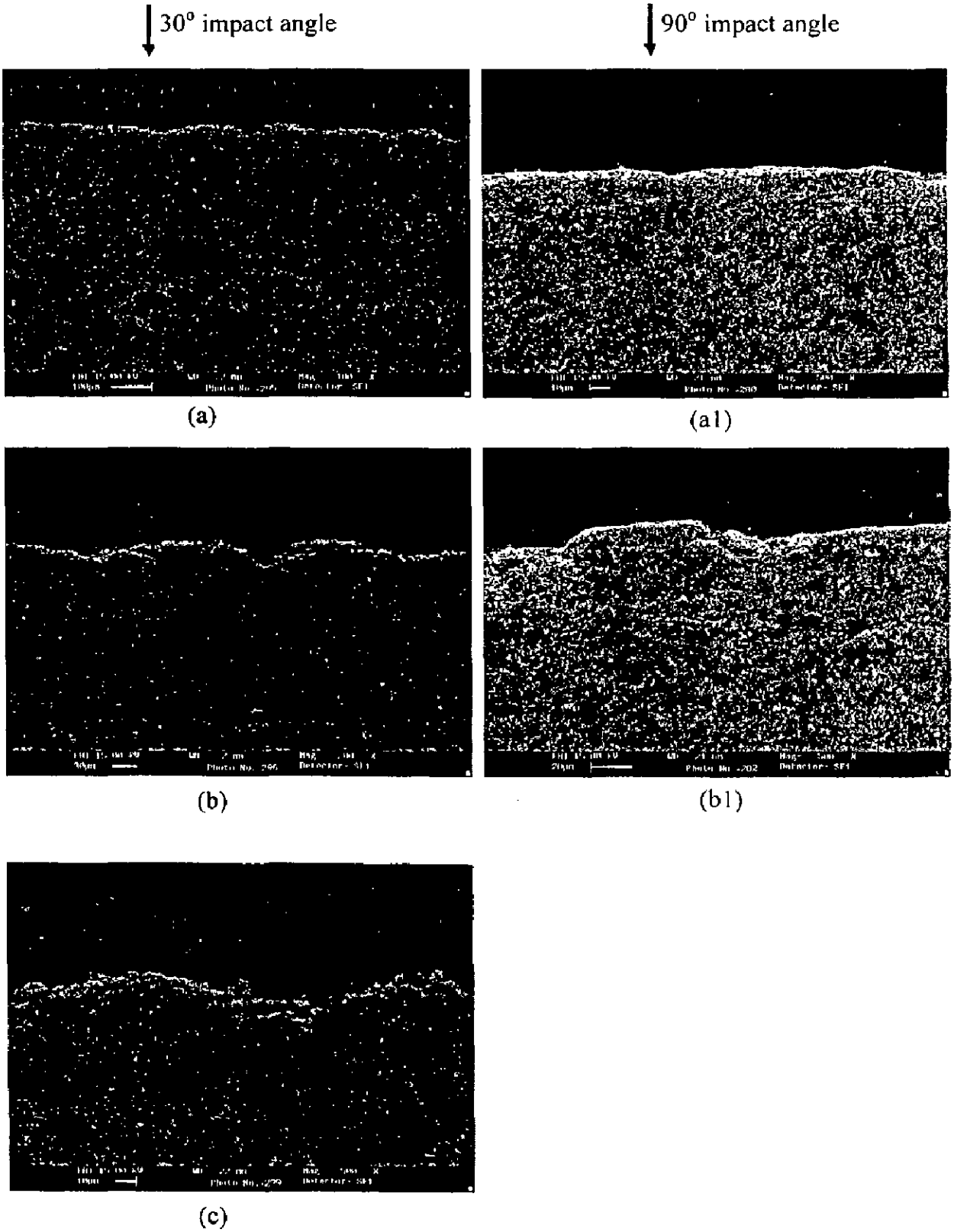

Fig. 5. 32 Scanning electron micrographs across the cross-section at different positions from the eroded area of Ni-20Cr coating on Superni 600 superalloy eroded at 30° and 90° impact angle.
(a), (b) and (c) at 30° impact angle; (a1) and (b1) at 90° impact angle.

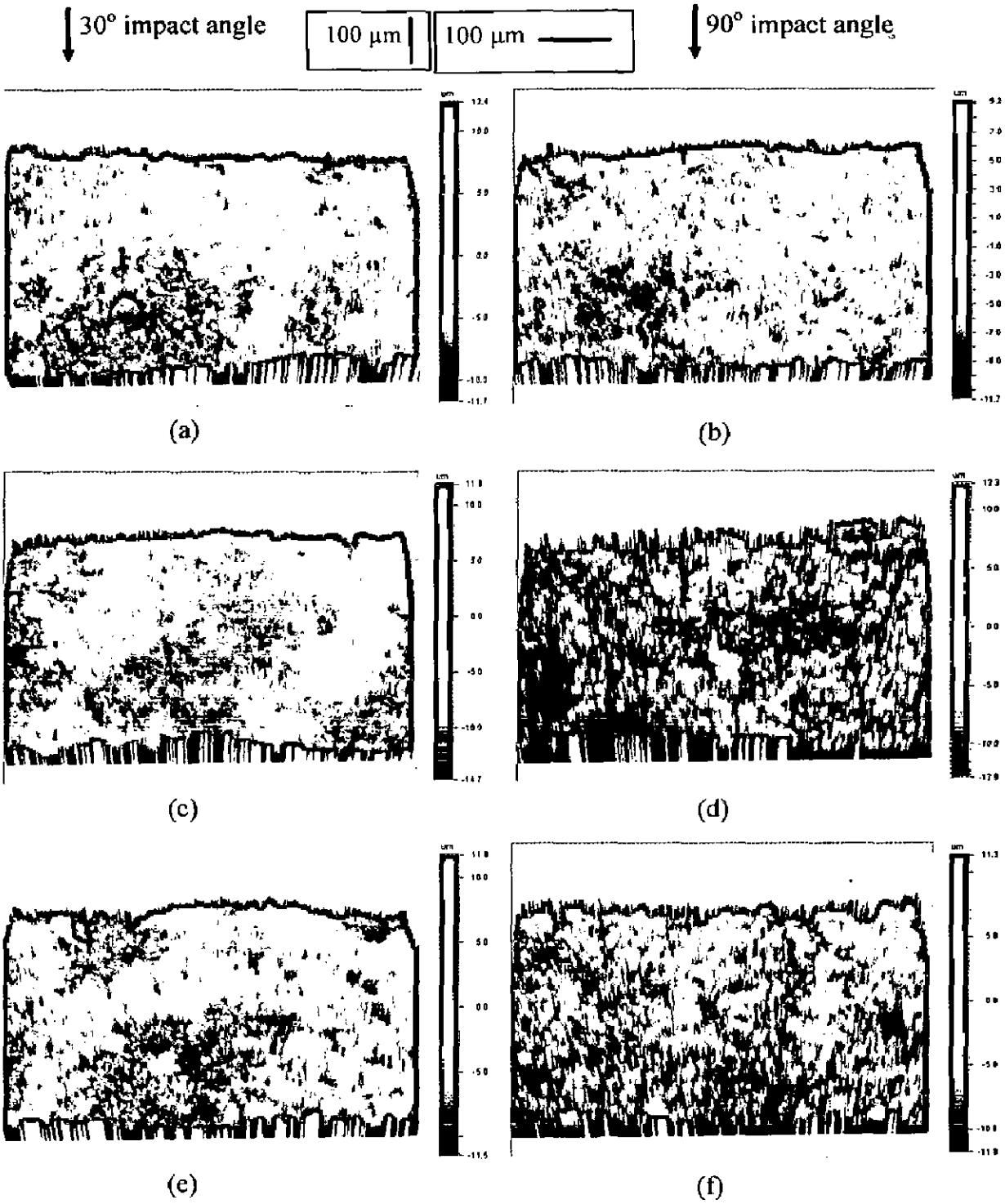

Fig. 5.33 3D optical profile of the eroded Ni-20Cr coated superalloys (a) & (b) *Superni 75*, (c) & (d) *Superni 600*, (e) & (f) *Superfer 800H*, respectively at 30° and 90° impact angle. Dimension of scanned area is 591 µm × 449 µm.

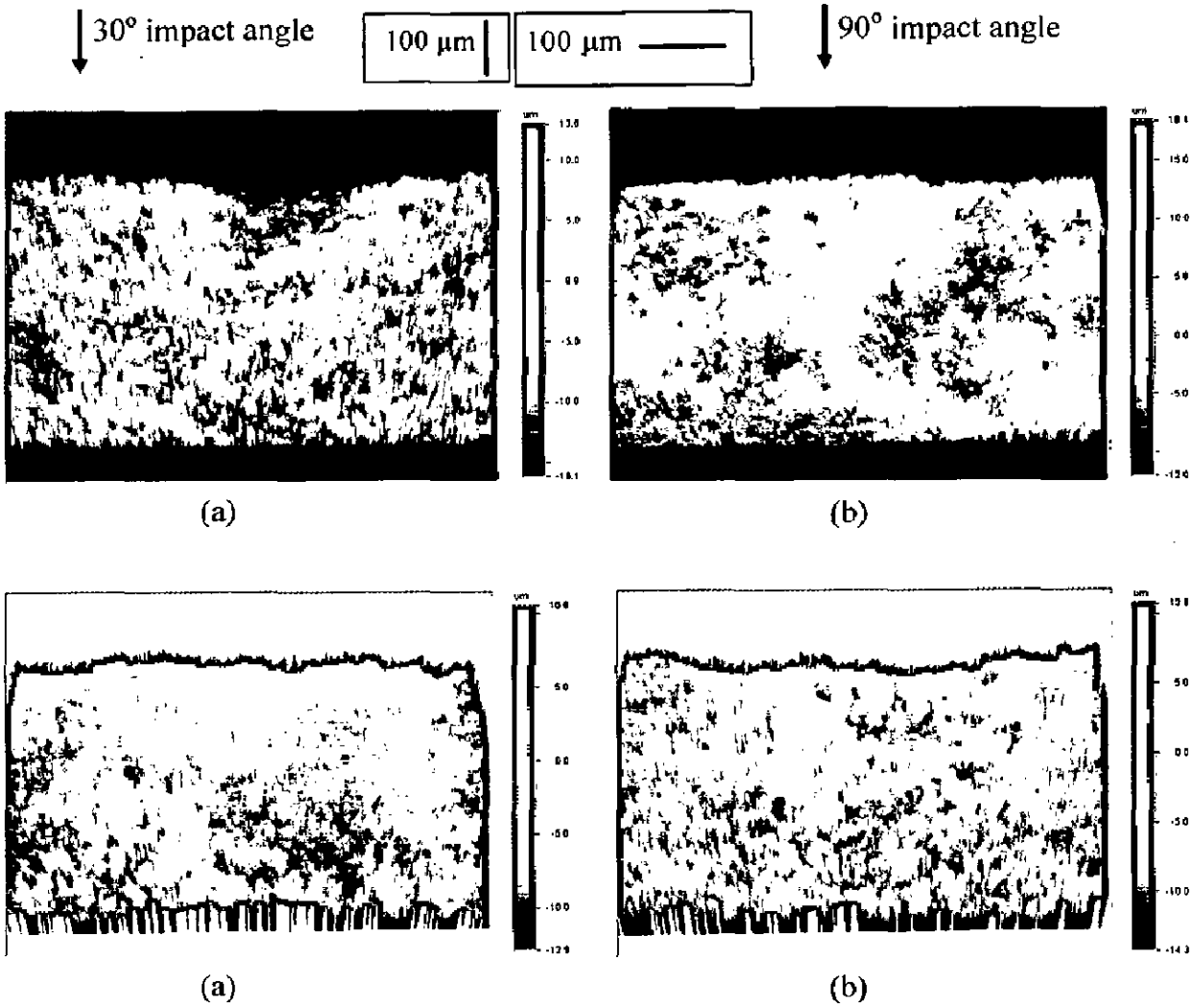

Fig. 5.34 3D optical profile of the eroded Ni-20Cr coated superalloys (a) & (b) Superco 605, (c) & (d) Superni 718, respectively at 30° and 90° impact angle. Dimension of scanned area is 591 µm × 449 µm.

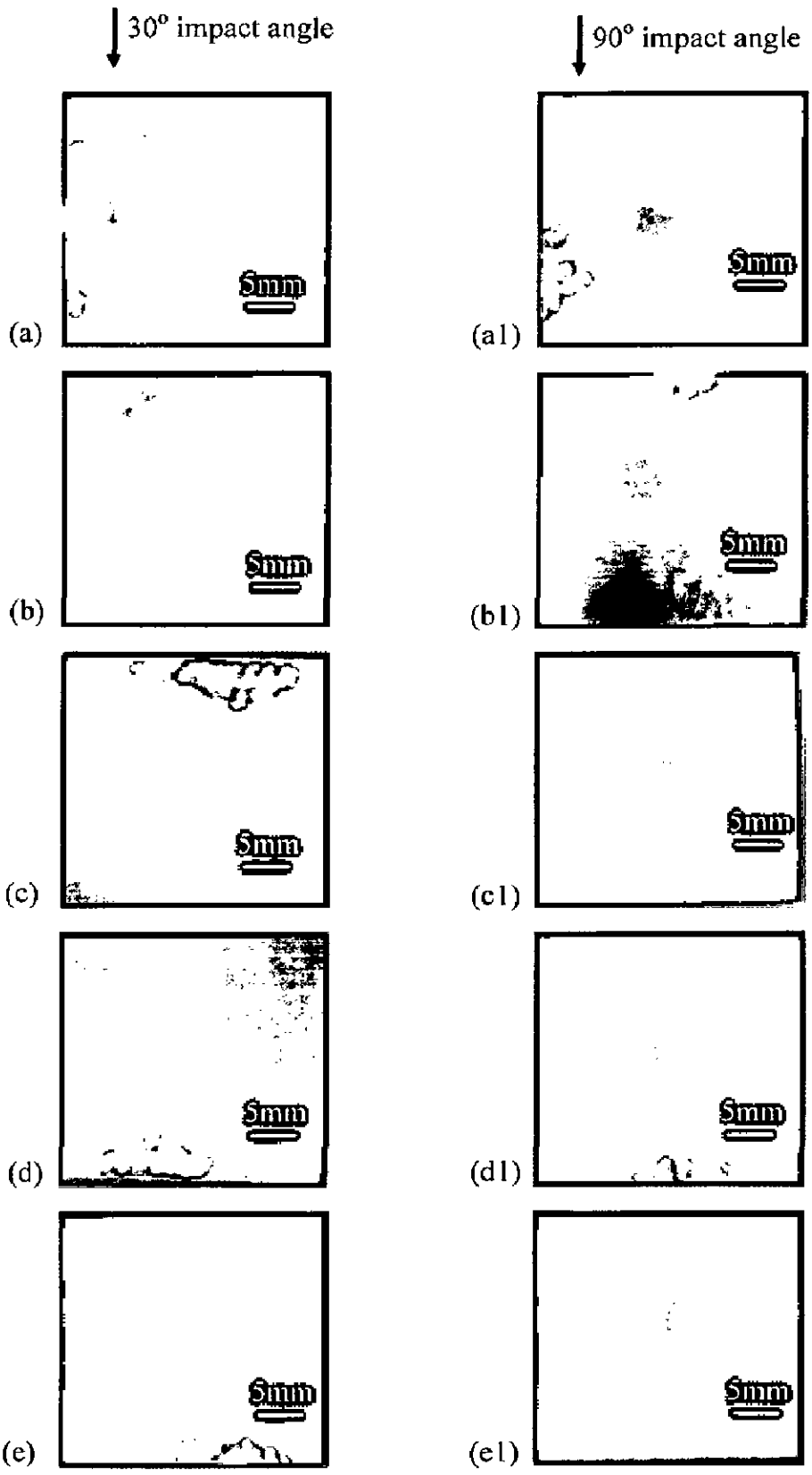

Fig. 5.35 Macrographs of plasma sprayed Ni_3Al coated superalloys eroded at a velocity of 40 ms^{-1} and impact angle of 30°.
(a) and (a1) Superni 75; (b) and (b1) Superni 600; (c) and (c1) Superfer 800H; (d) and (d1) Superco 605; (e) and (e1) Superni 718.

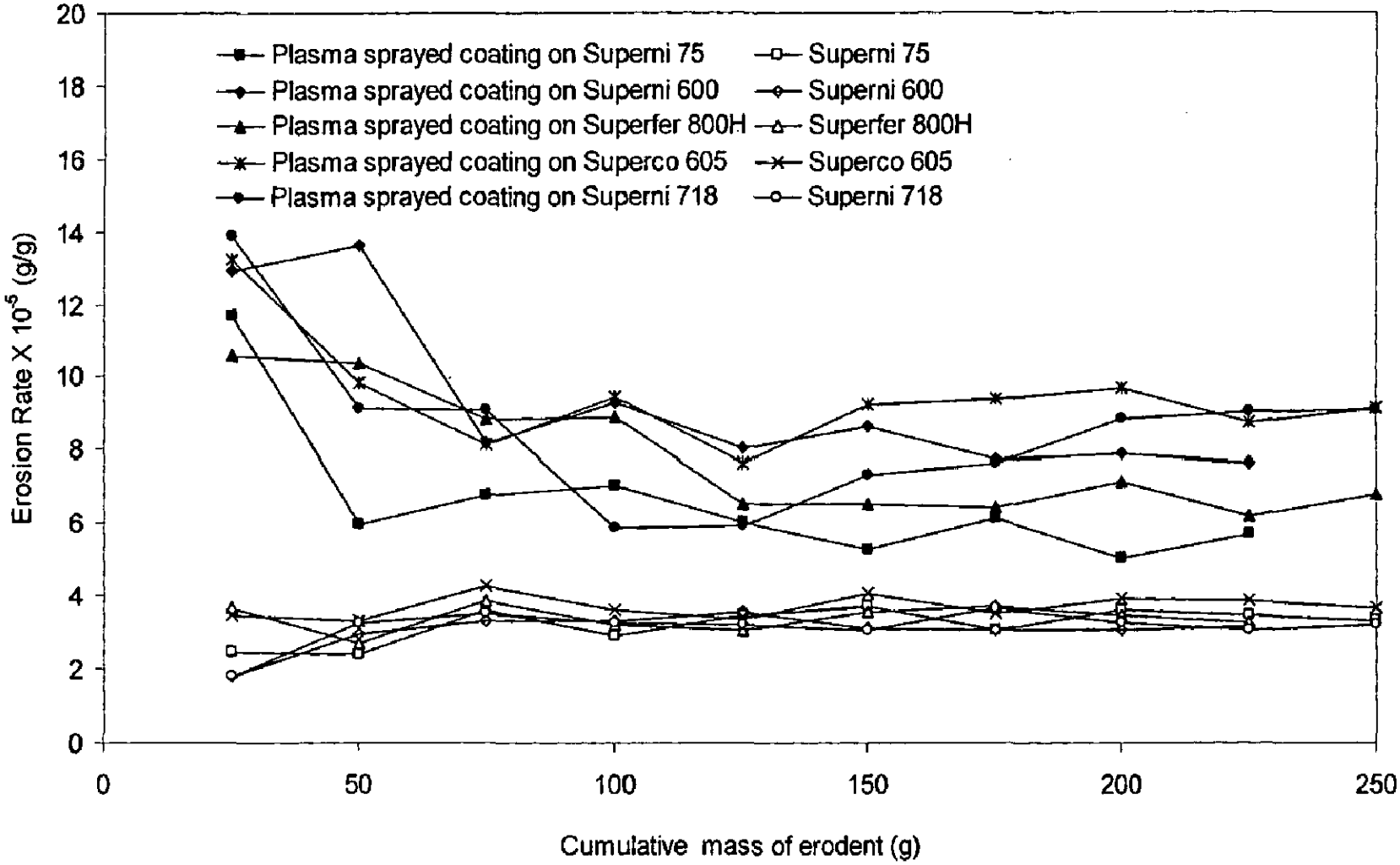

Fig. 5.36 Erosion rate (g/g) against cumulative mass of erodent for uncoated and plasma sprayed Ni_3Al coated superalloys at a velocity of $40ms^{-1}$ and 30^{o} impact angle.

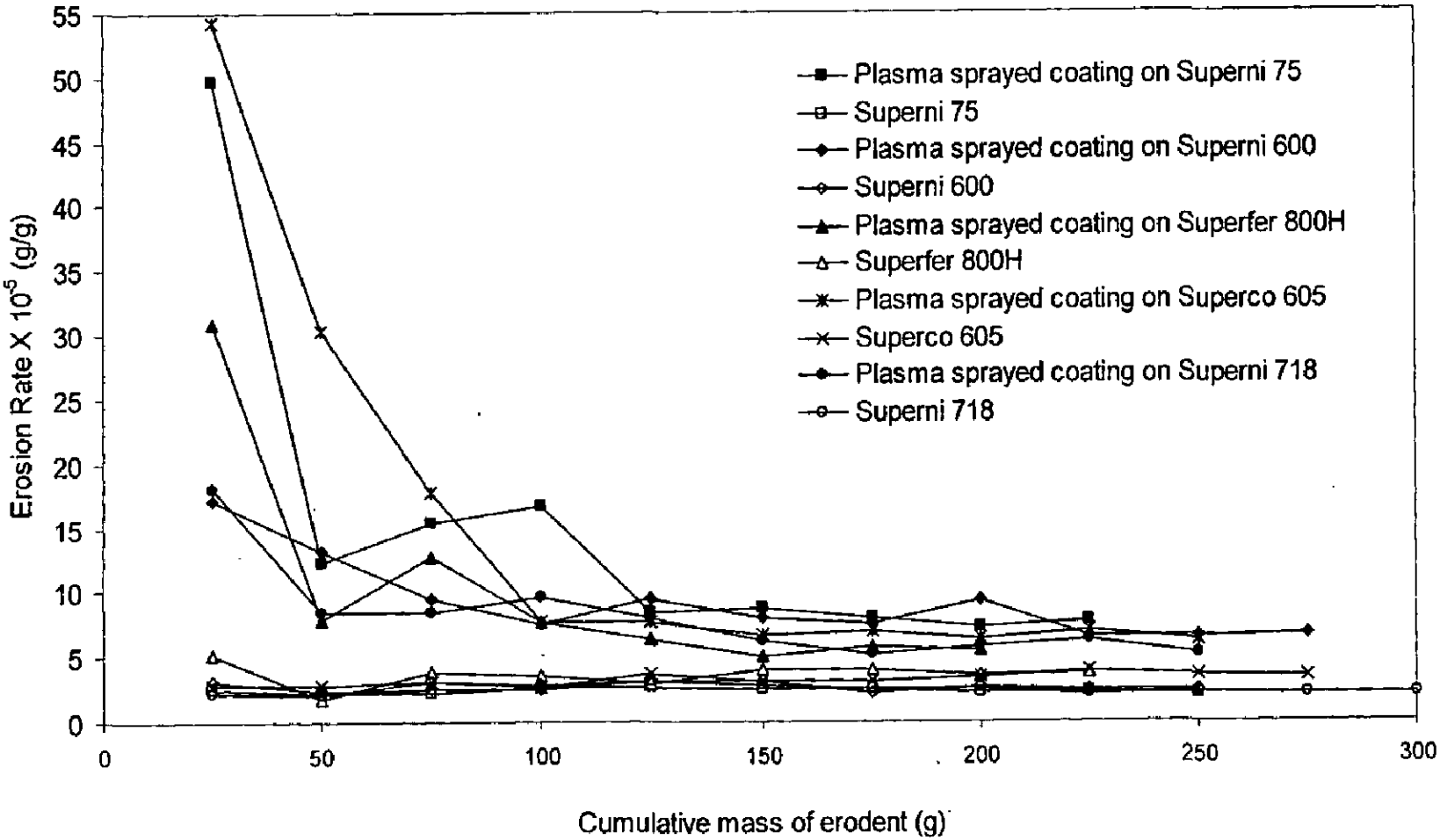

Fig. 5.37 Erosion rate (g/g) against cumulative mass of erodent for uncoated and plasma sprayed Ni_3Al coated superalloys eroded at a velocity of 40 ms^{-1} and 90° impact angle.

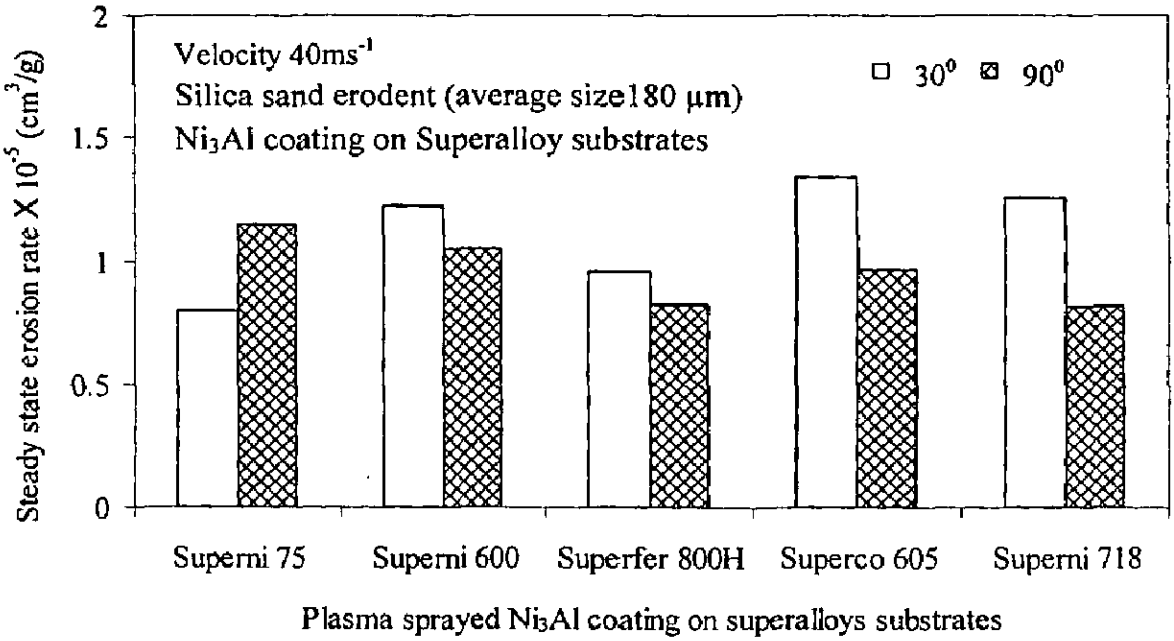

Fig. 5.38 A histogram illustrating the steady-state erosion rate of plasma sprayed Ni_3Al coating on different superalloy substrates subjected to erosion at a velocity of 40 ms^{-1} and impact angle of 30° and 90° using silica sand particles of average size 180 μm as erodent.

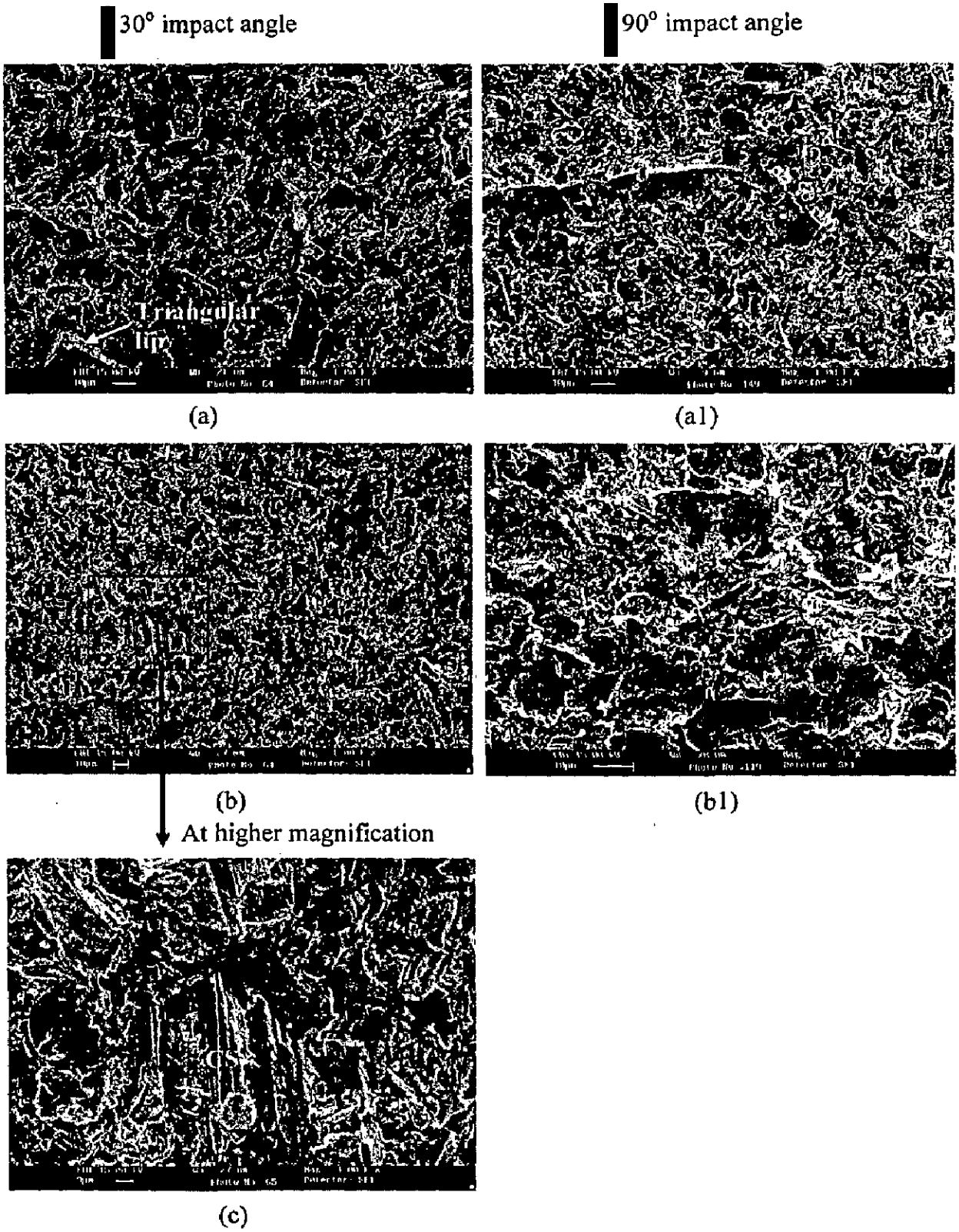

Fig. 5.39 Scanning electron micrographs of plasma spray Ni_3Al coated superalloys subjected to erosion at a velocity of 40 ms^{-1} at impact angle of 30° and 90°.
(a) and (a1) Superni 75; (b) and (b1) Superni 600;
(c) Superni 600 of 30° impact angle at higher magnification.

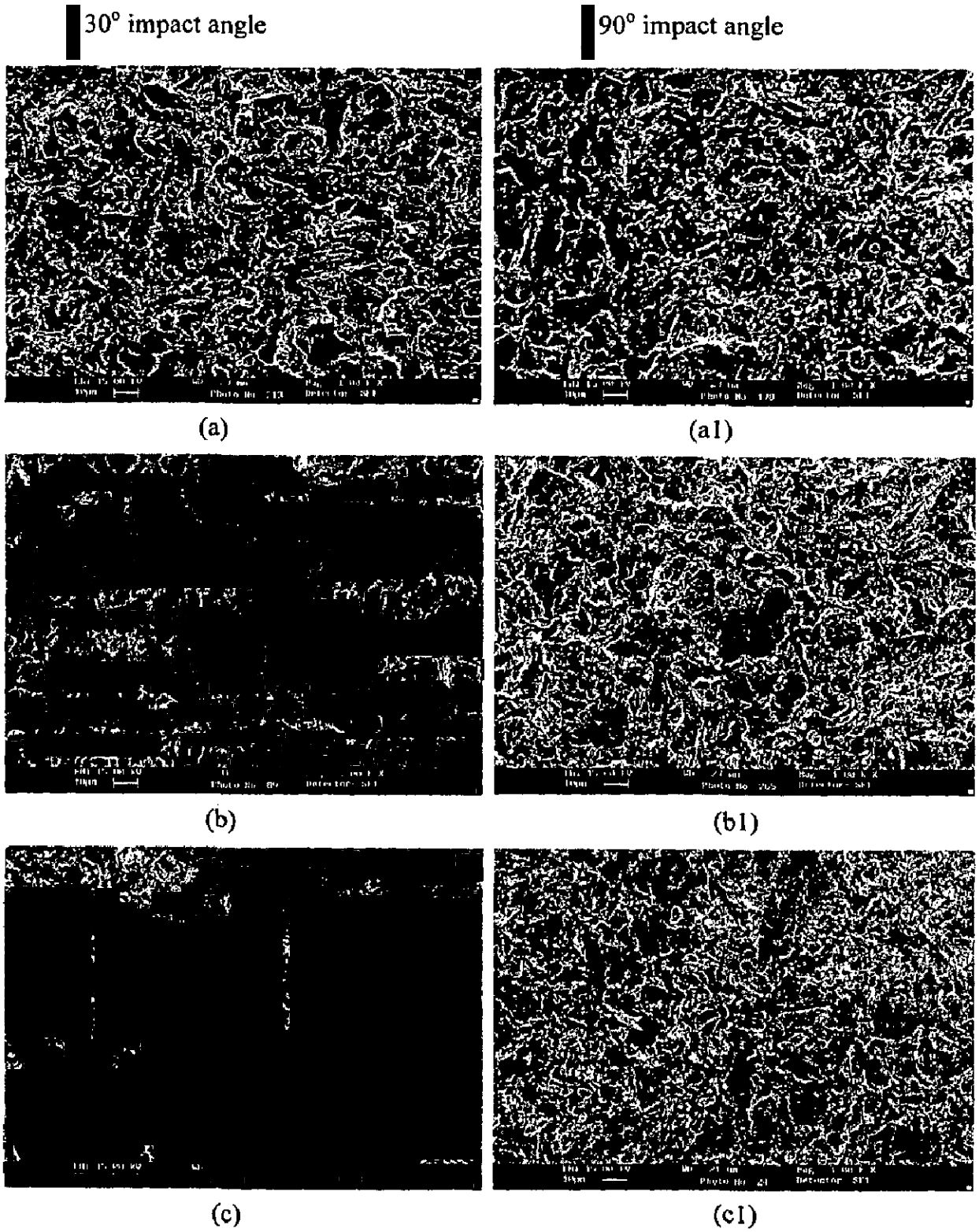

Fig. 5.40 Scanning electron micrographs of plasma spray Ni_3Al coated superalloys subjected to erosion at a velocity of 40 ms^{-1} at impact angle of 30° and 90°.
(a) and (a1) Superfer 800H; (b) and (b1) Superco 605;
(c) and (c1) Superni 718.

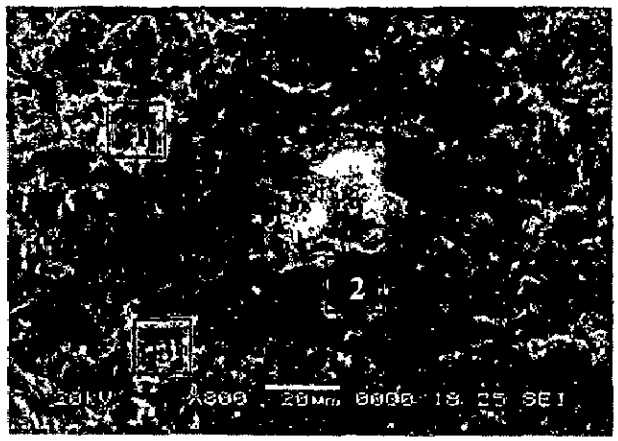

(a)

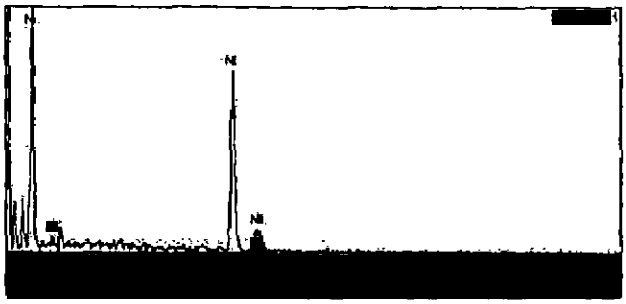

(b)

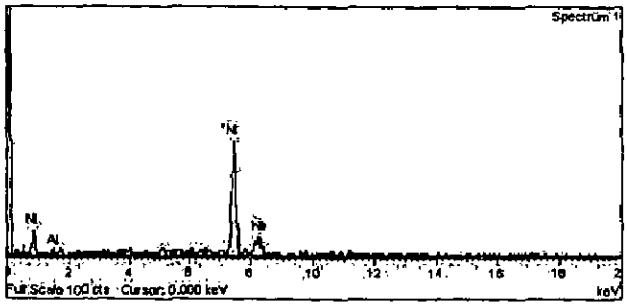

(c)

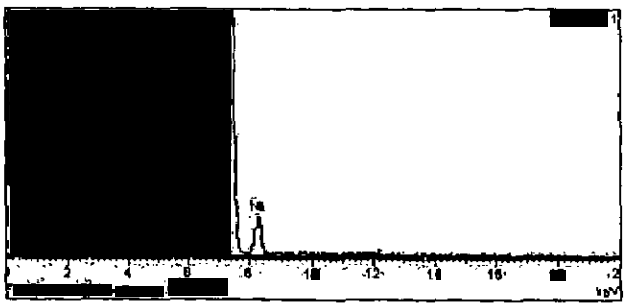

(d)

Fig. 5.41 Scanning electron micrographs with compositions of the Ni_3Al coating on Superco 605 superalloy substrate eroded at 90° impact angle. (a) Superco 605. (b), (c) and (d) respectively are the compositions at positions 1, 2 and 3 of the surface micrographs (a).

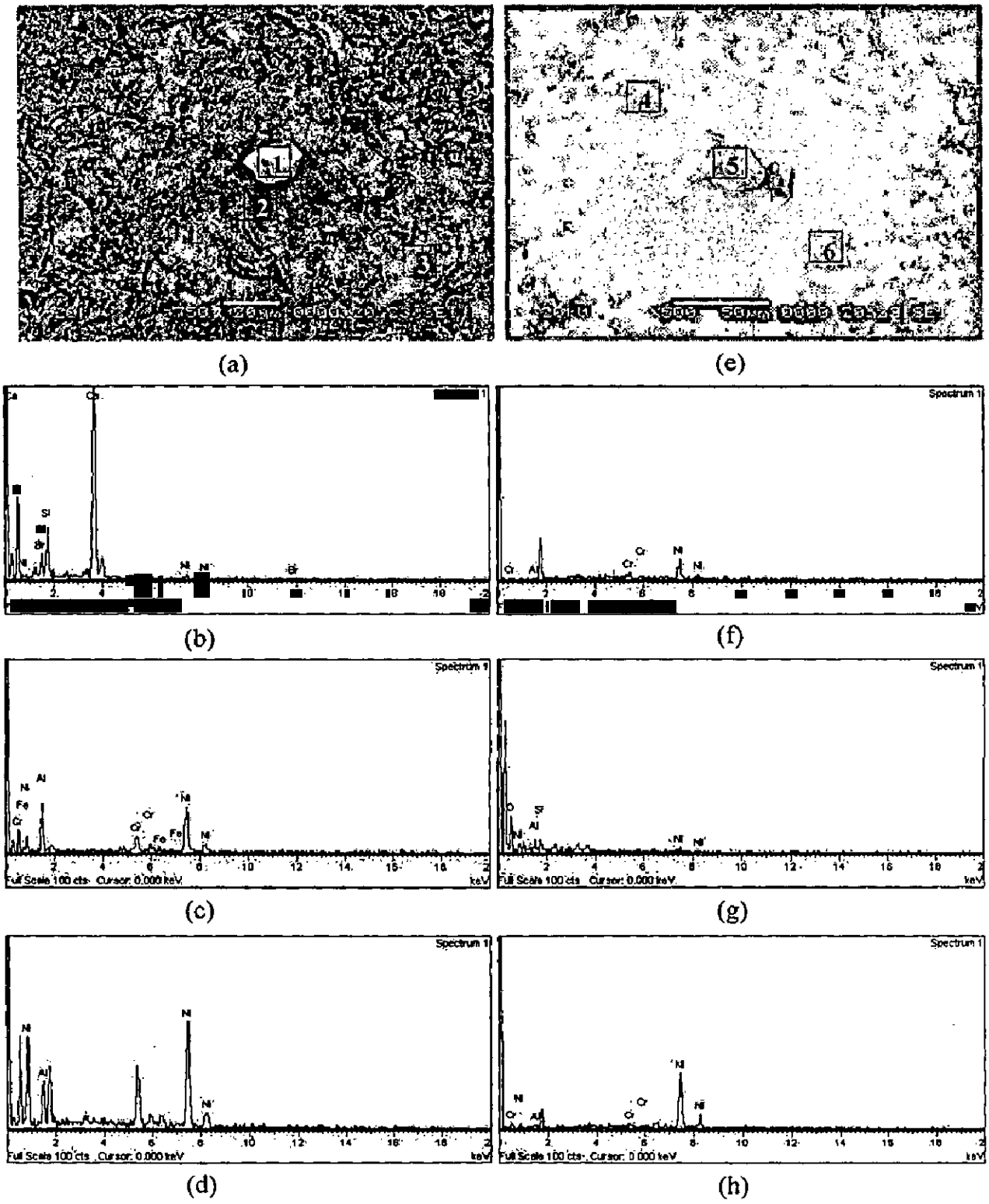

Fig. 5.42 Scanning electron micrographs with compositions of the eroded Ni_3Al coating on Superni 718 superalloy substrate. (a) 30° impact angle and (e) 90° impact angle. (b), (c), (d), (f), (g) and (h) respectively are the compositions at positions 1, 2, 3, 4, 5 and 6 of the surface micrographs (a) and (e).

5.1.4.3.2 Cross-Sectional Analysis

The cross-sectional SEMs of the Ni_3Al coating on Superni 600 superalloy substrate eroded at 30° and 90° impact angle have been depicted in Fig. 5.43. The micrograph of the coating eroded at 30° impact angle show a bigger hillock on right side of Fig. 5.43 (a) along with some smaller hillocks at several locations. The cross-sectional SEM micrograph of the coating eroded at normal impact angle indicate plastically deformed platelets on top surface as shown in Fig. 5.43 (b) which may get removed by subsequent impacts of the sand particles.

5.1.4.4 Surface Roughness

The surface roughnesses of the eroded plasma spray Ni_3Al coated superalloys are reported in Table 5.1. The surface roughness of all the coated superalloys eroded at 30° impact angle was found to be in the range of 2.88-4.5 μm, whereas for normal impact angle the surface roughness lies in the range of 2.78-4.19 μm. The maximum value of average surface roughness was found to be 4.5 μm for coated Superni 718, whereas the minimum was 2.88 μm for Superni 600 at 30° impact angle. At 90° impact angle, the highest value of average surface roughness was 4.19 μm, obtained for coated Superni 718, whereas lowest was 2.78 μm for Superni 600. The 3D surface roughness optical profiles of the eroded plasma sprayed Ni_3Al coating on different superalloys are shown in Figs. 5.44 and 5.45.

5.2 SUMMARY OF RESULTS

The results of erosion studies in air for coated and uncoated superalloys are summarised in Table 5.1 to understand the comparative behaviour of different coatings.

Table 5.1 Summary of the results for coated and uncoated superalloys eroded at a velocity of 40 ms^{-1} at impingement angle of 30° using silica sand (150-250 μm size, Knoop Hardness of 880) as erodent.

Base superalloy	Coating	Microhardness (HV)	Steady state erosion rate × 10^{-3} (mm^3g^{-1})		Average surface Roughness, μm		Remarks
			30° impact angle	90° impact angle	30° impact angle	90° impact angle	
Superni 75	Uncoated	324	3.995	2.7523	1.53	1.33	Erosion by cutting and ploughing with lip fracture 30° impact angle, whereas platelets with craters are visible at normal impact angle
Superni 600	Uncoated	260	3.713	2.986	1.45	1.45	Removal of material by cutting and ploughing at 30° impact angle, whereas platelets with plastic deformation are dominant at normal impact angle
Superfer 800 H	Uncoated	320	4.396	4.912	1.34	1.62	Lips and craters formed by ploughing are visible in the micrographs 30° impact angle, whereas platelets formed with plastic deformation can be seen at normal impact angle
Superco 605	Uncoated	512	4.121	3.989	1.28	1.28	Microcutting scar along with raised lips and craters are visible on highly plastic deformed surface at 30° impact angle, whereas platelets formed can be seen at normal impact angle, also series of slip band is visible

Superni 718	Uncoated	478	4.048	2.588	1.45	1.34	Cutting and ploughing were dominant at oblique impact angle, while platelets with craters visible in the micrograph at 90° impact angle.
Superni 75	NiCrAlY	510	13.308	17.33	3.24	3.07	cutting scar along with lips and craters are visible from micrograph of 30° impact angle, whereas platelets and craters formed can be seen at normal impact angle
Superni 600	NiCrAlY	350	12.169	14.948	2.91	2.69	Material removal by lips formation and plastic deformation at 30° impact angle, whereas erosion by platelets formation was dominant at normal impact angle
Superfer 800 H	NiCrAlY	452	12.573	10.382	2.78	2.2	plastically deformed surface with craters and lips are visible at 30° impact angle, whereas platelets formed by plastic deformation can be seen at normal impact angle
Superco 605	NiCrAlY	470	9.088	13.794	2.31	3.16	Lips and craters formed by ploughing are visible at oblique impact angle, while micrograph at 90° impact angle reveals plastic deformation, also a broken piece of sand particle embedded in the surface can be seen
Superni 718	NiCrAlY	468	16.544	14.853	2.57	2.34	Lips formed are visible at oblique impact angle, while platelets and craters are visible in the micrograph at 90° impact angle

Superni 75	Ni-20Cr	456	13.22	15.232	2.67	2.18	Erosion by cutting and ploughing at 30° impact angle, whereas erosion by platelets are revealed at normal impact angle
Superni 600	Ni-20Cr	284	12.743	15.007	3.88	2.72	Erosion by ploughing at 30° impact angle, also unmelted particle is visible, whereas for 90° impact angle, micrographs show the highly plastic deformed surface with platelets and lips or ridges
Superfer 800 H	Ni-20Cr	686	15.592	26.266	3.13	2.4	Micrograph at oblique impact angle reveals the ploughing with lips and craters, whereas at 90° impact angle erosion take place by plastic deformation and lip fracture
Superco 605	Ni-20Cr	490	13.425	18.350	3.64	2.51	Erosion by ploughing at 30° impact angle, whereas platelets and craters are visible at normal impact angle
Superni 718	Ni-20Cr	475	20.202	14.212	3.04	2.8	Lips formed are visible at oblique impact angle, while platelets and craters are visible in the micrograph at 90° impact angle, also distortion of the splat boundaries forming grooves in the surface can be seen
Superni 75	Ni_3Al	267	7.959	11.418	3.69	3.99	Ploughing was dominant, triangular portion of raised lip and cuttings scars are visible, at 30° impact angle, whereas platelet erosion was dominant at normal impact angle

Superni 600	Ni_3Al	279	12.228	10.463	2.88	2.78	Micrograph at oblique impact angle reveals the microploughing and microcutting were dominant, whereas at 90° impact angle platelet erosion was dominant
Superfer 800 H	Ni_3Al	173	9.580	8.176	3.43	2.84	the ploughing with lips formed are visible at oblique impact angle, whereas micrograph reveals that at 90° impact angle erosion take place by platelet mechanism
Superco 605	Ni_3Al	240	13.343	9.609	3.08	4.13	Micrograph at oblique impact angle reveals the plastic deformation with lips and craters, whereas the platelets, lips and craters formed on the eroded surface are visible at 90° impact angle
Superni 718	Ni_3Al	276	12.503	8.104	4.5	4.19	lips formed by ploughing of the coating are visible and vulnerable to remove by subsequent particle impacts for oblique impact angle

5.3 DISCUSSION

In all the samples, the erosion starts at the centre first, and then proceeds towards the edges of the samples. At a 30° impact angle, material is eroded creating an elliptical shape depression; while at a 90° impact angle, material is eroded forming a circular depression. The macrographs of eroded samples clearly reveal three zones; a central area from where most of the eroded material has been produced, a second zone of faint color where somewhat lesser erosion can be seen and a third outside region where a negligible amount of erosion is observed. The erosion scar produced, in general, on all the surfaces of the tested samples at both the impact angles have been schematically illustrated in Fig. 5.46.

All the uncoated and coated superalloys have shown relatively higher erosion rate in the early cycles of study, followed by steady state erosion rate with increase in number of cycles. The variation in erosion rate was more during the incubation period (up to 4-5 cycles) and thereafter, because of smooth surface, variation reduces. Also sand particles are embedded in the material during erosion, and results in the variation of the erosion rate (increases when embedded and decreases when removed) of the coating. This can be well seen from the graphs (Figs. 5.2, 5.3, 5.14, 5.15, 5.25, 5.26, 5.36 and 5.37) of erosion rate against cumulative mass of erodent. Tabakoff (1999) and Davis et al (1986) also observed the similar behaviour for the Inconel 718 superalloy and plasma sprayed ceramic thermal barrier coatings, respectively.

It has been observed that all the plasma sprayed coated superalloys, in general, gave higher erosion rate than that of uncoated superalloys. Also the average surface roughness of all the coated superalloys was found higher than that of bare superalloys. Further, all the coatings have maintained adherence with all the superalloy substrates under study during the erosion tests, and can be seen from the respective SEMs.

5.3.1 Uncoated Superalloys

In general, the superalloys under study that is Superni 75, 600, 718, Superfer 800H and Superco 605 have shown good erosion resistance. All the superalloys have given very low erosion rates and lie in a narrow range of 2.588-4.912 $\times 10^{-3}$ mm^3/g. The generalized behaviour of the superalloys was ductile in nature as observed from their scanning electron micrographs. Based on the present data the erosion rates for 30° impact angle can be arranged in following order:

Superfer 800H > Superco 605> Superni 718 > Superni 75 > Superni 600

This suggests that the relative erosion resistance of Superfer 800H at oblique impact angle is least among the superalloys under study, while Superni 600 has shown maximum erosion resistance. The difference in erosion rate is very marginal, only 1.2 times higher for the Superfer 800H than that for Superni 600. However this order is in relative terms, otherwise the erosion rates for different superalloys do not vary much at 30° impact angle.

The sequence of superalloys based on the data for erosion rate at normal impact angle is:

Superfer 800H > Superco 605 > Superni 600 > Superni 75 > Superni 718

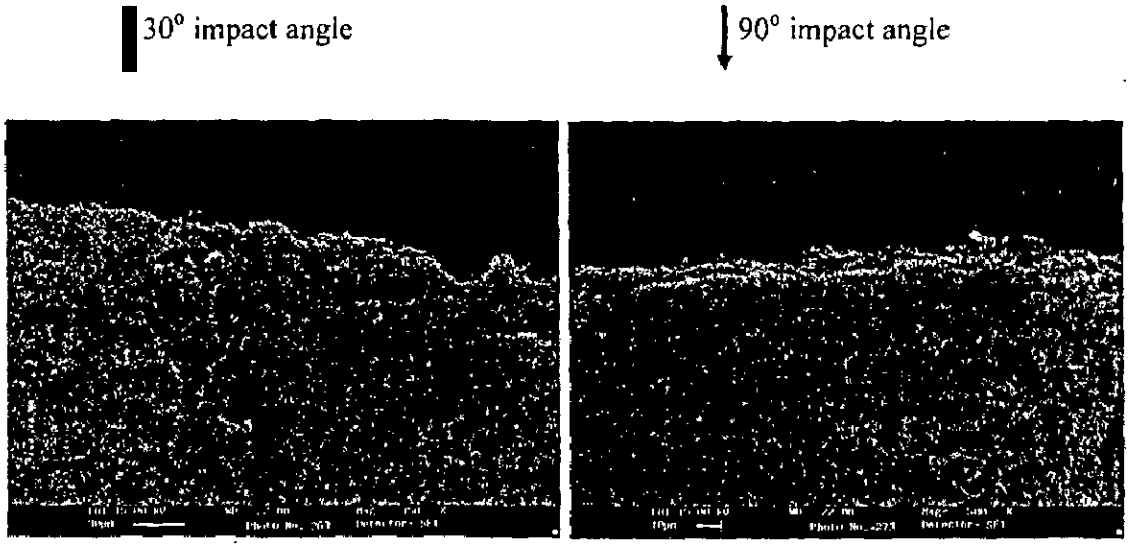

Fig. 5. 43 Scanning electron micrographs across the cross-section at different positions from the eroded region of Ni_3Al coating on Superni 600 superalloy eroded at 30° and 90° impact angle.
(a) at 30° impact angle (b) at 90° impact angle.

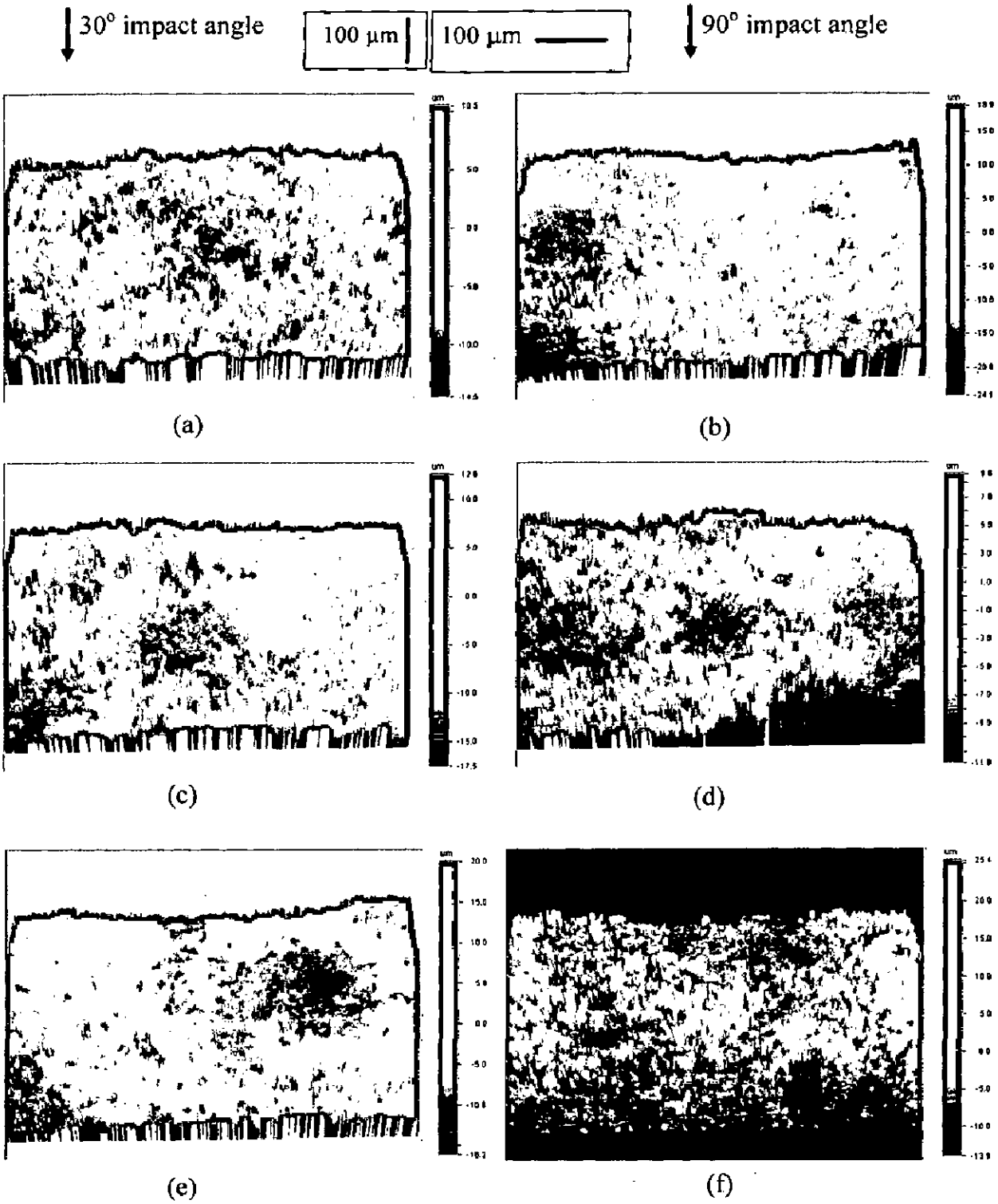

Fig. 5.44 3D optical profile of the eroded Ni_3Al coated superalloys (a) & (b) Superni 75; (c) & (d) Superni 600; (e) & (f) Superfer 800H; respectively at 30° and 90° impact angles. Dimension of scanned area is 591 µm × 449 µm.

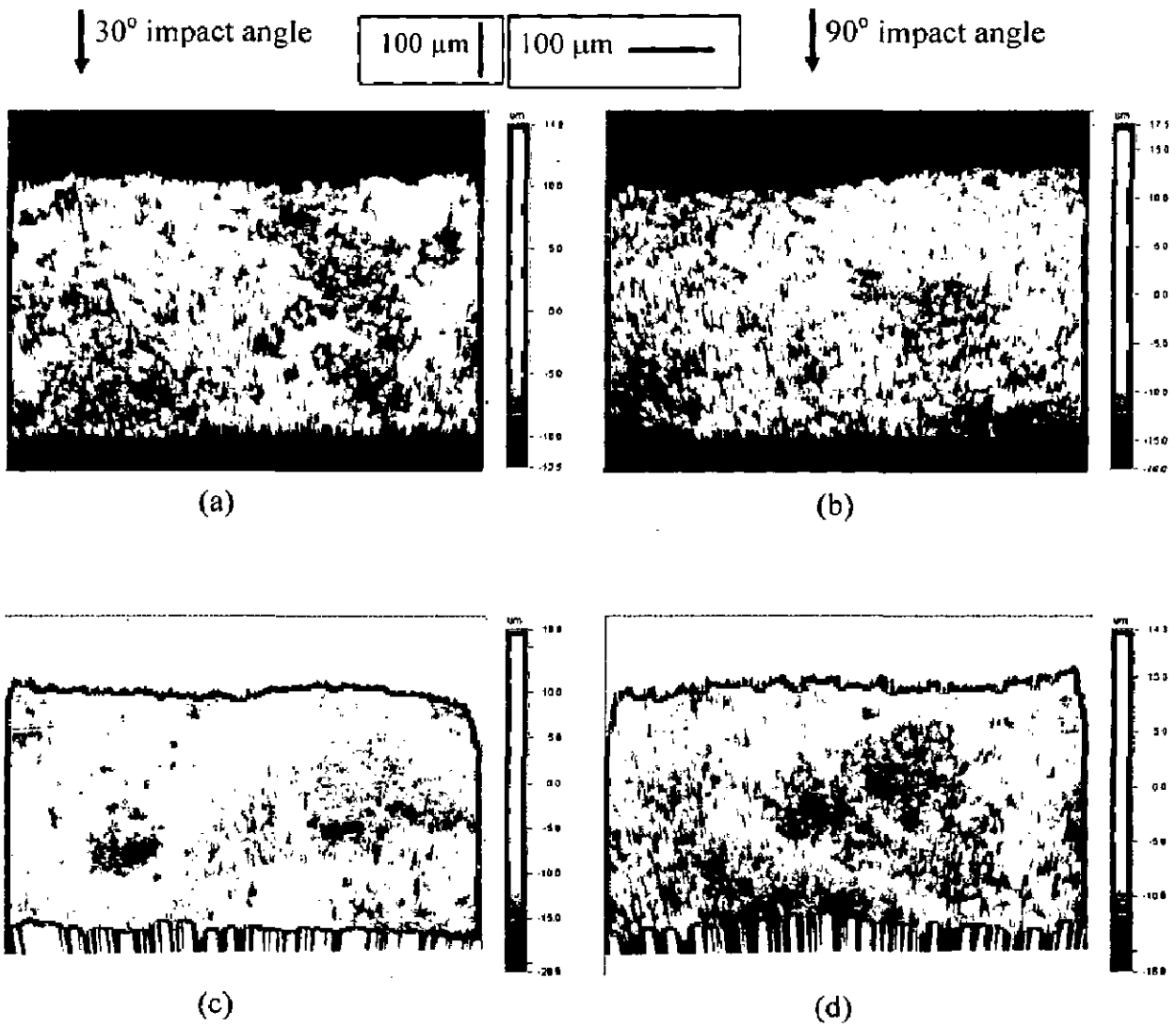

Fig. 5.45 3D optical profile of the eroded Ni_3Al coated superalloys (a) & (b) Superco 605, (c) & (d) Superni 718, respectively at 30° and 90° impact angle. Dimension of scanned area is 591 μm × 449 μm.

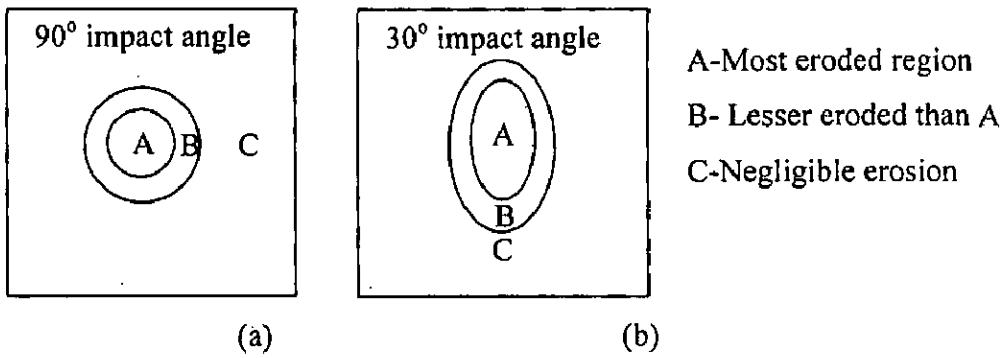

Fig. 5.46 A schematic diagram showing the erosion scar produced, in general, on all the materials tested at 90° and 30° impact angle.

From this sequence, it can be inferred that the relative erosion resistance of Superfer 800H is minimum among the superalloys under study, while Superni 718 has shown maximum erosion resistance at normal impact angle. The erosion rate for the Superfer 800H is about twice than that for Superni 718.

From the erosion rate data of the present study (Fig. 5.4), it is perceived that the steady state erosion rates of Superni 75, 600, 718 and Superco 605 were greatest at 30° impact angle, which is the characteristic erosion behaviour of ductile material. Whereas the steady state erosion rate of Superfer 800H was maximum at 90° impact angle, showing the brittle behaviour of the material. However the differences in erosion rates were marginal in case of Superfer 800H and Superco 605 and lie in a very narrow range. Thus it can be inferred that these two superalloys have shown almost similar erosion rates at both the impact angles.

Similar observations for the erosion rates of the superalloys have been reported by Ninham (1988). He found that the erosion response of high-strength materials, particularly when eroded by quartz, is weakly dependent upon impact angle. Further Tabakoff (1995) also reported the similar behaviour for cobalt-based alloy X-40. He reported the ductile erosion behaviour of the cobalt-based alloy with maximum erosion at 45° impact angle.

From the scanning electron micrographs of all the eroded superalloys at 30° impact angle, it can be inferred that the cutting and ploughing play the dominant role in erosion of materials. Cutting scars are visible in most of the SEM of the eroded superalloys at 30° impact angle, thus indicating the cutting mechanism of material removal. Also lips formed by ploughing of the superalloys by erodent particles are revealed from the micrographs. Form this it can be suggested that the material removal by erosion is complex in case of superalloys at oblique impact angle, with a combination of cutting and ploughing mechanisms.

At normal impact angle, the erosion occurred by the platelet mechanism in all the superalloys in general, similar to that described by Hutchings and Levy (1989). They reported that in the steady state condition, the three phases occur simultaneously at different locations over the surface. In the initial phase the impacting particle forms a crater, and material is extruded or displaced from the crater to form a raised lip or mound. In the second phase the displaced metal is deformed by subsequent impacts; this may lead to lateral displacement of the material, and can be accompanied by some ductile fracture in heavily strained regions. Finally, after a relatively few impacts, the

displaced material becomes so severely strained that it is detached from the surface by ductile fracture.

Fig. 5.6 (a) and (b) clearly show the craters (C) and lips (L) formed by the impact of erodent particles on the surface of Superco 605 superalloy. The general erosion mechanism is thus similar to one defined by Hutchings and Winter (1974) in which material is raised above the mean surface, followed by deformation during subsequent impacts and ultimate removal of the deformed material. Fig. 5.8 (e) also shows a series of slip bands along one side. Bellman and Levy (1981) have suggested that these bands generally occur along the walls of already formed craters where a fresh crater has been formed immediately adjacent to them. The particle impact forces that cause plastic deformation of the new crater act on the unsupported surface of already existing crater, resulting in slip band formation. The distance of these bands down the inclined surface of the existing crater is indicative of the depth of the new crater which formed them. This important observation was used by them in developing the suggested erosion mechanism. The schematic diagrams Figs. 5.47 and 5.48 have been suggested to explain the erosion phenomena at a 30° and 90° impact angle, which can be taken as representative case for all the superalloys under study.

5.3.2 NiCrAlY Coating

Based on the weight loss data, the erosion rates of the NiCrAlY coated superalloys for 30° impact angle can be arranged in following order:

Superni 718 > Superni 75 > Superni 600 > Superfer 800H > Superco 605

Thus it can be inferred that the relative erosion resistance of coated Superco 605 at oblique impact angle is maximum among these coated superalloys under study, while the one with Superni 718 as substrate has shown minimum erosion resistance.

The sequence of coated superalloys based on the data for erosion rate at normal impact angle is:

Superni 75 >Superni 600 > Superni 718 > Superco 605 > Superfer 800H

From this sequence, it can be perceived that the relative erosion resistance of coated Superfer 800H is greatest among the NiCrAlY coated superalloys under study, while coated Superni 75 has shown minimum erosion resistance at normal impact angle. The erosion rate for the coating on Superni 75 is about 1.8 times higher than that on Superfer 800H.

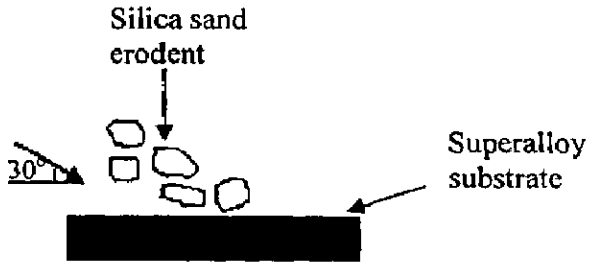

(a) Impact of silica sand erodent at 30° on superalloy surface

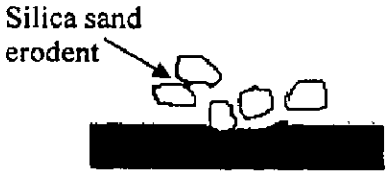

(b) Plastic deformation of superalloy surface by sand particles

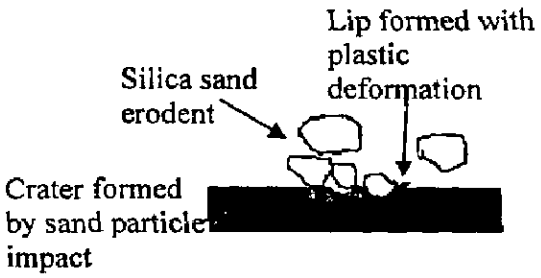

(c) Craters and lips formed by impacting sand particles on the superalloy surface

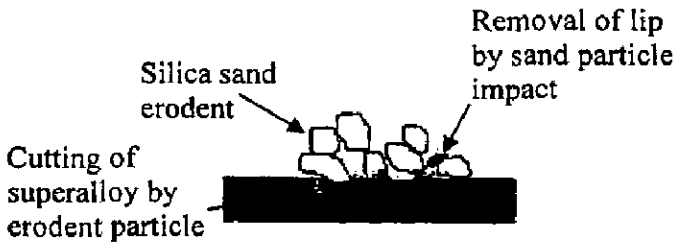

(d) Removal of material from superalloy surface

Fig. 5. 47 A schematic diagram showing probable erosion mechanism of superalloy when impacted by silica sand particles at a velocity of 40 ms^{-1} and impact angle of 30°.

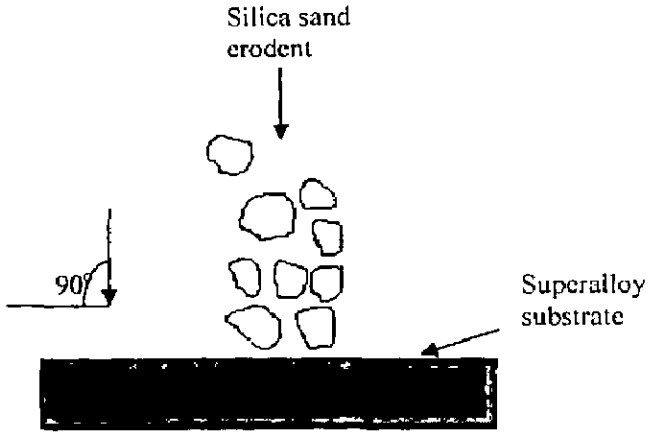

(a) Impact of silica sand erodent at 90° on superalloy surface

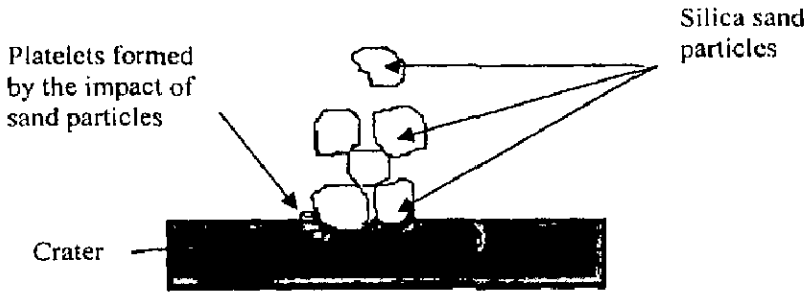

(b) Craters and lips or platelets formed by impacting sand particles on the superalloy surface by sand particles

(c) Removal of material from superalloy surface by sand particle impact

Fig. 5. 48 A schematic diagram showing probable erosion mechanism of superalloy when impacted by silica sand particles at a velocity of 40 ms^{-1} and impact angle of 90°.

From the erosion rate data of the present study (Fig. 5.16), it can be seen that the steady state erosion rate of NiCrAlY coating on Superfer 800H and Superni 718 was greatest at 30° impact angle, which is the characteristic erosion behaviour of ductile material. Whereas the steady state erosion rate of NiCrAlY coating on Superni 600 and Superco 605 was maximum at 90° impact angle, showing the brittle behaviour of the material. However the variation in magnitude of steady state erosion rates of plasma sprayed NiCrAlY coating on all these superalloys substrates is marginal.

The SEM micrographs of the NiCrAlY coating is indicating (Figs. 5.17-5.20) the ductile mechanism of coating removal despite the earlier results obtained for the steady state erosion rate vs. impact angle which showed maximum erosion at normal impact angle. The material subjected to erosion initially undergoes plastic deformation and is later removed by subsequent impacts of the erodent on the surface. The ploughing occurs by the impact of the sand particles, and lips or ridges are formed at the bank of the grooves. These lips are fractured or removed from the grooves with further erosion. Material removal takes place by the ductile mechanism described by Bellman and Levy (1981), where they suggested that the creation of platelet-like edges by impact extrusion protrude outward over adjacent material, and the loss of these platelets appears to be responsible for the mass loss. Further explained that repeated deformation of craters and forming of new craters is common, and some platelets are extruded several times before they are knocked off.

5.3.3 Ni-20Cr Coating

From the Fig. 5.25, it is evident that the coated superalloys Superfer 800H and Superni 718 have shown higher erosion values, whereas coated Superni 75, 600 and Superco 605 have shown a little lower erosion rates. The coated superalloys can be arranged in the following order with regard to their erosion resistance at 30° impact angle:

Superni 600 > Superni 75 > Superco 605 > Superfer 800H > Superni 718

The coating was found to be successful in retaining its surface contact with the substrate superalloys in general.

The sequence of coated superalloys with regard to their erosion resistance at 90° impact angle is:

Superni 718 > Superni 600 > Superni 75 > Superco 605 > Superfer 800H.

The erosion rate of Superfer 800H was found to be 1.85 times higher than that of coated Superni 718 at normal impact angle.

Further the steady state erosion rate (volumetric loss) of the coating on Superni 718 superalloy (Fig. 5.27) was maximum at 30° impact angle than that at normal impact angle, thus indicating the ductile behaviour of the coating on this superalloy. Whereas for Ni-20Cr coated Superni 75, 600, Superfer 800H and Superco 605 superalloys, steady state erosion rate was maximum at 90° impact angle, indicating the brittle behaviour of the coating. However the difference is so marginal that it may not be conclusive in predicting the ductile or brittle nature of the coating. Branco et al (2004) has made similar observation.

From the SEM micrographs of the Ni-20Cr coating on Superni 75, 600, Superfer 800H and Superco 605 (Fig. 5.28-5.29) ductile mechanism of coating erosion can be inferred whereas the results obtained for the steady state erosion rate vs. impact angle, showed maximum erosion at normal impact angle thereby indicating the brittle nature of coating. Hearley et al (1999) have also reported similar behaviour of the NiCr and NiAl metallic coatings. According to them the explanation of these apparently contradictory results lies in an examination of the erodent characteristics, i.e. morphology, size and hardness, which are known to influence the erosion behaviour. Further they concluded that brittle behaviour is not characterised by typical fracture or chipping mechanisms but rather by intense localized plastic flow producing lips round the craters periphery. They observed the plastic flow around particle impact sites resulted in surface smearing similar to the morphologies for present study shown in Figs. 5.28 and 5.29. The effect of hardness, porosity and bond strength of the coatings are discussed in the section 5.4.

5.3.4 Ni_3Al Coating

The Ni_3Al coated superalloys have shown steady state erosion rates in a very narrow range of 7.959-13.342 × 10^{-3} mm^3g^{-1}. Further, among these coated superalloys, the Ni_3Al coating on a Fe-based superalloy has shown better erosion resistance, as compared to the other coated superalloys, as the steady state erosion rate is 9.580 × 10^{-3} mm^3g^{-1} at 30° impact angle, and 8.176 × 10^{-3} mm^3g^{-1} at 90° impact angle. These indicate the protective nature of this coating on all the five substrate superalloys for erosion wear under

the evaluated conditions. Moreover, the coating was found to be successful in retaining its surface contact with the substrate superalloys in general.

The Ni_3Al coated superalloys can be arranged in the following order with regard to their erosion resistance at 30° impact angle:

Superni 75 > Superfer 800H > Superni 600 > Superni 718 > Superco 605.

The sequence of coated superalloys with regard to their erosion resistance at 90° impact angle is:

Superni 718 > Superfer 800H > Superco 605 > Superni 600 > Superni 75.

The steady state erosion rates of the Ni_3Al coating on Superni 600, 718, Superfer 800H and Superco 605 superalloys were maximum at 30° impact angle than that at normal impact angle. This indicates the ductile behaviour of these coated superalloys. Whereas for Ni_3Al coated Superni 75 superalloys, steady state erosion rate was maximum at 90° impact angle, indicating the brittle behaviour of the coating. Brittle erosion behaviour of the HVOF sprayed NiAl intermetallic coating has also been reported by Hearley et al (1999).

The plausible mode of the erosion for all the coated superalloys at a 30° and 90° impact angle may be described as shown in Figs. 5.49 and 5.50.

5.4 EFFECT OF HARDNESS AND POROSITY ON THE EROSION BEHAVIOUR OF THE COATINGS

The hardness of the coating is a major consideration in the erosion of metals and coatings. To study the effect of hardness on the erosion behaviour of coatings, the graphs have been plotted as shown in Figs. 5.51 and 5.52. From the graph it can be inferred that the hardness of coatings and superalloys have negative effect on the erosion rates. Fig. 5.51 shows at 30° impact angle whereas Fig. 5.52 indicates the linear trend of microhardness on erosion rate with R^2 value of 0.5996 at normal impact angle with a steeper line. The microhardness of the Ni_3Al coating was found lowest amongst the coatings and is showing better erosion resistance at both the impact angles. Davis et al (1986) have also similar findings for hardness of the ceramic thermal barrier coatings. Further Levy (1988) and Takeda et al (1993) have observed that hardness does not contribute directly to the improvement of the erosion resistance. Levy (1995) has reported that increasing hardness has either no effect or a negative effect on erosion resistance. In the present study, the range of porosity content in Ni_3Al coating has been observed in the range of 1.4-4.2 %, whereas

for NiCrAlY and Ni-20Cr coatings the porosity contents was in the range of 2-4.5 and 2.2-5% respectively. The relative comparison of porosity contents of the coatings and respective erosion rates of coatings also suggest negative effect of porosity content on the erosion rate of the plasma sprayed coatings. Thus indicating the better performance of plasma sprayed Ni_3Al coating as compared to NiCrAlY and Ni-20Cr coatings. Thus the variation in the porosity contents of the coatings might have contributed to the variation in erosion rates of the different coatings. Regarding the effect of porosity contents on the erosion behaviour of the coatings, Levy (1988) has reported that the greater the porosity of the coating, the easier it is for the erodent particles to knock off pieces of exposed surface, and the greater is the removal rate.

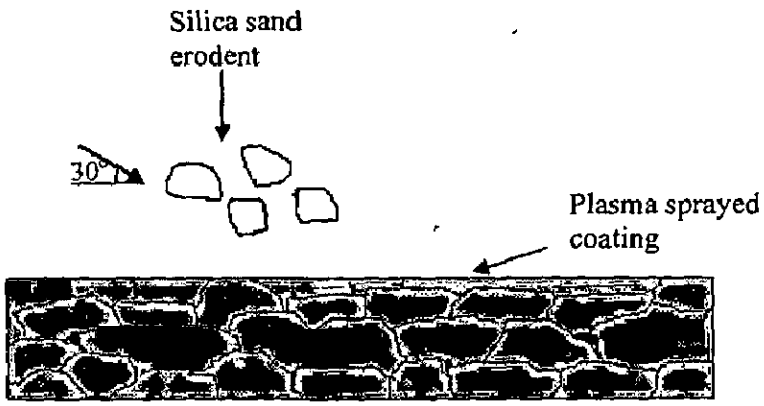

(a) Impact of silica sand erodent at 30° on plasma spray coated surface

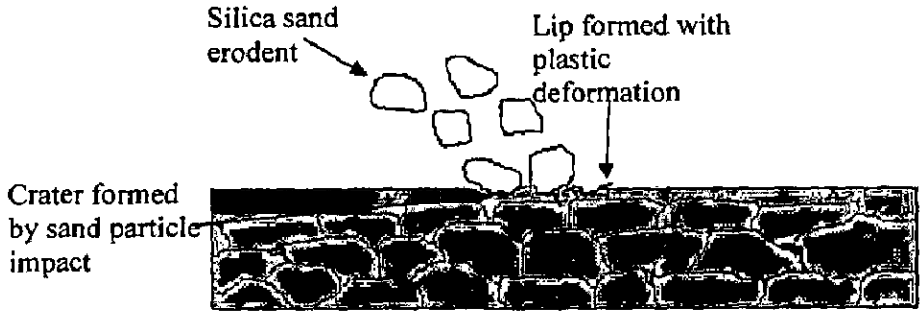

(b) Craters and lips formed by impacting sand particles on the coated surface

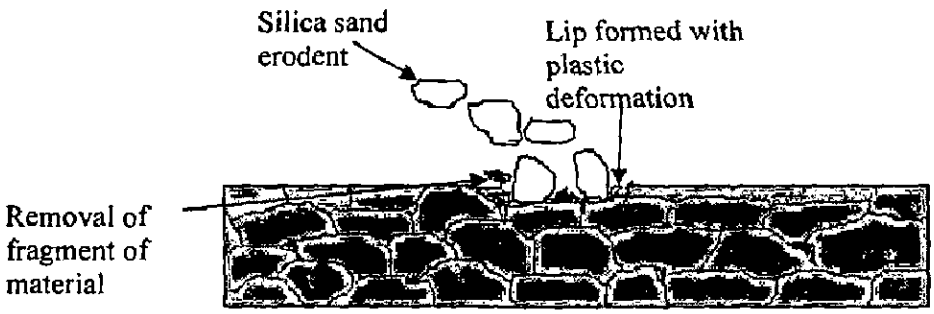

(c) Removal of fragment of material from the coating surface

Fig. 5. 49 A schematic diagram showing probable erosion mechanism of plasma spray coated superalloy when impacted by silica sand particles at a velocity of 40 ms^{-1} and impact angle of 30°.

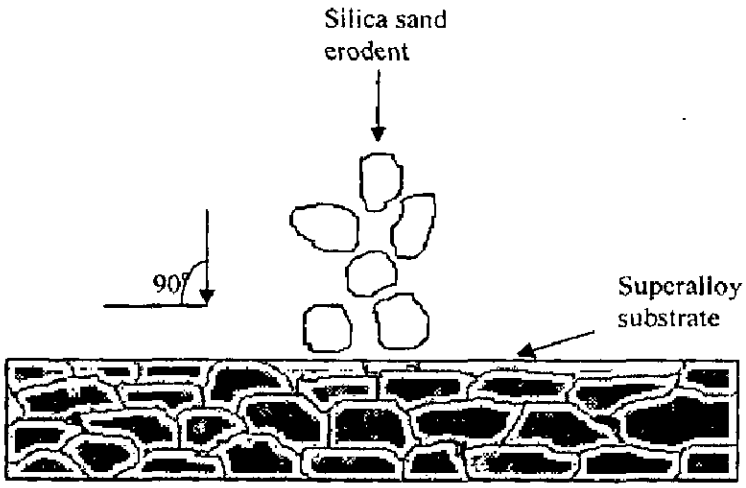

(a) Impact of silica sand erodent at 90° on plasma sprayed coating

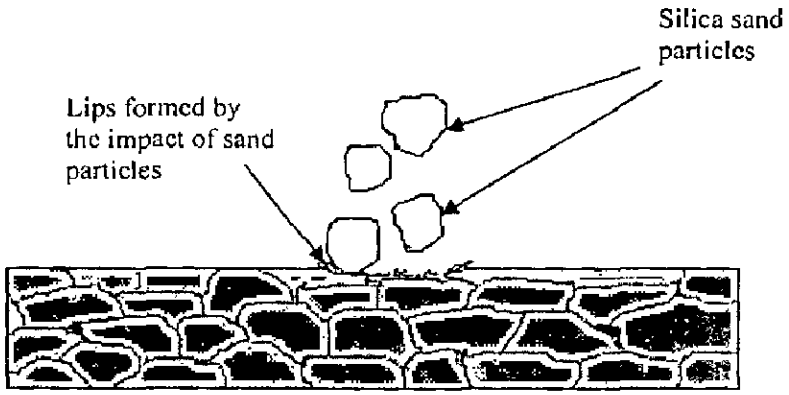

(b) Lips or platelets formed by plastic deformation on the plasma sprayed coating surface by sand particles

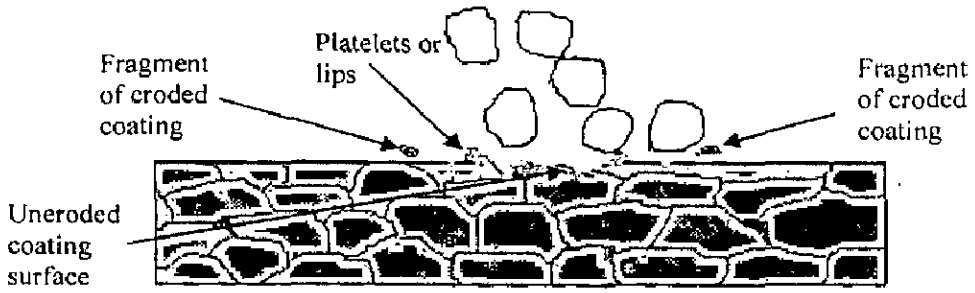

(c) Removal of material from the plasma spray coated surface by sand particles impact

Fig. 5. 50 A schematic diagram showing probable erosion mechanism for plasma spray coated superalloy when impacted by silica sand particles at a velocity of 40 ms^{-1} and impact angle of 90°.

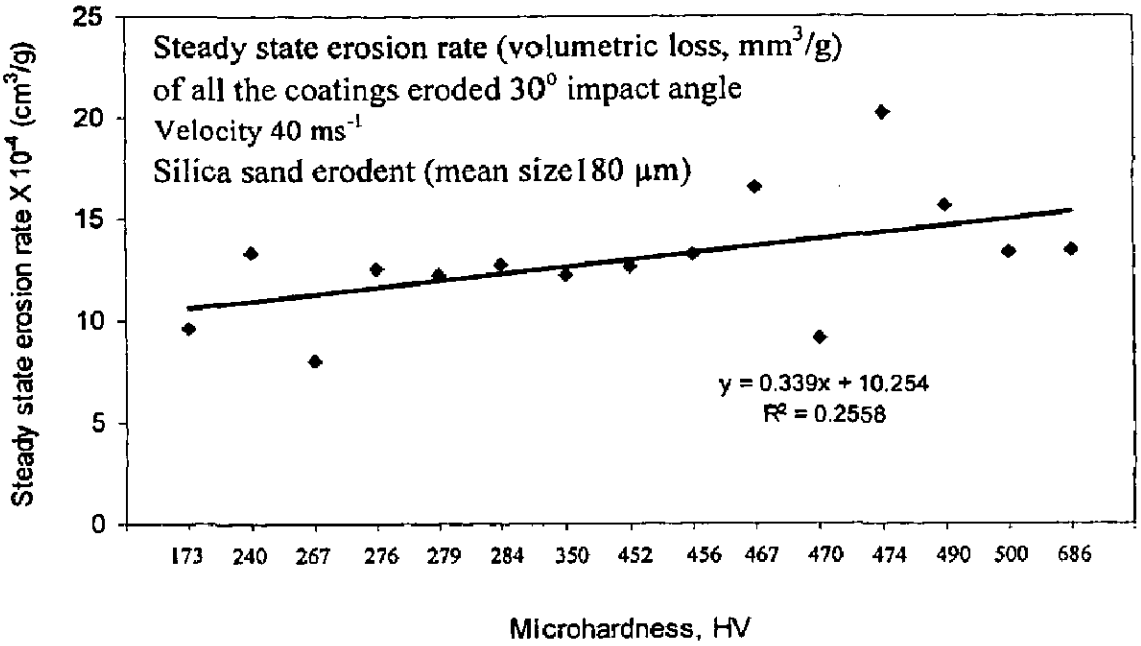

Fig. 5.51 Variation of steady state erosion rate (volumetric loss, cm^3/g) against increasing microhardness for all the plasma sprayed coatings eroded at a Velocity 40 ms^{-1} and impact angle of 30° using silica sand particles of average size180 μm as erodent.

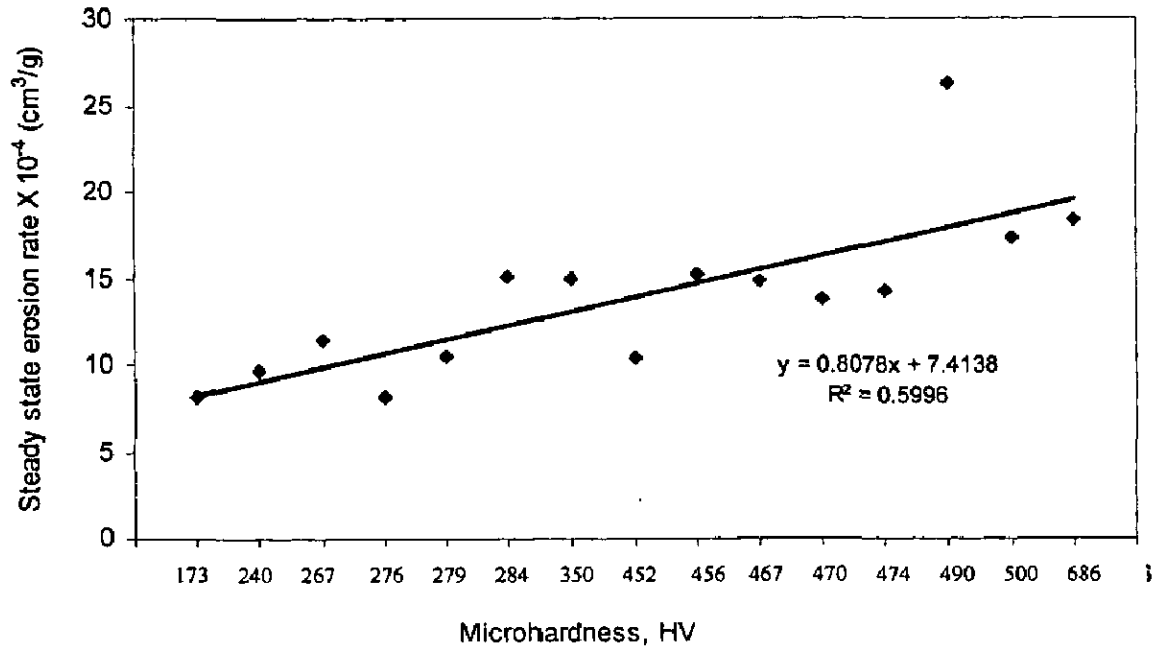

Fig. 5.52 Variation of steady state erosion rate (volumetric loss, cm^3/g) against increasing microhardness for all the plasma sprayed coatings eroded at a Velocity 40 ms^{-1} and impact angle of 90° using silica sand particles of average size180 μm as erodent.

Chapter 6

SLIDING WEAR STUDIES USING PIN-ON-DISC WEAR TEST RIG

Dry sliding wear behaviour of the superalloys as well as plasma sprayed coatings on the Superfer 800H superalloy substrate investigated in the present study has been described in this chapter. The dry sliding wear experiments were carried out using pin-on-disc wear test rig at a normal load of 9.8 N and sliding speed of 1 ms^{-1}. Wear test on bare superalloys have been carried out for a total sliding distance of about 3000 m (10 cycles of 5 min. duration). Whereas for coated specimens, wear test has been carried out for a total sliding distance of 1200 m (10 cycles of 2 min. duration).

The coefficients of friction have been plotted with sliding time for the substrate superalloys as well as plasma spray coated superalloys. Also cumulative wear volume and the specific wear rate data (mm^3/N-m) have been plotted against sliding distance for the substrate superalloys as well as plasma spray coated superalloys for comparison of the results. The worn samples were analysed with SEM. Whereas the wear debris collected during the study were analysed using XRD and SEM techniques. The results have been compiled to provide the performance of superalloys and coatings in this chapter.

6.1 RESULTS

6.1.1 Frictional Behaviour

The friction study cannot be split from wear, keeping in view the integrated tribological performance of a material. The variation of coefficient of friction with sliding distance provides the basic data for understanding the friction behaviour of a material. Therefore measurements of frictional force have been carried out at definite interval of time without interrupting the test. It has been monitored continuously throughout the sliding distance covered during the test. The coefficient of friction has been computed by dividing the frictional force by normal load and has been plotted against the time interval as shown in Fig. 6.1. It can be seen that the friction coefficient of the superalloys is unstable and varies continuously in case of all the five superalloys.

Superni 600 superalloy has shown the highest average coefficient of friction amongst the worn superalloys, whereas that of Superco 605 superalloy was found to be the least. Fig. 6.2 presents the variation of coefficient of friction for plasma sprayed coatings with sliding time. The graph indicates the highest coefficient of friction for Ni-20Cr coating whereas least average coefficient of friction for NiCrAlY coating.

6.1.2 Wear

Fig. 6.3 shows the variation of cumulative wear volume with sliding distance under a fixed normal load of 9.8 N at a sliding velocity of 1 m/s for Ni-, Fe- and Co-based superalloys. It is observed that the volume loss increases linearly with sliding distance. However, the cumulative volume loss of Superni 600 superalloy is highest amongst the superalloys followed by Superni 75. The cumulative wear volume of Superfer 800H and Superco 605 are almost similar and their trend lines overlap, whereas trend line of Superni 718 is slightly steeper than that of Superfer 800H and Superco 605 superalloy. The cumulative wear volume of plasma sprayed NiCrAlY, Ni-20Cr and Ni_3Al coatings on Superfer 800H substrate has been illustrated in Fig. 6.4. The cumulative wear volume loss of the Ni-20Cr coating is lower than that observed in other two coatings. Further the cumulative wear volume loss of Ni_3Al coating is found to be highest amongst the coatings.

Fig. 6.5 shows the variation of specific wear rate (mm^3/N-m) of the Superni 75, Superni 600, Superfer 800H, Superco 605 and Superni 718 superalloys with the sliding distance. From the graph, it can be inferred that the wear rate of Superni 600 was highest, whereas that of Superfer 800H was lowest, followed by Superco 605 with negligible difference, amongst the uncoated superalloys. Fig. 6.6 depicts the graph of wear rate against sliding distance for the plasma sprayed NiCrAlY, Ni-20Cr and Ni_3Al coatings. The average wear rate of Ni-20Cr coating was found to be least amongst the coatings whereas Ni_3Al coating on Superfer 800H superalloy substrate has shown maximum average specific wear rate (6.1914×10^{-4} mm^3/N-m).

6.1.1.3 SEM Analysis

6.1.1.3.1 Morphology of Worn Samples

The SEM micrographs (Figs. 6.7 and 6.8) have been obtained for the worn surfaces of all the superalloys and coatings. These micrographs clearly reveal the wear track and indicate the wear of the samples. Figure 6.7 shows the transferred layers of

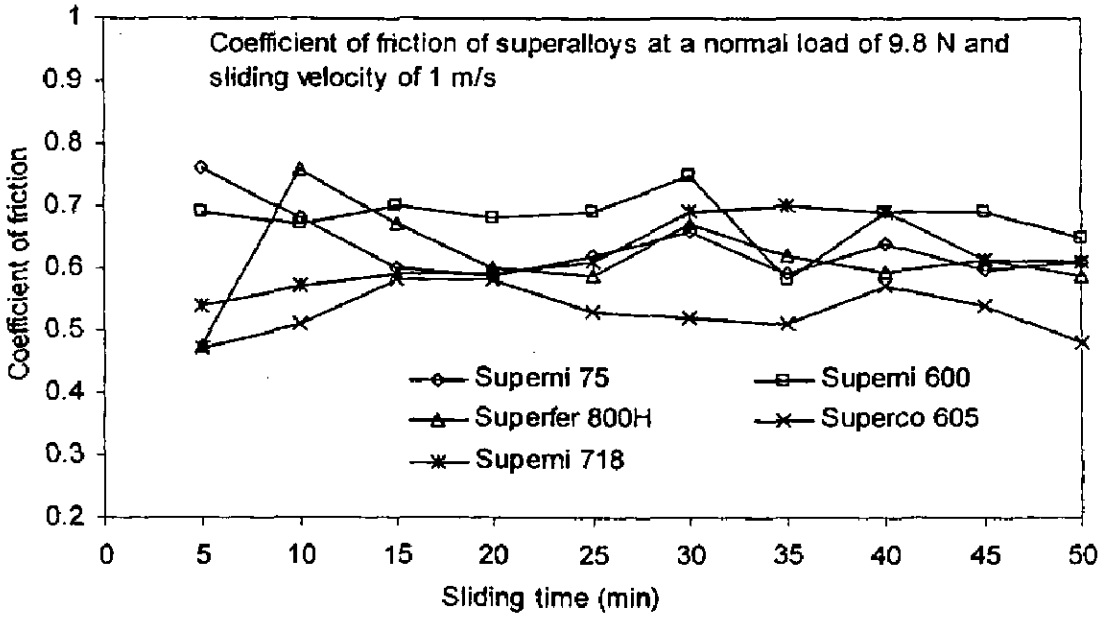

Fig. 6.1 Coefficient of friction versus sliding time curves of superalloys at a normal load of 9.8 N and sliding velocity of 1 ms^{-1}.

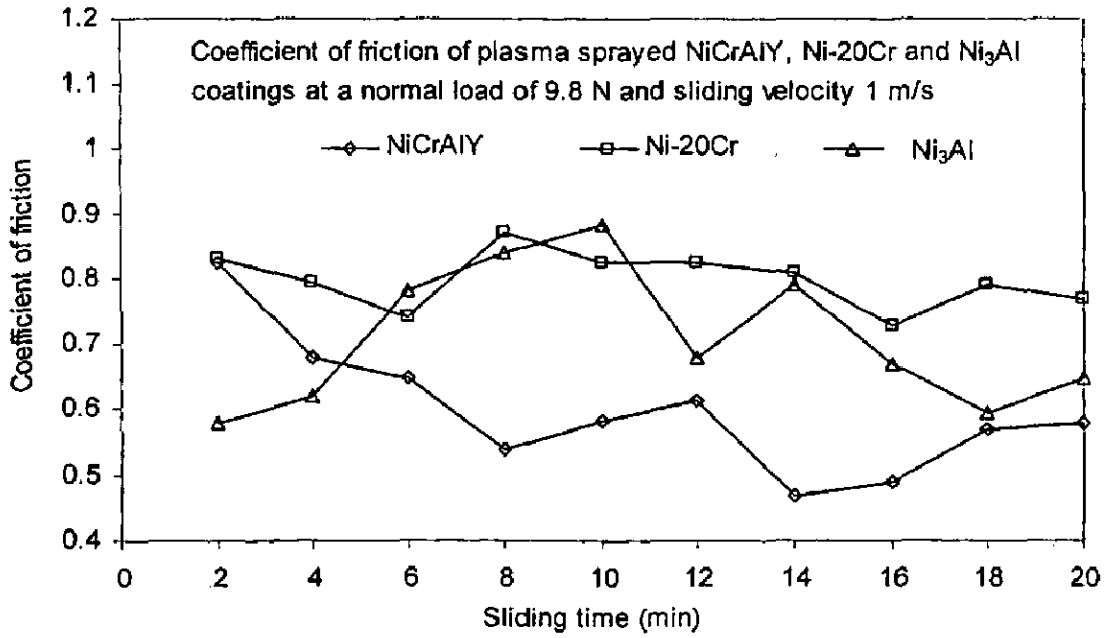

Fig. 6.2 Coefficient of friction for plasma sprayed coatings on Superfer 800H superalloy substrate versus sliding time curves at a normal load of 9.8 N and sliding velocity of 1 ms^{-1}.

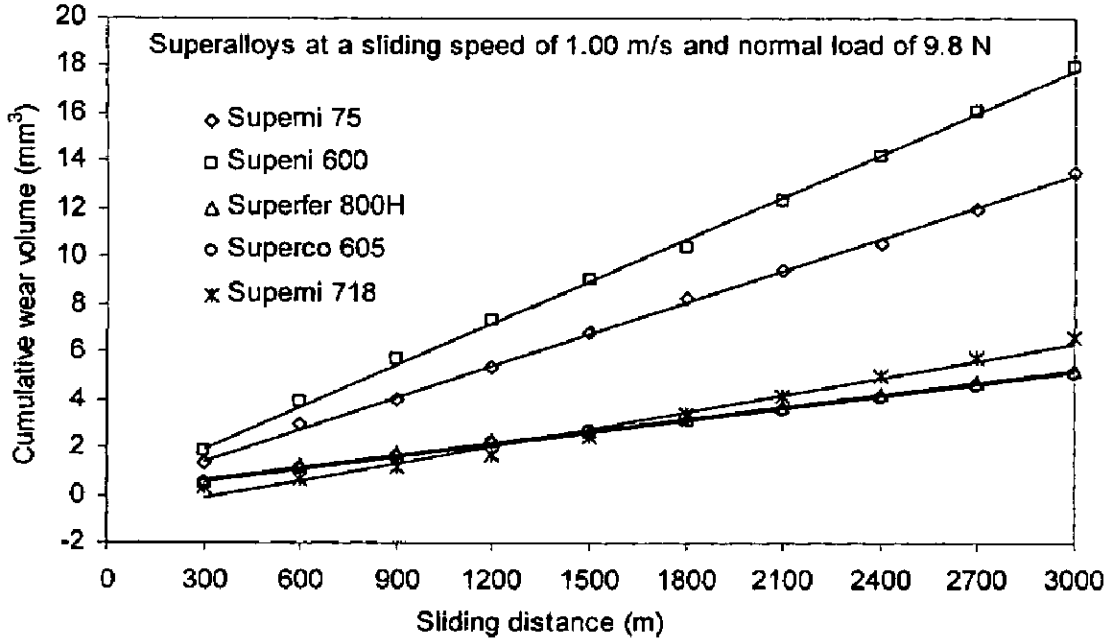

Fig. 6.3 Variation of cumulative wear volume of superalloys with sliding distance at a normal load of 9.8 N and sliding velocity of 1 ms^{-1}.

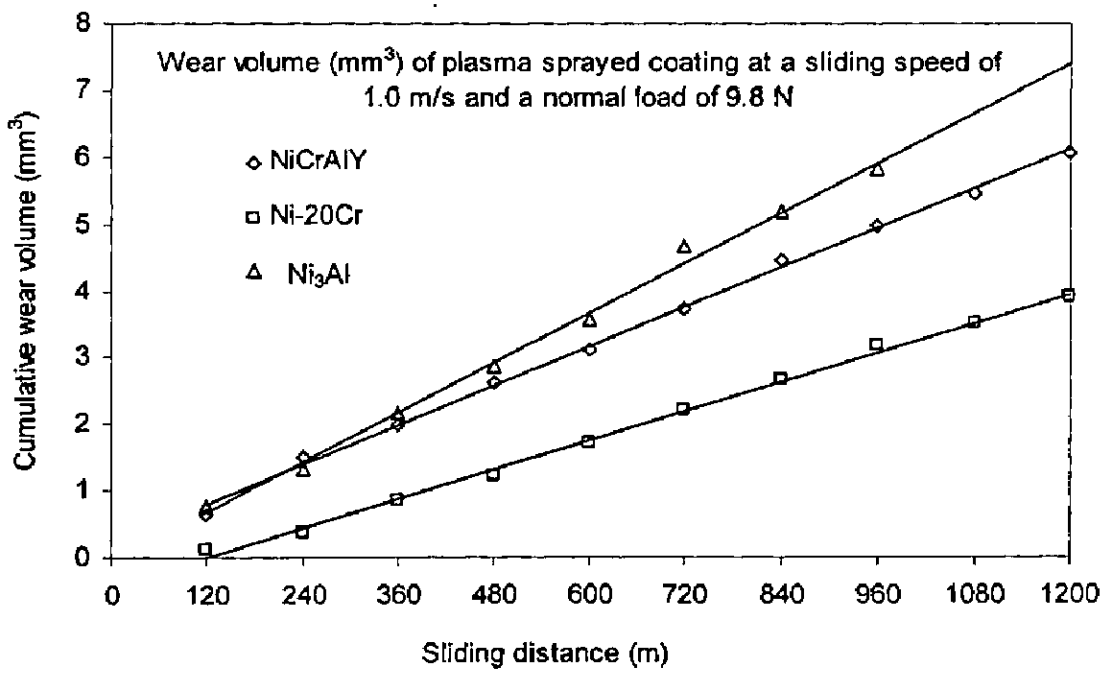

Fig. 6.4 Variation of cumulative wear volume of plasma sprayed coatings on Superfer 800H superalloy substrate with sliding distance at a normal load of 9.8 N and sliding velocity of 1 ms^{-1}.

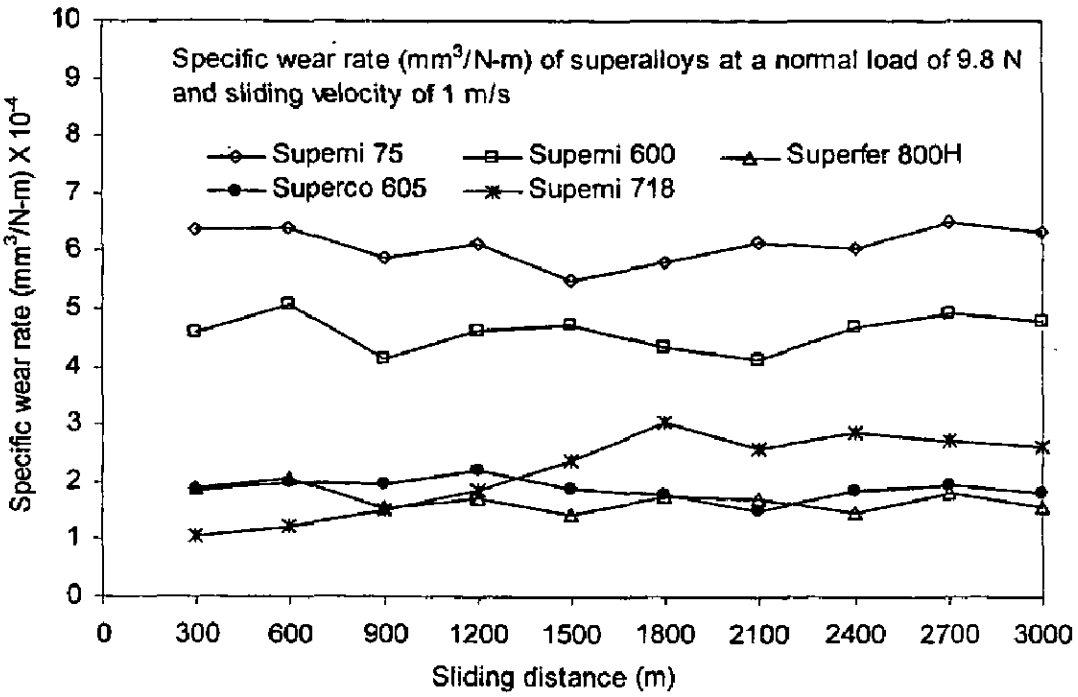

Fig. 6.5 Variation of specific wear rate of superalloys with sliding distance at a normal load of 9.8 N and sliding velocity of 1 ms^{-1}.

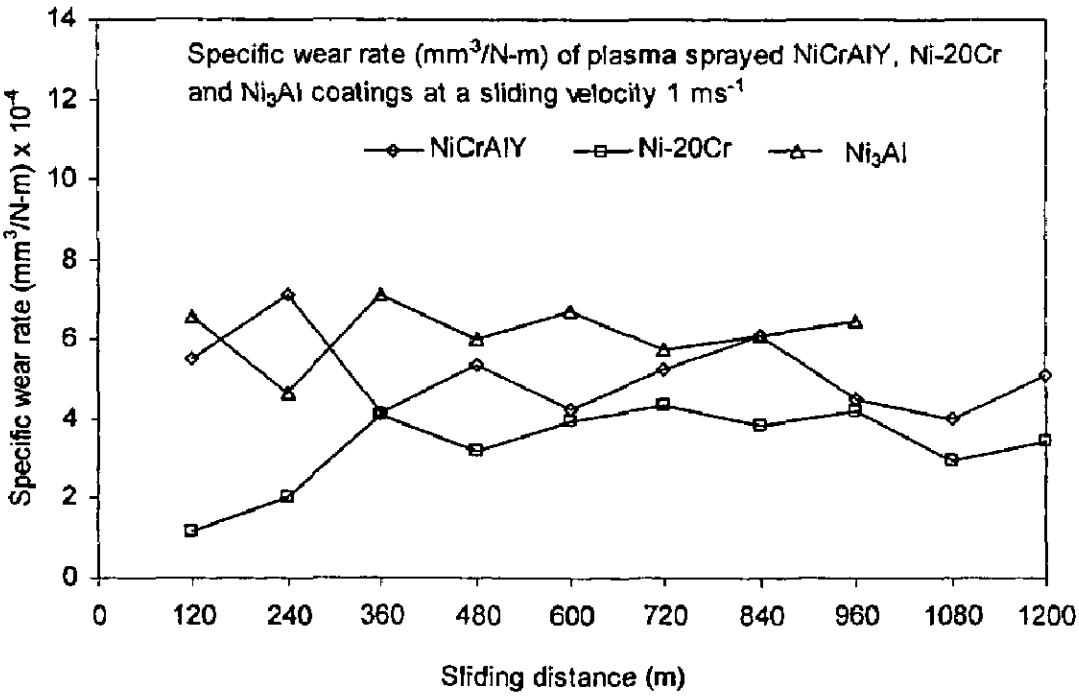

Fig. 6.6 Variation of specific wear rate of plasma sprayed coatings on Superfer 800H superalloy substrate with sliding distance at a normal load of 9.8 N and sliding velocity of 1 ms^{-1}.

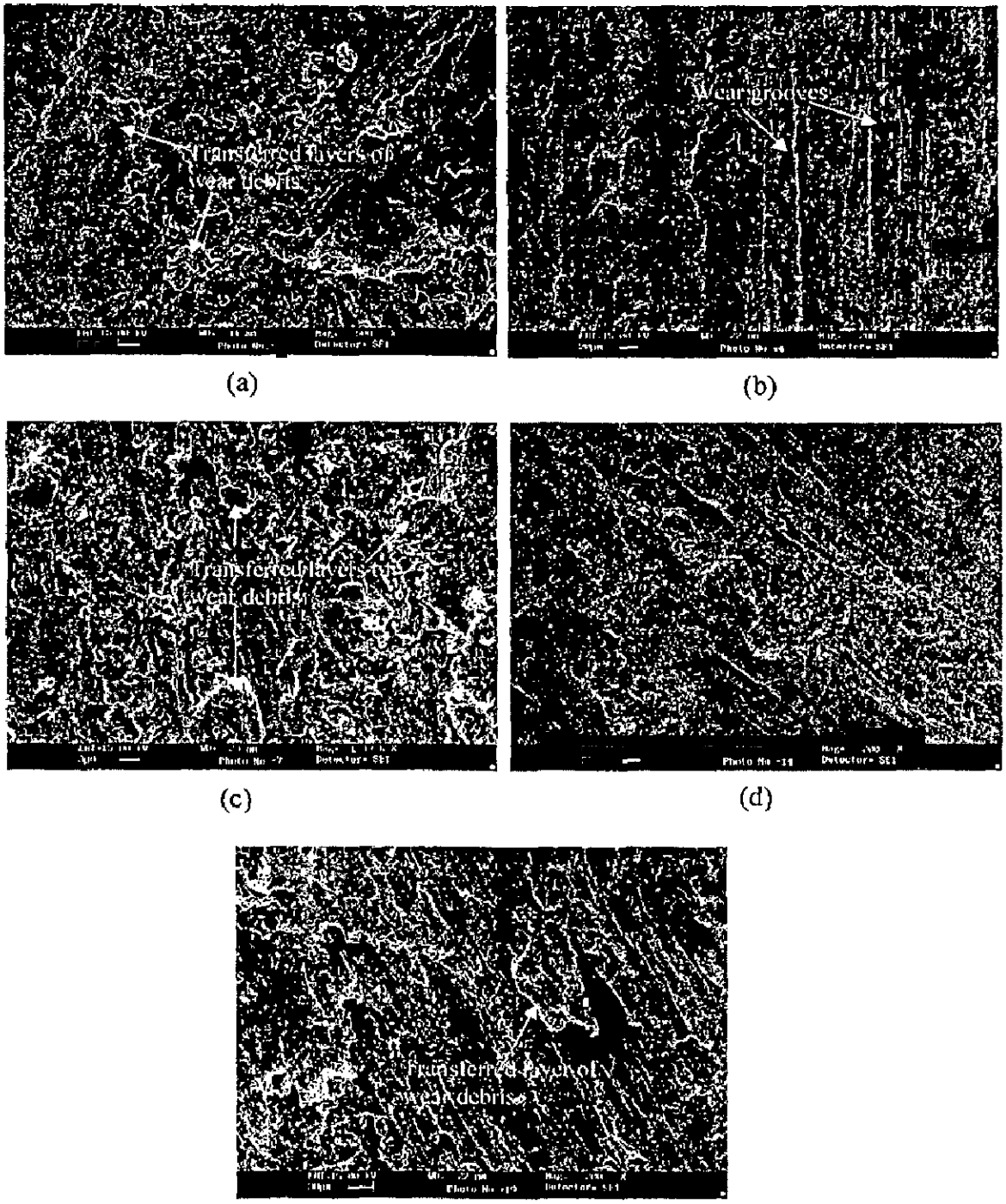

(a) (b)

(c) (d)

(e)

Fig. 6.7 Scanning electron micrographs of worn surfaces of superalloys subjected to sliding distance of 3000 m at an average sliding speed of 1 ms^{-1} on a pin-on-disc wear test rig.

(a) Superni 75 (b) Superni 600 (c) Superfer 800H

(d) Superco 605 (e) Superni 718.

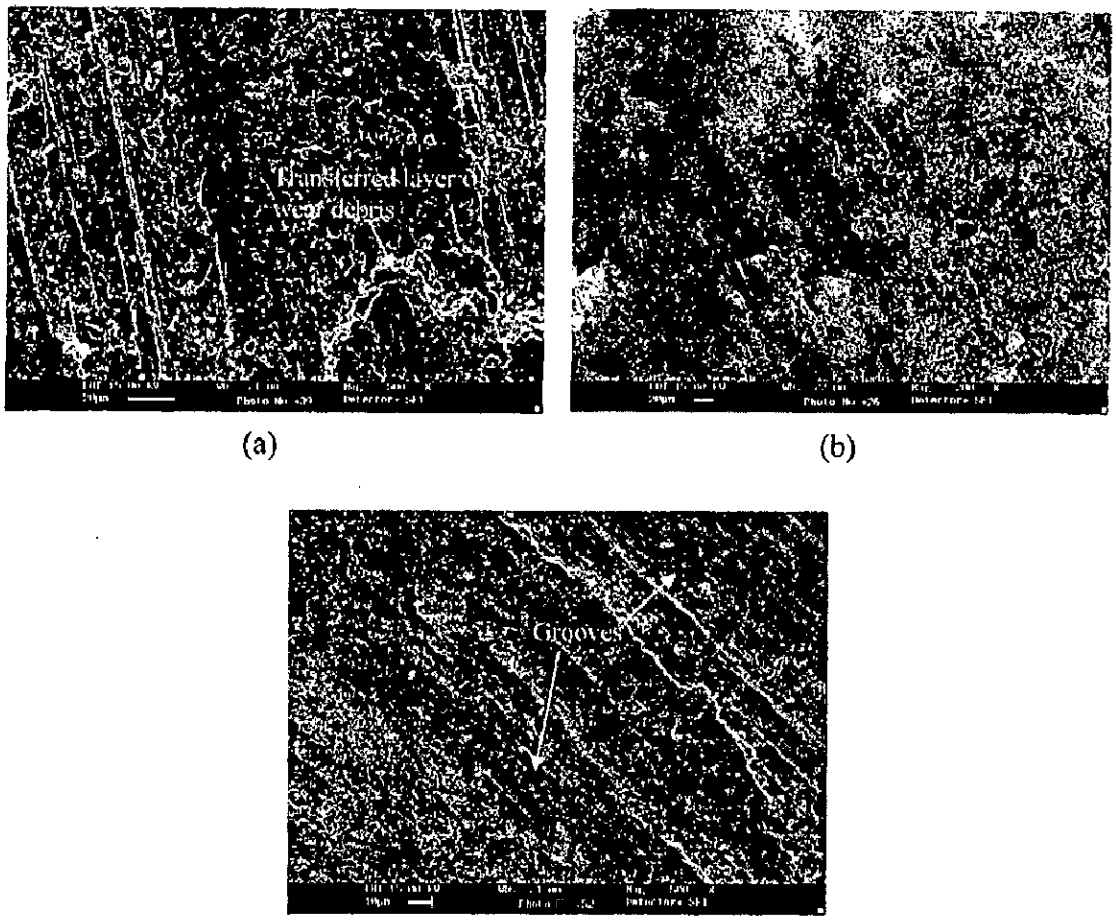

(a) (b)

(c)

Fig. 6.8 Scanning electron micrographs of worn surfaces of plasma sprayed coatings on Superfer 800H superalloy substrate subjected to sliding distance of 1200 m at an average sliding speed of 1 ms^{-1} on a pin-on-disc wear test rig.

(a) NiCrAlY coating (b) Ni-20Cr coating (c) Ni_3Al coating.

wear debris accompanied with large grooves formed on the worn surfaces of the superalloys subjected to a sliding distance of 3000 m. In case of coated samples, the transferred layers of wear debris are also visible (Fig. 6.8). The worn surfaces of NiCrAlY and Ni_3Al coatings also reveal grooves formed on the surfaces.

6.1.3.2 SEM of Wear Debris

The wear debris of all the worn out samples are collected for SEM studies. The micrographs (Figs. 6.9 and 6.10) of wear debris clearly reveal the severe wear of the samples under the tested condition.

6.1.1.3 XRD Analysis

X-ray diffraction patterns of wear debris of all the worn out samples have been shown in Figs. 6.11 through 6.17. The amounts of wear debris were not sufficient to detect the phases formed after sliding wear using XRD analysis for Ni-20Cr coatings. The XRD profiles of superalloys and coatings have shown some peaks of NiO and Al_2O_3 also.

6.2 SUMMARY OF RESULTS

The results of sliding wear studies for coated and uncoated superalloys are summarised in Table 6.1 to understand the comparative behaviour of different coatings.

Table 6.1 Summary of the results for coated and uncoated superalloys subjected to pin-on-disc wear test rig at a normal load of 9.8 N and a constant sliding velocity of 1 ms^{-1}.

Base superalloy	Coating	Average Microhardness (HV)	Average coefficient of friction	Specific sliding wear rate × 10^{-4} (mm^3/N-m)
Superni 75	-----	324	0.5942	4.5999
Superni 600	-----	260	0.679	6.1062
Superco 605	-----	512	0.529	1.6926
Superni 718	-----	478	0.6203	2.24
Superfer 800H	-----	320	0.5972	1.6788
Superfer 800 H	NiCrAlY	452	0.5998	5.1426
Superfer 800 H	Ni-20Cr	626	0.7985	3.3102
Superfer 800 H	Ni_3Al	173	0.7087	6.1973

6.3 DISCUSSION

The coefficient of friction of all the superalloys and coatings are found in the range of 0.529-0.798. The coefficient of friction was found fluctuating within the above range in all the uncoated and the coated superalloys. This may be due to variation in contact between the sample and the counterface. Similar range of coefficient of friction for Ni-based superalloy has also been reported by Panagopoulos et al (2003).

The superalloys Superfer 800H, Superco 605 and Superni 718 have shown good wear resistance under the test conditions. The specific wear rates of these three superalloys lie in a narrow range of 1.6925-2.2426 × 10^{-4} mm^3/N-m. The wear rates of these superalloys do not differ much. Whereas other two Ni- based superalloys, that is, Superni 75 and Superni 600 have shown higher wear rates. The wear rate for the Superni 600 is about 3.6 times higher than that for Superfer 800H. Based on the present data of the wear rate, the superalloys can be arranged in order to their wear resistance as:

Superfer 800H > Superco 605> Superni 718 > Superni 75 > Superni 600

The Superni 600 superalloy has shown highest wear rate may be due its lower hardness. The hardness is a major consideration in the sliding wear of metals and coatings. Further superior wear resistance of Superco 605 might have been contributed by its higher hardness. The Superfer 800H superalloy has also shown lower specific wear rate regardless of its lower hardness as compared to Superni 718 and Superco 605 superalloy. The oxidation rate of Superfer 800H superalloy was found to be higher as compared to the Ni-based superalloy (Singh, 2005, Ph.D. Thesis). Thus in the present case oxide layers might have formed on the Superfer 800H superalloy, thus protecting the direct metal to metal contact, contributing for lower wear rate.

Based on the weight loss data, the wear rates of the coated superalloys can be arranged in following order:

Ni_3Al coating > NiCrAlY coating > Ni-20Cr coating

Thus, it can be inferred that the relative wear resistance of Ni-20Cr coating is maximum amongst the three coatings under the test conditions. The wear rate of Ni_3Al coating is about 1.86 times to that of Ni-20Cr coating. This may be attributed to the higher hardness of Ni-20Cr coating as compared to the other two coatings (Table 6.1). The specific wear resistance of Ni-20Cr coating is found to be better than that of Superni 75 and Superni 600 superalloys, and may be due to its higher hardness. Although Ni-20Cr

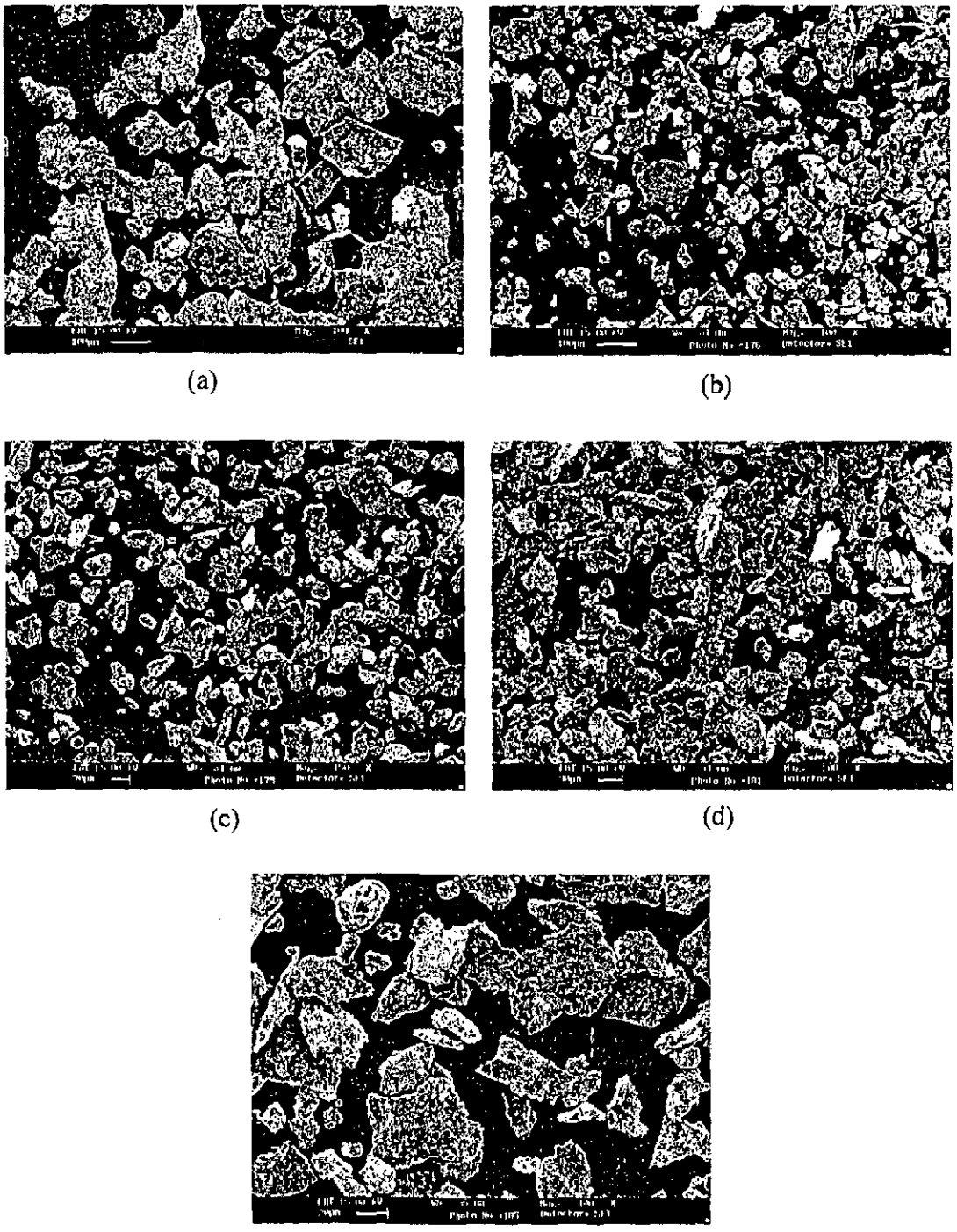

(a) (b)

(c) (d)

(e)

Fig. 6.9 Scanning electron micrographs of wear debris of superalloys subjected to sliding distance of 3000 m at an average sliding speed of 1 ms^{-1} on a pin-on-disc wear test rig.

(a) Superni 75 (b) Superni 600 (c) Superfer 800H

(d) Superco 605 (e) Superni 718.

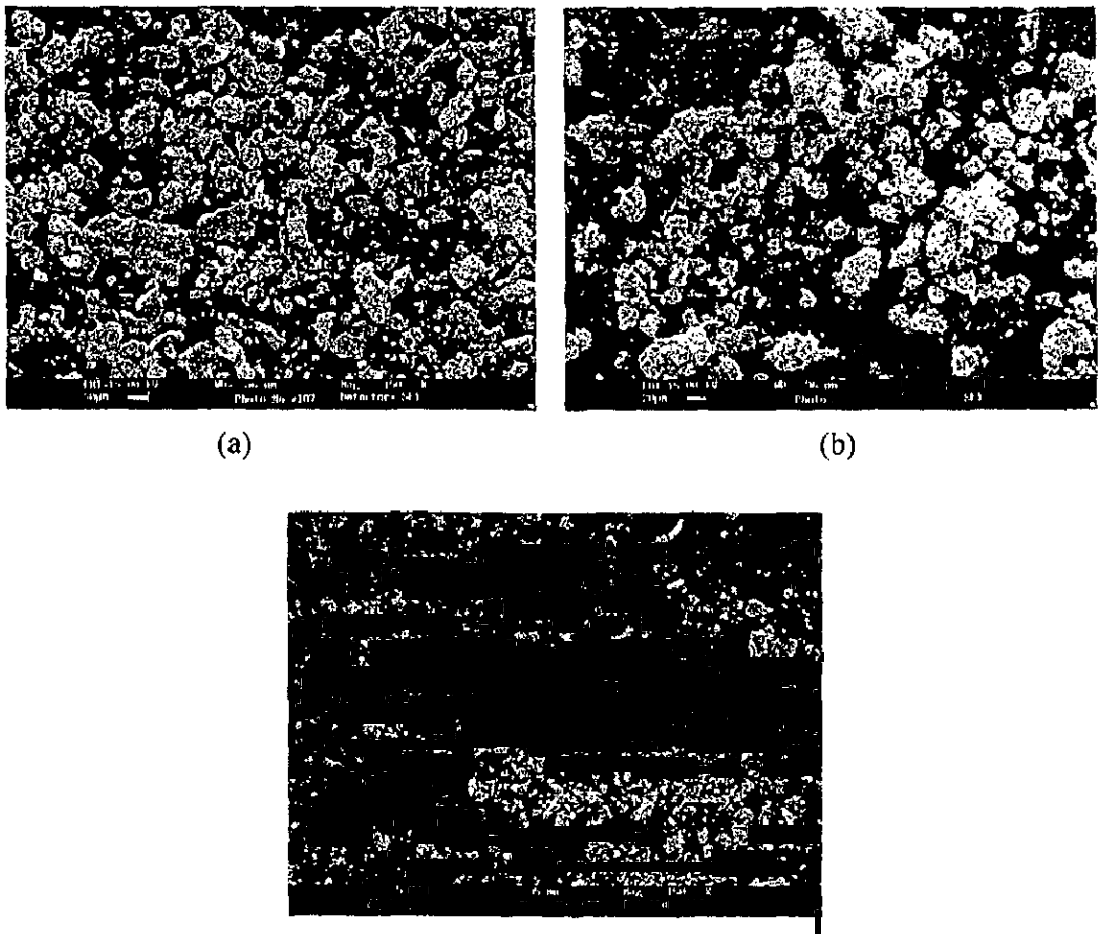

Fig. 6.10 Scanning electron micrographs showing wear debris of plasma sprayed coatings on Superfer 800H superalloy substrate subjected to sliding distance of 1200 m at an average sliding speed of 1 ms^{-1} on a pin-on-disc wear test rig.

(a) NiCrAlY coating (b) Ni-20Cr coating (c) Ni_3Al coating.

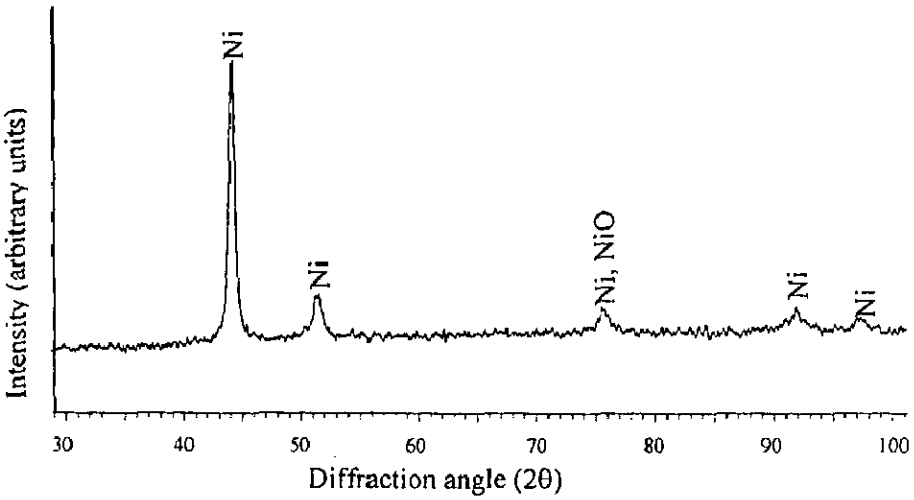

Fig. 6.11 X-ray diffraction profile of wear debris of Superni 75 superalloy substrate subjected to sliding wear studies at a normal load of 9.8 N and sliding velocity of 1 m/s.

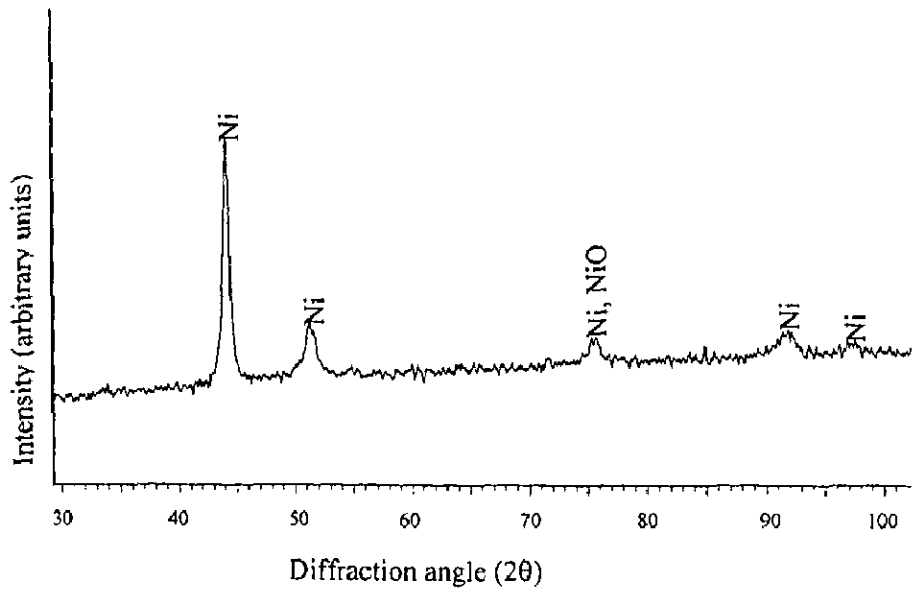

Fig. 6.12 X-ray diffraction profile of wear debris of Superni 600 superalloy substrate subjected to sliding wear studies at a normal load of 9.8 N and sliding velocity of 1 m/s.

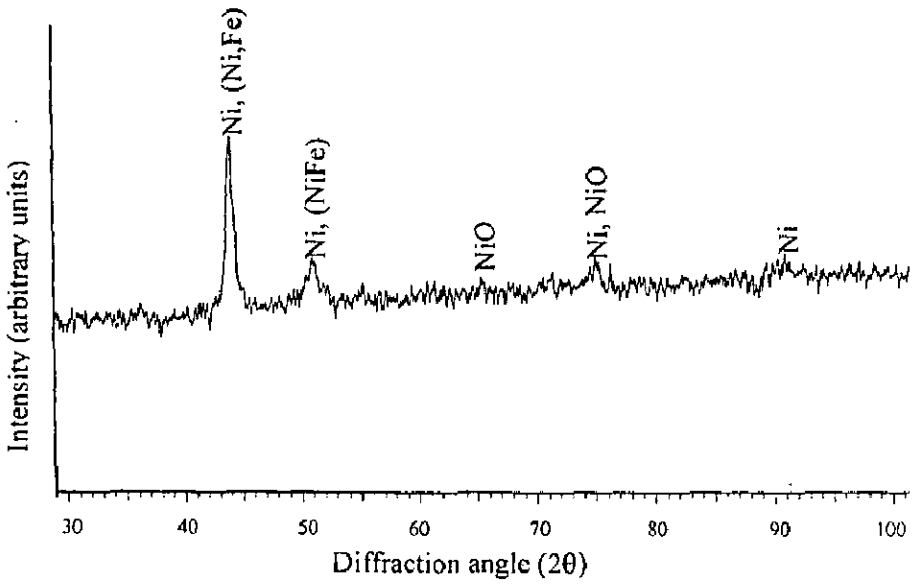

Fig. 6.13 X-ray diffraction profile of wear debris of Superfer 800H superalloy substrate subjected to sliding wear studies at a normal load of 9.8 N and sliding velocity of 1 m/s.

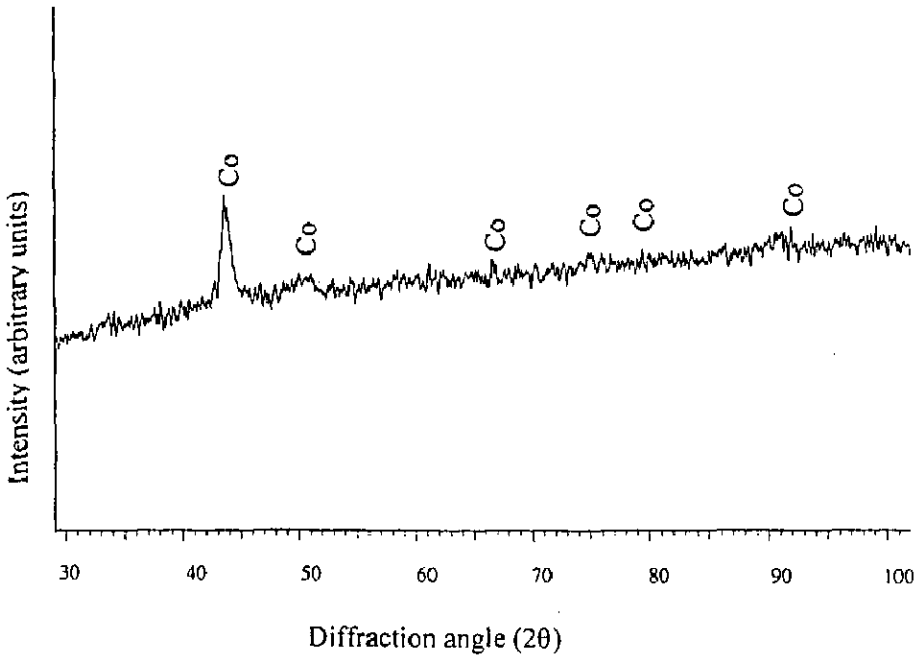

Fig. 6.14 X-ray diffraction profile of wear debris of Superco 605 superalloy substrate subjected to sliding wear studies at a normal load of 9.8 N and sliding velocity of 1 m/s.

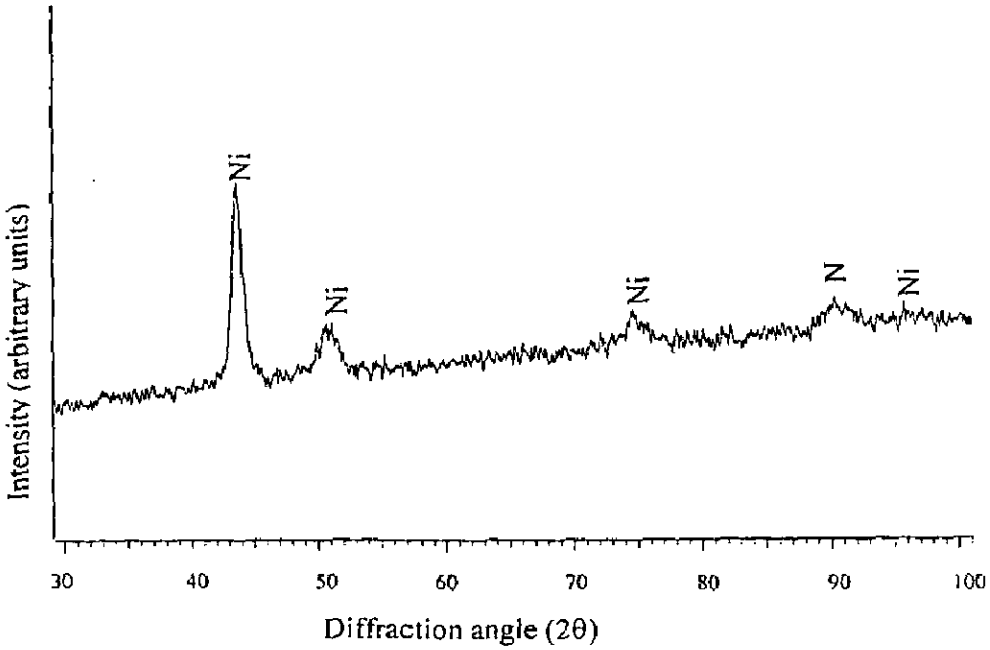

Fig. 6.15 X-ray diffraction profile of wear debris of Superni 718 superalloy substrate subjected to sliding wear studies at a normal load of 9.8 N and sliding velocity of 1 m/s.

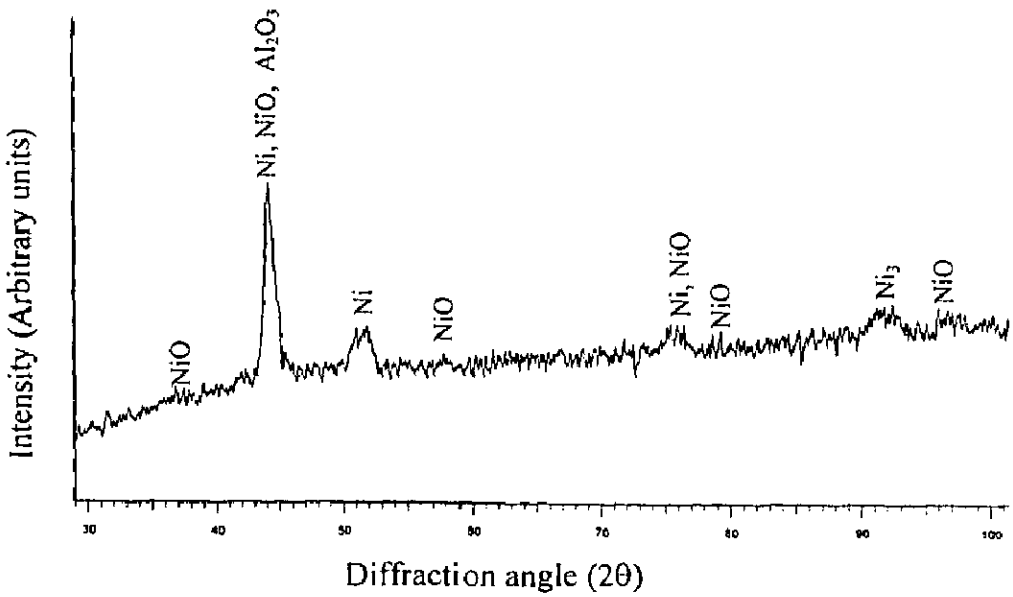

Fig. 6.16 X-ray diffraction profile of wear debris of plasma spray NiCrAlY coating on Superfer 800H superalloy substrate subjected to sliding wear studies at a normal load of 9.8 N and sliding velocity of 1 m/s.

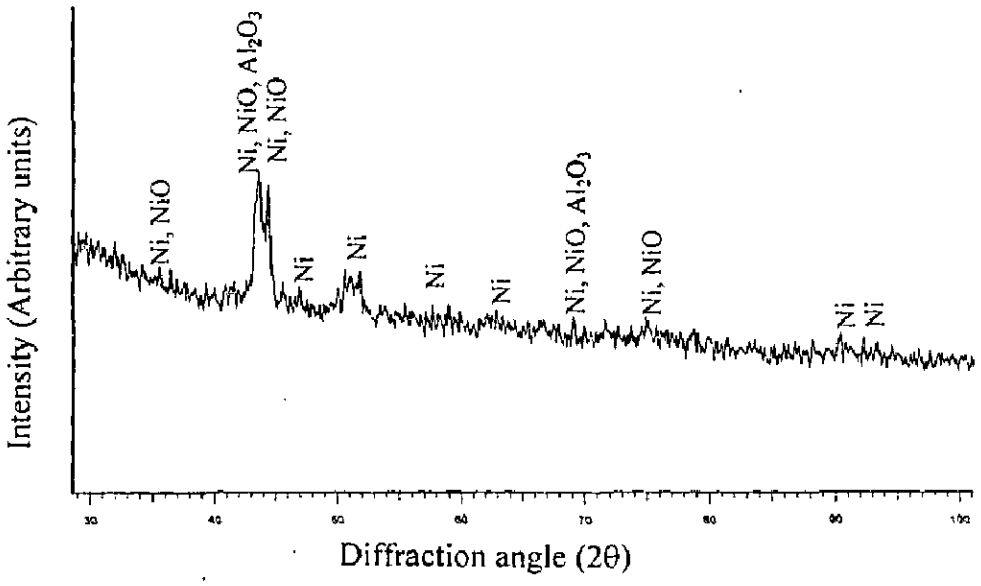

Fig. 6.17 X-ray diffraction profile of wear debris of plasma spray Ni_3Al coating on Superfer 800H superalloy substrate subjected to sliding wear studies at a normal load of 9.8 N and sliding velocity of 1.0 m/s.

coating is having higher hardness as compared to the bare superalloys, but has higher wear rate compared to Superco 605, Superfer 800 H and Superni 718 superalloys. This might be due the effect of porosity and oxide contents in the coating. Martin et al (2001) have also reported the higher wear of plasma sprayed coatings due to the pores. The wear rate should have been higher for the material with high coefficient of friction however it is not so in the present study indicating that the other factors such as the materials chemistry and processing parameters greatly affects the wear.

The transferred layers of compacted wear debris along with the wear tracks can be observed over the sliding surfaces (Figs. 6.7 and 6.8) for all the bare alloys and coated specimens. These layers reach critical thickness before getting detached as wear debris. The general mechanism of wear for both the bare superalloys and coatings involves mild-oxidational nature similar to that suggested by Stott (1998). The transferred layer provides a protective cover to the underlying material inhibiting thus the metal-metal contact.

Figure 6.9 indicates the existence of relatively larger size wear debris of superalloys. The morphology of wear debris of Superni 75 superalloy indicates the larger size range of 100-120 μm whereas the minimum size range is 20-60 μm for Superco 605 superalloy. The wear debris of coated superalloys is of smaller size as compared to the uncoated superalloys. The XRD profiles of superalloys as well as coatings have shown the very weak peaks of oxides. Panagopoulos et al (2000 and 2003) have also reported similar results phases in case of Ni-based superalloy.

Chapter 7

EROSION-CORROSION STUDIES IN INDUSTRIAL ENVIRONMENT

In this chapter the results of erosion-corrosion studies of coated and uncoated specimens in actual boiler (Low temperature primary super heater (LTSH) of coal fired boiler) environment have been compiled and discussed. In this zone of the boiler the temperature of flue gases was around 540^0C. The uncoated and plasma spray coated superalloys were exposed to this environment for total duration of 1000 hours (10 cycles of 100 hrs duration followed by 1 hour cooling at ambient temperature). The samples were examined critically at the end of each cycle for any change in the colour, luster and spalling tendency of scale, if any. Weight change was measured after each cycle of 100 hours exposure. The erosion-corrosion products were analysed through XRD, SEM/EDAX and EPMA.

7.1 RESULTS

7.1.1 Uncoated Superalloys

7.1.1.1 Visual Examination

The macrographs for Superni 75, Superni 600, Superni 718 and Superfer 800H superalloys after 1000 hours exposure in the Low Temperature Primary Super Heater (LTSH) zone of coal fired boiler are shown in Fig. 7.1. Thin light brown colour scale appeared on the surfaces of all the superalloys during first cycle of 100 hours and after that turned to brown colour. The scale appeared to be robust and no spalling of the scale was observed in all the four exposed superalloys.

7.1.1.2 Thermogravimetric Data and Thickness Monitoring

Weight change per unit area expressed in mg/cm^2 has been plotted as a function of time expressed in hours for Superni 75, Superni 600, Superni 718 and Superfer 800H superalloys in Fig. 7.2. All the superalloys have shown decrease in weight when the exposed for 1000 hours. The weight loss per unit area is highest in case of Superni 600 superalloy, whereas it is lowest in case of Superni 718 superalloy. All the exposed substrate superalloys have shown weight loss indicating their erosion in the given

environment. The extent of erosion-corrosion has been measured in terms of metal thickness lost and thickness of oxidised layer formed after 1000 hours of exposure. The total thickness loss as shown in Fig. 7.3 has been obtained by adding the loss of metal thickness measured after exposure of 1000 hours duration and the average thickness of the remained layer/scale which is measured from BSEIs as shown in Fig. 7.4. The total thickness loss is 0.085, 0.19, 0.124 and 0.17 mm for Superni 75, Superni 600, Superni 718 and Superfer 800H superalloys respectively as indicated in Fig. 7.3. The rough surfaces as shown in Fig. 7.4 indicate the contribution of erosion whereas the layer formed on the surfaces suggests the oxidation of the alloys. The minimum erosion-corrosion rate has been indicated by Superni 75 superalloy whereas maximum erosion-corrosion is shown by Superni 600 superalloy.

7.1.1.3 X-ray Diffraction Analysis

The X-ray diffractograms for Superni 75, Superni 600, Superni 718 and Superfer 800H superalloy after exposure to actual boiler environment for 1000 hours are shown in Figs. 7.5 and 7.6. In the given environment all the superalloys have indicated Ni as the main constituent in the scale. In addition the diffractograms also indicated the peaks of NiO, Al_2O_3 and $NiFe_2O_4$.

7.1.1.4 SEM/EDAX Analysis

7.1.1.4.1 Surface Morphology

The SEM micrograph shown in Fig. 7.7 (a) for the eroded surface of Superni 75 in the given environment indicates a very fine scale along with the presence of some embedded ash. The scale mainly consists of Cr_2O_3 and NiO (point 1 and 3 in Fig. 7.7 a). Analysis at point 2 reveals ash deposition, having 52 wt. % SiO_2, 21 wt. % Al_2O_3 and small amount of Cr_2O_3 and NiO. In case of Superni 600 superalloy exposed to boiler conditions SEM indicates a thin scale consisting mainly NiO (wt. % 64) and some amounts of Cr_2O_3, Fe_2O_3, SO_3, SiO_2 and Al_2O_3 (point 2 in Fig. 7.7 b). Ash particle embedded in the scale was indicated by EDAX analysis (point 1 in Fig. 7.7 b), that has 32 wt. % SiO_2, 19 wt. % Al_2O_3, 23 wt. % NiO, 12 wt. % Cr_2O_3 and some amount of Fe_2O_3 and SO_3 as shown in Fig. 7.7 (b). Micrograph of Superfer 800H superalloy (Fig. 7.8a) has shown a thin scale having 43 wt. % Fe_2O_3, 26 wt. % Cr_2O_3, 24 wt. % NiO, 4 wt. % SiO_2, 2 wt. % Al_2O_3 and 1 wt. % TiO_2 on the surface. Superni 718 superalloy subjected to boiler environment shows the thin scale consisting of mainly NiO (55 wt. %) with embedded ash particle rich in silica (Fig. 7.8 (b).

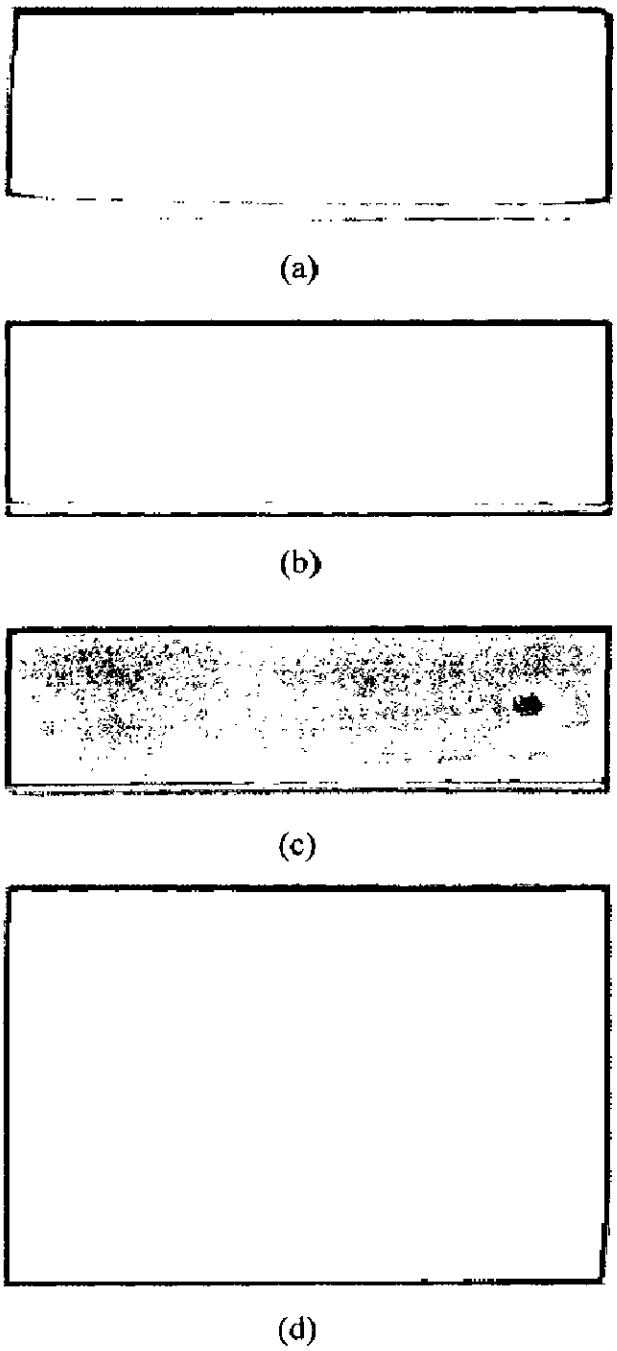

Fig. 7.1 Macrographs of uncoated superalloys subjected to coal-fired boiler at 540°C for 1000 hours.
(a) Superni 75 (b) Superni 600 (c) Superfer 800H
(d) Superni 718.

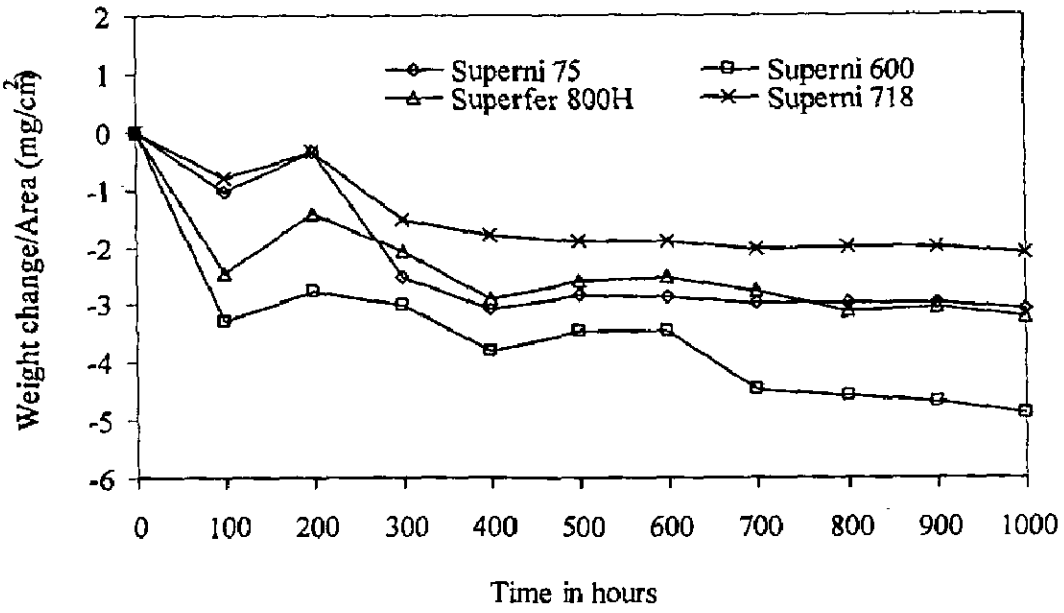

Fig. 7.2 Weight change against time in hours plot for uncoated superalloys exposed to the coal fired boiler for 1000 hours at 540°C.

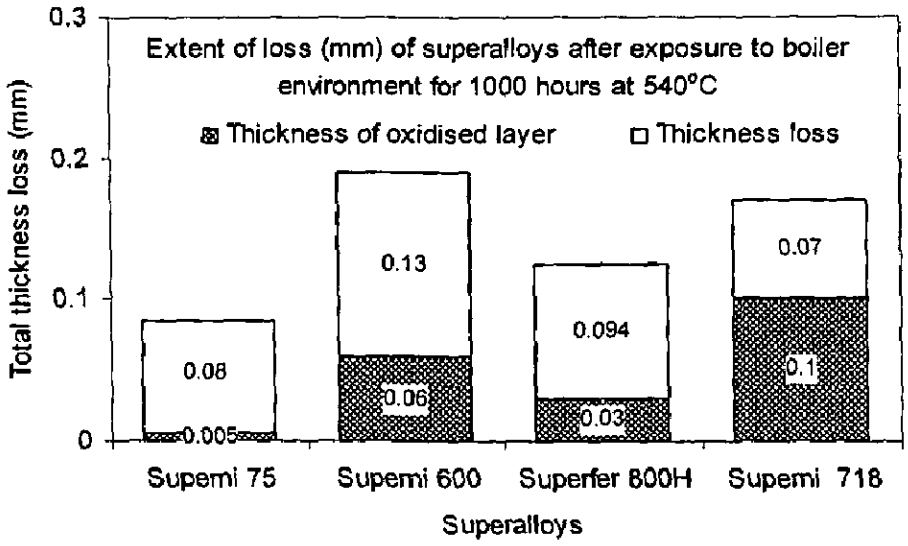

Fig. 7.3 Bar chart indicating the total thickness loss in mm by the uncoated superalloys after 1000 hours exposure to the coal fired boiler at 540°C.

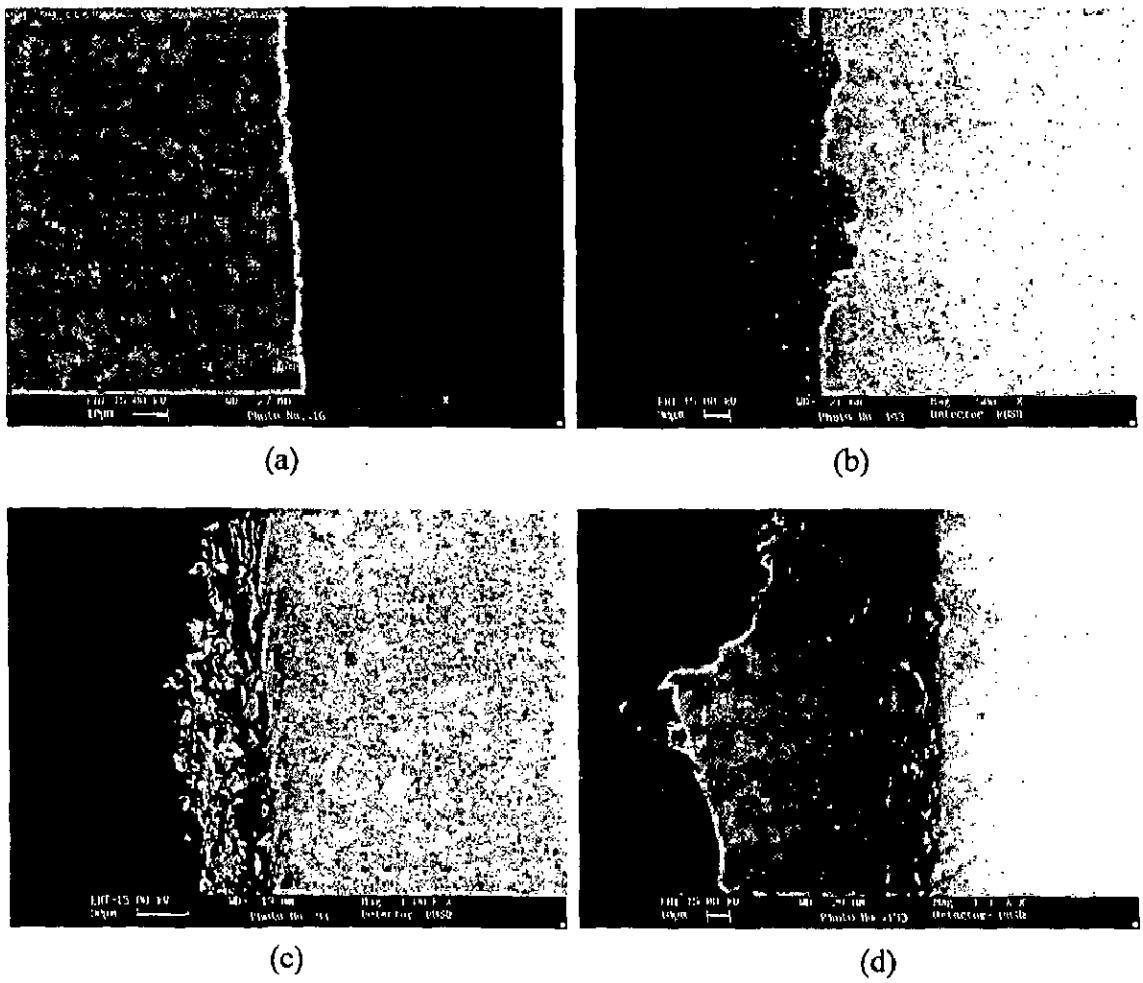

Fig. 7.4 SEM back scattered electron image along the cross-section for the uncoated superalloys exposed to the coal-fired boiler at 540°C for 1000 hours.

(a) Superni 75 (b) Superni 600 (c) Superfer 800H

(d) Superni 718

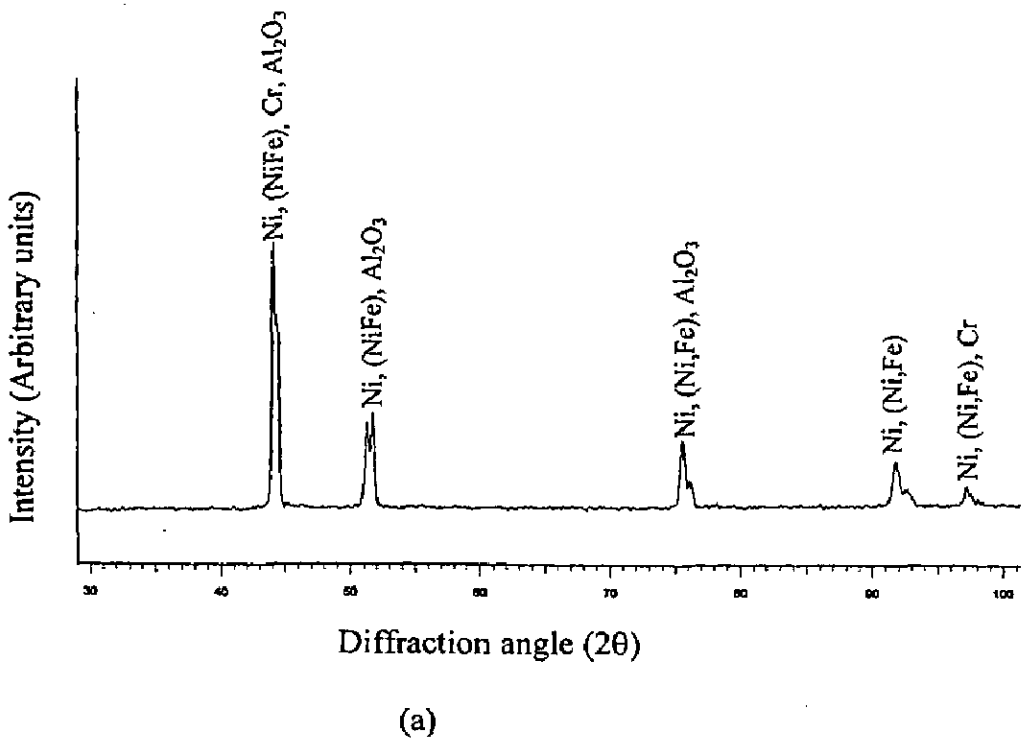

(a)

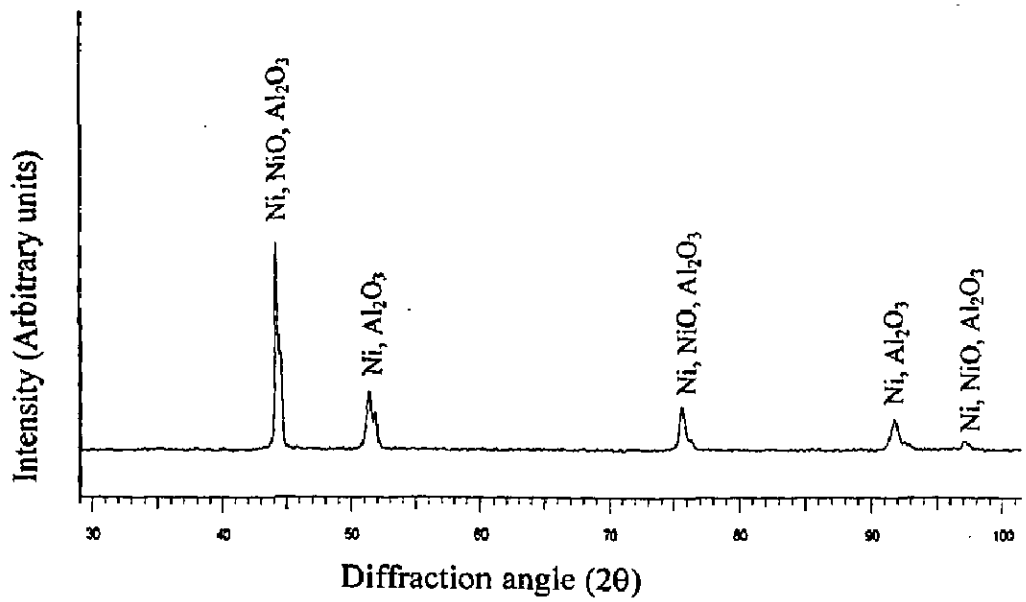

(b)

Fig. 7. 5 X-ray diffraction profiles for superalloys exposed to Low Temperature Primary Super Heater of the coal fired boiler for 1000 hours at 540°C.
(a) Superni 75 (b) Superni 600.

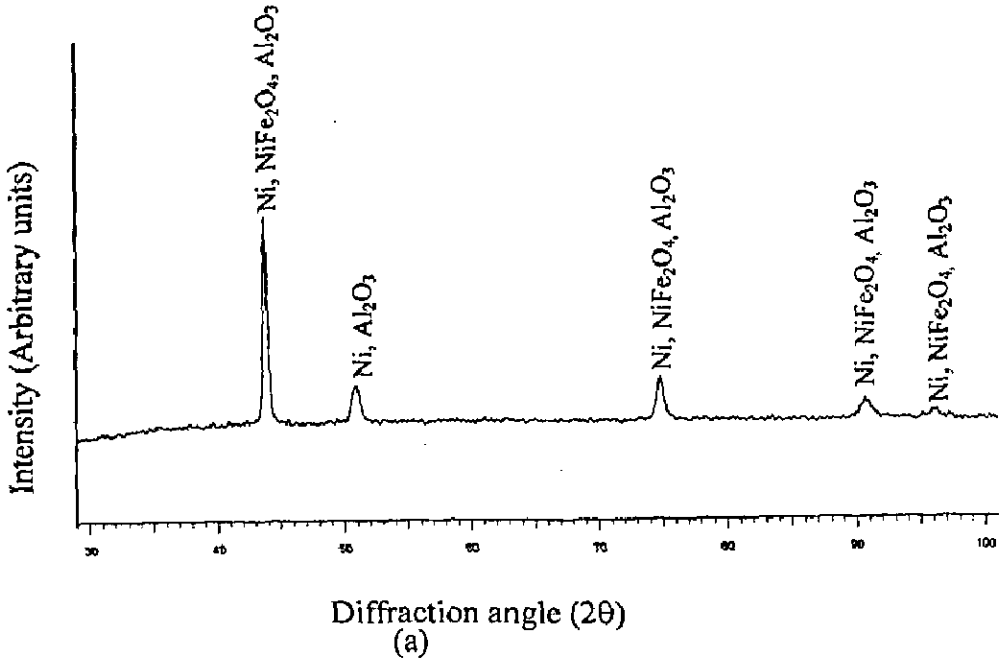

(a)

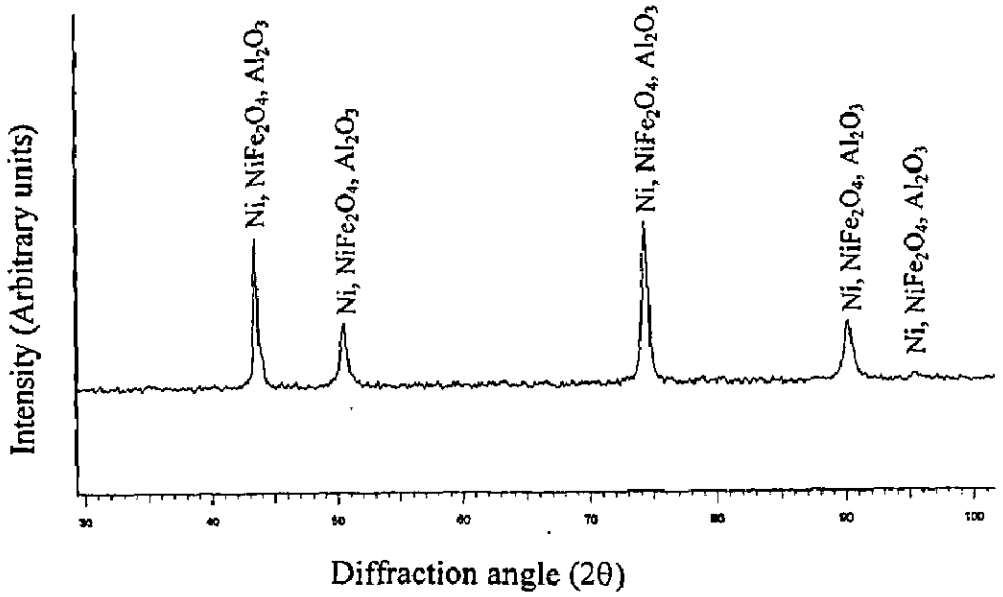

(b)

Fig. 7. 6 X-ray diffraction profiles for superalloys exposed to Low Temperature Primary Super Heater of the coal fired boiler for 1000 hours at 540°C.
(a) Superfer 800H (b) Superni 718.

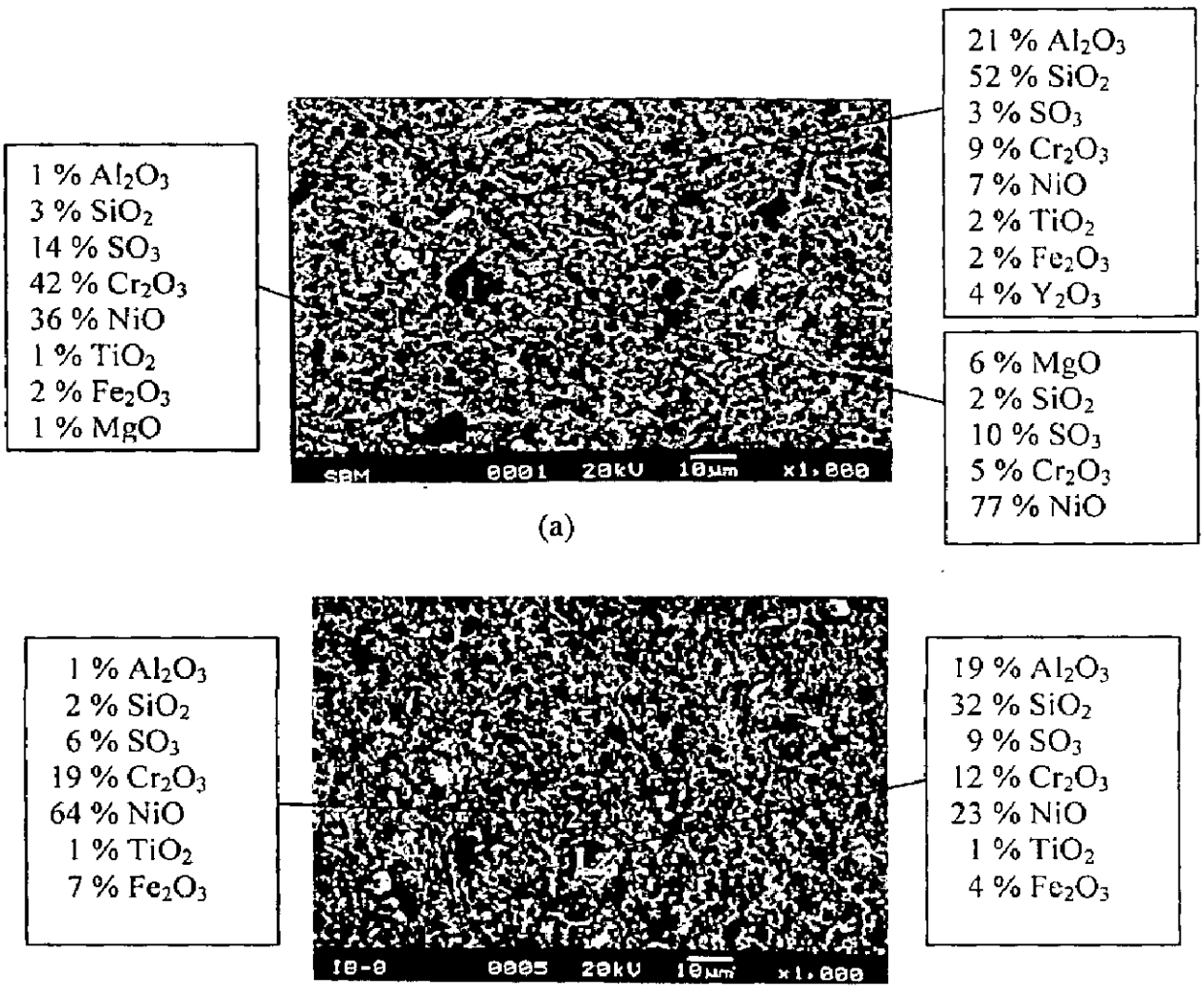

Fig. 7.7 SEM micrographs showing the surface morphology and EDAX analysis of superalloys exposed to coal-fired boiler for 1000 hours at 540°C.
(a) Superni 75 (b) Superni 600

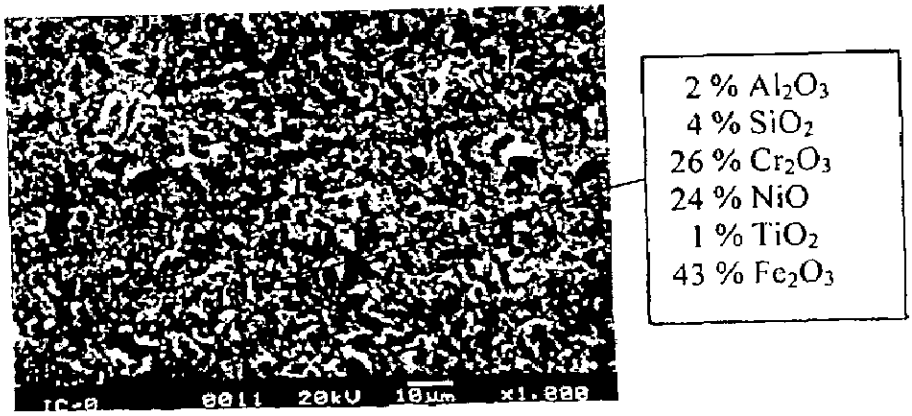

(a)

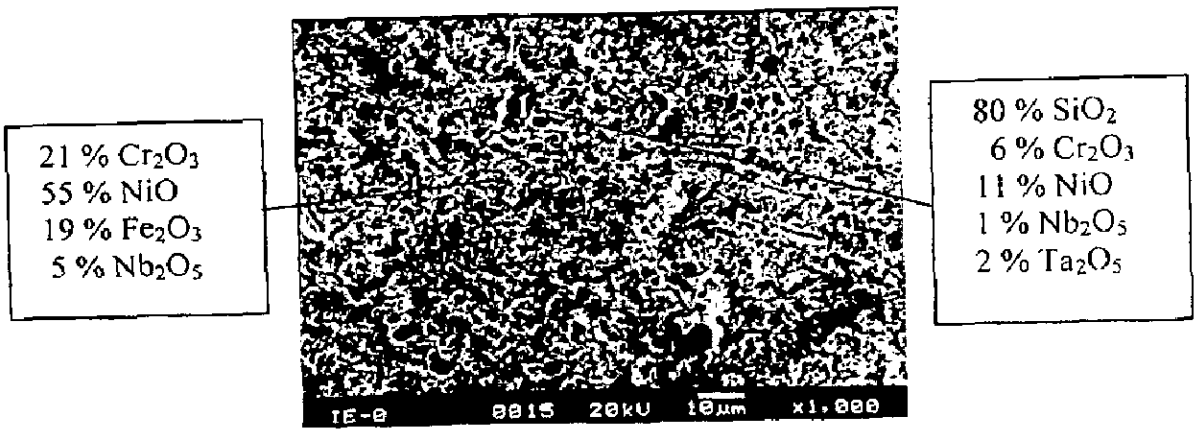

(b)

Fig. 7.8 SEM micrographs showing the surface morphology and EDAX analysis of superalloys exposed to coal-fired boiler for 1000 hours at 540°C.
(a) Superfer 800H (b) Superni 718.

7.1.1.4.1s Cross-Sectional Analysis

Cross-section morphologies for the Superni 75, 600, 718 and Superfer 800H superalloys after 1000 hrs exposure to the actual environment of the coal fired boiler are shown in Figs. 7.9 and 7.10. The SEM micrographs show scales for these superalloys after 1000 hrs of study, which consists of mainly nickel and iron oxides. Outer thin layer of the scale of Superfer 800H superalloy contains silicon whereas in case of Superni 718 superalloy this layer has higher percentage of silicon which is about 20 % at point 2 and 5 as evident from Fig. 7.10 (b). All the superalloys have also revealed presence of chromium in their scale and is about 20 % in case Superfer 800H and is 4 % in case of Superni 718. In case of Superni 600 and Superfer 800H, Mn is also present.

7.1.1.5 EPMA Analysis

BSEI and elemental X-ray maps obtained for the superalloys exposed to the boiler environment are shown in Figs. 7.11-7.14. The top layer contains mainly aluminium and silicon in all the exposed superalloys. EPMA analysis of exposed Superni 600 superalloy (Fig. 7.12) indicates a relatively thicker layer, which consists of mainly nickel, chromium, aluminium, silicon and oxygen. BSEI image of Superfer 800H (Fig. 7.13) shows the layer which consists of mainly nickel, chromium, aluminium and iron. Top thin layer of about 8 μm thickness is visible from the EPMA of Superni 718 (Fig. 7.14), which consists of mainly aluminium, silicon and oxygen.

7.1.2 Ni-Cr-Al-Y Coating

7.1.2.1 Visual Examination

Macrographs of NiCrAlY coated superalloys exposed to the given environment are shown in Fig. 7.15. No cracks and signs of spalling are observed on all the NiCrAlY coated superalloys. The colour of scale for NiCrAlY coated superalloys was grey which has turned to dark grey with increase in the exposure time. Even after 1000 hours of exposure there were no major sign of degradation of sample surfaces.

7.1.2.2 Thermogravimetric Data and Thickness Monitoring

The weight change data shown in Fig. 7.16 as a function of time expressed in hours for exposed NiCrAlY coated and uncoated superalloys have been plotted in order to assess the coating performance in actual coal-fired boiler environment. Coated Superni 75 superalloy has shown negligible weight change and seems to be providing very good protection. Exposed NiCrAlY coated Superni 600 superalloy has indicated weight loss and

was about 2 mg/cm^2. Whereas coated Superfer 800H has indicated lesser weight loss. Weight increase of about 1 mg/cm^2 was indicated by exposed NiCrAlY coating on Superni 718 superalloy substrate. The bar chart indicating the thickness loss for the exposed NiCrAlY coating on different superalloy substrates is shown in Fig. 7.17, whereas the cross-sectional BSEI image depicting the layer after exposure of 1000 hours at 540°C has been shown in Fig. 7.18. In case of exposed plasma sprayed coatings, the total thickness loss as shown in Fig. 7.17 has been obtained by adding the thickness change of exposed samples to the partially oxidised layer of coating. Erosion-corrosion loss of the exposed NiCrAlY coated Superni 75, Superni 600, Superfer 800H and Superni 718 superalloys are 0.46, 0.464, 0.02 and 0.4045 mm respectively.

7.1.2.3 X-ray Diffraction Analysis

The X-ray diffractograms for NiCrAlY coated superalloys after 1000 hours exposure to the coal fired boiler environment are shown in Fig. 7.19. The phases revealed by XRD analysis are Ni, NiO, $NiAl_2O_4$ and Al_2O_3.

7.1.2.4 SEM/EDAX Analysis

7.1.2.4.1 Surface Morphology

Surface EDAX of NiCrAlY coated superalloys subjected to boiler environment show mainly Cr_2O_3 and NiO on the top surface with embedded ash particles rich in alumina (Figs. 7.20 and 7.21). The micrograph of Superfer 800H superalloy reveals the white region (marked as 1 in Fig. 7.21) which contains higher percentage of oxides of aluminium (60%, Al_2O_3) along with chromium (27%, Cr_2O_3) whereas the dark region (indicated as 2) contains oxides of aluminium (29%, Al_2O_3), silicon (16% SiO_2), chromium (23% Cr_2O_3) and nickel (25% NiO). The surface micrograph of NiCrAlY coating on Superni 718 (Fig. 7.21(b)) has indicated NiO as the main phase along with small amount of chromium and aluminium oxides.

7.1.2.4.2 Cross-Sectional Analysis

Elemental variations across the cross-section of NiCrAlY coated superalloys after 1000 hours exposure in coal fired boiler are given in Figs. 7.22 and 7.23. EDAX analyses of the exposed coatings show the nickel rich splat regions of the coatings. Oxygen is present in the coatings at the places where nickel is absent or less. Further oxygen was higher at the points where aluminium is present, also chromium and yttrium exist in the oxygen rich region. These indicate the oxides of Al, Cr and Y along the splat boundaries of the exposed coating.

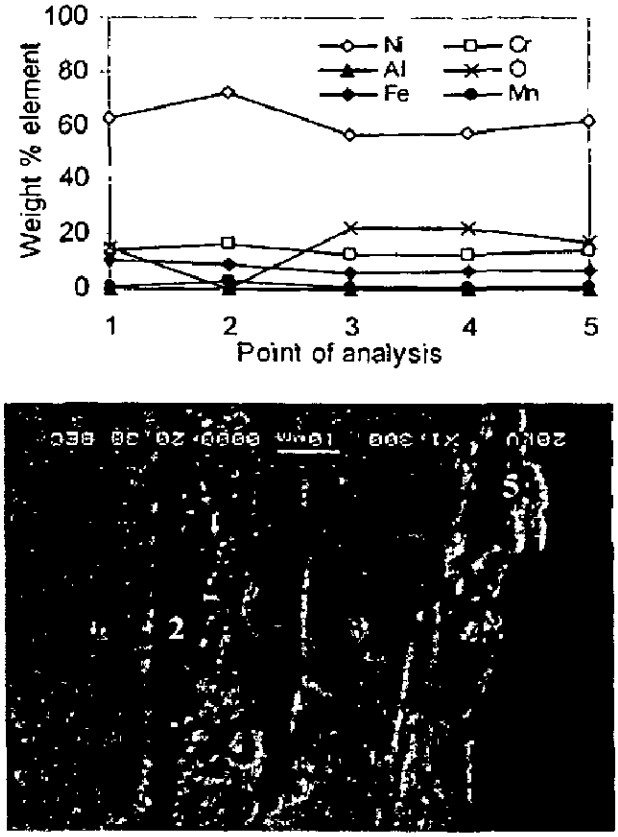

Fig. 7.9 Oxide scale morphology and elemental composition variation across the cross-section of Superni 600 superalloy exposed to boiler of thermal power plant for 100 hours at 540°C.

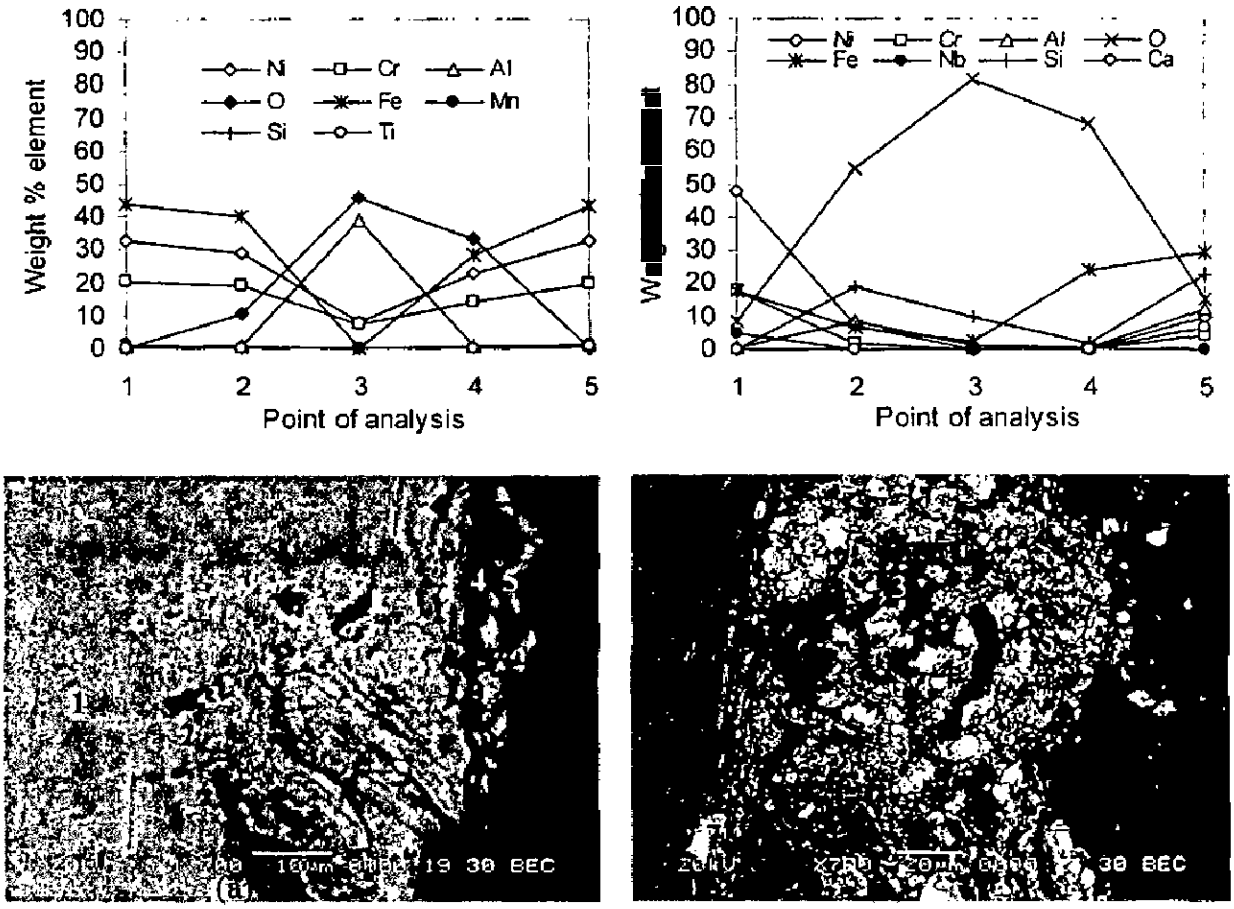

Fig. 7.10 Oxide scale morphology and elemental composition variation across the cross-section of superalloys exposed to boiler of thermal power plant for 1000 hours at 540°C.

(a)Superfer 800H (b) Superni 718.

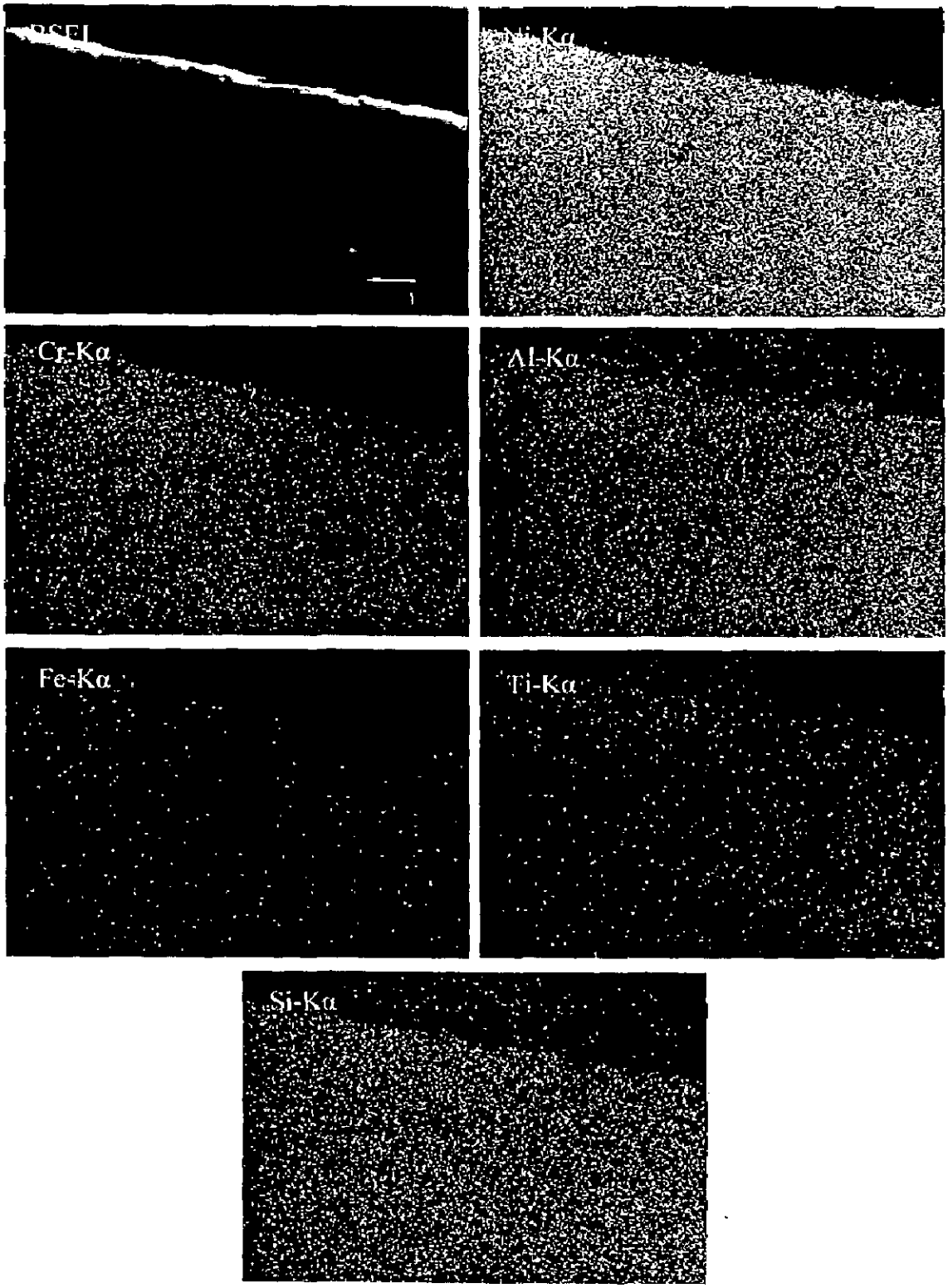

Fig. 7. 11 BSEI and X-ray elemental mapping of the cross-section of Superni 75 superalloy exposed to the boiler of the thermal power plant at 540°C for 1000 hours.

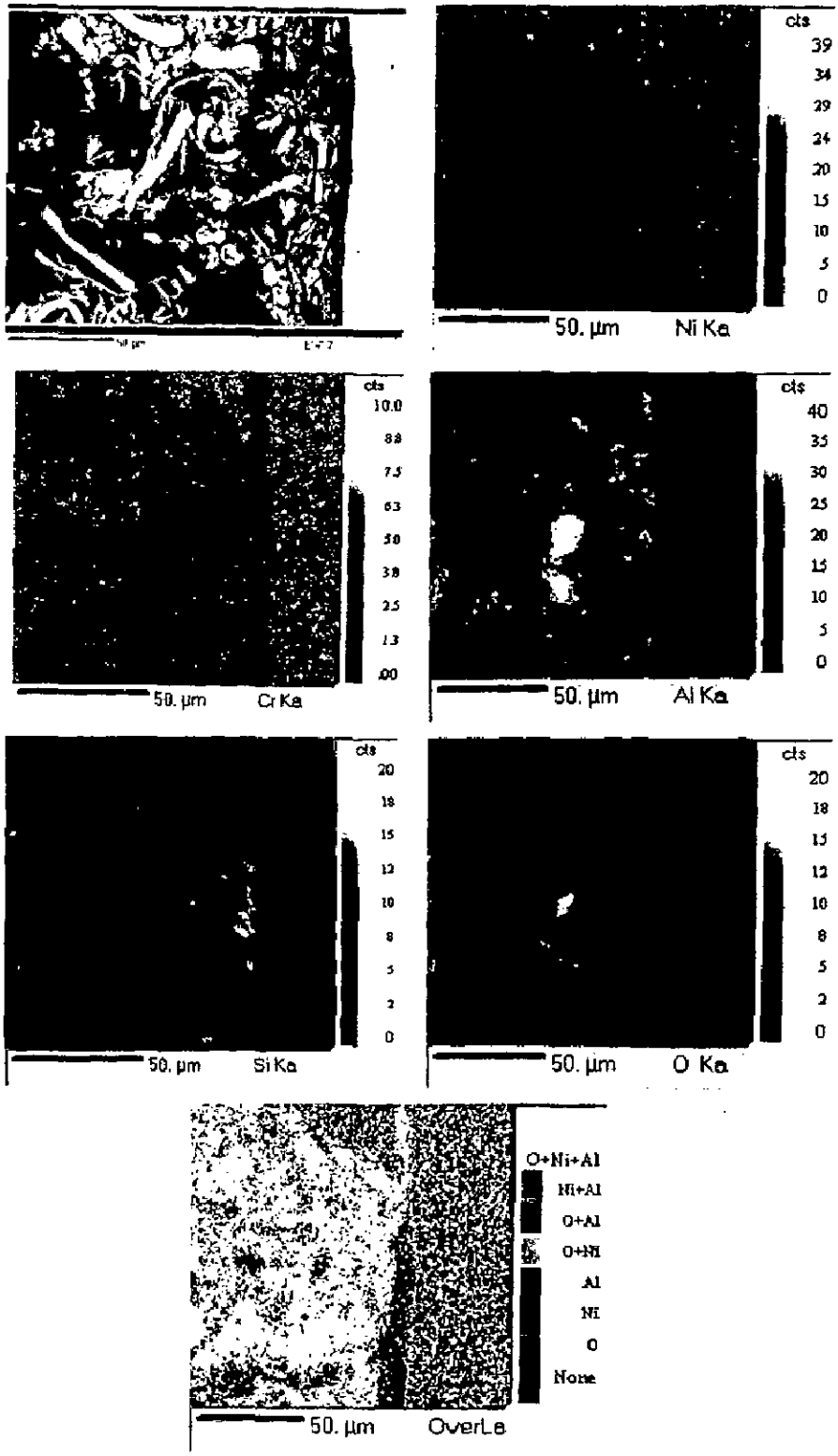

Fig.7.12 BSEI and elemental X-ray mapping of the cross-section of Superni 600 superalloy substrate exposed to boiler of thermal power plant for 1000 hours at 540°C.

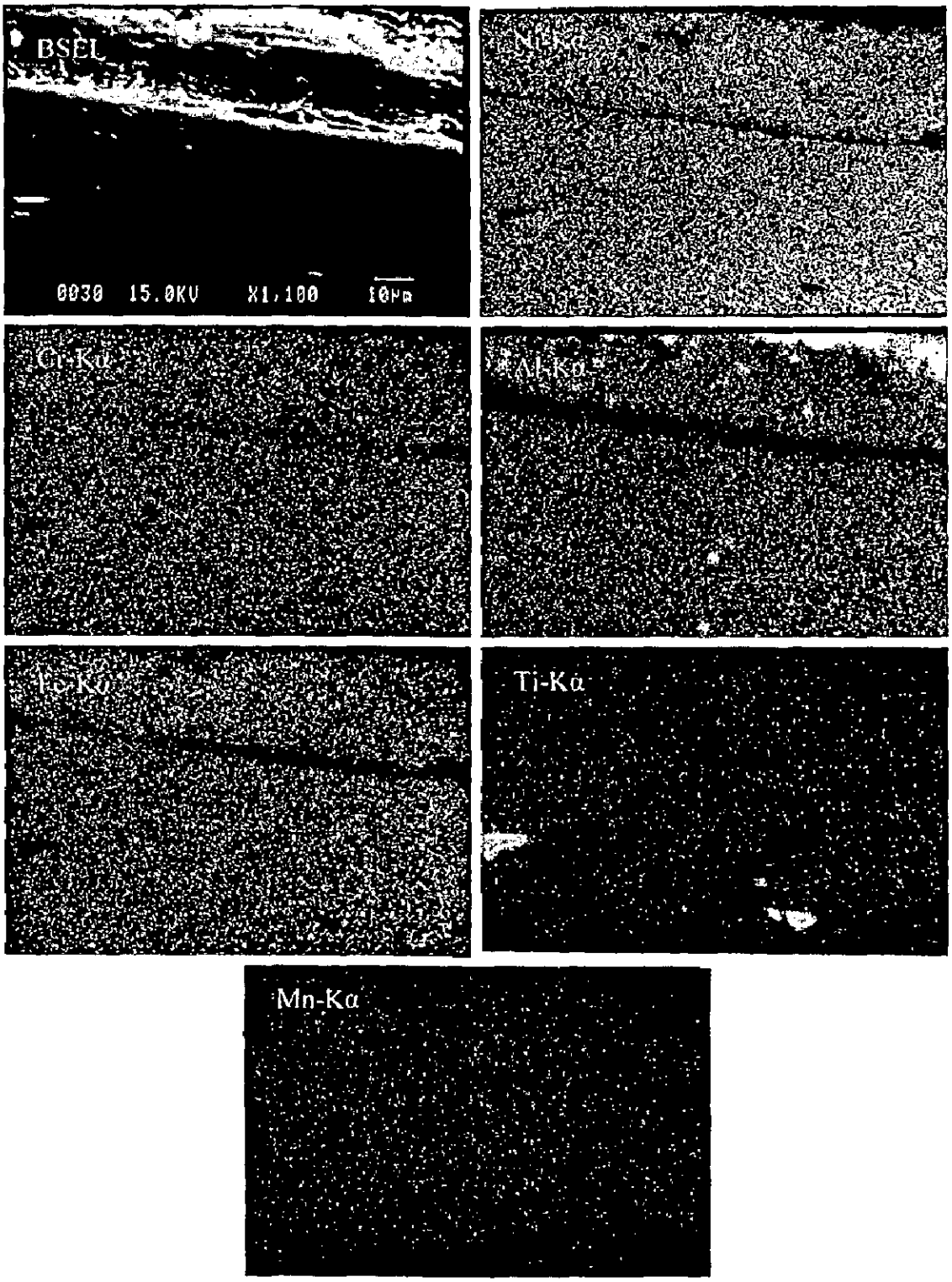

Fig.7. 13 BSEI and elemental X-ray mapping of the cross-section of Superfer 800H superalloy substrate exposed to boiler of thermal power plant for 1000 hours at 540°C.

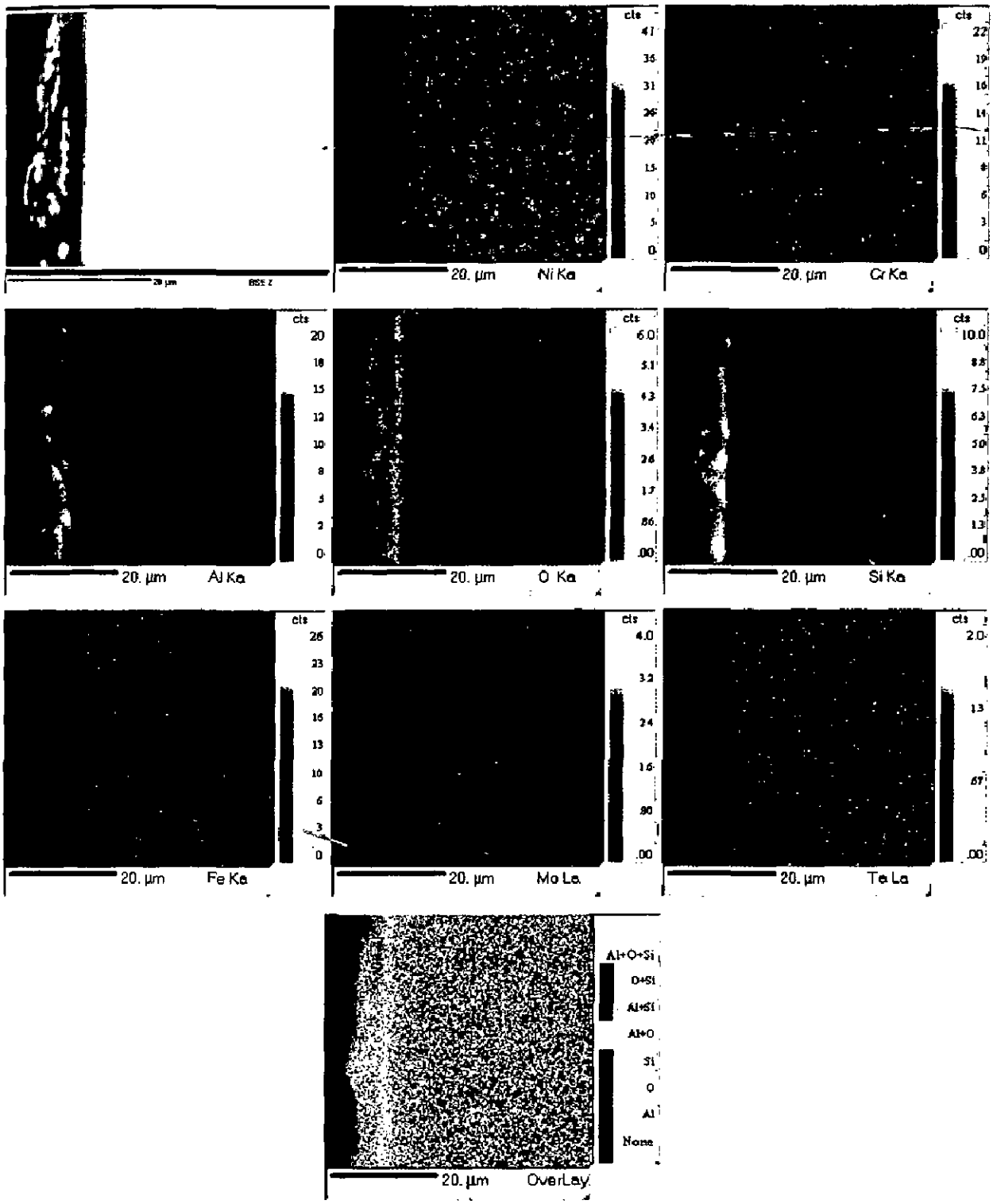

Fig. 7.14 BSEI and elemental X-ray mapping of the cross-section of Superni 718 superalloy substrate exposed to boiler of thermal power plant for 1000 hours at 540°C.

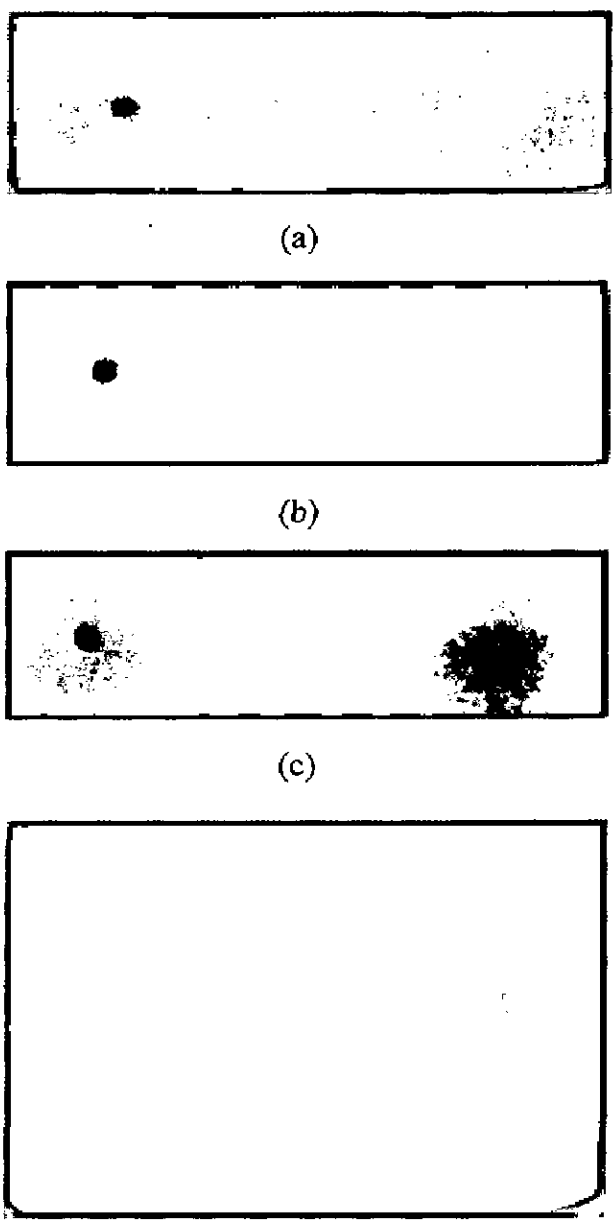

Fig. 7.15 Macrographs of plasma sprayed NiCrAlY coating on superalloys exposed to coal-fired boiler at 540°C for 1000 hours.

(a) Superni 75 (b) Superni 600

(c) Superfer 800H (d) Superni 718.

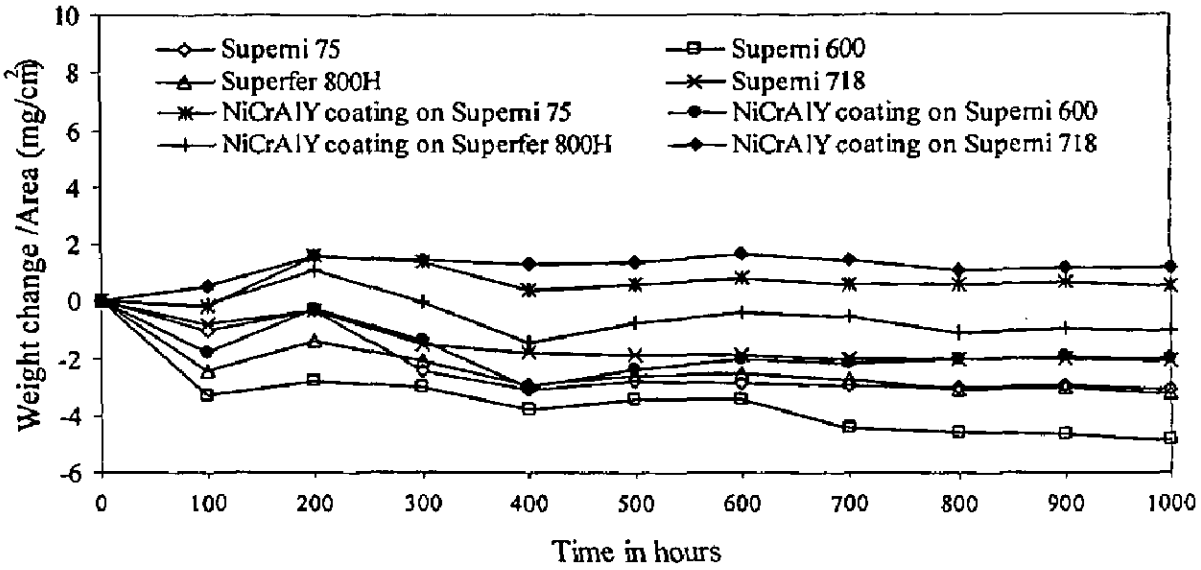

Fig. 7.16 Weight change versus time in hours plot for uncoated and NiCrAlY coated superalloys exposed to the coal fired boiler for 1000 hours at 540°C.

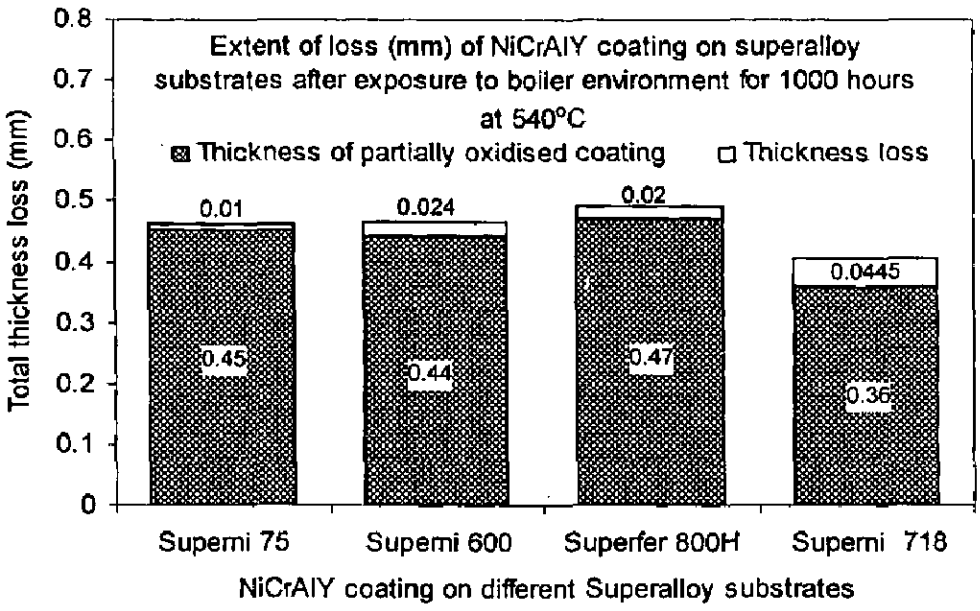

Fig. 7.17 Bar chart indicating the total thickness loss in mm for NiCrAlY coating on different superalloy substrates after 1000 hours exposure to the coal fired boiler at 540°C.

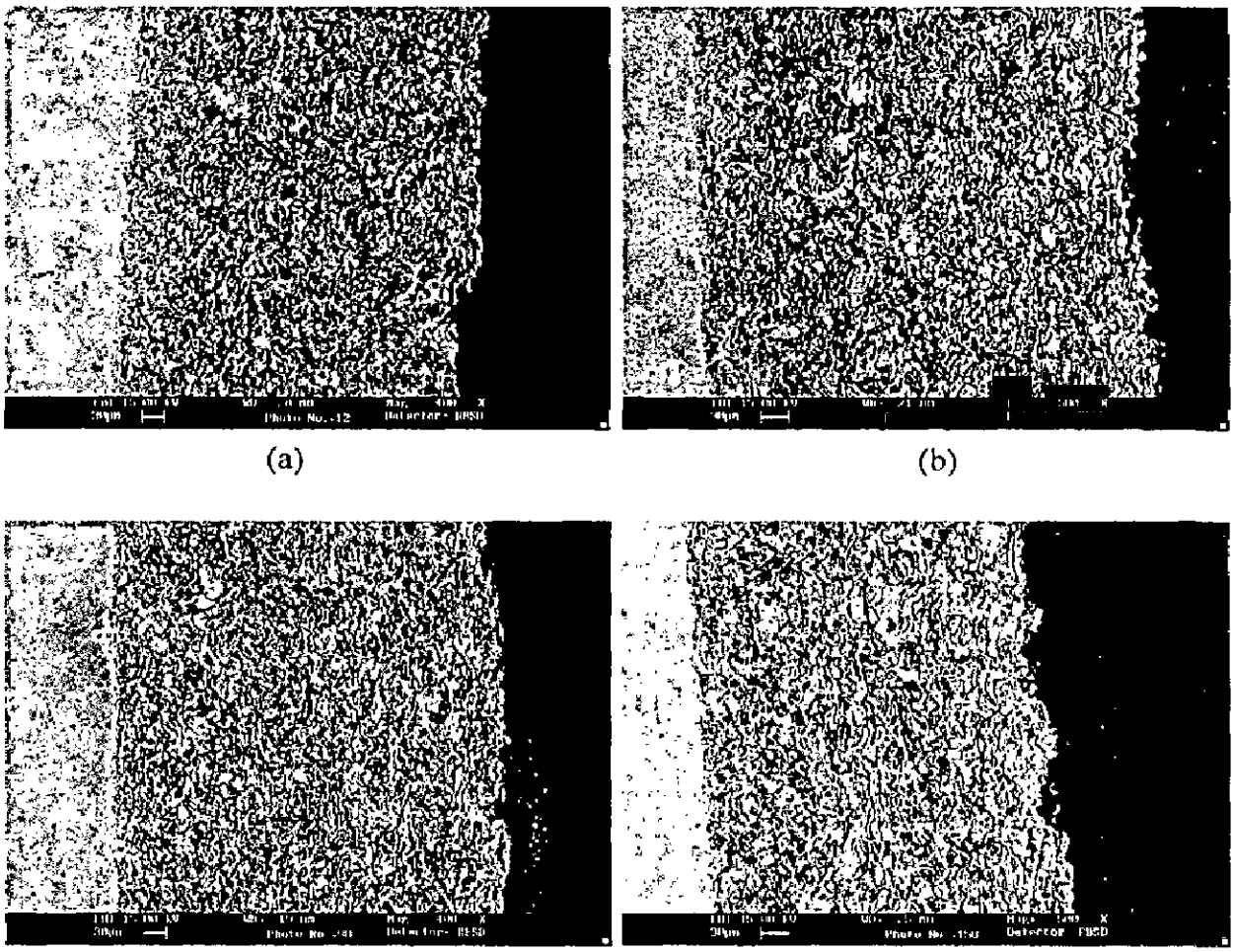

(a) (b)

(c) (d)

Fig. 7.18 SEM back scattered electron image along the cross-section for the NiCrAlY coated superalloys exposed to the coal-fired boiler at 540°C for 1000 hours.

(a) Superni 75 (b) Superni 600 (c) Superfer 800H

(d) Superni 718

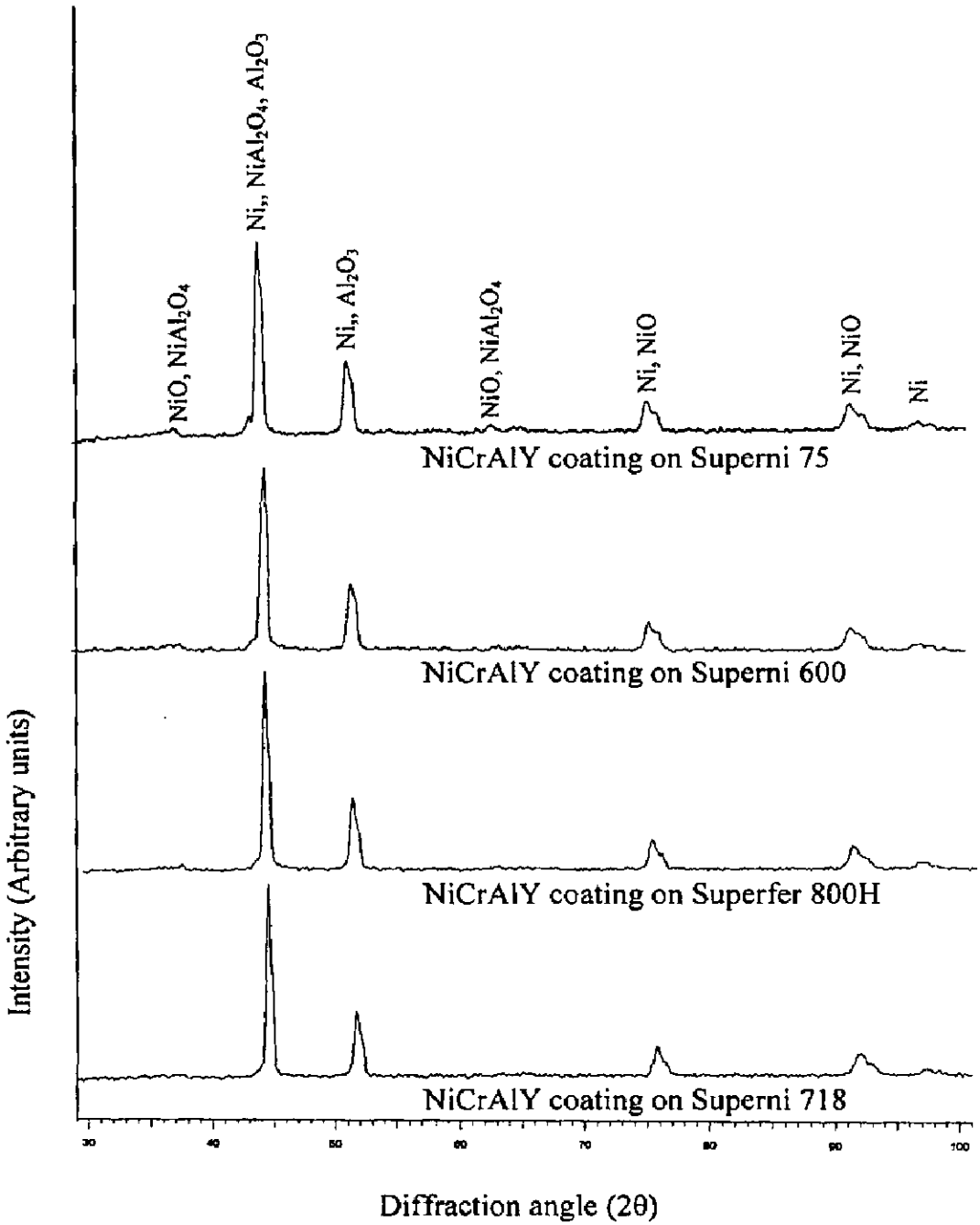

Fig. 7.19 X-ray diffraction profiles for Plasma Spray NiCrAlY coating on Superni 75, Superni 600, Superfer 800H and Superni 718 superalloy substrates exposed to Low Temperature Primary Super Heater of the coal fired boiler for 1000 hours at 540°C.

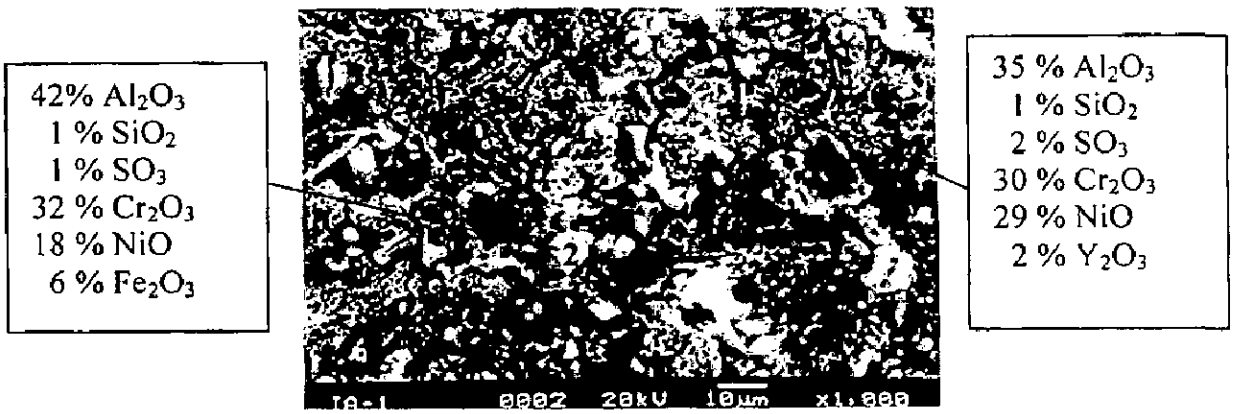

(a)

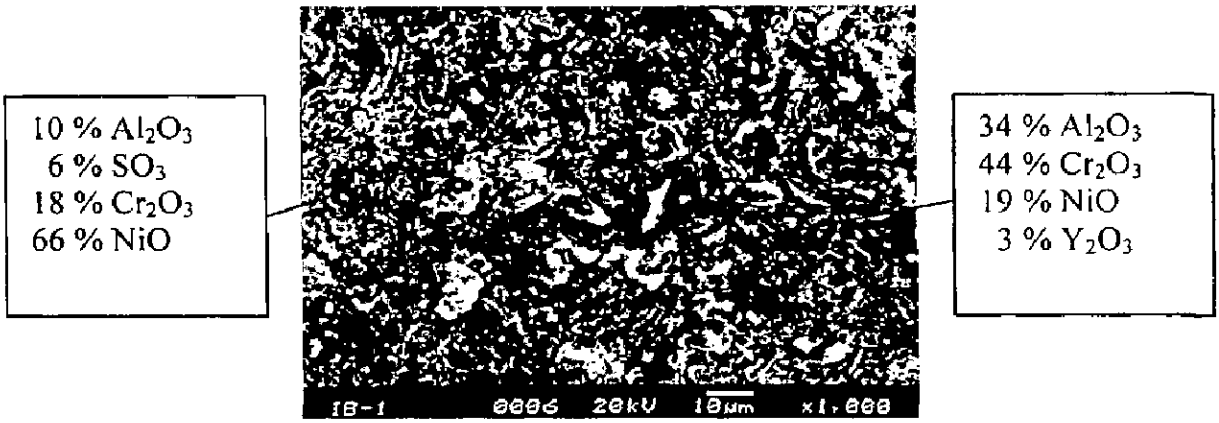

(b)

Fig. 7.20 SEM micrographs showing the surface morphology and EDAX analysis for NiCrAlY coating on superalloys exposed to coal fired boiler for 1000 hours at 540°C

(a) Superni 75 (b) Superni 600.

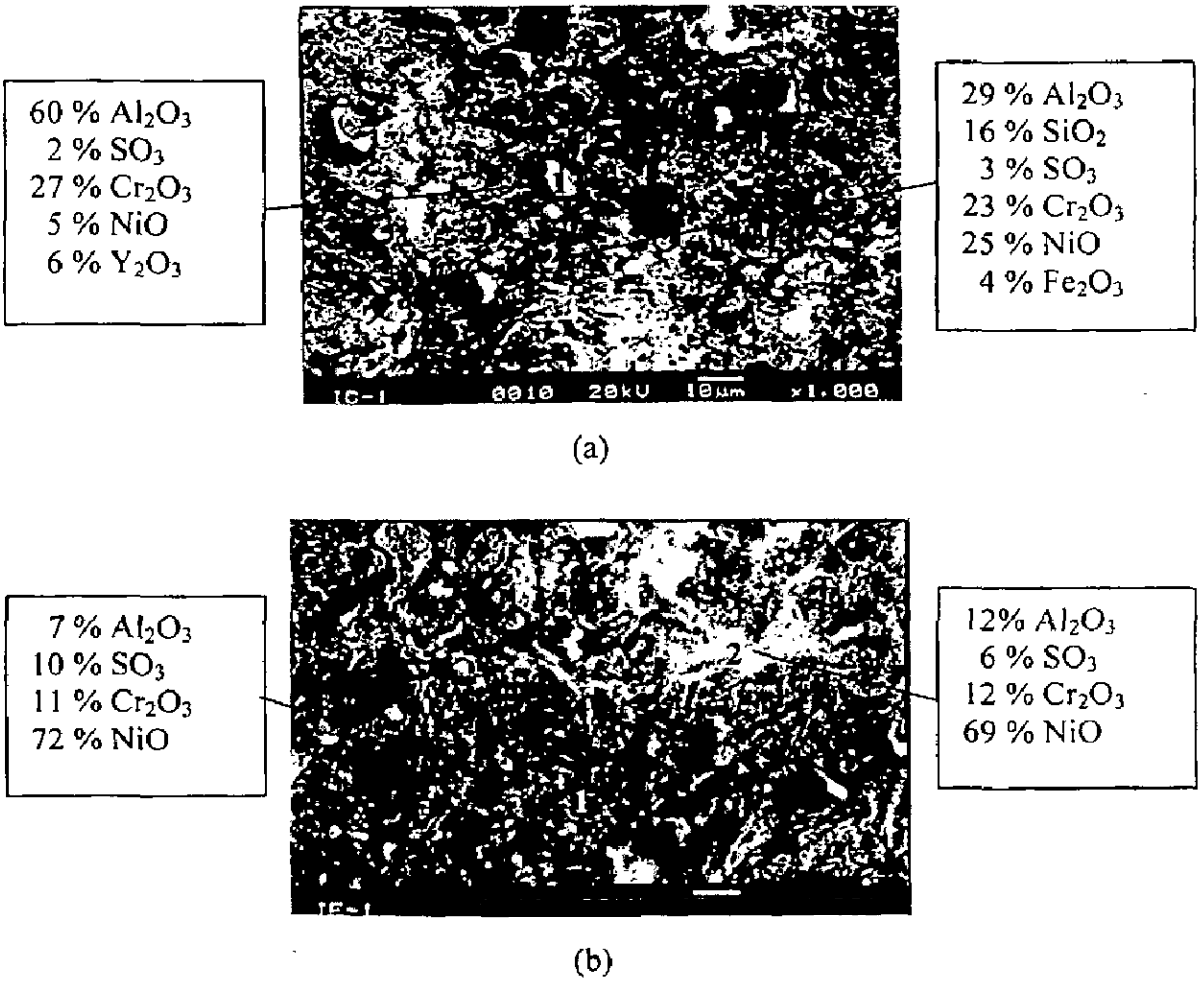

Fig.7.21 SEM micrographs showing the surface morphology and EDAX analysis for NiCrAlY coating on superalloys exposed to coal fired boiler for 1000 hours at 540°C.

(a) Superfer 800H (b) Superni 718.

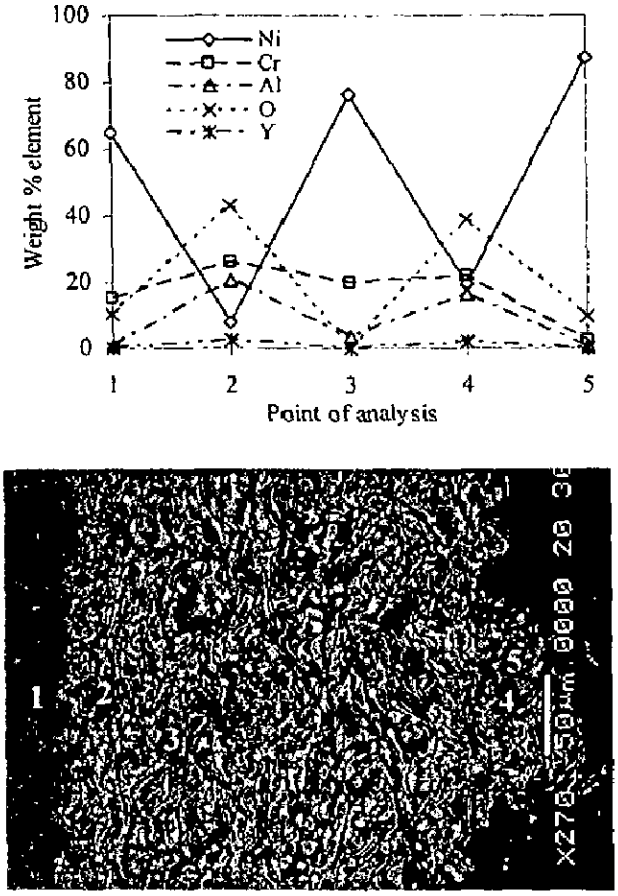

Fig. 7.22 Oxide scale morphology and elemental composition variation across the cross-section of NiCrAlY coated Superni 600 superalloy exposed to boiler of thermal power plant for 1000 hours at 540°C.

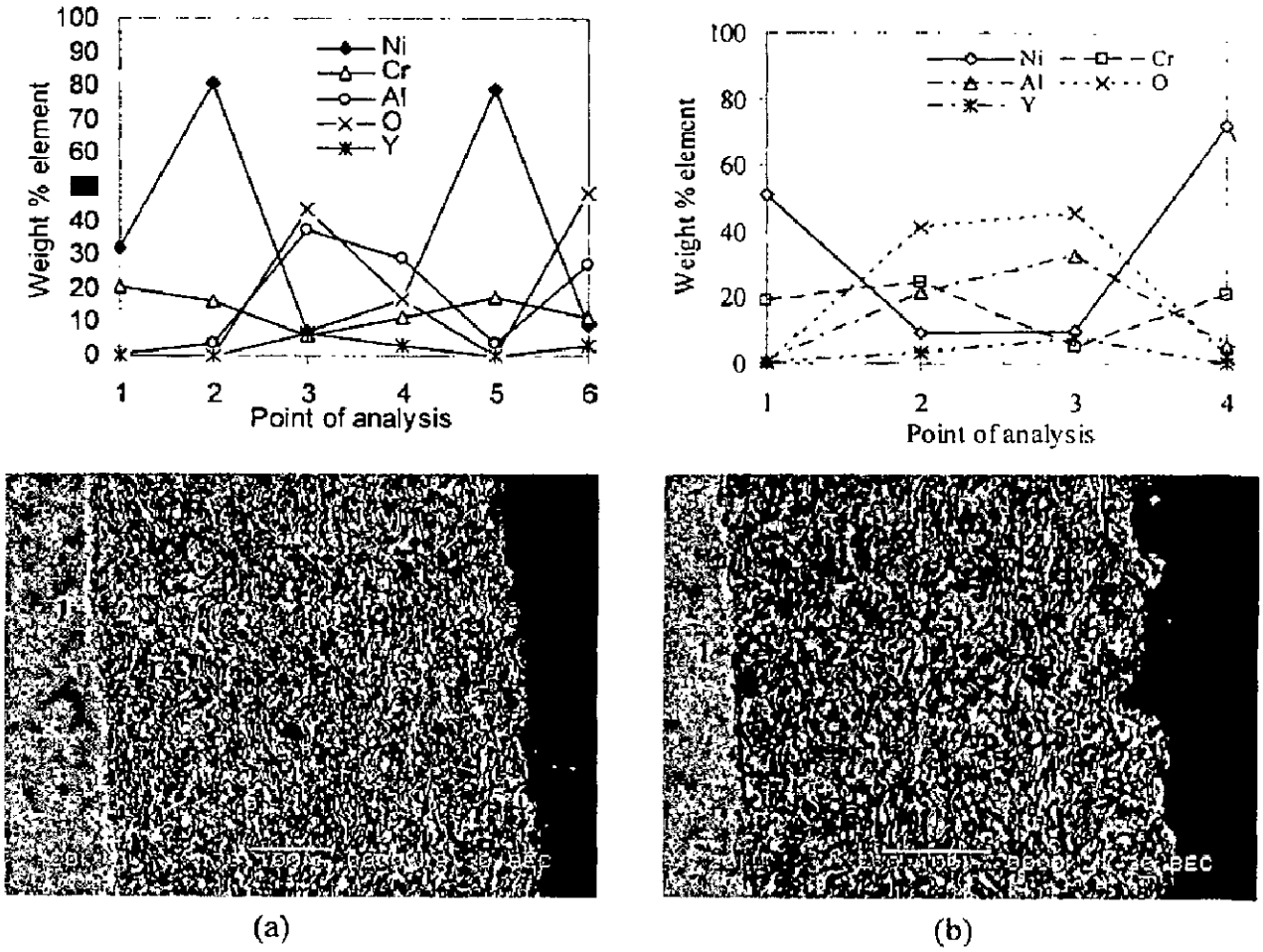

Fig. 7.23 Oxide scale morphology and elemental composition variation across the cross-section of NiCrAlY coating on superalloys exposed to boiler of thermal power plant for 1000 hours at 540°C
(a) Superfer 800H (b) Supermi 718.

7.1.2.5 EPMA Analysis

EPMA along the cross-section for the exposed NiCrAlY coating on different superalloys substrates can be seen in the Figs. 7.24-7.27. Nickel, chromium, aluminium and yttrium are the main elements present in the coatings. Presence of iron is also indicated in all the exposed coatings indicating the diffusion of iron from the substrates. Titanium and silicon are present in the exposed coated Superni 75 and 718 superalloys whereas manganese is observed in exposed coated Superni 600 and Superfer 800H superalloys, indicating the diffusion of these elements from the respective substrate superalloys into the coatings. Also traces of tantalum and molybdenum are present in the exposed coated Superni 718 superalloy indicating the diffusion of these elements from the substrate. The presence of Si and Al at the top of the scale along with Fe might be the indication of ash deposition. BSEI and elemental mapping of NiCrAlY coating on Superni 600 superalloy substrate (Fig. 7.25) shows the top layer of about 20 μm thickness and consists of mainly oxygen, aluminium and silicon.

7.1.3 Ni-20Cr Coating

7.1.3.1 Visual Examination

Macrograph of the plasma sprayed Ni-20Cr coated superalloys after exposure of 1000 hours in coal fired boiler of the power plant at about 540 ^{0}C are shown in Fig. 7.28. For all the coated superalloys the light grey colour scale was noticed after first cycle of 100 hours. Even after 1000 hours of exposure the coating was intact and did not show any crack. Final thin layer in case of all the Ni-20Cr coated superalloys was basically of dark brown colour.

7.1.3.2 Thermogravimetric Data and Thickness Monitoring

Weight change values as a function of time for Ni-20Cr coated superalloys are presented in Fig. 7.29. For this Ni-20Cr coating, the weight loss is noticed for coated Superni 75 superalloy and weight gain is observed in coated Superni 600, 718 and Superfer 800H superalloys. The lowest weight gain value was observed for coated Superni 718 superalloy, followed by Superni 600. The weight gain per unit area was highest in case of Ni-20Cr coated Superfer 800H and it was four times than that of coated Superni 718. Coated Superni 75, 600, 718 and Superfer 800H superalloys allowed the oxidising interface to penetrate up to 0.388, 0.359, 0.48 and 0.33 mm respectively into the specimen respectively after 1000 hours exposure in the coal fired boiler as evident from Fig. 7.30 and Fig. 7.31.

7.1.3.3 X-ray Diffraction Analysis

The XRD pattern of the scale on the coated superalloys after exposure to coal fired boiler environment at about 540 ^{0}C for 1000 hours shows similar phases for all the superalloys as indicated in Fig. 7.32. The phases revealed by XRD analysis are manily NiO, Cr_2O_3, $NiCr_2O_4$ and Al_2O_3.

7.1.3.4 SEM/EDAX Analysis

7.1.3.4.1 Surface Morphology

Fig. 7.33 (a) is an SEM micrograph of coated Superni 75 superalloy and indicates a spongy scale which mainly contains NiO, Cr_2O_3, Al_2O_3, and SiO_2. In the black area marked as point 1, there is perhaps ash embedded in the scale which consists of Al_2O_3 and SiO_2 with some amount of sulphur and iron oxide. There are white particles rich in NiO and Cr_2O_3 having some sulphur (point 2). The scale of Ni-20Cr coated Superni 600 superalloy after exposure contains mainly NiO and Cr_2O_3 as evident from Fig. 7.33 (b). There is a white area (point 2) that contains mainly NiO along with some amount of Cr_2O_3 (2%) and SO_3 (22%).

The Ni-20Cr coating on Superfer 800H superalloy after exposure of 1000 hours shows mainly NiO and Cr_2O_3 with small amounts of sulphur, silicon and iron oxides (Fig. 7.34 (a)). Whereas for Ni-20Cr coated Superni 718 superalloy again main scale contains NiO and Cr_2O_3 with sulphur and silicon oxides as seen from Fig. 7.34 (b).

7.1.3.4.2 *Cross-Sectional Analysis*

Scale morphology and EDAX analysis for the corroded cross-section of Ni-20Cr coated superalloys after 1000 hours exposure is shown in Figs. 7.35 and 7.36. In all the exposed Ni-20Cr coated superalloys nickel and chromium exist in the outer part with some amount of oxygen. Further it can be seen from Fig. 7.35 and Fig. 7.36 that the points where nickel is higher, oxygen content is lower, whereas higher amount of oxygen was observed with chromium, aluminium and yttrium along the splat interface. Aluminium has diffused into the top coat from bond coat whereas iron has remained confined in the substrate. Bond coat has retained its identity by forming oxides of aluminium, chromium and yttrium along the nickel rich splats. These are the indication of oxygen penetration into the coated superalloys along the intersplat interface.

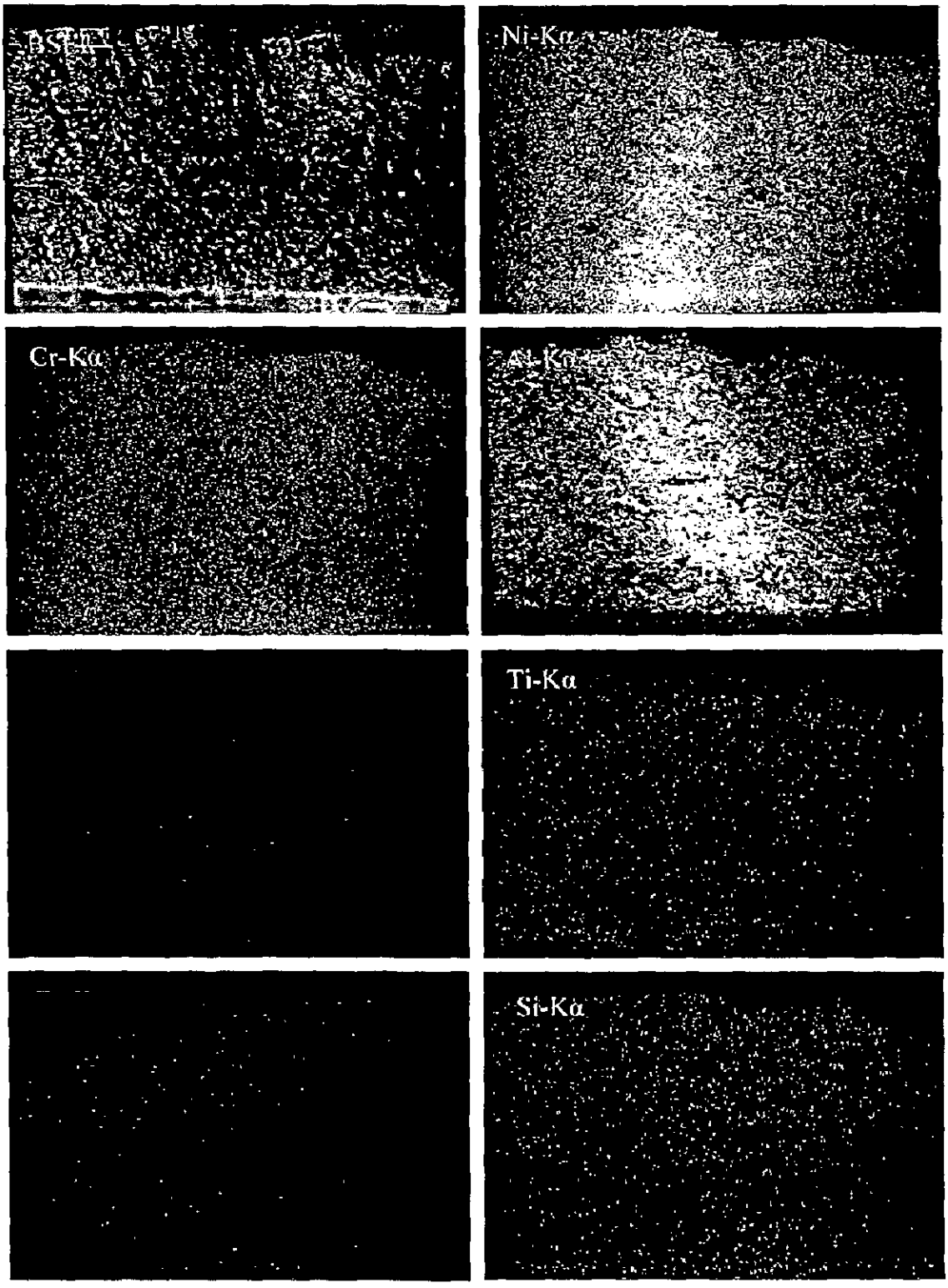

Fig. 7.24 BSEI and elemental X-ray mapping of the cross-section of NiCrAlY coating on Superni 75 superalloy substrate exposed to boiler of thermal power plant for 1000 hours at 540°C.

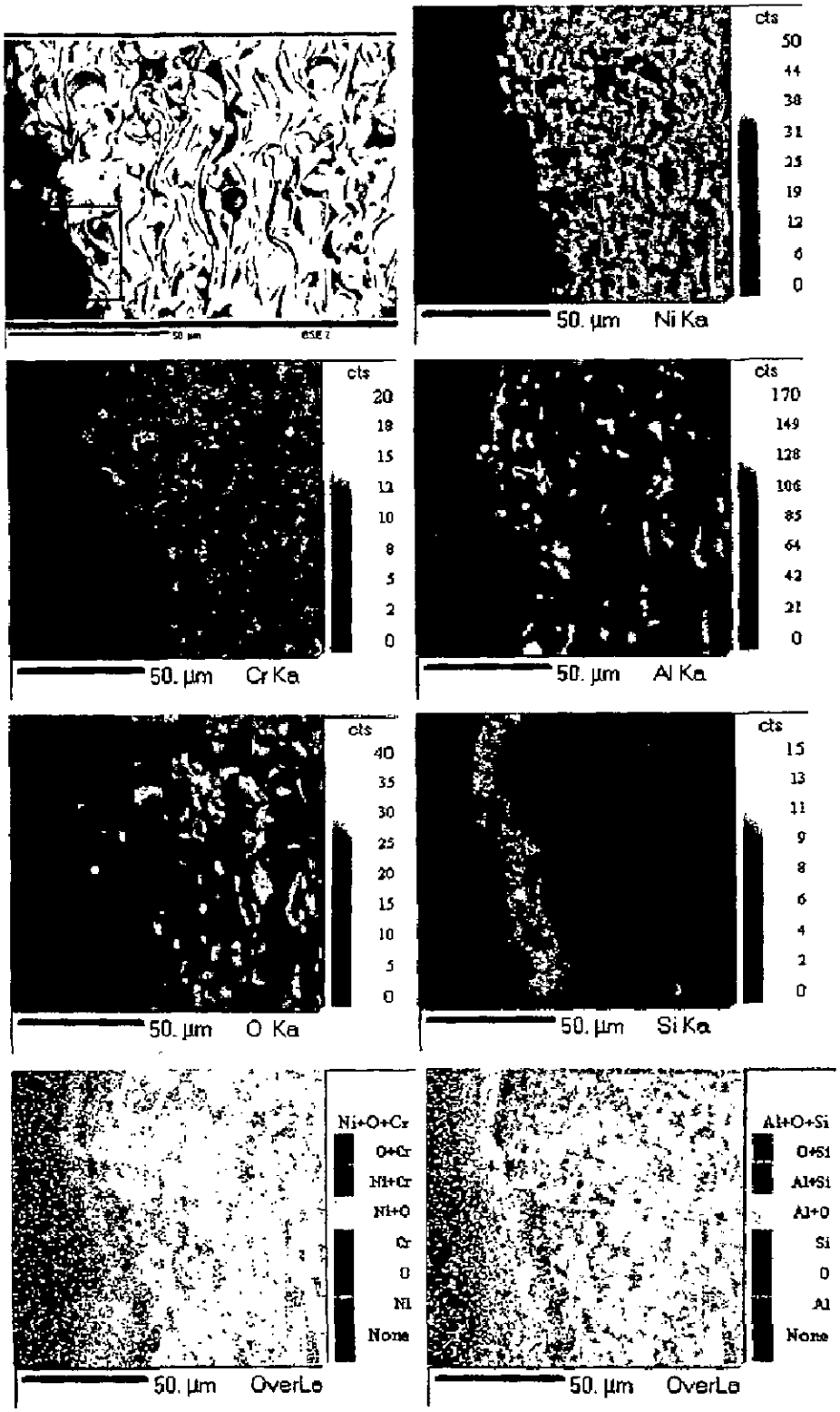

Fig.7.25 BSEI and elemental X-ray mapping of the cross-section of NiCrAlY coating on Superni 600 superalloy substrate exposed to boiler of thermal power plant for 1000 hours at 540°C.

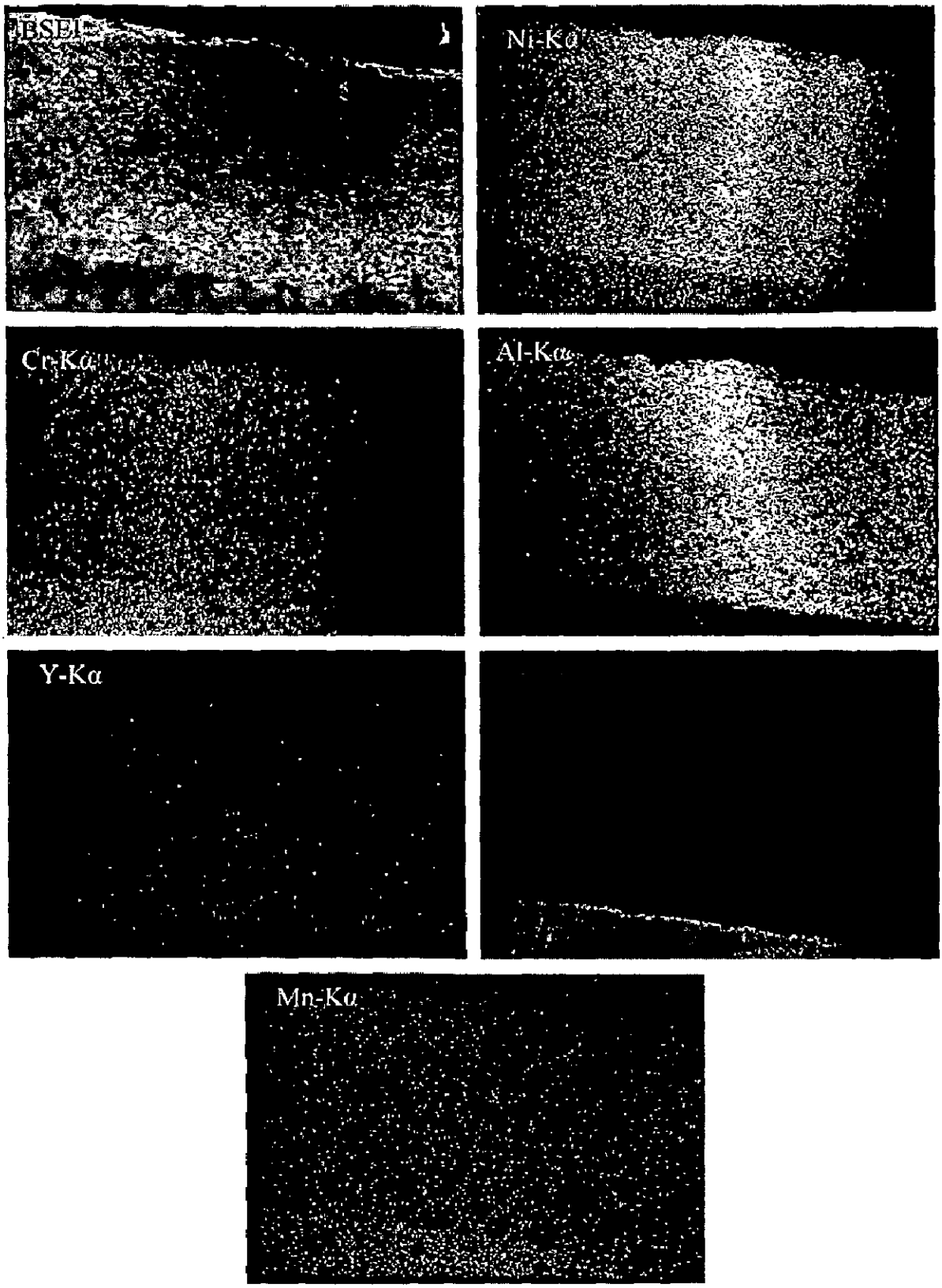

Fig. 7.26 BSEI and elemental X-ray mapping of the cross-section of NiCrAlY coating on Superfer 800H superalloy substrate exposed to boiler of thermal power plant for 1000 hours at 540°C.

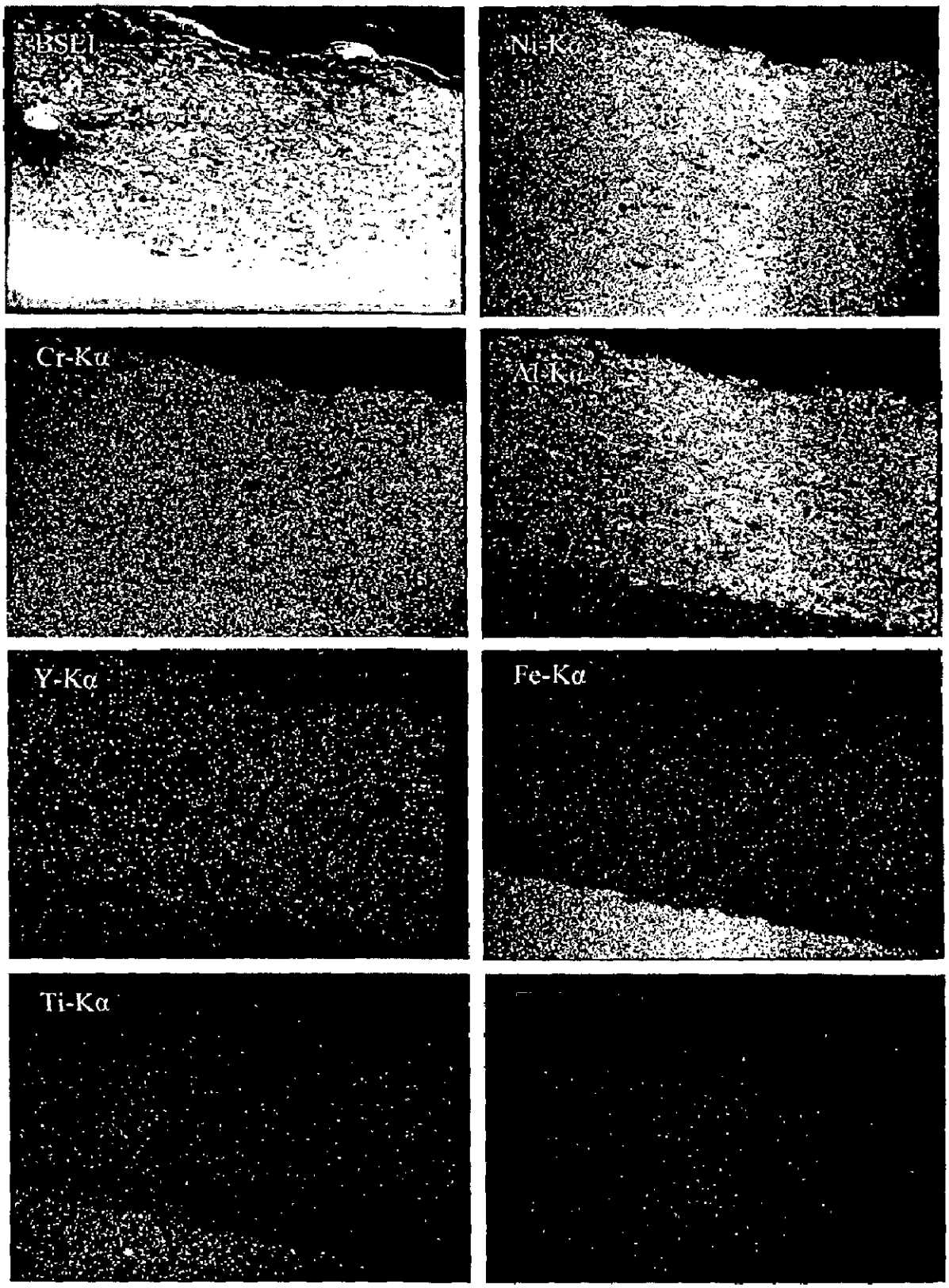

Fig. 7.27 BSEI and elemental X-ray mapping of the cross-section of NiCrAlY coating on Supemi 718 superalloy exposed to boiler of thermal power plant for 1000 hours at 540°C.

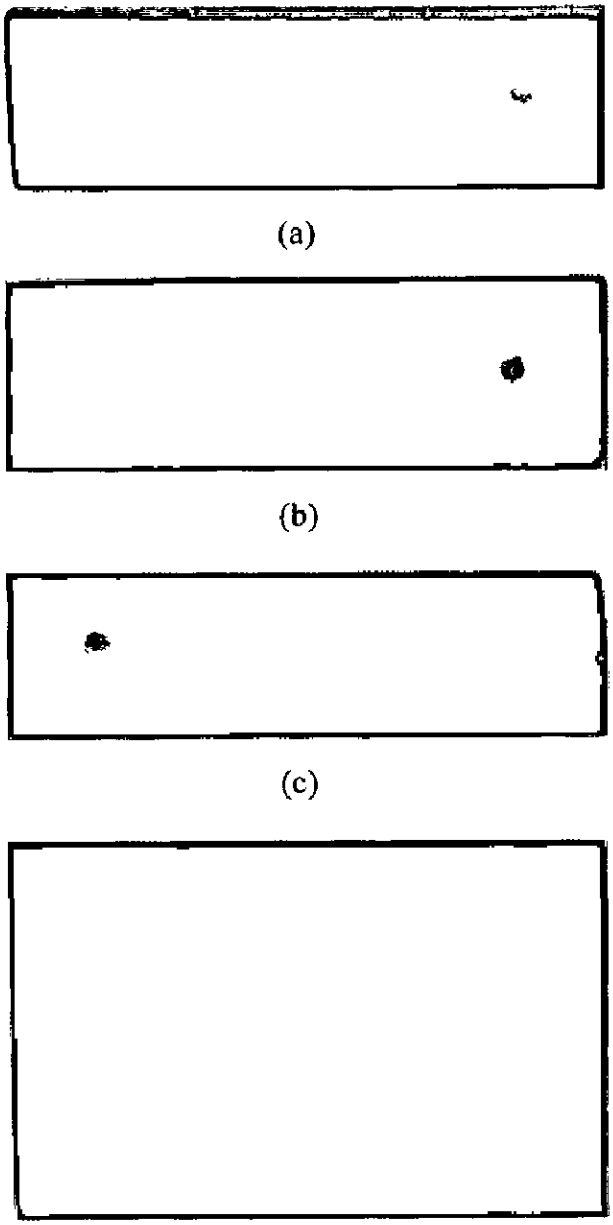

Fig. 7.28 Macrographs of plasma sprayed Ni-20Cr coating with bond coat of NiCrAlY coating on superalloys subjected to coal-fired boiler at 540°C for 1000 hours.

(a) Superni 75 (b) Superni 600 (c) Superfer 800H

(d) Superni 718

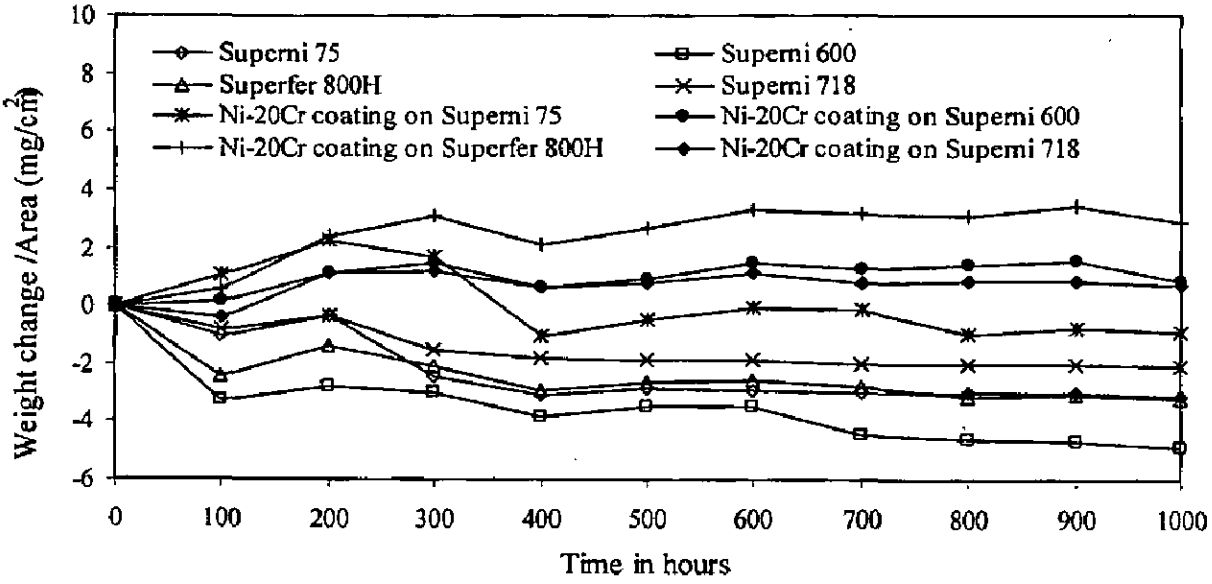

Fig. 7.29 Weight change versus time in hours plot for uncoated and Ni-20Cr coated superalloys with bond coat of NiCrAlY coating exposed to coal fired boiler for 1000 hours at 540°C.

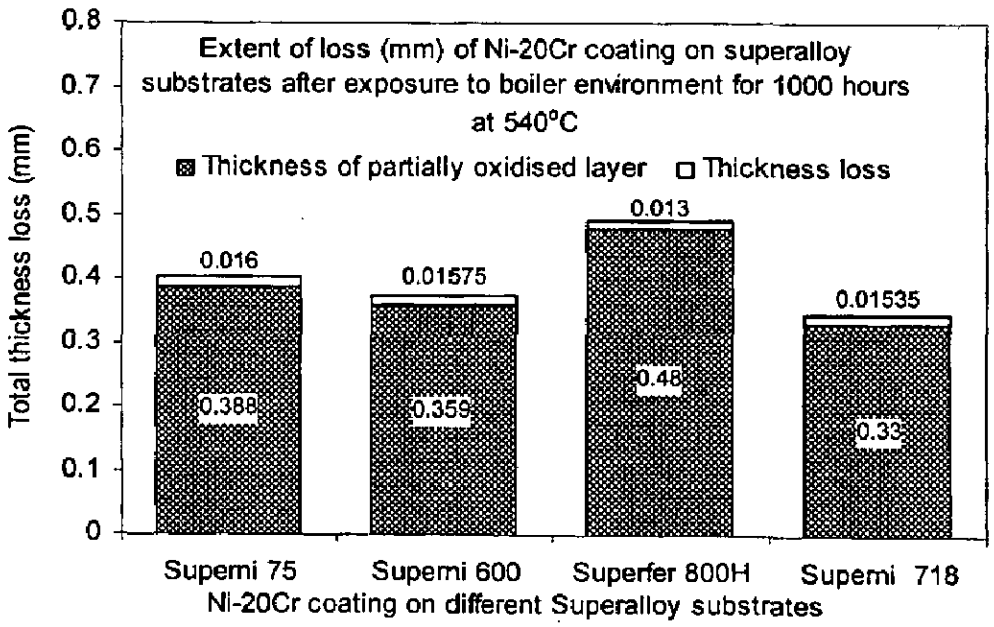

Fig. 7.30 Bar chart indicating the total thickness loss in mm for Ni-20Cr coating on different superalloy substrates after 1000 hours exposure to the coal fired boiler at 540°C.

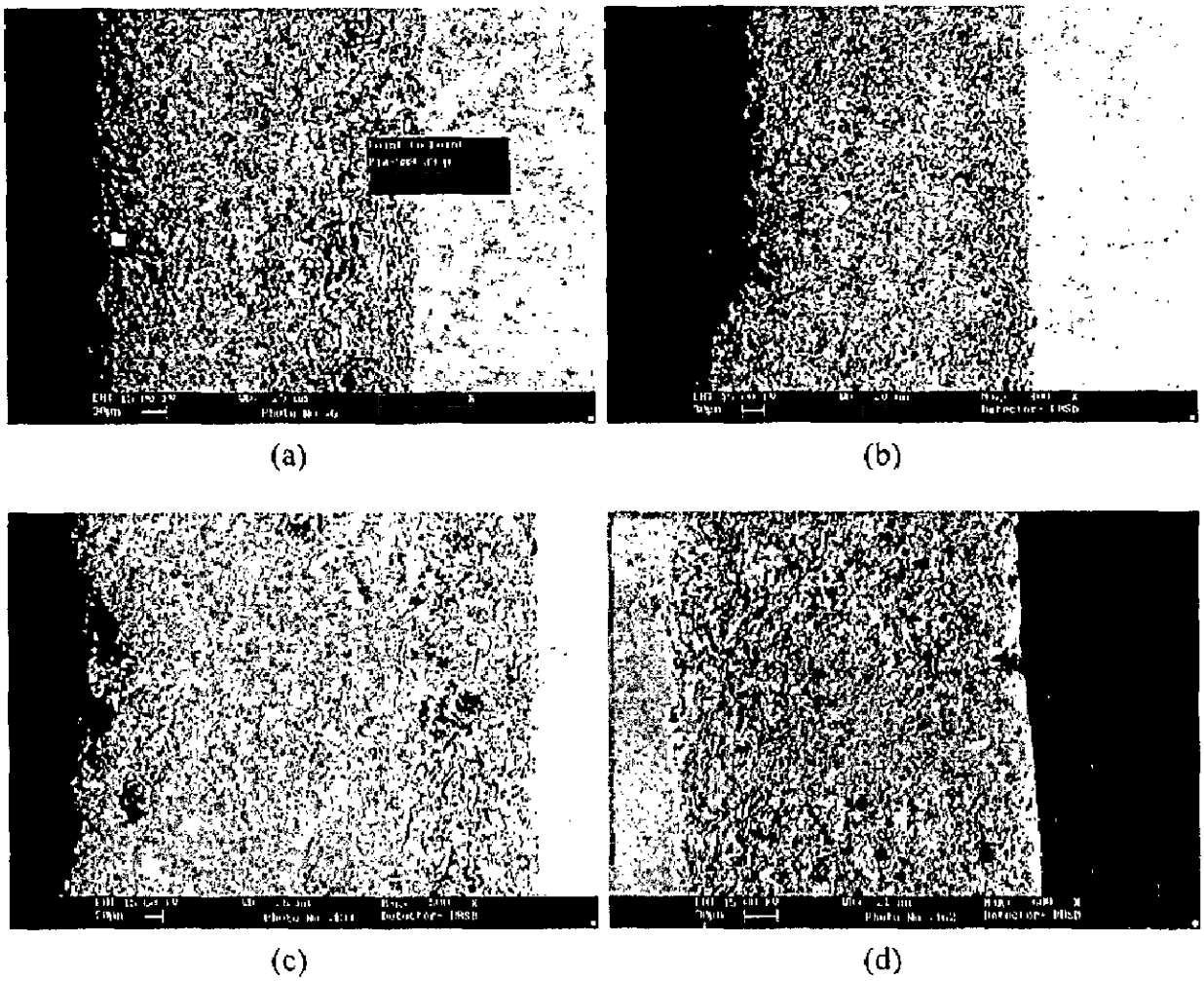

Fig. 7.31 SEM back scattered electron image along the cross-section for the Ni-20Cr coating on different substrate superalloys exposed to the coal-fired boiler at 540°C for 1000 hours.

(a) Superni 75 (b) Superni 600 (c) Superfer 800H

(d) Superni 718

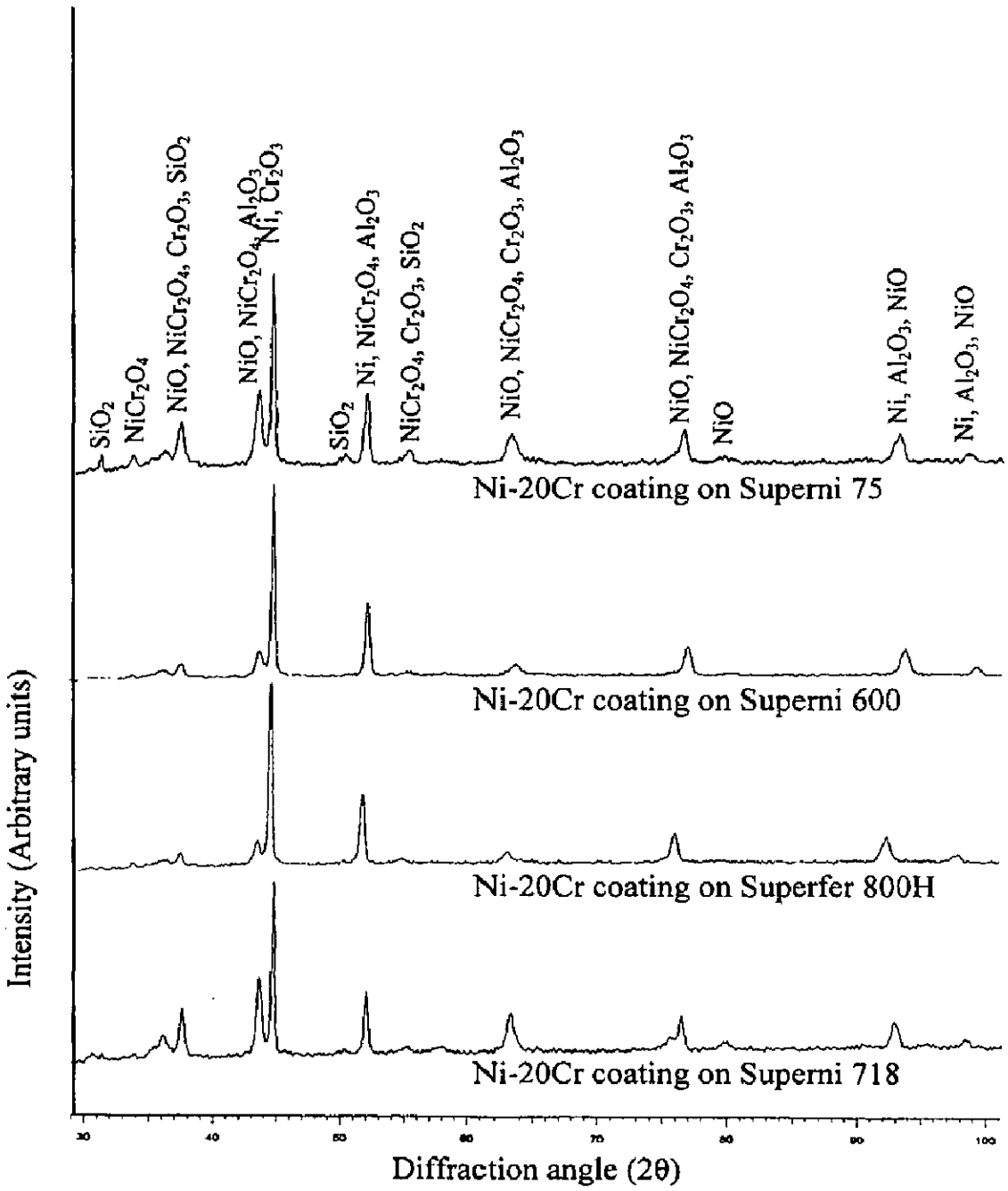

Fig. 7.32 X-ray diffraction profiles for Plasma Sprayed Ni-20Cr coating with bond coat of NiCrAlY coating on Superni 75, Superni 600, Superfer 800H and Superni 718 superalloys substrates exposed to Low Temperature Primary Super Heater of the coal fired boiler for 1000 hours at 540°C.

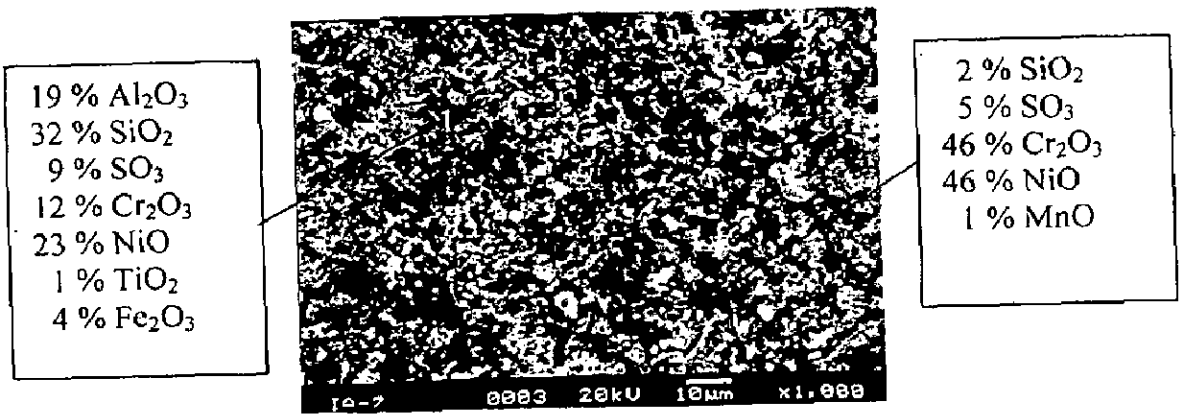

(a)

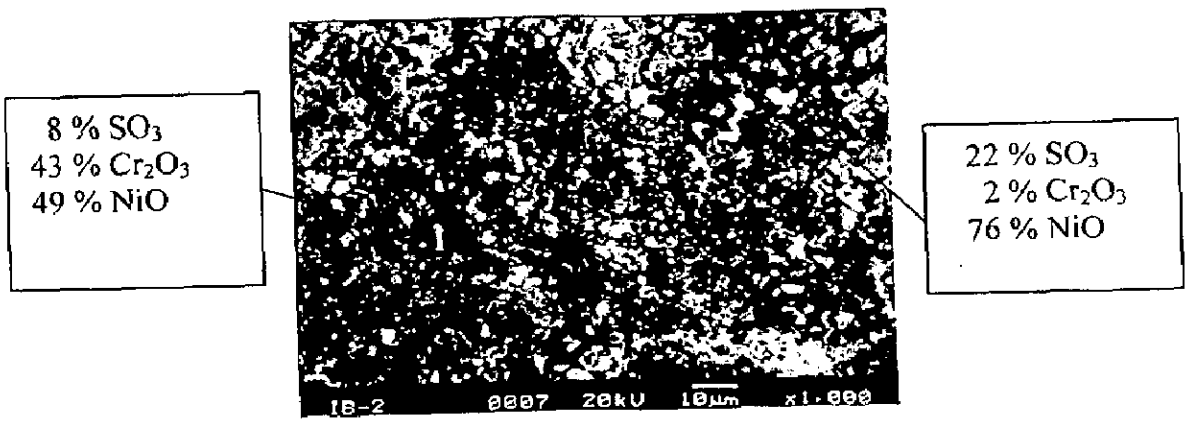

(b)

Fig. 7.33 SEM micrographs showing the surface morphology and EDAX analysis for Ni-20Cr coating with bond coat of NiCrAlY coating on superalloys exposed to coal fired boiler for 1000 hours at 540°C.

(a) Superni 75 (b) Superni 600

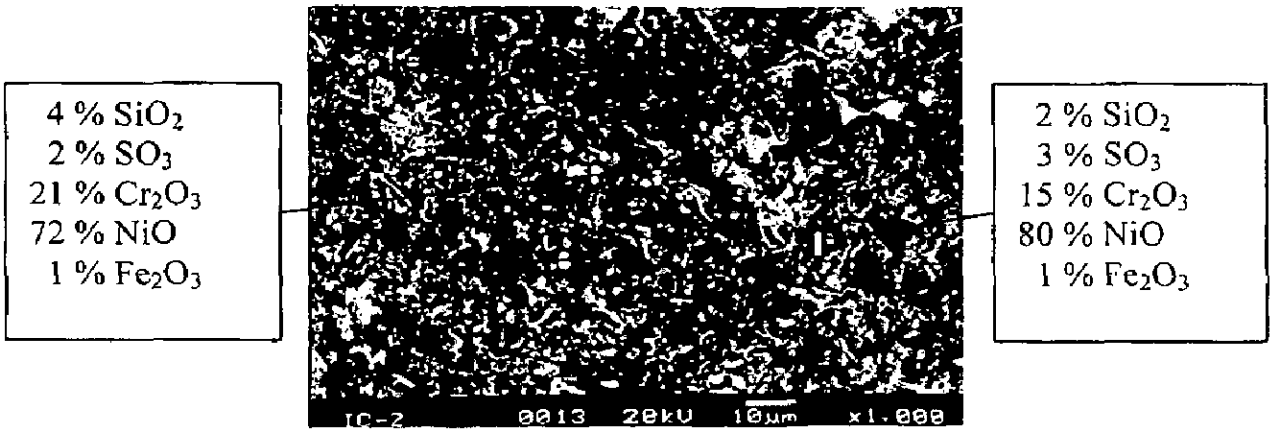

(a)

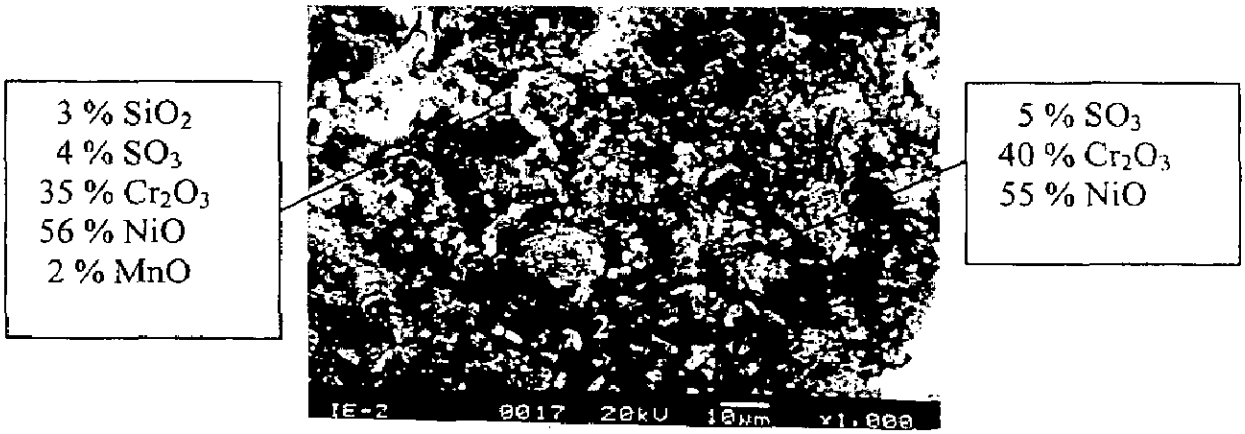

(b)

Fig. 7.34 SEM micrographs showing the surface morphology and EDAX analysis for Ni-20Cr coating with bond coat of NiCrAlY coating on superalloys exposed to coal fired boiler for 1000 hours at 540°C.

(a) Superfer 800H (b) Superni 718

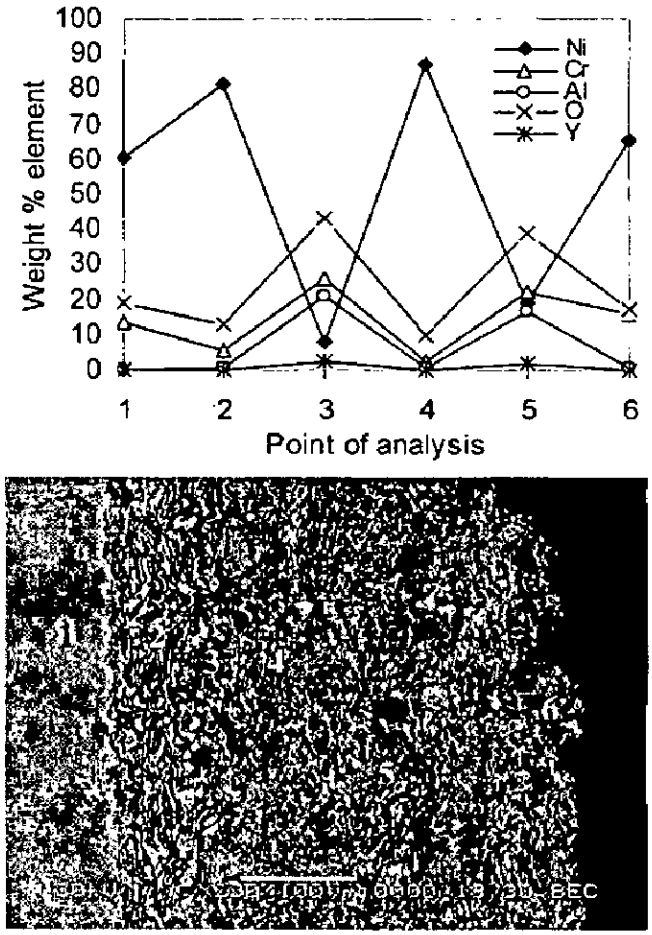

Fig. 7.35 Oxide scale morphology and elemental composition variation across the cross-section of Ni-20Cr coating with bond coat of NiCrAlY on Superni 600 superalloy exposed to boiler of thermal power plant for 1000 hours at 540°C.

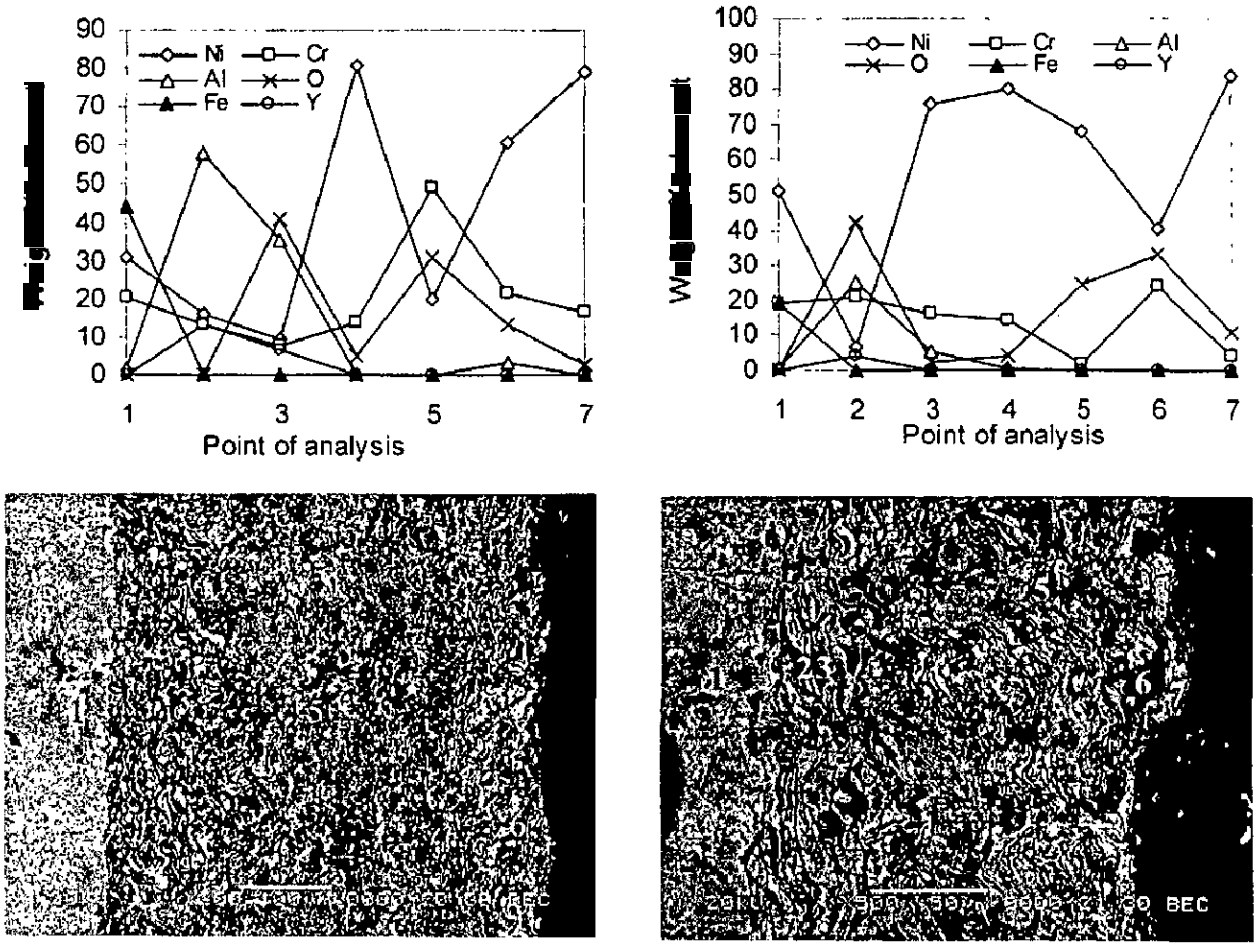

Fig. 7.36 Oxide scale morphology and elemental composition variation across the cross-section of Ni-20Cr coating with bond coat of NiCrAlY on superalloys exposed to boiler of thermal power plant for 1000 hours at 540°C
(a) Superfer 800H (b) Superni 718.

7.1.3.5 EPMA Analysis

From the EPMA of Ni-20Cr coated superalloys exposed to the boiler as shown in Figs. 7.37-7.40, bond coat of NiCrAlY can be clearly identified. Exposed coating layer is consisting of uniformly distributed nickel and chromium with diffusion of aluminium and yttrium from bond coat and iron and titanium from the substrate. Further in case of exposed coated superalloys, outer layer was rich in aluminium and silicon indicating the deposition of ash particles on the specimens' surfaces. X-ray mapping of the exposed Ni-20Cr coating deposited on Superfer 800H (Fig. 7.39) with oxygen analysis shows the diffusion of oxygen into the coating layer upto the coating-substrate interface. Aluminium and silicon are also visible on the top of the coating along with oxygen as seen from Figs. 7.39 and 7.40. The elemental mapping of the cross-section of exposed Ni-20Cr coating on Superni 718 superalloy with oxygen (Fig. 7.40) also indicates the diffusuion of oxygen upto the coating-substrate interface. Overlapping of aluminium, silicon and oxygen reveals the Al+O+Si on the top surface of the coating thereby indicating the deposition of fly ash at the surfaces.

7.1.4 Ni_3Al Coating

7.1.4.1 Visual Examination

Macrographs for Ni_3Al coated superalloys after 1000 hours exposure in coal fired boiler are shown in Fig. 7.41. After exposure the colour of scale is changed from shining grey to reddish brown. None of the coated superalloys have indicated cracking and spalling.

7.1.4.2 Thermogravimetric Data and Thickness Monitoring

The weight change per unit area for exposed Ni_3Al coated superalloy plotted as a function of time expressed in hours is given in Fig. 7.42. Ni_3Al coating on Superni 600 superalloy gained maximum weight (5.45 mg/cm^2) after 1000 hours exposure in the coal fired boiler at temperature of about 540°C. Coated Superni 718 superalloy showed decrease in weight gain after 800 hours of exposure time to 3/5th of the previous cycle. The cumulative weight change data of these exposed Ni_3Al coated superalloys have indicated weight gain per unit area whereas the data obtained for corresponding uncoated superalloys substrates have shown weight loss. The metal thickness loss after 1000 hours exposure to coal fired boiler for Ni_3Al coated Superni 75, Superni 600, Superfer 800H and Superni 718 superalloys are 0.071, 0.0961, 0.105

and 0.085 mm respectively (Fig. 7.43). The BSEI images depicting the layers along the cross-section are shown in Fig. 7.44, which indicates the thickness of partially oxidised coatings on Superni 75, Superni 600, Superfer 800H and Superni 718 superalloy substrates as 0.21, 0.215, 0.226 and 0.288 mm respectively.

7.1.4.3 X-ray Diffraction Analysis

The XRD profiles for Ni_3Al coated Superni 75, 600, 718 and Superfer 800H superalloy after 1000 hours of exposure in the coal fired boiler at about 540 ^0C are shown in Fig. 7.45. All the three coated superalloys have formed identical phases. The XRD analysis has shown the formation of mainly NiO, $NiAl_2O_4$ and indicates the presence of Ni_3Al, Ni and Al_2O_3 also.

7.1.4.4 SEM/EDAX Analysis

7.1.4.4.1 Surface Morphology

The SEM/EDAX analysis for Ni_3Al coated Superni 75 superalloy exposed to the coal fired boiler (Fig. 7.46 (a)) mainly indicates the formation of nickel and aluminium oxides. Silicon and some amount of sulphur oxides are also revealed by EDAX analysis. The SEM/EDAX of exposed Ni_3Al coated Superni 600 superalloy indicates top surface consisting mainly of NiO. Also oxides of aluminum, silicon and sulphur can be seen from Fig. 7.46 (b). The scale of coated Superfer 800H superalloy (Fig. 7.47 (a)) after 1000 hours exposure to the boiler environment contains NiO and SO_3 with some amounts of alumina and silica. The Ni_3Al coating on Superni 718 superalloy (Fig. 7.47 (b)) indicates the formation of NiO and Al_2O_3 in the top scale with some amounts of silicon, sulphur and iron oxides.

7.1.4.4.2 Cross-Sectional Analysis

Outer layer of the exposed Ni_3Al coated Superni 600 superalloy is rich in NiO (Fig. 7.48). Whereas bond coat layer contains nickel, chromium, aluminium and oxygen as can be seen from Fig. 7.48. The EDAX analysis at top area (point 6 in Fig. 7.49 (a)) for coated Superfer 800H superalloy shows mainly oxygen, aluminium, iron and silicon with small amount of nickel (5 wt. %). For the Ni_3Al coated Superni 718 superalloy (Fig. 7.49 (b)), nickel and oxygen are mainly visible in the outer layer of coating. Further from the cross-sectional EDAX analysis (Figs. 7.48 and 7.49), it is observed that the splat region is rich in nickel whereas along the splat interface higher amount of oxygen is present mainly with chromium, aluminium and yttrium.

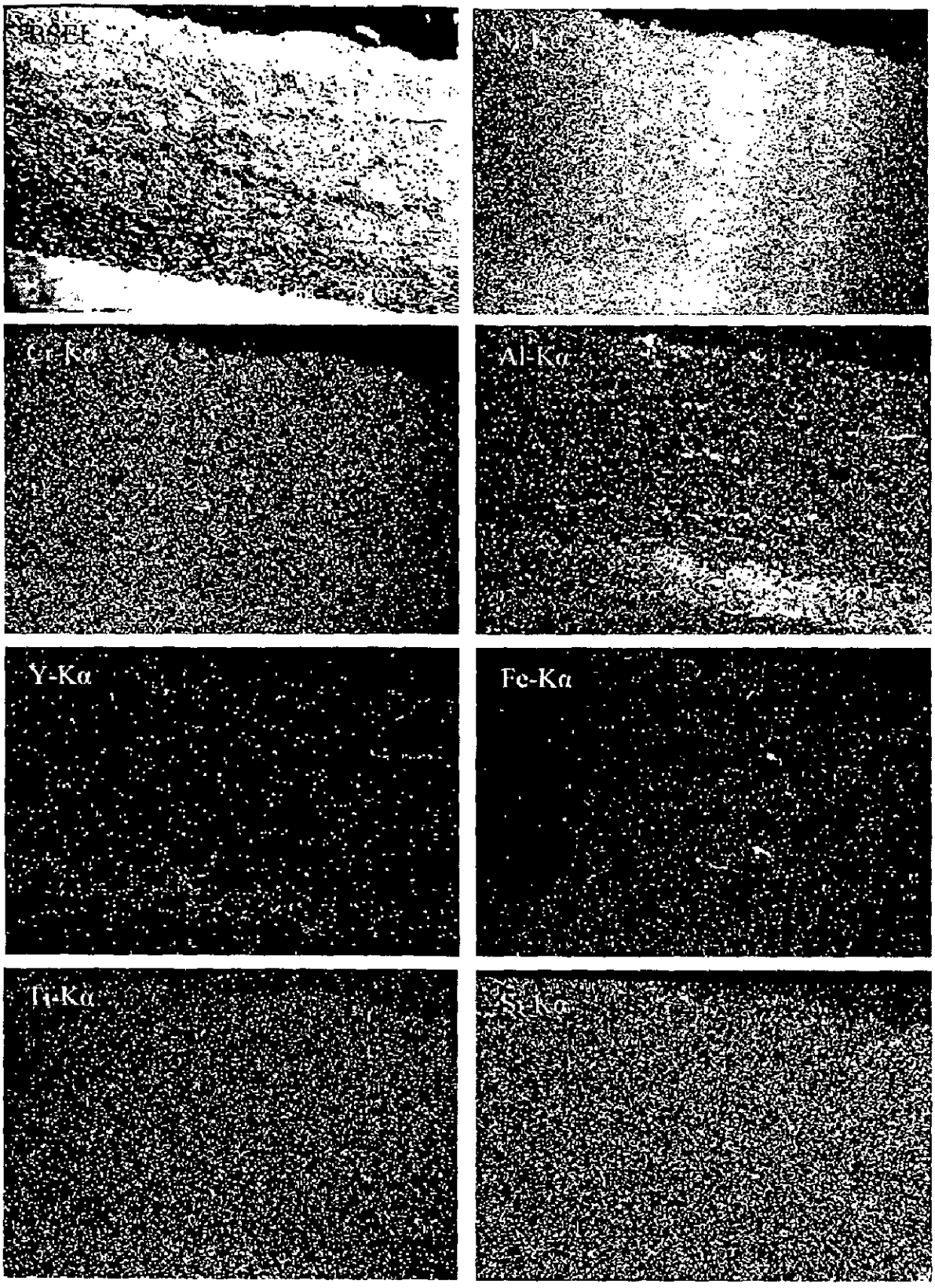

Fig. 7.37 BSEI and elemental X-ray mapping of the cross-section of Ni-20Cr coating on Superni 75 superalloy with bond coat of NiCrAlY exposed to boiler of thermal power plant for 1000 hours at 540°C.

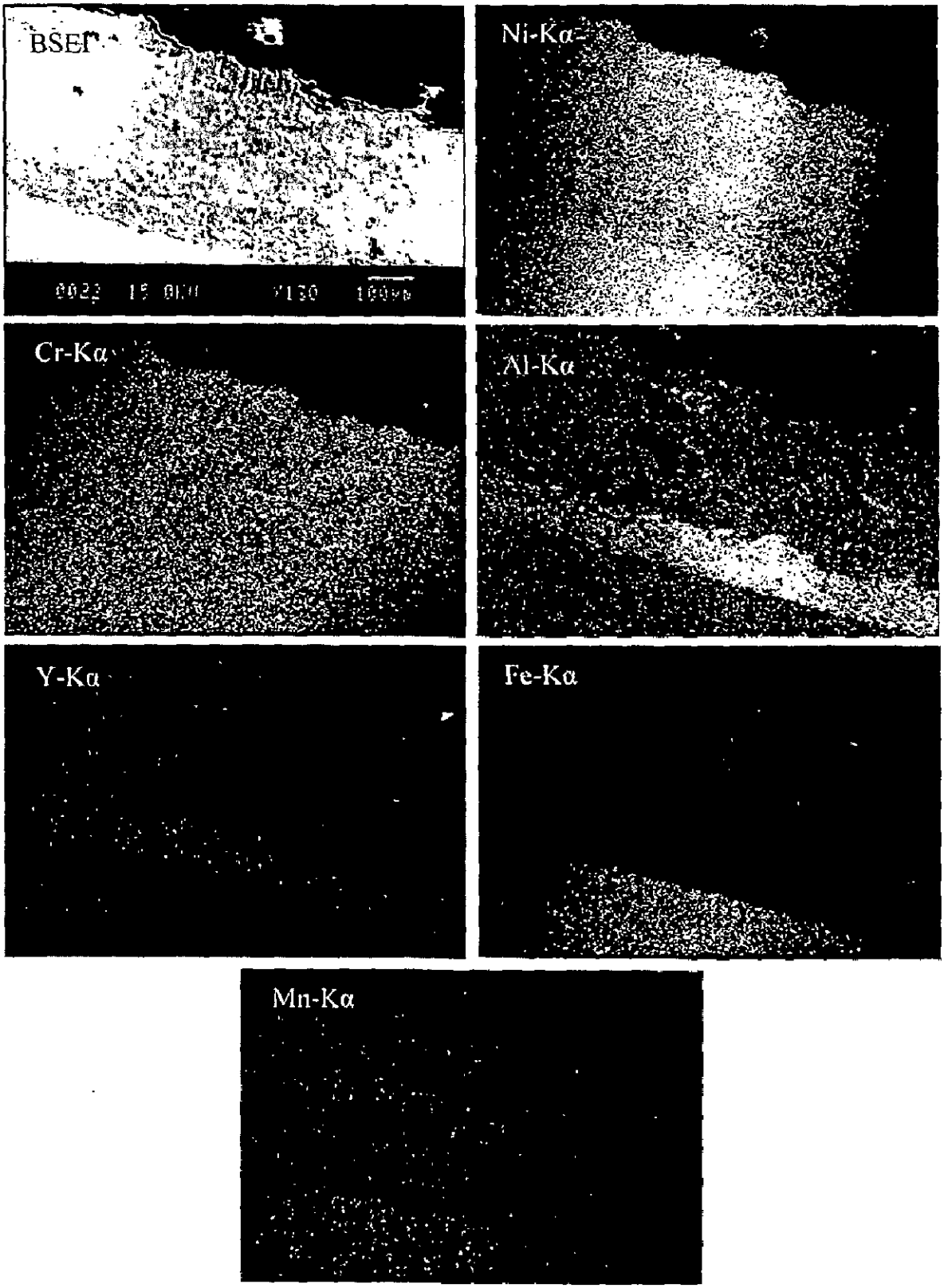

Fig. 7.38 BSEI and elemental X-ray mapping of the cross-section of Ni-20Cr coating on Superni 600 superalloy with bond coat of NiCrAlY exposed to boiler of thermal power plant for 1000 hours at 540°C.

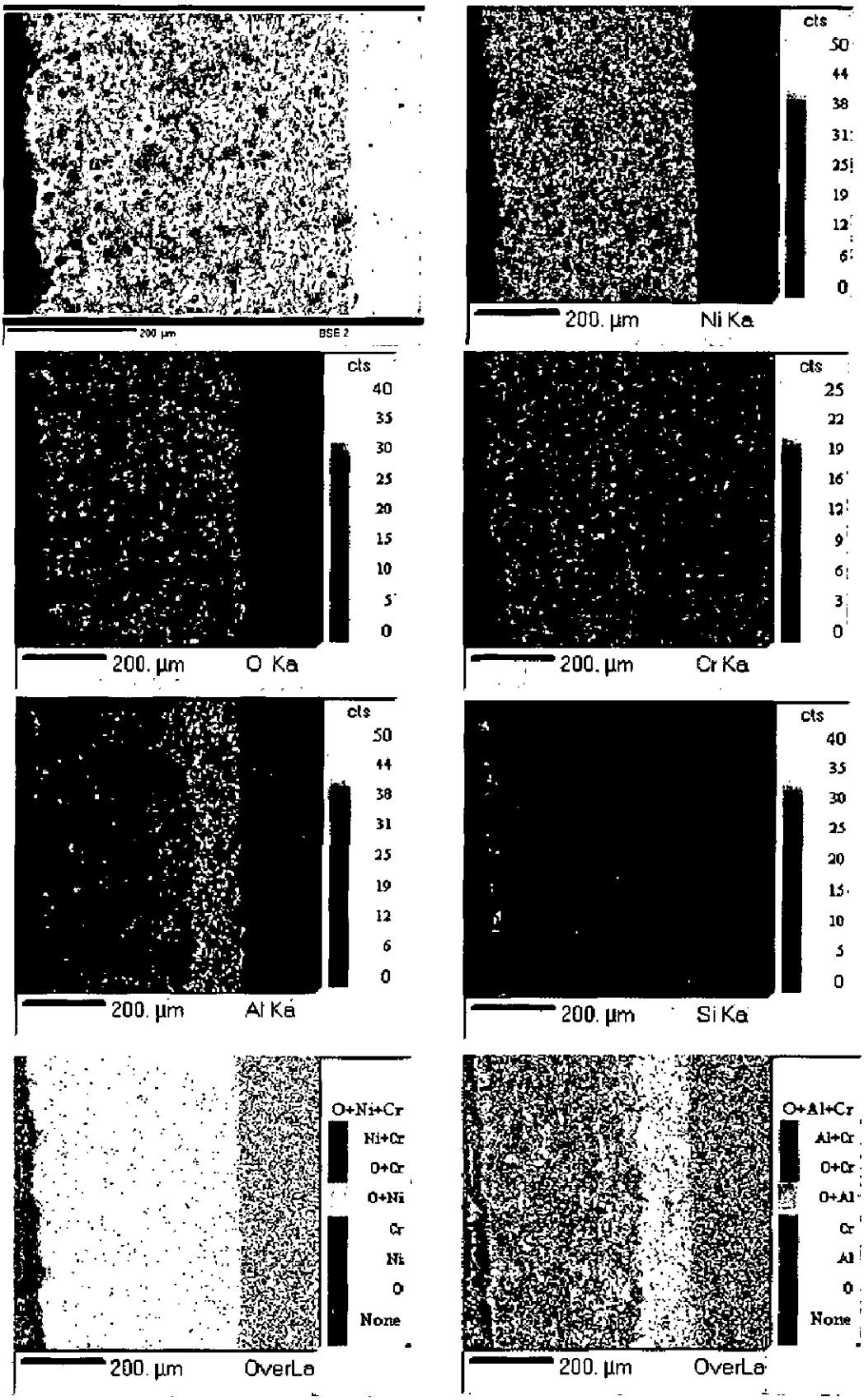

Fig. 7.39 BSEI and elemental X-ray mapping of the cross-section of Ni-20Cr coating with bond coat of NiCrAlY on Superfer 800H superalloy substrate exposed to boiler of thermal power plant for 1000 hours at 540°C.

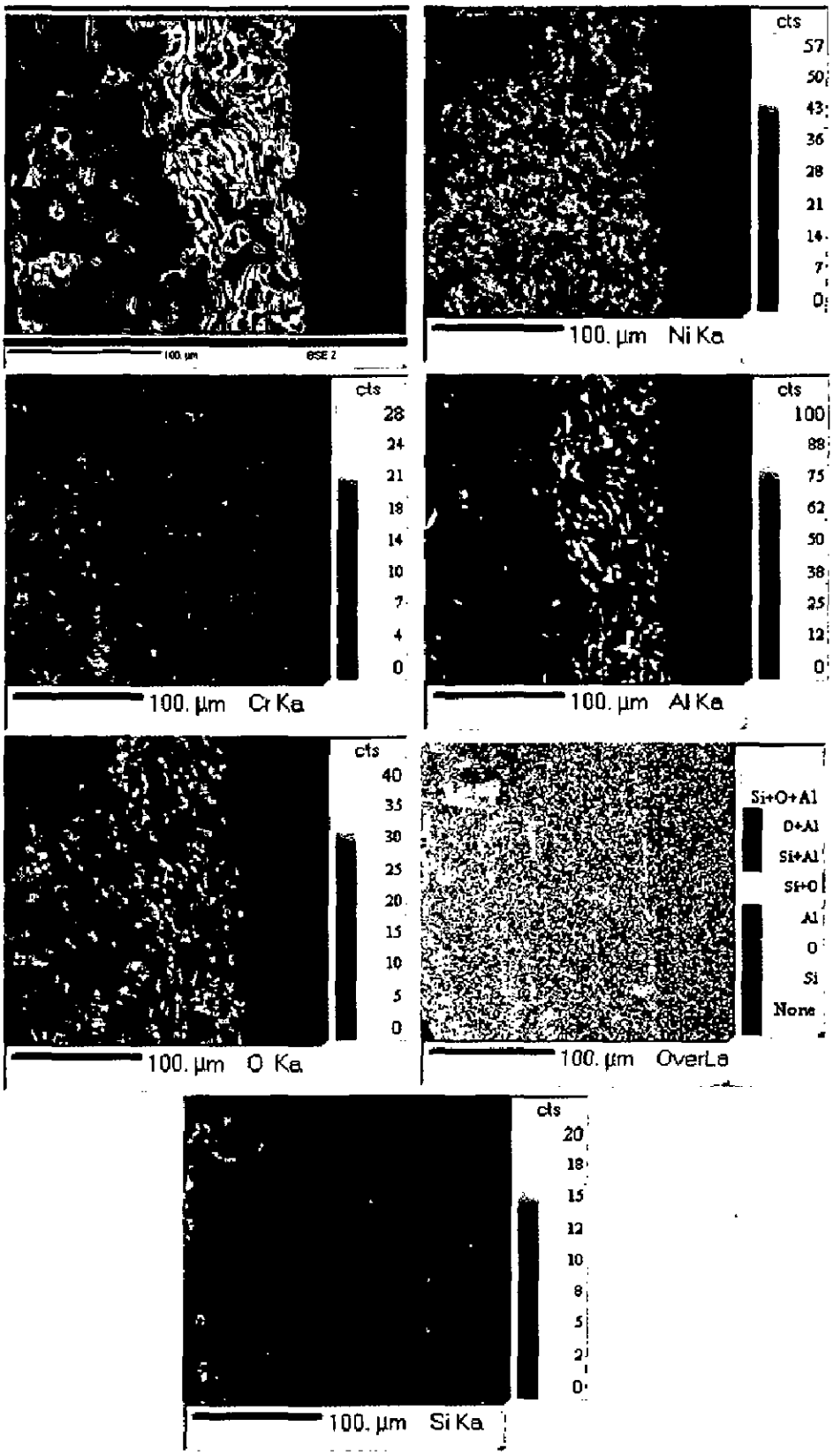

Fig. 7.40 BSEI and elemental X-ray mapping of the cross-section of Ni-20Cr coating on Supernı 718 superalloy with bond coat of NiCrAlY exposed to boiler of thermal power plant for 1000 hours at 540°C.

(a)

(b)

(c)

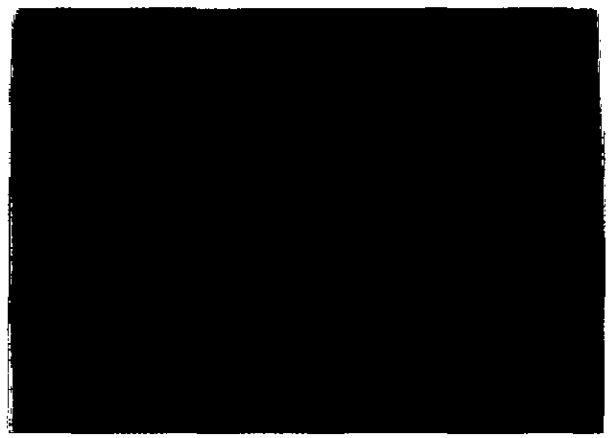

(d)

Fig. 7.41 Macrographs of plasma sprayed Ni_3Al coating with bond coat of NiCrAlY coating on superalloys exposed to coal-fired boiler at 540°C for 1000 hours.
(a) Superni 75 (b) Superni 600 (c) Superfer 800H
(d) Superni 718

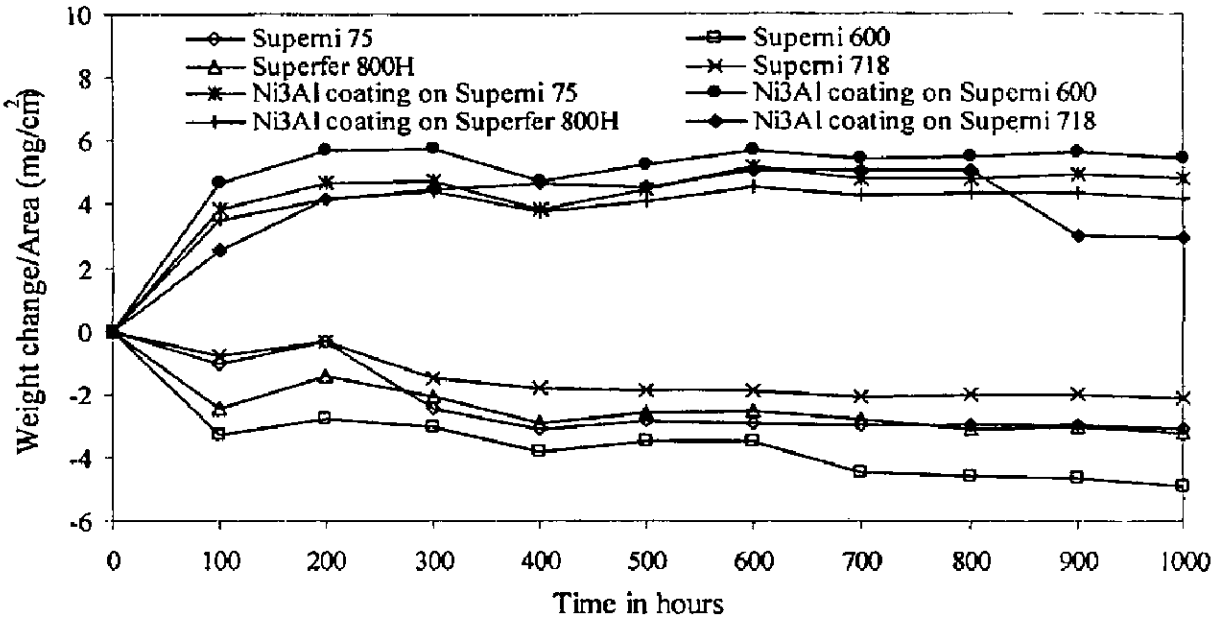

Fig. 7.42 Weight change versus time in hours plot for uncoated and Ni_3Al coated superalloys with bond coat of NiCrAlY coating exposed to coal fired boiler for 1000 hours at 540°C.

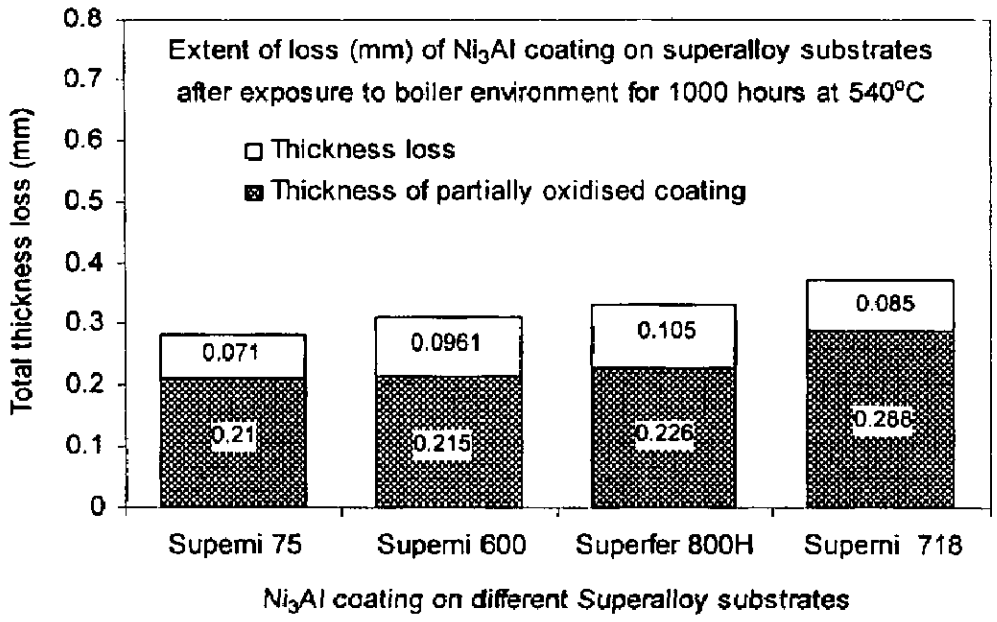

Fig. 7.43 Bar chart indicating the total thickness loss in mm for Ni_3Al coating on different superalloy substrates after 1000 hours exposure to the coal fired boiler at 540°C.

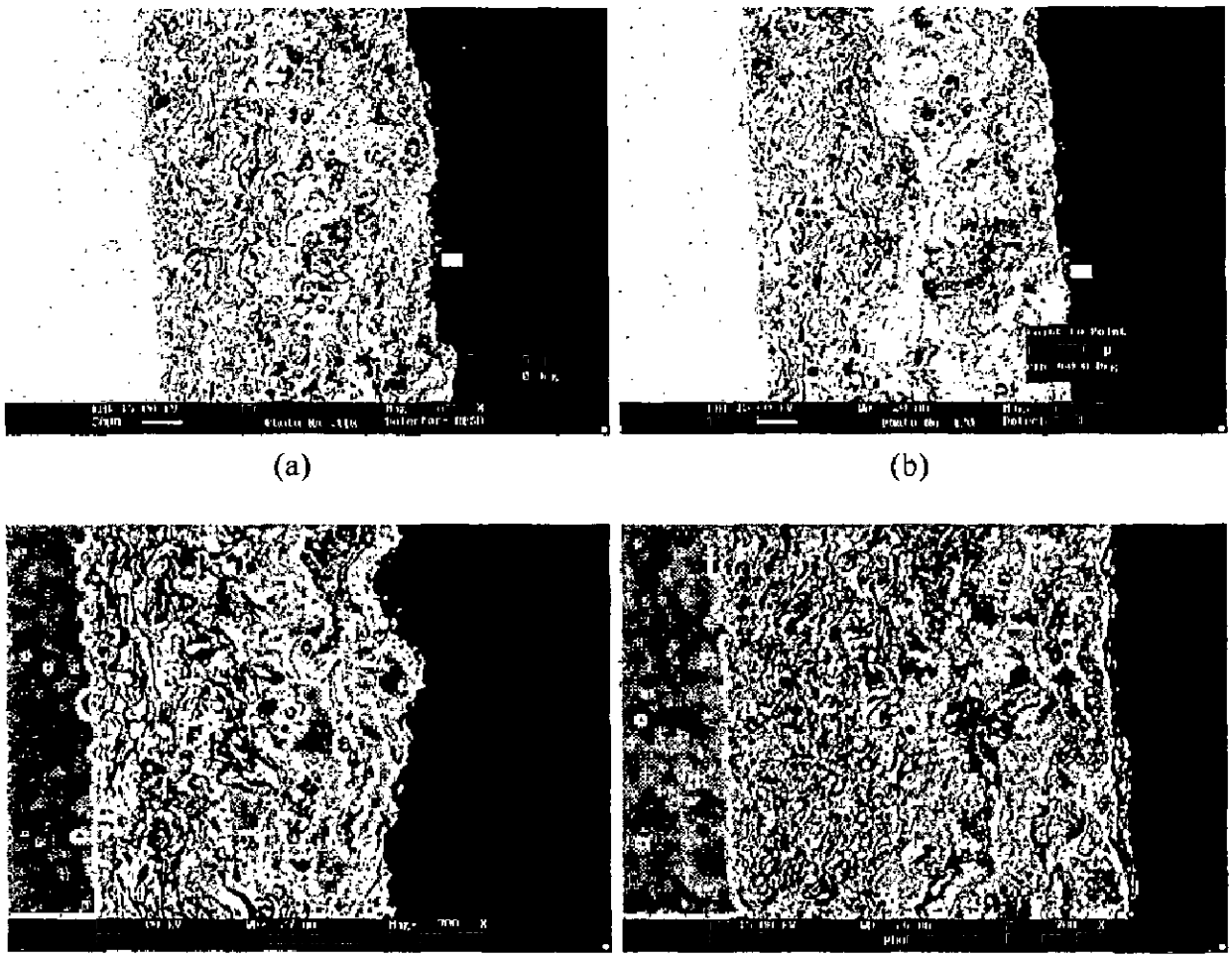

Fig. 7.44 SEM back scattered electron image along the cross-section for the Ni_3Al coating on different substrate superalloys exposed to the coal-fired boiler at 540°C for 1000 hours.

(a) Superni 75 (b) Superni 600 (c) Superfer 800H

(d) Superni 718

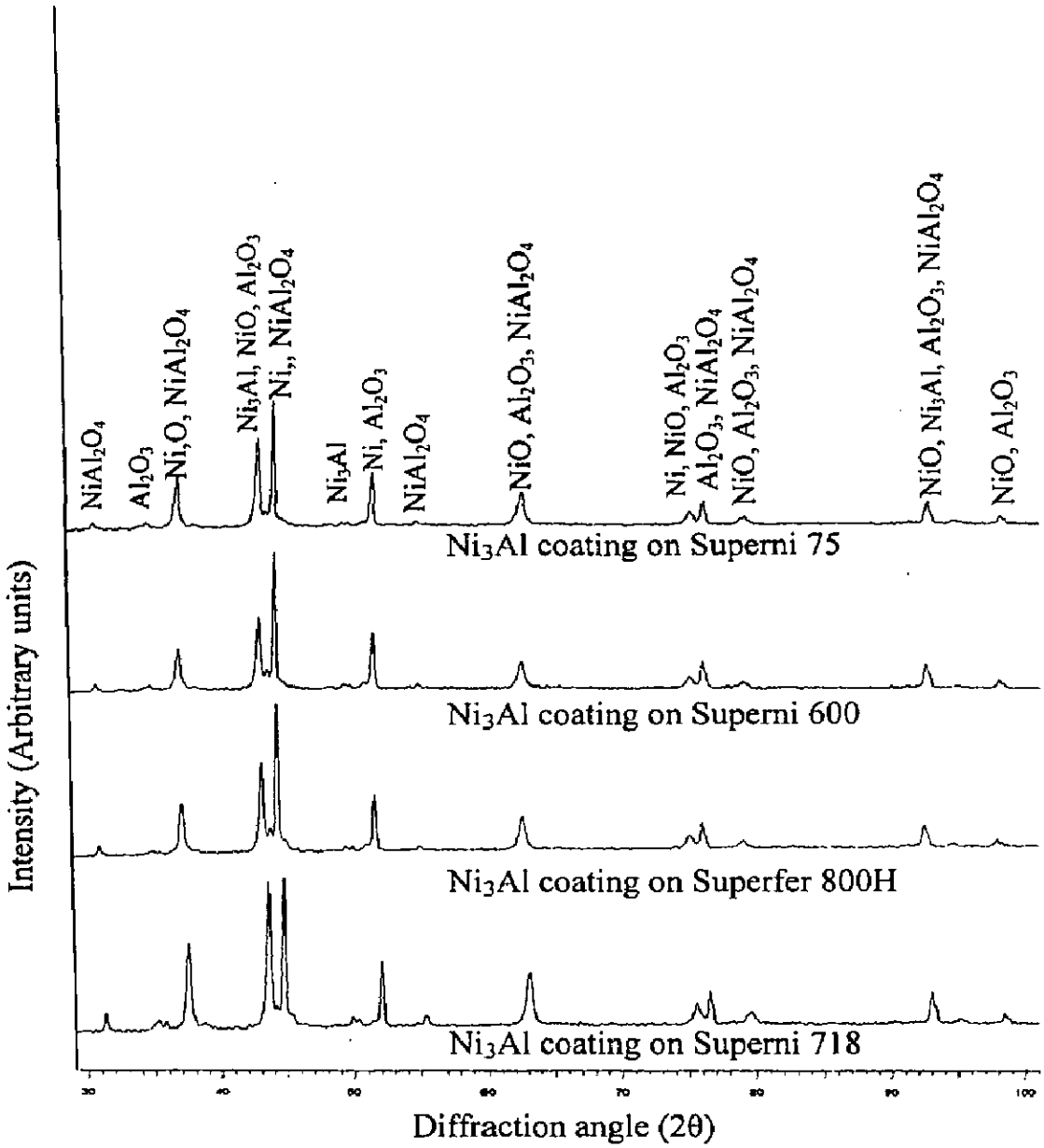

Fig. 7.45 X-ray diffraction profiles for Plasma Sprayed Ni_3Al coating with bond coat of NiCrAlY coating on Superni 75, Superni 600, Superfer 800H and Superni 718 superalloys substrates exposed to Low Temperature Primary Super Heater of the coal fired boiler for 1000 hours at 540°C.

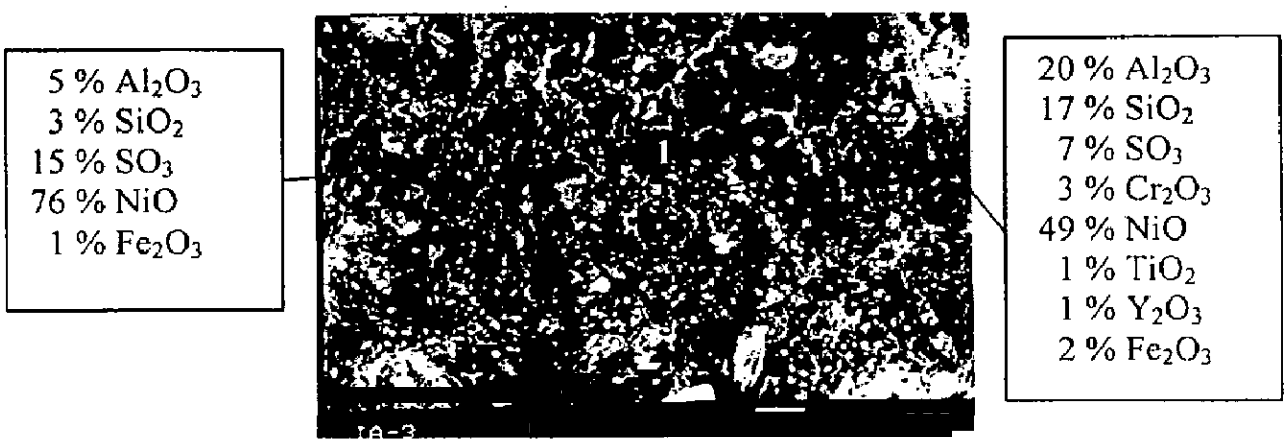

(a)

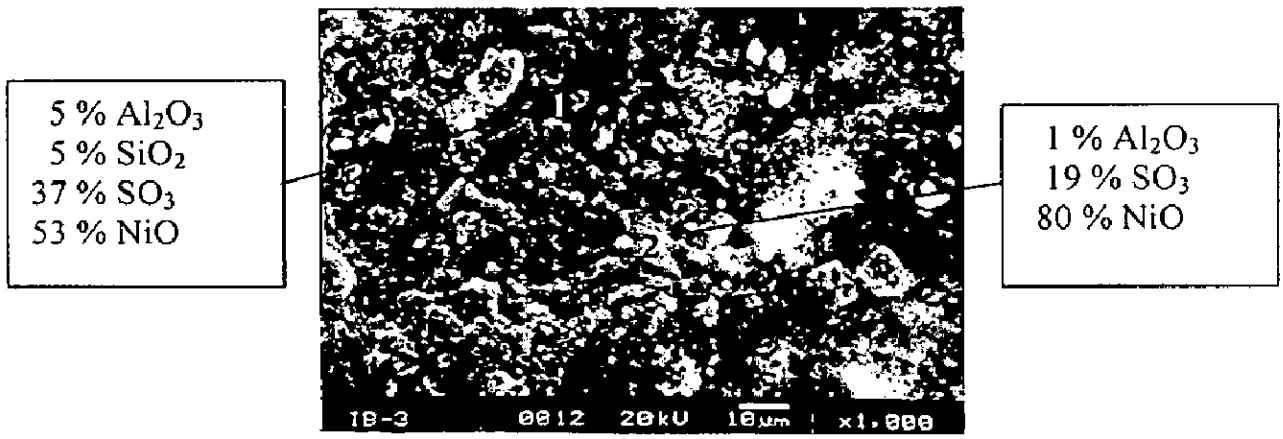

(b)

Fig. 7.46 SEM micrographs showing the surface morphology and EDAX analysis for Ni_3Al coating with bond coat of NiCrAlY coating on superalloys exposed to coal fired boiler for 1000 hours at 540°C.
(a) Superni 75 (b) Superni 600

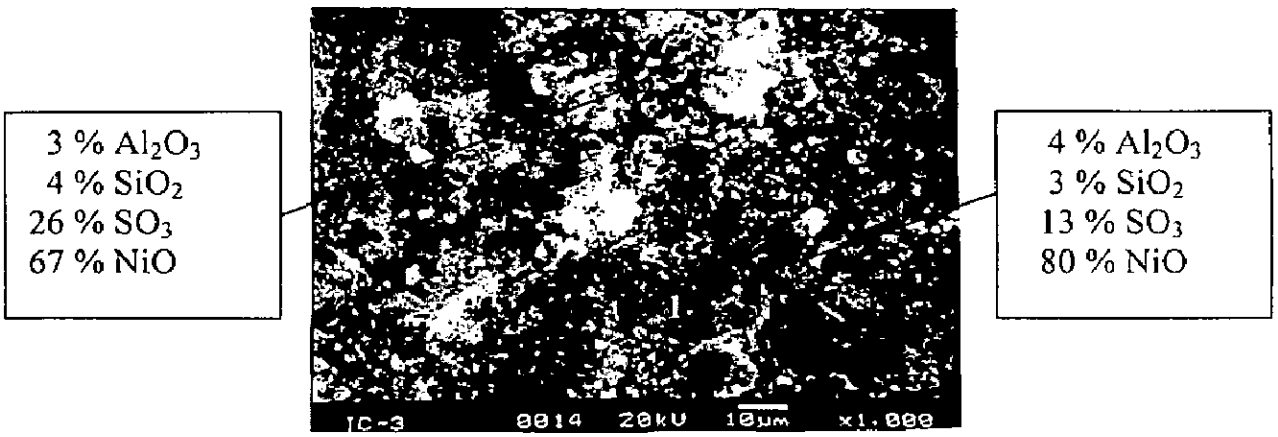

(a)

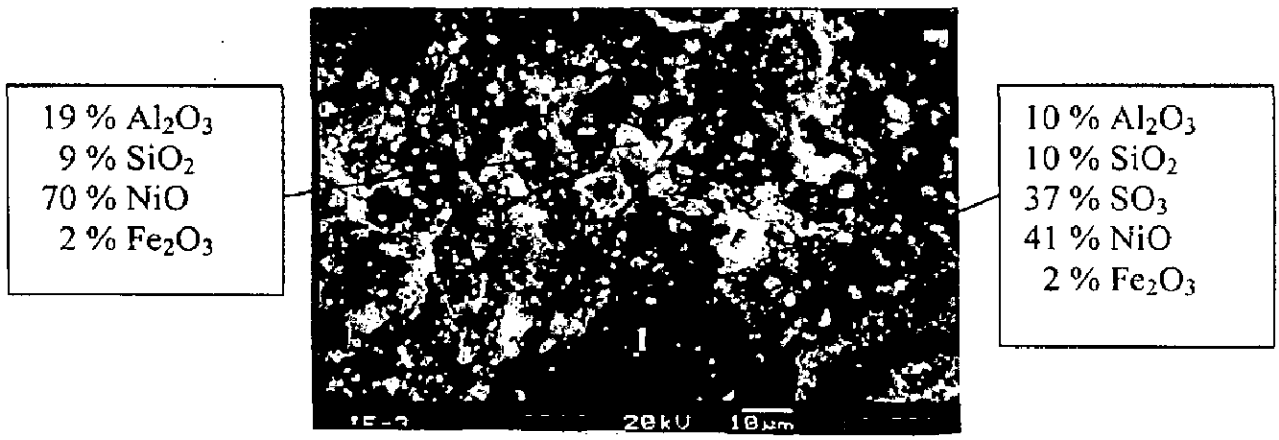

(b)

Fig. 7.47 SEM micrographs showing the surface morphology and EDAX analysis for Ni_3Al coating with bond coat of NiCrAlY coating on superalloys exposed to coal fired boiler for 1000 hours at 540°C.
(a) Superfer 800H (b) Superni 718.

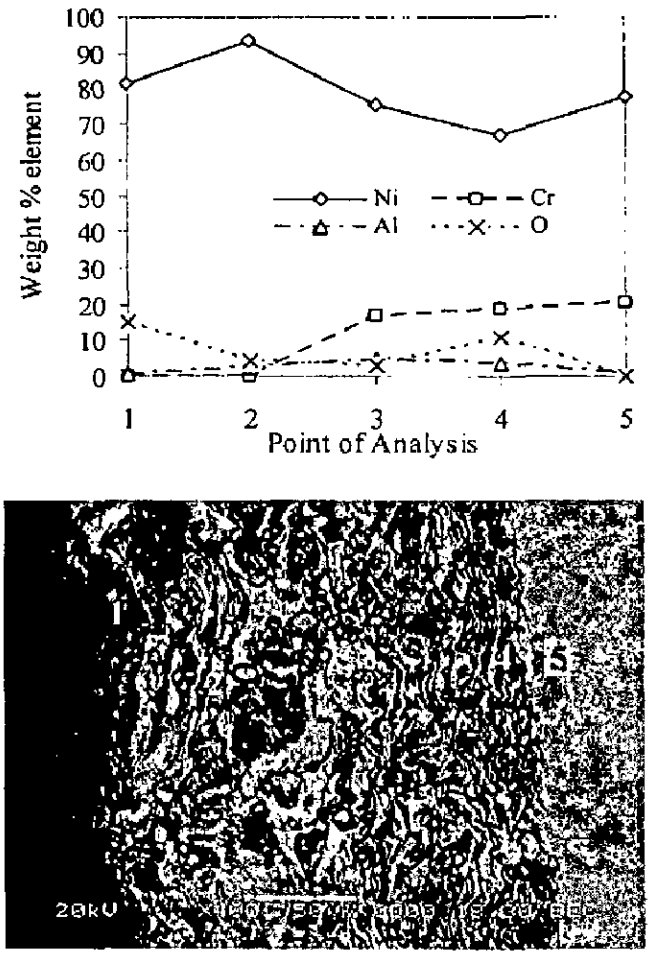

Fig. 7.48 Oxide scale morphology and elemental composition variation across the cross-section of Ni_3Al coating with bond coat of NiCrAlY on Superni 600 superalloy exposed to boiler of thermal power plant for 1000 hours at 540°C.

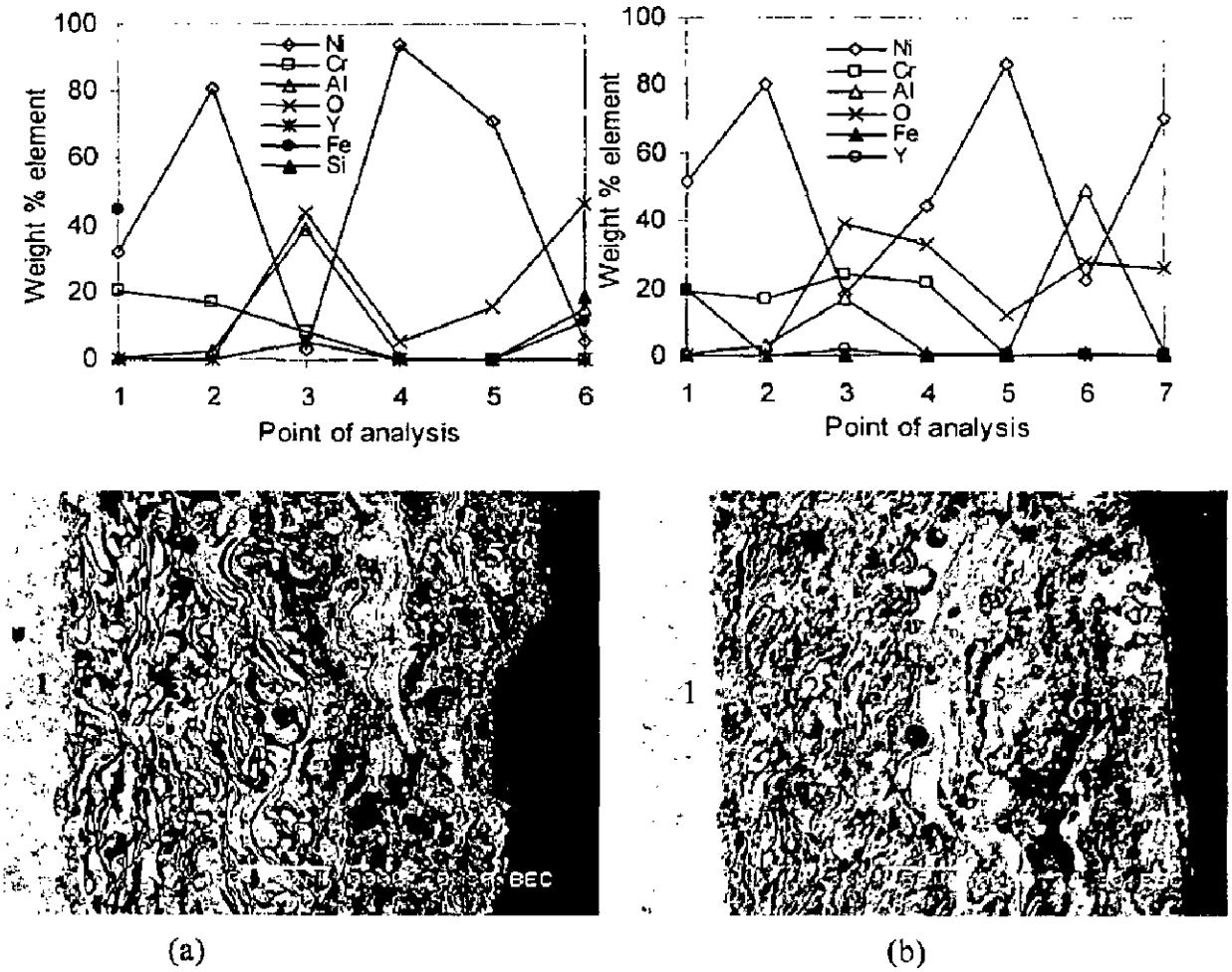

Fig. 7.49 Oxide scale morphology and elemental composition variation across the cross-section of Ni_3Al coating with bond coat of NiCrAlY on superalloys exposed to boiler of thermal power plant for 1000 hours at 540°C
(a) Superfer 800H (b) Superni 718.

7.1.4.5 EPMA Analysis

The EPMA for the exposed cross-section of Ni_3Al coated Superni 75 superalloy indicated the formation of Ni and Al rich layer in the top scale containing small amounts of Cr, Fe, Ti and Si (Fig. 7.50). Fig. 7.51 reveals the EPMA of coated Superni 600 superalloy exposed to the coal fired boiler for 1000 hours duration. It also shows nickel and aluminium rich layer with some amounts of iron, manganese, silicon and tantalum. The EPMA of coated Superfer 800H superalloy with oxygen analysis (Fig. 7.52) shows mainly aluminium, nickel, oxygen and silicon on the top of the coated layer after 1000 hours exposure in the industrial environment. Composition image and elemental distribution (Fig. 7.53) for Ni_3Al coated Superni 718 superalloy indicates the outer layer rich in nickel and aluminium. Also existence of yttrium, iron, titanium, molybdenum, tantalum and silicon in the coating are revealed by the EPMA analysis.

7.2 SUMMARY OF RESULTS

Results obtained after 1000 hours exposure of coated and uncoated superalloys to the coal fired boiler environment at around 540^0C are summarised in Table 7.1.

Table 7.1 Summary of the results for coated and uncoated superalloy after 1000 hours of exposure to the low temperature primary superheater of the coal fired boiler at around 540^0C.

Base superalloy	Coating	Weight change, mg/cm^2	Thickness Loss, mm	Thickness of oxidised layers, mm	XRD analysis	Remarks
Superni 75	---	-3.10	0.08	0.005	Ni, (Ni,Fe), Al_2O_3, Cr	Surface EDAX shows Al_2O_3, SiO_2, NiO, Fe_2O_3, Cr_2O_3 and SO_3. EPMA show top scale of Ni, Cr, Al and Si.
Superni 600	---	-4.90	0.13	0.06	Ni, (Ni,Fe), NiO	Surface EDAX shows NiO, Cr_2O_3, Al_2O_3, SiO_2, Fe_2O_3 and SO_3. Cross-sectional EDAX confirms NiO, Cr_2O_3 and Fe_2O_3. Scale of about 100 μm as seen from EPMA, and mainly consists of Ni, Cr, Al, Si and O.

Superfer 800H	---	-3.24	0.094	0.03	Ni, FeNi, Al_2O_3	Surface EDAX show Fe_2O_3, NiO, Cr_2O_3, SiO_2 and Al_2O_3. Cross sectional EDAX indicate scale of mainly Fe, Ni and Cr. EPMA shows thick scale of Ni, Cr, Al, Fe and Si in the top.
Superni 718	---	-2.19	0.07	0.1	(Ni,Fe), Al_2O_3	Surface EDAX shows mainly Fe_2O_3, NiO, Cr_2O_3 and SiO_2. Cross sectional EDAX indicate scale of Fe, Al and Cr. From EPMA Al, Si, and Oxygen is visible in the top scale, indicating ash deposition.
Superni 75	NiCrAlY	0.51	0.01	0.45	Ni, NiO, $NiAl_2O_4$, Al_2O_3	Surface EDAX show Al_2O_3, NiO and Cr_2O_3. EPMA shows Al in the top and traces of Si & Fe in the coated layer.
Superni 600	NiCrAlY	-2.04	0.024	0.44	NiO, $NiAl_2O_4$, Al_2O_3	Surface EDAX show mainly oxides of Al, Ni and Cr. EPMA shows oxygen, silicon, chromium and aluminium on the top scale.
Superfer 800H	NiCrAlY	-1.08	0.02	0.47	NiO, $NiAl_2O_4$, Al_2O_3	Surface EDAX shows mainly Al_2O_3, NiO and Cr_2O_3. Cross sectional EDAX indicates Al, Ni, Cr and Y with O.
Superni 718	NiCrAlY	1.12	0.0445	0.36	Ni, NiO, Al_2O_3	Surface EDAX shows mainly NiO with small amount of Cr_2O_3, Al_2O_3 and SO_3. Cross sectional EDAX also shows mainly Ni in the top layer with Cr, Al, Y and O.
Superni 75	Ni-20Cr	-0.90	0.016	0.388	Ni, NiO, $NiCr_2O_4$, Cr_2O_3, Al_2O_3, SiO_2	NiO and Cr_2O_3 are visible from surface EDAX with some amount of SiO_2, Al_2O_3 and SO_3. From EPMA, traces of Al and Si are visible in the top region, indicating ash deposition.
Superni 600	Ni-20Cr	0.86	0.01575	0.359	Ni, NiO, $NiCr_2O_4$, Cr_2O_3, Al_2O_3	Surface EDAX shows mainly NiO and Cr_2O_3 with small amount of SO_3. Cross sectional EDAX also shows mainly Ni in the top layer with Cr, Al, Y and O.

Superfer 800H	Ni-20Cr	2.86	0.013	0.480	Ni, NiO, $NiCr_2O_4$, Cr_2O_3, Al_2O_3	NiO and Cr_2O_3 are mainly visible from surface EDAX. Cross-sectional also shows Ni, Cr and O. Scale is not visible, only minor traces of Si and Al can be seen, Aluminum seems to be diffused in the top scale, oxygen has diffused onto the coating layer without affecting the substrate.
Superni 718	Ni-20Cr	0.72	0.01535	0.33	Ni, NiO, $NiCr_2O_4$, Cr_2O_3, Al_2O_3, SiO_2	NiO and Cr_2O_3 are mainly seen from surface and cross-sectional EDAX, along with SO_3. Ni, Cr and O are revealed from cross-sectional EDAX. EPMA shows diffusion of silicon from the environment into the top surface of the coated layer, also oxygen is visible in the coated layer.
Superni 75	Ni_3Al	4.78	0.071	0.21	Ni, NiO, Ni_3Al, $NiAl_2O_4$, Al_2O_3	Surface EDAX shows mainly NiO with small amount of Al_2O_3, SiO_2 and SO_3.
Superni 600	Ni_3Al	5.45	0.0961	0.215	Ni, NiO, Ni_3Al, $NiAl_2O_4$, Al_2O_3	NiO and SO_3 are visible from surface EDAX. Cross sectional EDAX also shows mainly Ni and O in the top layer. From EPMA traces of Al and Si are visible in the top scale, indicating ash deposition.
Superfer 800H	Ni_3Al	4.13	0.105	0.226	Ni, NiO, Ni_3Al, $NiAl_2O_4$, Al_2O_3	Surface EDAX shows mainly NiO and SO_3 with small amounts of Al_2O_3 and SiO_2. Al with O is mainly visible in the top scale with Ni. Top scale consists of Ni, Al and Si along with oxygen as revealed by EPMA.
Superni 718	Ni_3Al	2.91	0.085	0.288	Ni, NiO, Ni_3Al, $NiAl_2O_4$, Al_2O_3	Surface EDAX shows mainly NiO with some amount of Al_2O_3, SiO_2 and SO_3. Cross sectional EDAX shows mainly Ni in the top layer with O. From EPMA Ni, Al and Si are visible in the top scale.

7.3 DISCUSSION

In this section, the results of erosion-corrosion studies on superalloys (Superni 75, Superni 600, Superfer 800H and Superni 718) and plasma sprayed coatings (NiCrAlY, Ni-20Cr and Ni_3Al coatings) on these superalloys substrates exposed to the coal-fired boiler environment of thermal power plant for 1000 hours at 540°C have been discussed.

7.3.1 Uncoated Superalloys

The graph of weight change per unit area with number of cycles of 100 hours duration (Fig. 7.2) has indicated perceptible variation in weight change during the initial cycles of present study. This may be attributed to loss in weight by erosion and gain in weight by oxidation of the specimens. Also the increase in weight may also be contributed by the deposition of ash particles on the exposed surface of the specimen. Levy (1995) has also reported that surfaces of the specimen, other than the erodent impacted area, can add or subtract weight from chemical reactions such as oxidation. The erodent particles can deposit or embed themselves on the test surface. Mixtures of erodent particles and oxide scales can form on the eroding surfaces. Thin layers consisting of deposited material and oxidised scale have been observed for all the superalloys studied in present investigation. Further the top layer on Superni 75 is superficial whereas it is significant in case of other superalloys. The superalloys can be arranged based on their weight loss as

Superni 600 > Superfer 800H > Superni 75 > Superni 718.

Scales that form to a critical thickness would spall as a result of repeated impacts followed by oxide re-growth. A deposit layer forms on the specimen surface to render protection against wastage seems to depend on two competing processes; one is the growth of the oxide scale and the other the formation of a dense bed material layer on the specimen surface. At higher temperature, above 500°C in the boiler the wastage rate is perhaps dominated by oxidation, which itself was affected by the erosion process similar to the wear enhanced oxidation regime described by Rishel et al (1991).

In the present investigation all the superalloys have shown weight loss with maximum by Superni 600, thus suggesting the contribution of erosion. Fig. 7.5 & Fig. 7.6 show mainly the peaks of Ni and (Ni,Fe) and indicate the presence of some oxides. Also existence of some oxides has been shown by EDAX analysis of the surface (Fig. 7.7 and Fig. 7.8) as well as from the cross-sectional SEM/EDAX analysis (Fig 7. 9 and

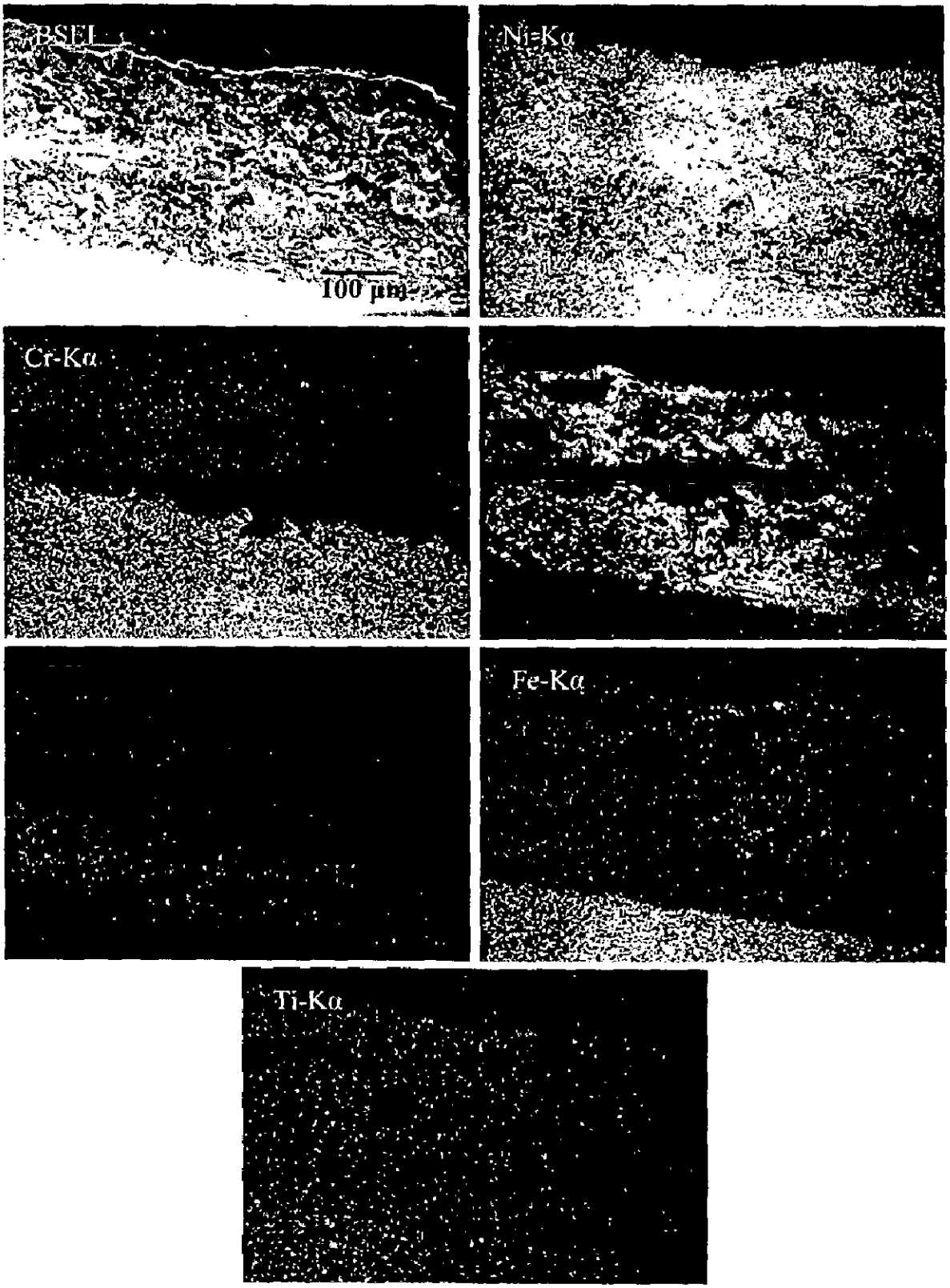

Fig. 7.50 BSEI and elemental X-ray mapping of the cross-section of Ni_3Al coating on Superni 75 superalloy with bond coat of NiCrAlY exposed to boiler of thermal power plant for 1000 hours at 540°C.

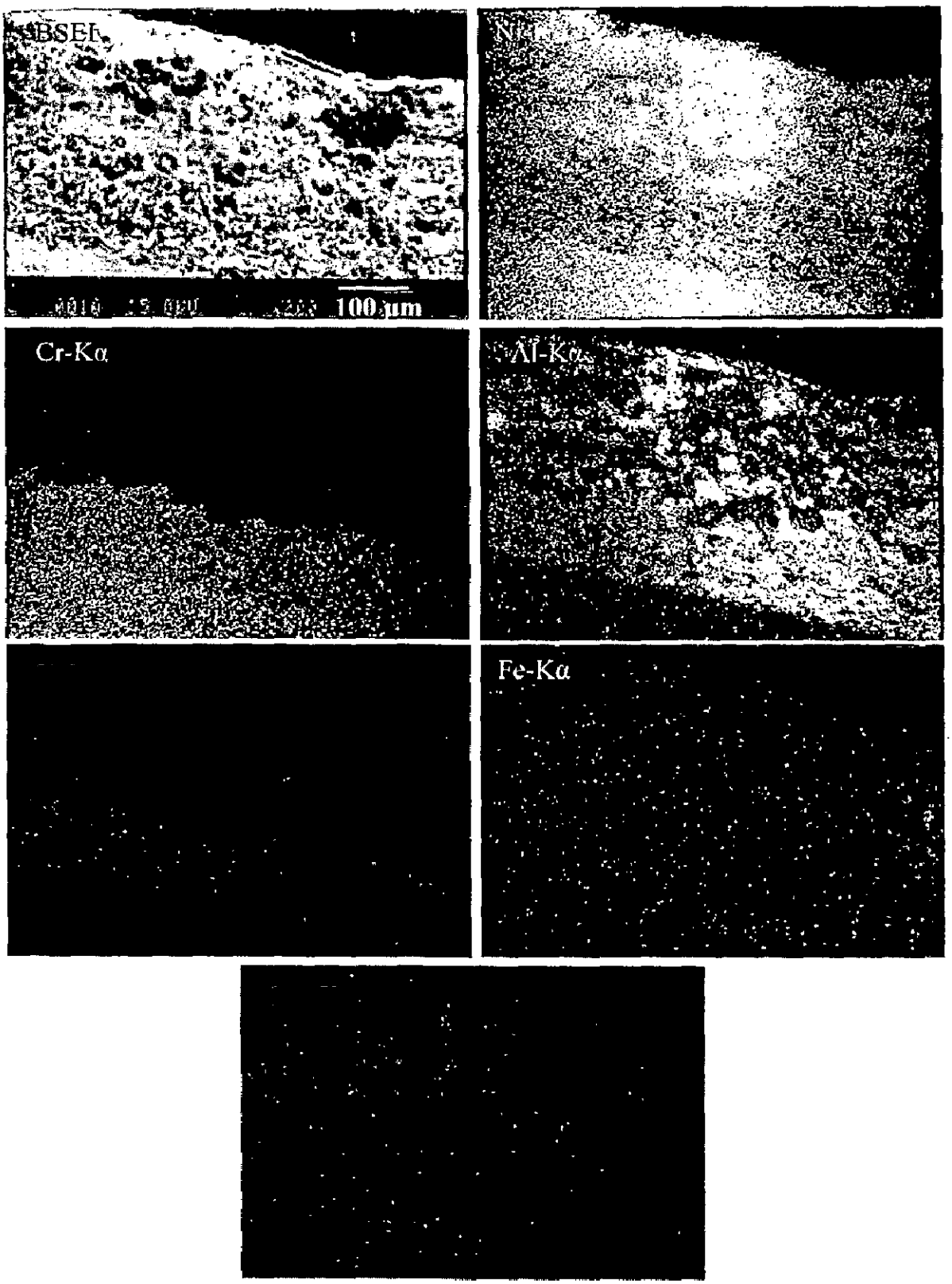

Fig. 7.51 BSEI and elemental X-ray mapping of the cross-section of Ni_3Al coating on Superni 600 superalloy with bond coat of NiCrAlY exposed to boiler of thermal power plant for 1000 hours at 540°C.

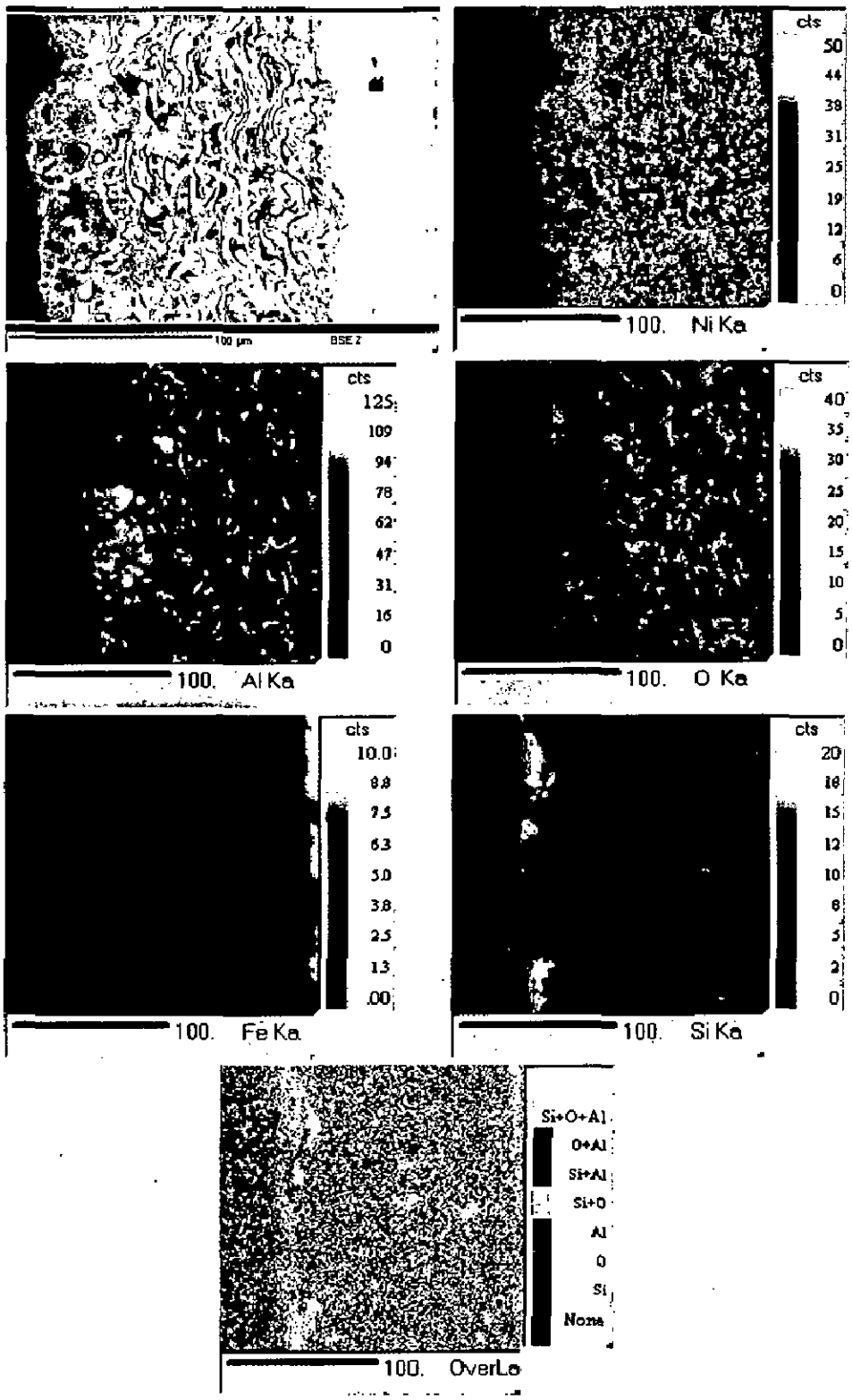

Fig. 7.52 BSEI and elemental X-ray mapping of the cross-section of Ni_3Al coating on Superfer 800H superalloy with bond coat of NiCrAlY exposed to boiler of thermal power plant for 1000 hours at 540°C.

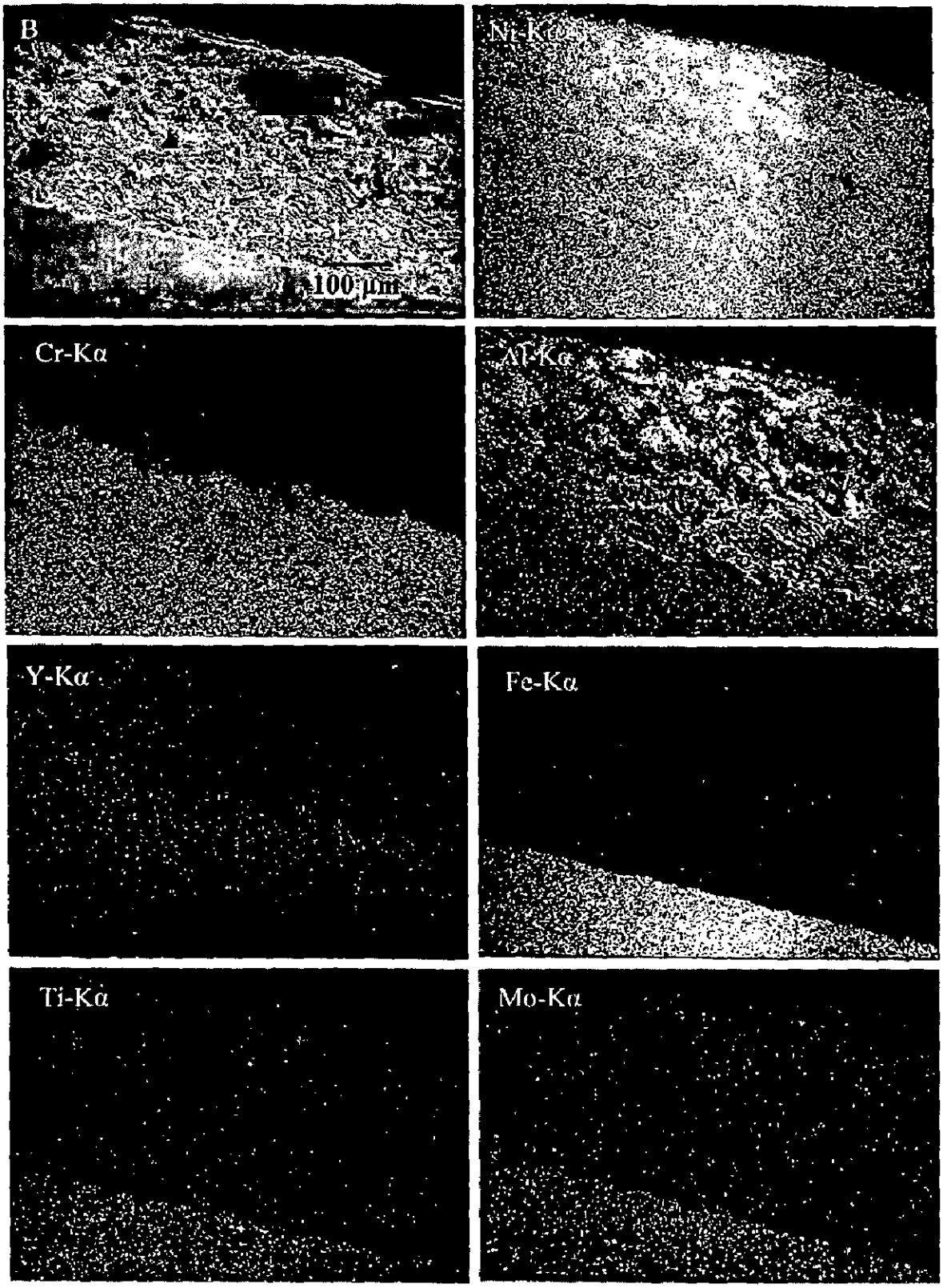

Fig. 7.53 BSEI and elemental X-ray mapping of the cross-section of Ni_3Al coating on Superni 718 superalloy with bond coat of NiCrAlY exposed to boiler of thermal power plant for 1000 hours at 540°C.

Fig. 7.10) for the specimens exposed to the boiler of the thermal power plant. The layers shown on the surfaces of the superalloys consist of silicon and aluminium (fly ash constituents) along with NiO, Cr_2O_3, Fe_2O_3, $NiFe_2O_4$. From this it can be inferred that the superalloys have also been oxidised accompanied with erosion by fly ash impact. The embedment of ash particles in the top layer of exposed superalloys has been further confirmed by the EPMA analysis. Levy (1993) has also observed the presence of mixture of bed material constituents in the outer scale deposits during erosion-corrosion of tubing superalloys in combustion boiler environments.

A schematic diagram shown in Fig. 7.54 has been suggested to explain the erosion-corrosion phenomenon for the case of Superni 600 superalloy.

7.3.2 Ni-Cr-Al-Y Coating

From weight change data it can be inferred that the protection to the base metals has been provided by the NiCrAlY coating. NiCrAlY coating on Superni 600 and Superfer 800 H has shown weight loss whereas the coating on Superni 75 and 718 has shown weight gain. Maximum weight loss of 2.04 mg/cm^2 was given by NiCrAlY coating on Superni 600 superalloy substrate whereas maximum weight gain of 1.12 mg/cm^2 was observed in case of Superni 718 coated superalloy. The weight loss might have contributed by erosion of coating whereas weight gain might have resulted by oxidation of coatings. Since weight change data may be insufficient to estimate degradation rate. The thickness change of the coated superalloys has been noted and total thickness loss has been calculated adding the thickness of oxide layer to this. Further from the EDAX analysis along the cross-section and EPMA analysis with oxygen, it has been perceived that the oxygen has penetrated upto the coated layer and has not affected the substrate superalloys. This suggest the protection of the substrate superalloys by the coated layer by forming oxides, which further blocks the progress of oxygen into the substrate superalloys. This resulted in the lower metal loss of the coated superalloys. Rao et al (1991) suggested that the scales at 450°C and 650°C consist of a relatively loosely packed mixture of oxidation product and erodent material. Lower erosion-corrosion temperatures promote denser and more impact-resistant scales which together with slower oxidation kinetics lead to lower metal loss rates.

Main phases identified in all the NiCrAlY coated superalloys are NiO, Cr_2O_3, Al_2O_3 and SiO_2 after 1000 hours exposure to the coal fired boiler environment by XRD

analysis. Whereas XRD analysis of coated superalloys has also indicated the formation of spinels $NiAl_2O_4$ along with the phases revealed for as coated superalloys. These identified phases are in agreement with those observed by Wu, Y. N. et al (2001) and Wu, X. et al (2001). Overlapping of Ni and Cr (Fig. 7.25) indicates that these elements lie along the splat boundaries, and might have formed $NiCr_2O_4$ spinels.

Wherever nickel is present, oxygen is less, thereby indicating that splats of nickel have not oxidised or oxidised to a lesser extent, although oxygen seems to have penetrated along the splat boundaries and reacted with aluminium, chromium and yttrium which have shown there existence along the interface between the splats (Fig. 7.22 and Fig. 7.23). Further from EPMA it is confirmed that the places devoid of nickel are rich in oxygen, aluminium, chromium and yttrium. These oxides are recognized as protective oxides for high temperature oxidation and hot corrosion. The probable mechanism of attack for this coating in the given boiler environment is shown in Fig. 7.55.

7.3.3 Ni-20Cr Coating

This coating has shown good resistance to erosion-corrosion in the given environment. No visual crack is indicated and the green colour in the top layer might be due to the presence of NiO. The weight change and erosion-corrosion rate values indicate the protective behaviour of this Ni-20Cr coating. The erosion-corrosion rate of Ni-20Cr coating on Superni 718 superalloy is least amongst the coated superalloys. Kunioshi et al (2005) has also obtained similar lower erosion-oxidation rate for HVOF sprayed Ni-20Cr coating using laboratory test rig.

The phases revealed by XRD diffractograms are found to be in agreement with those reported by Calvarin et al (2000). Presence of SiO_2, Al_2O_3, SO_3 and Fe_2O_3 in micrographs of Figs. 7.33 and 7.34 as revealed by the EDAX analysis may be attributed to ash embedment into the scale. The possibility for formation of such phase in ash constituents during combustion has further been reported by Nelson et al (1959).

The cross-sectional EDAX analyses shown in Figs. 7.35 & 7.36 indicate the outer layer of scale to be rich in nickel. Further similar to exposed NiCrAlY coating, these analyses shows that wherever nickel is present, oxygen is less, although higher percentage of oxygen seems to have penetrated along the splat boundaries and reacted with chromium in the top coat and with aluminium, chromium and yttrium in the bond

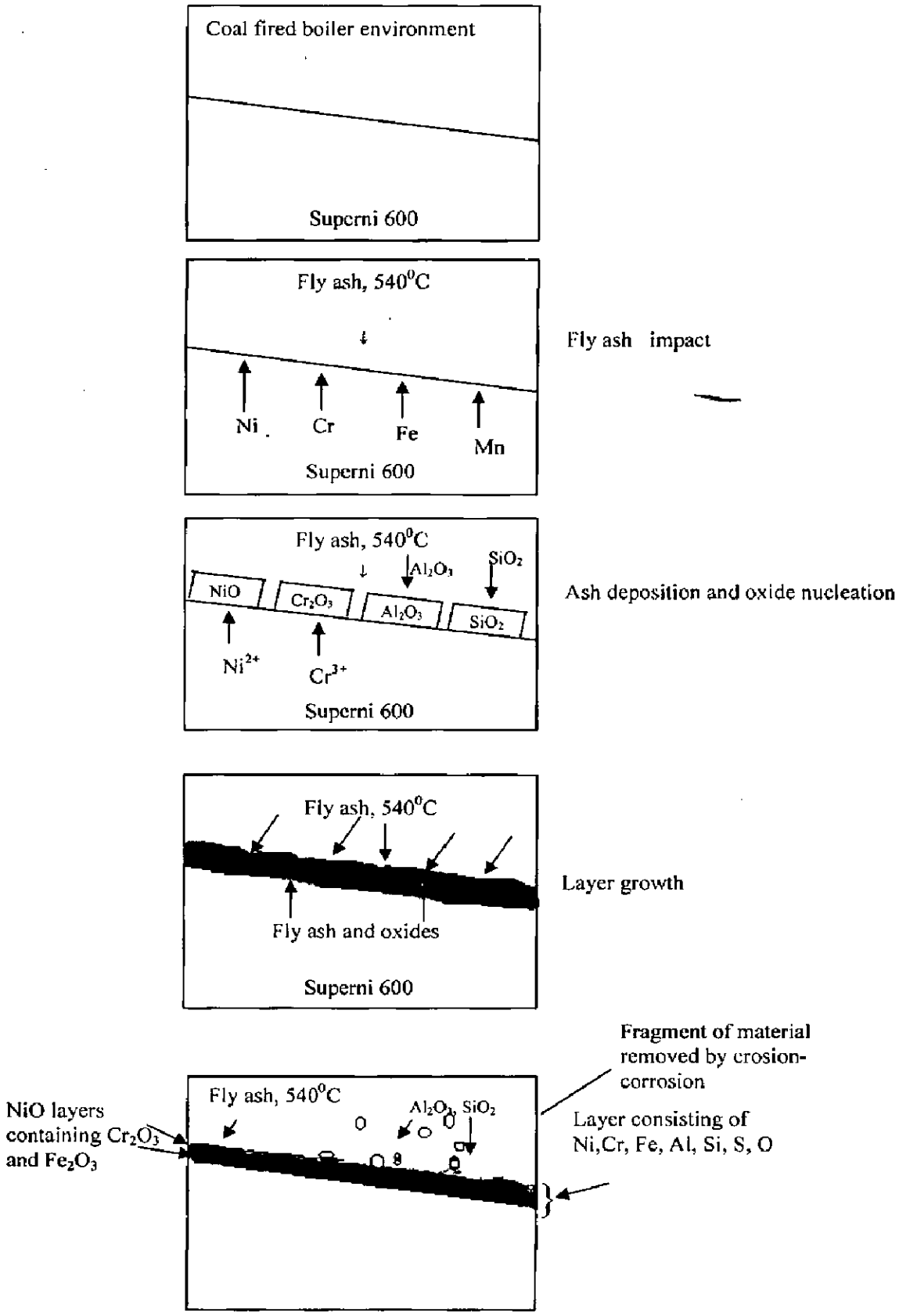

Fig. 7.54 Schematic diagram showing probable erosion-corrosion mechanism for the uncoated Superni 600 superalloy exposed to boiler environment at 540°C for 1000 hours.

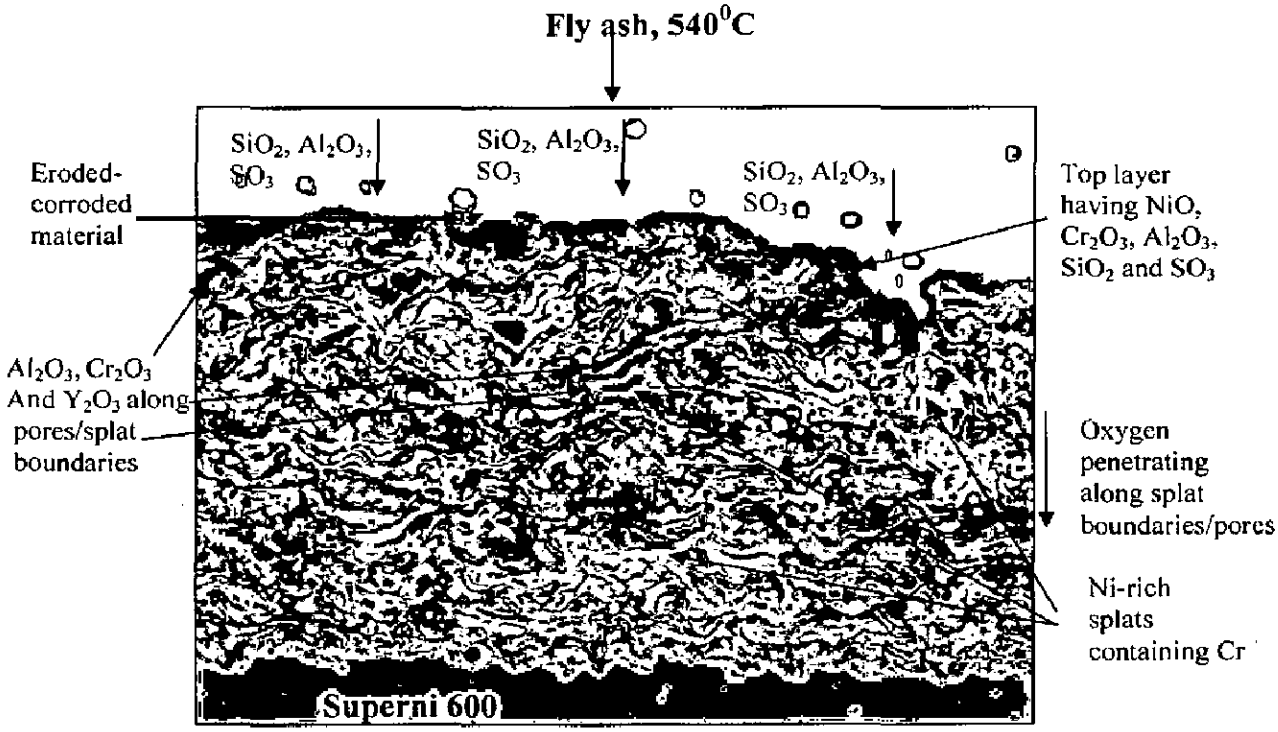

Fig. 7.55 Schematic diagram showing probable erosion-corrosion mode for the NiCrAlY coated Superni 600 superalloy exposed to boiler environment at 540°C for 1000 hours.

coating which have shown there existence along the interface between the splats (Fig. 7.35 and Fig. 7.36). This indicates that nickel has either not oxidised or oxidised to a lesser extent, whereas Cr, Al and Y have oxidised and generally persisted along the splat interfaces. Further from EPMA it is confirmed that the places devoid of nickel are rich in oxygen, aluminium, chromium and yttrium. EPMA analysis also confirms the formation of outer layer of oxides of Ni and Cr (Figs. 7.39 and 7.40). Identical results have also been reported by Calvarin et al (2000) where they have observed the growth of outward layer of NiO and an intermediate layer of NiO and Cr_2O_3 during oxidation studies at 500°C and have reported the absence of both internal oxidation and continuous chromia layer. They further suggested that at 600°C, in addition to NiO and Cr_2O_3 layer, the intermediate layer of $NiCr_2O_4$ is present. The mechanism for the Ni-20Cr coating under oxidising condition might be as given below:

$$Ni + \frac{1}{2}O_2 \rightarrow NiO$$

The oxygen might have penetrated through this porous layer of NiO and reacted with chromium to form chromia:

$$2Cr + \frac{3}{2}O_2 \rightarrow Cr_2O_3$$

Outer interface of this inner chromia layer is richer in nickel which might have led to the growth of spinel of nickel-chromium as per the reaction (Calvarin et al, 2000):

$$Cr_2O_3 + Ni + \frac{1}{2}O_2 \rightarrow NiCr_2O_4$$

In the present investigation cross-sectional EDAX analyses has further confirmed the penetration of reacting species upto the coating-substrate interface in case of coated superalloys but have not attacked the base superalloys (Fig. 7.47). This has also been confirmed by the EPMA analysis. The probable mechanism of attack for this coating is shown in Fig. 7.56.

7.3.4 Ni_3Al Coating

From weight change values it is apparent that the highest weight change per unit area was shown by Ni_3Al coatings on the base superalloys in the given boiler environment. The higher weight gain in case of coated Superni 600 may be attributed to the formation of Al_2O_3. The formation of Al, Cr, and Y oxides along the intersplats block the further entrance of oxygen into the substrate and provide protection to the base superalloys.

The nickel-aluminide coated specimens, when tested at 540°C for 10 cycles, still retain features of the coating microdroplets. This reveals that the coating stays on the surface to prevent scale flaking and therefore resulted in the larger weight gain shown in Fig. 7.38. In this regard, we can perceive that the nickel-aluminide coating protects superalloys from flaking of the oxide scale. Similar results have been obtained by He et al (2001). They suggested that $NiAl_3$ transforms into NiAl by converting aluminium into the γ-Al_2O_3 phase when exposed at 500°C. Further it is worth noting that no iron oxide is detected, indicating that the weight gain observed is predominantly contributed by Al_2O_3 formation. The probable mode of attack for this coated superalloy might be suggested as shown in Fig. 7.57.

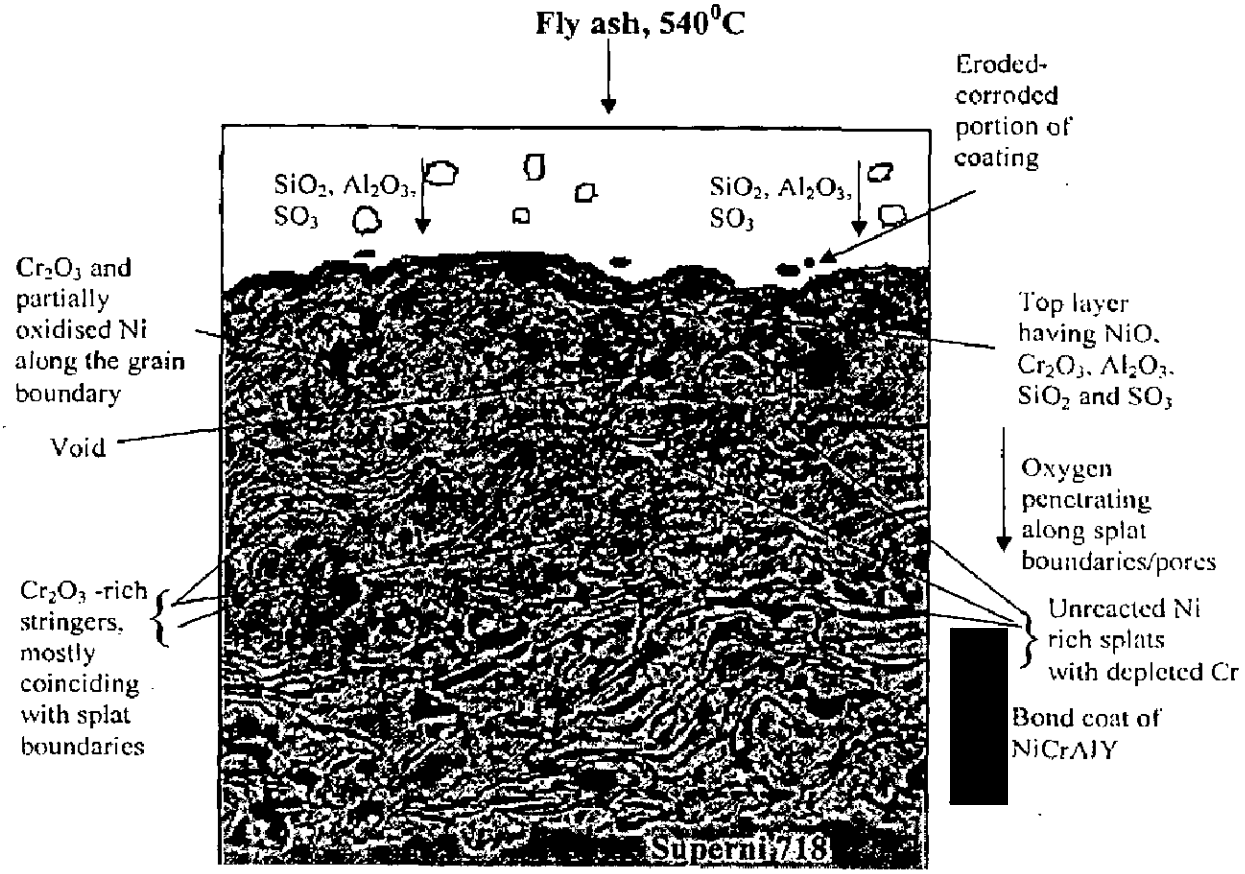

Fig. 7.56 Schematic diagram showing probable erosion-corrosion mode for the Ni-20Cr coated Superni 718 superalloy exposed to boiler environment at 540°C for 1000 hours.

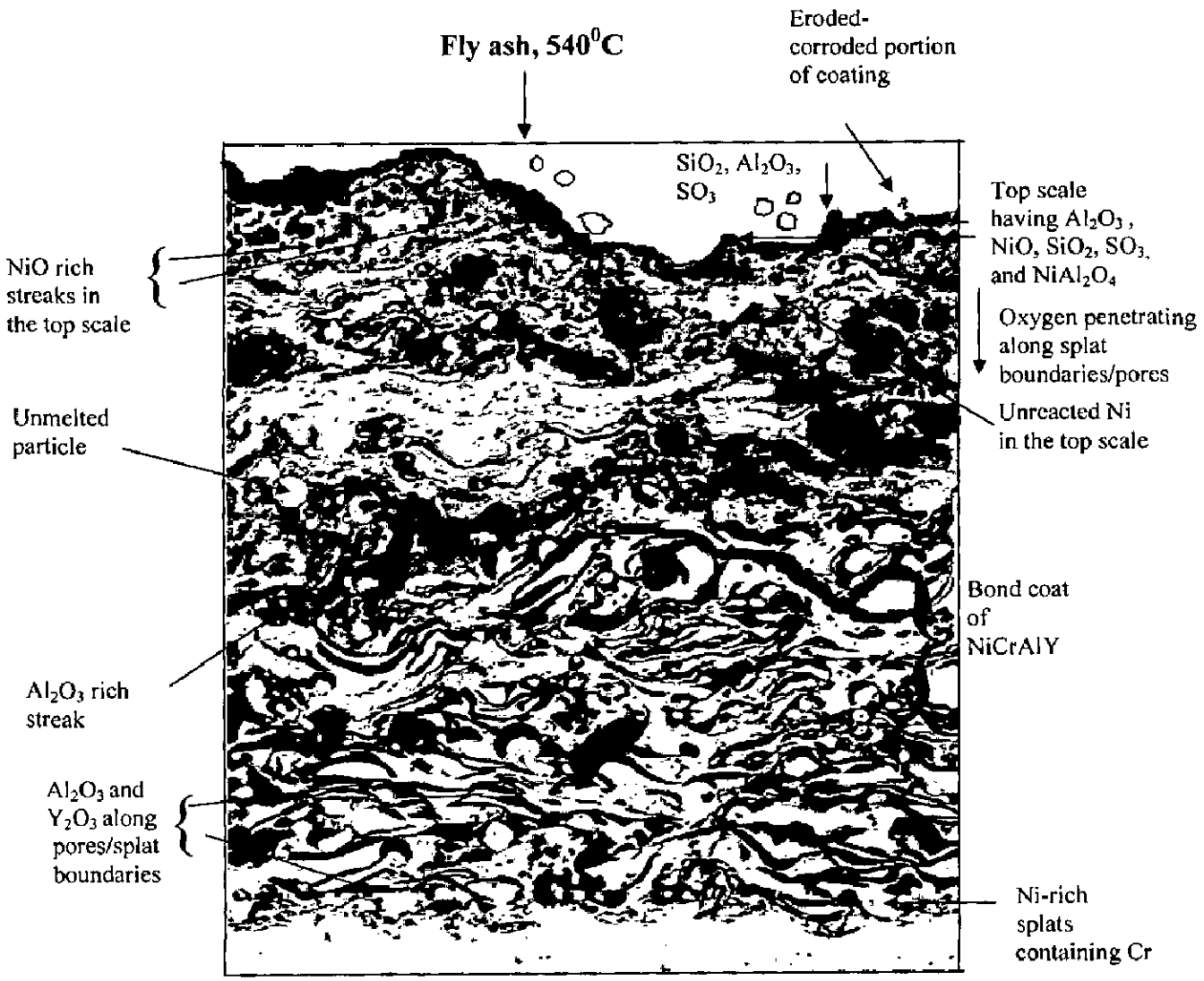

Fig. 7.57 Schematic diagram showing probable erosion-corrosion mode for the Ni_3Al coated Superfer 800H superalloy exposed to boiler environment at 540^{0}C for 1000 hours.

Chapter 8

COMPARATIVE DISCUSSION

In this chapter, the results of the current investigation giving comparative performance of the superalloys and superalloys coated with various coatings by the plasma spray process for room temperature erosion, sliding wear and actual industrial environment in coal fired thermal plant have been discussed.

8.1 ROOM TEMPERATURE EROSION STUDIES

The bar charts showing the room temperature average volumetric erosion loss at 30° and 90° impact angles, for the coated and uncoated superalloys are presented in Figs. 8.1 and 8.2. From the bar charts, it can be inferred that all the uncoated superalloys under study have shown slightly better erosion resistance against the impact of silica sand particles at 90° impact angle. There is no significant difference in the erosion loss of superalloys at 30° impact angle, whereas at 90° impact angle, the Ni-based superalloys have shown better erosion resistance as compared to Fe- and Co- based superalloys.

The sequence of superalloys based on the erosion resistance at 90° impact angle is:

Superni 718 > Superni 75 > Superni 600 > Superco 605 > Superfer 800H

No clear cut correlation with the hardness of the superalloys against the erosion loss has been obtained. The relatively higher erosion loss of Superfer 800H might have been contributed by the presence of manganese and silicon. Further the difference in erosion rate of all these superalloys is marginal and may be affected by their properties such as grain size, thermomechanical factor, types of microconstituents and their distribution, impurities shape and size, etc, which have not been investigated in the present work.

Comparing the erosion resistance of NiCrAlY, Ni-20Cr and Ni_3Al coatings for the room temperature erosion condition at 30° impact angle (Fig. 8.1), sequences observed for the different coated superalloys are as follows:

Ni_3Al > NiCrAlY > Ni-20Cr	for	Superni 75, Superfer 800H and Superni 718
NiCrAlY > Ni_3Al > Ni-20Cr	for	Superni 600 and Superco 605

Comparing the erosion resistance of NiCrAlY, Ni-20Cr and Ni_3Al coatings for the room temperature erosion condition at 90° impact angle (Fig. 8.2), sequences observed for the different coated superalloys are as follows:

Ni_3Al > Ni-20Cr > NiCrAlY	for	Superni 75 and Superni 718
Ni_3Al > NiCrAlY > Ni-20Cr	for	Superni 600 , Superfer 800H and Superco 605

Ni_3Al coating has shown better erosion resistance at 90° impact angle amongst the coated superalloys which may be attributed to its higher ductility. The volumetric erosion loss of the Ni_3Al coated superalloys is significantly lower than that for the NiCrAlY and Ni-20Cr coated superalloys under the room temperature erosion conditions. The higher volumetric erosion rate of the plasma sprayed coatings in general might be attributed partly to the presence of some porosity in the coatings.

Further the difference in erosion resistance of NiCrAlY and Ni_3Al coatings for Superni 600 substrate is very little at 30° impact angle. Also the difference in erosion resistance of NiCrAlY and Ni-20Cr coatings for Superni 75 and Superni 718 substrates is very little at 90° impact angle.

Thus, in general the sequence for the overall protective behaviour of coatings in room temperature erosion condition can be arranged as:

Ni_3Al > NiCrAlY > Ni-20Cr

Further the behaviour of these plasma sprayed coatings is different on different superalloy substrates, which might have been due to a little diffusion of elements from the substrate to the coatings. The EPMA analyses of as sprayed coatings have shown some traces of substrate elements into the coatings as illustrated in the schematic diagram, Fig. 8.3. Minor amount of Fe and Ti have been observed into the coated Superni 75 superalloys. Coated Superni 600 indicates the diffusion of Fe and Mn, whereas Superfer 800H indicates presence of Fe, Mn, Al and Ti in the coatings. Traces of Co, W, Fe and Mn have migrated into the coatings from the Superco 605 substrates. The coatings on Superni 718 have shown the minor amounts of Fe, Mo, Ti, Mn and Ta.

8.2 SLIDING WEAR STUDIES

The bar chart, Fig. 8.4, indicates the highest specific wear rate or the lowest sliding wear resistance of Superni 600 which might be attributed to its lower hardness (260 Hv) whereas highest sliding wear resistance is found for Superfer 800H followed by

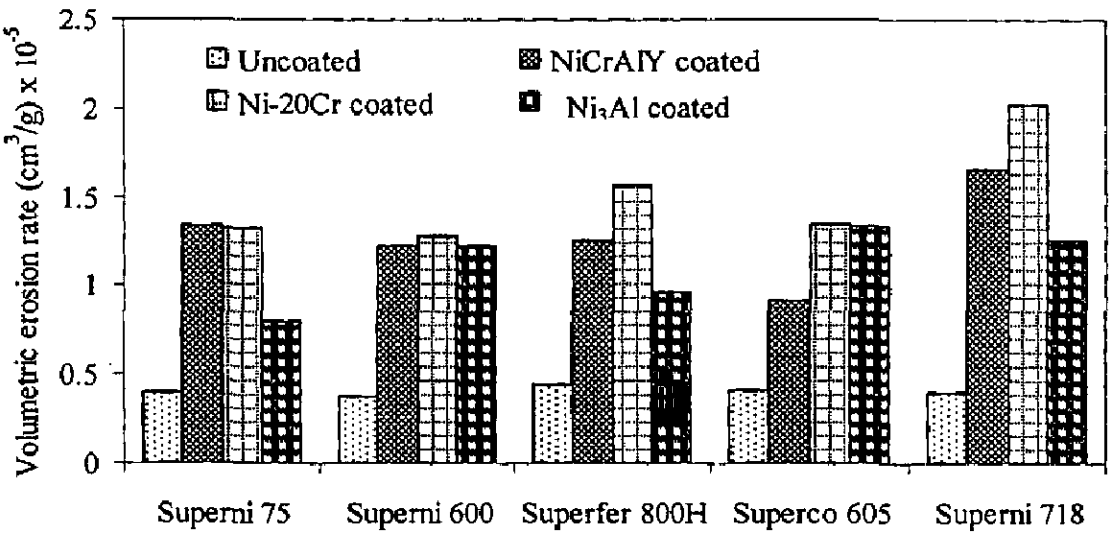

Fig. 8.1 Bar chart indicating volumetric erosion rate in cm^3/g for the coated and uncoated superalloys subjected to erosion at a velocity of 40 ms^{-1} and impact angle of 30° using silica sand of average particle size 180 μm as erodent.

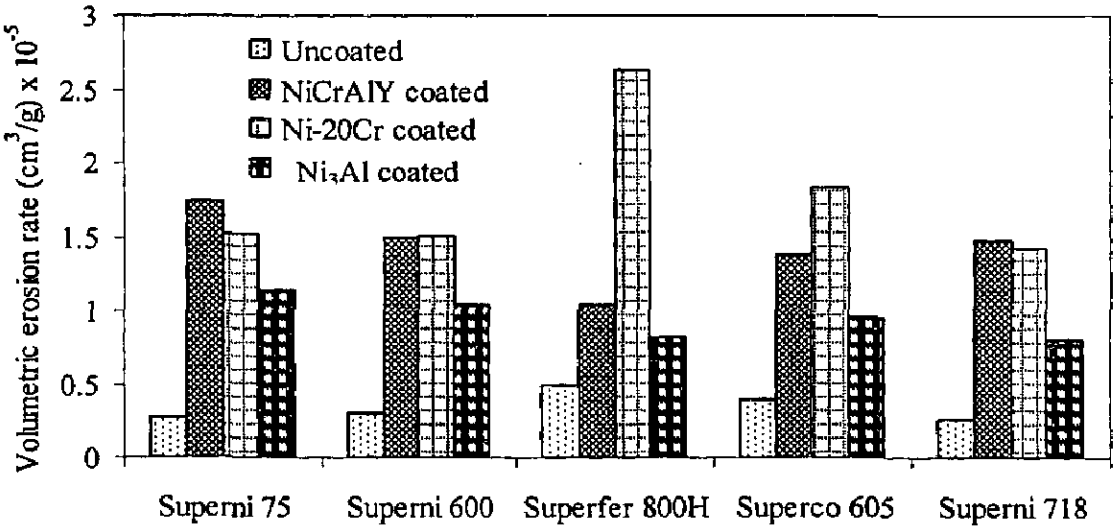

Fig. 8.2 Bar chart indicating volumetric erosion rate in cm^3/g for the coated and uncoated superalloys subjected to erosion at a velocity of 40 ms^{-1} and impact angle of 90° using silica sand of average particle size 180 μm as erodent.

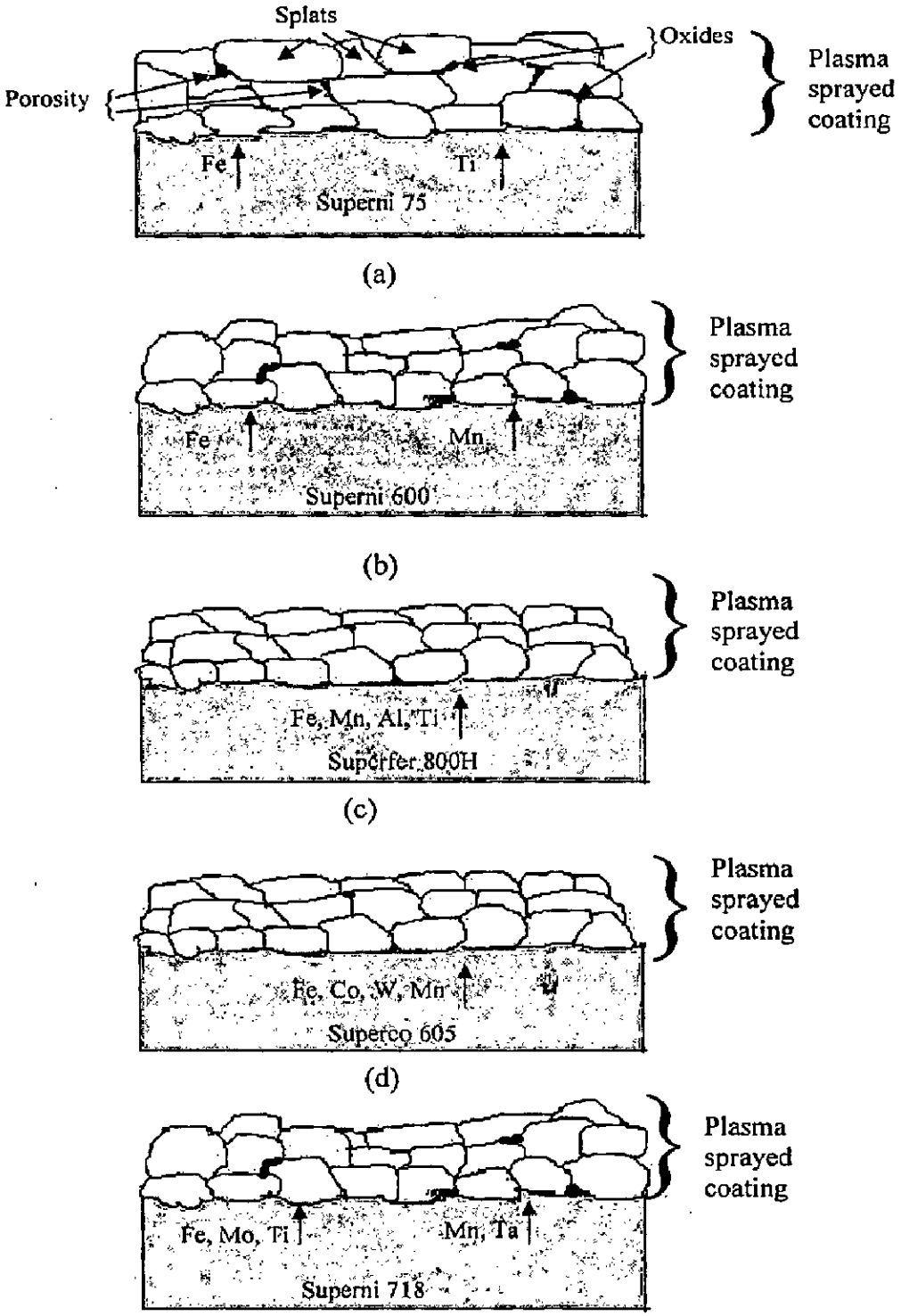

Fig. 8.3 Schematic diagram of plasma sprayed coatings on different superalloy substrates indicating minor diffusion of elements from substrate into the coatings.

(a) Superni 75 (b) Superni 600 (c) Superfer 800H

(d) Superco 605 (e) Superni 718

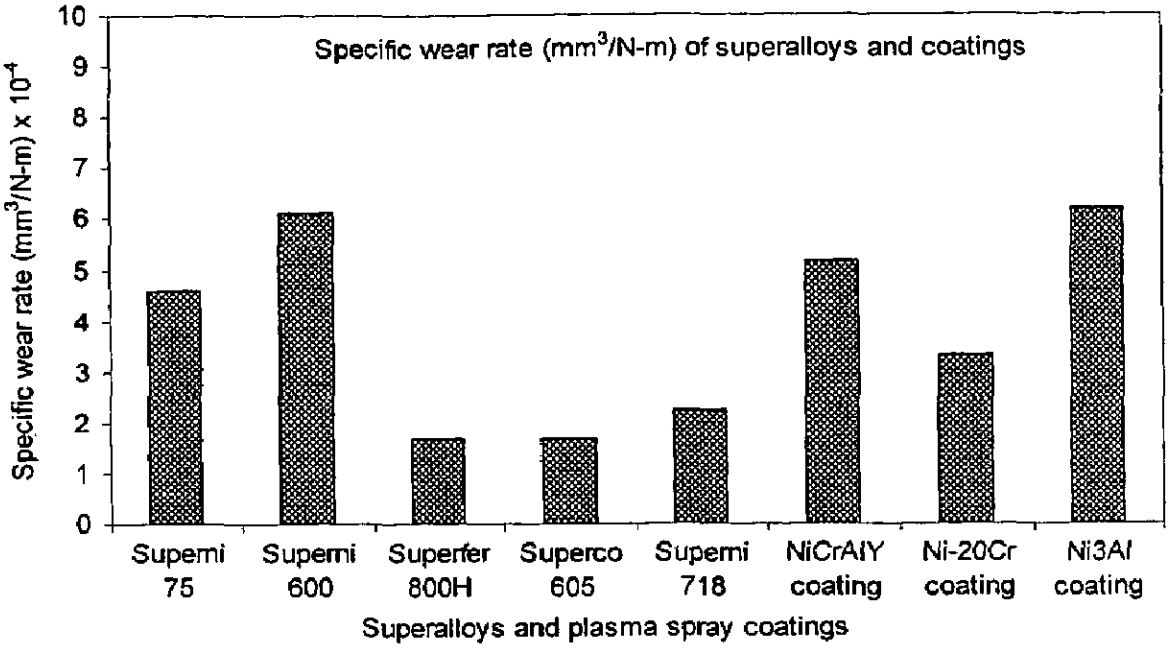

Fig. 8.4 A histogram illustrating the specific wear rate of different superalloys and plasma sprayed coatings on Superfer 800H superalloy substrate.

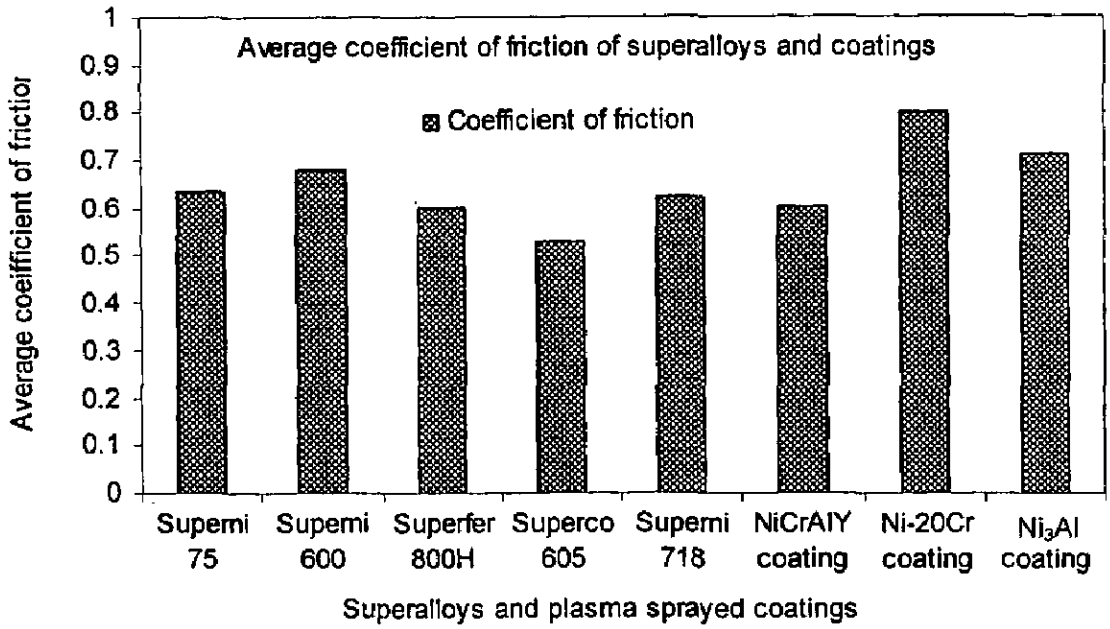

Fig. 8.5 A histogram illustrating the average coefficient of friction for different superalloys and plasma sprayed coatings on Superfer 800H superalloy substrate.

Superco 605 having highest hardness (512 Hv). The relatively higher sliding wear resistance of Superfer 800H might have been also contributed to its chemical composition and other factors as discussed in section 8.1.

Comparing the sliding wear resistance of NiCrAlY, Ni-20Cr and Ni_3Al coatings, sequences observed for the different coated superalloys are as follows:

Ni-20Cr > NiCrAlY > Ni_3Al for Superfer 800H

The Ni-20Cr coating is having the highest hardness amongst the coatings, which might have contributed to its better wear resistance. Whereas the inferior wear resistance of Ni_3Al coating may be due to its lower hardness.

Superni 600 superalloy has shown the highest average coefficient of friction (0.679) amongst the worn superalloys, whereas that of Superco 605 superalloy was found to be least (0.529), as shown in Fig. 8.5. Amongst the plasma sprayed coatings the highest coefficient of friction is revealed for Ni-20Cr coating (average 0.7985) whereas least average coefficient of friction was given by NiCrAlY coating (0.5998). The wear rate should have been higher for the material with high coefficient of friction however it is not so in the present study indicating that the other factors such as the materials chemistry and processing parameters greatly affects the wear.

8.3 EROSION-CORROSION IN LOW TEMPERATURE PRIMARY SUPERHEATER OF COAL-FIRED BOILER AT 540°C FOR 1000 HOURS

The bar chart Fig. 8.6, indicating the total extent of erosion-corrosion for the uncoated and coated superalloys exposed to the boiler environment, consists of two portions. The upper portion denotes the change in thickness of material whereas the lower portion denotes the thickness upto which oxygen has penetrated. From the bar chart, it can be inferred that minimum resistance to thickness loss has been shown by Superni 600 superalloy followed by Superfer 800H. It indicates the higher thickness of oxidised scale for Superni 718 superalloy followed by Superni 600 superalloy. The Superni 75 superalloy has shown better erosion-corrosion resistance in the boiler environment in terms of thickness loss.

Comparing the erosion-corrosion loss of NiCrAlY and Ni-20Cr coated superalloys in boiler environment, it can be inferred that the difference in thickness loss with respect to substrate is negligible. In case of Ni_3Al coated superalloy the thickness loss is perceptible and is follows:

Superfer 800H > Superni 600 > Superni 718 > Superni 75

Further all the coated superalloys are partially oxidised upto the coating substrate interface. The substrate superalloys remain unaffected by the environment attack. Amongst the three coatings, Ni-20Cr coated superalloys have provided maximum resistance against the fly ash impact at 540°C. The slightly higher thickness loss has been shown by NiCrAlY coated superalloys. The Ni_3Al coated superalloys have shown similar coating thickness removal as obtained for uncoated superalloys. Although the thickness removal of material is low for the coated superalloys, the thickness of partially oxidised coated layer is significant. The EDAX and EPMA analysis (Chapter 7) indicate the partial oxidation of the coated superalloys upto the coating thickness. From the EDAX and EPMA analyses of the coated samples, it is clear that the Ni exists at the centre of splats and remains unoxidised. Whereas aluminium, chromium and yttrium which exist along the splat boundaries get oxidised. Thus the bar chart illustrates the higher overall thickness loss of the coated superalloys.

During erosion-corrosion under the boiler environment, oxygen penetrates along the interconnected splat boundaries of the plasma sprayed coatings and pores, and oxidises mainly Al and Y present at the periphery of splats alongwith the Cr. These oxides might be responsible for blocking/slowing down the transport of oxygen along the splat boundaries and pores. The protection shown by these coatings might also be contributed by the simultaneous formation of a hard protective oxide α-Al_2O_3 alongwith Cr_2O_3 and $NiCr_2O_4$. According to Toma et al (1999), α-Al_2O_3 grows very slow and is thermodynamically stable. This hard oxides formed on the surface protects the coatings from the erosive attack by fly ash. Thus in the boiler environment coating layers get partially oxidised, and acts as a perfect barrier against erosion-corrosion of superalloys. Further the partially oxidised coatings remain intact even after 1000 hours cycle exposure, thus it can be presumed that it will enhance the life of boiler tube in the evaluated environment.

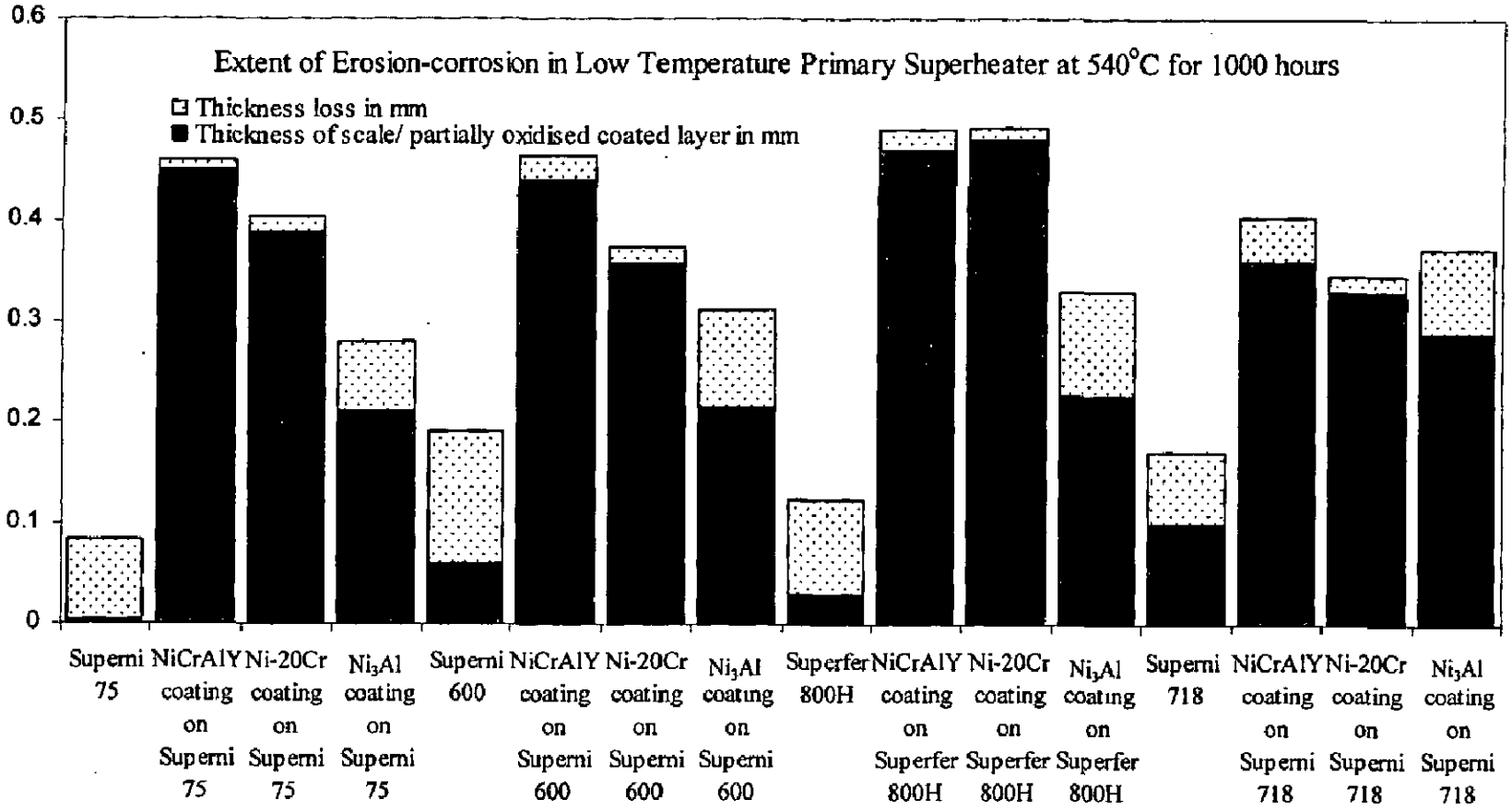

Fig. 8. 6 Bar chart indicating total extent of thickness loss in mm of uncoated and NiCrAlY, Ni-20Cr and Ni_3Al coated superalloys when exposed to the Low Temperature Primary Superheater of coal fired boiler at 540°C for 1000 hours.

Fly ash deposited together with scale formed by slower oxidation rate at 540°C in the boiler environment might be promoting denser and more impact resistant top layers resulting in lower metal loss. The improvement in erosion resistance of plasma sprayed coatings against superalloys at higher temperature in the boiler environment as compared to the room temperature might also be due to increase in ductility of the eroding material without a commensurate significant reduction in its strength as suggested by Levy and Hickey (1986).

The erosion behaviour at room temperature of these alloys and coatings indicate that the coatings are having relatively higher erosion rates. But these coatings are adherent and will definitely be useful in protecting the substrate alloy against erosion and will act as a sacrificial material. The coatings have not been very effective in improving the wear resistance under sliding condition. The superalloys with the coatings may be used in the boiler environment as they will provide the requisite protection against erosion-corrosion.

Chapter 9
CONCLUSIONS

In the present study, investigations have been carried out on the erosion behaviour of NiCrAlY, Ni-20Cr and Ni_3Al coated and uncoated superalloys namely Superni 75, Superni 600, Superfer 800H, Superco 605 and Superni 718. These coatings are produced by argon shrouded plasma spray process with a bond coat of NiCrAlY. The first two coating powders were commercially available whereas the third coating powder i.e. Ni_3Al was prepared using stochiometric mixture of nickel-aluminium. The uncoated and coated superalloys have been investigated for their room temperature erosion behaviour, sliding wear behaviour and their behaviour in erosive environment of coal fired thermal power plant. The important conclusions from the present study are enumerated below:

Characterisation of Coatings

(1) The requisite coatings NiCrAlY, Ni-20Cr and Ni_3Al of thickness in the range of approximately 350-500 μm including bond coat of around 150 μm were successfully obtained by shrouded plasma spray process on the given superalloy substrates.

(2) As-sprayed NiCrAlY coating revealed presence of γ (nickel solid solution) and γ′ (Ni_3Al) phases. Ni-20Cr coating has indicated nickel solid solution matrix. Ni_3Al formation was confirmed in NiAl.coating.

(3) The microhardness along the cross-section of the coatings is found varying with the distance from the coating-substrate interface. The Ni-20Cr coating has shown a maximum microhardness while Ni_3Al coating exhibited a minimum microhardness amongst the coatings.

(4) A little diffusion of various elements into the plasma sprayed coatings from the substrate has been indicated by EPMA. The diffusion between the bond coat and top coat is relatively high. Aluminium is found to be the most vulnerable element to the diffusion phenomenon.

Room Temperature Erosion Studies

(5) Among the uncoated superalloys, Nickel based superalloys showed the better erosion resistance, whereas Fe- and Co- based superalloys exhibited marginally higher erosion rate at both the impact angles.

(6) The steady state erosion rates for the investigated superalloys at 30° impact angle is found in following order:

Superfer 800H > Superco 605> Superni 718 > Superni 75 > Superni 600

(7) The sequence of superalloys based on the data for erosion rate at 90° impact angle is:

Superfer 800H > Superco 605 > Superni 600 > Superni 75 > Superni 718

(8) All the three Ni- based superalloys have shown higher erosion rate at 30° impact angle as compare to that at 90° impact angle indicating the ductile behaviour of these superalloys.

(9) A negligible effect of the change in impact angle on the steady state erosion rate of Fe- and Co- based superalloys has been observed.

(10) All the uncoated and coated superalloys have shown relatively higher erosion rate in the early cycles of study up to 4-5 cycles, followed by steady state erosion rate with increase in number of cycles. Embedment of sand particles has been observed during erosion, which might also be contributing to the variation of the erosion rate (increases when embedded and decreases when removed) of the coating.

(11) Based on the weight loss data, the erosion rates of the NiCrAlY coated superalloys are as follow:

for 30° Superni 718> Superni 75> Superni 600> Superfer 800H > Superco 605

for 90° Superni 75> Superni 600> Superni 718> Superco 605> Superfer 800H

(12) The Ni-20Cr coated superalloys depending upon their erosion resistance are:

for 30° Superni 600 > Superni 75 > Superco 605 > Superfer 800H > Superni 718

for 90° Superni 718 > Superni 600 > Superni 75 > Superco 605 > Superfer 800H

(13) The Ni_3Al coated superalloys with regard to their erosion resistance are:

for 30° Superni 75 > Superfer 800H > Superni 600 > Superni 718 > Superco 605

for 90° Superni 718 > Superfer 800H > Superco 605 > Superni 600 > Superni 75

(14) The overall ductile behaviour in erosion studies has been revealed by the scanning electron microscope for all the bare and coated superalloys in the present study.

(15) In general, the sequence for the overall protective behaviour of coatings in room temperature erosion condition can be arranged as:

Ni_3Al > NiCrAlY > Ni-20Cr

Sliding Wear Studies

(16) Superni 600 superalloy has shown the highest average coefficient of friction amongst the worn superalloys, whereas that of Superco 605 superalloy is found to be least.

(17) Amongst the plasma sprayed coatings the highest average coefficient of friction is revealed for Ni-20Cr coating whereas least average coefficient of friction was given by NiCrAlY coating.

(18) The cumulative volume loss of Superni 600 superalloy is the highest amongst the superalloys followed by Superni 75. The cumulative wear volume of Superfer 800H and Superco 605 are almost similar.

(19) The cumulative wear volume loss of the Ni-20Cr coating is lowest among the three coatings which might be attributed to its highest hardness.

(20) Among the uncoated superalloys, Superfer 800H has shown the lowest value of specific wear rate. Specific wear rate of Superco 605 superalloy is only slightly higher as compared to Superfer 800H, followed by Superni 718. Whereas Superni 600 superalloy has given highest specific wear rate, followed by Superni 75. Among the coated superalloys, lowest value of specific wear was revealed from Ni-20Cr coating and highest wear rate was shown by Ni_3Al coating.

Erosion Studies in Boiler Environment

(21) In actual industrial environment that is running boiler in low temperature primary superheater zone where average temperature is around 540°C, all the superalloys have shown weight loss suggesting the contribution of erosion.

(22) The alloy constituents are getting oxidised and scale is developing which simultaneously being eroded by fly ash impact. The embedment of ash particles in the top layer of exposed superalloys has been indicated.

(23) Main phases identified in all the exposed coated superalloys after 1000 hours exposure to the coal fired boiler environment are NiO, Cr_2O_3, Al_2O_3 and SiO_2.

(24) In case of the boiler exposed plasma sprayed coatings, elemental analysis along the cross-section showed that wherever nickel is present, oxygen is negligible, although higher percentage of oxygen seems to have penetrated along the splat boundaries and reacted with chromium in the top coat, and with aluminium, chromium and yttrium in the bond coat, which have shown there existence along the interface between the splats.

(25) From weight change data it can be inferred that the protection to the base metal has been provided by the NiCrAlY coating. NiCrAlY coating on Superni 600 and Superfer 800 H has shown weight loss whereas the coating on Superni 75 and 718 has shown weight gain.

(26) Ni-20Cr coating has shown good resistance to erosion-corrosion in the boiler environment. The erosion-corrosion rate of Ni-20Cr coating on Superni 718 superalloy in the boiler environment is least amongst the coated superalloys.

(27) Amongst the boiler exposed coated superalloys Ni_3Al coatings on all the substrate superalloys have shown relatively higher weight gain as compared to the other coatings. This may be attributed to the formation of Al_2O_3 along the splat interfaces.

(28) Fly ash deposited together with scale formed by slower oxidation rate at 540°C in the boiler environment might be promoting denser and more impact resistant top layers resulting in lower metal loss of the coatings.

(29) The erosion behaviour at room temperature of these alloys and coatings indicate that the coatings are having relatively higher erosion rates. But these coatings are adherent and will definitely be useful in protecting the substrate alloy against erosion and will act as a sacrificial material. The coatings have not been very effective in improving the wear resistance under sliding condition. The superalloys with the coatings may be used in the boiler environment as they will provide the requisite protection against erosion-corrosion.

SUGGESTIONS FOR FUTURE WORK

1. All the investigated coatings have maintained continuous surface contact with their respective substrate superalloys during erosion-corrosion studies in boiler environment. These coatings should be investigated for other applications such as jet engines, gas turbines.
2. Studies may be conducted to investigate the erosion-corrosion behaviour of the thermal spray coatings developed by other processes such as high-velocity oxy-fuel and detonation spray processes using conventional and nano-powders introducing some rare earth elements.
3. Cost effectiveness analysis should be done for different types of coatings.
4. Attempts may be made to estimate the useful life of these coated superalloys by extrapolation of the laboratory data using mathematical modeling.
5. The post coating treatments may be adopted to eliminate the porosity of these coatings so as to enhance their erosion resistance.

Table A.1 Mechanisms of erosion of various metals, alloys and coatings as reported by various researchers.

Material	Brief Details
	According to **Kapoor and Johnson (1994)** slivers are formed as a result of progressive plastic extrusion, a process termed as 'ratchetting', in which small increments of plastic deformation are accumulated with each pass of the slider or cycle of loading. **Kapoor and Johnson (1995)** further reported that when a component of elastic-plastic material is subjected to cyclic loading it may respond in one of four different ways: (i) At sufficiently light loads no element of material reaches yield so that the response is perfectly elastic. The limit load below which this occurs is known as the elastic limit. (ii) Above the elastic limit some material elements may yield on first loading, but the development of protective residual stresses and/or strain hardening may cause the component to shakedown such that the steady cyclic state is perfectly elastic. The maximum load for shakedown is known as elastic shakedown limit. If the shakedown limit is exceeded, plastic deformation will occur in each cycle of load with one of the two possible consequences. (iii) If the steady cyclic state consists of a closed cycle of plastic strain it is described as a state of plastic shakedown. On the other hand a steady accumulation of unidirectional plastic strain may occur and this incremental process is known as ratchetting. It is this behaviour which is believed to account for the extrusion of slivers. The load above which it occurs is the plastic shakedown limit or the ratchetting threshold.

Boiler tube steel (AISI1015)	**Zhang et al (2001)** have reported that the material removal mechanisms mainly depend on the particle collision angle and fall into four regimes. According to them they are rubbing and scratching regime when the particle collision angle α is below 20°, cutting and cracking regime when α is between 20 and 30°, forging and extrusion regime when α varies from 30 to 80° and sputtering and adhesion regime when the angle is beyond 80°, but <90°. They added that however, since the transition from one regime to the other is gradual, the above boundary division is not absolutely exact. They suggested that highest wear rate take place with the cutting and cracking mechanism when the particle collision angle is in the range of 20–30°.
Laser treated and untreated carbon steel	An air jet erosion tester utilizing SiC particles as erodent was used for comparing the erosion behavior of laser-treated steels with those of untreated steel and annealed Armco iron (HV 76) by **Rao et al, 1993**. They carried out erosion tests at two impact velocities (46 and 96 ms^{-1}) and three impact angles (30°, 60° and 90°). They concluded that laser surface hardening does not improve the erosion resistance of 0.4% C steel and that the erosion rates of the steels are very similar to that of annealed Armco iron.
sodalime glass, Pyrex glass and single crystalline {100} silicon	**Wensink and Elwenspoek (2002)** studied the transition from brittle to ductile erosion for three brittle materials: sodalime glass, Pyrex glass and single crystalline {100} silicon. Besides the erosion rates, they also measured the erosion classification value (E_{cv}), which is the ratio of the erosion rate at 45° and 90° impact angle. Further they suggested that brittle erosion has an E_{cv} of about 0.45, whereas E_{cv} of ductile erosion is larger than 1 and this can give a quick indication of the erosion mechanism. The investigators concluded that the transition is not suddenly, but extends over a larger change of kinetic energy. And during this transition, the E_{cv} slowly rises to a value >1. Further they proposed that the large kinetic energy exponent during the transition has two effects on the E_{cv}. First due to the higher energy exponent the E_{cv} slightly decreases, second when kinetic energy is further reduced the ductile erosion

	mechanisms become more and more important and the E_{cv} can eventually increase to a ductile value. According to them this progressive transition is a result of the many unequal impact events in erosion. Further particles shapes, size, velocities and impact orientations are not identical so each impact has a different degree of effectiveness. And the chance a lateral crack is initiated from a particle impact becomes smaller as the kinetic energy decreases.
WC/Co (coarse grained hard metal)	**Gee et al (2003)** studied the stepwise erosion of the WC/Co (coarse grained hard metal) sample and reported that wear occurred by the accumulation of damage, fracture and removal of single grain of WC. It is shown that the wear occurs by progressive damage process that involves: ❖ Removal of binder phase from the surface layer of the sample almost immediately. ❖ Build up of considerable plastic deformation in WC grains. ❖ When further plastic deformation cannot be accommodated, or when local impact forces are too high, individual grains fracture and fragment. ❖ Growth of cracking between individual grains in the WC skeleton of material. ❖ Final breakaway of single WC grains. They concluded no evidence for large scale lateral cracking. However in the high speed steel, they reported some evidence for cracking and local grooving, but the main mechanism for removal of material was fracture of unsupported and grossly deformed layers of material on the surface.

Erosion – Oxidation	
	Wright et al (1995) have proposed an approach for describing the rate of loss from a metal surface subjected to the simultaneous action of high-temperature oxidation and mechanical erosion, in terms that involve the major parameters that determine the oxidation behavior of the alloy and the "erosion potential" of the environment. Different regimes are identified where oxidation or erosion is dominant, and where the two processes act together. It is shown that under conditions where exfoliation of the oxide scale (or of an adherent deposit) can occur, surface loss by erosion-oxidation is a strong function of the metal temperature and the erodent flux. Some simplifying assumptions are made to provide a workable framework for incorporating the parameters in a way that is consistent with the observed modes of material loss. The effects of erodent impacts on scale spallation are statistical in nature, and an initial attempt to address this issue is illustrated. In most simplified forms, three broad but distinct regimes of possible erosion-oxidation interactions can be envisioned which, although they may overlap, may be described in terms of the parameters that control the competing processes and with a logic that follows the observations of the actual process of material loss. ***Regime 1: erosion dominates*** In this regime, the rate of oxide formation is so slow that oxide removal makes a negligible contribution to the overall material loss, which occurs predominantly by the removal of metal. However, the presence of an oxide film may modify the erosion-oxidation interaction by changing the physical (for instance, coefficient of friction) or mechanical (for instance, hardness) properties of the eroding surface. This regime will be encountered at low temperatures and, for very oxidation-resistant alloys, under conditions of very aggressive erosion where the erosive component completely overwhelms the contribution from oxidation. Modeling of the material behavior in this regime probably will rely on the established models of metallic erosion, with the environmental effects (temperature, for instance) being accounted for through their influences on the mechanical properties of the target and erodent materials.

Regime 2: erosion-oxidation interactions

There are obviously several scenarios whereby interactions between erosion and oxidation can result, depending on the relative rates of oxide growth (alloy composition, temperature) and the severity of the erosive action (particle flux, velocity, angle of impingement) in an acceleration of the rate of material loss. Therefore, there is a need to distinguish the circumstances under which each is the dominant cause of material loss, and to describe the actual mode of loss. Also, in some circumstances **(Edington and Wright, 1978)**, parts of the erodent particles may become detached and embedded in the target surface, or parts of the scale itself may be hammered into the surface, resulting in the development of a surface layer that could modify the oxidation and/or erosion behavior of the target, and possibly reduce the rate of material loss. There are some similarities here with the formation of glazes on alloys subjected to sliding wear under conditions of high-temperature oxidation. Depending on the severity of the impact (particle kinetic energy), the thickness of the oxide scale, and the properties of the alloy substrate, the erosion event may lead to the removal of fragments of the oxide scale, or to shedding of the oxide over larger areas, or to the actual removal of substrate metal.

Wright et al (1995) assumed that the conditions of erosion-oxidation are such that no metal is directly removed by the erosion process. Instead, erosion is assumed to accelerate the overall material loss process, and the major mode of material removal is through loss of the oxide scale, so that the material response may be termed "erosion-assisted scale loss." As a starting point, it is assumed that each particle impact is an erosive event that removes the oxide scale completely over an area referred to as the "erosion footprint", and that the erosion-oxidation process occurs uniformly over the target surface. The situation where erosion removes only a fraction of the oxide thickness has also been considered by **Wright et al (1990)**. Energy may be transferred by the erodent particles to the target surface in several ways, for instance, in the form of a shock wave that travels along the scale-substrate interface, or as a shearing action from displacement of the oxide structure or deformation of the metal substrate, and is sufficient to overcome the scale-substrate bonding so that the growing scale is effectively spalled from the surface. The net result of the erosion-oxidation process in this regime is that the rate of oxidation increases as the scale is thinned locally, the magnitude of the increased oxidation rate depending on the thickness of oxide removed by the erosive impact.

	Regime 3: oxidation dominates In this regime, the erosive component removes only the outer part of a continuous and growing oxide scale and effectively reduces the oxide thickness, thereby leading to a more rapid rate of oxidation than expected (if the oxidation rate is controlled by diffusion across the oxide). This behavior may be termed "erosion-accelerated oxidation". If the oxidation rate is sufficiently rapid relative to the rate of oxide thinning by erosion, and the oxide is adherent to the metal, then the oxide will continue to thicken at a parabolic rate so that the effectiveness of the erosive component becomes less with time. For every set of erosive conditions, it is suggested that there is a eventual thickness of oxide which, if attained, will resist removal (spallation) by the erosive impacts. This regime is likely to be encountered with alloys that oxidize rapidly, at high temperatures, and for mildly erosive conditions **[Wright et al (1995)]**.
	The erosion of metals operating at elevated temperatures will clearly be influenced by the formation of surface scales such as oxides. Based on bulk properties, the metal substrate will respond in a ductile manner whereas the oxide scale may exhibit a brittle response. Thus in the first instance, high temperature erosion can be considered as material removal from a composite system, consisting of a ductile substrate and a brittle surface oxide **(Stephenson and Nicholls, 1995).** They developed the high temperature erosion mechanism maps which predict the conditions under which various material removal mechanism predominate.
Mechanisms of coating removal	
Ni and Ni-20Cr alloy	**Link et al. (1998)** reviewed that the principle mechanism by which pure metals deteriorate under simultaneous erosion and corrosion conditions at high temperature. Basically the erosion of metal in the absence of oxidation proceeds more slowly at high temperature. This is because the more ductile metal at high temperature absorbs more of the energy of the erosive

impacts in the form of plastic deformation, thus less energy is available to take part in the removal mechanism. Under erosion, a material surface can respond in a brittle or ductile manner, and the energy of the erosive impact can be absorbed in plastic deformation, material removal processes, or in rebound. When the material is brittle, the energy is spent primarily in developing intersecting crack systems and in rebound energy. With ductile materials, energy can be absorbed by causing the material to deform plastically during processes of removal such as cutting and ploughing as well as in the rebound particle.

When a pure nickel is exposed to erosion and oxidation simultaneously, the two processes interact in several different ways that form a logical sequence of interaction regimes. Primarily, these regimes deal with the way in which oxide scale formed by oxidation and is then removed by the erosive processes. Whereas erosion of the metal is not very efficient at temperatures where it has substantial ductility, removal of the less ductile oxide by erosion proceeds much more efficiently. Thus, in the presence of oxidation and erosion conditions simultaneously, the deterioration of the metal proceeds substantially more rapidly than in the presence of either oxidation or erosion alone.

In the first regime, where erosion is not very energetic, an oxide scale will form according to the parabolic growth laws for diffusion control. The surface of the growing scale is removed at a constant rate by the erosion. Thus, the scale will continue to grow until it reaches a thickness at which the rate of growth is equal to the rate of removal by erosion. The more rapid the erosive removal rate, the thinner the scale will be, when this steady state condition reaches and the sooner this situation will be achieved.

With very strong erosion, the steady-state scale may be extremely thin, theoretically, but not be observed on the metal surface. In this condition, the highest rate of degradation of the metal is observed. This is readily understood in the sense that oxide-scale formation is more rapid when the scale is very thin. Thus, if erosion is removing the oxide scale very efficiently, the synergism will cause very rapid material degradation. In this situation, a coherent surface scale is not

	observed, because there is no time for it to form between impacts. Consequently, under such conditions, the metal surface is represented by a composite layer of metal, embedded erodent and oxide particles. Under these conditions also, with no oxide layer to absorb the erosive impact, the metal surface shows substantial plastic deformation and takes on a rippled or hill-and-valley appearance. These mechanisms and the existence of regimes of interaction between erosion and oxidation have been well established for pure metals.
boiler tube	According to **Stringer and Wright (1987),** the two distinct patterns of wastage are commonly observed around the circumference of tubes. These are as follows: ***Type A***, characterized by a maximum wastage somewhere on the lower sides with flats formed about these locations; loss at 180° is relatively low or non-existent. The second wastage pattern, ***Type B***, is characterized by a maximum loss at 180°, and decreasing losses at either side. They reported that while both patterns have been observed in practice, attempts to simulate BFBC wastage in the laboratory almost always result in a Type A pattern. According to them, the distinction between Type A and B is important because it has been suggested, by **Birkby and Gibb** (1987) among others, that they (type A and B) may be due to two separate loss mechanisms. **Stringer and Wright** (1987) further reported that the delineation between the two profiles has in specific cases been attributed to the following. **Ductile metal erosion vs. brittle oxide erosion (Holtzer and Rademakers, 1991)** At low temperatures, erosion would be ductile in nature, and would confirm to the standard dependence on incident angle, i.e. a maximum loss near an impact angle of 20°, and a minimum for glancing and normal impacts. Thus the losses at a

tube location of 180° (normal impact) would be relatively low compared with those on either side, and a Type A pattern could develop. At higher temperatures, as the oxidation rate increases, the wastage mechanism might shift from ductile erosion of metal, to brittle erosion of oxide. Brittle erosion typically shows a maximum loss at angles of normal incidence, and so a Type B pattern would result.

Erosion vs. abrasion (Stringer and Wright, 1987)

Here it is suggested that different particle flow regimes, and possibly different wear mechanisms are responsible for the distinction. For Type A, it has been suggested that tubes are within flow channels consisting of a relatively low concentration of particles travelling at a high velocity, and therefore ductile erosion occurs with a resulting Type A pattern as discussed above. Type B is linked to abrasion from dense aggregates of particles thrown against the tube undersides as a result of the collapse of voids or bubble wakes.

Erosion vs. erosion-enhanced corrosion (Minchener et al, 1985)

Here Type A results from classic erosion with a negligible corrosion component. Type B occurs where corrosion is high, and is preferentially enhanced towards the tube bottom by impact-induced deformation.

While these explanations may apply in some specific situations, they cannot be generally applicable since exceptions to each are widespread. Type B wear has been observed for carbon steel at low metal temperatures of 250-300°C, where brittle erosion of oxide (case I), and erosion-enhanced corrosion (case 3) are unlikely to be of relevance [**NCB (IEA Grimethorpe) Ltd., (1985)**]. Also, a fast low density particle flow channel is not necessary to cause Type A (case 2) wear since it has been found where high density, relatively slow aggregate impacts during passage of bubbles were known to have been the source of wastage (**Tsutsumi et al, 1988**).

Table A.2 Factors affecting erosion

Factors	Brief Description
Impact velocity	The particle impact velocity (v) is the most important variable that influences erosion rate. The erosion rate is proportional to the power of impingement velocity (v). Erosion rate is directly proportional to the particle kinetic energy. As particle velocity increases erosion rate increases **(Finnie and McFadden, 1978 and Hutchings, 1978)**. $E = kv^n$ Where k is a constant and n is a velocity exponent that generally depends on material and erosion conditions.
Impingement angle (angle of incidence)	Specimen orientation relative to the impinging particles stream is an important feature to be studied. The influence of impingement angle (α) is dependent on the type of material **(Rickbery and Macmillon, 1982 and Brown and Edington, 1982)**. For ductile materials the maximum damage occurs at low impact angle in the range of 15° to 30°, where as for brittle material, it occurs at 90°. In case of ductile materials, significant erosion occurs even at normal impact angles. Usually the erosion rate at 90° is 20 to 50% of maximum erosion rate obtained in the angle range of 15 to 30°.
Erodent Flux (particle concentration)	Systematic measurements of the steady state erosion rate as a function of erodent particle flux were made for a range of different erosion conditions **(Anand et al, 1987)**. They reported a significant decrease in erosion rate with increasing flux. And have demonstrated that because of interference of rebounding particles with incident particles, the surface is effectively shielded-the result being that **Erosion (E)** decreases exponentially with increasing flux. They further reported that the effect increases with decreasing velocity or particle size and depends on material through the effect of rebound velocity, which affects the time during which the rebounding particles shield the surface. Impact models predict no effect of erodent particle flux on erosion, because only one particle is considered. **Levy (1995)** has also reported that the lower the concentration or feed rate, much higher is the erosion rate. This indicates that there is particle-to-particle interference at higher solids loading, reduced the effectiveness of the particles to erode the surface. The primary mode of this interference is probably due to particles rebounding up from surface, deflecting the incoming particles in the downward moving stream.

Erodent particle shape	In general it is found that angular particles are more effective in causing erosion than the spherical particles (**Levy and Chik, 1983 and Liebhard and Levy, 1991**). At angularity and at low impact angle, erosion is maximum. From observations, angular particles form lips or platelets more efficiently than the spherical particles. The angular steel grit caused much sharper, deeper craters, caused a more efficient production of extruded plates. The spherical steel shot developed shallower, rounded craters that did not produce extruded plates efficiently. **Levy and Man (1989)** reported that angular-shaped particles remove oxide scale as it forms and directly erode the base metal at fast rates. Whereas rounded particles permit a continuous, somewhat protective, oxide scale to form on the metal surface which is eroded at much slower rates.
Erodent particle size and density	The erosion increases rapidly with grit size up to some critical diameter (50μ-100μ) and then increases at much slower rate or remains constant. It is observed from the literature that, the higher the density of the impacting particle, the greater is the rate of erosion (**Levy, 1995**). According to **Liebhard and Levy (1991)** the erosivity of spherical particles increases with particle size to a peak and then decreases at still larger particle sizes. And the angular particle erosivity increases with particle size to a level which became more or less constant with size at lower velocities, but increases continuously at higher velocities. The variation of erosion is studied with changes in size of erodent particles by **Bahadur and Badruddin (1990)**. They found that erosion rate increases with increasing particle size for SiC and Al_2O_3 particles upto a certain value and decreases for SiO_2 particles.
Erodent hardness	The hardness of the erodent particle relative to the material being eroded is an important factor in erosion (**Kosel, 1992**). According to Wellinger and Uetz (1957-58), the erosion rates drops dramatically when particle hardness decreases below that of the material being knocked eroded. They also noted that as long as the hardness of the erodent particles was at least twice that of the target material, the erosion rate was independent of the particle hardness. **Srinivasan and Scattergood (1988)** investigated the effect of relative hardness values of the erodent particles and the target material. They reported that when the ratio of target hardness to the hardness of the erodent particle approaches unity, there is a sharp transition in erosion rates. Relatively soft erodents lead to less erosion.

Erodent particle friability	**Sundararajan (1984)** has found that the friable particles result in high erosion rates. This effect is readily explainable on the basis of secondary erosion model of **Tilly (1973).**
Temperature	The rate and mechanism of erosive wear are influenced by temperature. The primary effect of temperature is to soften the eroded material and increase wear rates **(Stachowiak and Batchelor, 1993).** Under many typical industrial environments, erosion occurs at high temperature (up to $0.7T_m$, where T_m is the melting point of the eroding material) **(Sundararajan and Shewmon, 1983).** According to **Levy (1995),** erosion rate generally increase with increasing temperature, because with increasing temperature the material becomes softer. He reported that in case of metals, below $0.3T_m$ (target point) erosion resistance increases with increasing temperature, while above 0.5 T_m the erosion resistance decreases with increasing temperature. At low impact angles erosion rate decreases with increasing temperature up to 0.6 T_m and at higher temperature, erosion rate increases. At high impact angle, erosion rate attained a round $0.4T_m$ itself.
Mechanical Properties of target material	Metal hardness and toughness are among the most important characteristics to consider while selecting the metals for minimum erosion. Generally wear resistance increases with hardness and decreases as toughness increases. But in case of erosion, high hardness increases the erosion rate and it decreases as toughness increases. This is an important relationship in application that requires both wear resistance and impact resistance. The erosion resistance of ductile metals has been repeatedly correlated to their hardness by **Finnie et al (1967).** If the material is tough, it will have more resistance to erosion and also resistance to crack propagation. According to **Davis et al (1986)** and **Takeda et al (1993)** the hardness does not contribute directly to the improvement of the erosion resistance. Thus the variation of erosion with mechanical properties does not seem to follow any universal pattern as learnt from literature so far. **Naim and Bahadur (1986)** reported that the erosion rate varies directly with the hardness when the ductility remains constant and it varies inversely with the square of the percent area reduction when the hardness remains constant in case of 18 Ni (250) maraging steel. Effect of the material surface hardness on the erosion of AISI316 stainless steel has been evaluated by **Divakar et al (2005).** According to them, increase in the hardness shows higher erosion resistance as a result of compressive stresses, which are induced in to the

	target surface by the cold rolling and a compound layer produced on the target surface by nitriding. The cold rolling and nitriding improved the erosion resistance of 316 austenitic stainless steel by increasing its hardness while retaining sufficient ductility. **Nava et al (1993)** have suggested the general trends of erosion resistance as a function of material hardness under erosion-dominated, erosion-corrosion-dominated and corrosion-dominated conditions. According to them at relatively low temperatures, where erosion dominates, there is no obvious correlation between the two parameters. They suggested that however, at higher temperatures where oxidation plays a more significant role, the rate of erosion generally increases with increasing substrate hardness.
Microstructure of target material	Effect of microstructure on erosion has been studied by various authors **[Finnie et al (1967), Naim and Bahadur (1986, 1988, 1990), Levy (1988), Hutchings (1975)]**. Generally it is observed that fine grain size structure is more erosion resistant than coarse grain structure. The erosion rate of poly crystalline alumina has been found to be strongly dependent on grain size. In both dry erosion and wet erosion, the erosion rate increases with grain size **(Franco and Roberts, 1998)**. For the coatings, according to **Qureshi et al (1986)** when the grain size of the coating is very small and there is a minimum of pores, the loss rate is very low. **Levy (1981)** studied the effect of microstructure of two ductile steels on their erosion behavior. They concluded that the pearlite steels exhibited cracking at the eroded surface as well as beneath it and that this caused greater material removal. Whereas the spheroidized structure showed no surface cracking; however, cracking did occur at a depth of approximately 20 μm below the surface.

Table A.3 Summary of sliding wear studies of superalloys and coatings relevant to the present study.

Coating	Substrate	Equipment of wear test	Sliding distance	Load	Sliding Speed	Results	Reference
nickel-fly ash composite coatings	mild steel	Pin-on-disc wear test rig		7-11.8 kgf	1.26 & 1.89 m/s	They concluded that nickel-fly ash composite coatings possess better wear resistance than nickel coating. Further the lower wear loss of the composite coatings may be attributed to smearing-out of fly ash on both the specimen surface and the counter disk.	Ramesh et al (1991)
Nickel Silicon Nitride composite coating (150μm) using the sediment electro-co-deposition technique	Mild steel	Axially loaded bearing type wear testing machine with a disc of high carbon high Cr steel hardened to HRC60	10 min to 30 min	Conta-ct pre-sure 1.23, 3, 1.40 & 1.50 Mpa	1.26 & 1.57 m/s	They suggested that wear resistance of nickel-silicon nitride electrodeposited composite coatings increases with increase in volume per cent of silicon nitride in the nickel matrix. They reported sliding as the most dominant wear process in the composite coatings under study.	Ramesh et al (1992)
Al2O3 ambient Plasma Sprayed coating	AISI1020steel	Block on ring: block of Al2O3; Ring of AISI D2 steel	40000 m cycle duration	45-133 N	100-200 rpm; 0.183-0.366 m/s	They suggested that failure types of plasma-sprayed Al_2O_3 coating when sliding against steel AISI D2 in conformal contact are plastic deformation, adhesive wear as well as brittle fracture.	Fernandez et al (1995)
NiCoCrAlYTa and CoNiCrAlY by HVOF, APS,	NC20T and HastelloyX	Fretting test	100 cycl;e with displac-	10-20 daN	5 HZ	They concluded that after 100 hrs tribologically transformed structures were observed on the wear tracks of the three CoNiCrAlY coatings. This	Li et al (1998)

andArgon shrouded plasma spray processes			ement of ± 100 μm & 200000 cycles with ± 100 μm	& 20 daN		brittle structure led to debris formation. This was the main wear mechanism occurring in longer tests conducted with the ASPS CoNiCrAlY, which has a homogeneous structure. The oxides and porosity present in APS and HVOF CoNiCrAlY induced detachment of entire splats and more severe wear. In all cases adhesive transfer from the counterbody was observed and debris was oxidized.	
Chromium or Nickel plated coating	iron	pin-on-block	Several number of sliding strokes of 1 mm	13.2 N	0.02 mm/s	The failure of coating was classified mainly into three cases such as the fracture of coating, wear of coating, and the flaking by cracks in coating. It was revealed that the fracture of coating appeared with thin coating and large plastic deformation of substrate, the wear occurred when the substrate appeared less deformation, and the generation of cracks and flaking was observed with relatively thick hard coating which had quite little wear. It is suggested that the mechanical failure is by the intrinsic properties of coating and substrate materials, e.g. the relation between the thickness of coating and the depth of the plastically deformed region in the substrate.	Mishina (1999)
NiCrAlY, NiCrAlY		a reciprocating friction and wear test;	Stroke length	100 N	Cycle frequency	They concluded that chromium carbide coating by plasma spraying is superior to all other coatings	Mann et al (2000)

by plasma; Al O NiAl, Al O NiAl by plasma. 2 3 2 3		test duration 3 hrs, 550°C	2mm		25 Hz	except chromium oxide under graphite lubrication conditions, because graphite is filled in the pores. Further they reported excellent wear and friction characteristics of chromium oxide.	
Al_2O_3 plasma sprayed coating	S.G. cast iron	Pin on disc tribometer with counterface of quenched and tempered D2 tool steel (60HRC)	10000 rev.	50, 100, 160 N	1.40 m/s (620 rpm)	They suggested that the wear rate of Al_2O_3 presents three stages. During the first one, the wear rate decreases rapidly and the wear of the coating proceeds via adhesion mechanism. During the second stage, wear rate remains almost constant and the wear of the coating is taking place via a combined "polishing/ abrasion/ fatigue" wear mechanism, which leads to the formation of mainly small size debris (<1 μm). During the last stage, wear rate increases rapidly until the total worn of the ceramic layer due to the "easy" removal of the completely cracked remained coating.	Pantelis et al (2000)
75% Cr_3C_2, 20% Ni and 5% Cr by Plasma spraying	AISI 1043 steel blocks	Sliding wear tribometer	6300 m (40,000 cycles)	57-465 N	0.2 to 1.3 m s^{-1}	They suggested more wear resistant of ceramic coatings than steel. The wear rate of the steel was far superior to that of the coatings during the running-in period. In the steady state period, however, the wear rates of both materials are similar.	Mateos et al (2001)

Cr_3C_2–NiCr coatings by controlled atmosphere plasma system (CAPS)		ball-on-disc tribometer using 6-mm diameter counterbodies composed of WC+6%Co	1000 m	10 N	0.1 m s^{-1}	They concluded coating consisting of chromium carbide, Ni–Cr, carbo-nitride phase and graphitic carbon had excellent sliding wear resistance and was approximately 23 times better than that reported for conventional HVOF Cr_3C_2–25NiCr coating.	Staia et al (2001B)
Ni-17Cr-2.5Fe-2.5Si-2.5B-0.15C (Metco), Fe-30Mo-2C (Diamalloy), Co-30Cr-12W-2.4C (Stellite), and Zn-50SiC (Zn-SiC) by thermal spray process	Cast iron	Pin on disc tribometer	3 hr	1.72, 3.45, and 6.89 MPa	1 and 3 m/s	They concluded that wear rate for the stellite coating was lowest for all sliding speeds used in their study. Further the coefficient of friction was found to decrease with sliding speed for all the coatings. However, stellite coating exhibited stable friction behavior from 3.45 to 6.89 MPa pressure. For the Metco coating, though the friction was high, it tended to decrease under severe sliding conditions. They suggested that this coating is more prone to fade than the others.	Stanford and Jain (2001)
Ni_3Al-Cr_7C_3 (23 wt.%) coating by SHS casting process	1045 carbon steel	Ball on disc with disc of coating and ball of GCr15 steel of hardness 62-63HRC	Stroke length 1m duration 20min.	20-70N & 30 N	0.05 m/s & 0.02-0.14 m/s	Brittle fragmentation and abrasive wear of coatings was reported by the investigators.	La et al (2001)
Plasma sprayed WC-NiCrBSi coatings	A carbon steel	Oscillating friction machine	1000 m	50 and 200 N	0.15 m/s	The Ni-based alloy plasma-sprayed coatings studied in this work maintain their wear resistance at a bulk temperature of 500°C.	Martin et al (2001)

cobalt and two iron-based superalloys, Stellite #S2, Stellite#6, M1 MSA 2001 A M2 MSA 2020 A T1 Tribaloy		Submerged bearing test rig		45–13.4 kN	0–500 rpm	They found that a commonly used cobalt-based alloy (Stellite #6) not only suffered severe wear but also reacted with the zinc bath to form intermetallic compounds that participated in the wear process. According to them although other cobalt-based superalloys and newly developed iron-based superalloys appeared to have negligible reaction with the zinc alloy baths in the test conditions, cracks developed near the contacting surface. The wear mechanisms include abrasive wear, adhesive wear and surface fatigue wear in this short-term submerged test.	Zhang and Battiston (2002)
Cao-stabilized zirconia coating and NiAlMo- bond coat	Ni and Co base alloy	Carbon steel as counter face.	30 min. duration test	150 N	60 rpm	They suggested that coatings applied by plasma-transferred arc technology on mixed Ni- and Co-based alloys possess good resistance to erosion and abrasion. According to them abrasive and erosive resistances of deposits were almost independent of their chemical compositions. In practice, hardfacing can be built through successive application of layers from mixed powders, or a Ni-based deposit can be used as a primer below the Co-based deposit. They concluded that cobalt can be partly replaced by nickel for ambient-temperature dry wear applications.	Hejwowski et al (2002)

Nickel composite coatings prepared by sediment electro-co-deposition (SECD) technique.	Mild steel	an axially loaded thrust bearing type wear test rig with counter disc of high carbon high chromium steel hardened	10 min for friction-al tests and 30 min for wear tests	1.10 and 1.23 MPa	1.26, 1.57 and 1.73 $m\ s^{-1}$	They concluded that nickel–silicon nitride, nickel–fly ash and nickel–calcium fluoride composite coatings exhibited lower coefficient of friction and better wear resistance as compared to nickel coatings at all the studied loads and sliding velocities. However, nickel–calcium fluoride composites possess lowest coefficient of friction as well as the lowest wear rates. Further they suggested that delamination wear processes dominates at higher loads.	Ramesh and Seshadri (2003)
	Nimonic 80A superalloy	High temperature reciprocating wear test rig (block on cylinder) counterface of stellite 6	Temperat ure 0f 20° C	7 N	0.314 m/s	The sliding wear of Nimonic 80A allowed the development of a wear resistant nanostructur-ed glaze layer. The improved wear resistance of such a layer has been attributed to the absence of Hall–Petch softening and the lack of significant degree of work hardening and enhanced fracture toughness of the surface.	Du et al (2003)
NiCrBSi coatings by APS and HVOF spraying	Mild steel	Ball on Disk (BOD) tests with a martensitic plain steel as disc	1000 m	15 N	0.11 m/s	Main wear mechanisms are investigated by the characterisation of the coating wear track and debris using Scanning Electron Microscopy (SEM). It is observed that different wear mechanisms take place in the coatings obtained by the diverse processes.	Miguel et al (2003)

HVOF and plasma sprayed Alumina/titania coatings		Pin on disc tribometer with disc of SiC abrasive of 120 Grit (106 μm)	38 m	2-17 N		They suggested that a combination of brittleness and porosity results in fracture that dominates the abrasion wear of plasma-sprayed coatings.	Liu et al (2003)
NiCrBSi by plasma and flame spray plus fusion	Carbon steel SAE1045.	Oscillating friction machine of pure alumina cylinder	1000 m	50 and 200 N	Stroke length 15 mm, frequent-cy 5 Hz	Load is found much more influential on wear resistance than temperature within the ranges analysed.	Rodriguez et al (2003)
Flame sprayed and furnace fused NiCrBSiC coatings	Low carbon steel	Pin on disc with SiC grinding papers of # 120 (grit size of 120 μm) and # 400 (grit size of 30 μm)	3 h & 168 m	3 kg	0.07 m/s	They concluded that the dry sliding wear resistance of the 20% (and/or 30%) WC–NiCrBSiC composite coating is almost 10 times better than that of the quenched and tempered JIS SUJ2 bearing steel.	Kim et al (2003)
------	Monocrys-talline samples of CMSX-186 superalloy	pin-on-disk with martensitic stainless steel disc	500 m	200, 500, 1000, 1700 g	16 m/s	According to them the main wear mechanism of Ni superalloy CMSX-186 might be attributed to the ductile and brittle friction mechanism. The collected debris consisted of the fundamental faces of Ni and $Ni(Al,Ti)_3$ of CMSX-186 in addition to elements such as Fe and C, which probably sprang from the counter material.	Panagopo-ulos et al (2003)

Al-SI-Mo plasma sprayed coatings	Case hardened steel (16MnCr5) of 55HRC	Pin on disc tribometer with WC-6% Co pin against coatings		2-30 N	20 cm/s	They suggested that there no clear relationship between the coating hardness and their wear rate.	Form et al (2003)
$MgZrO_3$ coating with NiCrAl (Metco 443) as a bond coat by atmospheric plasma spray	AISI 304 L stainless steel	Pin-on-plate with AISI303 pin	15 min.	89, 109 and 209 N	0.5 and 1Hz	According to them the applied loads played a significant role in the wear behaviour of FGM and were more dominant at lower sliding speeds than that at higher ones. Also, the coating layers showed the better wear resistance by depth.	Cetinel et al (2003)
TiC/(NiAl-Ni_3Al) composite coating by laser cladding	electrolyzed nickel	block-on-wheel wear tester at room-temperature	_	147 N	0.42 m/s	They concluded the excellent wear resistance of the coating under the room temperature sliding wear test condition.	Chen and Wang (2004)
Ni-Al based intermetallic coating	Cast iron	Pin-on-disc sliding wear test with counter disc of AISI 1040	5 km	2 N	2 to 7 m/s	They concluded that the wear of intermetallic compound coating layer at that range progressed with the form of pitting during sliding contact repeated. Further they reported that with the increasing sliding speed, wear properties were significantly improved.	Lee et al (2006)

REFERENCES

1. **Allen**, C. and Ball, A., (1996), "Review of the Performance of Engineering Materials under Prevalent Tribological and Wear Situations in South African Industries," Tribology International, Vol.29, No. 2, pp.105-116.
2. **Anand**, K., Hevis, S.K., Conrad, H. and Scattergood, R.O., (1987), "Flux Effects in Solid Particle Erosion," Wear, Vol. 118, pp. 243-257.
3. **ASM** Handbook, (1995), "Metallography and Microstructures," Vol. 9, Sixth Printing, ASM Publication, Metals Park Ohio, U.S.A.
4. **ASTM** Standard C633-01, Standard Test Method for Adhesion or Cohesion Strength of Termal Spray Coatings, 100 Barr Harbor Drive, west Conshohocken, PA 19428-2959, United States, pp. 1-7.
5. **ASTM** Standard, Designation: G76-95 (2000), Standard Test Method for Conducting Erosion Tests by Solid Particle Impingement Using Gas Jets, 100 Bar Harbor Drive, West Conshohocken, PA 19428-2959, United States, pp.1-5.
6. **Bahadur**, S. and Badruddin, R., (1990), "Erodent Particle Characterization And The Effect of Particle Size And Shape On Erosion" Wear, Vol. 138, No. 1-2, pp. 189-208
7. **Barber**, J., Mellor, B.G. and Wood, R.J.K., (2005), "The Development of Sub-Surface Damage During High Energy Solid Particle Erosion of a Thermally Sprayed WC-Co-Cr Coating," Wear, Vol. 259, No. 1-6, pp. 125-134.
8. **Barkalow**, R.H. and Pettit, F.S., (1979), "Corrosion/Erosion of Materials in Coal Combustion Gas Turbines," Proc. Conf. Corrosion/Erosion of Coal Conversion System Materials, Berkeley, USA, Jan 24-26 1979, NACE, Houston, TX, pp. 139-173.
9. **Batchelor**, A.W., Lam, L.N. and Chandrasekaran, M, (2003), "Discrete Coatings," in Materials Degradation and its Control by Surface Engineering, 2nd Edition, Imperial College Press.
10. **Bellman**, R., Jr. and Levy, A., (1981), "Erosion Mechanism in Ductile Metals," Wear, 70 (1) 1-27.
11. **Berndt**, C.C. and McPherson, R., "The Adhesion of Flame and Plasma Sprayed Coatings - A Literature Review -Awra Report P 11-1-78," Australian Welding Research 6 (1979) 75-85.

12. **Bhusari**, M., (2001), "Plasma Spray: The Job Shop Perspective," Proc. Inter. Thermal Spray Conf., May 28-30, Singapore, pp. 1289-1297.

13. **Bhushan**, B. (2002), "Introduction to tribology," Pub. John Wiley and Sons NewYork, USA, Chapter 7, pp. 332.

14. **Birkby**, C. and Gibb, J., (1987), "Commentary of Fluidisation Characteristics Changes at Grimethorpe," Proc. of a Workshop on Wastage of In-Bed Surfaces in Fluidized-Bed Combustors, EPRI, Palo Alto, CA, paper 6.5.

15. **Bitter**, J.G.A., (1963), "A Study of Erosion Phenomena," Part I, Wear, Vol. 6, pp.5-21.

16. **Bitter**, J.G.A., (1963), "A Study of Erosion Phenomena," Part I, Wear, Vol. 6, pp.169-190.

17. **Bluni**, S.T., and Marder, A.R., (1996), "Effects of Thermal Spray Coating Composition and Microstructure on Coating Response and Substrate Protection at High Temperatures" Corrosion (Houston), Vol. 52, No.3, pp.213-218.

18. **Bose**, K., Wood, R.J.K., and Wheeler, D.W., (2005), "High Energy Solid Particle Erosion Mechanisms of Superhard CVD Coatings," Wear, Vol. 259, No. 1-6, pp. 135-44,

19. **Brach**, R.M., (1988), "Impact Dynamics with Applications to Solid Particle Erosion" International Journal of Impact Engineering," Vol. 7, No. 1, pp. 37-53.

20. **Branco**, J.R.T., Gansert, R., Sampath, S., Berndt, C.C., and Herman, H., (2004), "Solid Particle Erosion of Plasma Sprayed Ceramic Coatings," Materials Research, Vol. 7, No. 1, pp.147-153.

21. **Brown**, R., Jun, E., and Edington, J., (1982), "Mechanisms of Solid Particle Erosive Wear for 90° Impact on Copper and iron," Wear, Vol. 74, No.1, pp. 143-156.

22. **Buckley**, D.H., (1981), "Surface Effects in Adhesion, Friction, Wear and Lubrication, in: Tribology Series 5," Elsevier Scientific Publishing Company, Amsterdam, Netherlands.

23. **Budinski**, K. G., (1998), 'Engineering Materials, Properties and Selection,' Pub. Prentice-Hall of India, New Delhi, India.

24. **Budinski**, K.G., (1998), "Use of Wear Tests for Plastics," American Chemical Society, Polymer Priprints, Division of Polymer Chemistry, Vol. 39, No. 2, pp. 1217.

25. **Burakowski,** T. and Wierzchon, T., (1999), "Surface Engineering of Metals, Principles, Equipment, Technology,' CRC Press, N. W., Boca Raton, Florida.

26. **Calvarin,** G., Molins, R. and Huntz, A. M., (2000), "Oxidation Mechanism of Ni-20Cr Foils and its Relation to the Oxide-Scale Mircrostructure," Oxid. Met., Vol. 53, No. 1-2, pp. 25-48.

27. **Cetinel,** H., Uyulgan, B., Tekmen, C., Ozdemir, I. and Celik, E., (2003), "Wear Properties of Functionally Gradient Layers on Stainless Steel Substrates for High Temperature Applications," Surface and Coatings Technology, Vol. 174-175, pp.1089-1094.

28. **Chatterjee,** U.K., Bose, S.K. and Roy, S.K., (2001), "Environmental Degradation of Metals," 270, Madison Avenue, New York, Marcel Dekker.

29. **Chen,** H.C., Liu, Z.Y., and Chuang, Y.C., (1993), "Degradation of Plasma-Sprayed Alumina and Zirconia Coatings on Stainless Steel During Thermal Cycling and Hot Corrosion" Thin Solid Films, Vol. 223, No. 1, pp. 56-64..

30. **Chen,** Y., and Wang, H.M., (2004), "Microstructure and Wear Resistance of A Laser Clad TiC Reinforced Nickel Aluminides Matrix Composite Coating," Materials Science and Engineering, (Structural Materials: Properties, Microstructure and Processing), Vol. A368, No. 1-2, pp. 80-87.

31. **Chinnadurai,** S. and Bahadur, S., (1995), "High-Temperature Erosion of Haynes and Waspaloy: Effect of Temperature and Erosion Mechanisms," Wear, Vol. 186-187 pp. 299-305.

32. **Christman,** T. and Shewmon, P.G., (1979), "Erosion of a Strong Aluminium Alloy," Wear, Vol. 52, pp.57-70.

33. **Clark,** H.M., (1992), "The Influence of the Flow Field in Slurry Erosion," Wear, Vol. 152, pp. 223-240.

34. **Dallaire,** S., "Hard Arc-Sprayed Coating with Enhanced Erosion and Abrasion Wear Resistance," Proceedings of the 2000 International Thermal Spray Coference-ITSC'2000-Montreal, Quebec, Canada, 8-10 May 2000, ASM International, pp. 575-582.

35. **Dallaire,** S., Dube, D. and Fiset, M., (1999), "Laser Melting of Plasma-Sprayed Copper-Ceramic Coatings for Improved Erosion Resistance," Wear, Vol. 231, No. 1, pp. 102-107.

36. **Das**, S., Saraswathi, Y.L. and Mondal D.P., (2005), "Erosive–Corrosive Wear of Aluminum Alloy Composites: Influence of Slurry Composition and Speed," in press.

37. **Davis**, A.G., Boone, D.H., and Levy, A.V., (1986), "Erosion of Ceramic Thermal Barrier Coatings," Wear, Vol. 110, pp. 101-116.

38. **Davis**, J.R. (2001), "Surface Engineering for Corrosion and Wear Resistance," ASM International, Materials Park, OH 44073-0002 U.S.A

39. **Demirkiran**, A.S. and Avci, E., (1999), "Evaluation of Functionally Gradient Coatings Produced by Plasma-Spray Technique," Surface and Coatings Technology, Vol. 116-119, pp. 292-295.

40. **Dent**, A.H., DePalo, S. and Sampath, S., (2002), "Examination of the Wear Properties of HVOF Sprayed Nanostructured and Conventional WC-Co Cermets with Different Binder Phase Contents," Journal of Thermal Spray Technology, Vol. 11, No. 4, pp. 551-558.

41. **Divakar**, M., Agarwal, V.K. and Singh, S.N., (2005), "Effect of the Material Surface Hardness on the Erosion of AISI316," Wear, Vol. 259, No. 1-6, pp. 110-117.

42. **Du**, H.L., Datta, P.K., Inman, I., Geurts, R. and Kubel, C., (2003), "Microscopy of Wear Affected Surface Produced During Sliding of Nimonic 80A against Stellite 6 at 20°C," Materials Science and Engineering A, Vol. 357, No. 1-2, pp. 412-422.

43. **Dundar**, M., Inal, O.T. and Stringer, J., (1999), "Effect of Particle Size on the Erosion of A Ductile Material at the Low Particle Size Limit," Wear, Vol. 233-235, pp. 727-736.

44. **Eaton**, H. E. and Zajchowski, P., (1999), "High Temperature Particulate Erosion of Plasma Sprayed YSZ verses selected Powder Characterization & Plasma Torch Designs," Surface and coatings Technology, Vol. 120-121, pp.28-33.

45. **Edington**, J.W. and Wright, I.G., (1978), "Study of Particle Erosion Damage in Haynes Stellite 6B. II: Transmission Electron Microscopy of Eroded Surfaces," Wear, Vol.48, pp.145-155.

46. **Edrisy**, A., Perry, T., Cheng, Y.T. and Alpas A.T., (2001), "Wear of Thermal Spray Deposited Low Carbon Steel Coatings on Aluminum Alloys" Wear Vol. 251, pp. 1023-1033.

47. **Erickson**, L.C., Westergard, R., Wiklund U., Axen N., Hawthorne H.M. and Hogmark S., (1998), "Cohesion in Plasma-Sprayed Coatings-A Comparison between Evaluation Methods," Wear, Vol. 214, pp. 30-37.

48. **Fauchais**, P, Vardelle, A. and Vardelle, M., (1991), 'Modelling of Plasma Spraying of Ceramic Films and Coatings,' Ed. Vinenzini, Pub. Elsevier State Publishers B.V.

49. **Fauchais**, P., Vardelle, A. and, Dussoubs, B., (2001), "Quo Vadis Thermal Spray," J. Therm. Spray Technol, Vol. 10, No. 1, pp. 44-46.

50. **Fauchais**, P., (2004), "Topical Review: Understanding Plasma Spraying," J. Phys. D: Appl. Phys., Vol. 37, pp. R86-R108.

51. **Fernandez**, J.E., Rodriguez, R., Wang, Y., Vijande, R. and Rincon, A., (1995), "Sliding Wear of A Plasma-Sprayed Al_2O_3 Coating," Wear, Vol. 181-183, pp. 417-425.

52. **Finnie**, I., (1958), "The mechanism of erosion of ductile metals," Proceedings of the Third U.S. National Congress of Applied Mechanics, pp. 527–532.

53. **Finnie**, I., (1960), "Erosion of Surfaces by Solid Particles," Wear, Vol. 3, pp. 87–103.

54. **Finnie**, I., (1995) "Some Reflections on the Past and Future of Erosion," Wear, 186-197, pp.1-10.

55. **Finnie**, I., Wolak, J., and Kabil, Y., (1967), "Erosion of Metals by Solid Particles," ASTM J. Mater. Vol. 2, pp. 682–700.

56. **Finnie**, I. and McFadden, D.H., (1978), "On the Velocity Dependence of the Erosion of Ductile Metals by Solid Particles at Low Angles of Incidence," Wear, Vol. 48, pp.181-190.

57. **Forn**, A., Picas, J.A. and Simon, M.J., (2003), "Mechanical and tribological properties of Al-Si-Mo plasma-sprayed coatings," J. of Mat. Processing Tech., Vol. 143-144, pp. 52-57.

58. **Franco**, A. and Roberts, S.G., (1998), "The effect of impact angle on the erosion rate of polycrystalline α-Al_2O_3," Journal of the European Society, Vol. 18, pp. 269-274.

59. **Gee**, M.G, Gee, R.H., Mcnaught, I., (2003), "Stepwise Erosion as a Method for Determining the Mechanisms of Wear in Gas Borne Particulate Erosion," Wear, Vol. 255, pp.44-54.

60. **Goebel,** J.A., Pettit, F.S. and Goward, G.W., (1973), "Mechanisms for the Hot Corrosion of Nickel-Base Alloys," Metall. Trans., Vol. 4, pp. 261-275.

61. **Goward,** G.W., (1986), "Protective Coatings-Purpose, Role and Design," Mater. Sci. Technol., Vol. 2, No. 3, pp. 194-200.

62. **Grainger,** S. and Blunt, J., (1998) "Engineering Coatings: Design and App.lications," Abington Publishing, 2nd Ed.

63. **Gulden,** M.E., and Kubarych, K.G., (1982), "Erosion Mechanisms of Metals," Report SR-81-R-4526-02, Solar Turbines, Inc. San Diego.

64. **Guo,** D.Z., Li, F.L., Wang, J.Y. and Sun, J.S., (1995), "Effects of Post-Coating Processing on Structure and Erosive Wear Characteristics of Flame and Plasma Spray Coatings," Surface and Coatings Technology, Vol. 73, No. 1-2, pp. 73-78.

65. **Halling,** J., and Arnell, R.D., (1984), "Ceramic Coatings in the War of Wear," Wear, Vol. 100, pp. 367-380.

66. **Hamner,** N. E., (1977), "Coatings for Corrosion Protection," in NACE Basic Corro. Course," Houston, Texas, Ch. 14.

67. **Hancock,** P. and Nicholls, J.R., (1988), "Application of Fracture Mechanics to Failure of Surface Oxide Scales," Mater. Sci. Technol., Vol. 4, pp. 398-406.

68. **Hansen,** J.S., (1979), "Relative Erosion Resistance of Several Metals, Erosion: Prevention and Useful Applications," STP 664 ASTM, pp.148-162.

69. **Hansson,** C.M. and Hansson, I.L.H., (1992), "Cavitation Erosion in: Friction, Lubrication and Wear Technology, ASM Handbook, Vol.18, pp. 214-220.

70. **Hawthorne,** H.M., Erickson, L.C., Ross, D., Tai, H. and Troczynski, T., (1997), "The Microstructural Dependence of Wear and Indentation Behaviour of Some Plasma-Sprayed Alumina Coatings," Wear, Vol. 203-204, pp. 709-714.

71. **He,** J. L., Chen, K. C., Chen, C. C., Leyland A., and Matthews, A., (2001), "Cyclic Oxidation Resistance of Ni–Al Alloy Coatings Deposited on Steel By A Cathodic Arc Plasma Process," Surface and Coatings Technology, Vol. 135, pp. 158-165.

72. **Hearley,** J.A., Little, J.A., Strugeon, A.J., (1999), "The Erosion Behaviour of NiAl Intermetallic Coatings Produced by High Velocity Oxy-Fuel Thermal Spraying," Wear, Vol. 233-235, pp. 328-333.

73. **Heath,** G.R., Heimgartner, P., Irons, G., Miller, R. and Gustafsson, S., (1997), "An Assessment of Thermal Spray Coating Technologies for High Temperature Corrosion Protection," Mater. Sci. Forum, Vol. 251-54, pp. 809-816.

74. **Hedenqvist,** P. and Olsson M., (1990), "Solid Particle Erosion of Titanium Nitride Coated High Speed Steel, Tribology International, Vol. 23, No.3, pp. 173-181.

75. **Hejwowski,** T., (2002), "Wear Resistance of Graded Coatings," Vacuum, Vol. 65, pp. 515-520.

76. **Heymann,** F.J., (1992), "Liquid Impingement Erosion in: Friction, Lubrication and Wear Technology," ASM Handbook, Vol.18, pp. 221-232.

77. **Hidalgo,** V.H., Varela, F.J.B. and Rico, E.F., (1997), "Erosion Wear and Mechanical Properties of Plasma-Sprayed Nickel- and Iron-Based Coatings Subjected to Service Conditions in Boilers," Trib. Int., Vol. 30, No. 9, pp. 641-649.

78. **Hidalgo,** V.H., Varela, F.J.B., Calle, J.M., and Menendez, A.C., (2000), "Characterisation of NiCr Flame and Plasma Sprayed Coatings for Use in High Temperature Regions of Boilers," Surface Engineering, Vol. 16, No. 2, pp. 137-142.

79. **Hidalgo,** V.H, Varela, J.B., Menendez, A.C., Martinez, S.P., (2001A), "High temperature Erosion Wear of Flame and Plasma Sprayed Nickel-Chromium Coatings under Coal-Fired Boiler Atmospheres," Wear, Vol.247, pp.214-222.

80. **Hidalgo,** V.H., Varela, F.J.B., Menendez, A.C. and Martinez, S.P., (2001B), "A Comparative Study of High-Temperature Erosion Wear of Plasma-Sprayed NiCrBSiFe and WC-NiCrBSiFe Resistance Coatings under Simulated Coal-Fired Boiler Conditions," Tribology International, Vol.34, pp.161-169.

81. **Hocking,** M.G., (1993), "Coatings Resistant to Erosive/Corrosive and Severe Environments, Surface and Coatings Technology," Vol. 62, pp. 460-466.

82. **Hocking,** M.G., Vasantshree, V., Sidky, P.S., (1989), "Metallic and Ceramic Coatings," UK: Longman Scientific and Technical, pp.566-588.

83. **Holtzer,** G.J. and Rademakers, P.L., in E.J. Anthony (ed.), (1991), "Studies of 90 MWth AK20 and 4 MWth TN0 FBC Show Excellent Erosion-Corrosion Results," Proc. 11th Int. Conf. on Fluidized Bed Combustion, ASME, New York, NY, pp. 743-753.

84. **Hoop**, P.J. and Allen, C., (1999), "The High Temperature Erosion of Commercial Thermally Sprayed Metallic and Cermet Coatings by Solid Particles," Wear, Vol.233-235, pp.334-341.

85. **Hou**, P., MacAdam, S., Niu, Y. and Stringer, J., (2004), "High Temperature Degradation by Erosion-Corrosion in Bubbling Fluidized Bed Combustors," Materials Research, Vol. 7, No. 1, pp. 71-80.

86. **Hutchings**, I.M. and Levy, A.V., (1989), "Thermal Effects in The Erosion of Ductile Metals," Wear 131, pp.105-121.

87. **Hutchings**, I. M., (1979), "Some Comments on the Theoretical Treatment of Erosive Particle Impacts," Proceedings of the Annual Industrial Pollution Conference, pp. 1-36.

88. **Hutchings**, I.M., in Edler, W.F. (Ed.), (1979), "Erosion: Prevention and Useful Applications," ASTM Sp. Tech. Pub., Vol. 664, pp.59-76.

89. **Hutchings**, I.M. and Winter, R.E., (1974), "Particle Erosion of Ductile Metals: A Mechanism of Material Removal," Wear, Vol.27, pp.121-128.

90. **Hutchings**, I.M. and Winter, R.E., (1975), "The Erosion of Ductile Metals by Spherical Particles," Journal of Physics D (Applied Physics), Vol. 8, No. 1, pp. 8-14.

91. **Illavsky**, J., Pisacka, J., Chraska, P., Margandant, N., Siegmann, S., Wagner, W., Fiala, P. and Barbezat, G., (2000), "Microstructure-Wear and Corrosion Relationships for Thermally Sprayed Metallic Deposits," Proc. 1st Inter. Thermal Spray Conf., Montreal, Quebec, Canada, May 8-11, pp. 449-454.

92. **Kamaraj**, M., (2003), "Rafting in Single Crystal Nickel-Base Superalloys - An Overview," Sadhana - Academy Proceedings in Engineering Sciences, Vol. 28, No. 1-2, pp. 115-128.

93. **Kang**, C.T., Pettit, F.S. and Birks, N., (1987), "Mechanisms in the Simultaneous Erosion-Oxidation Attack of Nickel and Cobalt at High Temperature," Metallurgical Transactions A (Physical Metallurgy and Materials Science), Vol. 18A, No. 10, pp. 1785-1803.

94. **Kang**, C.T., Chang, S.L., Pettit, F.S. and Birks, N., (1985), "Synergisms in the Degradation of Metals Exposed to Erosive High-Temperature Oxidising Environments," in G. Simkovich and VS. Stubican (eds.), Transport in Non-sroichiometric Compounds, Plenum, New York, pp. 41 l-427.

95. **Kapoor**, A. and Johnson, K.L., (1994), "Plastic Ratchetting as a Mechanism of Metallic Wear," Proc. R. Soc. London, Ser., Vol. 445, pp.367-384.

96. **Kapoor**, A. and Johnson, K.L., (1995), "Plastic Ratchetting as a Mechanism of Erosive Wear," Wear, Vol. 186-187, pp.86-91.

97. **Kim**, H.J., Hwang S.Y., Lee, C.H. and Juvanon P., (2003), "Assessment of wear performance of flame sprayed and fused Ni-based coatings," Surface and Coatings Technology, Vol. 172, No.2-3, pp. 262-269.

98. **Knotek**, O., (2001), "Thermal Spraying and Detonation Spray Gun Processes," in Handbook of Hard Coatings: Deposition Technologies, Properties and Applications, Ed. Bunshah, R.F., Noyes Pub. Park Ridge, New Jersey, U. S. A./William Andrew Publishing, LLC, Norwich, New York, U.S.A., Chapter 3, pp. 77-107.

99. **Kosel**, T.H., (1992), "Solid Particle Erosion, in: Friction Lubrication and Wear Technology, ASM Handbook, Vol.18, pp. 199-213.

100. **Krishnamoorthy**, P.R., Seetharamu, S. and Sampathkumar, P., (1993), "Influence of the Mass Flux and Impact Angle of the Abrasive on the Erosion Resistance of Materials Used in Pulverized Fuel Bends and Other Components in Thermal Power Stations," Wear, Vol. 165, pp. 151-157.

101. **Kucuk**, A., Lima, R. S. and Berndt, C. C., (2001), "Influence of Plasma Spray Parameters on Formation and Morphology of ZrO_2-8 wt% Y_2O_3 Deposits," J. Am. Ceram. Soc., Vol. 84, No. 4, pp. 693-700.

102. **Kunioshi**, C.T., Correa, O.V. and Ramanathan, L.V., (2005), "Erosion-Oxidation Behavior of Thermal Sprayed Ni20Cr Alloy and WC and Cr_3C_2 Cermet Coatings," Materials Research, Vol. 8, No. 2, pp. 125-129.

103. **La**, P., Bai, M., Xue, Q. and Liu, W., (1999), "A Study of Ni_3Al Coating on Carbon Steel Surface Via The SHS Casting Route," Surface and Coatings Technology Vo. 113, pp. 44-51.

104. **La**, P., Xue, Q. and Liu, W., (2001), "Effects of Boron Doping on Tribological Properties of Ni_3Al-Cr_7C_3 Coatings Under Dry Sliding," Wear, Vol. 249, pp. 94-100.

105. **Lee**, H.Y., Roe, J. K. and Ikenaga, A., (2006), "Sliding Wear Properties for Ni-Al Based Intermetallic Compound Layer Coated on Ductile Cast Iron by Combustion Synthesis," Wear, Vol. 260, No.1-2, pp. 83-89.

106. **Levy**, A.V., (1982), "The Erosion of Metal Alloys and Their Scales," Proc. NACE Conf. Corrosion-Erosion-Wear of Materials in Emerging Fossil Energy Systems (Berkeley, CA), pp.298-376.

107. **Levy**, A.V., (1988), "The Erosion-Corrosion Behavior of Protective Coatings," Surface and Coatings Technology, Vol. 36, pp.387-406.

108. **Levy**, A.V., (1993), "The Erosion-Corrosion of Tubing Steels in Combustion Boiler Environments, Corros. Sci., Vol. 35 No.5–8, pp. 1035–1043.

109. **Levy**, A., (1995), "Solid Particle Erosion and Erosion-Corrosion of Materials," ASM International, Materials Park, OH 44073-0002, U.S.A.

110. **Levy**, A.V., Azhazadeh, M., and Hickey, G., (1984), "The Effect of Test Variables on the Platelet Mechanism of Erosion," Rep. LBL-17835, (Lawrence Berkeley Laboratory, University of California, Berkeley, CA, U.S.A.).

111. **Levy**, A.V. and Hickey, G. , (1986), "Erosion of Corrosion-Resistant Surface Treatments on Alloy Steels," Wear, Vol. 108, No. 1, pp. 61-79.

112. **Levy**, A.V. and Man Y.F., (1989), "Erosion-Corrosion Mechanisms and Rates in Fe-Cr Steels," Wear, Vol. 131, pp. 39-51.

113. **Levy**, A.V. and Chik, P. (1983), "The Effects of Erodent Composition and Shape on the Erosion of Steel," Wear, Vol. 89, No.2, pp. 151-162.

114. **Levy**, A.V., Wang, B.Q., Man, Y.F. and Jee, N., (1989), "Erosion-Corrosion of Steels in Simulated and Actual Fluidized Bed Combustor Environments," Wear, Vol. 131, pp. 39-51.

115. **Li**, S., Langlade, C., Fayeulle, S. and Treheux, D., (1998), "Influence of the Microstructure of Plasma Deposited MCrAlY Coatings on their Tribological Behaviour," Surface and Coatings Technology, Vol. 100-101, pp. 7-11.

116. **Li**, M. H., Sun, X. F., Li, J. G., Zhang, Z. Y., Jin, T., Guan, H.R. and Hu, Z. Q., (2003A), "Oxidation Behaviour of a Single-Crystal Ni-Base Superalloy in Air-I: At 800 and 900^{0}C," Oxid. Met., Vol. 59, No. 5-6, pp.591-605.

117. **Li**, M. H., Sun, X. F., Jin, T., Guan, H.R. and Hu, Z.Q., (2003B), "Oxidation Behaviour of a Single-Crystal Ni-Base Superalloy in Air-II: At 1000, 1100, and 1150^{0}C," Oxid. Met., Vol. 60, No.1-2, pp.195-210.

118. **Li**, M. H., Zhang, Z. Y., Sun, X. F., Li, J. G., Yin, F. S., Hu, W. Y., Guan, H. R. and Hu, Z. Q., (2003C), "Oxidation Behaviour of Sputter-Deposited NiCrAlY coating," Surf. Coat. Technol., Vol. 165, No. 3, pp. 241-247.

119. **Li**, Y., Yuan, C., Guo, J. T. and Yang, H. C., (2003), "Oxidation Kinetics of Cast Ni-Base Superalloy K35," J. Northeastern Uni., Vol. 24, No. 1, pp. 75-78.

120. **Liebhard**, M., Levy, A.V., (1991), "Effect of Erodent Particle Characteristics on the Erosion of Metals Wear of Materials," International Conference on Wear of Materials, Vol. 1, pp. 123-127.

121. **Lin**, D. S., Stott, F. H., Wood, G. C., Wright, K. W. and Allen, J. H., (1973), "The Friction and Wear Behaviour of Nickel-Base Alloys in Air at Room Temperature," Wear, Vol. 24, pp. 261-278.

122. **Lindsley**, B., Stein, K. and Marder, A.R., (1995), "The Design of a High-Temperature Erosion app.aratus for Studying Solid Particle Erosion," Meas. Sci. Technol., Vol.6, pp. 1169-74.

123. **Link**, R.J., Birks N., Petit, F.S. and Dethorey, F., (1998), "The Response of Alloys to Erosion-Corrosion at High Temperatures" Oxidation of Metals, Vol. 49, No. 34, pp. 213-236.

124. **Liu**, Z. and Gao, W., (2001), "Oxidation Behaviour of Cast Ni_3Al Alloys and Microcrystalline Ni_3Al + 5% Cr Coatings with and without Y Doping," Oxidation of Metals, Vol. 55, No. 5-6, pp. 481-504.

125. **Liu**, Y., Fischer, T.E. and Dent, A., (2003), "Comparison oOf HVOF and Plasma-Sprayed Alumina/Titania Coatings—Microstructure, Mechanical Properties and Abrasion Behavior," Surface and Coatings Technology, Vol. 167, pp. 68-76.

126. **MacAdam**, S.S. and Stringer J., (1995) "The Circumferential Distribution of Wastage on In-Bed Tubes in Fluidized Bed Combusters," Wear, Vol. 186-187, pp. 325-331.

127. **Margadant**, N., Siegmann S., Patscheider J., Keller T., Wagner W., Ilavsky J., Pisacka J., Barbezat G. and Fiala P., (2001), "Microstructure- Property Relationships and Cross-Property-Correlations of Thermal Sprayed Ni-Alloy Coatings," Thermal Spray 2001 New Surfaces for a New Millennium: Proceedings of the International Thermal Spray Conference, pp. 643-652.

128. **Martin**, A., Rodriguez, J., Fernandez, J.E., and Vijande, R., (2001), "Sliding wear behaviour of plasma sprayed WC-NiCrBSi coatings at different temperatures," Wear, Vol. 251, pp. 1017-1022.

129. **Mateos**, J., Cuetos, J.M., Vijande, R. and Fernandez, E., (2001), "Tribological Properties of Plasma Sprayed and Laser Remelted 75/25 Cr_3C_2/NiCr Coatings," Tribology International, Vol. 34, pp. 345-351.

130. **Mazar**, P., Maresse, D. and Lopvet, C., (1986), "High Temperature Alloys for Gas Turbines," Eds. Betz, M. et al, Pub. Dordrecht, Netherlands, D. Reidel Publishing Co., pp. 1183-1192.

131. **Mbabazi**, J.G., Sheer, T.J. and Shandu., R., (2004), "A Model to Predict Erosion on Mild Steel Surfaces Impacted by Boiler Fly Ash Particles," Wear, Vol. 257, pp. 612-24.

132. **Metals Handbook**, (1972), "Atlas of Microstructures of Industrial Alloys," Vol. 7, ASM Publication, Metals Park OH, USA.

133. **Miguel**, J.M., Guilemany, J.M. and Vizcaino. S., (2003), "Tribological Study of NiCrBSi Coating Obtained by Different Processes," Tribology International, Vol. 36, pp. 181-187.

134. **Minchener**, A.J., Stringer, J., Brooks, S., Lloyd, D.M., Swift, W.M., Anderson, J.S. and Mainhardt, P.J., (1985), "Materials studies at the IEA Grimethorpe PFBC experimental facility," Proc. 8th Int. Conf on Fluidized Bed Combustion, DOEMETC-9516021, pp. 760-771.

135. **Mishina**, H., (1999), "Microscopic Real Time Observation of Failure, Wear and Deformation on Coating/Subsurface," Tribology International, Vol. 32, pp. 137-144.

136. Mishra, S.B., Chandra, K., Prakash, S. and Venkataraman, B., (2005), "Characterisation and Erosion Behaviour of a Plasma Sprayed Ni_3Al Coating on a Fe-Based Superalloy," Materials Letters, Vol. 59, No. 28, pp.3694-3698.

137. **Mishra**, S.B., Prakash, S. and Chandra, K., (2006), "Studies on Erosion Behaviour of Plasma Sprayed Coatings on a Ni-Based Superalloy," Wear, Vol. 260, No. 4-5, pp. 422-432.

138. **Murthy**, J.K.N., Rao., D.S. and Venkataraman, B., (2001), "Effect of Grinding on the Erosion Behavior of a WC-Co-Cr Coating Deposited by HVOF and Detonation Gun Spray Processes," Wear, Vol.249, pp.592-600.

139. **Nafari**, A. and Nylund, A., (2002), "Erosion Corrosion of Steel Tubes in the Loop Seal of a Biofuel Fired CFB Plant," in: Proceedings of the 7th Liege Conference Materials for Advanced Power Engineering, Liege, Belgium.

140. **Naim**, M. and Bahadur, S., (1986), "Effect of Microstructure and Mechanical Properties on the Erosion of 18 Ni (250) Maraging Steel," Wear, Vol. 112, No. 2, pp. 217-34.

141. **Naim**, M. and Bahadur, S., (1988), "Erosion Behavior of Prestrained and Aged 2024 Aluminum," Wear, Vol. 128, No. 3, pp. 239-247.

142. **Naim**, M. and Bahadur, S., (1990), "Effect of Precipitated and Dispersed Hard Particles on Erosion," Lubrication Engineering, Vol. 46, No. 1, pp. 53-57

143. **NCB** (IEA Grimethorpe) Ltd., (1985), "Materials-Related Activities During Test Series 2.2 and 2.3," Report No. GEF/U/84/15.

144. **Neilson**, J.H. and Gilchrist, A., (1968), "Erosion by a Stream of Solid Particles," Wear, Vol. 11, No., pp.111-122.

145. **Nelson**, H.W., Krause, H.H., Ungar, E.W., Putnam, A.A., Slunder, C.J., Miller, P.D., Hummel, J.D. and Landry, B.A., (1959), "A Review of Available Information on, Corrosion and Deposits in Coal- and Oil-Fired Boilers and Gas Turbines," Report of ASME Research Committee on Corrosion and Deposits from Combustion Gases, Pub. Pergamon Press and ASME, New York.

146. **Nicholls**, J.R., (2000), "Designing Oxidation-Resistant Coatings," JOM, Vol. 52, No. 1, pp. 28-35.

147. **Nickel**, H., Quadakkers, W.J. and Singheiser, L., (2002), "Analysis of Corrosion Layers on Protective Coatings and High Temperature Materials in Simulated Service Environments of Modern Power Plants Using SNMS, SIMS, SEM, TEM, RBS and X-ray Diffraction Studies," Anal. Bioanal. Chem., Vol. 374, pp. 581-587.

148. **Nicoll**, A.R., (1984), "Chapter 13: The Production and Performance Evaluation of High Temperature Coatings," in 'Coatings and Surface Treatment for Corrosion and Wear Resistance,' Eds. Strafford, K. N., Datta, P. K. and Googan, C. G., Institution of Corros. Sci. and Techol., Birmingham, Pub. Ellis Horwood Ltd., Chichester.

149. **Ninham**, A., (1988), "The Effect of Mechanical Properties on Erosion," Wear, Vol. 121, pp. 307-324.

150. **Niranatlumpong**, P., Ponton, C. B. and Evans, H.E., (2000), "The Failure of Protective Oxides on Plasma-Sprayed NiCrAlY Overlay Coatings" Oxid. Met., Vol. 53, No.3-4, pp. 241-258.

151. **Norling**, R. and Olefjord, I., (2003), "Erosion-Corrosion of Fe- and Ni-based Alloys at 555°C," Wear, Vol. 254, pp. 173-184.

152. **Olefjord**, I., (1975), "Application of ESCA to Oxide Films Formed on Stainless Steels at Intermediate and High Temperatures," Met. Sci., Vol. 9, pp. 263–268.

153. **Panagopoulos**, C.N., Papachristos, V.D., and Christoffersen, L.W., (2000), "Lubricated Sliding Wear Behaviour of Ni-P-W Multilayered Alloy Coatings Produced by Pulse Plating," Thin Solid Films, Vol. 366, No. 1-2, pp. 155-163.

154. **Panagopoulos**, C.N., Giannakopoulos K.I., Saltas V., (2003), "Wear Behavior of Nickel Superalloy, CMSX-186," Materials Letters, Vol. 57, pp. 4611-4616.

155. **Pantelis**, D. I., Psyllaki, P. and Alexopoulos, N., (2000), "Tribological Behaviour of Plasma-Sprayed Al_2O_3 Coatings Under Severe Wear Conditions," Wear, Vol. 237, pp.197-204.

156. **Peterson**, B., Rishel, D. M., Birks, N. and Pettit, F. S., (1995), "The Development of Surface Features on Nickel during Erosion-Corrosion," Wear, Vol.186-187, pp. 56-63.

157. **Pfender**, E., (1988), "Fundamental Studies Associated with the Plasma Spray Processes," Surface and Coatings Technology, Vol.34, pp.1-14.

158. **Prakash**, S., Singh, S., Sidhu, B. S. and Madeshia, A., (2001), "Tube Failures in Coal Fired Boilers," Proc. National Seminar on Advances in Material and Processing, Nov., 9-10, IITR, Roorkee, India, pp. 245-253.

159. **Qureshi**, J., Levy, A. and Wang, B., (1986), "Characterization of Coating Processes and Coatings for Steam Turbine Blades," Proc. 13th Int. Conf. on Metallurgical Coatings, San Diego, CA, April 1986, American Institute of Physics, New York, pp. 2638-2647.

160. **Ramesh**, C.S. and Seshadri, S.K., (2003) "Tribological Characteristics of Nickel Based Composite Coatings," Wear, Vol. 255, pp. 893-902.

161. **Ramesh**, C.S., Seshadri S.K. and Iyer, J.L., (1992), "A Model for Wear Rates of Composite Coatings," Wear, Vol. 156, pp.205-209.

162. **Ramesh**, C.S., Seshadri, S.K. and Iyer, K.J.L., (1991), "A Survey of Aspects of Wear of Metals," Ind. J. of Tech., Vol. 29, pp.179-85.

163. **Rao**, D.R.K., Venkataraman, B., Asundi M. K. and Sundararajan G., (1993), "The Effect of Laser Surface Melting on the Erosion Behavior of a Low Alloy Steel," Surface and Coatings Technology, Vol.58, pp.85-92.

164. **Rao**, M., Keiser, J., Levy, A.V. and Wang, B., (1991), "Mechanical Behavior of Erosion-Corrosion Scales on Steels as Characterized by Single-Particle Impacts," Wear, Vol. 150, pp. 135-152.

165. **Restall**, J.E. and Stephenson, D.J., (1987), "High Temperature Erosion of Coated Superalloys for Gas Turbines," Material Science and Engineering, Vol. 88, pp. 273-282.

166. **Reyes**, M. and Neville, A., (2003), "Degradation mechanisms of Co-based alloy and WC metal–matrix composites for drilling tools offshore," Wear, Vol. 255, No. 7-12, pp. 1143-1156.

167. **Rickerby**, D. G. and Macmillan, N. H., (1982), "The Erosion of Aluminum by Solid Particle Impingement at Oblique Incidence," Wear, Vol. 79, No. 2, pp. 171-281.

168. **Rishel**, D.M., Pettit, F.S. and Birks, N., (1990), Proc. of Conf. on Corrosion-Erosion-Wear of Materials at Elevated Temperatures, ed. levy, A.V., NACE, Houston, TX, paper no. 16, pp.1-23.

169. **Rishel**, D.M., Pettit, F.S. and Birks, N., (1991), "Some Principal Mechanisms in the Simultaneous Erosion and Corrosion Attack of Metals at High Temperatures," Proc. of Conf. on Erosion-Corrosion-Wear of Materials at Elevated Temperatures, ed. Levy, A.V., NACE, Houston, TX, paper no. 16.

170. **Rodríguez**, J., Martin. A., Fernandez, R., and Fernandez, J.E., (2003), "An Experimental Study of The Wear Performance of NiCrBSi Thermal Spray Coatings," Wear, Vol. 255, pp. 950-955.

171. **Rogers**, P.M., Hutchings, I.M., Little, J.A. and Kara, F., (1997), "Microstructural Characterization of Surface Layers Formed on a Low Alloy Steel during Erosion-Oxidation in a Fluidized Bed," Journal of Materials Science, Vol. 32, pp. 4575-4583.

172. **Rosso**, M., Bennani, A. and Rastrelli, R., (1998), "Properties of Coated Tools for Improved Performances Properties of Coated Tools for Improved Performances," Proceedings of the International Thermal Spray Conference, Vol. 2, pp. 1007-1012.

173. **Roy**, M., Ray, K.K. and Sundararajan, G., (1998), "An Analysis of the Transition from Metal Erosion to Oxide Erosion," Wear, Vol. 217, pp.312-320.

174. **Roy**, M., Ray, K.K., and Sundararajan G., (1999), "The Influence of Erosion-Induced Roughness on the Oxidation Kinetics of Ni and Ni-20Cr Alloys," Oxidation of Metals, Vol. 51, No. 314, pp.251-272.

175. **Ruff**, A.W. and Ives, L.K., (1975), "Measurement of Solid Particle Velocity in Erosive Wear," Wear, Vol. 35, pp. 195-199.

176. **Sahoo**, M., Lui, A., Morin, G. and Sikka, V.K., (1981), "Mechanical Properties and Erosion Behaviour of Nickel Aluminide," Report MTL 89-68 (J), Canada Centre for Mineral and Energy Technology, CANMET.

177. **Sampath**, S., Jiang, X., Kulkarni, A., Matejicek, J., Gilmore, D. L. and Neiser, R. A., (2003), "Development of Process Maps for Plasma Spray: Case Study for Molybdenum," Mat. Sci. and Engg. A, Vol. 348, No. 1-2, pp. 54-66.

178. **Sampath**, S., Jiang X.Y., Matejicek, J., Prchlik, L., Kulkarni, A., and Vaidya, A., (2004), "Role of Thermal Spray Processing Method on the Microstructure, Residual Stress and Properties of Coatings: An Integrated Study of Ni-5 Wt. % Al Bond Coats," Materials Science and Engineering A, Vol. 364, pp.216-231.

179. **Shanov**, V. and Tabakoff, W., (1996), "Erosion Resistance of Coatings for Metal Protection at Elevated Temperature," Surface and Coatings Technology, Vol. 86-87, pp. 88-93.

180. **Shanov, V.**, Tabakoff, W. and Gunaraj, J. A., (1997), "Erosion Behavior of Uncoated Waspaloy and Waspaloy Coated with Titanium Carbide," Surface and Coatings Technology, Vol.94-95, pp.64-69.

181. Sheldon, G.L. and Finnie, I., (1966), "The Mechanism of Material Removal in the Erosive Cutting of Brittle Materials," Trans. ASME, 88B, pp. 393-400.

182. **Sheldon**, G.L. and Kanhere, A., (1972), "An Investigation of Impingement Erosion Using Single Particles," Wear, Vol. 21, pp.195-209.

183. **Singh**, B., (2003), "Studies on the Role of Coatings in Improving Resistance to Hot Corrosion and Degradation," Ph.D. Thesis, Dept. of Met. & Mat. Engineering, Indian Institute of Technology Roorkee, India.

184. **Sidhu**, B.S., Puri, D. and Prakash, S., (2005) "Mechanical and Metallurgical Properties of Plasma Sprayed and Laser Remelted Ni–20Cr and Stellite-6 Coatings," Journal of Materials Processing Technology, Vol. 159, pp. 347-355.

185. **Sidhu**, B.S., D. Puri, S. Prakash, (2004) "Characterisations of Plasma Sprayed and Laser Remelted NiCrAlY Bond Coats and Ni_3Al Coatings on Boiler Tube Steels," Materials Science and Engineering A368 149–158.

186. **Sidhu**, B.S., S.Prakash, (2003) "Evaluation of the corrosion behaviour of plasma-sprayed Ni_3Al coatings on steel in oxidation and molten salt environments at 900°C," Surface & Coatings Technology, Vol. 166, pp. 89-100.

187. **Sidky**, P.S., Hocking, M.G., (1999), "Review of Inorganic Coatings and Coating Processes for Reducing Wear and Corrosion," British Corrosion Journal, Vol. 34, No. 3, pp. 171-183.

188. **Simms**, N.J., Oakey, J.E., Stephenson, D.J., Smith, P.J., and Nicholls, J.R., (1995) "Erosion-Corrosion Modeling of Gas Turbine Materials for Coal-Fired Combined Cycle Power Generation," Wear, Vol. 186-187, pp. 247-255.

189. **Singh**, T. and Sundararajan, G., (1990), Erosion Behavior of 304 Stainless Steel at Elevated Temperatures," Metallurgical Transactions A (Physical Metallurgy and Materials Science), Vol. 21A, pp. 3187-3199.

190. **Singh**, H., (2005), "Hot Corrosion Studies on Plasma Spray Coatings Over Some Ni- and Fe- Based Superalloys," Studies on the Role of Coatings in Improving Resistance to Hot Corrosion and Degradation," Ph.D. Thesis, Dept. of Met. & Mat. Engineering, Indian Institute of Technology Roorkee, India.

191. **Soderberg**, S., Hogmark, S., Engman, U. and Swahn, H., (1981), "Erosion Classification of Materials Using a Centrifugal Erosion Tester," Tribology International, Vol. 14, pp. 333-343.

192. **Stachowiak**, G. W. and Batchelor A.W., "Abrasive, Erosive and Cavitation Wear," Chapter 11 from Engg. Tribology (Tribology series-2), Elsevier Science Publishers, Amsterdam, New York, 1993, pp.586.

193. **Stack**, M.M., Stott, F.H. and Wood, G.C., (1991), "Erosion-corrosion of Preoxidized Incoloy 800H in Fluidized Bed Environments: Effects of Temperature, Velocity, and Exposure Time," Mater. Sci. Tech., Vol. 7, pp.1128-37.

194. **Stack**, M.M., Stott, F.H. and Wood, G.C., (1991), "Erosion-Corrosion f Preoxidised Incoloy 800H in Fluidised Bed Environments: Effects of Temperature, Velocity, and Exposure Time," Marer. Sci. Technol., Vol. 7, pp.1128-37.

195. **Stack**, M.M., Stott, F.H. and Wood, G.C., (1992), "Effect of Pre-oxidation of Chromia and Alumina Forming Alloys on Erosion in Laboratory Simulated Fluidized Bed Conditions," Corrosion Sci., Vol. 33, pp.965-83.

196. **Staia**, M. H., Valente, T., Bartuli, C., Lewis, D. B., Constable, C. P., Roman, A., Lesage, J., Chicot, D. and Mesmacque, G., (2001B) "Part II: Tribological Performance of Cr_3C_2-25% NiCr Reactive Plasma Sprayed Coatings Deposited at Different Pressures," Surface and Coatings Technology, Vol. 146-147 pp. 563-570.

197. **Stanford**, M.K. and Jain V.K., (2001) "Friction and Wear Characteristics of Hard Coatings," Wear, Vol. 251, pp. 990-996.

198. **Steffens**, H.D. and Mack, M., Pure and App.l. Chem., (1990), "Plasma Spraying as an Advanced Tool in Surface Engineering," Vol. 62, No. 9, pp. 1801-08.

199. **Stein**, K. J., Schorr, B.S. and Marder, A.R., (1999), "Erosion of Thermal Spray MCr-Cr_3C_2 Cermet Coatings," Wear, Vol. 224, pp.153-159.

200. **Stephenson**, D.J. and Nicholls, J.R., (1995), "Modelling the Influence of Surface Oxidation on High Temperature Erosion," Wear, Vol. 186-187, No. 1, pp. 284-290

201. **Stephenson**, D.J. and Nicholls, J.R., (1990), "Role of Surface Oxides in Modifying Solid Particle Impact Damage," Mater. Sci. Technol., Vol. 6, pp. 96-99.

202. **Stephenson**, D.J. and Nicholls, J.R., (1993), "Modelling Erosive Wear" Corros. Sci., Vol. 35, pp. 1015-26.

203. **Stephenson**, D.J., (1989), "Predicting the High Temperature Erosion Behaviour of Materials Used in Gas Turbines," Corros. Sci., Vol. 29, pp. 647-656.

204. **Stephenson**, D.J., Nicholls, J.R., and Hancock, P., (1985), "Erosion of Gas Turbine Blade Materials by Solid Sea Salt," Corros. Sci., Vol. 25, pp. 1181-1192.

205. **Stephenson**, D.J., Nicholls, J.R., and Hancock, P., (1986), "Particle-Surface Interactions during the Erosion of a Gas Turbine Material (MARM002) by Pyrolytic Carbon Particles," Wear, Vol. 15- 29, pp.31-39.

206. **Stott,** F. H., (1998), "The Role of Oxidation in the Wear of Alloys," Trib. Int., Vol. 31, No. 1-3, pp. 61-71.

207. **Stott**, F.H. and Jordan, M.P., (2001), "The Effects of Load and Substrate Hardness on the Development and Maintenance of Wear-Protective Layers during Sliding at Elevated Temperatures," Source: Wear, Vol. 250-251, No. 1, pp. 391-400.

208. **Strafford**, K. N., Datta, P. K. and Googan, C. G., (1984), "Coatings and Surface Treatment for Corrosion and Wear Resistance," Institution of Corros. Sci. and Techol., Birmingham, Pub. Ellis Horwood Ltd. Chichester.

209. **Stringer**, J. and Wright, LG., (1987), "Erosion/Corrosion in FBC Boilers," Proc. of a Workshop on Wastage of In-Bed Surfaces in Fluidized-Bed Combustors, EPRI, Palo Alto, CA, paper 1.1.

210. **Stringer**, J., Stallings, J.W. and Wheeldon, J.M., (1989), "Wastage in Bubbling Fluidized-Bed Combustors: An Update, in: A.M. Manaker (Ed.)," Proc. 10th Int. Conf. on Fluidized Bed Combustion, San Francisco, CA, April 30–May 3, 1989, ASME, New York, NY, pp. 857–862.

211. **Stringer**, J., (1995), "Practical Experience With Wastage at Elevated Temperatures in Coal Combustion Systems Source: Wear, Vol. 186-187, No. 1, pp. 11-27.

212. **Stringer**, J., (1998), "Coatings in the Electricity Supply Industry: Past, Present and Opportunities for the Future," Surface and Coatings Technology, Vol. 108-109, pp. 1-9.

213. **Stroosnijder**, M. F., Mevrel, R. and Bennett, M. J., (1994), "The Interaction of Surface Engineering and High Temperature Corrosion Protection," Materials at High Temperature, Vol.12, No. 1, pp.53-66.

214. **Suckling**, M. and Allen C., (1995) "The Design of An AppAratus to Test Wear of Boiler Tubes," Wear 186-187, pp.266-272.

215. **Sundararajan**, G. and Roy, M., (1997), "Solid Particle Erosion Behavior of Metallic Materials at Room and Elevated Temperatures," Tribology International, Vol.30, No. 5, pp.339-359.

216. **Sundararajan**, G., (1991), "An Analysis of the Erosion-Oxidation Interaction Mechanisms," Wear, Vol.145, pp.251-282.

217. **Sundararajan**, G. and Shewmon, P.G., (1983), "A New Model For The Erosion of Metals at Normal Incidence," Wear, Vol. 84, pp. 237-58.

218. **Sundararajan**, G., (1983), "An Analysis of the Localization of Deformation and Weight Loss during Single-Particle Normal Impact," Wear, Vol. 84, pp. 217-35.

219. **Sundararajan**, G., (1984), "The Effect of Temperature on Solid Particle Erosion," Wear, Vol. 98, pp. 141-149.

220. **Sundararajan**, T., Kuroda, S., Itagaki, T. and Abe F., (2003), "Steam Oxidation Resistance of Ni-Cr Thermal Spray Coatings on 9Cr-1Mo Steel. Part 2: 50Ni-50Cr," ISIJ Int., Vol. 43, No.1, pp. 104-111.

221. **Tabakoff**, W., (1999A) "Erosion Resistance of Superalloys and Different Coatings Exposesd to Particulate Flows at High Temperature," Surface and Coatings Technology, Vol.120-121, pp.542-547.

222. **Tabakoff**, W., (1999B) "Protection of Coated Superalloys from Erosion in Turbomachinery and other Systems Exposed to Particulate Flows," Wear, Vol.233-235, pp.200-208.

223. **Tabakoff**, W., (1992), "High-Temperature Erosion Resistance of Coatings for Use in Gas Turbine Engines," Surface and Coatings Technology, Vol.52, pp.65-79.

224. **Tabakoff**, W., "High-Temperature Erosion Resistance of Coatings for Use in Turbomachinery," Wear, 1995, Vol.186-187, pp.224-229.

225. **Tabakoff**, W., Shanov, V., (1995), "Erosion Rate Testing at High Temperature for Turbomachinery Use," Surface and Coatings Technology, Vol.76-77, pp.75-80.

226. **Takeda**, K., Ito, M., Takeuchi, S., Sudo, K., Koga, M. and Kazama, K., (1993), "Erosion Resistant Coating by Low Pressure Plasma Spraying," ISIJ International, Vol.33, No.9, pp.976-981.

227. **Tiainen**, T., Siitonen, P. and Kettunen, P., (1987), "Laboratory and full scale Testing of Candidate Materials for Fluidized Bed Combustors," EPRI Workshop Proc. Wastage of In-bed Surfaces in Fluidized Bed Combustors, Argonne, IL, Paper 20.

228. **Tilly**, G.P., (1973), "A Two Stage Mechanism of Ductile Erosion," Wear, Vol. 23, pp.87-96.

229. **Toma,** D., Brandl, W. and Koester, U., (1999), "Studies on the Transient Stage of Oxidation of VPS and HVOF Sprayed MCrAlY Coatings," Surf. Coat. Technol., Vol. 120-121, pp. 8-15.

230. **Tsutsumi**, K., Tatebayashi, J., Hasegawa, K., Takamori, M., Okada, Y. and Furubayashi, K., (1988), "Development of Erosion-Resistant in-Bed Tubes," unpublished work, Kawasaki Heavy Industries Ltd., Akashi, Japan.

231. **Tucker**, R.C., Jr., (1994), "Advanced Thermal Spray Deposition Techniques, in: R.F. Bunshah (Ed.)," Handbook of Deposition Technologies for Films & Coatings, Chapter 11, William Andrew Publ./Noyes, pp., 617-668.

232. **Vardelle,** M., Vardelle, A., Li, K.I. and Fauchais, P., (1996), "Coating generation: Vaporization of particles in plasma spraying and splat formation," Pure and Applied Chemistry, Vol. 68, No. 5, pp. 1093.

233. **Walsh**, P. and Tabakoff, W, (1990), "Comparative Erosion Resistance of Coatings Intended for Steam Turbine Components," ed. Bellanca, C. (Warrendale, P.A.: ASME), Advances in Steam Turbine Technology for Power Generation, Vol.10, pp.1-8.

234. **Wang**, B.Q. and Luer K., (1994), "Erosion-oxidation Behavior of HVOF Cr_3C_2-NiCr Cermet Coating," Wear, Vol. 174, No.1-2, pp. 177-185.

235. **Wang**, Y., Chen, W. and Wang, L., (2003), "Micro-indentation and Erosion Properties of Thermal Sprayed NiAl Intermetallic-based Alloy Coatings," Wear, Vol.254, pp.350-355.

236. **Wang**, F., Lou, H., Bai, L. and Wu, W., (1989), "Hot Corrosion of Yttrium-Modified Aluminide Coatings," Mater. Sci. Eng. A-Struct., Vol. 121, pp. 387-389.

237. **Wang**, B.Q., (1995), "Erosion-Corrosion of Coatings by Biomass-Fired Boiler Fly Ash, Wear, Vol. 188, pp.40-48.

238. **Wang**, B., (1996), "Erosion-Corrosion of Thermal Sprayed Coatings in FBC Boilers," Wear, Vol. 199, No. 1, pp. 24-32.

239. **Wang**, H.M., Wang, C.M., Cai, L.X., (2003), "Wear and Corrosion Resistance of Laser Clad Ni_2Si/Nisi Composite Coatings," Surface and Coatings Technology, Vol. 168, pp.202-208.

240. **Wells**, J.J., Wigley, F., Foster, D.J., Livingston, W.R., Gibb, W.H. and Williamson, J., (2005), "The Nature of Mineral Matter in a Coal and the Effects on Erosive and Abrasive Behaviour," Fuel Processing Technology, Vol. 86, No. 5, pp. 535-550.

241. **Wensink**, H. and Elwenspoek, M.C., (2002), "A Closer Look at the Ductile-Brittle Transition in Solid Particle Erosion," Wear, Vol. 253, No. 9-10, pp. 1035-1043.

242. **Westergard**, R., Erickson, L.C., Axen, N., Hawthorne, H.M., and Hogmark, S., (1998), "The Erosion and Abrasion Characteristics of Alumina Coatings Plasma Sprayed Under Different Spraying Conditions," Tribology International, Vol.31, No. 5, pp. 271-279.

243. **Westergard**, R., Axen, N., Wiklund, U. and Hogmark, S., (2000), "An Evaluation of Plasma Sprayed Ceramic Coatings by Erosion, Abrasion and Bend Testing," Wear, Vol.246, pp.12-19.

244. **Wielage**, B., Hofmann, U., Steinhauser, S. and Zimmermann, G., (1998), "Improving Wear and Corrosion Resistance of Thermal Sprayed Coatings," Surface Engineering, Vol. 14, No. 2, pp. 136-138.

245. **Winter**, R.E. and Hutchings, I.M., (1974), "Solid Particle Erosion Studies Using Single Angular Particles," Wear, Vol.29, pp.181-194.

246. **Winter**, R.E. and Hutchings, I.M., (1975), "The Role of Adiabatic Shear in Solid Particle Erosion," Wear, Vol.34, pp.141-148.

247. **Wood**, R.J.K. and Wheeler D., (1998), "Design and Performance of a High Velocity Air-Sand Jet Impingement Erosion Facility," Wear, Vol. 220, pp. 95-112.

248. **Wood**, R.J.K., (1999), "The Sand Erosion Performance of Coatings," Materials and Design, Vol.20, pp.179-191.

249. **Wood**, R.J.K., Mellor, B.G. and Binfield, M.L., (1997), "Sand Erosion Performance of Detonation Gun Applied Tungsten Carbide/Cobalt-Chromium Coatings," Wear, Vol. 211, pp. 70-83.

250. **Wright**, I.G., Nagarajan, V., and Stringer, J., (1986), "Observations on the Role of Oxide Scales in High-Temperature Erosion-Corrosion of Alloys," Oxidation of Metals, Vol. 25, pp.175-199.

251. **Wright**, I.G., Sethi, V.K. and Nagarajan, V., (1990), "An Approach to Describing the Simultaneous Erosion and High-Temperature Oxidation of Alloys," ASME paper 90-GT-361.

252. **Wright**, I.G., Sethi, V.K. and Nagarajan, V., (1991), J. Eng Gas Turbines Power, Trans. ASME, Vol. 113, pp. 616-620.

253. **Wright**, I.G., Sethi, V.K., and Markworth, A.J., (1995), "A Generalized Description of the Simultaneous Processes of Scale Growth by High-Temperature Oxidation and Removal by Erosive Impact," Wear, Vol. 186-187, pp. 230-37.

254. **Wu**, Y.N., Zhang, G., Feng, Z.C., Zhang, B.C., Liang, Y. and Liu, F.J., (2001), "Oxidation Behavior of Laser Remelted Plasma Sprayed NiCrAlY and NiCrAlY-Al_2O_3 Coatings," Surface and Coatings Technology, Vol. 138, pp. 56-60.

255. **Wu**, X., Weng, D., Chen, Z. and Xu, L., (2001), "Effects of Plasma-Sprayed NiCrAl/ZrO_2 Intermediate on the Combination Ability of Coatings," Surf. Coat. Technol.,Vol. 140, pp. 231-237.

256. **Yamada**, K., Tomono, Y., Morimoto, J., Sasaki, Y. and Ohmori, A., (2002), "Hot Corrosion Behavior of Boiler Tube Materials in Refuse Incineration Environment," Vacuum, Vol. 65, No. 3-4, pp. 533-40.

257. **Yoshiba**, M., (1993), "Effect of Hot Corrosion on the Mechanical Performances of Superalloys and Coating Systems," Corros. Sci., Vol. 35, No. 5-8, pp. 1115-1124.

258. **Zambelli**, G. and Levy, A.V., (1981), "Particulate Erosion of NiO Scales," Wear, Vol. 68, No. 3, pp. 305-331.

259. **Zhang**, K. and Battiston, L., (2002), "Friction and Wear Characterization of Some Cobalt- and Iron-Based Superalloys in Zinc Alloy Baths," Wear, Vol. 252, pp. 332–344.

260. **Zhang**, L., Sazonov, V., Kent, J., Dixon, T. and Novozhilov, V., (2001), "Analysis of Boiler-Tube Erosion by Technique of Acoustic Emission Part I: Mechanical Erosion," Wear, Vol. 250-251, pp. 762-769.

261. **Zhang**, T. and Li, D.Y., (2000), "Beneficial Effect of Oxygen-Active Elements on the Resistance of Aluminide Coatings to Corrosive Erosion and Dry Erosion," Surface and Coatings Technology, Vol. 130, No. 1, pp. 57-63.

262. **Zhang**, X. S., Clyne, T. W. and Hutchings, I. M., (1997), "Relationship Between Microstructure and Erosive Wear Resistance of Plasma Sprayed Alumina Coatings," Surface Engg., Vol. 13, No. 5, pp. 393-401.

263. **Zhang**, Y., Cheng, Y.B., Lathabai, S., (2000), "Erosion of Alumina Ceramics by Air- and Water-Suspended Garnet Particles," Wear, Vol. 240, pp.40-51.

264. **Zhao**, S., Xie, X. and Smith, G.D., (2004), "The Oxidation Behaviour of the New Nickel-Based Superalloy Inconel 740 with and without Na_2SO_4 Deposit," Surf. Coat. Technol., Vol. 185, pp. 178-183.